

CORRECTED VERSION

(19) World Intellectual Property
Organization
International Bureau



(43) International Publication Date
17 July 2003 (17.07.2003)

PCT

(10) International Publication Number
WO 2003/058307 A3

(51) International Patent Classification⁷: G02B 6/13

(21) International Application Number:
PCT/US2002/041592

(22) International Filing Date:
27 December 2002 (27.12.2002)

(25) Filing Language: English

(26) Publication Language: English

(30) Priority Data:
10/032,702 28 December 2001 (28.12.2001) US

(63) Related by continuation (CON) or continuation-in-part (CIP) to earlier application:
US 10/032,702 (CIP)
Filed on 28 December 2001 (28.12.2001)

(71) Applicant (for all designated States except US): XTAL-
LIGHT, INC. [US/US]; 83 Nehoiden Road, Newton, MA
02468 (US).

(72) Inventors; and

(75) Inventors/Applicants (for US only): SALERNO, Jack,

P. [US/US]; 83 Nehoiden Road, Newton, MA 02468 (US).
JIN, Guanghai [CN/US]; 49 Prescott Road, Boxborough,
MA 01719 (US). BRADY, David, J. [US/US]; 2801 Dog-
woodt, Durham, NC 27705 (US). DOUGHTY, Christo-
pher [US/US]; 251 Granville Lane, North Andover, MA
01845 (US).

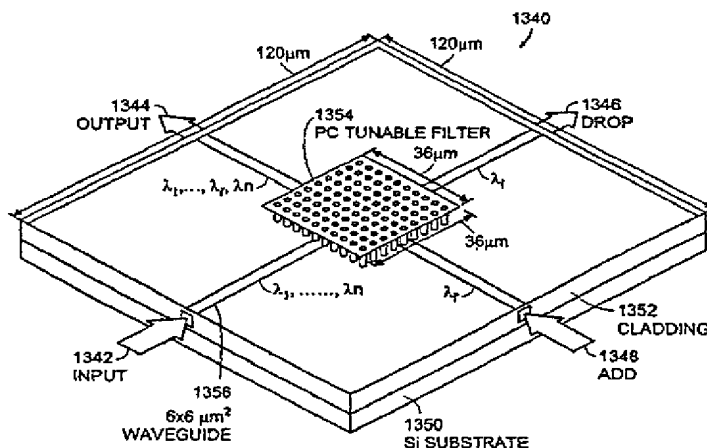
(74) Agents: HOOVER, Thomas, O. et al.; Bowditch &
Dewey, LLP, 161 Worcester Road, P.O. Box 9320, Fram-
ingham, MA 01701-9320 (US).

(81) Designated States (national): AE, AG, AL, AM, AT, AU,
AZ, BA, BB, BG, BR, BY, BZ, CA, CH, CN, CO, CR, CU,
CZ, DE, DK, DM, DZ, EC, EE, ES, FI, GB, GD, GE, GH,
GM, HR, HU, ID, IL, IN, IS, JP, KE, KG, KP, KR, KZ, LC,
LK, LR, LS, LT, LU, LV, MA, MD, MG, MK, MN, MW,
MX, MZ, NO, NZ, OM, PH, PL, PT, RO, RU, SC, SD, SE,
SG, SK, SL, TJ, TM, TN, TR, TT, TZ, UA, UG, US, UZ,
VC, VN, YU, ZA, ZM, ZW.

(84) Designated States (regional): ARIPO patent (GH, GM,
KE, LS, MW, MZ, SD, SL, SZ, TZ, UG, ZM, ZW),
Eurasian patent (AM, AZ, BY, KG, KZ, MD, RU, TJ, TM),
European patent (AT, BE, BG, CH, CY, CZ, DE, DK, EE,

[Continued on next page]

(54) Title: SYSTEMS AND METHODS OF MANUFACTURING INTEGRATED PHOTONIC CIRCUIT DEVICES



(57) Abstract: The systems and methods of the present invention includes the manufacturing of integrated photonic circuit devices using deposition processes such as, for example, supercritical fluid deposition (SFD). The present invention further includes the coupling of photonic crystal structures and planar waveguides to provide high performance, low-cost and scalable photonic components. Preferred embodiments of the methods in accordance with the present invention produce high quality metal, metal oxide, polymers, semiconductor and metal alloy deposits of precisely tailored composition in the form of thin films, conformal coatings on topologically complex surfaces, uniform deposits within high aspect ratio features, and both continuous and discrete deposits within microporous supports. Moreover, the absence of surface tension inherent to supercritical solutions ensures complete wetting of surfaces of varying complexities.



ES, FI, FR, GB, GR, IE, IT, LU, MC, NL, PT, SE, SI, SK,
TR), OAPI patent (BF, BJ, CF, CG, CI, CM, GA, GN, GQ,
GW, ML, MR, NE, SN, TD, TG).

(48) Date of publication of this corrected version:

8 July 2004

Published:

— with international search report

(15) Information about Correction:

see PCT Gazette No. 28/2004 of 8 July 2004, Section II

(88) Date of publication of the international search report:

21 May 2004

For two-letter codes and other abbreviations, refer to the "Guidance Notes on Codes and Abbreviations" appearing at the beginning of each regular issue of the PCT Gazette.

-1-

APPLICATION FOR A UNITED STATES PATENT

UNITED STATES PATENT AND TRADEMARK OFFICE

(B&D Docket No. 301541.3000-101)



Title: Systems and Methods of Manufacturing Integrated Photonic Circuit Devices

Inventors: Jack P. Salerno, a citizen of the United States of America and a resident of Massachusetts;
Guanghai Jin, a citizen of China and a resident of Massachusetts;
David J. Brady, a citizen of the United States of America and a resident of North Carolina
Chris Doughty, a citizen of the United States of America and a resident of Massachusetts

Assignee: Xtalight, Inc.
83 Nehoiden Road
Newton, MA 02468

CROSS REFERENCES TO RELATED APPLICATIONS

The present application is a continuation-in-part of co-pending U.S. Patent Application Serial No. 10/032,702, filed December 28, 2001. The entire contents of the application is incorporated herein by reference in its entirety.

5 BACKGROUND OF THE INVENTION

Photonic crystals including, for example, low loss periodic dielectrics allow the propagation of electromagnetic energy, for example, light, to be controlled in otherwise difficult or impossible ways. They are of great interest in the field of electromagnetics because certain types of photonic crystals exhibit a photonic band
10 gap or stop band. The band gap defines a range of frequencies at which electromagnetic radiation striking the crystal is reflected by the crystal rather than being permitted to propagate through the crystal.

The typical photonic crystal is a spatially periodic structure. One well-known photonic crystal is formed of multiple elements of a dielectric material arranged in a
15 three-dimensional lattice. Other crystals exhibit two-dimensional periodicity in which elongated, for example, cylindrical, elements made of dielectric material are arranged in a two-dimensional periodic pattern with their longitudinal axes parallel to each other. In these crystals, the dimensions of the lattice structures and the dielectric elements are selected to produce band gaps having desired center
20 frequencies and bandwidths. Electromagnetic radiation at a frequency within the band gap is reflected from the structure via, for example, the Bragg reflection phenomenon.

The development of photonic crystals, structures with band gaps that prevent the propagation of light in a certain frequency range, has led to several proposals of
25 many novel devices for important applications in lasers, opto-electronics, and communications. These devices, however, require the fabrication of photonic crystals allowing confinement of light in three dimensions. Moreover, the dimensional period of the features in a structure must be on the order of microns in order to control light of wavelengths typical in opto-electronics and other
30 applications.

The market for optical networking components is one of the fastest growing segments of the data and telecommunications equipment and infrastructure industry. However, as recent market conditions have illustrated, most optical component manufacturers cannot scale manufacturing costs to meet industry demands due to the inherent limitations of the hand-assembly methods employed for their predominantly hybrid-component product lines. Moreover, even if these component suppliers introduce automated assembly methods, the level of cost reductions required to fuel industry growth cannot be achieved due to barriers that limit hybrid-architecture manufacturing capability. Further, component vendors who are trying to implement integrated component architectures are typically doing so with technologies that are not scalable to achieve increasingly higher levels of integration and the ensuing cost reductions. There is a need for technologies with the ability to scale, to enable photonic component and device architectures that can fuel the growth of optical networking components which provide continual reduction in functional cost.

SUMMARY OF THE INVENTION

The systems and methods of the present invention includes the manufacturing of integrated photonic circuit devices using deposition processes such as, for example, supercritical fluid deposition (SFD). The present invention further includes the coupling of photonic crystal structures and planar waveguides to provide high performance, low-cost and scalable photonic components.

Preferred embodiments of the methods in accordance with the present invention produce high quality metal, metal oxide, polymers, semiconductor and metal alloy deposits of precisely tailored composition in the form of thin films, conformal coatings on topologically complex surfaces, uniform deposits within high aspect ratio features, and both continuous and discrete deposits within microporous supports. Moreover, the absence of surface tension inherent to supercritical solutions ensures complete wetting of surfaces of varying complexities.

Preferred embodiments of these devices include optical filters, waveguides permitting tight bends with low losses, channel-drop filters, efficient LEDs, and enhanced lasing cavities.

In accordance with a preferred embodiment, a photonic crystal structure includes a substrate having a surface characteristic and at least a first material disposed over the surface characteristic. A preferred embodiment includes the first material conformally covering the surface.

5 The first material is disposed using deposition processes such as, but not limited to, supercritical fluid deposition processes. The surface characteristic can be a patterned substrate wherein the patterned substrate has submicron features. The features have an aspect ratio of between approximately five and thirty. Further, the first material can be one of at least a metal, a semiconductor, a polymer, a monomer,
10 a mixture of metals, a metal dioxide, a metal sulphide, a metal nitride, a metal phosphide, a metal fluoride, a metal carbide, a metal chloride and metal alloys.

 The photonic crystal structure of a preferred embodiment includes a silicon wafer, and/or a silicon wafer having a silicon dioxide cladding layer. In a preferred embodiment, the photonic crystal structure forms a thin film filter. In alternate
15 preferred embodiments the photonic crystal structure forms an integrated circuit.

 A preferred embodiment of the present invention is an integrated waveguide device which includes a substrate having a first refractive index characteristic, a material disposed over the substrate having a second refractive index characteristic, and forming a waveguide layer. A second material is disposed at least within the
20 first material having a third refractive index characteristic wherein the second refractive index characteristic is greater than the first and third refractive index characteristics. The integrated waveguide device further includes a cladding layer disposed over the first material. The integrated waveguide device has a waveguide layer having dimensions between approximately $4 \times 4 \mu\text{m}^2$ and $7 \times 7 \mu\text{m}^2$. The
25 integrated waveguide device of a preferred embodiment includes the second material deposited in one of a plurality of at least holes, trenches, ribs, posts and/or cylinders. In a preferred embodiment, the aspect ratio of the plurality of holes is between approximately five and thirty.

 In a preferred embodiment of the integrated waveguide device the first
30 material has at least one patterned array of submicron features wherein the second material is deposited therein.

In accordance with another aspect of the present invention, a photonic crystal filter includes an input waveguide which carries a signal having at least one frequency including at least one desired frequency, an output waveguide, and a photonic crystal resonator system coupled between the input and output waveguides.

- 5 The resonator is operable for the adjustable transfer of at least one desired frequency to the output waveguide. The photonic crystal filter is a fixed single-wavelength filter in one preferred embodiment. The photonic crystal filter is tunable for wavelength and polarization.

- In a preferred embodiment, the photonic crystal filter includes a multi-cavity
10 Fabry- Perot resonator. In the alternate, the photonic crystal filter includes a photonic crystal resonator system which is a single cavity Fabry- Perot resonator. The photonic crystal filter includes a photonic crystal resonator which has a first photonic crystal mirror and a second photonic crystal mirror, the second photonic crystal mirror is spaced from the first photonic crystal mirror to form a resonant
15 cavity. In a preferred embodiment, the first and second photonic crystal mirrors are a two-dimensional hexagonal structure. In an alternate embodiment the first and the second photonic crystal mirrors are a three-dimensional structure.

- In accordance with a preferred embodiment, the photonic crystal filter is a tunable filter wherein a change in a refractive index characteristic of the photonic
20 crystal resonator system provides for tuning of the filter. The refractive index can be controlled by using one of either thermal optics, electro-optics, magneto-optics and piezo-optics means.

- According to another aspect of the present invention, the photonic crystal filter has a photonic crystal resonator system which includes a photonic crystal that
25 is a three-dimensionally periodic dielectric structure. In an alternate embodiment, the photonic crystal filter includes a photonic crystal that is a two-dimensionally periodic dielectric structure. Further, another embodiment includes a photonic crystal resonator system having a one-dimensionally periodic photonic crystal structure.

- 30 In accordance with another aspect of the present invention, a photonic crystal wavelength router includes at least a first input waveguide, at least a first output waveguide, a chromatic dispersion compensator, at least one wavelength division

5 multiplex filter and photonic crystal reflectors. In a preferred embodiment the photonic crystal wavelength router further includes a power tap disposed therein. The photonic crystal wavelength router includes a material with tunable dielectric or absorbing properties. The photonic crystal wavelength router includes one of at least a one-dimensionally periodic photonic crystal, a two-dimensionally periodic photonic crystal or a three-dimensionally periodic photonic crystal.

10 In another preferred embodiment, a photonic crystal dynamic optical add/drop multiplexer includes a plurality of input waveguides, a plurality of output waveguides, a plurality of photonic crystal resonator systems disposed between the plurality of input waveguides and plurality of output waveguides, and a photonic crystal reflector coupled to the plurality of photonic crystal resonator systems.

15 Another aspect of the present invention includes a photonic crystal optical add/drop multiplexer having an input waveguide, at least a first output waveguide, an optical performance monitor, a photonic crystal wavelength router, and a dispersion compensation module.

20 A method of producing an integrated photonic circuit device, includes providing a substrate with a surface characteristic and a first refractive index characteristic, disposing at least a first material with a second refractive index characteristic onto the surface characteristic, wherein the second refractive index characteristic is higher than the first. The method of producing an integrated photonic circuit device further includes etching the surface characteristic of the substrate to form a plurality of features such as cavities having an aspect ratio characteristic and depositing a second material having a third refractive index characteristic in the plurality of cavities, the second refractive index characteristic being higher than the first and the third refractive index characteristic. The aspect ratio characteristic of the features is between approximately five and thirty. The method also includes disposing a cladding layer over the first material. The first material comprises, but is not limited to, amorphous silicon doped with increasing dopants. The method can also include oxidizing the first material.

30 In another preferred embodiment, a periodic three-dimensional photonic crystal structure includes a substrate having a surface characteristic, at least one thin film deposited on the surface characteristic to result in a multi-layer photonic crystal,

the multi-layer photonic crystal being adapted to have an induced variation in an index of refraction characteristic and wherein a plurality of the multi-layer photonic crystals are placed in a stack configuration. Further, a material is deposited in-situ using supercritical fluid deposition processes into interstitial gaps formed in the stack configuration. The substrate in a preferred embodiment is spherical in shape.

5 A method of fabricating an integrated photonic circuit device, includes providing a substrate having a surface characteristic and a first refractive index characteristic depositing a film over the substrate, fabricating a waveguide structure having a second refractive index characteristic, fabricating a lattice structure, and
10 providing a lattice fill having a third refractive index characteristic. The second refractive index characteristic is higher than the first and third refractive index characteristic. The film comprises an undercladding including a thermal oxide. The waveguide structure is deposited using a plasma enhanced chemical vapor deposition process. The step of fabricating a waveguide structure further comprises
15 guide mask deposition.

The foregoing and other features and advantages of the system and method of manufacturing integrated photonic circuit devices will be apparent from the following more particular description of preferred embodiments of the system and method as illustrated in the accompanying drawings in which like reference
20 characters refer to the same parts throughout the different views.

BRIEF DESCRIPTION OF THE DRAWINGS

Figure 1 illustrates a substrate coated with a prior art deposition process;
Figure 2 illustrates the results of a prior art method of sealing interstitial gaps in the substrate layer;
25 Figure 3 illustrates another prior art method of sealing interstitial gaps in the substrate layer;
Figure 4 illustrates a preferred embodiment of a substrate coated with a method of supercritical fluid deposition in accordance with a present invention;
Figure 5A illustrates preferred embodiment of a guided wave thin film filter
30 in accordance with the present invention;

Figure 5B is a cross sectional view of a patterned substrate resulting from supercritical fluid deposition nanostructure processing in accordance with a preferred embodiment of the present invention;

Figure 5C is a cross section of a planar waveguide structure in accordance
5 with a preferred embodiment of the present invention;

Figure 6 illustrates a preferred multilayer embodiment of photonic crystals in accordance with the present invention;

Figure 7 illustrates a preferred embodiment of a stack configuration of multilayer photonic crystals in accordance with the present invention;

10 Figure 8 illustrates a preferred embodiment of a stack configuration with in-situ deposition in accordance with the present invention;

Figure 9 is a diagram illustrating a preferred embodiment of an integrated planar and fiber waveguide device in accordance with the present invention;

Figure 10 illustrates a preferred embodiment of a multilayer lens device in
15 accordance with the present invention;

Figures 11A and 11B illustrate preferred embodiments of mode conversion devices in accordance with the present invention;

Figure 12 is a preferred embodiment of a device having cavities formed by skewed deposition techniques in accordance with the present invention;

20 Figures 13A-13C are preferred embodiments of devices having skewed axis elements such as, for example, a detector and source in accordance with the present invention;

Figure 14 illustrates a preferred embodiment of a wavelength division multiplexer (WDM) processing circuit in accordance with the present invention;

25 Figure 15 is a preferred embodiment of a mode-matching device in accordance with the present invention;

Figure 16 is a preferred embodiment of a method for manufacturing structured fibers in accordance with the present invention;

30 Figure 17 illustrates a preferred embodiment of a device manufactured with thick depositions on device surfaces using supercritical fluid deposition methods in accordance with the present invention;

Figures 18A through 18D illustrate a method of stacking two different media through a deposition/etch cycle in accordance with the present invention;

Figure 19 is a preferred embodiment of an integrated circuit device including partial reflectors, beam splitters and lenses in accordance with the present invention;

5 Figure 20 illustrates a Fabry- Perot cavity structure in accordance with a preferred embodiment of the present invention;

Figure 21 illustrates graphically the transmission spectra of a Fabry- Perot resonant cavity in accordance with a preferred embodiment of the present invention;

10 Figure 22 is a top view of a waveguide Fabry- Perot filter using photonic crystal mirrors in accordance with a preferred embodiment of the present invention;

Figure 23 graphically illustrates the reflectivity of a preferred embodiment photonic crystal Fabry- Perot reflector versus wavelength for both polarizations, transverse electric (TE) mode and transverse magnetic (TM) mode, optimized for C-band operation;

15 Figure 24 illustrates a sectional view of a double cavity Fabry- Perot structure in accordance with a preferred embodiment of the present invention;

Figure 25 graphically illustrates the transmission spectrum in a double cavity Fabry- Perot structure wherein the x axis is expressed in wavelength (nm) in accordance with a preferred embodiment of the present invention;

20 Figure 26 graphically illustrates the transmission spectrum in a single cavity Fabry- Perot structure wherein the x axis is expressed in wavelength (nm) in accordance with a preferred embodiment of the present invention;

Figure 27 is a graphical illustration of the transmission spectrum for full width at half maximum (FWHM) in a double cavity Fabry- Perot structure, wherein 25 the x axis is expressed as a frequency differential and 25 GHz corresponds to 0.2 nm in accordance with a preferred embodiment of the present invention;

Figure 28 graphically illustrates a transmission spectrum for FWHM in a single cavity Fabry- Perot structure wherein the x axis is expressed in frequency differential and 25 GHz corresponds to 0.2 nm, in accordance with a preferred embodiment of 30 the present invention;

Figures 29A-29C illustrate the relation between electric vectors in successive layers of double or single cavity Fabry- Perot structures, in accordance with preferred embodiments of the present invention;

Figure 30A is a sectional view of a tunable filter in accordance with a
5 preferred embodiment of the present invention;

Figure 30B is a graphical illustration of a tuning spectrum for a 25 GHz space dense wavelength division multiplexer (DWDM) by using a direct tuning method in accordance with a preferred embodiment of the present invention wherein $\lambda_c = 1550$ nm, $\Delta n = \pm 2 \times 10^{-4}$;

10 Figure 31 is a graphical illustration of the numerical comparison between a direct tuning method and a resonant tuning method to account for vernier effects in accordance with preferred embodiments of the present invention;

Figure 32 graphically illustrates the spectral plots for the refractive index (n) and the absorption coefficient (k) for copper dioxide (Cu_2O) in accordance with a
15 preferred embodiment of the present invention;

Figure 33 graphically illustrates the spectral plots for the refractive index (n) and absorption coefficient (k) for copper dioxide (CuO) in accordance with a preferred embodiment of the present invention;

Figure 34 graphically illustrates a portion of the spectral plots for the
20 refractive index (n) and absorption coefficient (k) illustrated in Figure 33, in particular for a wavelength range of 1 to 2 μm in accordance with a preferred embodiment of the present invention;

Figure 35 graphically illustrates the spectral plots for the refractive index (n) and absorption coefficients (k) for lead sulphide in accordance with a preferred
25 embodiment of the present invention;

Figure 36 graphically illustrates the spectral plots for the refractive index (n) and absorption coefficients (k) for titanium dioxide in accordance with a preferred embodiment of the present invention;

Figure 37 graphically illustrates a portion of the spectral plots for the
30 refractive index (n) and absorption coefficient (k) for the wavelength range of 1-2 μm in accordance with a preferred embodiment of the present invention;

Figure 38 graphically illustrates the spectral plots for the refractive index (n) and absorption coefficient (k) for zinc selenide (ZnSe) in a preferred embodiment of the present invention;

Figure 39 graphically illustrates a portion of the spectral plots illustrated in
5 Figure 38 for the wavelength range of 0.5 to 1.5 μm ;

Figure 40 graphically illustrates the optical properties (n and k) at 1.55 microns for different materials of interest in accordance with preferred embodiments of the present invention;

Figures 41A and 41B graphically illustrate the real and imaginary values of
10 the dielectric constants for metals such as gold, copper, silver and aluminum in accordance with preferred embodiments of the present invention;

Figure 42A is a preferred embodiment of a tunable filter in accordance with the present invention;

Figure 42B and Figure 42C are cross-sectional views of the filter illustrated in
15 Figure 42A in accordance with a preferred embodiment of the present invention;

Figure 42D is a sectional view and a view along the lines A-A in accordance with the preferred embodiment illustrated in Figure 42A;

Figures 43A and 43B illustrate a preferred embodiment of a tunable filter having two-dimensional photonic crystals and the related directions of propagation,
20 respectively, in accordance with the present invention;

Figures 44A and 44B illustrate a three-dimensional photonic crystal tunable filter along with a diagram of the direction of propagation in accordance with a preferred embodiment of the present invention;

Figures 45A and 45B illustrate a preferred embodiment of a multicavity
25 tunable filter in accordance with the present invention;

Figure 45C is a graphical plot of reflectivity versus wavelength for a mirror used in the filter described with respect to Figures 45A and 45B;

Figures 46A and 46B graphically illustrate the reflectivity in the transverse electric mode and transverse magnetic mode of tunable filter devices in accordance
30 with a preferred embodiment of the present invention;

Figure 47 is a preferred embodiment of a dual wavelength tunable filter in accordance with the present invention;

Figures 48A and 48B illustrate a preferred embodiment of an optical add/drop multiplexer device and the directions of propagation respectively in accordance with the present invention;

Figures 49A and 49B illustrate a preferred embodiment of an optical add/drop multiplexer using a three-dimensional photonic crystal tunable filter and the related spectrum respectively in accordance with the present invention;

Figure 49C is a view of a three-dimensional photonic crystal structure realized by a lithographic pattern and exemplary angle-controlling etching methods in accordance with the present invention;

Figure 49D is a cross-sectional view of elements in a three-dimensional photonic crystal structure realized by a lithographic pattern and exemplary wet-dry mixed etching technologies in accordance with a preferred embodiment of the present invention;

Figure 50 illustrates a dynamic four port optical add/drop multiplexer in accordance with a preferred embodiment of the present invention;

Figure 51 illustrates a multi-port wavelength router in accordance with a preferred embodiment of the present invention;

Figures 52A and 52B graphically illustrate the levels of cross talk in a single-cavity filter and a multi-cavity device in accordance with preferred embodiments of the present invention;

Figure 53A illustrates a multi-functional device including at least an optical add/drop multiplexer, and an optical monitor in accordance with a preferred embodiment of the present invention;

Figure 53B is a schematic view for a 2 x 2 wavelength router with a tap mirror in accordance with a preferred embodiment of the present invention;

Figure 54A illustrates a schematic of an integrated photonic crystal device having zero-radius waveguide bends in accordance with a preferred embodiment of the present invention;

Figure 54B graphically illustrates the reflectivity versus the wavelength for the photonic crystal reflectors in the device illustrated in Figure 54A.

Figure 55 is a preferred embodiment of a variable optical attenuation spectral equalizer array in accordance with the present invention;

Figure 56 is a cross-sectional view of the spectral equalizer array illustrated with respect to the preferred embodiment in accordance with the present invention in Figure 55;

Figures 57A and 57B graphically illustrate the spectrums at the input port and the output port of the preferred embodiment illustrated in Figure 55;

Figure 58 illustrates a preferred embodiment of a resonant coupled waveguide structure in accordance with the present invention;

Figure 59 illustrates a schematic view of an asymmetric Fabry- Perot cavity (Gires-Tournois etalon) in accordance with a preferred embodiment of the present invention;

Figure 60 graphically illustrates the phase of the reflection of the light beam versus wavelength at $R = 0.9$ and $d = 20 \lambda c/n$ in accordance with a preferred embodiment of the present invention;

Figure 61 graphically illustrates the group velocity dispersions (ps/GHz) in the reflected light versus wavelength for $R = 0.95$ and $R = 0.9$ in accordance with a preferred embodiment of the present invention; and

Figure 62 graphically illustrates the group velocity dispersion compensation (ps/nm) tuning in the reflected light beams versus wavelength in accordance with a preferred embodiment of the present invention.

Figure 63 graphically illustrates the photonic bandgap effect, refractive index and the C-band Bragg dimensions in accordance with the present invention.

Figure 64A is a schematic view of an integrated multiple resonant cavity compensator in accordance with a preferred embodiment of the present invention.

Figure 64B illustrates graphically the numerical results of time delay (ps) versus relative wavelength (nm) at a wavelength of $\lambda_c = 1544$ nm in a cascaded Gires-Tournois structure in accordance with a preferred embodiment of the present invention.

Figures 65A and 65B are schematic diagrams of integrated circuit functional blocks integrated in application specific circuits in accordance with preferred embodiments of the present invention;

Figures 66A and 66B are diagrams illustrating a module-on-a-chip, for example, a multiplexed ROADM Optical node application and a multi-channel

ROADM metro access application, respectively, in accordance with a preferred embodiment of the present invention.

Figure 67 graphically illustrates the spectral plots for the refractive index (n) and the absorption coefficient (k) with respect to wavelength for silicon dioxide (silica) in accordance with a preferred embodiment of the present invention.

Figures 68A and 68B is a top view and a cross-sectional view, respectively, of a one-dimensional photonic crystal in photonic lightwave circuits in accordance with a preferred embodiment of the present invention.

Figure 69 graphically illustrates the reflection spectrum of one-dimensional photonic crystals composed of silica as the waveguide material and silicon as the filling material at the normal and 10° incidences of light in accordance with a preferred embodiment of the present invention.

Figure 70 graphically illustrates the reflection spectrum of a one-dimensional photonic crystal composed of silica and oxide material ($n = 2.5$), having a period of $1.54 \mu\text{m}$ and the same value of d_1 and d_2 in accordance with a preferred embodiment of the present invention.

Figure 71 illustrates a general cascaded N-cavity of a Gires-Tournois structure in accordance with a preferred embodiment of the present invention.

Figure 72 illustrates a view of a cascaded Gires-Tournois cavity with a photonic lightwave circuit for chromatic dispersion compensation in which the input and output are separated in accordance with a preferred embodiment of the present invention.

Figures 73A-C illustrate a plurality of characteristics for a sample oxidized at 700°C , such as ellipsometric data and optical constants along with a XPS depth profile for a thermally oxidized sample in accordance with a preferred embodiment of the present invention.

Figure 73D illustrates a flowchart of a method for fabricating a three-dimensional photonic crystal structure in oxide materials based on waveguide oxidation in accordance with a preferred embodiment of the present invention.

Figures 74A-74D illustrate the methods for fabricating a three-dimensional photonic crystal structure in oxide materials in accordance with preferred embodiments of the present invention.

Figures 75A-75D illustrate a method for fabricating three-dimensional photonic crystal structures using planar etch techniques in accordance with a preferred embodiment of the present invention.

5 Figures 76A and 76B illustrate the method of fabricating a photonic crystal structure by defining the photonic crystal followed by filling of a waveguide structure in accordance with a preferred embodiment of the present invention.

Figures 77A-77D illustrate a method of manufacturing a photonic crystal waveguide device in which both the photonic crystal and waveguide are etched in one step in accordance with a preferred embodiment of the present invention.

10 Figures 78A-78F illustrate a method for manufacturing a planar waveguide device with integrated photonic crystal structures using oxidized waveguides in accordance with a preferred embodiment of the present invention.

Figures 79A-79D illustrate a method for fabricating GaAs, InP or other III-V photonic crystals embedded in silicon oxide materials in accordance with a preferred
15 embodiment of the present invention.

Figures 80A-80J illustrate cross-section views of a preferred embodiment of a photonic integrated circuit fabrication process flow in accordance with a preferred embodiment of the present invention.

20 Figure 81 is a top level flow chart of a method for fabricating a photonic crystal device in accordance with the Figures 80A-80J of the present invention.

The drawings are not necessarily to scale, emphasis instead being placed upon illustrating the principles of the invention.

DETAILED DESCRIPTION OF THE INVENTION

25 The system and methods of the present invention are directed to manufacturing integrated photonic circuit devices. Preferred embodiments of the devices in accordance with the present invention are manufactured using chemical fluid deposition processes and in particular embodiments employing supercritical fluid deposition processes.

30 Supercritical fluid deposition (SFD) is a surface wetting deposition process that applies a uniform conformal coating. SFD enables the fabrication of one-dimensional, two-dimensional and three-dimensional photonic crystal structures,

materials and devices. SFD further enables the layering of materials in directions skewed relative to the deposition surface normal. Critical photonic devices such as, for example, but not limited to, spectral filters, mode and polarization matching filters, wave formers and cavity mirrors include layered media. Conventional
5 deposition processes produce layers that fill interstitial gaps according to, for example, surface tension constraints. The conventional deposition processes struggle with having sufficient quantities of reactants and/or control of conditions under which reactions occur only on the surfaces and tend to minimize deposition layer bends. Figure 1 illustrates a substrate coated with a conventional prior art deposition
10 process. The layers 14, 16, 18, having different indices of refraction n_1 , n_2 and n_3 , respectively, are deposited over a substrate 12.

Figure 2 illustrates the results of a prior art method of sealing interstitial gaps in the substrate layer. Gaps such as gap 24, in the substrate layer 22 are sealed by prior art deposition techniques. Figure 3 illustrates another prior art method of
15 sealing interstitial gaps. The gap 36 is filled with a fluid. In contrast, the SFD process conformally coats surface bends and distortions as illustrated in Figure 4 which illustrates a preferred embodiment of a coated substrate 42 in accordance with the present invention. The coating layer 44 has a particular index of refraction and is conformally applied over the substrate.

20 Chemical, or SFD methods as described in U.S. Patent No. 5,789,027 issued on August 4, 1998 to Watkins et al., entitled "Method of Chemically Depositing Material Onto A Substrate," and in International publication WO 01/32951 A2, having an application number PCT/US00/30264 filed on November 2, 2000 by Watkins et al., entitled "Chemical Fluid Deposition for the Formation of Metal and
25 Metal Alloy Films on Patterned and Unpatterned Substrates", the entire teachings of both being incorporated herein by reference, are used in preferred embodiments of the methods of the present invention.

A method for depositing a material onto a substrate surface or into a porous solid is referred to herein as chemical fluid deposition (CFD) or SFD. CFD involves
30 dissolving a precursor of the material into a solvent under supercritical or near-supercritical conditions and exposing the substrate (or porous solid) to the solution. A reaction reagent is then mixed into the solution and the reaction reagent initiates a

chemical reaction involving the precursor, thereby depositing the material onto the substrate surface (or within the porous solid). Use of a supercritical solvent in conjunction with a reaction reagent produces high purity thin films at temperatures that are much lower than conventional Chemical Vapor Deposition (CVD)

5 temperatures.

Preferred embodiments of the present invention include a method for depositing a film of a material, for example, without limitation, a metal, mixture of metals, metal dioxide, metal sulfide, insulator, polymer or monomers which can be subsequently cross-linked to form a polymer, or semiconductor, onto the surface of a
10 substrate, for example, a silicon wafer or preprocessed silicon wafer, as containing a patterned silicon dioxide surface, by dissolving a precursor of the material into a solvent, for example, carbon dioxide, under supercritical or near-supercritical conditions to form a supercritical or near-supercritical solution; exposing the substrate to the solution under conditions at which the precursor is stable in the
15 solution; and mixing a reaction reagent, for example, hydrogen, into solution under conditions that initiate a chemical reaction involving the precursor, for example, but not limited to, a reduction, oxidation, decomposition or hydrolysis reaction, thereby depositing the material onto the surface of the substrate, while maintaining supercritical or near-supercritical conditions.

20 For example, the method for supercritical fluid deposition can be conducted so that the temperature of the substrate is maintained at no more than approximately 200° C, 225° C, 275° C or 300° C. The solvent has a reduced temperature between 0.8 and 2.0, the solvent has a density of at least 0.1 g/cm³, the solvent has a density of at least one third of its critical density, or the solvent has a critical temperature of less
25 than 150° C. In addition, preferred embodiments of the method in accordance with the present invention can be carried out so that the temperature of the substrate measured in Kelvin is less than twice the critical temperature of the solvent measured in Kelvin, or so that the temperature of the substrate measured in Kelvin divided by the average temperature of the supercritical solution measured in Kelvin is between
30 0.8 and 1.7. A preferred embodiment of the method of SFD can also be conducted such that the average temperature of the supercritical solution is different from the temperature of the substrate.

In another preferred embodiment of the present invention, a method for depositing material within a microporous or nanoporous solid substrate, includes dissolving a precursor of the material into a solvent under supercritical or near-supercritical conditions to form a supercritical or near-supercritical solution; ii) 5 exposing the solid substrate to the solution under conditions at which the precursor is stable in the solution; and iii) mixing a reaction reagent into the solution under conditions that initiate a chemical reaction involving the precursor, thereby depositing the material within the solid substrate while maintaining supercritical or near-supercritical conditions. A preferred embodiment of the method can be 10 conducted such that the temperature of the solid substrate is maintained at no more than approximately 200° C.

In another preferred embodiment of the present invention, a film of a material, for example, but without limitation, a metal, a metal dioxide, a polymer or semiconductor, on a substrate, the coated substrate itself, and microporous or 15 nanoporous solid substrates have such materials deposited on and within them.

Further, preferred embodiments include methods for depositing a material, for example, a thin film of a pure metal, a mixed metal, a metal dioxide, semiconductor, a polymer or a metal alloy, or a layer, for example, a discontinuous layer of discrete uniformly distributed clusters, onto a substrate surface or into a porous solid 20 substrate. The substrate surface can include one or more layers, which may be patterned. When patterned substrates are used, for example, having deep sub-micron, high-aspect ratio features such as, but not limited to, trenches or cylinders, SFD can provide uniform conformal coverage and uniform filling of the features.

Preferred embodiments of the present invention include a two-step process 25 that involves the deposition of a catalytic seed layer, for example, of palladium, platinum, or copper, by SFD, followed by plating, for example, electrolyses or electrolytic plating, or additional SFD, of more of the same metal or another metal or alloy. The seed layer need not be continuous, i.e., the seed layer can be made of clusters of deposited material, but the isolated catalytic seed clusters are distributed 30 uniformly in any patterns, for example, trenches or invaginations, in the surface of the substrate. The surface can be functionalized prior to deposition using coupling

agents, for example, chlorotrimethoxysilane, for example, to control the concentration and location of the seed layer deposit.

In another two-step process, a seed layer and a thin film is created simultaneously by a first thermal disproportionation step using a precursor such as copper, for example, Cu(I) followed by the addition of a reaction reagent such as H₂ to reduce the products of the disproportionation reaction in a CFD method to obtain high yield deposition of the precursor onto a substrate.

The substrate can be a patterned substrate, formed using processes such as photolithography which are used similar to one used in the microelectronics industry. The patterned substrate can have submicron features which may have an aspect ratio greater than about two. Preferably the aspect ratios are in the range of between approximately five and thirty. The material can be deposited to conformally cover the features. The features may be at angles other than an angle normal to the surface. In one embodiment, the substrate is a patterned silicon wafer and the material is palladium or a palladium alloy that conformally covers the patterned features. In another embodiment, the substrate is a patterned silicon wafer and the material is copper or a copper alloy that conformally covers or fills the patterned features.

In another aspect, a preferred embodiment of the present invention features an integrated circuit including a patterned substrate having submicron features and a film including palladium or copper conformally covering the features. The aspect ratio of the patterned features can be greater than about two and preferably in the range of 20 to 30.

As used herein, a "supercritical solution" (or solvent) is one in which the temperature and pressure of the solution (or solvent) are greater than the respective critical temperature and pressure of the solution (or solvent). A supercritical condition for a particular solution (or solvent) refers to a condition in which the temperature and pressure are both respectively greater than the critical temperature and critical pressure of the particular solution (or solvent). A "near-supercritical solution" (or solvent) is one in which the reduced temperature (actual temperature measured in Kelvin divided by the critical temperature of the solution (or solvent) measured in Kelvin) and reduced pressure (actual pressure divided by critical pressure of the solution (or solvent)) of the solution (or solvent) are both greater than

0.8 but the solution (or solvent) is not a supercritical solution. A near-supercritical condition for a particular solution (or solvent) refers to a condition in which the reduced temperature and reduced pressure are both respectively greater than 0.8 but the condition is not supercritical. Under ambient conditions, the solvent can be a gas
5 or liquid. The term solvent is also meant to include a mixture of two or more different individual solvents. The "aspect ratio" of a feature on a patterned substrate is the ratio of the depth of the feature and the width of the feature.

Preferred embodiments of the present invention include a number of advantages, including the use of process temperatures that are much lower than
10 conventional chemical vapor deposition (CVD) temperatures. A reduction in process temperature is advantageous in several respects: it aids in the control of depositions, minimizes residual stress generated by thermal cycling in multi-step device fabrication that can lead to optical artifacts, such as changing the refractive index, and/or thermal-mechanical failure, minimizes diffusion and reaction of the incipient
15 film with the substrates, renders the deposition process compatible with thermally labile substrates such as polymers, and suppresses thermally-activated side-reactions such as, for example, thermal fragmentation of precursor ligands that can lead to film contamination. Thus, the films produced by the processes and methods in accordance with preferred embodiments of the present invention are substantially
20 free of impurities.

An additional advantage of the preferred embodiments of the present invention is that they obviate the CVD requirement of precursor volatility since the processes are performed in solution. Furthermore, since the process is performed under supercritical or near-supercritical conditions, the diffusivity of precursors
25 dissolved in solution is increased relative to liquid solutions, thereby enhancing transport of precursor and reaction reagent to and decomposition products away from the incipient film. The supercritical fluid is also a good solvent for ligand-derived decomposition products, and thus facilitates removal of potential film impurities and increases the rate at which material forms on the substrate in cases where this rate is
30 limited by the desorption of precursor decomposition products. In addition, since the reactants are dissolved into solution, precise control of stoichiometry is possible.

Another advantage of the preferred embodiments of the present invention is that the supercritical solution is usually miscible with gas phase reaction reagents such as hydrogen. As a result, gas/liquid mass transfer limitations common to reactions in liquid solvents are eliminated, and so excess quantities of the reaction reagent can easily be used in the reaction forming the material.

Thus, the techniques produce high quality metal, metal dioxide, polymers, semiconductor and metal alloy deposits of precisely tailored composition in the form of thin films, conformal coatings on topologically complex surfaces, uniform deposits within high aspect ratio features, and both continuous and discrete deposits within microporous supports. Moreover, the absence of surface tension inherent to supercritical solutions ensures complete wetting of tortuous surfaces.

Using chemical fluid deposition (CFD) which may be defined as a chemical reaction of soluble precursors, desired materials can be deposited on a substrate, such as a silicon wafer, to form a high-purity (for example, better than 99%) thin film (for example, less than 5 microns). The supercritical fluid transports the precursor to the substrate surface where the reaction takes place and transports ligand-derived decomposition products away from the substrate thereby removing potential film impurities. Typically, the precursor is unreactive by itself and a reaction reagent (for example, a reducing or oxidizing agent) is mixed into the supercritical solution to initiate the reaction which forms the desired materials. The entire process takes place in solution under supercritical conditions. The process provides high-purity films at various process temperatures under 250° C, (for example, below 200° C, 150° C, 100° C, 80° C, 60° C, or 40° C), depending on the precursors, solvents, and process pressure used.

SFD can be used, for example, to deposit platinum (Pt) and palladium (Pd) films onto silicon wafers or fluoropolymer substrates. In these examples, process temperatures of as low as 80° C provide a film purity that can be better than 99%. SFD can also be used to deposit materials into mesoporous or microporous inorganic or polymer solids. Examples include the metallation of nanometer-size pores in catalyst supports such as silicalites and amorphous mesoporous aluminosilicate molecular sieves. Supercritical fluids have gas-like transport properties (for example, low viscosity and absence of surface tension) that ensure rapid penetration

of the pores. Uniform deposition throughout the pores is further facilitated by independent control of the transport (via solution) and deposition (via reaction reagent) mechanisms in SFD. By contrast, metallation of porous substrates by CVD often results in choking of the pores by rapid deposition at the pore mouth resulting
5 from high process temperatures.

A preferred embodiment of a method of the present invention includes a batch SFD run which involves the following general procedure. A single substrate and a known mass of precursor are placed in a reaction vessel (for example, a stainless steel pipe), which is sealed, purged with solvent, weighed and immersed in
10 a circulating controlled temperature bath. The vessel is then filled with solvent using a high pressure manifold. The contents of the reactor are mixed using a vortex mixer and conditions are brought to a specified temperature and pressure at which the solvent is a supercritical or near-supercritical solvent. The mass of solvent transferred into the reaction vessel is determined gravimetrically using standard
15 techniques. The vessel is maintained at this condition (at which the precursor is unreactive) for a period of time, for example, up to one hour or longer, sufficient to ensure that the precursor has completely dissolved and that the reaction vessel is in thermal equilibrium.

A reaction reagent is then transferred through a manifold connected to the
20 reaction vessel. The reaction reagent can be a gas or a liquid, or a gas, liquid, or solid dissolved in a supercritical solvent. The transfer manifold is maintained at a pressure in excess of that of the reaction vessel. The mass of reaction reagent transferred into the reaction vessel is usually in molar excess relative to the precursor. The reaction is typically carried out for at least one hour, though the reaction may be complete at
25 times much less than one hour, for example, less than 20 minutes or less than 30 seconds. The optimal length of reaction time can be determined empirically. When the reactor has cooled, the substrate is removed and can be analyzed.

A continuous SFD process is similar to the above batch method except that known concentrations of the supercritical (or near-supercritical) solution and reaction
30 reagent are taken from separate reservoirs and continuously added to a reaction vessel containing multiple substrates as supercritical solution containing precursor decomposition products or unused reactants is continuously removed from the

reaction vessel. The flow rates into and out of the reaction vessel are made equal so that the pressure within the reaction vessel remains substantially constant. The overall flow rate is optimized according to the particular reaction. Prior to introducing precursor-containing solution into the reaction vessel, the reaction vessel
5 is filled with neat solvent (which is the same as the solvent in the precursor solution) at supercritical or near-supercritical pressures and is heated to supercritical or near-supercritical temperatures. As a result, supercritical or near-supercritical conditions are maintained as the precursor-containing solution is initially added to the reaction vessel.

10 Alternate preferred embodiments include deposition processes other than SFD such as, for example, but not limited to, CVD, and/or electroplating and atomic layer deposition. Alternate embodiments may include post deposition treatments to optimize optical properties of photonic crystal devices. Such post processing treatments may include, but are not limited to, annealing, heat treatment, and
15 chemical treatment. In particular the properties such as the refractive index (n) and the absorption coefficient (k) may be optimized for the photonic materials used in the devices.

Multilayer deposition with SFD enables devices as illustrated in Figure 5A which is a preferred embodiment of a thin film filter having a waveguide in
20 accordance with the present invention. A waveguide 54 is disposed on a substrate 52. Thin films having different indices of refraction n_1 , n_2 , and n_3 are deposited on the waveguide.

Figure 5B is a cross-sectional view of a patterned substrate resulting from supercritical fluid deposition (SFD) nanostructure processing in accordance with the
25 present invention. The integrated waveguide includes photonic crystals in accordance with the present invention. The integrated device is manufactured by disposing a high refractive index material within a relatively low refractive index material. The device includes a waveguide having dimensions for maximizing fiber coupling. Fiber optic single mode propagation is maximized by using dimensions
30 such as, for example, $6 \times 6 \mu\text{m}^2$. Thus, coupling losses and propagation losses are minimized and preferably eliminated due to low transmission in transverse area. Further, the integrated devices in accordance with the present invention are

polarization independent. The fibers, and in particular, the cross-section of fibers may be aligned or coupled to the cross-section of the waveguides and attached using index matching adhesives in a preferred embodiment of the present invention. In an alternate embodiment the fibers may be coupled to the waveguides using a lens system.

The cladding 66 disposed over the substrate 65 has a low refractive index (no) and a thickness of approximately 20μ . The waveguide layer 64 has a thickness of approximately 6 microns. The second layer of cladding 68 has a thickness of approximately 2 to 4 microns. An etching process etches holes approximately in a range of 10 to 20 microns. The diameter of the holes etched is typically in the range of between approximately 0.1 to 1.5 microns, and is preferably 0.7 microns. The preferable spacing between the holes is typically 1.03 microns.

It should be noted that the simplest photonic crystal is a one-dimensional system and consists of alternating layers of material with different dielectric constants. This photonic crystal can act as a perfect mirror for light with a frequency within a sharply defined gap, and can localize light modes if there are any defects in its structure. This arrangement is used in dielectric mirrors and optical filters. A two-dimensional photonic crystal is periodic along two of its axes and homogenous along the third axis. A square lattice of dielectric columns is an example of a two-dimensional photonic crystal. For certain values of the column spacing, the crystal can have a photonic band gap in the XY plane, for example. Inside this gap, no extended states are permitted and incident light is reflected. But although the multilayer film (one-dimensional photonic crystal) only reflects light at normal incidence, this two-dimensional photonic crystal can reflect light incident from any direction in the plane. Further, a three-dimensional photonic crystal is a dielectric that is periodic along three different axes.

Conventional optical systems are limited to longitudinal designs with a well-defined optical axis or to waveguide designs in one-dimension (fiber) or two-dimensions (integrated optical). In preferred embodiments, SFD enables optical devices which combine longitudinal and waveguide components.

Figure 5C is a cross-sectional view of a planar waveguide structure. The silicon wafer 72 has disposed over it a silicon dioxide cladding 74 having a thickness

within the range of 20-40 microns. The refractive index of the cladding 74 layer is n_1 . The cladding layer 74 is blanketed with a dopant such as germanium. A material having a refractive index of n_2 which is greater than refractive index n_1 of the cladding is then patterned into the waveguide. The difference between the refractive indices in a preferred embodiment is approximately 0.002 to 0.02.

As described hereinbefore, conventional photonic crystal designs are constructed of periodic arrays of two materials, such as air and semiconductor. SFD deposition enables the generation of multilayer "photonic atoms". In an alternate embodiment, a photonic crystal configuration includes a stack of multilayer spheres formed using SFD deposition techniques. In a particular embodiment, the spheres are formed by a conventional CVD multilayer deposition process.

Figure 6 illustrates a preferred multilayer embodiment of photonic crystals in accordance with the present invention. A multilayer sphere 80 is formed by the deposition of a plurality of materials having different indices of refraction n_1 82 and n_2 84 on a substrate.

Figure 7 illustrates a preferred embodiment of a stack configuration of multilayer photonic crystals in accordance with the present invention. A stack 90 configuration includes a plurality of the multilayer spheres 92.

Figure 8 illustrates a preferred embodiment of a stack configuration 100 with in-situ deposition in accordance with the present invention. SFD deposition enables a different class of atoms combining stacking with in situ deposition as described herein. The core material 104 such as the multilayer spheres described with respect to the previous embodiments is arranged in a stack configuration. The interstitial gaps created during the stacking of the multilayer spheres are then filled with a coating 102 using SFD. The ability of SFD to internally coat a material enables three-dimensional photonic crystal growth. In one embodiment, the core material is etched out, for example, as it may be, but is not limited to, water soluble. A three-dimensional semiconductor photonic crystal is created by coating the semiconductor on a polymer bead matrix and then removing, for example, by washing the bead matrix out. Alternatively, a silica bead matrix may be used which is removed after a hydrofluoric acid etch process.

Figure 9 is a diagram illustrating a preferred embodiment of an integrated thin film component, in particular an integrated planar and fiber waveguide device 110 in accordance with the present invention. The embodiments of the present invention provide the ability to integrate longitudinal devices and materials with planar and
5 fiber waveguide devices as discussed hereinbefore. A reflector, for example, metal mirror 114 is coupled with a waveguide 112 to provide an integrated photonic circuit.

This ability to create optical elements transverse to the waveguide plane by high aspect ratio deposition enables the integration of layered devices, electro-optic modulators, metal optical elements and liquid crystal modulators with planar
10 components. Preferred embodiments of the present invention optical systems include lens and mirror based systems. It should be noted that any conventional optical system can be replicated in accordance with the present invention systems and methods in planar systems by this technology.

Figure 10 illustrates a preferred embodiment of another thin film component
15 in particular an embedded multilayer lens device in accordance with the present invention. A multilayer lens 122 is embedded in the device 124. The multilayer lens may be coated for anti-reflection. The direction of propagation of light is perpendicular to the lens surface. In preferred embodiments at least two classes of lenses are included: cylindrical lenses are created by etching and alternatively filling
20 a lens-shaped hole in a planar structure.

Figures 11A and 11B illustrate preferred embodiments of alternate thin film components, in particular mode conversion devices in accordance with the present invention. A longitudinal lens is created for mode conversion by deposition of materials on heterogeneous coupled devices. Multilayer SFD coating such as, for
25 example, of materials having different refractive indices (n_1) 152, (n_2) 154 create mode matching between the source 146 and the fiber 142.

Preferred embodiments of the present invention include SFD deposition on skewed and curved surfaces. SFD conformal coating of bulk optical components is of great interest for conventional optical applications. Figure 12 is a preferred
30 embodiment of a device 160 having cavities formed by skewed deposition techniques in accordance with the present invention. One such cavity 164 is formed by skewed deposition. Skewed surface deposition also enables new classes of devices, including

coupled cavity switches and memories. Preferred embodiments of the present invention include arbitrary three-dimensional structures for field processing. Processing is particularly strong with cavities. SFD enables compact devices to enhance both electrical non-linearities, by making gap sizes smaller and effective
5 fields bigger, and optical non-linearities by focusing fields.

Figure 13A is a preferred embodiment of a device 180 having skewed axis elements such as, for example, a detector 182 and a source 184 in accordance with the present invention. The skewed elements might be formed by stacking in accordance with a preferred embodiment of the present invention. The skewed axis
10 elements in a preferred embodiment may also be formed by projecting three dimensional structures such as holes 185 at an angle as depicted in Figure 13B. Further, by using processes such as etching, a skewed element 186 may be disposed in an integrated photonic crystal device as shown in Figure 13C. Etching methods that combine Chemical Amplifying of Resist Lines (CARL™) lithography, Inductive
15 Coupled Plasma (ICP) for dry development and high density plasma etching may be used to fabricate holes in the order of approximately 30 nm and trenches in the order of approximately 25 nm in dioxides with aspect ratios of up to 30:1 in accordance with preferred embodiments of the present invention. Such methods are described in a paper entitled "Fabrication of Sub-0.1 μm contacts with 193 nm CARL™
20 photolithography by a combination of ICP dry development and MØRI™ HDP dioxide etch," by Y.P. Song et al. as presented at The Electrochemical Society Conference, Hawaii, 1999, the entire contents of which being incorporated herein by reference.

Figure 14 illustrates a preferred embodiment of a wavelength division
25 multiplexer (WDM) processing circuit 192 in accordance with the present invention. Integrated transverse thin film filter systems enables two-dimensional WDM processing circuits. These circuits incorporate three or more port devices. The waveguide 194 is coupled to, for example, a thin film filter 196. Such devices may incorporate mode matching components into thin film filters using curved surface
30 deposition.

Figure 15 is a preferred embodiment of another integrated thin film component, in particular a mode-matching device 200 in accordance with the present

invention. Mode matching may be particularly significant in automated fiber coupling to two-dimensional circuits. In a preferred embodiment of the method of manufacturing photonic integrated circuits, mode matching may be selected to use both SFD and conventional deposition and etching processes. Skewed multilayer deposition may also be significant in optical switching by enabling both non-linear and electro-optic switching material integration and by enabling propagating field concentration in switching layers.

Figure 16 is a preferred embodiment of a method for manufacturing structured fibers 222 in accordance with systems of the present invention. Thus, SFD is used for fabrication of waveguides with "holes." Waveguides with complex transverse structures such as, for example, holes and trenches enables design of dispersion and polarization properties. SFD can be applied in fiber pulling processes to create structured fibers.

SFD can also be used to locally fill holes in a holey fiber for switch and/or laser fabrication. In a preferred embodiment, combinations of SFD and pulling create novel fibers. Further, in a particular embodiment, SFD is used to fill fiber cores after preferential core-specific etch processes.

Hereinbefore, SFD methods were discussed with respect to providing uniform thin films. Figure 17 illustrates a preferred embodiment of devices manufactured with thick depositions on surfaces using supercritical fluid deposition methods in accordance with the present invention. SFD enables thick device deposition 242 on surfaces 244 of substrates or materials. SFD fills deep into structured surfaces, enabling thick devices. Thick coatings may be particularly useful when combined with conventional etch and deposition technologies, in which case SFD is used to create three-dimensional devices and mode matching systems.

Figures 18A through 18D illustrate a method of stacking two different media through a deposition/etch cycle in accordance with a preferred embodiment of the present invention. The stacking process of two different media through a deposition/etch cycle includes etching the surface of the substrate in step 260, filling the high aspect ratio surfaces with a material having a refractive index n_1 per step 270, etching the surface and filling the gaps with a material having a second index of refraction n_2 per steps 280 and 290, respectively. SFD enable three-dimensional

device fabrication by allowing stacking, formation of cavities and heterogeneous deposition and etching.

Figure 19 is a preferred embodiment of an integrated circuit device 300 including a waveguide 316, partial reflectors 312, beam splitters 310, filters 306 and
5 lenses 308 in accordance with the present invention. SFD enables the integration of and processing of unique and heterogeneous materials. Since SFD is a low temperature process it enables device fabrication from a much wider class of materials than conventional devices. Integration of organic, metallic, semiconductor, polymeric, inorganic glass and ceramic materials is possible. Incorporation of
10 nanoparticles, liquid crystals and semiconductors into various lattices enables switch and source development. Heterogeneous devices may also be used to create a complete optical breadboard in planar circuits. The device 300 includes metal mirrors 312 and a waveguide 316 created by deep deposition channels.

Photonic circuit devices include wavelength management components and
15 extend from a fixed single-wavelength filter to a multi-channel tunable wavelength router. The core component of these devices is an optical resonator integrated into a conventional silica planar waveguide. An integrated Fabry-Perot resonator can be used to fabricate a wavelength filter. The resonator is designed to transmit the wavelength that is desired to be removed, or filtered, from the multi-channel signal.
20 The remaining wavelengths are reflected by the Fabry-Perot resonator. Moreover, the methods of fabrication in accordance with the present invention allows the fabrication of multi-cavity Fabry-Perot resonators to create flat-top optical filters. These flat top filters provide the pass-band and drop-off characteristics essential for low-cross talk wavelength selection in diverse dense WDM (DWDM) applications.

25 As discussed hereinbefore, the components in accordance with the preferred embodiments of the present invention are enabled by the precision fabrication of Fabry- Perot reflectors into a planar waveguide so that they are perpendicular to light propagation direction. This is accomplished by creating a photonic crystal within the planar waveguide using, for example, but not limited to, SFD processing. The use of
30 the photonic crystal reflector allows the photonic bandgap of the crystal to be engineered, thereby allow its reflective properties to be designed for its specific application. These devices can be tuned to operate on selected wavelengths over a

wide spectral range by inducing a small change in the refractive index of the Fabry-Perot cavity.

The components of preferred embodiments of the present invention combine the efficiency and manufacturability of planar waveguides for fiber-coupling,
5 packaging and waveguiding with the performance and functional advantages of the photonic crystal structures. Moreover, the photonic crystals in the integrated circuits of the present invention are formed only in microscopic regions along the planar waveguide structure where they offer critical functional advantage. This eases processing and maximizes circuit yield.

10 Preferred embodiments of the present invention include wavelength filter and routing devices that utilize resonant Fabry-Perot cavities for wavelength selection. The waveguide Fabry-Perot structural filter is composed of a photonic circuit and photonic crystal mirrors. As discussed hereinbelow, the Fabry-Perot resonant cavity is explained, and the operation of wavelength filters based on integrated Fabry-Perot
15 resonators is further explained. Further the implementation of Fabry-Perot resonators using photonic crystal reflectors is illustrated, and the analysis of the requirements for wavelength tunable components is presented.

The Fabry-Perot structure is an important optical device which works based on multi-path interference of a beam of light. The interference provides a resonance
20 at a particular wavelength, resulting in the transmission of light for only a very narrow band centered around the resonant wavelength. This provides a transmission output with a very sharp peak. The Fabry-Perot structure consists of two partially transmitting mirrors 322, 324 that are separated by a distance "d" to form a reflective cavity 326 between the mirrors, as illustrated in Figure 20. To understand the
25 operation of the Fabry-Perot resonator, consider that light impinges on the first mirror surface 324. From classical optics, the rays of light are partially reflected and partially transmitted from the first mirror 324 and then also partially reflected and partially transmitted from the second mirror 322. These multiple reflected and transmitted beams of light interfere with each other to define the reflection and
30 transmission spectrum of the Fabry-Perot cavity 326. Specifically, the Fabry-Perot resonant cavity is designed such that light of only a particular wavelength is passed

through the cavity, for example, transmitted, while all other wavelengths are reflected.

Classically, and for visible light wavelengths, this structure is fabricated by coating the surfaces of an optically flat glass plate of precise thickness with a gold
5 film so thin that it is semi-transparent. The properties of these mirrors are extremely important as the magnitude of both the transmission and reflection of light off the mirror surface is critical for optimum performance of the resonant cavity.

Analytically, when a plane wave is incident on the mirror at angle θ , the transmission of the cavity is given by the following formula

$$10 \quad T(\lambda) = \frac{(1-R)^2}{(1-R)^2 + 4R \sin^2(\delta/2)} \quad (1)$$

where,

$$\delta = \frac{4\pi nd}{\lambda} \cos(\theta) \quad (2)$$

In these equations, R is the reflectivity of the mirrors, n is the refractive index of the cavity material between the mirrors, and d is the separation distance between
15 the mirrors, referred to as the cavity length. This relationship shows the strong dependence of the transmission through the Fabry-Perot resonator on the reflectivity value of the mirror. Physically, the transmission and reflection intensities are the product of the complex conjugates of the superimposed wave amplitude sum. Figure 21 shows the spectral transmission characteristics 330 of a Fabry-Perot cavity for a
20 range of reflectivity values.

The transmission equation clearly shows zero transmission through the resonator if the mirror is perfectly reflecting, for example, if $R=1$. The value of the reflectivity is determined to optimize transmission and other critical attributes as follows. The width of the transmission peak, given by its full width at half-
25 maximum (FWHM) is governed by the following:

$$\delta\lambda = \frac{1-R}{R^{1/2}} \cdot \frac{\lambda^2}{2nd} \quad (3)$$

This relationship shows that increasing either the mirror reflectivity, R, or the cavity length, d, results in a smaller FWHM, or sharper spectral transmission peak.

As with any resonant structure, there are a set of resonant peaks that occur at fixed periods in the wavelength spectrum. The wavelength difference between these resonant peaks is defined as the free spectral range (FSR) and is given by the following:

$$\Delta\lambda = \frac{\lambda^2}{2nd} \quad (4)$$

This relationship illustrates that increasing the cavity length, d , moves the resonant peaks closer together. This is an important consideration for wavelength filter design. For instance, the design of a fixed wavelength filter can benefit from a short cavity length since the adjacent resonant peaks may have a large wavelength separation from the desired transmitted wavelength. Conversely, the operation of a tunable filter can benefit from a longer cavity length, where a smaller separation between transmitted peaks can be utilized to maximize the tuning range.

Over the free spectral range of the Fabry-Perot resonator, the maximum transmission can reach unity (100%), while the minimum transmission depends on the reflectivity of mirror and is given by the following:

$$T_{\min} = \frac{(1-R)^2}{(1+R)^2} \quad (5)$$

An important figure of merit for the quality of the resonator is the ratio of the maximum to minimum transmission taken over the entire free spectral range. This is termed the extinction ratio (ER) and is determined from the following equation:

$$\frac{T_{\max}}{T_{\min}} = 10 \log \left[\frac{(1+R)^2}{(1-R)^2} \right] \text{ (dB)} \quad (6)$$

and indicates, for example, that to achieve an ER of 30 dB the reflectivity R be higher than 0.95 (or 95%).

These properties show that a major consideration in the design of the Fabry-Perot resonant cavity filter is the value of the mirror reflectivity. For a filter designed around a selected cavity length, allowing selection of the desired spectral range, the mirror reflectivity must be optimized for maximum transmission (minimizing signal loss) and peak sharpness (minimizing channel cross-talk). The use of photonic

crystal reflectors allows the design and implementation of these optimized Fabry-Perot resonators for wavelength filter and routing applications.

As discussed hereinbefore, a photonic crystal is composed of the periodic distribution of different dielectric materials in a macroscopic range. When
5 considering the true quantum nature of light, this periodic structure provides a periodic "potential" to photons, resulting in a photonic bandgap. This is a direct analogy to the electronic bandgap, which results from the periodic electrical potential field created by the periodic arrangement of atoms in a semiconductor crystal. In a material having a photonic bandgap, light can only propagate in certain directions
10 and is literally excluded from occupying certain regions of the photonic crystal. Photonic crystals can be formed with periodicities in one, two or three orthogonal directions. Only the three-dimensional structure has a truly complete bandgap. However, both one and two dimensional photonic crystals can be practically utilized because of the optical confinement they offer in specific directions and they can be
15 more readily implemented with conventional optical systems.

In preferred embodiments of the present invention Fabry-Perot resonant cavity filters are formed in conventional planar waveguides by depositing an optical material into arrays of sub-micron features lithographically patterned into the waveguide in selected areas. These patterned areas, which have lateral dimensions of
20 only a few to a tenth microns, define the Fabry-Perot reflector. The deposited optical material has a significantly different refractive index than the waveguide material. This process creates a photonic crystal within the waveguide. The bandgap properties of this photonic crystal are designed to act on light propagating along the waveguide as a Fabry-Perot resonator mirror with optimized performance for the
25 specific wavelength filtering application. Two such mirrors are formed separated from each other by the precise dimensions required for the specified cavity length.

In this integrated Fabry-Perot filter configuration, light is confined for straight propagation by the waveguide geometry, in which the refractive index of guiding layer is higher than that in the cladding. This configuration is illustrated in Figure
30 22, as viewed from the top of a waveguide Fabry-Perot filter using photonic crystal mirrors in accordance with a preferred embodiment of the present invention. The

photonic crystal 354 illustrated is a two-dimensional hexagonal structure with a lattice dimension 'a'.

When used as a wavelength filter in a preferred embodiment for a DWDM application, the optical signal includes multiple wavelengths propagating along the planar waveguide and is input onto the first photonic crystal mirror 348. There is no optical loss with incidence on the photonic crystal, as the optical front simply sees a mirror. The mirrors 348, 352 are identical and are designed for an optimal reflectivity to allow resonant optical interference within the Fabry-Perot cavity 350, which is the planar waveguide media 344. When this occurs, a particular wavelength peak is transmitted through the Fabry-Perot resonator and the output signal 356 continues to propagate along the planar waveguide. The full optical signal, minus the transmitted peak spectrum, is reflected back from the Fabry-Perot resonator. Photonic crystal structures typically have a propagation loss of between approximately 1 to 10 dB per centimeter of propagation length. In a preferred embodiment Fabry-Perot structure, the optical signal transverses a length of the photonic crystal on the order of 10 microns. Therefore, in a preferred embodiment the anticipated signal loss from this Fabry-Perot cavity is less than approximately 0.1 dB, including the multi-pass resonance.

As discussed hereinbefore, the ability to design an optimal reflector with photonic crystals is enabling. This is achieved by forming a two-dimensional photonic crystal within a planar waveguide. While the two-dimensional photonic crystal structure does not provide a complete band-gap, this reflection configuration readily achieves the desired resonator mirror properties. Importantly, the photonic crystal mirror is designed to be polarization independent, working in both transverse electric (TE) and transverse magnetic (TM) modes. The simulation results in Figure 23 illustrate the design of a photonic crystal Fabry-Perot reflector optimized for C-band operation. The vertical markers 362, 364 show the C-band operating window. According to the transparent characteristics in optical glass, the transmission spectra is divided into several wavelength ranges, such as, for example, the C, L, S bands. In preferred embodiments the bands have the following ranges: C-band: 1530 nm ~ 1565 nm, L-band: 1565 nm ~ 1625 nm, and S-band: 1460 nm ~ 1530 nm.

The transmission characteristics of a single Fabry-Perot, as described hereinbefore, provide an extremely narrow transmission peak with sloping sidewalls. Due to this narrow FWHM, it is difficult to use this kind of filter in the DWDM system. A filter using multiple resonant Fabry-Perot cavities addresses the problem of a narrow transmission peak. For example, an illustration of a dual cavity Fabry-Perot structure is shown in Figure 24. The double cavity Fabry-Perot type of filter 370 is composed of two common Fabry-Perot resonators 372, 374 separated at a certain coupling distance L. In preferred embodiments the channel spacing for particular frequencies is as follows: at 100 GHz the channel spacing is 0.8 nm; at 50 GHz the channel spacing is 0.4 nm and at 25 GHz the channel spacing is 0.2 nm.

Figures 25-28 illustrate the comparisons of the transmissions at -40 dB and -3 dB extinction ratio between a double cavity and single cavity. Figures 25 and 27 illustrate the transmission spectra in a double cavity Fabry-Perot structure with the x axis expressed in wavelength (nm) and a frequency differential Δf (GHz), respectively, in accordance with preferred embodiments of the present invention. In comparison Figures 26 and 28 graphically illustrate the transmission spectra in a single cavity Fabry-Perot structure with the x axis expressed in wavelength (nm) and Δf (GHz), respectively, in accordance with preferred embodiments of the present invention. The phase difference between the cavities is determined by the distance between the cavities (denoted as d2 in Figure 24). Pass band characteristics can be simplistically viewed as the product of two slightly offset spectra. The offset of spectra is determined by the distance between the cavities.

Another form, more convenient for computation, can be obtained if the relations between the electric vectors in successive layers are expressed in terms of Fresnel coefficients. For the system of n layers shown in the Figures 29A-29C, according to the continuity at the boundary, the recurrence relation of the electric field may be written in the matrix form as the following.

$$\begin{pmatrix} E_{m-1}^+ \\ E_{m-1}^- \end{pmatrix} = \frac{1}{t_m} \begin{pmatrix} e^{i\delta_{m-1}} & r_m e^{i\delta_{m-1}} \\ r_m e^{-i\delta_{m-1}} & e^{i\delta_{m-1}} \end{pmatrix} \begin{pmatrix} E_m^+ \\ E_m^- \end{pmatrix} \quad (7)$$

The relationship between E_0 and E_{n+1} may be written as the following:

$$\begin{pmatrix} E_0^+ \\ E_0^- \end{pmatrix} = \frac{(C_1)(C_2) \dots (C_{n+1})}{t_1 t_2 \dots t_{n+1}} \begin{pmatrix} E_{n+1}^+ \\ E_{n+1}^- \end{pmatrix} \quad (8)$$

wherein

$$C_m = \begin{pmatrix} e^{i\delta_{m-1}}, r_m e^{i\delta} \\ r_m e^{-i\delta_{m-1}}, e^{i\delta_{m-1}} \end{pmatrix} \quad (9)$$

The product of the matrix is rewritten for simplicity as the following:

$$\begin{pmatrix} A, B \\ C, D \end{pmatrix} = (C_1)(C_2) \dots (C_{n+1}) \quad (10)$$

Thus the following relationship may be obtained under the reality $E_{n+1}^- = 0$

$$\begin{pmatrix} E_0^+ \\ E_0^- \end{pmatrix} = \frac{1}{t_1 t_2 \dots t_{n+1}} \begin{pmatrix} A E_{n+1}^+ \\ C E_{n+1}^+ \end{pmatrix} \quad (11)$$

Consequently, the transmission T and reflection R can be expressed as the following:

$$R = \frac{(E_0^-)(E_0^-)^*}{(E_0^+)(E_0^+)^*} = \frac{CC^*}{AA^*} \quad (12)$$

$$T = \frac{(E_{n+1}^+)(E_{n+1}^+)^*}{(E_0^+)(E_0^+)^*} = \frac{(t_1 t_2 \dots t_{n+1})(t_1 t_2 \dots t_{n+1})^*}{AA^*} \quad (13)$$

wherein r_i and t_i are the Fresnel coefficients of reflection and transmission on the i th interface, respectively, which are polarization dependent at normal incidence, as well as

$$\delta_i = \frac{2\pi n_i d_i \cos \phi_i}{\lambda} \quad (14)$$

The filter may be tuned by any effects that can change the refractive index of the cavity material, such as thermal-optics (TO), electro-optics (EO), magneto-optics (MO) and piezo-optics (PO). Figure 30A is a sectional view of a tunable filter in accordance with a preferred embodiment. The index of refraction of the cavity material 456 is adjusted by changing, for example, the current or voltage using thermal-optics or electro optics, respectively. The direct tuning process may be

accomplished over the full C-band to account for a high refractive index differential (Δn). In preferred embodiments, the C-band range of wavelengths is 1.53 to 1.57 μm while the L-band range is approximately 1.57 to 1.62 μm . A resonant tuning process to account for a vernier effect may be used in preferred embodiments wherein tuning
5 over the same range is conducted for two such Fabry-Perot resonators. In the preferred embodiment, one Fabry-Perot resonator is tuned with respect to the other to account for the vernier effect.

The tuning range of the wavelength $\Delta\lambda$ is determined by an index change Δn expressed as the following:

$$10 \quad \frac{\Delta\lambda}{\lambda} = \frac{\Delta n}{n} \quad (15)$$

For 1% wavelength tuning of $\Delta\lambda$, a 1% index change Δn can be made in a preferred embodiment. For the entire C or L band, the wavelength range $\delta\lambda$ is approximately 30 nm thus, a 2% index change is required in a preferred embodiment. In addition, for preferred embodiments of waveguide based devices, a 2% index
15 change may alter guiding mode properties. In alternative embodiments, a dual-cavity structure with a small difference in resonant frequencies with respect to each other are used. This method of a preferred embodiment results in discrete wavelength tuning or wavelength jumping, which can be matched to wavelength series in DWDM.

20 Figure 30B is a graphical illustration of a tuning spectrum for a 25 GHz space DWDM resulting from a direct tuning method in accordance with a preferred embodiment. The center wavelength λ_c is 1550 nm and the differential refractive index is approximately $\pm 2 \times 10^{-4}$.

Figure 31 graphically illustrates the numerical comparison of the direct tuning
25 method and the resonant tuning method that accounts for vernier effects. In a numerical simulation in accordance with a preferred embodiment, the resonant tuning method can be tuned to approximately 10 times the wavelength tuning ($\Delta\lambda \sim 8 \text{ nm}$) than made by the direct tuning ($\Delta\lambda \sim 0.8 \text{ nm}$).

Figures 32 through 40 graphically illustrate the spectral plots of the optical
30 properties such as, for example, the refractive index (n) and absorption coefficient (k) for several materials of interest in accordance with preferred embodiments of the

present invention. These materials include copper dioxide, both Cu_2O and CuO , lead sulphide (PbS), titanium dioxide (TiO_2), and zinc selenide (ZnSe). These varieties of materials have a refractive index that is higher than the refractive index of substrates used and are disposed in the hole structures. The transmission properties of these materials vary but are appropriate for the wavelengths used in optical circuit devices in accordance with preferred embodiments of the present invention.

Further, the metals are used to provide appropriate values of reflectivity for mirrors disposed in the devices in accordance with preferred embodiments. SFD provides an appropriate processing method to manufacture devices having mirrors or reflectors and/or resonators.

Figures 41A and 41B illustrate the dielectric constants for copper, silver, gold and aluminum in accordance with the preferred embodiments of the present invention. The real and imaginary values for the dielectric constants are illustrated, respectively. The dielectric constant relationship is given by the following:

$$\varepsilon = \varepsilon' + i\varepsilon'' = (n + ik)^2 \quad (16)$$

wherein the ε is the dielectric constant, ε' and ε'' are respectively the real and imaginary parts of dielectric constant; n is the refractive index, and k is the absorption coefficient of material.

Figure 42A is a preferred embodiment of a tunable filter 1340 in accordance with the present invention. The function of this preferred embodiment is the tuning of the transmission wavelength. The device 1340 includes an input port 1342, an output port 1346, an add port 1348, and a drop port 1346. The substrate 1350 has disposed over it a cladding layer 1352. A waveguide 1356 is formed in the cladding. Preferably the dimensions of the waveguide are $6 \times 6 \mu\text{m}^2$ to optimize fiber coupling. A photonic crystal tunable filter is coupled to the waveguide 1356. Based on the theoretical analysis of a three-dimensional photonic crystal, the filtering performance can be realized with polarization independency. This preferred embodiment realizes the same wavelength filtering both for two orthogonal polarized lights using a two-dimensional photonic crystal. However, another preferred embodiment includes a two-dimensional photonic crystal (PC) filter which has a band-gap reflector for one polarization mode while it has the filtering performance for another polarization

mode. Thus, the photonic crystal filter is configured to have the filter performance for the TE mode while having the band-gap reflection for TM mode in waveguide, or vice versa.

5 Figure 42B is a cross-sectional view of the filter 1340 illustrated in Figure 42A. The substrate layer 1362 has a low refractive index (n_0) in comparison to the refractive indices of the waveguide layer 1364, and the layer of material used to fill the structures such as holes disposed in the device.

10 Figures 42C and 42D are a cross-sectional view 1380 and a view 1400 along the line A-A, respectively, in accordance with the preferred embodiment illustrated in Figure 42A. A micro-view of the photonic crystal tunable filter 1354 illustrates a waveguide layer 1390, a cladding layer 1388 and an electrode 1386 disposed within a gap created in the cladding layer 1388 and waveguide layer. A central electrode 1382 is disposed in the gap along with an electro-optic polymer 1384.

15 Figures 43A and 43B illustrate a preferred embodiment of a tunable filter 1420 having two-dimensional photonic crystals and the related directions of propagation, respectively, in accordance with the present invention. There are two photonic crystal band-gap reflectors 1428, 1434 which reflect both TE and TM modes. The photonic crystal filter 1430 reflects approximately all wavelength TM and other TE modes while it allows wavelength λ_i in TE mode to pass through. The
20 second filter 1432 reflects approximately all wavelength TE and other TM modes while it allows wavelength λ_i in TM mode to pass through. Thus, when a group of wavelength light is injected from the input port 1422, λ_i wavelength TE mode signal passes through the filter 1430 while all TM and other TE modes are reflected. At the second filter 1432, λ_i wavelength TM mode signal passes through to combine with λ_i
25 wavelength TE mode signal while all other wavelengths of the TE and TM mode are reflected into the output port. When the passing central wavelength is tuned by some manner, using, for example, EO, MO, PO, TO effects, the tunable wavelength filter is included in the conventional photonic circuit using two-dimensional photonic crystal structures.

30 Figures 44A and 44B illustrate a three-dimensional photonic crystal tunable filter 1480 along with a diagram of the direction of propagation in accordance with a preferred embodiment of the present invention. The three-dimensional photonic

crystal tunable filter 1480 includes an input port 1482, an output port 1484, and a port 1486 to allow the propagation of desired frequencies. The tunable filter 1492 is coupled between the waveguides 1494. The desired frequency λ_i is transmitted while the unwanted frequencies are reflected toward the output port 1484 by the tunable filter 1492. The tunable filter 1492 is periodic along all three different axes. The filter 1492 has the ability to tune the frequency of a resonant mode.

Figures 45A and 45B illustrate a preferred embodiment of a multicavity tunable filter device 1520 in accordance with the present invention. The multi-cavity in particular, a three cavity filter 1522 is disposed between the waveguides 1530, 1531 that connect the input port 1526 and the output ports 1528, 1532. The photonic crystal filter 1522 includes three cavities such as cavity 1536. The photonic crystal micro-cavity contains non-linear materials. The photonic crystal microcavity is essentially a structure made of a first material having a first dielectric constant and of an electrode disposed in the center as described with respect to Figure 42C.

Figure 45C is a graphical plot of reflectivity versus wavelength for a mirror used in the filter described with respect to Figures 45A and 45B. The transmission illustrated is in the C-band.

Figures 46A and 46B graphically illustrate the reflectivity in the transverse electric (TE) mode and transverse magnetic (TM) mode of preferred embodiments of tunable filter devices in accordance with a preferred embodiment of the present invention. The reflectivity of the TE mode of a two-dimensional photonic crystal composed of a cylinder semiconductor on silica accounts for the mode whose electric field vector is normal to the direction of propagation. The TM mode, illustrated in graph 1560 illustrates low cross talk characteristics. The refractive index values for the waveguide layer and material used in the holes is as follows: $n_1 = 3.192$, $n_2 = 1.46$ with the respective dielectric constants being $\epsilon_1 = 10.2$ and $\epsilon_2 = 2.1316$.

Figure 47 is a preferred embodiment of a dual wavelength tunable filter 1580 in accordance with the present invention. The multiport wavelength router and particularly, the dual wavelength top-flat tunable filter device 1580 includes two multi-cavity tunable filters 1594, 1600 disposed between the photonic crystal waveguide such as waveguide 1598.

Figures 48A and 48B illustrate a preferred embodiment of an optical add/drop multiplexer device and the directions of propagation respectively in accordance with the present invention. The multiplexer device 1620 provides the ability of selectively dropping wavelength λ_i in an Optical Add/Drop multiplexing (OADM) system.

5 Based on the theoretical analysis of photonic crystal, the filtering performance can be realized with polarization independency. The two-dimensional photonic crystal (PC) filters 1634, 1636 have the band-gap reflector for one polarization mode while they have the filtering performance for another polarization mode. Thus, the photonic crystal filter can be made to have the filter performance for TE mode while
10 having the band-gap reflection for TM mode in waveguide, or vice versa and thus providing the wavelength selectable add/drop multiplexer.

 There are two photonic crystal band-gap reflectors 1640, 1642 which reflect both TE and TM modes. The filter 1634 reflects all wavelength TM and absorb TE modes totally while it lets wavelength λ_i in TE mode to pass through. The second
15 filter 1636 reflects all wavelength TE and absorb TM modes totally while it lets wavelength λ_i in TM mode to pass through. When multi-wavelength light is injected from the input port 1622, λ_i wavelength TE mode signal passes through the filter 1634 while all TM and other TE modes are reflected. At the second filter 1636, λ_i
20 wavelength TM mode signal passes through to combine with λ_i wavelength TE mode signal while all other wavelength TE and TM modes are reflected into the output port 1624. This preferred embodiment is also a wavelength selectable 1 x 2 switch.

 For the adding function, λ_i wavelength light is injected from the add port 1626. The TE mode passes through the filter 1634 while the TM mode is reflected. At the second filter 1636, the TE mode is reflected while the TM mode passes
25 through. Thus, both TE and TM modes of adding wavelength λ_i join into the output port 1624. In a preferred embodiment, when the passing central wavelength is tuned, the tunable wavelength OADM is formed in the conventional photonic circuit using two-dimensional photonic crystal structures.

 Figures 49A and 49B illustrate a preferred embodiment of an optical add/drop
30 multiplexer 660 using a three-dimensional photonic crystal tunable filter 1668 and the related spectrum, respectively, in accordance with the present invention. The

principles described with respect to Figure 48A apply here with the exception that the photonic crystal is periodic along all three different axes.

Figure 49C is a view of a three-dimensional photonic crystal structure 1680 realized by a lithographic pattern and exemplary angle-controlling etching methods in
5 accordance with the present invention.

Figure 49D is a cross-sectional view 1690 of elements in a three-dimensional photonic crystal structure realized by a lithographic pattern and exemplary wet-dry mixed etching technologies in accordance with a preferred embodiment of the present invention.

10 Figure 50 illustrates a dynamic four port optical add/drop multiplexer 1700 in accordance with a preferred embodiment of the present invention. The multiplexer 1700 provides the ability to dynamically add or drop signals. The device employs a photonic crystal tunable filter which includes a resonator system disposed between waveguides such as waveguides 1708, 1718. The input port 1702 is coupled to an
15 input waveguide 1708 which carries a signal having a plurality of frequencies. The optical multiplexer is disposed between the input waveguide 1708 and the add and drop ports 1710, 1712.

Figure 51 illustrates a multi-port wavelength router in accordance with a preferred embodiment of the present invention. The multi-port dual-wavelength
20 router 1750 has a plurality of multicavity tunable filters 1758, 1772 and a photonic crystal band gap reflector 1774. Additional wavelengths are carried by waveguides 1762 and 1782 while signals are dropped by ports 1776 and 1780.

Figures 52A and 52B illustrate graphically the levels of cross talk in a single cavity filter and a multi-cavity device, respectively, in accordance with preferred
25 embodiments of the present invention. The level of cross talk in a multi-cavity filter device as illustrated in graph 1800 is lower than the level of cross talk in the graph 1810. The integrated multi-cavity filter forms a flat top filter, with low cross talk and polarization independent characteristics. In a preferred embodiment, the multi-cavity filters can be formed as circuit chips and approximately 650 circuit chips can
30 populate a square inch.

Figure 53A is a multi-functional device 1850 including an optical add/drop multiplexer, an optical performance monitor 1852, a power tap, a dispersion

compensation module 1854 and a wavelength router 1856. The output port in a preferred embodiment is a multi-output port with separate add and drop channels.

Figure 53B is a schematic illustration of a 2 x 2 wavelength router 1860 with an integrated tap. The wavelength router includes the dynamic chromatic dispersion compensator, WDM filters, and a power tap as well as the approximately 100% reflectors 1862. Several integrated taps are used to split several percentages of optical signals into the optical performance monitors.

Figure 54A is a schematic diagram of a photonic crystal device having zero-radius waveguide bends in accordance with the present invention. The device includes photonic crystal reflectors with low loss characteristics. The waveguides, such as waveguide 1890, have dimensions to enable optimal fiber coupling. For example, the waveguide dimensions are $6 \times 6 \mu\text{m}^2$. The device configuration includes a fan-in and fan-out configuration for the inputs and outputs.

Figure 54B graphically illustrates the reflectivity versus the wavelength of the photonic crystal device illustrated with respect to Figure 54A. The curves illustrate the polarization independence of the 90° photonic crystal reflectors.

Figure 55 is a preferred embodiment of a variable optical attenuation spectral equalizer array 2820 in accordance with the present invention. The spectral equalizer array 2820 makes the multi-channel optical power level flat in dense wavelength division multiplexer (DWDM) amplification. Based on the theoretical analysis of three-dimensional volume grating, the optical diffraction ratio can be dependent on the wavelength with polarization independency. The two-dimensional photonic crystal (PC) diffraction grating such as present in the tunable photonic crystals diffracts only one polarization electric field while another polarized light is transmitted through. Thus, the photonic crystal grating can be made to diffract the TE mode only in wavelength dependency, while the TM mode passes through without loss in waveguide, or vice versa.

There are several groups of photonic crystal diffraction gratings. Each group is composed of two diffraction gratings as a central wavelength λ_i and with bandwidth $\Delta\lambda_i$, one working for TE mode and another for TM mode. Diffraction of light is adjustable independently in different group of gratings, resulting in a flat power level over a desired wavelength range.

Figure 56 is a cross-sectional view 2840 of the spectral equalizer array illustrated with respect to the preferred embodiment in accordance with the present invention in Figure 55.

Figures 57A and 57B graphically illustrate the spectrums 2860, 2870 at the
5 input port and the output port of the preferred embodiment illustrated in Figure 55. The output spectrum is flattened over the desired wavelength range.

Figure 58 illustrates an alternate preferred embodiment of a resonant coupled waveguide structure 2900 in accordance with the present invention. A silicon
substrate 2906 has a cladding 2908 disposed over the substrate. A plurality of
10 photonic crystal waveguides 2910a...n are disposed in the cladding. The use of this alternative embodiment of the waveguide structure comports with the increasing interest in photonic integrated circuits (PIC's) and the increasing use of all-optical fiber networks as backbones for global communication systems which have been based in large part on the extremely wide optical transmission bandwidth provided by
15 dielectric materials. This has accordingly led to an increased demand for the practical utilization of the full optical bandwidth available. In order to increase the aggregate transmission bandwidth, it is generally preferred that the spacing of simultaneously transmitted optical data streams, or optical data channels, be closely packed to accommodate a larger number of channels, such as guides 2910a...n. In
20 other words, the difference in wavelength between two adjacent channels is preferably minimized.

This configuration 2900 accesses one channel of a wavelength division multiplexed (WDM) signal while leaving other channels undisturbed and can be used for optical communication systems. The resonant coupled waveguide structure
25 provides for channel dropping because it can potentially be used to select a single channel with a very narrow linewidth. The waveguides, for example, 2910a...n, the bus 2902 and the drops, are coupled through the waveguide structure. While WDM signals, (i.e. multi-frequency signals) propagate inside one waveguide (the bus), a single frequency-channel is transferred out of the bus and into the other waveguide
30 (the drop) either in the forward or backward propagation direction, while completely prohibiting cross talk between the bus and the drop for all other frequencies.

The performance of the resonant coupled waveguide structure may be determined by the transfer efficiency between the waveguides. Perfect efficiency corresponds to 100% transfer of the selected channel into either the forward or backward direction in the drop, with no forward transmission or backward reflection into the bus. All other channels remain unaffected by the presence of the waveguide structure.

The forward propagating wave in the bus excites a rotating mode in the waveguide structure, which in turn couple into the backward propagating mode in the drop. Ideally, at resonance, a 100% transfer can be achieved. However, radiation losses inside the waveguide structure have the effect of reducing the transfer efficiency. Furthermore, the resonant coupled waveguide structure supports multiple resonances. The photonic crystal microcavities do not suffer from intrinsic radiation losses, and can be truly single mode, and are somewhat insensitive to fabrication-related disorder.

In alternate preferred embodiments of the present invention, a Gires-Tournois etalon is an asymmetric Fabry-Perot cavity with a rear mirror reflectivity of 100 %, while the front mirror is a partially reflecting dielectric coating with $R < 100\%$. Figure 59 illustrates the asymmetric Fabry-Perot cavity in accordance with the present invention. The reflectivity of the whole stack is approximately 100%, because light cannot pass through the second mirror 3006 and the whole stack is lossless. All the electromagnetic energy is reflected provided the mirror reflectivity remains approximately 100% in the spectral regions of interest. It is an ideal configuration to have a purely phase modulation, which in preferred embodiments is used in the application of a chromatic dispersion compensation.

In this preferred embodiment of a Gires-Tournois etalon device 3000, the reflection coefficient can be written as the following:

$$r = e^{i\varphi} = \frac{-\sqrt{R} + e^{-2i\varphi}}{1 - \sqrt{R} \cdot e^{-2i\varphi}} \quad (17a)$$

where φ is given by

$$\varphi = \frac{2\pi}{\lambda} n d \cos\theta \quad (17b)$$

The phase shift upon reflection, Ψ is defined in equation (17a) and can be expressed in terms of ϕ as

$$\psi = 2 \arctg \left[\frac{1 + \sqrt{R}}{1 - \sqrt{R}} \tg \theta \right] \quad (18)$$

In the limit when the reflectivity of the front mirror vanishes ($R = 0$), this phase is reduced to 2ϕ , which can be defined simply as the round trip optical phase gained by the light beam. When the reflectivity is greater than zero ($R > 0$), the phase Ψ may be substantially increased because of the multiple reflections in the asymmetric Fabry-Perot cavity. It means that the chromatic dispersion of the cavity material can be magnified. Figure 60 shows the phase Ψ plotting versus wavelength from equation (18) in accordance with a preferred embodiment of the present invention.

This result illustrates that the chromatic dispersion is nearly zero at most wavelength ranges, except in the narrow band wavelengths that fulfill the cavity resonant conditions. This characteristic is very useful to the applications like as chromatic dispersion compensation and optical delay lines at discrete wavelengths.

In the material, components and transmission systems, the traveling time τ for a group of velocity v_g and optical path L is

$$\tau = \frac{L}{V_g}, \text{ or } \tau = L\beta' = L \frac{\partial \beta}{\partial \omega} = \frac{\partial \psi}{\partial \omega} \quad (19)$$

where β is the propagation constant and β' is the first derivative with respect to ω . The variation of traveling time τ with respect to frequency ω is

$$\frac{\partial \tau}{\partial \omega} = L\beta'' = L \frac{\partial^2 \beta}{\partial \omega^2} = \frac{\partial^2 \psi}{\partial \omega^2} \quad (20)$$

where β'' is the second derivative with respect to ω .

For a signal with a spectral width $\Delta\omega$, then the traveling time extension $\Delta\tau$ is

$$\Delta\tau = L\beta'' \Delta\omega = \frac{\partial^2 \psi}{\partial \omega^2} \Delta\omega \quad (21a)$$

or

-47-

$$\Delta\tau = -\frac{2\pi c}{\lambda^2} \frac{\partial^2 \psi}{\partial \omega^2} \Delta\lambda \quad (21b)$$

The optical pulse extension can be expressed by the Group Velocity Dispersion (GVD) coefficient α as the following:

$$\begin{aligned} \Delta\tau &= \alpha L \Delta\omega \\ \alpha &= \frac{1}{L} \frac{\partial^2 \psi}{\partial \omega^2} \end{aligned} \quad (22)$$

5 Thus, the pulse spread caused chromatic dispersion depends on ψ .

Starting from (18) equation, the second derivative (group-velocity dispersion coefficient) of the phase of light reflected from G-T etalon can be expressed as

$$\Delta\Phi = \alpha L = \frac{\partial^2 \psi}{\partial \omega^2} = -2 \left(\frac{nd}{c} \right)^2 \cdot \frac{1 + \sqrt{R}}{1 - \sqrt{R}} \cdot \frac{4\sqrt{R}(1 - \sqrt{R})^2 \sin(2\varphi)}{\left[(1 - \sqrt{R})^2 + 4\sqrt{R} \sin^2(\varphi) \right]^2} \quad (23)$$

By equation from (18) and (23), the group-velocity dispersions can be
 10 calculated for the light beams through the Gires-Tournois (G-T) etalon device in accordance with a preferred embodiment, as shown in the Figure 61, in which the front mirror reflectivities are respectively 0.95 and 0.9. The value of $d = 50 \lambda c/n$ and the center wavelength λc is 1550 nm.

The group-velocity dispersion (GVD) has a number covering a range from the
 15 negative and positive ones in the wavelength range around the cavity resonance, which can be adjusted by the fitness of the cavity according to the relation (23). These characteristics are very useful to correct the signal pulse extension caused by the chromatic dispersion. The propagation of light in a long fiber is supposed to create the extension $\Delta\tau$ of optical pulse, because of the chromatic dispersion of
 20 guiding mode and material of fiber. The extension $\Delta\tau$ is positive. The central wavelength of pulse λc is within the resonant range in G-T etalon and $\Delta\Phi_\lambda < 0$. The pulse width is compressed by $\Delta\tau' = \Delta\Phi \Delta\omega$. To achieve $\Delta\tau' + \Delta\tau = 0$, the pulse extension can be completely compensated through the Gires-Tournois etalon.

As mentioned hereinbefore, group-velocity dispersion exists only around the
 25 resonant wavelength, and the resonant wavelengths are determined by the cavity length and the refractive index of etalon materials. These characteristics provide the

way to tune the compensating wavelengths. Thus, either index or the etalon length can be used to realize the tuning functionality for the chromatic dispersion compensation. Figure 62 shows one such simulation result of tuning for GVD compensation.

5 Moreover, this kind of chromatic dispersion compensation can be achieved for a series of wavelengths at one Gires-Tournois etalon, if the etalon has the multi-resonant longitudinal modes. Supposing mode separation in wavelength is equal to the channel space in DWDM, the tunable chromatic dispersion compensation is feasible to whole channels of DWDM at one tunable Gires-Tournois etalon.

10 In a preferred embodiment, heterogeneous integration devices are formed by combining formation and etch processes, including coating interior surfaces of optical MEMs and microfluidic devices, interior surfaces of fibers and fiber bundles, and creating three-dimensional structures by cycles of etch, SFD and/or conventional deposition. Preferred embodiments include free space integrated optics, which are
15 small Micro-Electromechanical Systems (MEMs) longitudinal designs on surfaces, but which do not involve waveguides.

Table 1.0

	MEMs Technology	Photonic Crystal Technology (3-cavity)
Insertion Loss	2.5-3dB	1.5dB
Contrast ratio	40dB	40dB
Channel selectivity	50dB	60dB
Filter width @3dB	40pm	100pm
Filter width @25dB	400pm	150pm
Tuning range	45nm	45nm
Wavelength	1500-1630nm	1500-1600nm
Operating Temperature	0-70C	0-70C
Operating Humidity	5-95%	5-95%
Price (1-10)	\$5,000	\$1,000
Price (1000+)	\$3,500	\$500

Table 1.0 illustrates a comparison of photonic crystal technology and MEMs technology. Recent advances in micro-electro-mechanical systems (MEMS) have made it possible to produce compact optomechanical structures and microactuators at low-cost, using batch-processing techniques. Movable optomechanical structures, micromotors rotating at record speeds (over a million revolutions per minute), and linear microactuators with extremely high accuracy (on the order of 10 nm) are just a few examples. MEMS technology has opened up many new possibilities for optical and optoelectronic systems, including optomechanical devices that can be monolithically integrated on a single chip. Compared with macro-scale optomechanical devices, micromechanical devices are smaller, lighter, faster (higher resonant frequencies), and more rugged. Very efficient light modulators, switches, broadly tunable lasers, detectors, and filters can now be realized. This family of new devices is called micro-opto-electro-mechanical systems (MOEMS) or, simply, optical MEMS. The applications of optical MEMS include projection and head-mounted displays, optical data storage, printing, optical scanners, switches, modulators, sensors, and optoelectronic components packaging. Preferred embodiments of the present invention integrate MEMs devices and photonic crystal devices discussed hereinbefore.

MEMS technology includes both bulk and surface micro machining in bulk micromachining, precise mechanical structures created on silicon wafers by anisotropic etching. The etching rate of silicon in crystal planes is much slower than in other planes in etchants such as EDP, KOH, or TMAH. As a result, bulk micromachining can create very precise V-grooves, pyramidal pits, and cavities. These V-grooves for positioning or aligning optical fibers and micro-optics can then be coated with materials using SFD technology discussed herein.

In contrast to bulk micromachining, in preferred embodiments of the present invention, surface micromachined structures can be made entirely from thin films deposited on the surface of a wafer using SFD. Alternating layers of structural and sacrificial layers are successively grown and patterned on the substrate. Sacrificial etching, the key technology for surface micromachining, selectively removes sacrificial layers from underneath the structural layers, creating free-standing thin-

film mechanical structures. Polysilicon thin films and silicon dioxide sacrificial layers are popular surface micromachining materials because of their mechanical properties and the high selectivity of sacrificial etching. Other material combinations may be configured, for example, using aluminum structural layers and organic
5 sacrificial layers for a digital micromirror device and integrating micromirrors on silicon chips with a complementary metal dioxide-semiconductor (CMOS) transistor driving circuit for projection display application.

MEMS technology has made it possible, for the first time to integrate an entire optical table onto a single silicon chip. Optical elements such as lenses,
10 mirrors, and gratings are batch fabricated along with the XYZ stages and the microactuators. Several XYZ stages are used to align the microlenses and a tunable optical delay line to form a femtosecond optical autocorrelator. Similarly, many other optical functions can be implemented on a free space micro-optical-bench (FS-MOB) in accordance with preferred embodiments of the present invention. FS-
15 MOBs offer many advantages over conventional optical systems.

One of the most important building blocks of FS-MOB is the out-of-plane micro-optical elements. Their optical axes are parallel to the substrate so that the optical elements can be cascaded, similar to the bulk optical systems built on optical tables. Conventional micro-optics fabrication techniques can only produce in-plane
20 microlenses, that is, microlenses lying on the surface of the substrate. In MEMS FS-MOB, the surface-micro-machined microhinges can "flip up" the microlenses after they are fabricated.

The out-of-plane micro-optical elements can also be integrated with actuated translation or rotation stages for optical alignment or tuning of an optical circuit such
25 as one formed in accordance with preferred embodiments of the present invention using SFD. Instead of anchoring the optomechanical plates to the substrate, it is attached to another suspended polysilicon plate, which is free to move in the direction determined by the confinement structures.

The preferred embodiments are simulated and analyzed using simulation tools
30 such as, but not limited to, Translight, provided by the University of Glasgow, which provides the ability of theoretical modeling.

Preferred embodiments of the present invention include at least one integrated functional block such as, for example, a wavelength filter, a chromatic dispersion compensator, a signal router and a variable optical attenuator. The wavelength filter includes a fixed, tunable or hitless tunable filter. The chromatic dispersion
5 compensator provides for a plurality of magnitudes and slope matching. As discussed previously the signal router includes zero radius bends and/or taps. Thus, photonic circuits are fabricated by integrating nano-scale optical elements within conventional high-performance silica planar waveguides.

The preferred embodiments include filling silicon waveguides with silica,
10 titania, copper oxide or air. Filling the waveguides with materials other than air allows for larger features to be utilized. Silica waveguides are thin and the cladding may be air or thin silica to reduce the fill aspect ratio. The silica waveguides can have dimensions such as, for example, $4 \times 4 \mu\text{m}$ or $4.5 \times 4.5 \mu\text{m}$, without limitation.

Figure 63 graphically illustrates the photonic bandgap effect, refractive index
15 and the C-band Bragg dimensions in accordance with the present invention. In this plot the x-axis is the index of refraction of the waveguide host material. For a device fabricated in silica this index is approximately 1.46. For devices fabricated in II-V or Si material systems the index is approximately 3.5. The curve labeled
20 "lattice fill, $n = 1$ " indicates on the left-hand axis the photonic band gap parameter for a photonic crystal etched into a waveguide host as a function of the waveguide host index. In this embodiment, the fill material is air with an index of 1.0. The exact photonic bandgap depends in detail on the structure and wavelength, however it is governed by the index contrast between the two materials of the photonic
25 crystal. The parameter plotted is $n^2 - m^2/n^2$ where n and m are the indices of the two materials. At a waveguide host index of 1.0 the waveguide is homogeneous and no photonic bandgap exists. As the host index increases the potential bandgap increases and becomes large at waveguide host index values > 2.0 . As a result, most embodiments including photonic crystals have focused on material sets such as, for example, Si, GaAs, InP, with high index values and hence large photonic bandgap
30 parameters.

The curve marked "lattice fill $n = 2.7$ " is representative of the performance of a photonic crystal structure fabricated with a TiO_2 material. At a waveguide host

index of 2.7 the waveguide is again homogeneous and there is no bandgap. At a waveguide host index of 1.46 a substantial index contrast and bandgap effect exist. Thus photonic crystal structures in silica waveguides with usable properties can be fabricated in silica host materials providing that structure are comprised of mixtures
5 of silica and high index materials. Structure fabricated solely by etching of features in silica may not in general have usable photonic bandgap effects. TiO_2 is used in preferred embodiments as a representative material without any limitation. Other high index materials such as other metal oxides, for example, CuOx , HfOx , TaOx , ZrOx , or semiconductors such as, for example, Si, Ge, or SiGe alloys, and III-V (for
10 example, GaAs) II-VI (for example, InP) materials also exhibit large photonic bandgaps and are used in preferred embodiments.

Figure 63 also addresses the manufacturability of these structures. The right axis plots the representative feature size required as a function of waveguide host index. The Bragg criteria dimension is chosen at a wavelength of 1.55 μm as a
15 figure of merit. This is defined as $(\lambda)/4n$, where n is the host index. For a large host index the wavelength is reduced and the required feature size shrinks. For an index > 3.0 this parameter is at the limits of manufacturability ($< 0.1 \mu\text{m}$) with all but the most advanced methods. When the dimensional tolerance of these features is included the task becomes even more difficult. In contrast silica hosts have much
20 reduced requirements and are easily manufactured.

Figure 64A is a schematic view of an integrated multiple resonant cavity compensator 3440 in accordance with a preferred embodiment of the present invention. The compensator 3440 includes planar waveguide circuits 3452 and GT cavity 3444. The compensator is characterized as having low insertion losses and
25 low PMD.

Figure 64B graphically illustrates the time delay of the dispersion compensation (ps/nm) versus channel spacing for the multiple resonant cavity compensator in accordance with the preferred embodiment illustrated in Figure 64A. The channel spacing is approximately 50 GHz and compensation is in the order of
30 approximately 2000 ps/nm.

Figures 65A and 65B are schematic diagrams of integrated functional blocks integrated in application specific circuits in accordance with preferred embodiments

of the present invention. The application specific circuit 3480 in Figure 65A includes a dispersion compensation 3482 that may be preset, a slope compensator 3484 and a wavelength filter 3486 that is hitless. The circuit 3500 in Figure 65B includes a dispersion compensator 3502, a plurality of tap and optical (OPM) filter
5 3504, 3512, and an n-channel optical add-drop multiplexer (OADM) 3506.

Figures 66A and 66B are diagrams illustrating a module on an integrated circuit chip 3520, for example, a multiplexed ROADM Optical node application, and a multichannel ROADM metro access application, respectively, in accordance with a preferred embodiment of the present invention. The insertion loss is less than
10 approximately 2.0 dB, PDL is less than approximately 0.2 dB, PMD less than approximately 0.1 ps and tuning time less than approximately 50 ms. The module on chip includes a plurality of flat-top tunable filters with four ports, cascaded by zero-radius bend reflectors 3524.

Figure 67 graphically illustrates the spectral plots for the refractive index (n) and the absorption coefficient (k) with respect to wavelength for silicon dioxide
15 (silica) deposited using the SFD process in accordance with a preferred embodiment of the present invention. This deposition can be performed with an organic silicon precursor, Tetraethoxysilane (TEOS) precursor in a supercritical CO₂ ambient at a temperature of approximately 250 degrees C. Similar alkyoxide precursors exist for
20 many metal species. These have very similar reaction pathways for the deposition of a metal oxide film. The demonstration of fully dense SiO₂ by this pathway indicates that the full range of metal oxides can in principle be deposited via this method.

Preferred embodiments of the present invention include one-dimensional photonic crystal lattice structure, in which the bandgap effect is still available for a
25 certain wavelength range and a relative small incidence angle (< 20 degrees). Figures 68A and 68B illustrate the schema of one-dimensional photonic crystal planted in a photonic lightwave circuit (PLC). The thickness d_i of each layer in such one-dimensional photonic crystal is equal to the quarter wavelength in materials. However in another embodiment, a modification of thickness of each layer is
30 possible if the following relation is satisfied for each layer and N_i is kept to a small number in the following equation.

$$d_i = \frac{\lambda}{4n_i} + N_i \frac{\lambda}{2n_i} \quad (24)$$

where $i = 1, 2, \dots$; $N_i = 0, 1, 2, \dots$

Moreover, equal thickness of each layer is also possible when the dimensions d_1 and d_2 are close to each other using a small N_i number.

5 Figure 69 illustrates the simulation results of one-dimensional photonic crystals composed of silica (waveguide material) and silicon (filling material) at the normal and 10 degree incidences of light. Whole C and L band are entirely covered by the one-dimensional photonic crystal bandgap. The reflection spectrum is illustrated in a one-dimensional photonic crystal composed of silica and silicon
10 having a period of 1.6 μm and d_1 and d_2 being the same.

 Figure 70 graphically illustrates a reflection spectrum of a one-dimensional photonic crystal composed of silica and oxide material having a refractive index of $n=2.5$, a period of 1.54 μm and a value of same d_1 and d_2 . A large feature (0.6 ~ 0.9 μm) of one-dimensional photonic crystal is provided by using high index material
15 such as silicon, thus utilizing the materials having the indices from 2.2 to 3.5 for the one-dimensional photonic crystal having a large feature. Further, the equal size feature of the one-dimensional photonic crystal is provided when the layer's thickness is close to each other as provided by using the Equation 24. By the simulation, entire C&L bands are still covered by bandgap when the feature ratio
20 (d_1/d_2) changes from 0.9 to 1.1, which results in acceptable tolerances for fabrication.

 Waveguide cascaded or a coupled cavity all-pass filters (W-CC) based on photonic crystal mirrors can provide compact, low-loss and highly stable compensation for chromatic dispersion. Fundamentally, it is an immigration of a
25 thin film based all-pass filter implemented in a waveguide platform. The article entitled "The Realization of All-Pass Filters for Third-Order Dispersion Compensation in Ultrafast Optical Fiber Transmission Systems," Jablonski, Mark et al., Journal of Lightwave Technology, Vol. 19, No. 8, August 2001 describes coupled cavity filters, the entire teachings of which are incorporated herein by
30 reference in its entirety. Each mirror in the waveguide cascade cavity all-pass filter is composed of a group of the photonic crystal structure, wherein the reflectivity is

determined by the parameters of the photonic crystal. Figure 71 illustrates the general cascaded N-cavity of the G-T structure, while Figure 72 illustrates one preferred embodiment of the cascaded cavity filter with photonic lightwave circuit for chromatic dispersion compensation, where the input and output are separated in accordance with the present invention.

Figure 64B illustrates graphically the numerical results of a simulation about a multi-channel waveguide cascaded cavity all-pass filter for a chromatic dispersion compensation in accordance with a preferred embodiment of the present invention. The waveguide cascaded cavity filter is composed of a four-cavity G-T structure. The slope of the time delay corresponds to the chromatic dispersion compensation, approximately -2000 ps/nm. The G-T etalon is designed for 10 GHz bandwidth channels centered at a wavelength of 1544 nm and a 50 GHz channel spacing.

A preferred embodiment of the present invention includes a method of fabricating photonic crystals in oxide waveguides and filling with silicon or silicon oxide or silicon air composites without limitation. The method consists of etching holes in oxide waveguides, and filling holes with a CVD process based on, for example, silane, dichlorosilane or other silicon precursors. Chemical vapor deposition processes for highly conformal deposition are well known in the microelectronics industry for fabrication of structures in memory, power device, and micromechanical devices. The preferred embodiment described herein applies these films and processes to the area of photonic devices, in particular photonic crystal devices. Alternate methods include the fill process occurring in a highly conformal manner to leave a small void or dimple behind. The effect of this void is to modify the effective refractive index of the fill, allowing for control of the effective index variation via control of the film thickness. A further alternative includes the use of germanium in place of silicon, or Si/Ge alloys. In addition, a multilayer stack can be deposited consisting of silicon, oxide, or silicon. This structure is analogous to a dynamic random access memory (DRAM) trench capacitor. By voltage biasing of the structure the carrier density, depletion widths, and optical properties can be shifted. Another alternative preferred embodiment includes the deposition of either an amorphous or polycrystalline film depending upon the deposition conditions. Either a-Si or poly-Si may be used as the fill material and may be deposited by

chemical vapor deposition. A number of methods are known for depositing these films in electronic or micro-mechanical applications. Precursor gases can include, for example, dichlorosilanes and other silanes and chlorosilanes SiH_xCl_y , where $x = 0, 1, 2, 3, 4$ and $\text{Cl} = 0, 1, 2, 3, 4$. Chemical vapor deposition methods include

5 atmospheric pressure CVD (APCVD), low pressure CVD (LPCVD) in either hot or cold wall reactors. Alternately, plasma enhanced CVD methods may be used. Typically in APCVD and LPCVD systems, temperatures are less than $575\text{-}600^\circ\text{C}$ give amorphous material while temperatures greater than 600°C give polycrystalline material. A preferred embodiment for producing optical devices is a LPCVD

10 method operating at a pressure of approximately 0.25-1 Torr and a temperature of less than $500\text{-}550^\circ\text{C}$. For device designs in which poly silicon is desired the deposition temperature may be in the range of $600\text{-}650^\circ\text{C}$. Alternately, amorphous silicon films can be deposited at a lower deposition temperature and recrystallized in a high temperature anneal step at greater than 600°C or via laser induced

15 recrystallization or by other methods well known in the art. In order to achieve highly conformal coatings it is desirable that the growth mechanism be limited by surface reaction rate and not be transported to the growth surface. This aspect of the reaction can be enhanced through either lower growth rates, lower temperature, or use of precursors with high stability on the growth surface.

20 Filling of high aspect ratio features requires that reactants be transported into the features to be filled prior to dissociation or reaction and that by-products can be transported out of the system without interfering with transport of additional precursors into the feature. Because of these considerations it is desirable to use precursors with relatively simple and high mobility by products such as silane as

25 opposed to more complex organo-silanes.

If Ge (amorphous or poly) or SiGe alloys are desired Ge may be supplied by similar precursors such as Germane (GeH_4) or GeCl_xH_y precursors. In addition to the precursors listed herein above other halides of Ge or Si can be used as well as organic compounds. Exemplary halides, but not limited to, are listed in Sorab K.

30 Ghandi's, VLSI Fabrication Principles, 2nd edition, Wiley, NY and are incorporated herein by reference in their entirety.

-57-

Further, metallic Ti, Ta, and other transition metals can be deposited by reduction of organic or halide compounds via a thermal or plasma-enhanced route. Common precursors are Chlorides (for example, TiCl_4) or organics such as, for example, tetrakis-(dimethylamido)titanium (TDMAT). Most metallic Ti is currently
5 deposited via a plasma process at low temperature, (for example, 350-500° C) which is not purely conformal. This temperature limitation is due to the specifics of microelectronics manufacturing which do not apply here. At a temperature of 600-700° C thermal CVD of Ti from TiCl_4 can be performed with good conformality. A preferred embodiment uses a temperature of 400-700° C which is sufficient to
10 achieve a highly conformal film. In addition, Cu films and liners can be deposited from organic compounds such as $\text{Cu}(\text{hfac})$, which is well known in the integrated circuits industry. No copper chlorides exist with high volatility at low temperatures.

For all metal depositions the metal films can be used in metallic reflector structures without modification. Alternately the metal films can be oxidized in an
15 ambient of O_2 , water vapor, or other oxidizing species to produce a film of the metal oxide. This film typically undergoes a volume expansion (for example, for TiO_2 by a factor of 1.7) and hence a lined feature can be filled with via this method. The teachings in Choi et al, Bull Korean Chem Society, Vol 16, pg 701, 1995 regarding thermal oxidation are incorporated herein by reference. Similar oxidation pathways
20 will exist for other metals for oxidation to metal oxides. Figures 73A-73B illustrate data of different characteristics for a sample oxidized at 700°C. Figure 73A illustrates ellipsometric data and fits, while Figure 73B illustrates the optical constants of the film derived from the fits. The optical fits include, for example, index of refraction and extinction coefficient. Figure 73C illustrates a XPS depth
25 profile for a thermally oxidized sample, oxidized in ambient atmosphere at a temperature of 700°C for eight hours. The composition of the film is 2:1 O:Ti and is uniform through the film bulk. The interface is comprised of a SiTiO grading. The XPS depth profile is for a 1700 Å thick film on SiO_2 . The interface intermixing of Ti and Si oxides may be due to diffusion or to an artifact of the sputter depth profile
30 process.

Alternatively, isotropic etch processes can be used in a sequential fashion followed by additional sequential deposition processes to open the top of the feature

and allow for enhanced filling. Further, for metal depositions a tungsten – CVD (WCVD) process can be used. Other metals, such as, for example, Ta, Ti, Cu can be used in the alternative. W-CVD typically occurs from a WF₆ precursor via a hydrogen (H₂) or silane reduction at temperatures of 400-800°C. Alternatively, plasma enhance chemical vapor deposition (PECVD) is based on the deposition of a gaseous compound near the substrate surface can also be used. Further, thermal CVD is used in another preferred embodiment. WO_x has a relatively low index of refraction and hence is less desirable than TiO₂ or CuO.

A preferred embodiment of the present invention includes a method 3700 as illustrated in Figure 73D for fabricating a three-dimensional photonic crystal structure in oxide materials based on waveguide oxidation. The method 3700 consists of the step 3702 of depositing a polymer or other easily anisotropically and isotropically etched first material A, for example, photoresist. The method then includes the step 3704 of deposition of a waveguide layer, for example, for a structure to be later oxidized, for example, amorphous silicon doped with Ge or other index increasing dopant can be used. The next step 3706 includes the deposition of the first material A over the silicon layer. Further, the method includes the deposition of a mask, photoresist or other mask materials including, for example, hard masks and other polymers and patterning of the hard mask by methods, for example, dry etching to a feature size consistent with the smallest desired features in the final device per step 3708.

The method then includes the step 3710 of etching of the stack consisting of material A/Ge:Si/A with an anisotropic etch to produce photonic crystal structures with a diameter or width of approximately 0.5-1 μm and a pitch of 1-1.5 μm . Per step 3712, the structure is etched with a selective isotropic etch, either dry or wet, which etches either the photoresist or the waveguide layer laterally increasing the feature diameter or width in that layer. As an alternate process flow to produce a three-dimensional or quasi three-dimensional structure the feature can be etched laterally with an isotropic Si or SiGe etch (per step 3712). In an embodiment that a one or two-D structure is desired this step can be eliminated. Note that Si with other dopants or even undoped Si may be used, hence SiGe is not essential to this method. The advantage of this method is that the materials to be etched (Si or SiGe and

material A), may be much easier to etch than SiO_2 , for example, Si etching of high aspect ratio features is well established using, for example, the Bosch Process, while etching of similar high aspect ratio features in Silica have not been demonstrated yet. Material A may be chosen such that it is relatively straightforward to etch at the
5 desired feature size and tolerance. A preferred embodiment can use a polymeric material which easily etches in oxygen chemistries.

The method 3700 then includes the step 3714 of filling of the feature with a method capable of filling small voids, for example, using CVD, electroplating, or chemical fluid deposition methods, without limitation. The material of the fill can
10 be either a metal or dielectric. The next step 3716 includes the removal of the resist layer by an isotropic etch, and in a preferred embodiment, following definition of a waveguide strip structure to expose the feature sides. This results in a suspended silicon line with photonic crystal structures which extend out of the silicon line. The method then includes the step 3718 of oxidizing of the silicon line to produce a
15 guide layer which is suspended and in which is completely encased, or partially encased, a photonic crystal structure with variation along the direction parallel to the original surface normal. The method 3700 then includes the step 3720 of depositing of a cladding layer with a method capable of filling under the suspended line and of void free filling around the photonic crystal structure. Alternately, the suspended
20 line can form a waveguide without encapsulation. In this embodiment the guiding structure is clad by air ($n = 1$).

In an alternate preferred embodiment, the silicon waveguide can be replaced by an oxide waveguide on silicon. In this embodiment the etch depth must be increased because the oxidation step and growth do not occur. This requires a depth
25 of approximately 6 μm . An amorphous or poly silicon mask can be used for material A, with the silicon wafer forming material A below. In this embodiment etches which are selective to either silicon or oxide can be used if desired to laterally etch either the Si or oxide layer and form a three-D or quasi three-D structure. For selective isotropic etching of Silicon oxide to silicon, for example, hydrofluoric acid
30 (HF) or buffered HF can be used, while for selective isotropic etching of oxide to silicon, for example, sulfuric acid based, hydrazine, or ethylenediamine-based etches or others known in the art may be used. Following filling the silicon can be

isotropically etched and replaced or can be oxidized in-situ forming the cladding. These methods allow for fabrication of a three-dimensional structure with only a single mask step. Further, these methods utilize relatively simple materials and etch processes.

- 5 Another preferred embodiment includes a method of fabrication of a three-dimensional photonic crystal structure, as illustrated in Figures 75A-75D, using planar etch techniques. This method includes fabricating an "hourglass" profile, or a periodic variation in width or diameter of an etched structure. The method consists of the following steps including etching the structure to a depth h_1 , depositing a
- 10 passivating film A, etching the structure to a depth h_2 , depositing a passivating film B, and repeating the aforementioned steps to produce a structure of depth $N * (h_1 + h_2)$ where N is the number of repetitions. At various points in the etch depth the sidewall is passivated with a stack composed of layers of, for example, A/B/A/B...., with the layer immediately adjacent to the substrate being alternately A or B. During
- 15 the etch process the plasma conditions are sufficient to prevent the deposition of either A or B on the feature bottom, but because of the lack of ion bombardment on the sidewall, the film at these locations is not removed. The method includes the structure being exposed to a selective etch that removes all B layers and is sufficient to remove A layers with underlying B layers by a lift-off mechanism. This results in
- 20 a structure with bands of A layers with a height h_1 remaining where there was no B layer adjacent to the substrate. These bands are separated with bands of no passivation, where originally B passivation was adjacent to the substrate. The method includes the substrate being exposed to a selective etch which etches the substrate but not the A passivated bands. In these regions the feature is etched
- 25 laterally, resulting in a periodic structure along the feature depth axis. The advantages of this method include allowing for fabrication of three-dimensional photonic crystal structures in materials where an isotropic in-situ etch and an anisotropic in-situ etch cannot be easily implemented. For example, in oxide systems a highly isotropic etch is difficult to achieve. This has the effect of limiting
- 30 device structures to vertical sidewalls. Isotropic chemical etches are available but typically do not have the fine linewidth required.

In an alternative preferred embodiment a method including surface defined waveguides, including ion exchange and in-diffused waveguides is used, for fabricating a planar waveguide in glass or a glass on another substrate, for example, silicon wafer, and fabricating a photonic crystal structure. In-diffusion is used to
5 form the waveguide, which can occur before or after waveguide formation. Further, glass wafers can be processed through standard wafer tools, either bare or with a backcoating. The advantages of this embodiment include the economical procurement of plane waveguides. Further, this embodiment offers waveguides with integrated gain medium, for example, Er⁺ as a relatively mature technology. Er⁺ or
10 other rare earth doping may allow for a gain medium to be added to the structure. This method is used in optical fiber amplifiers and similar materials in planar waveguide form, either in deposited waveguides or in-diffused waveguides. The addition of a gain medium allows for amplification of signals on the same die in an integrated fashion. It can also allow for gain flattening and for wavelength
15 conversion through use of a standard gain saturated operating condition.

An alternate preferred embodiment includes a method for fabricating a photonic crystal structure by defining the photonic crystal followed by filling of the waveguide structure. Figures 76A and 76D illustrate the method of defining the photonic crystal and subsequently filling the waveguide structure in accordance with
20 the preferred embodiment of the present invention. The method includes etching to define a template for the photonic crystal structure, filling of photonic crystal structure by conformal or near conformal techniques, an isotropic etch to release the photonic crystal structure, and encapsulation of the photonic crystal structure in a sacrificial layer. Alternately the photonic crystal can be etched and filled, followed
25 by a separate step to define a rib. In those areas where the rib is removed the photonic crystal structure resists the etch and results in a set of released photonic crystal features which can then be encapsulated by, without limitation, for example, SFD. The advantages of this embodiment include the implementation with a rib waveguide by exposing only those photonic crystal structures which are outside the
30 region of the waveguide, followed by filling with the cladding layer.

Figures 77A-77D illustrate a method of manufacturing a photonic crystal waveguide device in which both the photonic crystal and waveguide are etched in

one step in accordance with a preferred embodiment of the present invention. The method of fabricating a photonic crystal filled with a dielectric, metallic or semiconducting medium includes the step of deposition of a film stack comprising of lower cladding index layer, guide index layer, and an overcladding layer. Further, 5 the method includes the step of patterning by, for example, lithography and etching of the film stack to produce a photonic crystal structure and a rib or ridge waveguide structure. This is an alternative method to a fabrication flow in which the rib is patterned and covered with a cladding layer, followed by fabrication of the photonic crystal structure.

10 This structure results in a photonic crystal region which contains a higher index waveguide slab within it. By optimization of the design of the photonic crystal the waveguide propagation can be reduced along the direction perpendicular to the transmission waveguide and hence low loss can be achieved. It has the advantage of lower cost in that only one mask level is needed to both define the 15 photonic crystal and the waveguide. Additionally the lithography step is more straightforward as there is minimal surface topology present on the wafer.

The method further includes the step of filling of the photonic crystal structure by conformal or near conformal methods resulting in filled photonic crystal features and a blanket film over the remainder of the device. The method then 20 includes the step of removing of the photonic crystal fill material from all regions of the device with the exception of the photonic crystal structures by either isotropic etching which only minimally etches the structure due to either surface tension or aspect ratio dependent etch properties, timed etching which removes the blanket film but only a minimal portion of the photonic crystal fill, and patterning to protect the 25 top of the photonic crystal features followed by a removal of the blanket material. The method then includes the step of encapsulation of the entire structure with an upper cladding layer which is index matched to the lower clad. Alternately the device can be fabricated as is as a rib or ridge waveguide. The advantages of this embodiment include a simple device fabrication sequence requiring fewer mask 30 steps and no alignment of sequential masks. Because of the depth of the etch process used for the photonic crystal a rib can be etched at the same time without an additional process step. In order to maintain the propagation properties of the

waveguide and photonic crystal it may be necessary to modify the design of the photonic crystal to account for the fact that the entire region has a guide layer within the stack. This is an alternative to the applications in which the photonic crystal is etched into both the waveguide and the cladding layers after definition of the

5 waveguide.

Figures 78A-78F illustrate a method for manufacturing a planar waveguide device with integrated photonic crystal structures using oxidized waveguides in accordance with a preferred embodiment of the present invention. The method for making photonic crystal device structures includes regular arrays of features etched

10 or embedded in a waveguide structure fabricated in SiO_2 . The photonic crystal, for example, might include a square or hexagonal plan view array of circular or near circular holes etched into a $\text{SiO}_2/\text{Ge:SiO}_2/\text{SiO}_2$ waveguide. These photonic crystal structures have characteristic dimensions of approximately $0.75\text{ }\mu\text{m}$ on a $1\text{ }\mu\text{m}$ periodicity. The method includes the following steps of etching of a desired rib or

15 ridge structure in silicon or in a silicon layer on top of a SiO_2 or other layer. The bottom SiO_2 forms the bottom clad layer, etching of photonic crystal structure into silicon, oxidation of silicon structure with photonic crystal structure to form SiO_2 structure with hole structure embedded, and filling of photonic crystal hole structure to form photonic crystal device structure.

20 Alternatively, the filling step can occur prior to oxidation, followed by oxidation. The entire waveguide structure including doping profiles can be defined by doping and/or epi profiles in the silicon starting structure, which upon annealing and oxidation results in a doped oxide layer. Alternately, only a portion of the waveguide can be oxidized from silicon, for example, only the guide and upper clad.

25 Further, alternately the portion of the photonic crystal above the waveguide guide layer might be deposited in silicon or in a photoresist mask, followed by stripping and oxidation of the guide. At this point the remaining photonic crystal structure extends above the guide and can be encapsulated by a deposition of cladding layer. The advantages of this embodiment include the fabrication of the desired photonic

30 crystal structure directly in SiO_2 which requires the etching of structures with width of approximately $0.3\text{-}1\text{ }\mu\text{m}$ and height/depth ratio of approximately $15\text{ }\mu\text{m}$ for aspect ratios of $15:1$ to $> 45:1$. Such structures are difficult to manufacture in oxide due to

- difficulties in etching of SiO_2 . Compared to oxide, etching of silicon to high aspect ratios and depths is relatively straightforward. For example, etching using the Bosch Process to aspect ratios $> 100:1$ is well documented. The present invention allows for replacement of a difficult oxide etch process with a relatively mature silicon etch process. Further, because oxidation of silicon results in an increase in layer thickness of approximately 2.3 times the silicon layer required to produce the desired waveguide layer height is reduced by this factor. Thus in order to produce a waveguide stack of thickness approximately 6-10 μm a silicon layer thickness of approximately 2.6-4 μm is required. Thermal oxides with $> 10 \mu\text{m}$ thickness can be grown by standard methods on planar substrates. In addition, because the required silicon thickness that must be etched is reduced the etch requirements become even easier to meet and control over photonic crystal hole diameters that can be maintained to tighter tolerances. Further, because of the volumetric change upon oxidation some degree of stress is produced in the final device. This can be minimized by doping and use of oxidation temperature high enough to exceed the glass transition temperature or reflow temperature. Some residual stress due to differences in the coefficient of thermal expansion (CTE) of the oxide and substrate (silicon) result. By proper choice of doping level in the glass the CTE can be made equivalent to that of silicon (for example by P doping).
- The pitch and feature size requirements may be incompatible with oxidation prior to filling because of lateral growth of the oxide in the absence of fill material in the hole. Provided the fill material is stable to oxidation at the temperatures required, for example, use of most transition metal oxides, is not a problem. The waveguide device can have a gaussian doping profile or some similar diffusion dominated profile, unless a diffusion barrier is inserted on each side of the guide layer to stop lateral diffusion of the Ge or other dopant. Control of this profile through the initial layer profile and thermal process is possible. If wet oxidation is used the -OH groups remaining in the waveguide oxide may lead to somewhat higher loss.
- Figures 79A-79D illustrate a method of producing GaAs, InP or other III-V photonic crystals embedded in silicon oxide materials in accordance with a preferred embodiment of the present invention. This method can be used to provide emitters

and/or detectors, for example, GaN light emitting diodes. The method includes using the starting material, for example, a GaAs wafer with a AlGaAs layer, approximately 6 μm from the surface. This is an exemplary material system. Any material system with a high etch rate ratio etch stop layer can be used. The GaAs is
5 etched into a structure with the desired photonic crystal dimensions, for example, approximately 0.5 μm features on a 1 μm pitch. This can be done by a dry etching process, for example.

The method includes the deposition of silicon dioxide using a method capable of filling high aspect ratio gaps such as those defined hereinbefore. Further,
10 the method includes planarization of the wafer surface oxide. In a preferred embodiment where the GaAs layer is to be electrically active the top surface might be exposed. Alternately the oxide layer might cover the top surface. The method then includes deposition of a top cladding layer over the planarized structure, followed by silicon wafer bonding of the GaAs and silicon wafers. Alternately the
15 silicon wafer can have an oxide layer that forms the cladding. The GaAs wafer can be thinned from the back side either mechanically or with a highly selective etch down to the AlGaAs layer. The layer can then be precision lapped or dry etched to expose the oxide, leaving an oxide core layer with embedded GaAs structures. The method includes the step of the wafer then being capped by another oxide cladding
20 layer. Further, patterning of the waveguide in the SiO_2 can occur at several points in the process flow, either immediately after deposition of the guide, or at a later point prior to the final encapsulation.

Alternative embodiments include the incorporation of AlGaAs layers into the epi structure so that it is possible to etch back from the surface of the oxide on both
25 sides to a buried layer of Al and thus have a recessed GaAs surface relative to the guide layer. By anisotropically etching the oxide selectively to the GaAs it is possible to make a structure with the oxide surface recessed relative to the GaAs on each side (top and bottom) of the waveguide. Further, by starting with an appropriate epi structure it may be possible to fabricate three-dimensional photonic
30 crystal functionality. The advantages of this embodiment include allowing high quality III-V to be integrated into the oxide photonic crystal device. This allows for active functionality to be incorporated. The steps of selective etch and wafer

bonding are established. The fill technology for high quality oxides can include CFD methods.

A preferred alternative embodiment includes a method of fabricating filled photonic crystals with metal oxides based on deposition of metal liners followed by oxidation of the metal. Since oxidation typically results in a volume increase, proper choice of metal thickness can completely close the feature and leave a completely oxidized metal oxide filling the feature. The method includes lining a feature with appropriate thickness of metal using a technique such as CVD, ALD, or ionized PVD. Example of metals include the use of Ti, Ta, Cu, Al. The method includes the oxidization of the metal to produce a metal oxide via, for example, thermal oxidation, plasma oxidation, anodic oxidation. The oxidizing ambient can be one of a number well know in the art, for example, oxygen, air, water vapor, and NO compounds. The advantages of the embodiment include an ease to line features with material than to completely fill the approach minimizes the technical difficulty of achieving a full fill. The transport of oxidizing species to the oxidation front can be via either the silicon oxide layers or the metal and metal oxide. Lining technologies for W, Ti, Ta, Cu are well developed.

Figures 80A-80J illustrate cross-section views of a preferred embodiment of a photonic integrated circuit fabrication process flow in accordance with a preferred embodiment of the present invention. Figure 80A is a cross-sectional view illustrating the results of a blanket film deposition process. The undercladding deposition 4252 in a preferred embodiment includes a 15 um thermal oxide, followed by guide deposition 4254 of 4 um Ge (1%) LPCVD oxide. A topclad deposition 4256 of 2 um BPSG oxide then follows. The circuit is then subjected to an annealing process for stress reduction. The layers are deposited using methods employed in planar lightwave circuit fabrication. The bottom cladding uses thermal oxidation and high pressure oxidation at pressures of one atmosphere and greater than one atmosphere. And temperatures range between 900-1200° C for the process. The guide layer deposition uses plasma-enhanced CVD (pecvd) from silane and nitrous oxide at pressures of 20-500 mTorr and rf powers of 50-500 W for a 150 mm wafer. The temperatures range from 300-500° C. In order to control stress, power, pressure and silane to oxidant ratio can be adjusted. Low pressure CVD (LPCVD) at

-67-

pressures of 10mT to 10 Torr and temperatures of 350° C (low-temp oxide, LTO) to 750° C are used. The guide layer is deposited with a Ge doping to control index of refraction, to 1e-4. Alternately B and P (BPSG) may be used to control the index, for example, 4 wt% P in NSG (non-doped silicon glass) gives an index of 1.5% greater than thermal oxide appropriate for use as a guide layer with approximate dimensions 4 x 4 um. An overcoat is deposited with PECVD or LPCVD as described herein before and alternately, B, P or BP doping (BSG, PSG, BPSG) can be used. Because of the small size of these devices the extreme uniformity and index control required for conventional plc devices is not required. This makes it possible to use alternate material stacks. One preferred embodiment includes using a B/P doped gas which is a standard oxide composition which has better etch qualities than Ge glasses. Ge glasses etch differently due to the low volatility of GeCl₄ and different microstructure. In contrast B/P etch products are volatile, for example, BF₃.

Figure 80B is a cross-sectional view 4270 illustrating the results of waveguide fabrication. The waveguide fabrication includes guide-mask deposition (if hardmask). The guide mask, for example, has a 4 um linewidth, 1.0 um minimum space, and CD measured on space. A guide-mask etch is used if a hardmask is used. An alignment mark implementation prior to guide-mask etch is also used.

The mask can be either a hardmask, silicon, silicon nitride, metal for example, Cr, Ni, Ti, Ta, or photoresist. For the guide layer a preferred embodiment uses a photoresist to lower cost as fewer process steps are required. In order to facilitate the later fabrication of the waveguide with a planar surface, an alternate preferred embodiment uses a hardmask and uses the hardmask as a polish stop. In this embodiment, the mask can have a high selectivity for the etch process, be easily patterned, and have a high polish selectivity (low polish rate in an oxide polish process) to oxide.

The process flow then includes the step of accounting for process variations. The materials typically used as guide mask include, photoresist: 4-6 um thick, SiN_x: 1-2 um thick; Cr: 0.2-1 um; wet etched; WSi: 1-2 um dry etched; Poly-Si; a-Si; Ni. An important requirement includes very low sidewall roughness along waveguide

length. A preferred embodiment includes in the process flow using guide hardmask as polishstop for chemical-mechanical polishing (CMP) to control the final thickness of the topclad.

Figure 80C is a cross-sectional view 4300 illustrating the results of waveguide fabrication process. The guide etch preferably has a 4-6 μm etch depth, 85-90 degree sidewall, and low sidewall roughness (lateral runout). The strip includes photoresist, and the hardmask remains as polish stop. The overcoat uses LPCVD or PECVD BPSG oxide and is index matched to thermal oxide. The process then includes an annealing process for reflow and stress reduction.

Figure 80D is a cross-sectional view 4320 illustrating the results of a sequential waveguide fabrication process flow. The process flow includes a step of planarization which includes 2-4 μm surface topography, polish stop options, a final thickness controlled to 0.2 μm and the guidemask being polishstopped. Further, the guidemask strip is exposed as a polish stop layer. In addition, the final planarization step includes controlling the final top cladding layer thickness to 0.2 μm , and local flatness to $< 0.1 \mu\text{m}$.

The process flow then includes accounting for process variations. This flow utilizes the guide hardmask as a polish stop to control topclad thickness. This can be accomplished with several similar flows, which includes no polish stop layer wherein CMP is required to stop at $2 \mu\text{m} +0.3/-0$ topclad thickness. The disadvantage to this step is that the guide etch and overcoat non-uniformity lead to topclad non-uniformity. Further, the topclad layer is eliminated CMP wherein is stopped on top of the guide layer. Additional topclad deposition may be required. The disadvantage of this step is that the guide layer surface is subject to polishing. In addition, a polish stop above overcoat is implemented. A disadvantage of this step includes guide etch and overcoat non uniformity which may lead to topclad non-uniformity.

Figure 80E is a cross-sectional view 4340 illustrating the results of lattice fabrication in the process flow in accordance with a preferred embodiment of the present invention. The lattice fabrication includes the step of hardmask deposition with materials for example, Al, Si, SiN_x , and current flow of 0.75 μm for Al hardmask. The next step is lattice-mask definition which includes the use of stepper

lithography. A specification may be specified for dense line for space structures including 0.5 μm minimum CD, and for equal line/space. Line/space structures are used in preferred embodiments, for example.

For a preferred embodiment for the hardmask, materials, for example, Al, Cr, SiNx, Si are preferred. Al can be easily patterned at fine feature sizes with Cl chemistry (for example, CCl_4 , Cl_2 , BCl_3 , chlorofluoro carbons and derivatives). This can be done in parallel plate plasma reactors and in high density plasma systems with inductively coupled, helicon, helical resonator, and electron cyclotron resonance plasmas. These systems use a separate wafer bias applied to the wafer. An Al etch at $<0.25 \mu\text{m}$ features is used. The preferred embodiment uses processes that are known in the art operating in parallel plate and high density plasmas at pressures of 1-1000 mTorr and powers of 50-5000 W and wafer biases of 50-750 V rf-induced dc bias. For Cr masks a Cl_2 -based chemistry can be used. This is used in fabrication of photomasks where either wet or dry etch is used. For the feature CD control required where a dry etch is preferred, where a passivating chemistry is used to control CD bias during etch and where a 100-500 nm thick Cr is patterned. A similar set of process conditions can be used here, in either a parallel plate or high density plasma reactor.

The hardmask can be patterned with a photoresist mask. This mask can be exposed and developed using standard techniques. Preferred embodiments use either a contact, proximity mask aligner or a stepper or scanner lithography system. A photoresist thickness of 0.8-1.0 μm can be used. Antireflective coatings (either photodefinable or post-defined) can be used. Either a positive or negative resist can be used, but a positive is generally preferred. Alternately the mask can be defined by using a trimask technique, or other "image-enhanced" or siliated resist process flow, to give a thicker resist and eliminate the hardmask. A hardmask can also be used in the hardmask flow to pattern a thicker hardmask. One preferred embodiment uses a silicon oxide as a hardmask on Al to pattern Al in thicknesses $> 1 \mu\text{m}$ where it is difficult to control CD in thicker resist which might be required due to resist to Al selectivity. The preferred hardmask thickness is determined by the selectivity of the oxide etch process to the hardmask. For Si, a selectivity of 10-25:1 is typical. For Al and other metals a selectivity of $> 40:1$ can be achieved. With the current set of

processes a Al mask thickness of $> 0.75 \mu\text{m}$ is required. This mask thickness is sufficient to etch to a depth of $5\text{-}8 \mu\text{m}$ depending on whether the feature is a line/space feature or a hole feature. The etch typically exhibits an effect known as "rie lag" or "aspect ratio dependent etch (ARDE)" in which features with higher aspect ratios etch slower as the aspect ratio increases. Because of this effect the mask required to etch to a depth of $2\times$ those listed herein above may be substantially greater than $2\times$ the mask thickness (nominally $0.75 \mu\text{m}$) listed herein above

Figure 80F is a cross-sectional view 4370 of the results of further lattice fabrication process flow steps. The steps include lattice-mask hardmask etch with current flow, Al dry etch including CCl_4/Ar RIE. Further, a step of lattice etch is $8\text{-}10 \mu\text{m}$ deep, and has $0.5 \mu\text{m}$ line / space minimum feature for preferred embodiments.

The process further includes the accountability of process variations. For example, Al mask requires a low bias etch (HDP) to avoid excessive Al sputtering and micromasking. This is incompatible with standard RIE. Further, Si or SiN_x mask may be compatible with standard RIE and may offer better lateral runout/roughness.

In a preferred embodiment, the oxide etch may be done by reactive ion etching in either parallel plate or high density plasma systems. Alternately an ion beam or reactive ion beam can be used. Neutral particle beams or ion cluster beams can also be used. A preferred embodiment includes a plasma etch process. The oxide etch process is used in microelectronics manufacturing. Carbon and fluorine containing gases are used. Examples, without limitation, of preferred gases include CF_4 , CHF_3 , C_2F_4 , C_2F_6 , C_3F_8 , C_4F_8 , C_5F_8 , in addition to dilutents such as Ar, N_2 , He, and polymer etching gases such as O_2 , N_2O , CO_2 , CO. In a parallel plate reactor, a process chemistry of 100 Ar, 20 C_4F_8 , 50 CO, 10 O_2 is representative although many different permutations and combinations can be used. In a parallel plate reactor, the reactive species density is relatively low and it is generally not a preferred method for use with a metal mask where mask sputtering is a problem. For use with a metal mask, a high density plasma, where higher reactive density and a lower wafer bias can be used. In a high density plasma, gases which are more difficult to dissociate can be used. In addition much of the noble gas component can be removed leading

to less mask sputtering. Preferred process conditions include pressures of 1-100 mTorr for a HDP etcher at source powers of 1-5 kW and a wafer bias of 100-750 V rf induced dc bias. Preferred process conditions for a parallel plate system are 20-500 mT at a power of 2-10kW and a wafer bias of 200-750 V. Magnetically enhanced (MERIE) configurations fall into this category. ChlorFluorocarbons can also be used in other embodiments.

Figure 80G is a cross-sectional view 4400 of the results of a lattice fill process in accordance with a preferred embodiment. The lattice fill process includes the step of mask strip and clean, and filling the trench via structures with Si, preferably or TiO_2 using multiple routes. The requirements include being void-free, 1% index uniformity, low stress, and stable to 300° C.

Preferred embodiments include different lattice fill options. For example, deposition based on supercritical fluids which is capable of filling high aspect ratio structures with a variety of metals, metal oxides, and polymers can be used. Alternate approaches include, LPCVD-Si: undoped, high index at 1.55 um telecommunication wavelengths, and mature commercial processes. Alternatively CVD-Ti plus thermal oxidation can be used Ti liner process exists, with thermal oxidation demonstrated at 500-700° C. In another preferred embodiment, ALD- TiO_2 , processed can be used. In a preferred embodiment, MOCVD can be used to deposit a Cu liner followed by post oxidation. The preferred process uses a standard Cu alkoxide such as Cu (hfac) at a sub atmosphere pressure and at temperature ranging from 150-350° C. Under these conditions a conformal lining can be deposited without a liner or seed layer directly on SiO_2 . Cu can be thermally oxidized to several different oxides, for example, CuO and Cu_2O , among others. CuO is preferred in some embodiments. Under thermal oxidation or thermal annealing a metal silicide (Ti or Cu- Si) can be formed which can have the desirable effect of giving a graded index junction such as $\text{SiO}_2/\text{SiTiOx}/\text{TiO}_2$. This then has the effect of reducing dependence on interface roughness. TiSi is formed when TiSiO_2 is exposed to elevated temperatures (> 300° C). Under oxygen ambient, however, this silicide is reported to oxidize congruently (without formation of phase segregated layers). By controlling the anneal conditions and oxygen partial pressure between approximately 0 and 1 atmosphere this interface layer can be controlled. A

preferred method for post oxidation of Ti liner includes the conditions of temperature of > 500 C and a partial pressure of 0.1-1 Atmosphere partial pressure O_2 . Alternately H_2O or steam oxidation can be used. For CFD, the preferred process conditions are 2,000-10,000 psi in a CO_2 ambient at a temperature of 100-
5 500°C. Various precursors can be used, many of which are well known from MOCVD. In general however, less reactive precursors are desired to minimize gas phase reactions which lead to particulate formation.

Figure 80H illustrates a cross-sectional view 4420 of the results of a lattice fabrication process flow including lattice fill etch back in which the surface is
10 planarized, followed by an isotropic etch, and wet or dry etch. The planarization is performed by etching back the fill material with an isotropic etch. This can be either a wet or dry etch with low enough etch rate to allow the etch to stop just below the surface of the oxide. The etch must be selective to oxide. Endpoint methods based on the change in area between the blanket film and the fill area can also be
15 performed.

Figure 80I illustrates a cross-sectional view 4440 of the results of heater fabrication process flow in a preferred embodiment wherein thin film resistor metal deposition, has occurred using, for example, NiCr, TaN_x , a 50 ohm resistor target for example and low TCR. The Resistor define is > 1 μm CD and includes a resistor
20 etch or lift-off.

Figure 80J is a cross-sectional view 4460 of the results of a thermal isolation process flow in a preferred embodiment including, isolation define, and isolation etch, (15-20 μm deep, non-critical etch). The process flow can included the additional steps of dicing, fiber pigtailling, and packaging.

Figure 81 is a top level flow chart 4500 of a method for fabricating a photonic crystal device in accordance with the Figures 80A-80J of the present invention. The preferred embodiments for each step are detailed with respect to the Figures 80A-80J. The top level process includes the step 4502 of blanket film deposition, the step 4504 of waveguide fabrication, followed by a step 4506 of
25 accounting for process variations. The process then includes the step 4508 of lattice fabrication followed by step 4510 of accounting for process variations in the lattice fabrication process. Lattice fill process per step 4512 then follows with additional
30

-73-

lattice fabrication steps per step 4514 such as, for example, etching back the lattice fill. The process 4500 then includes fabrication of a heater per step 4516 and thermal isolation per step 4518. The process 4500 can include optional steps of dicing, fiber pigtailling and packaging without limitation.

- 5 The claims should not be read as limited to the described order or elements unless stated to that effect. Therefore, all embodiments that come within the scope and spirit of the following claims and equivalents thereto are claimed as the invention.

CLAIMS

What is claimed is:

1. A photonic crystal structure, comprising:
a substrate having a surface characteristic; and
5 at least a first material over the surface characteristic and covering the surface.
2. The photonic crystal structure of Claim 1 wherein the first material is disposed using supercritical fluid deposition processes.
- 10 3. The photonic crystal structure of Claim 1 wherein the surface characteristic is a patterned substrate.
4. The photonic crystal structure of Claim 1 wherein the first material
15 comprises one of at least a metal, a semiconductor, a polymer, a monomer, a mixture of metals, a metal di-oxide, a metal sulphide, a metal nitride, a metal phosphide, a metal fluoride, a metal carbide, a metal chloride and metal alloys.
- 20 5. The photonic crystal structure of Claim 3 wherein the patterned substrate has submicron features.
6. The photonic crystal structure of Claim 5 wherein the features have an aspect ratio of between five and thirty.
- 25 7. The photonic crystal structure of Claim 1 wherein the substrate is one of a silicon wafer, a silicon wafer having at least one layer of silicon dioxide cladding.
- 30 8. The photonic crystal structure of Claim 1 comprising a thin film filter.
9. The photonic crystal structure of Claim 1 comprising an integrated circuit.

10. The photonic crystal structure of Claim 3 wherein the patterned substrate has features with dimensions less than or equal to a wavelength of interest for light.
- 5
11. The photonic crystal structure of Claim 3 wherein the patterned substrate has features having a size of approximately 0.9 microns.
12. An integrated waveguide device, comprising:
- 10 a substrate having a first refractive index characteristic;
 a first material disposed over the substrate having a second refractive index characteristic, and forming a waveguide layer; and
 a second material disposed at least within the first material having a third refractive index characteristic wherein the second refractive index
15 characteristic is greater than the first and third refractive index characteristics.
13. The integrated waveguide device of Claim 12 further comprising a cladding layer disposed over the first material.
- 20
14. The integrated waveguide device of Claim 12 wherein the dimensions of the waveguide layer is between approximately 3 and 8 μm thick.
15. The integrated waveguide device of Claim 12 wherein the second material is deposited in one of a plurality of at least holes, trenches, ribs, posts and cylinders, and at least encapsulates a plurality of features.
- 25
16. The integrated waveguide device of Claim 15 wherein the aspect ratio of the plurality of holes, trenches, ribs, posts and cylinders is between
30 approximately five and thirty.

-76-

17. The integrated waveguide device of Claim 13 wherein the cladding layer has a fourth refractive index characteristic that is lower than the second refractive index characteristic.
- 5 18. The integrated waveguide device of Claim 12 wherein the first material has at least one patterned array of submicron features such that the second material is deposited therein.
- 10 19. A photonic crystal filter, comprising:
an input waveguide which carries a signal having at least one frequency including at least one desired frequency;
an output waveguide; and
a photonic crystal resonator system coupled between said input and output waveguides operable for the adjustable transfer of said at least one
15 desired frequency to said output waveguide.
20. The photonic crystal filter of Claim 19 wherein the filter is a fixed single-wavelength filter.
21. The photonic crystal filter of Claim 19 wherein the filter is tunable for at least one of wavelength and polarization.
- 20 22. The photonic crystal filter of Claim 19 wherein the photonic crystal resonator system is a multi-cavity Fabry-Perot resonator.
23. The photonic crystal filter of Claim 19 wherein the photonic crystal resonator system is a single cavity Fabry-Perot resonator.
- 25 24. The photonic crystal filter of Claim 19 wherein the photonic crystal resonator system comprises a first photonic crystal mirror and a second photonic crystal mirror, the second photonic crystal mirror being spaced from the first photonic crystal mirror to form a resonant cavity.

-77-

25. The photonic crystal filter of Claim 24 wherein the first and second photonic crystal mirrors include a two-dimensional structure.
26. The photonic crystal filter of Claim 24 wherein the first and the second photonic crystal mirrors include a three-dimensional structure.
- 5 27. The photonic crystal filter of Claim 19 wherein a change in a refractive index characteristic of the photonic crystal resonator system provides for tuning of the filter.
28. The photonic crystal filter of Claim 27 wherein the refractive index can be controlled by using one of at least thermal-optics, electro-optics, magneto-optics and piezo-optics means.
- 10 29. The photonic crystal filter of Claim 19 wherein said photonic crystal resonator system comprises a photonic crystal that is a three-dimensionally periodic dielectric structure.
30. The photonic crystal filter of Claim 19 wherein said photonic crystal resonator system comprises a photonic crystal that is a two-dimensionally periodic dielectric structure.
- 15 31. The photonic crystal filter of Claim 19 wherein the photonic crystal resonator system comprises a one-dimensionally periodic photonic crystal.
32. The photonic crystal filter of Claim 19 further comprising:
- 20 a substrate having a first refractive index characteristic;
- a first material disposed over the substrate having a second refractive index characteristic, and forming a waveguide layer; and
- a second material disposed at least within the first material having a third refractive index characteristic wherein the second refractive index
- 25 characteristic is greater than the first and third refractive index characteristics.

-78-

33. The photonic crystal filter of Claim 32 further comprising a cladding layer disposed over the first material.
34. The photonic crystal filter of Claim 32 wherein the dimensions of the waveguide layer is between approximately 3 and 8 μm thick.
35. The photonic crystal filter of Claim 32 wherein the second material is deposited in one of a plurality of at least holes, trenches, ribs, posts and cylinders, and at least encapsulates a plurality of features.
36. The photonic crystal filter of Claim 35 wherein the aspect ratio of the plurality of holes, trenches, rib, posts or cylinders is between approximately five and thirty.
37. The photonic crystal filter of Claim 33 wherein the cladding layer has a fourth refractive index characteristic that is lower than the second refractive index characteristic.
38. The photonic crystal filter of Claim 32 wherein the first material has at least one patterned array of submicron features such that the second material is deposited therein.
39. A photonic crystal wavelength router, comprising:
at least a first input waveguide;
at least a first output waveguide;
a chromatic dispersion compensator;
at least one wavelength division multiplex filter; and
at least one photonic crystal reflector.
40. The photonic crystal wavelength router of Claim 39 further comprising a power tap disposed therein.

-79-

41. The photonic crystal wavelength router of Claim 39 wherein the router comprises a material with tunable dielectric or absorbing properties.
42. The photonic crystal wavelength router of Claim 39 comprises one of at least a one-dimensionally periodic photonic crystal, a two-dimensionally periodic photonic crystal and a three-dimensionally periodic photonic crystal.
43. The photonic crystal wavelength router of Claim 39 further comprising:
a substrate having a first refractive index characteristic;
a first material disposed over the substrate having a second refractive index characteristic, and forming a waveguide layer; and
a second material disposed at least within the first material having a third refractive index characteristic wherein the second refractive index characteristic is greater than the first and third refractive index characteristics.
44. The photonic crystal wavelength router of Claim 39 further comprising a cladding layer disposed over the first material.
45. The photonic crystal wavelength router of Claim 39 wherein the dimensions of the waveguide layer is between approximately 3 and 8 μm thick.
46. The photonic crystal wavelength router of Claim 39 wherein the second material is deposited in one of a plurality of at least holes, trenches, ribs, posts, cylinders, and at least encapsulates a plurality of features.
47. The photonic crystal wavelength router of Claim 46 wherein the aspect ratio of the plurality of holes, trenches, rib, posts or cylinders is between approximately five and thirty.

48. The photonic crystal wavelength router of Claim 44 wherein the cladding layer has a fourth refractive index characteristic that is lower than the second refractive index characteristic.
- 5 49. The photonic crystal wavelength router of Claim 39 wherein the first material has at least one patterned array of submicron features such that the second material is deposited therein.
50. A photonic crystal optical add/drop multiplexer, comprising:
- 10 an input waveguide;
 at least a first output waveguide;
 an optical performance monitor coupled between the input waveguide and the at least first output waveguide;
 a photonic crystal wavelength router; and
 a dispersion compensation module.
- 15 51. The photonic crystal optical add/drop multiplexer of Claim 50 further comprising:
- a substrate having a first refractive index characteristic;
 a first material disposed over the substrate having a second refractive index characteristic, and forming a waveguide layer; and
- 20 a second material disposed at least within the first material having a third refractive index characteristic wherein the second refractive index characteristic is greater than the first and third refractive index characteristics.
- 25 52. The photonic crystal optical add/drop multiplexer of Claim 50 further comprising a cladding layer disposed over the first material.
53. The photonic crystal optical add/drop multiplexer of Claim 50 wherein the dimensions of the waveguide layer is between approximately 3 and 8 μm
- 30 thick.

54. The photonic crystal optical add/drop multiplexer of Claim 50 wherein the second material is deposited in one of a plurality of at least holes, trenches, ribs, posts and cylinders, and at least encapsulates a plurality of features.
- 5
55. The photonic crystal optical add/drop multiplexer of Claim 54 wherein the aspect ratio of the plurality of holes, trenches, rib, posts or cylinders is between approximately five and thirty.
- 10
56. The photonic crystal optical add/drop multiplexer of Claim 52 wherein the cladding layer has a fourth refractive index characteristic that is lower than the second refractive index characteristic.
- 15
57. The photonic crystal optical add/drop multiplexer of Claim 50 wherein the first material has at least one patterned array of submicron features such that the second material is deposited therein.
58. A photonic crystal dynamic optical add/drop multiplexer comprising:
- 20
- a plurality of input waveguides;
 - a plurality of output waveguides;
 - a plurality of photonic crystal resonator systems disposed between the plurality of input waveguides and plurality of output waveguides; and
 - a photonic crystal reflector coupled to the plurality of photonic crystal resonator systems.
- 25
59. The photonic crystal dynamic add/drop multiplexer of Claim 58 further comprising:
- a substrate having a first refractive index characteristic;
 - a first material disposed over the substrate having a second refractive index characteristic, and forming a waveguide layer; and
 - 30 a second material disposed at least within the first material having a third refractive index characteristic wherein the second refractive index

-82-

characteristic is greater than the first and third refractive index characteristics.

- 5 60. The photonic crystal dynamic add/drop multiplexer of Claim 58 further comprising a cladding layer disposed over the first material.
- 10 61. The photonic crystal dynamic add/drop multiplexer of Claim 58 wherein the dimensions of the waveguide layer is between approximately 3 and 8 μm thick.
- 15 62. The photonic crystal dynamic add/drop multiplexer of Claim 58 wherein the second material is deposited in one of a plurality of at least holes, trenches, ribs, posts and cylinders, and at least encapsulates a plurality of features.
- 20 63. The photonic crystal dynamic add/drop multiplexer of Claim 62 wherein the aspect ratio of the plurality of holes, trenches, ribs, posts and cylinders is between approximately five and thirty.
- 25 64. The photonic crystal dynamic add/drop multiplexer of Claim 60 wherein the cladding layer has a fourth refractive index characteristic that is lower than the second refractive index characteristic.
- 30 65. The photonic crystal dynamic add/drop multiplexer of Claim 58 wherein the first material has at least one patterned array of submicron features such that the second material is deposited therein.
66. A method of producing an integrated photonic circuit device, comprising:
providing a substrate having a surface characteristic and a first refractive index characteristic;
disposing at least a first material with a second refractive index characteristic over the surface characteristic, wherein the second refractive index characteristic is higher than the first.

67. The method of producing an integrated photonic circuit device of Claim 66 further comprising:
etching the surface characteristic of the substrate to form a plurality of cavities having an aspect ratio characteristic; and
5 depositing a second material having a third refractive index characteristic in the plurality of cavities, the second refractive index characteristic being higher than the first and the third refractive index characteristic.
- 10 68. The method of producing an integrated photonic circuit device of Claim 67 wherein the aspect ratio characteristic is between approximately five and thirty.
69. The method of producing an integrated photonic circuit device of Claim 66 further comprising disposing a cladding layer over the first material.
- 15 70. The method of Claim 66 wherein the first material comprises an amorphous silicon material doped with index increasing dopants.
71. The method of Claim 70 further comprising oxidizing the first material.
- 20 72. A periodic three dimensional photonic crystal structure comprising:
a substrate having a surface characteristic;
at least one thin film deposited over the surface characteristic to result in a multi-layer photonic crystal, the multi-layer photonic crystal being adapted to have an induced variation in an index of refraction characteristic
25 and wherein a plurality of the multi-layer photonic crystals are placed in a stack configuration and a material is deposited into interstitial gaps formed in the stack configuration using supercritical fluid deposition processes.
73. The periodic three-dimensional photonic crystal structure of Claim 72 wherein the substrate is spherical in shape.

74. An optical waveguide structure, comprising;
a first waveguide;
a second waveguide that intersects with said first waveguide; and
at least one photonic crystal resonator at the intersection of said first
and second waveguides to minimize cross talk between signals of said first
and second waveguides.
75. A method of fabricating an integrated photonic circuit device, comprising:
providing a substrate having a surface characteristic and a first
refractive index characteristic;
depositing a film over the substrate;
fabricating a waveguide structure having a second refractive index
characteristic;
fabricating a lattice structure; and
providing a lattice fill having a third refractive index characteristic.
76. The method of Claim 75 wherein the second refractive index characteristic is
higher than the first and the third refractive index characteristic.
77. The method of Claim 75 wherein the film comprises an undercladding
including a thermal oxide.
78. The method of Claim 75 wherein the waveguide structure is deposited using
a plasma enhanced chemical vapor deposition process.
79. The method of Claim 78 wherein the step of fabricating a waveguide
structure further comprises guide mask deposition.
80. The method of Claim 75 wherein the step of providing a lattice fill comprises
deposition using supercritical fluids to fill aspect ratio structures in the range
of between five and thirty.

1/100

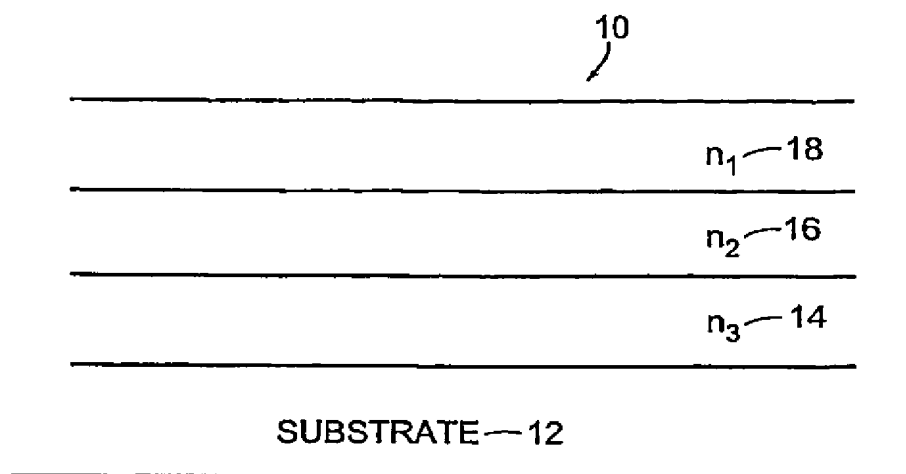


Figure 1

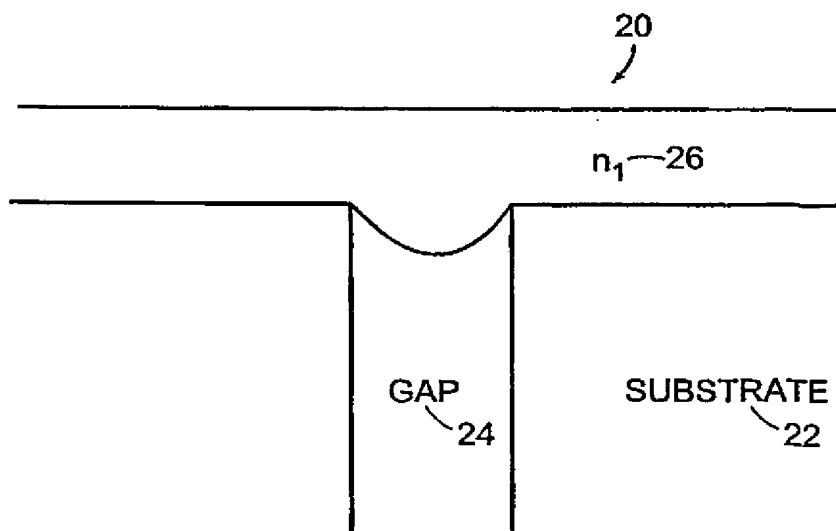


Figure 2

SUBSTITUTE SHEET (RULE 26)

2/100

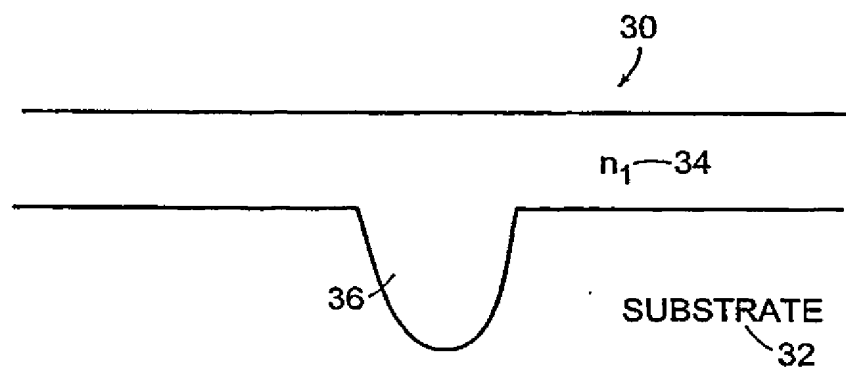


Figure 3

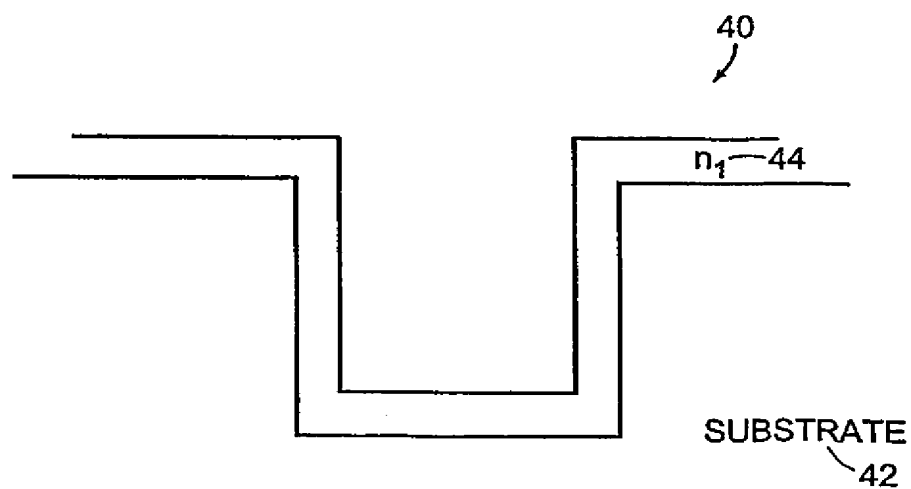
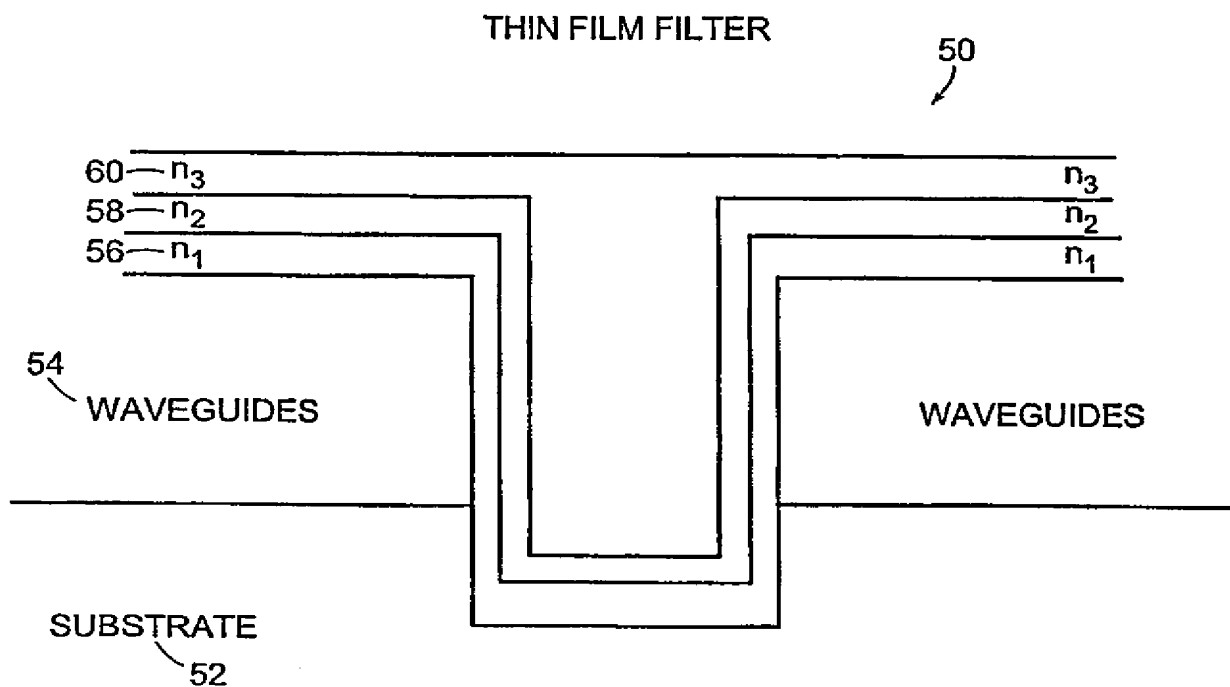


Figure 4

SUBSTITUTE SHEET (RULE 26)

3/100



GUIDED WAVE THIN FILM FILTERS

Figure 5A

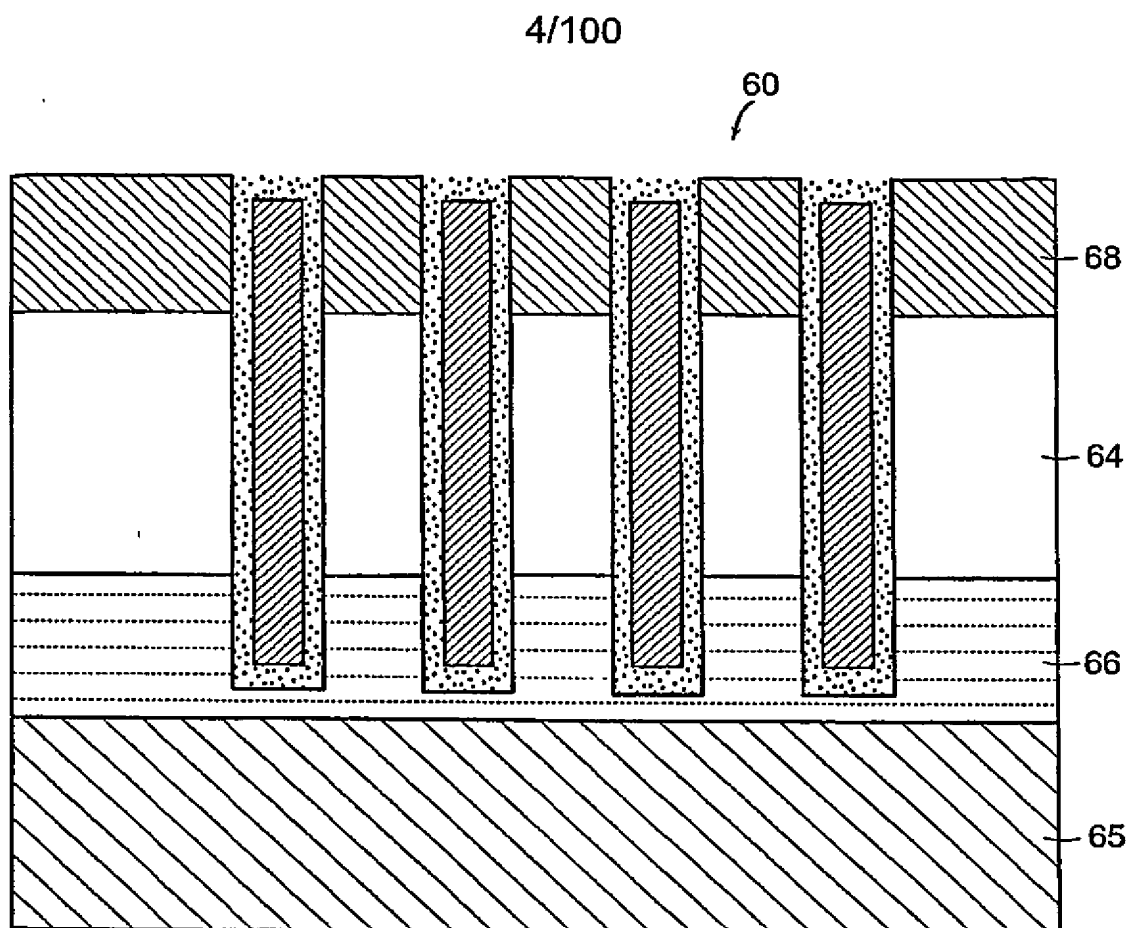


Figure 5B

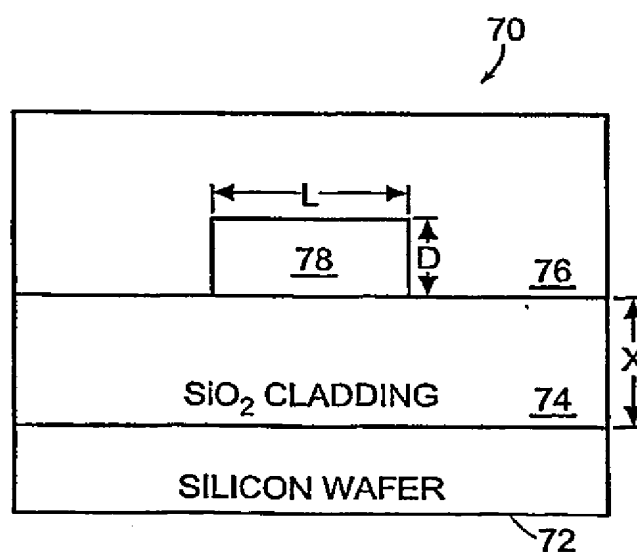


Figure 5C

SUBSTITUTE SHEET (RULE 26)

5/100

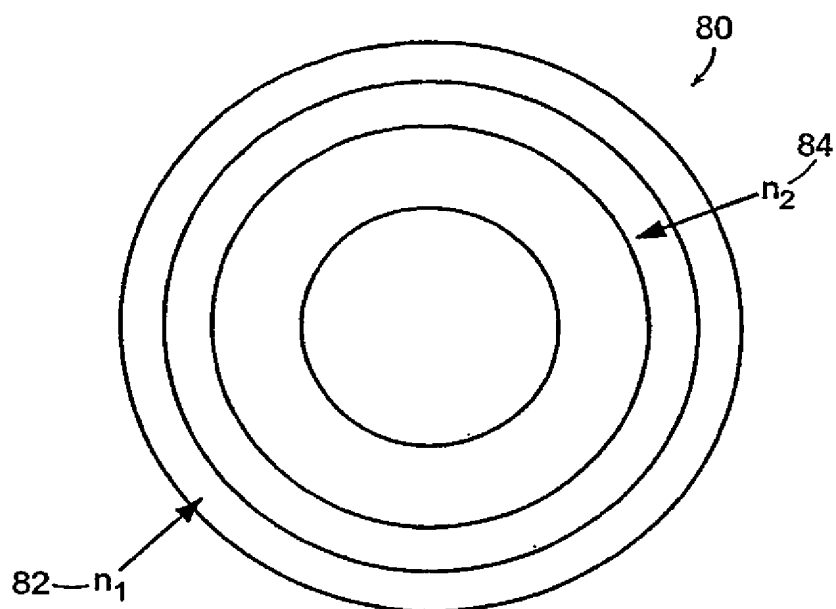


Figure 6

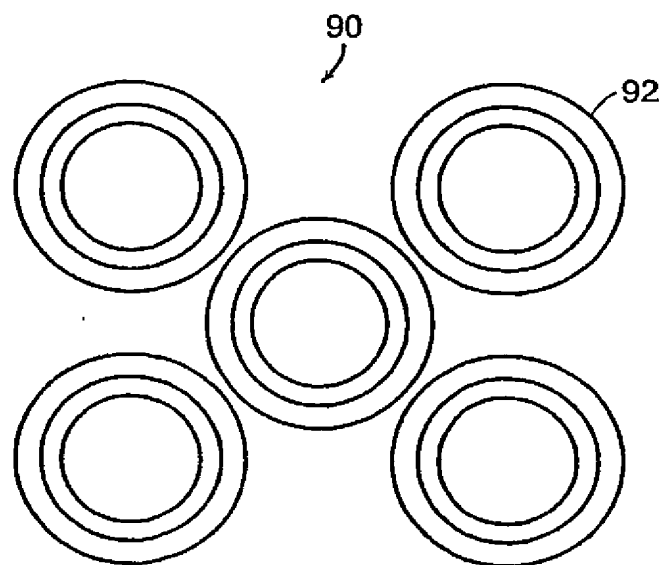


Figure 7

SUBSTITUTE SHEET (RULE 26)

6/100

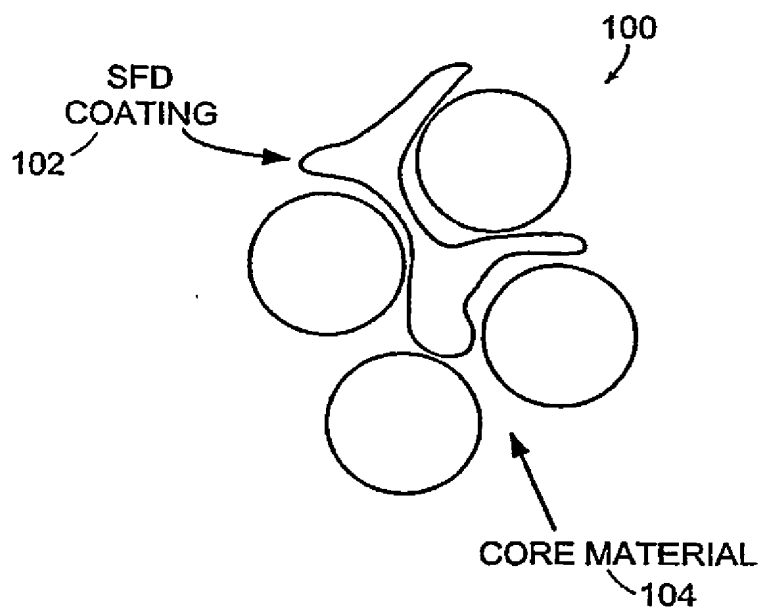


Figure 8

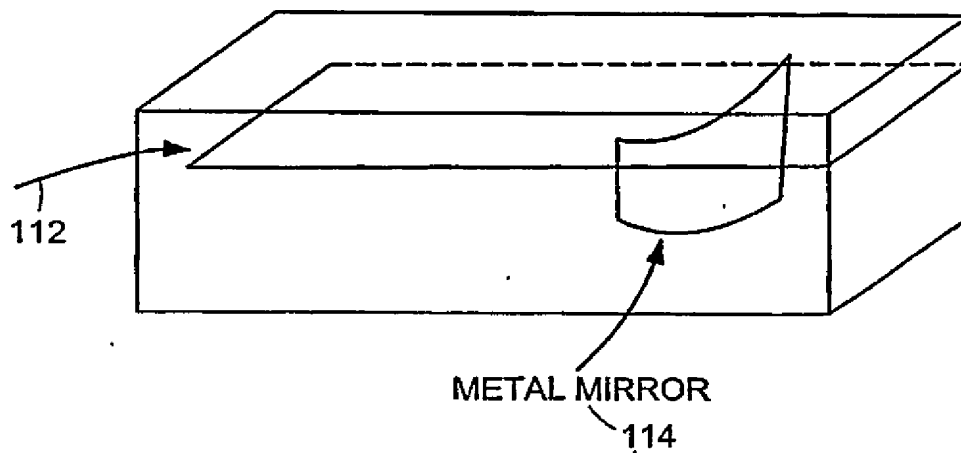


Figure 9

SUBSTITUTE SHEET (RULE 26)

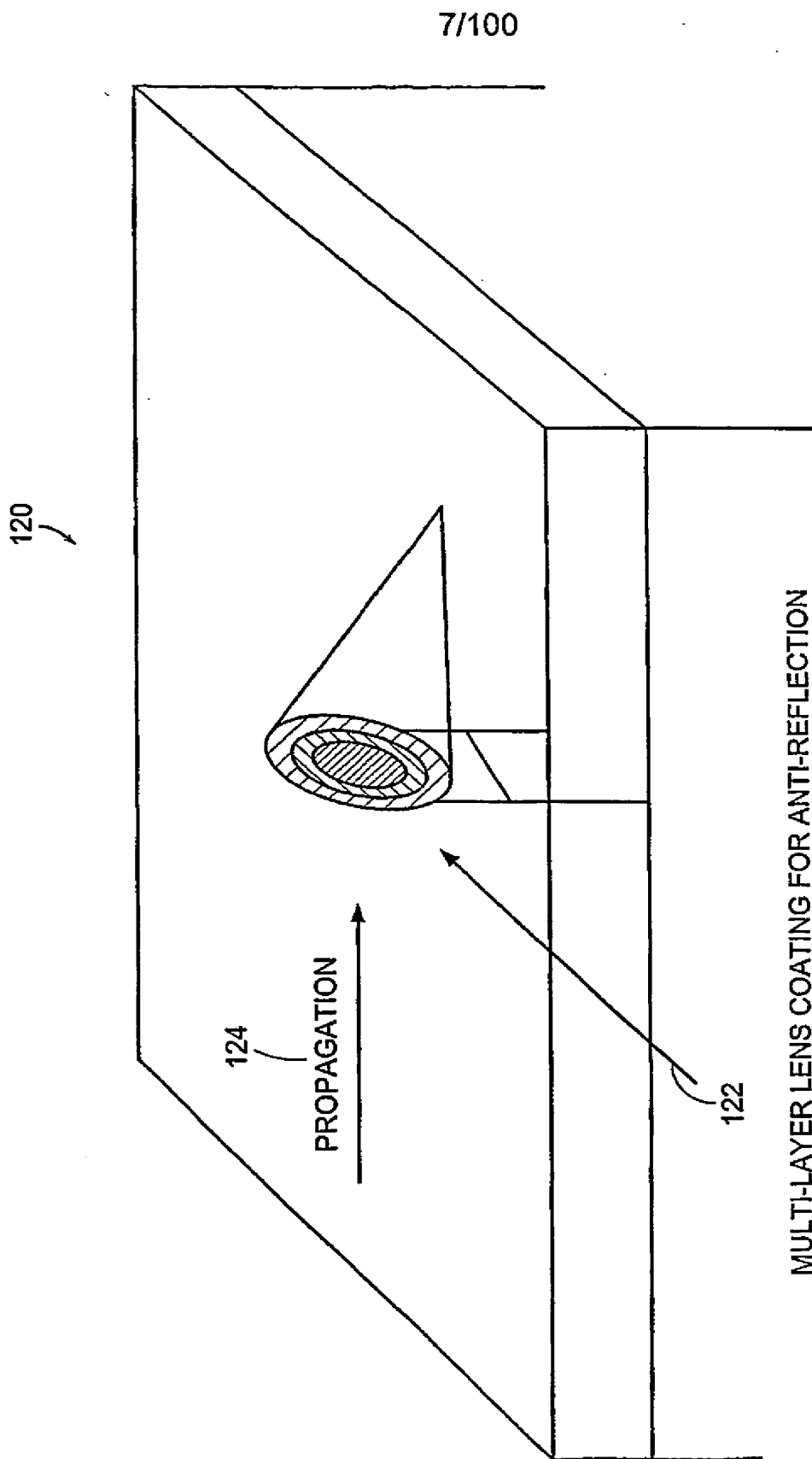


Figure 10

SUBSTITUTE SHEET (RULE 26)

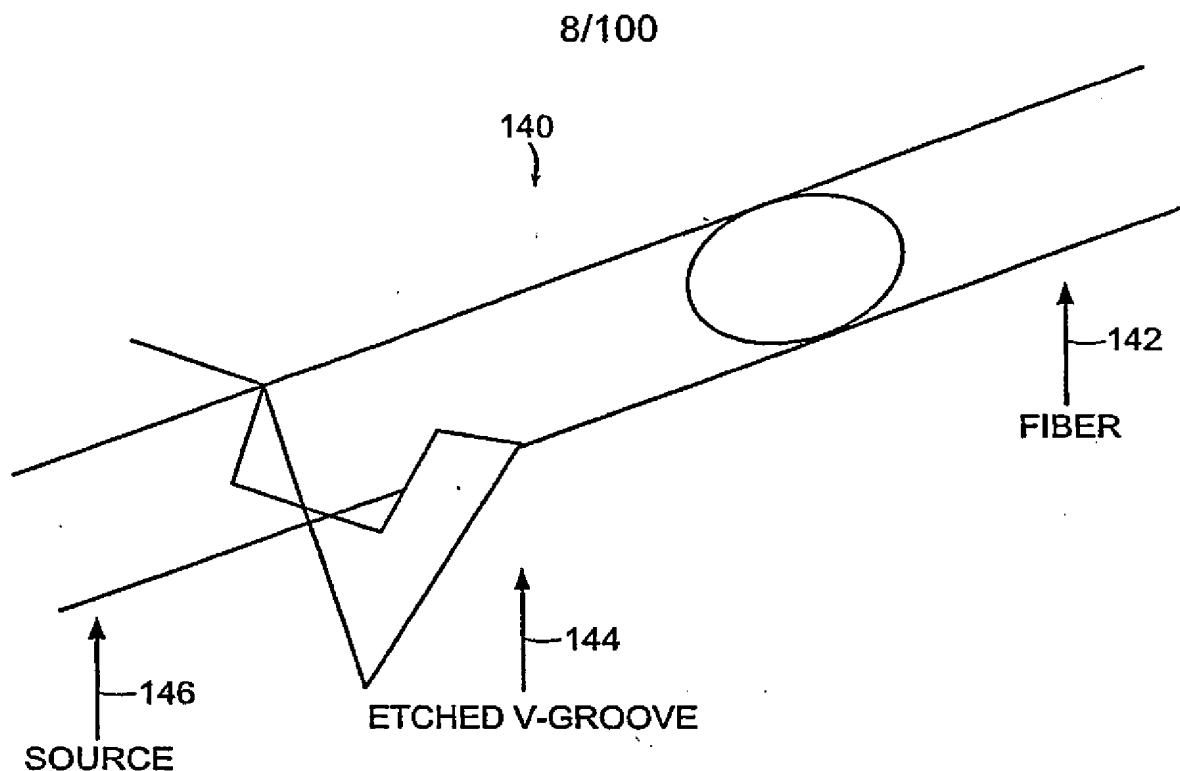


Figure 11A

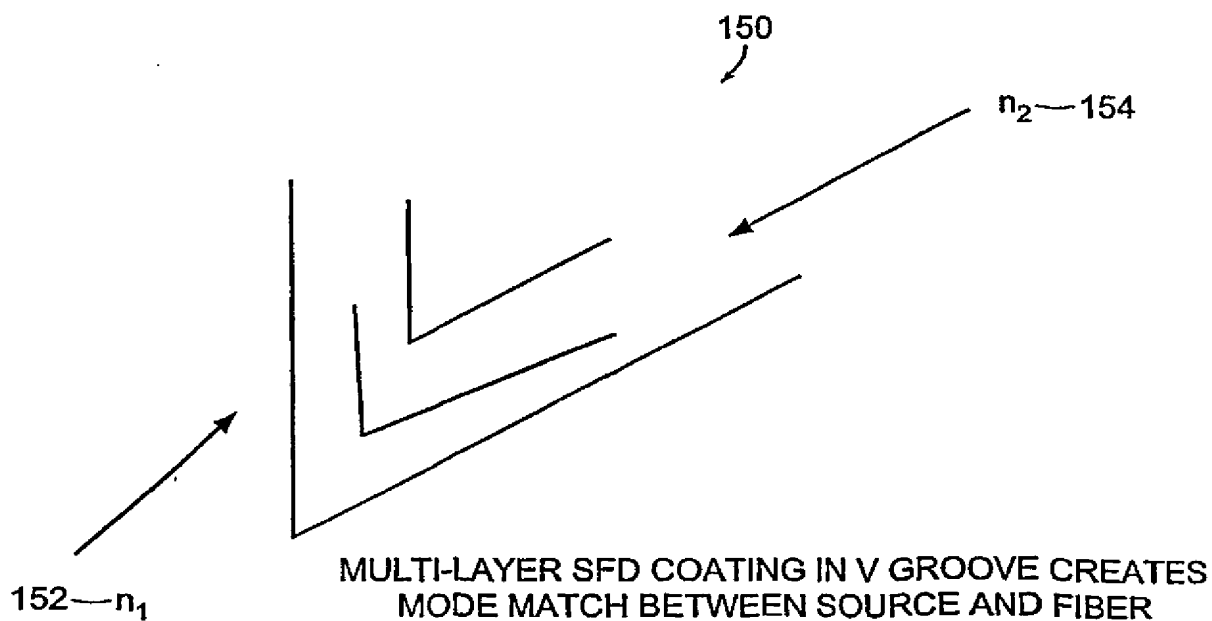


Figure 11B

9/100

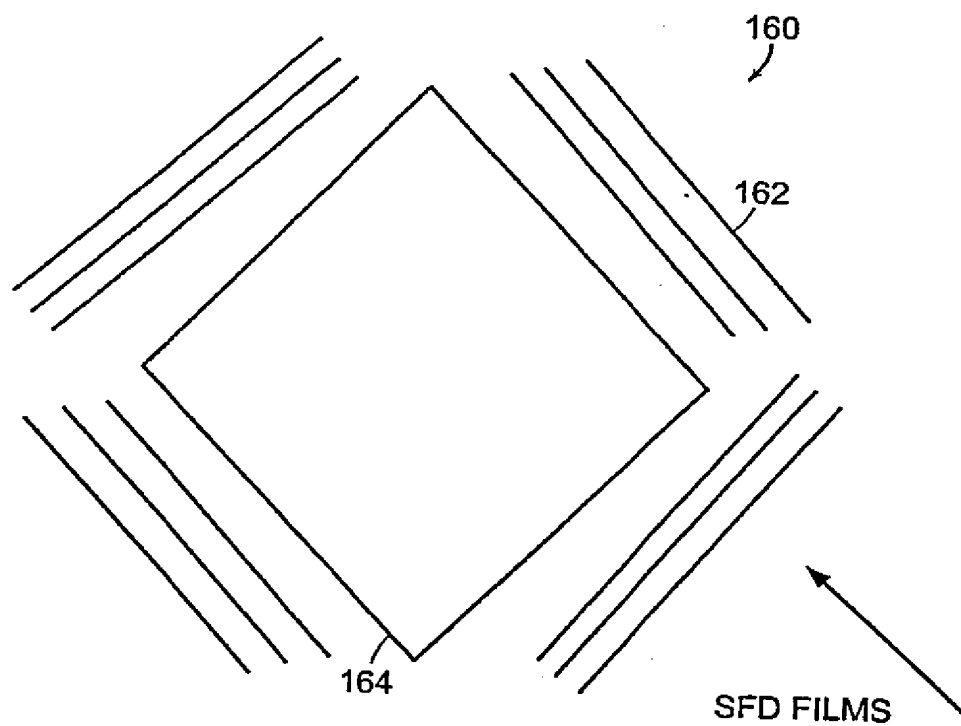


Figure 12

10/100

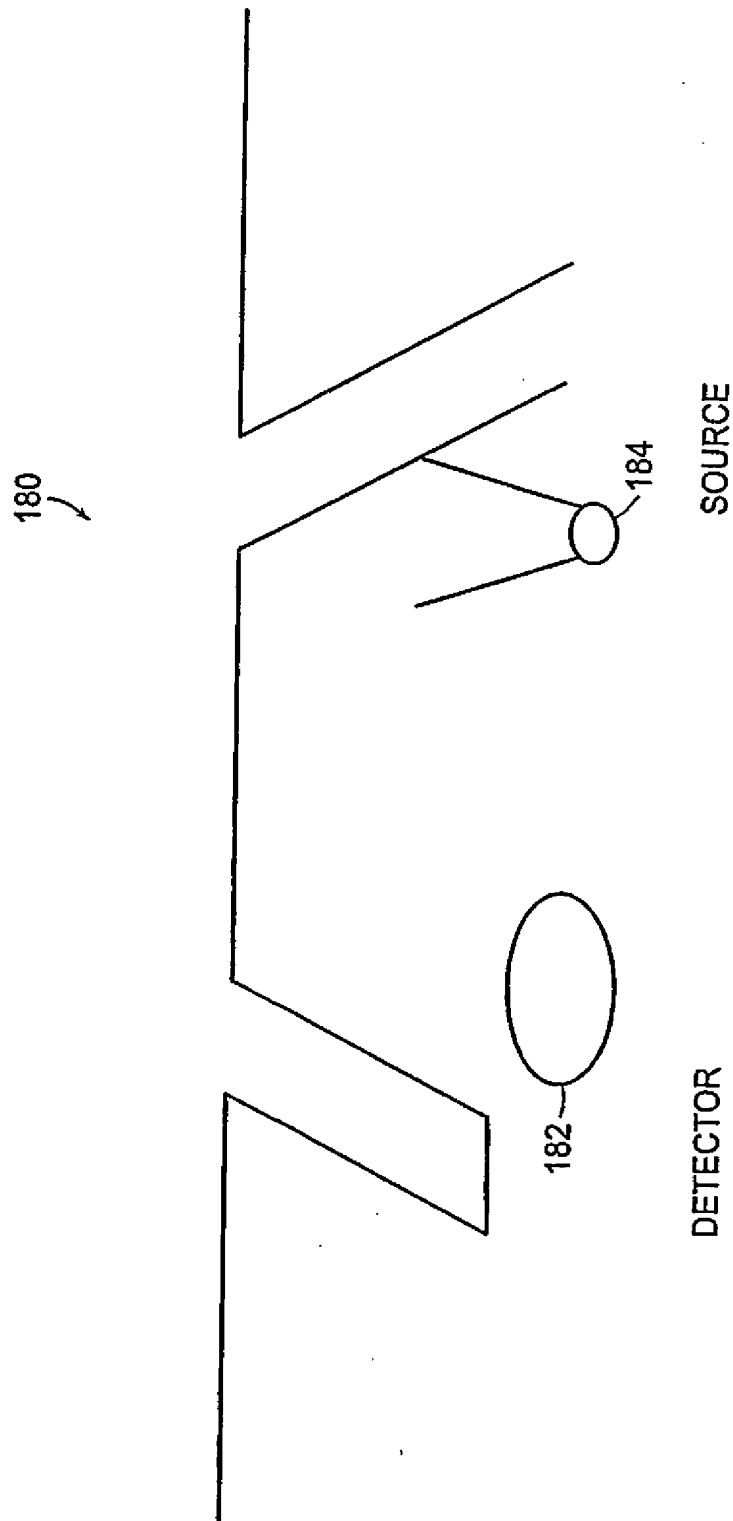


Figure 13A

SUBSTITUTE SHEET (RULE 26)

11/100

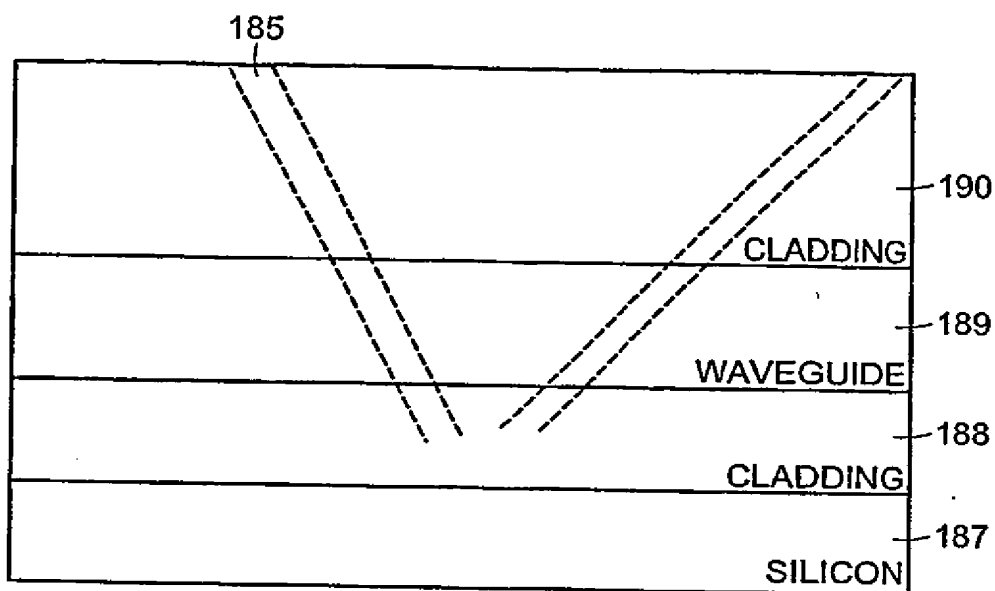


Figure 13B

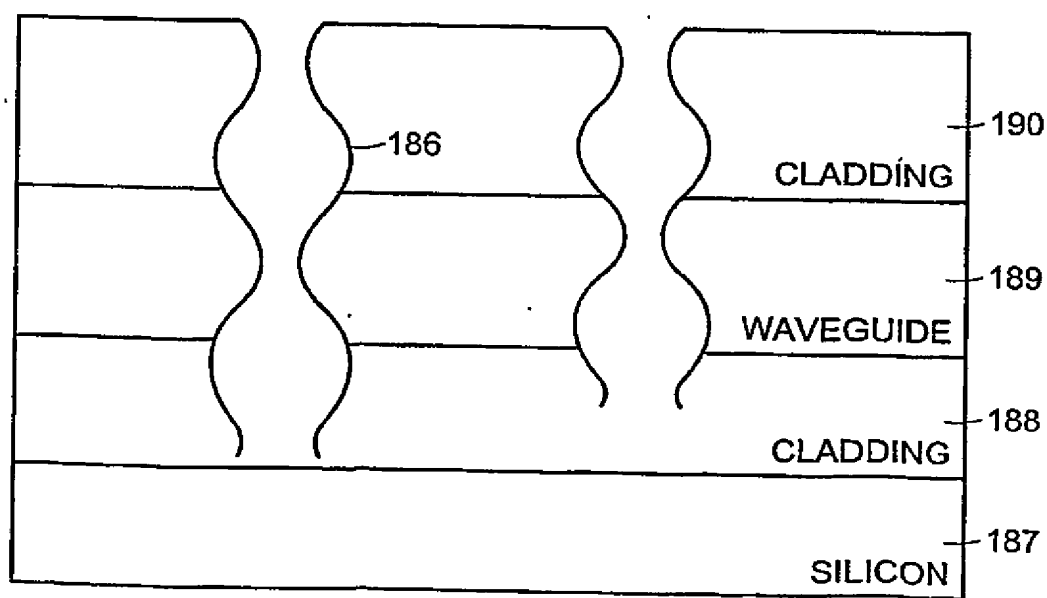


Figure 13C

SUBSTITUTE SHEET (RULE 26)

12/100

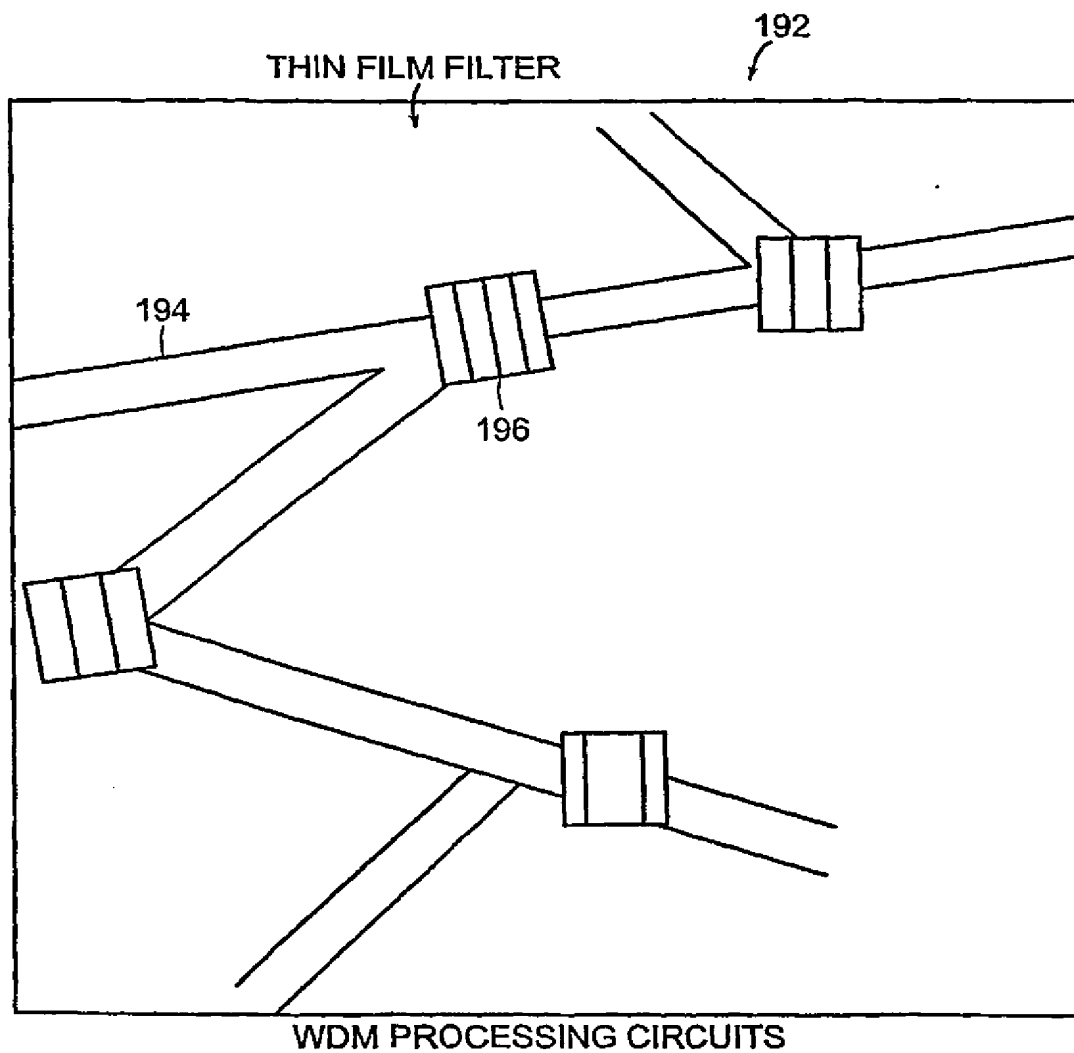


Figure 14

13/100

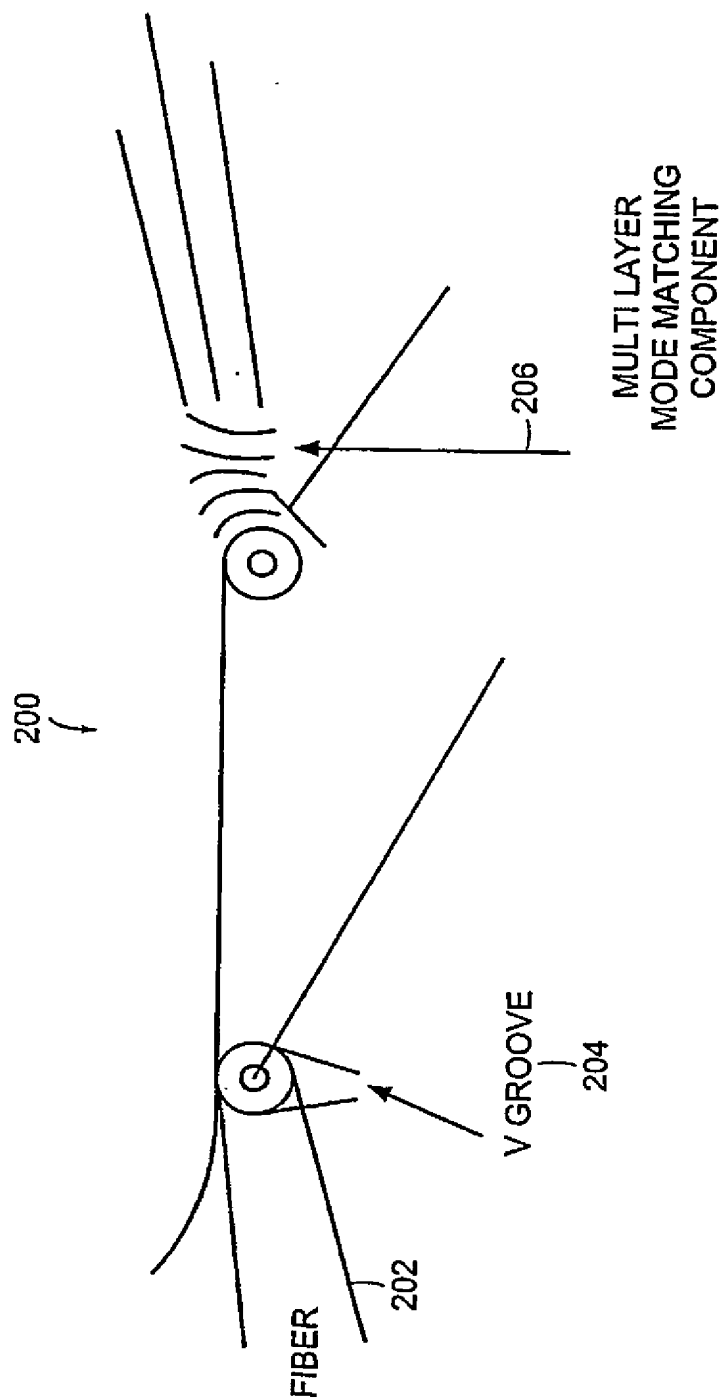


Figure 15

SUBSTITUTE SHEET (RULE 26)

14/100

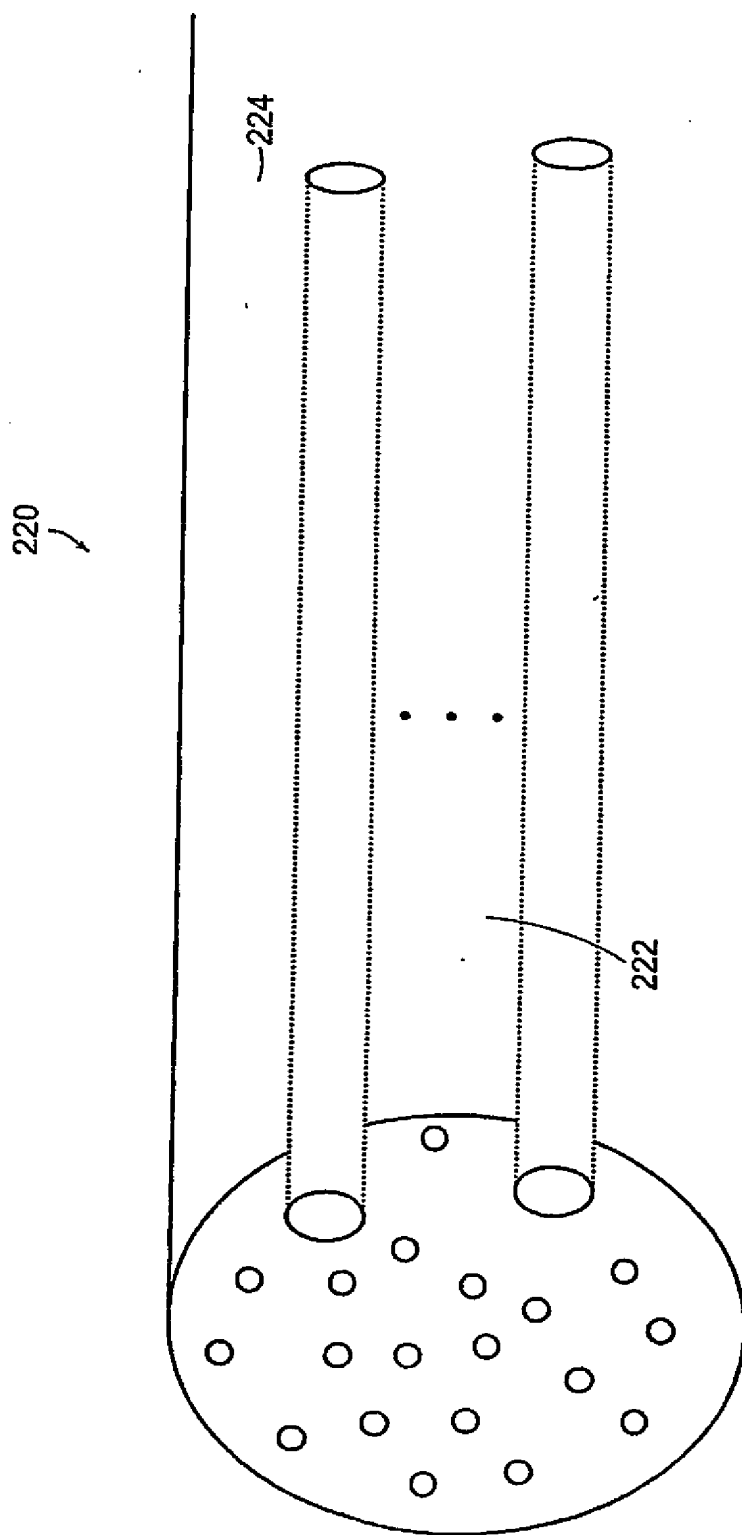


Figure 16

SUBSTITUTE SHEET (RULE 26)

15/100

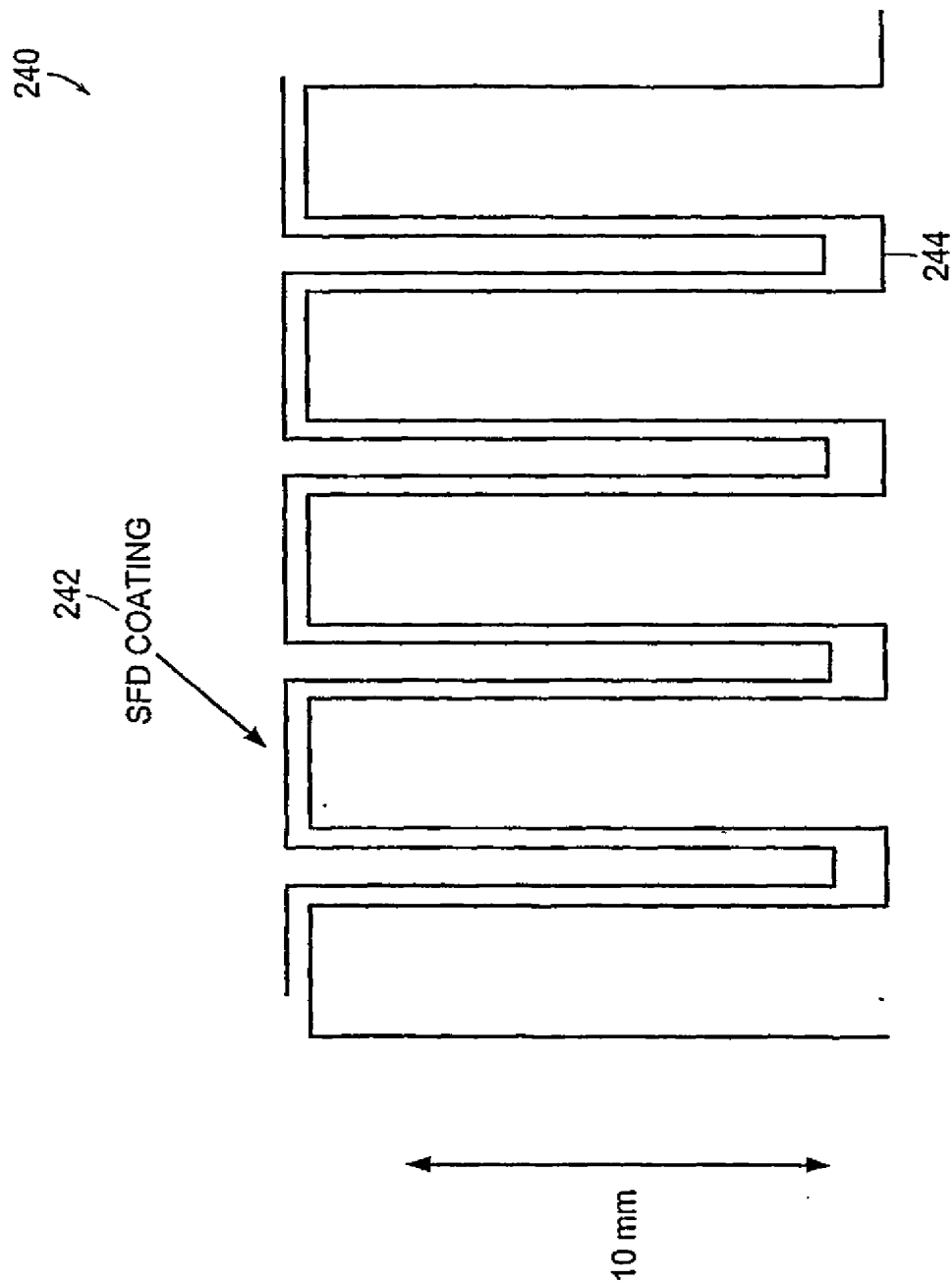


Figure 17

SUBSTITUTE SHEET (RULE 26)

16/100

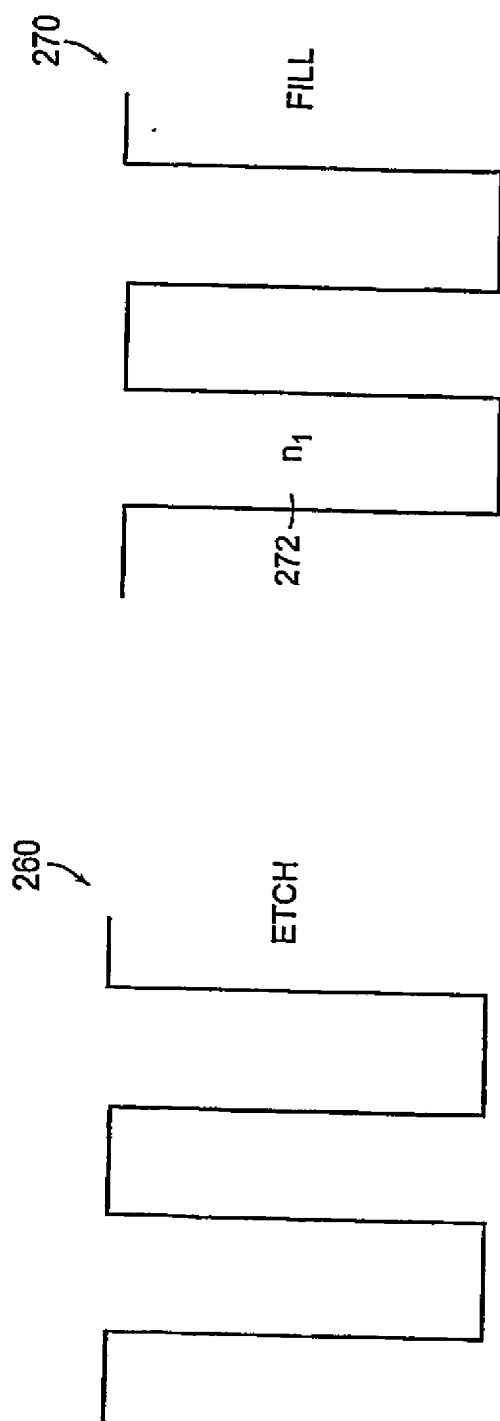


Figure 18A

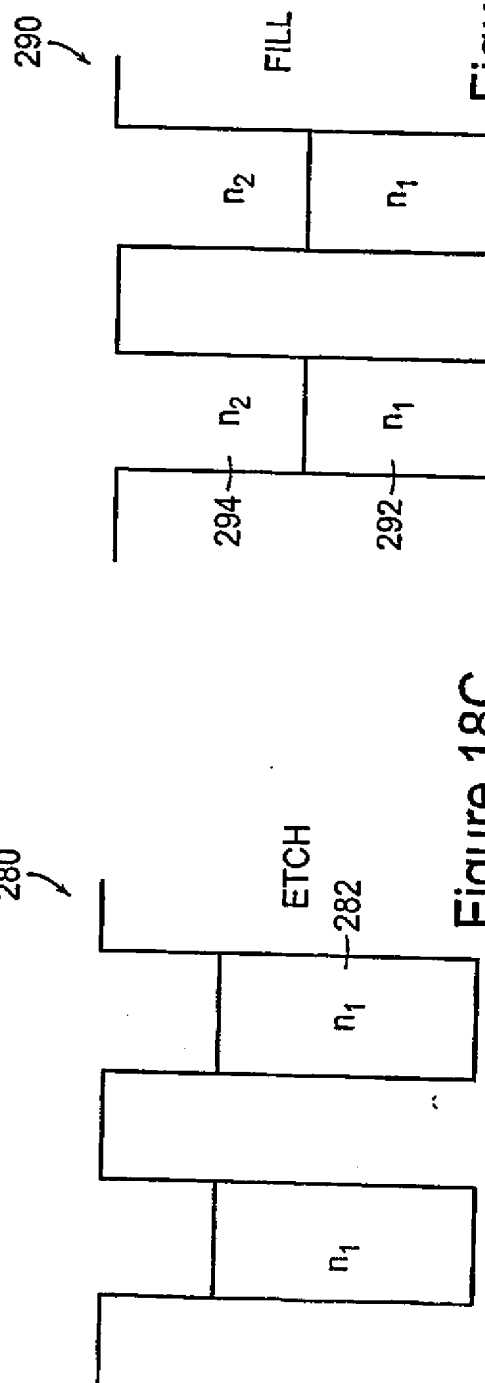


Figure 18B

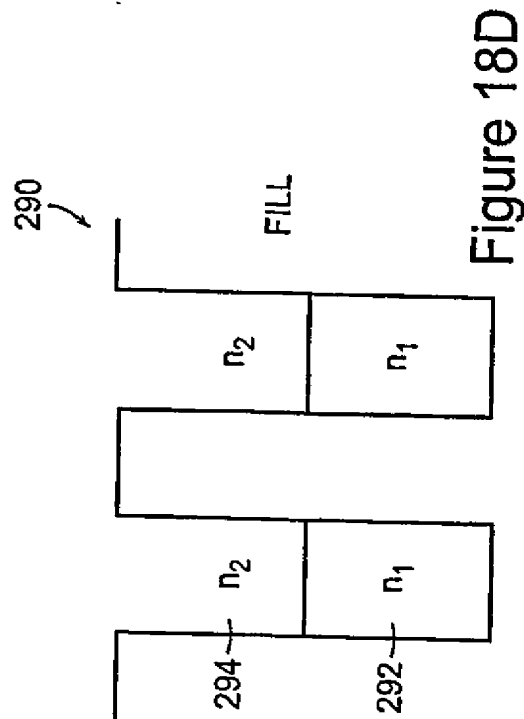


Figure 18C

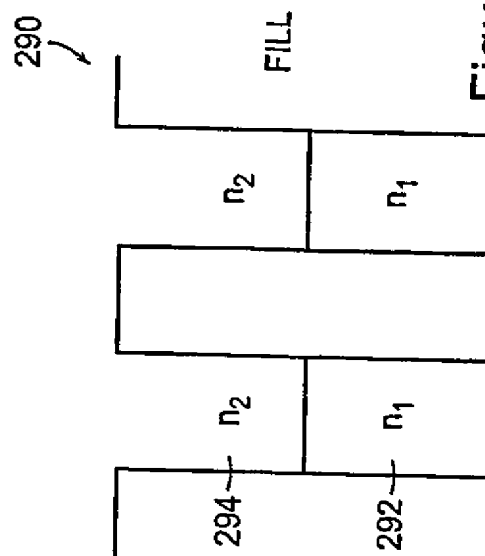


Figure 18D

17/100

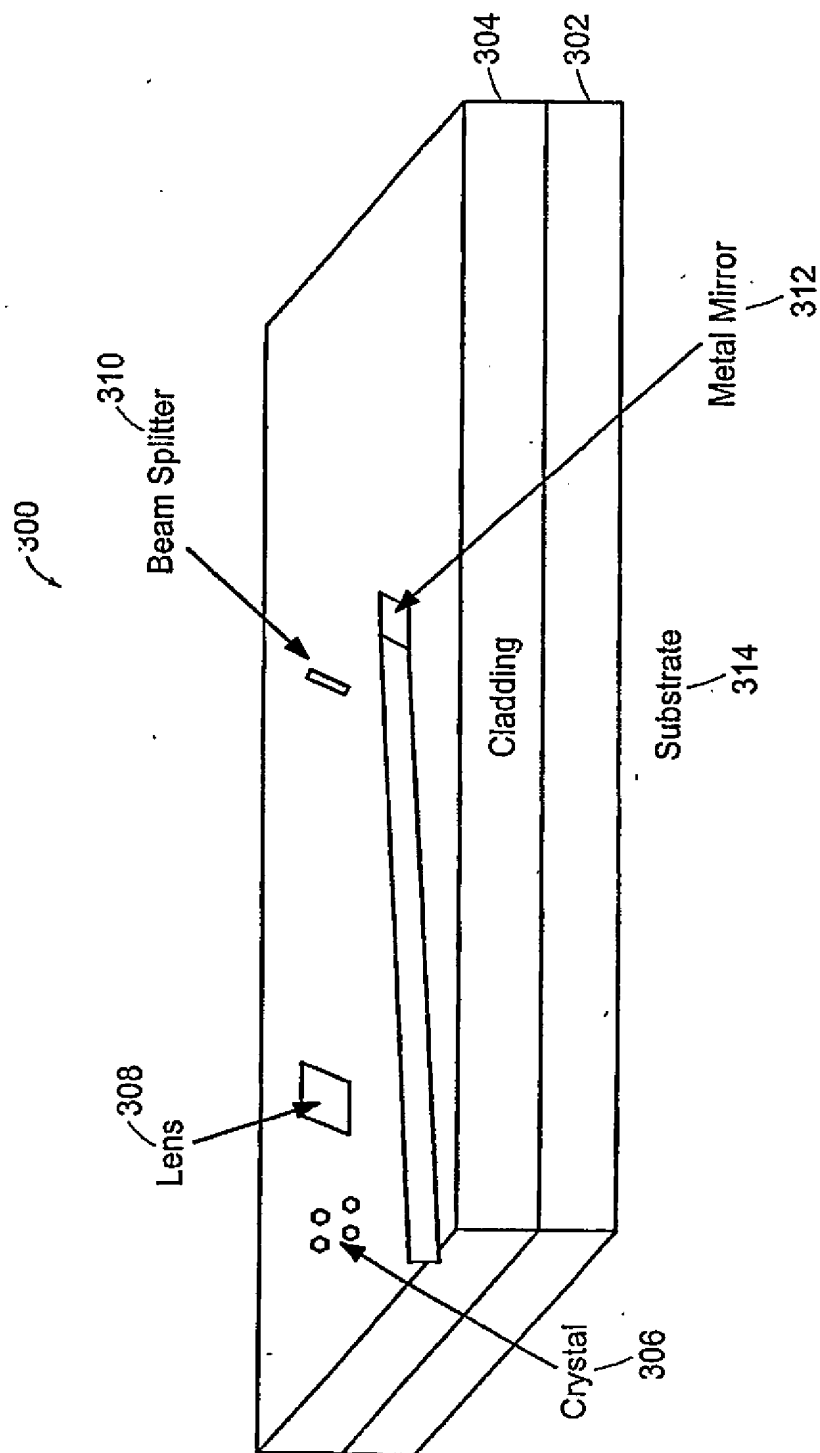


Figure 19

18/100

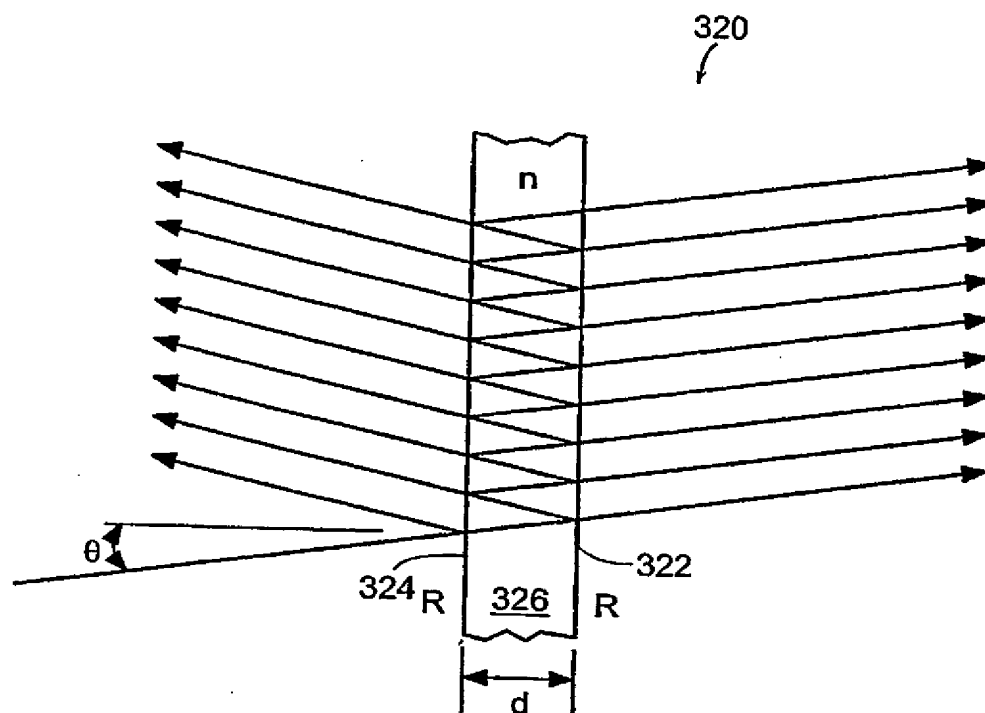


Figure 20

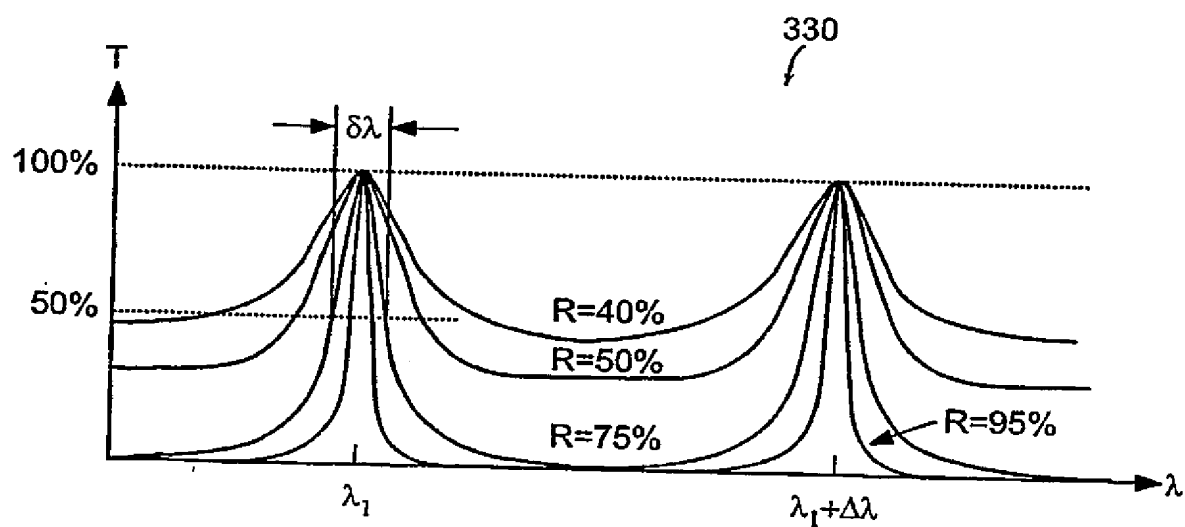


Figure 21

SUBSTITUTE SHEET (RULE 26)

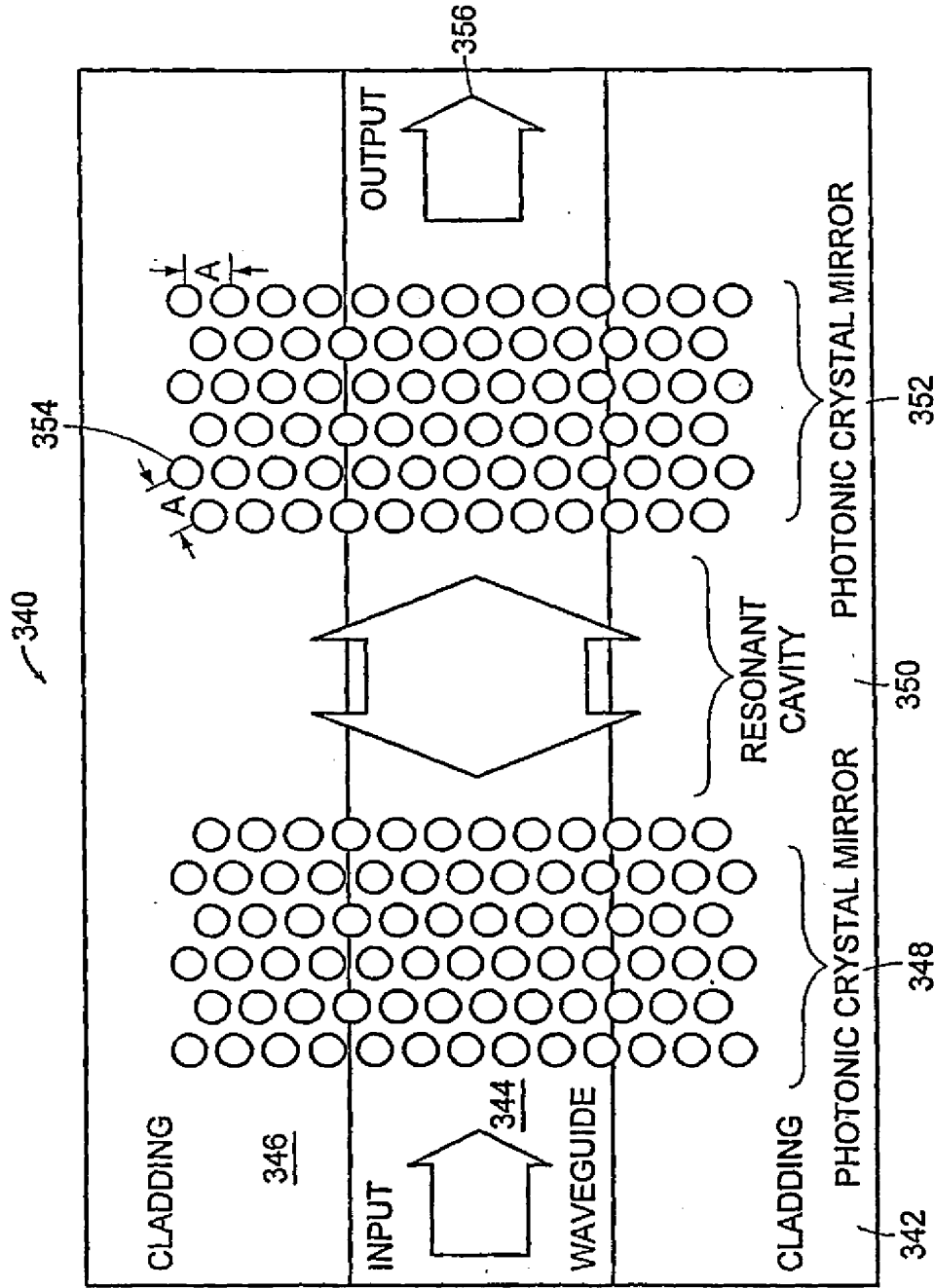


Figure 22

20/100

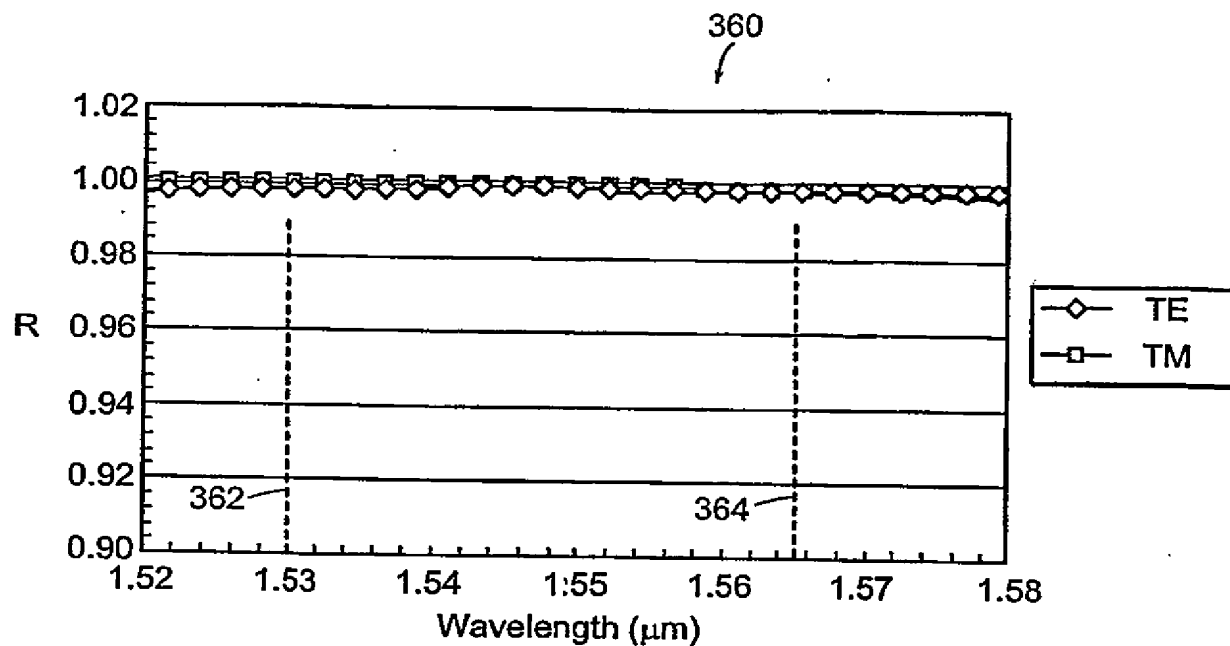


Figure 23

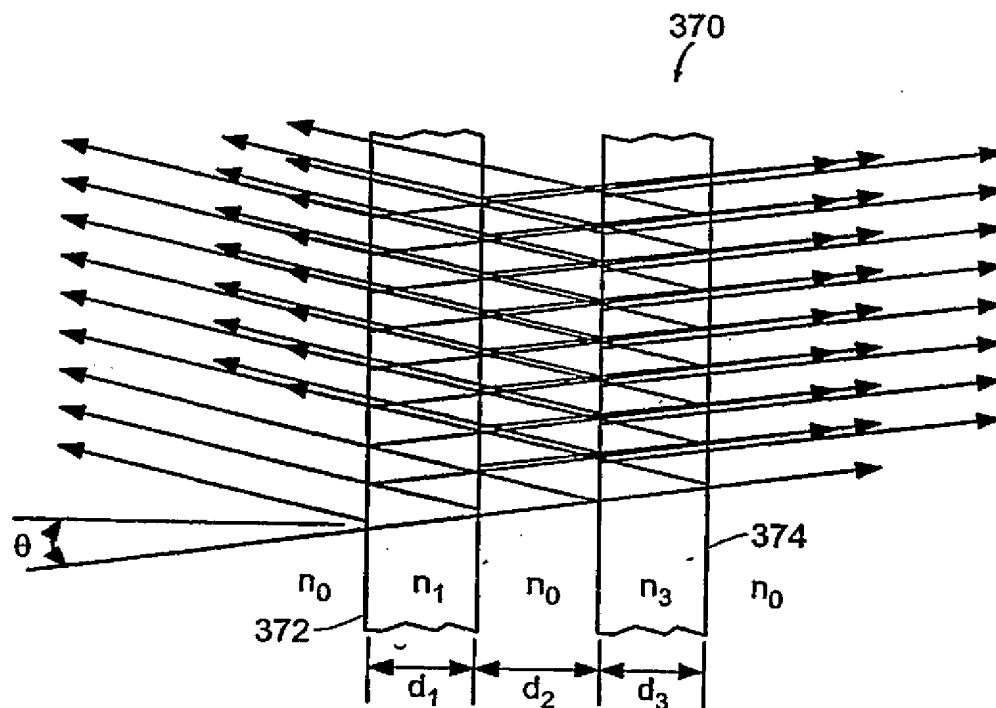


Figure 24

SUBSTITUTE SHEET (RULE 26)

21/100

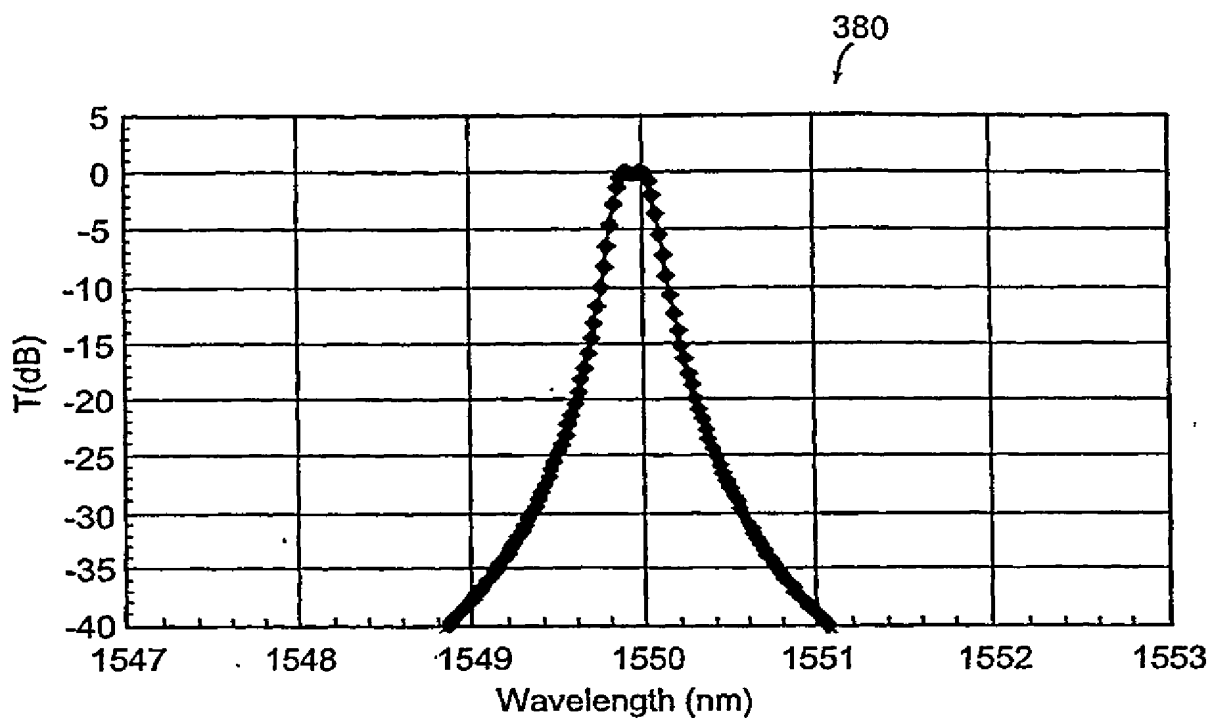


Figure 25

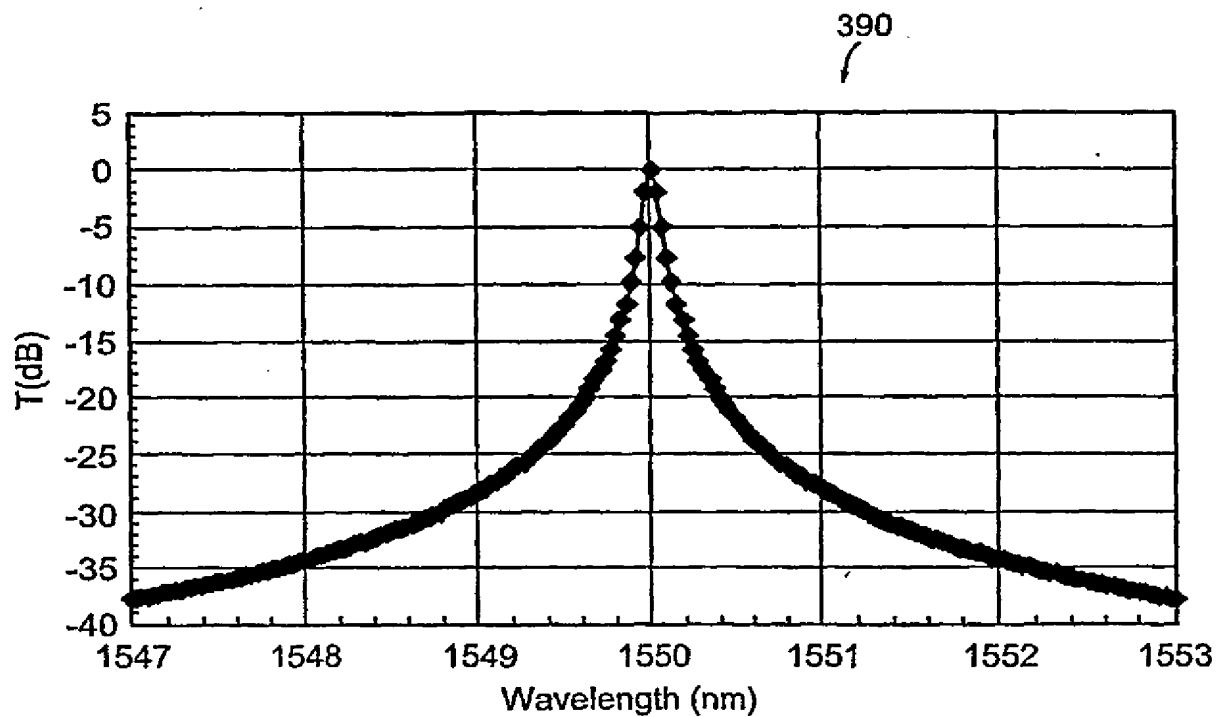


Figure 26

SUBSTITUTE SHEET (RULE 26)

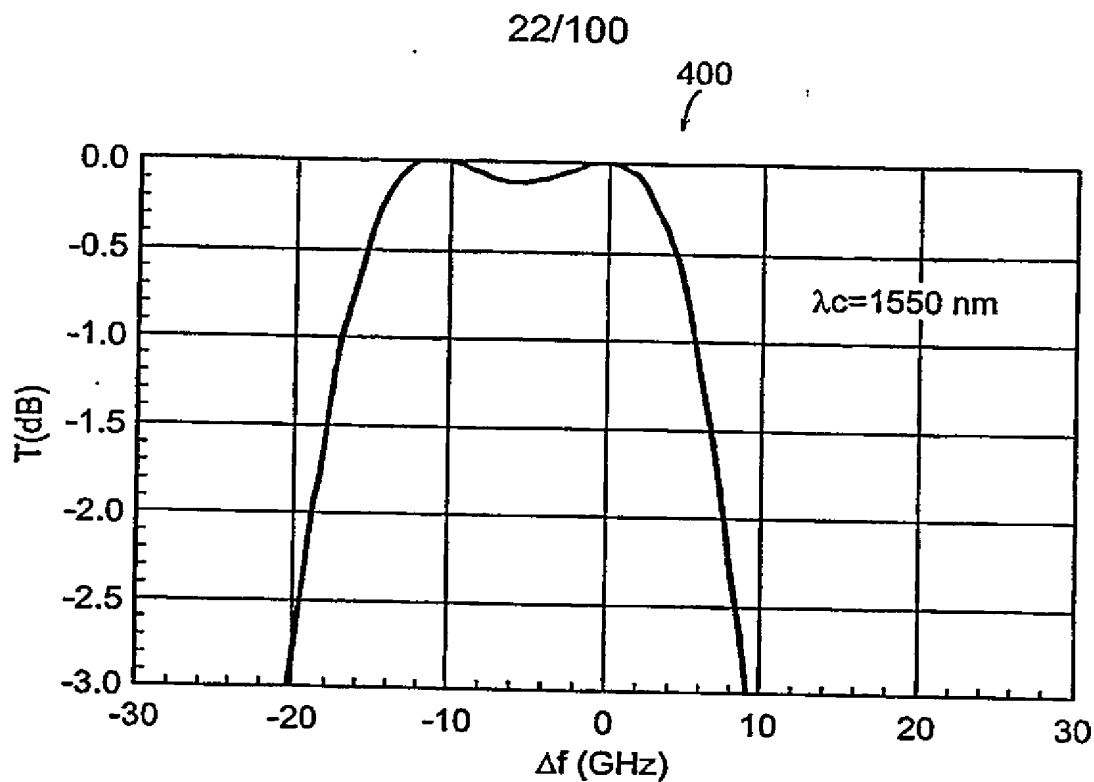


Figure 27

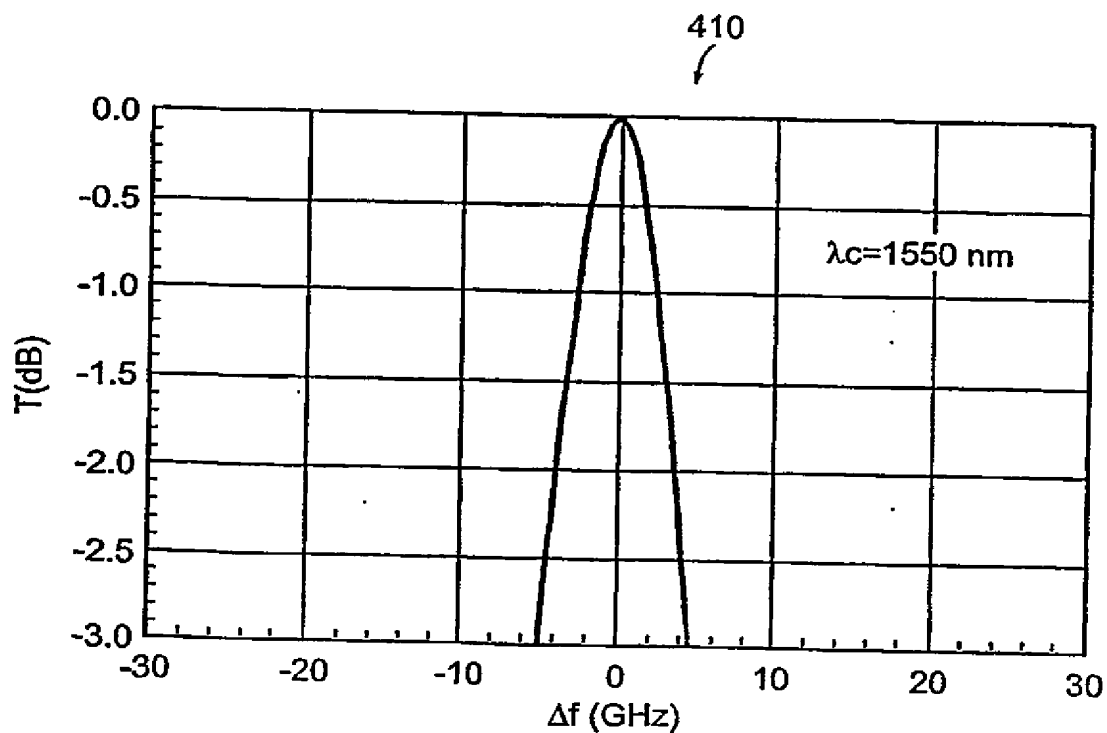


Figure 28

SUBSTITUTE SHEET (RULE 26)

23/100

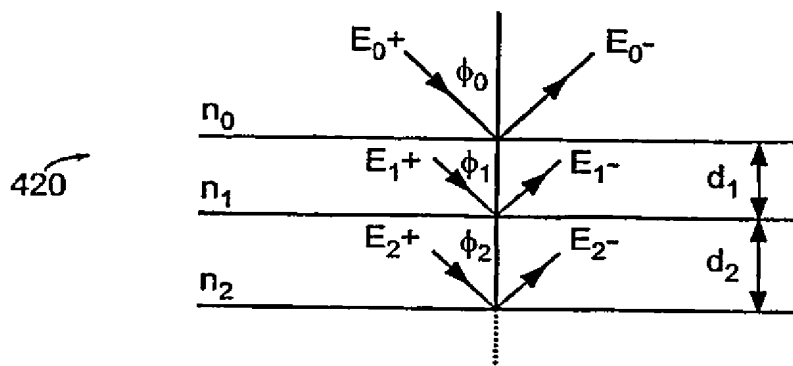


Figure 29A

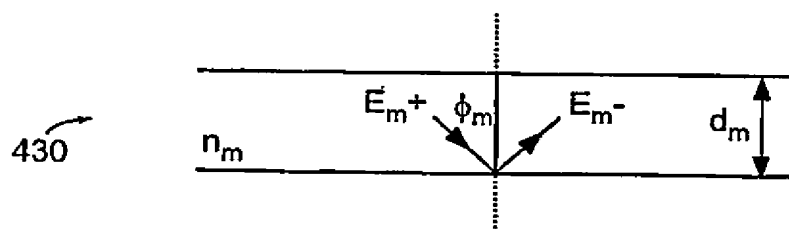


Figure 29B

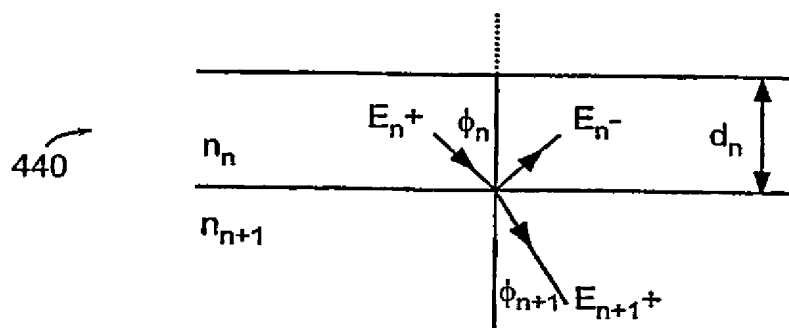


Figure 29C

SUBSTITUTE SHEET (RULE 26)

24/100

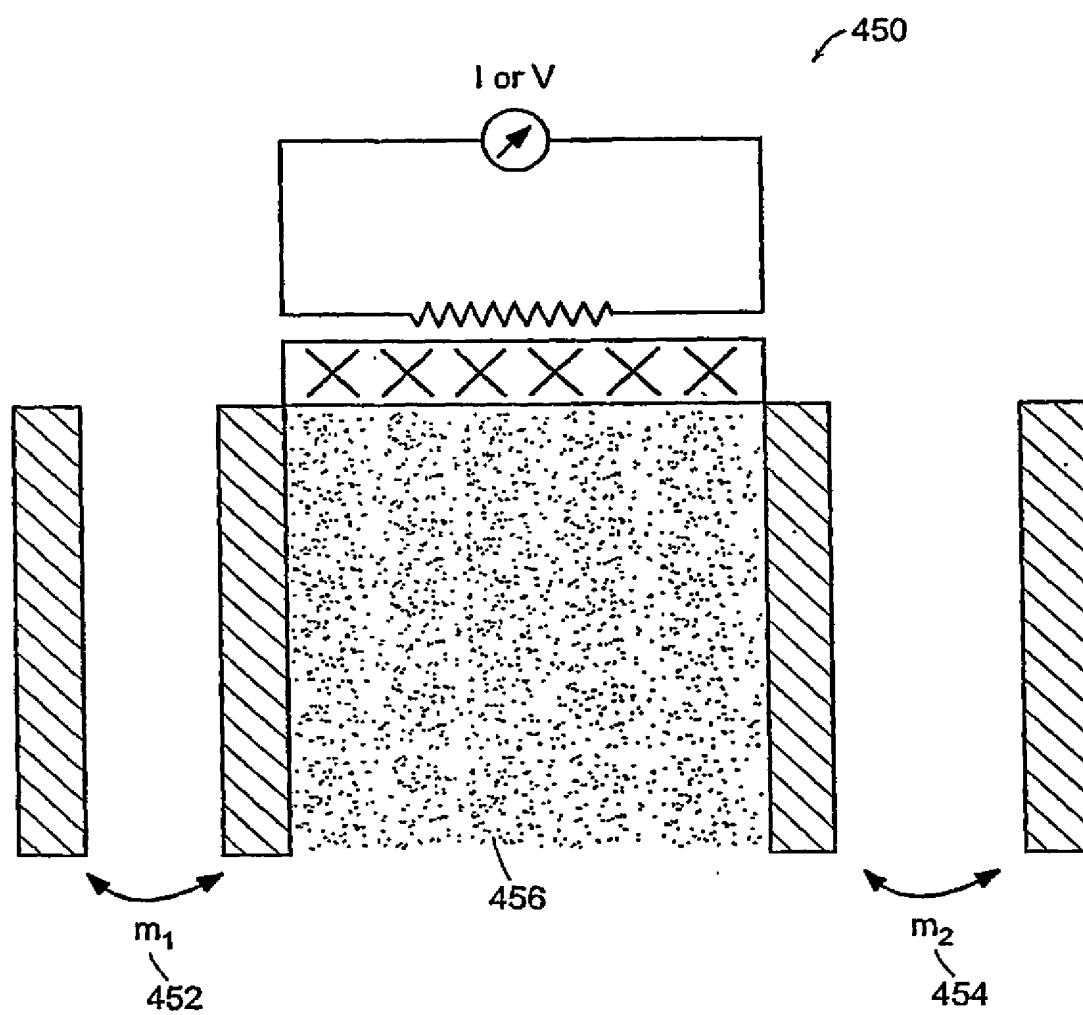


Figure 30A

SUBSTITUTE SHEET (RULE 26)

25/100

470

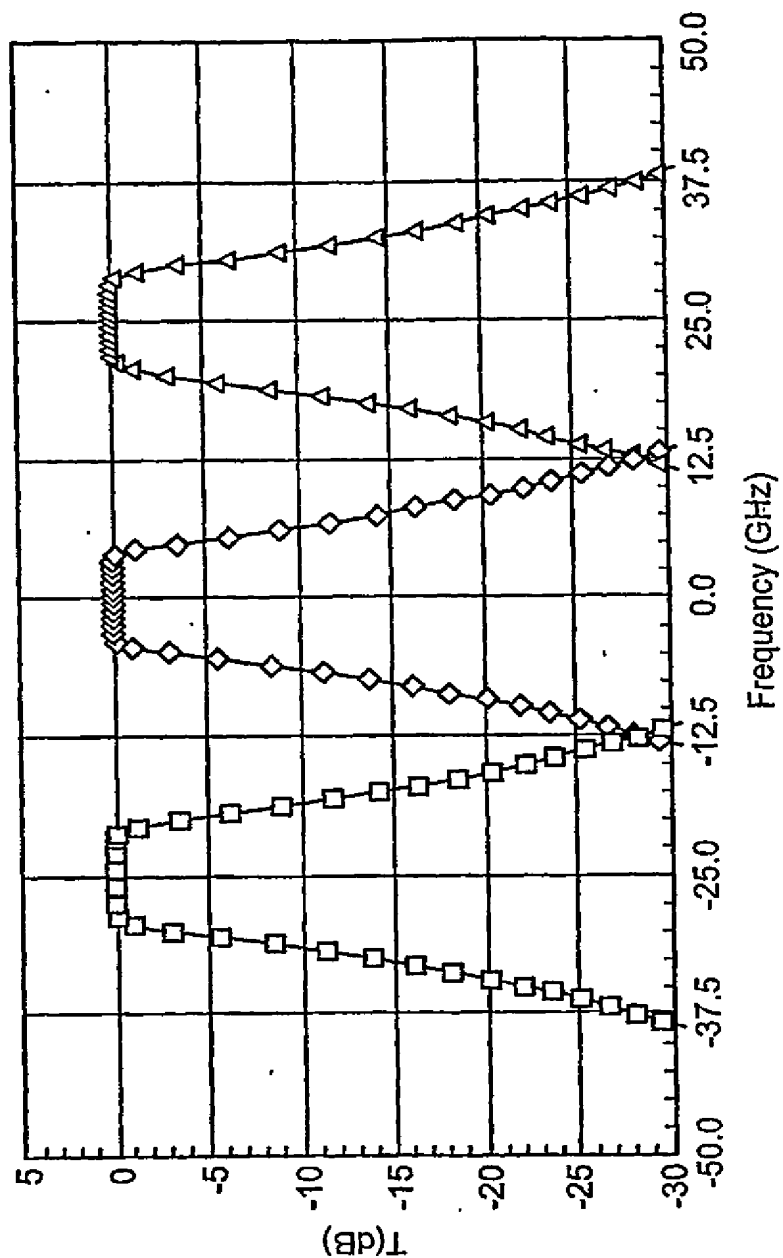


Figure 30B

26/100

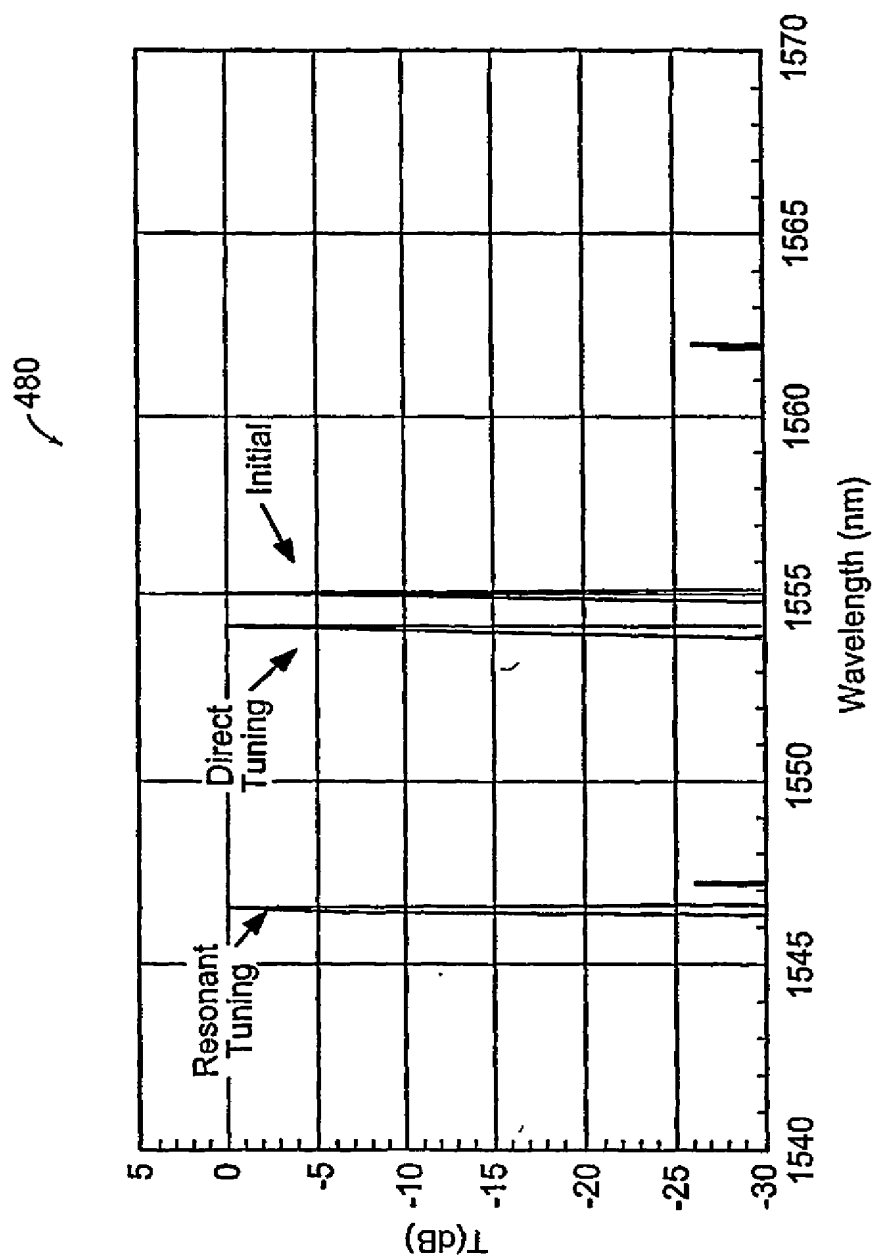


Figure 31

SUBSTITUTE SHEET (RULE 26)

27/100

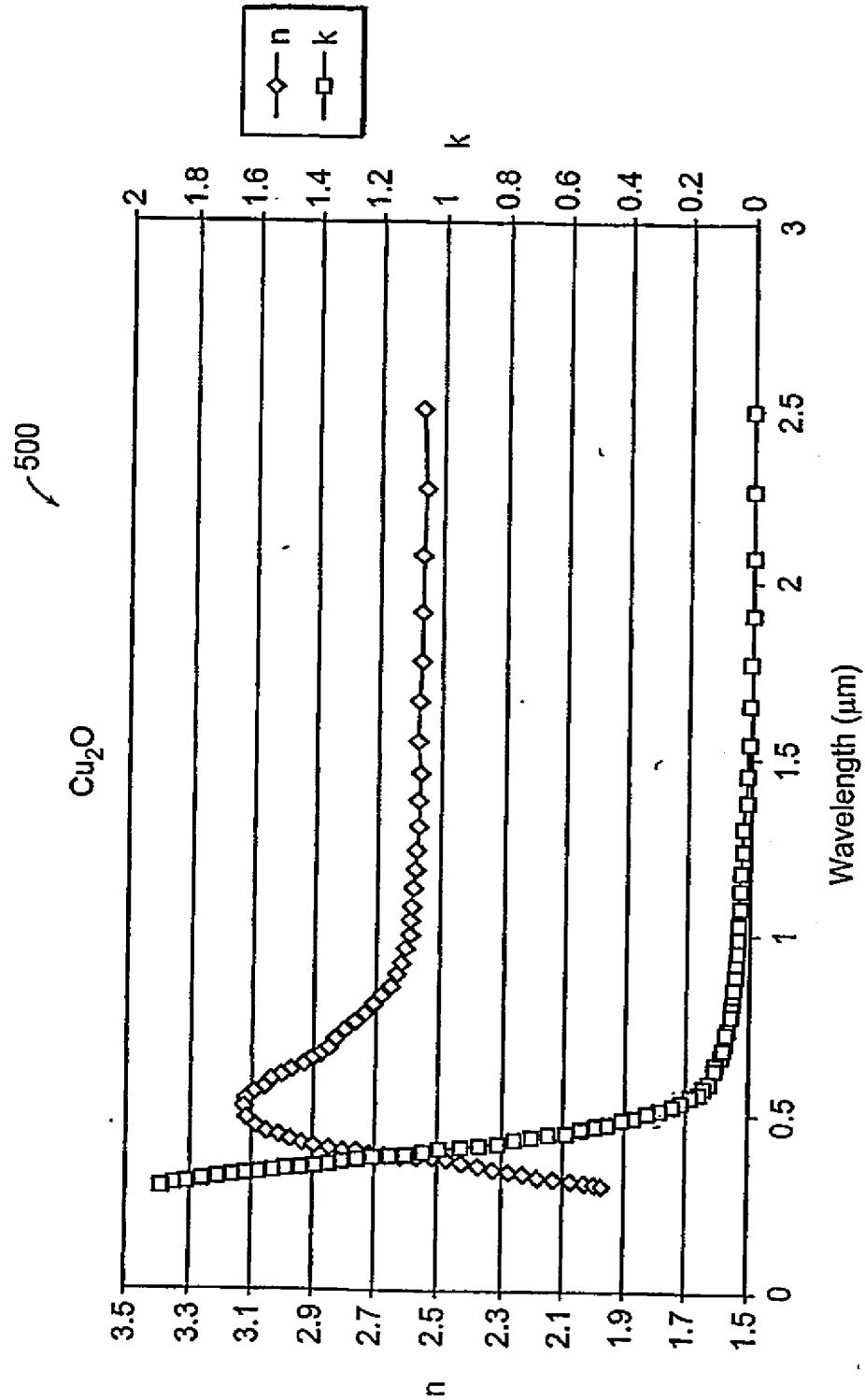


Figure 32

SUBSTITUTE SHEET (RULE 26)

28/100

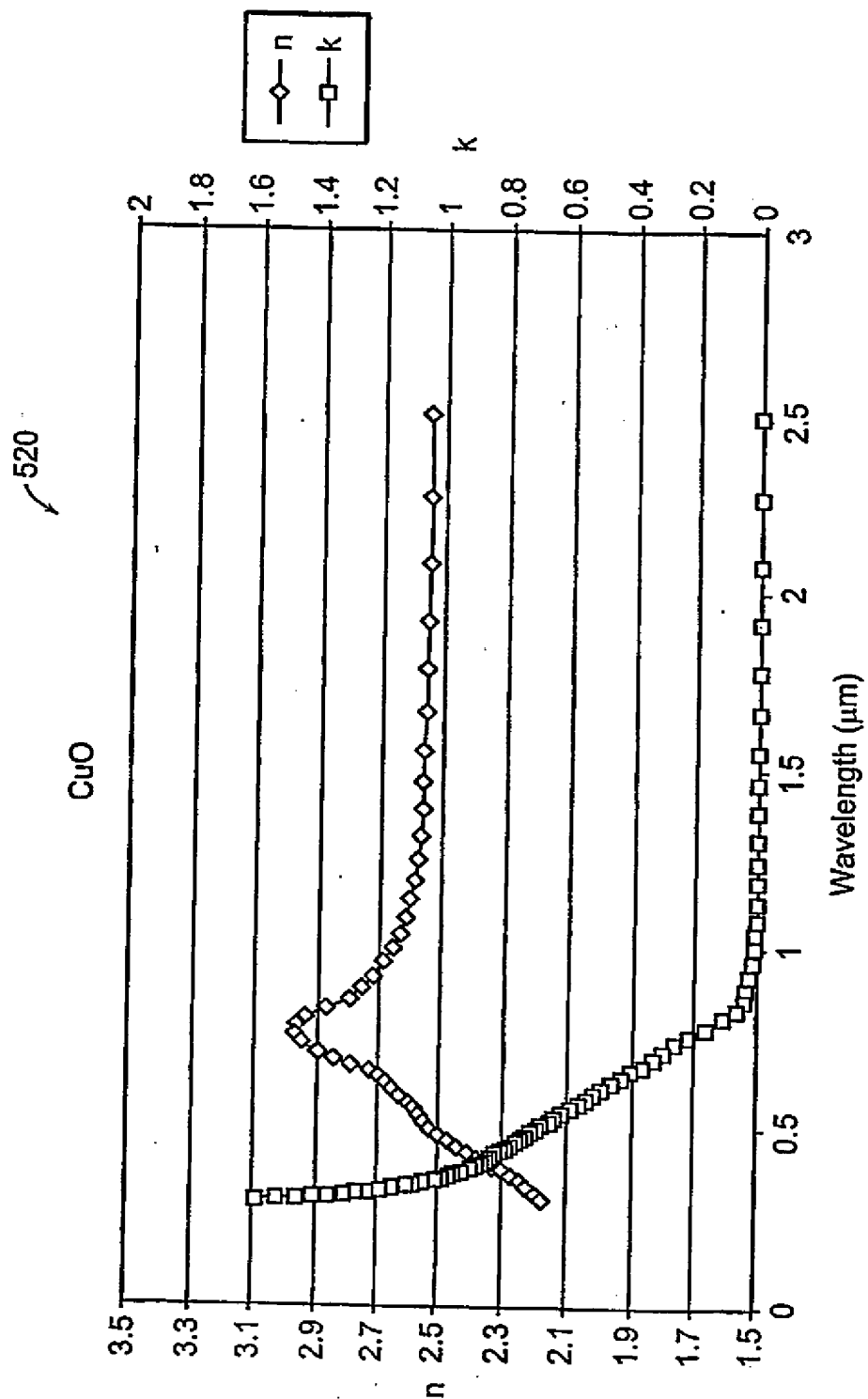


Figure 33

SUBSTITUTE SHEET (RULE 26)

29/100

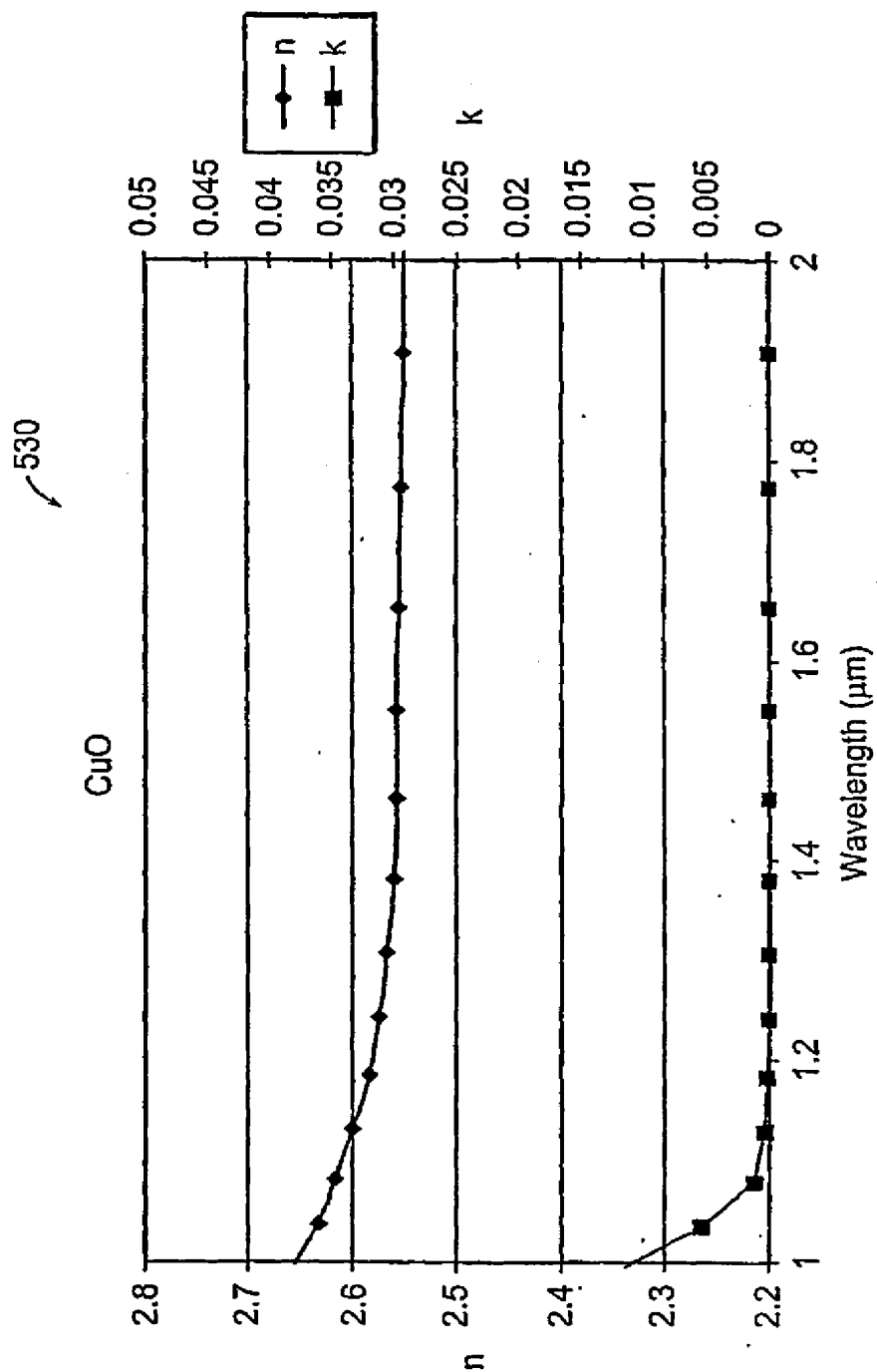


Figure 34

SUBSTITUTE SHEET (RULE 26)

30/100

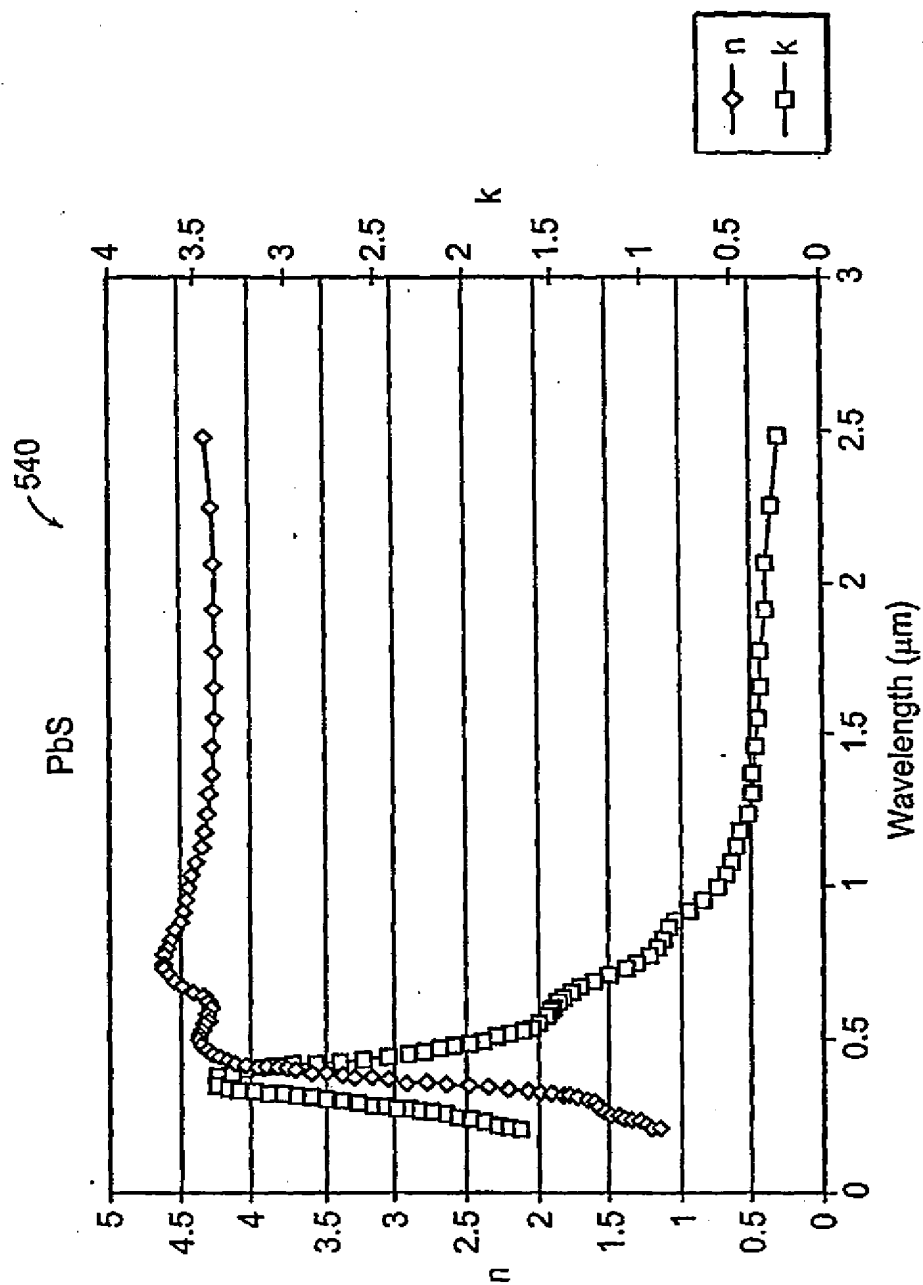


Figure 35

SUBSTITUTE SHEET (RULE 26)

31/100

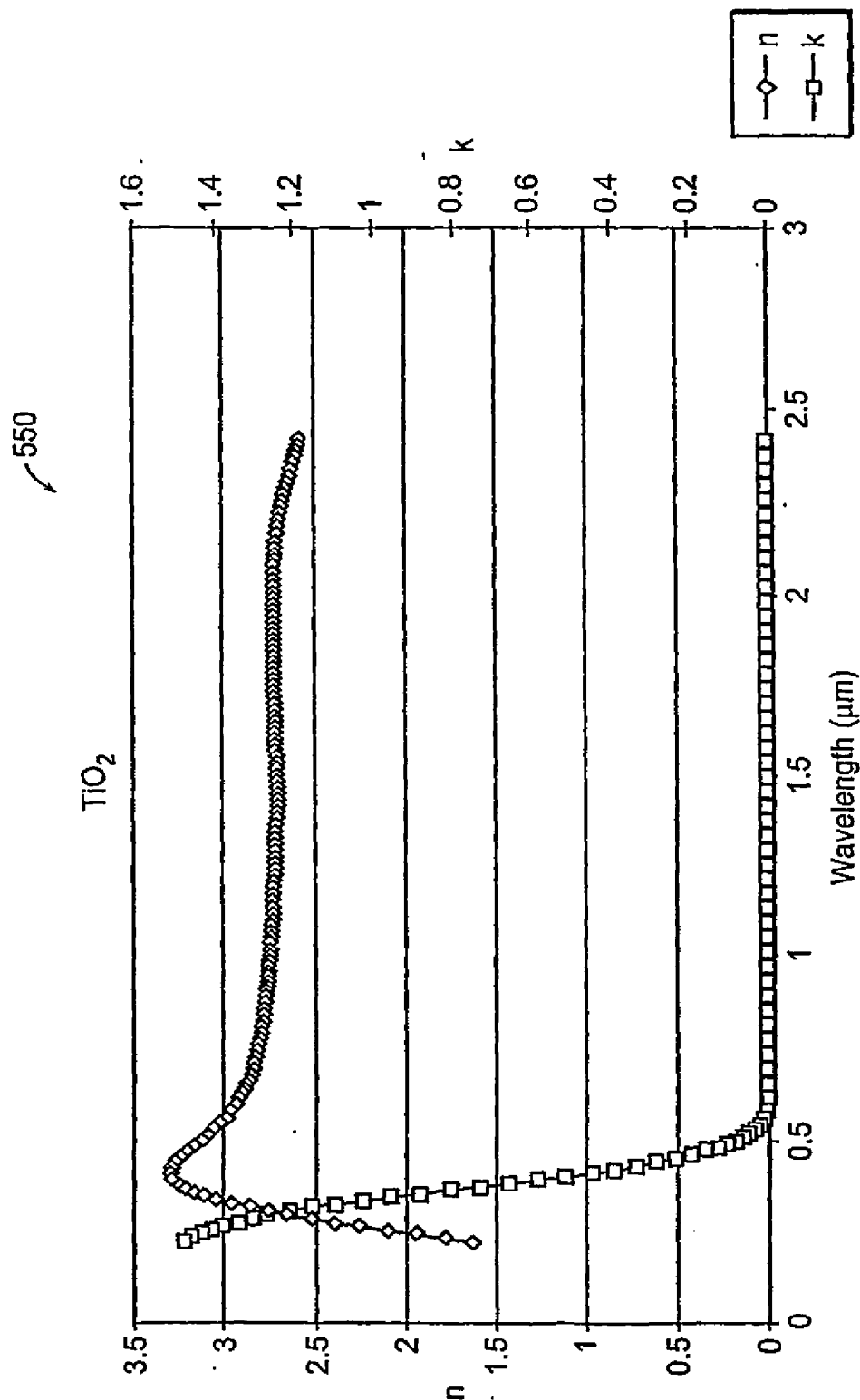


Figure 36

SUBSTITUTE SHEET (RULE 26)

32/100

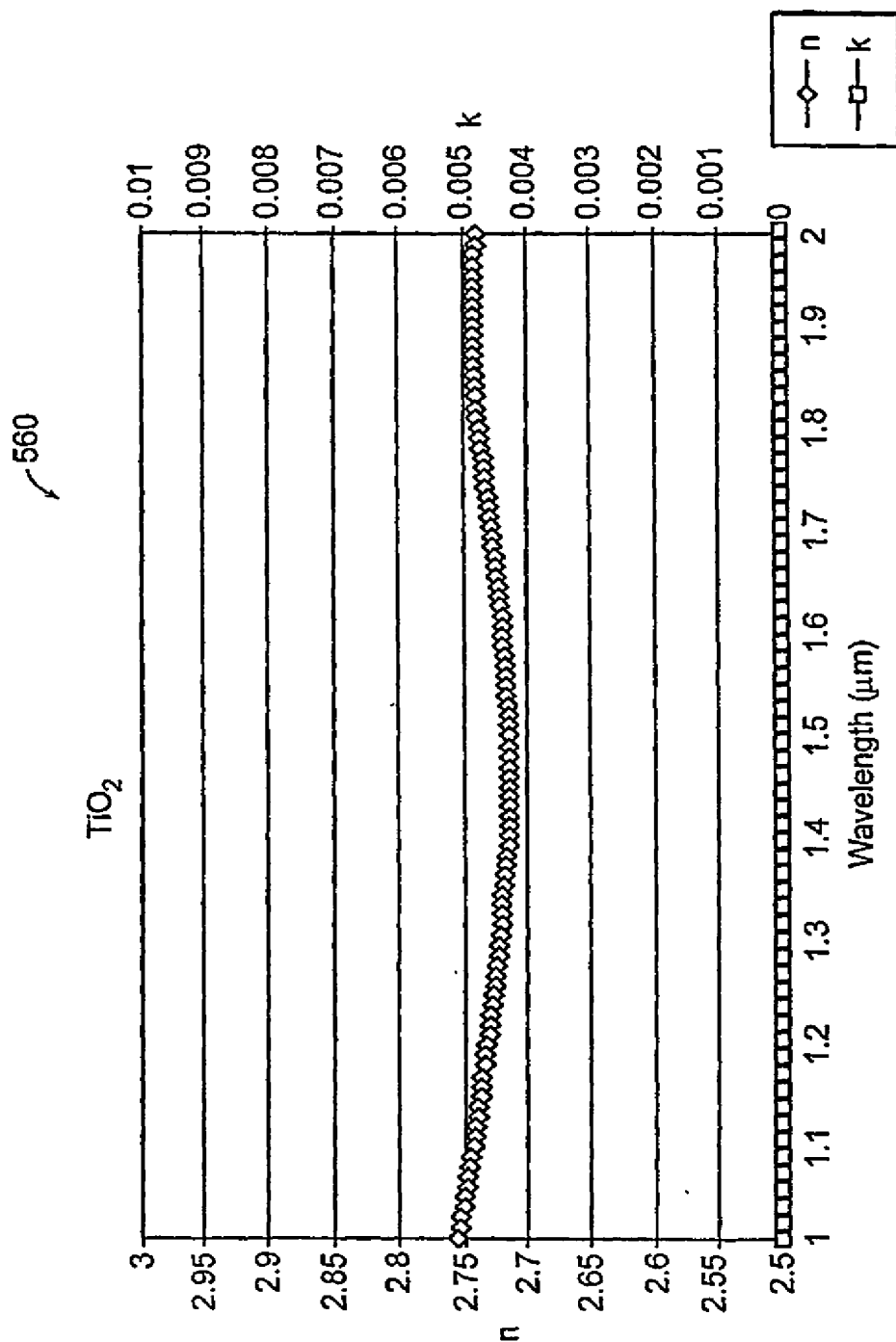


Figure 37

33/100

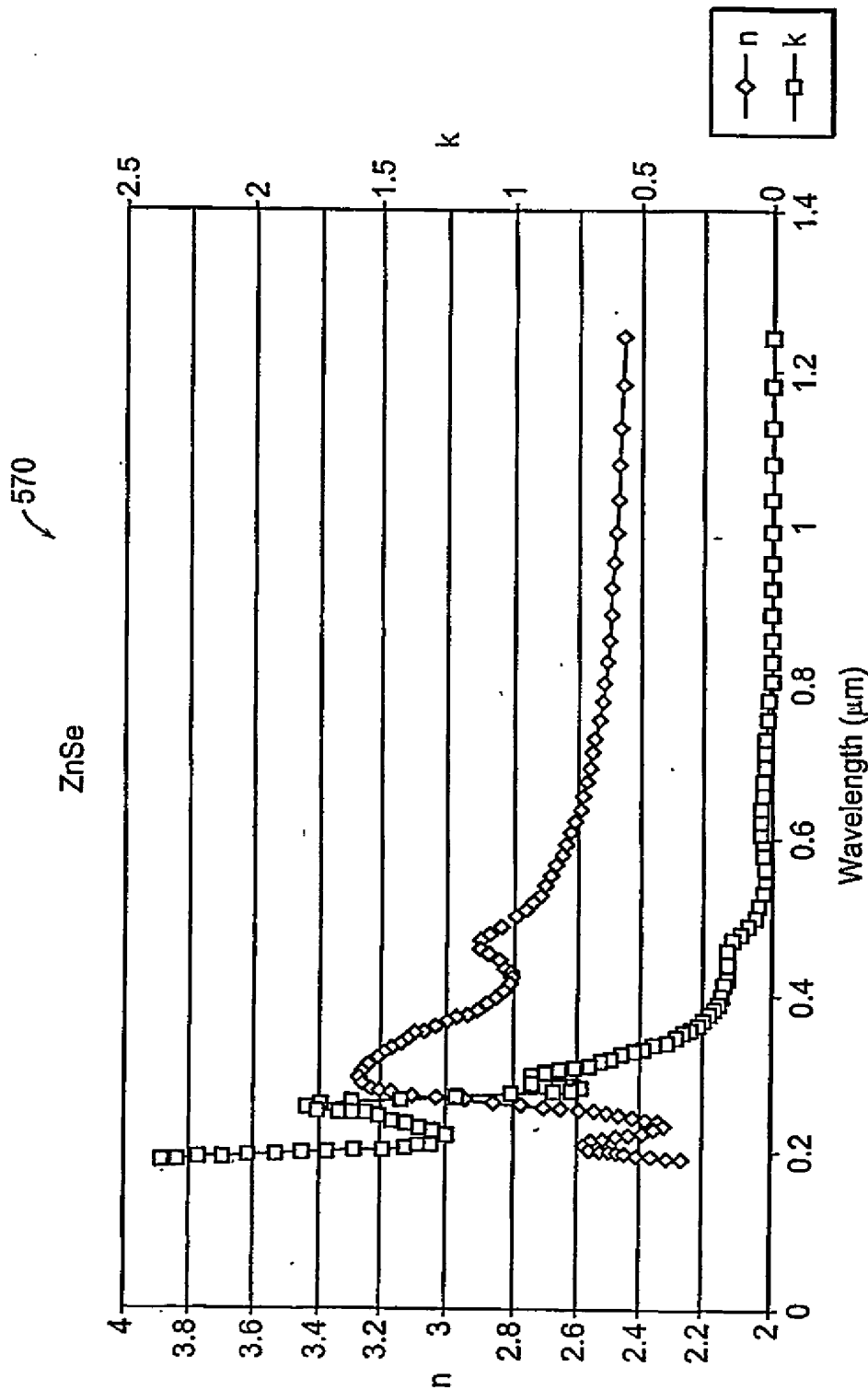


Figure 38

SUBSTITUTE SHEET (RULE 26)

34/100

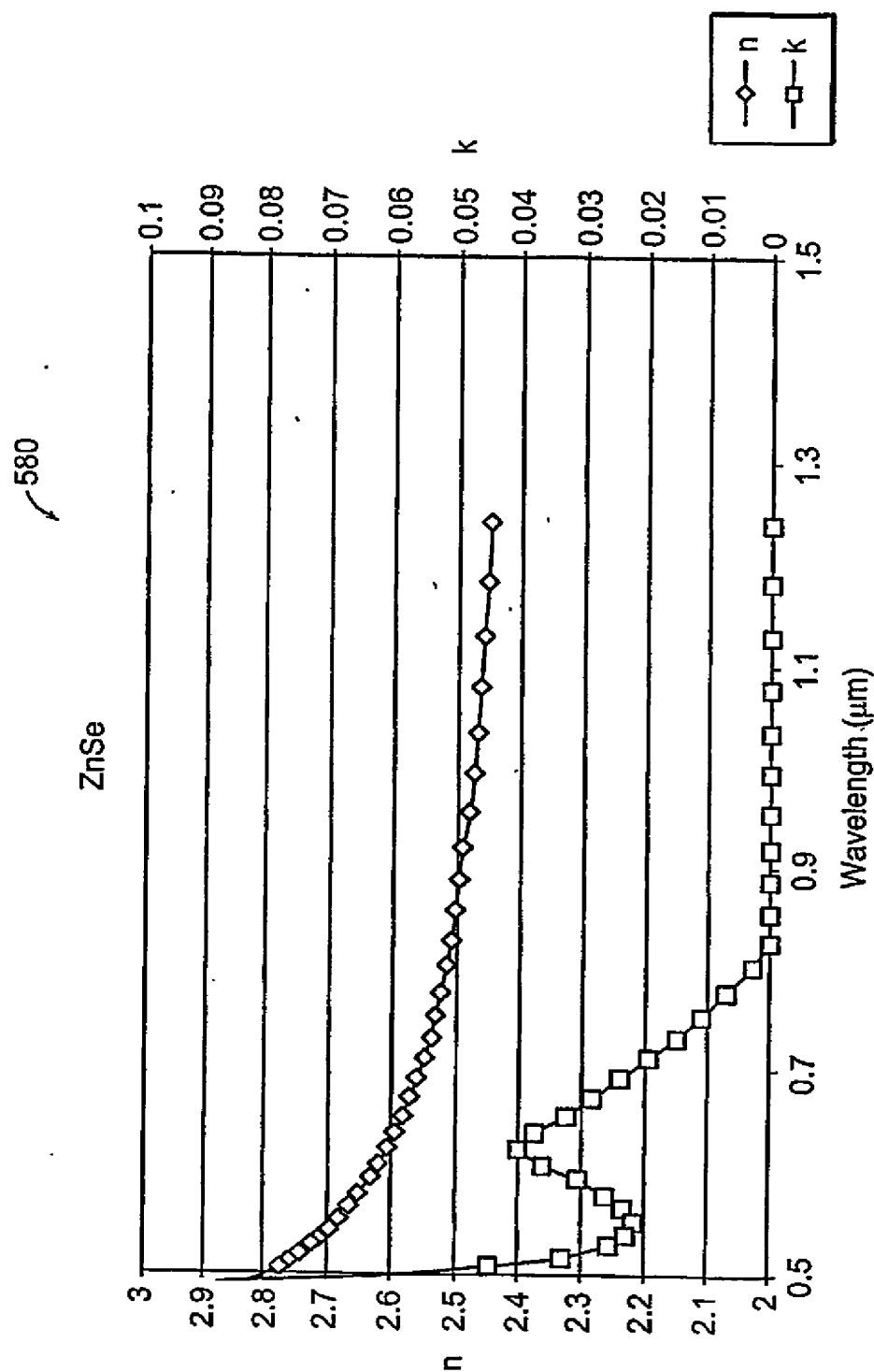


Figure 39

35/100

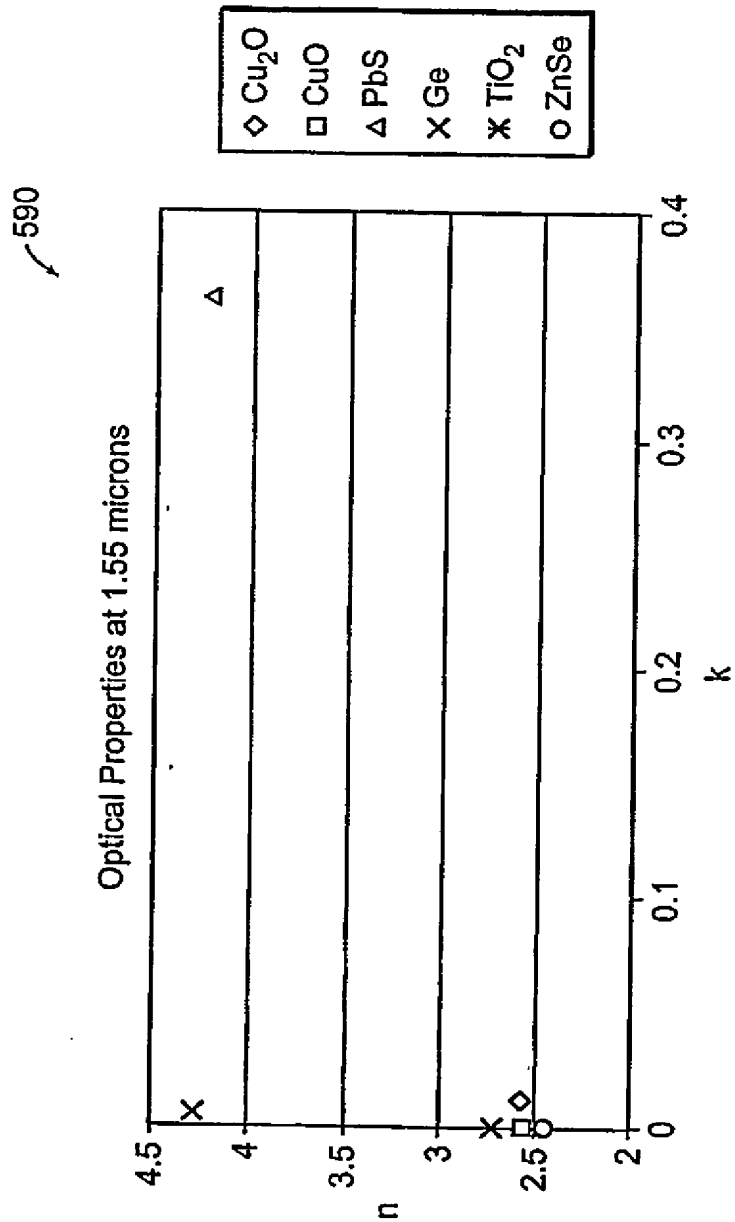


Figure 40

SUBSTITUTE SHEET (RULE 26)

36/100

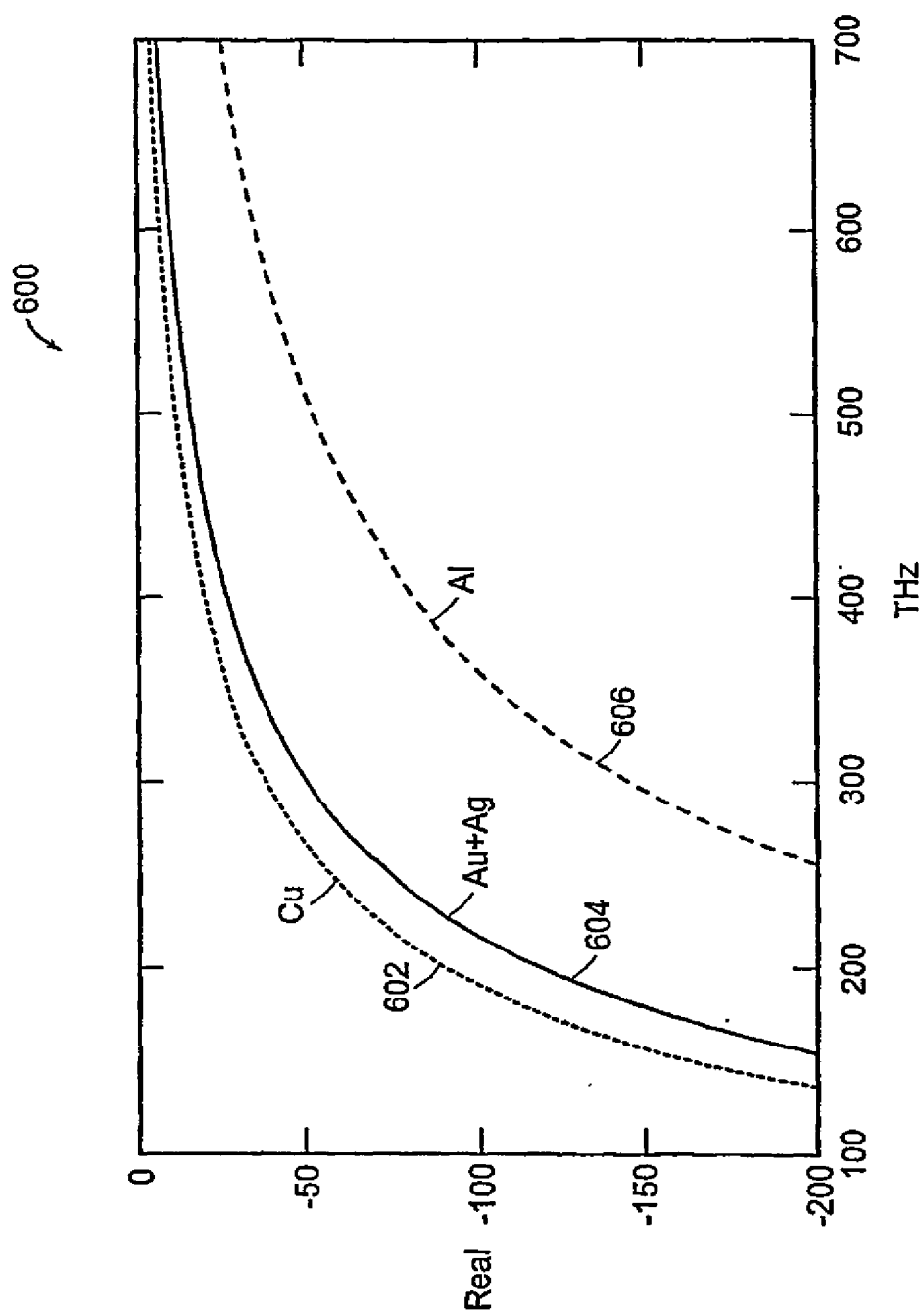


Figure 41A

SUBSTITUTE SHEET (RULE 26)

37/100

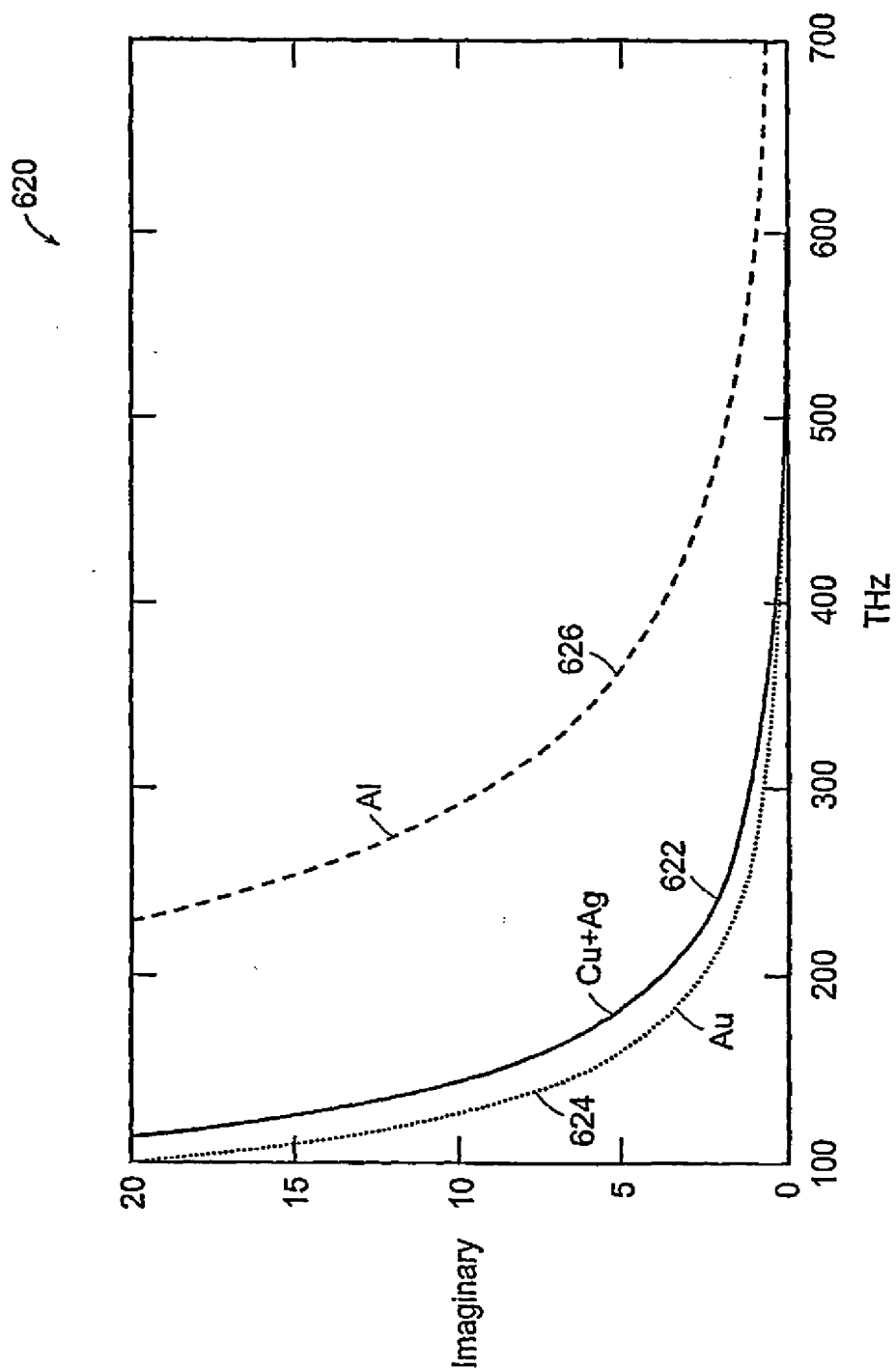


Figure 41B

SUBSTITUTE SHEET (RULE 26)

38/100

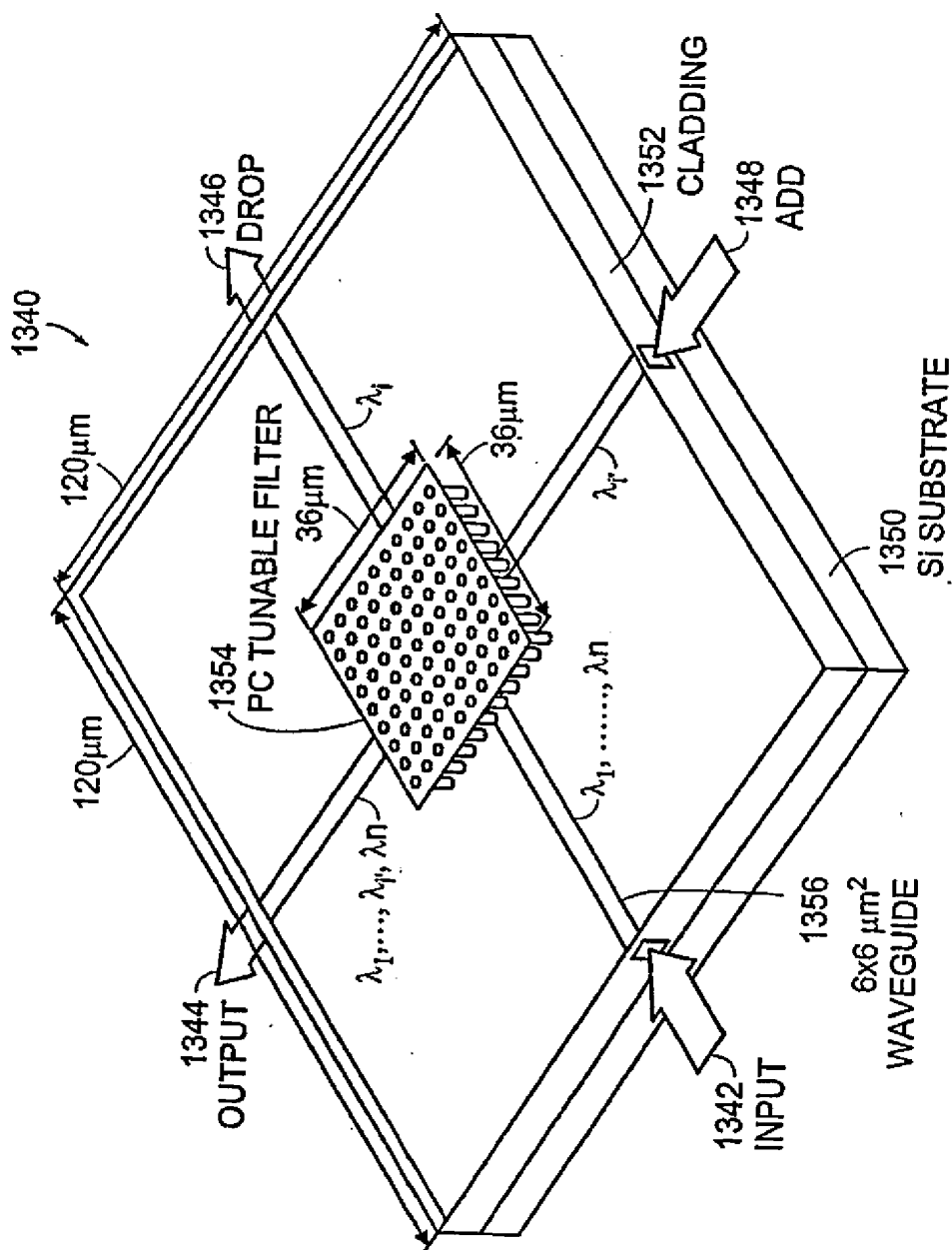


Figure 42A

SUBSTITUTE SHEET (RULE 26)

39/100

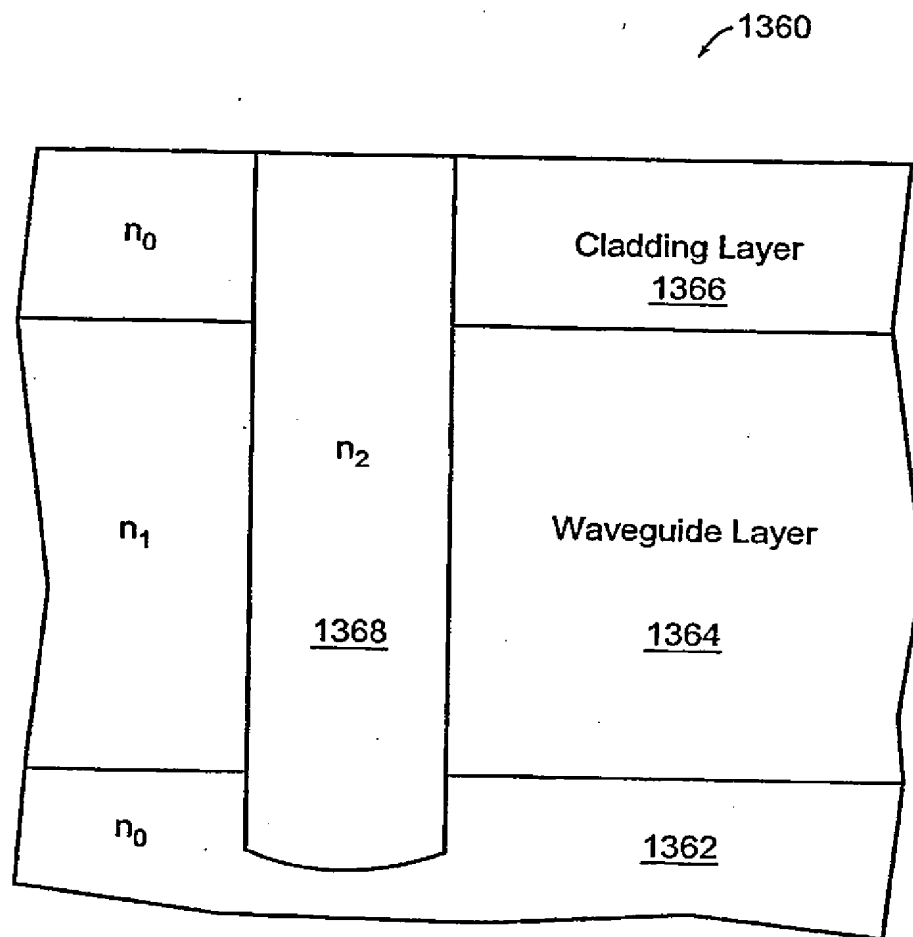


Figure 42B

SUBSTITUTE SHEET (RULE 26)

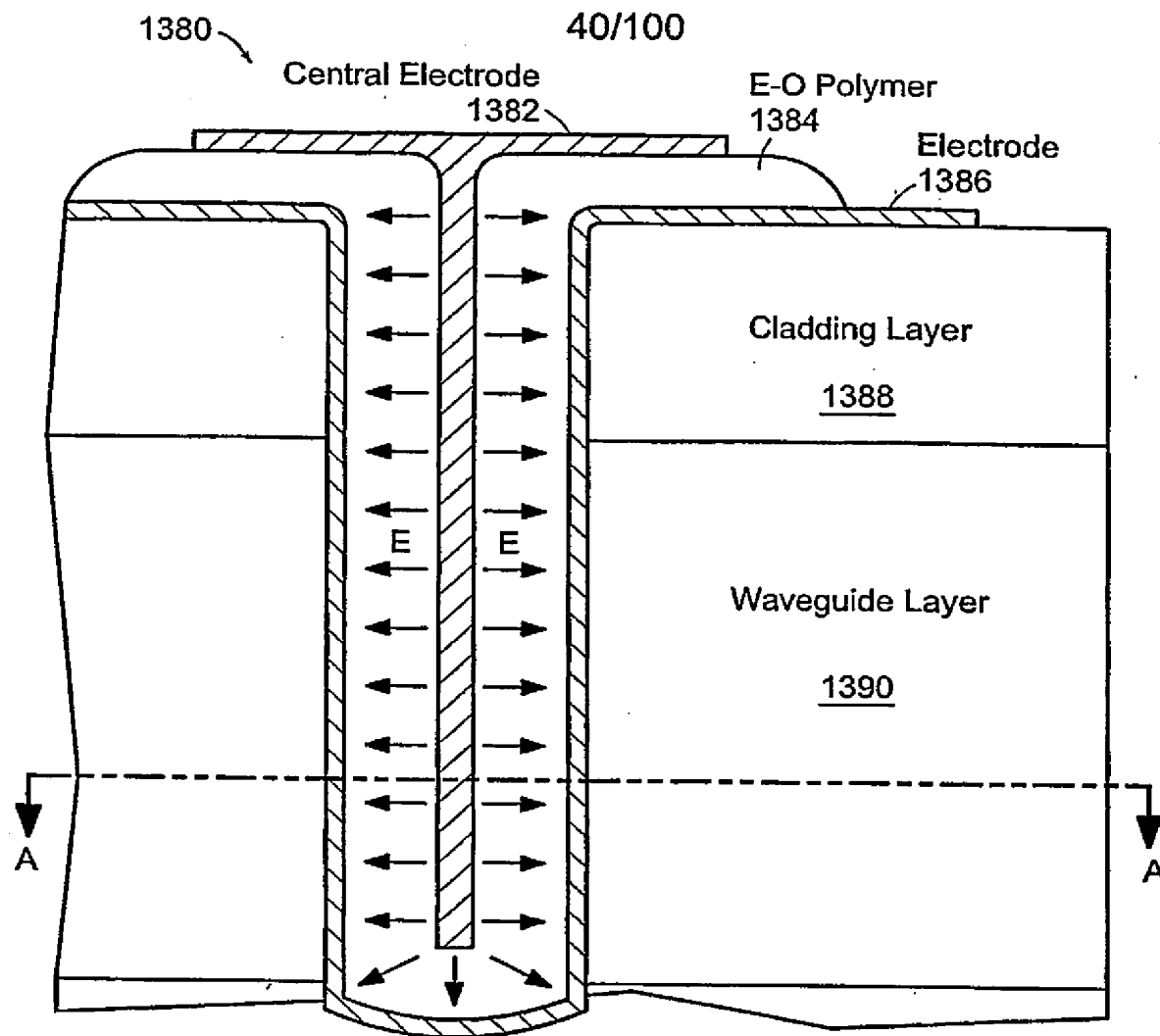


Figure 42C

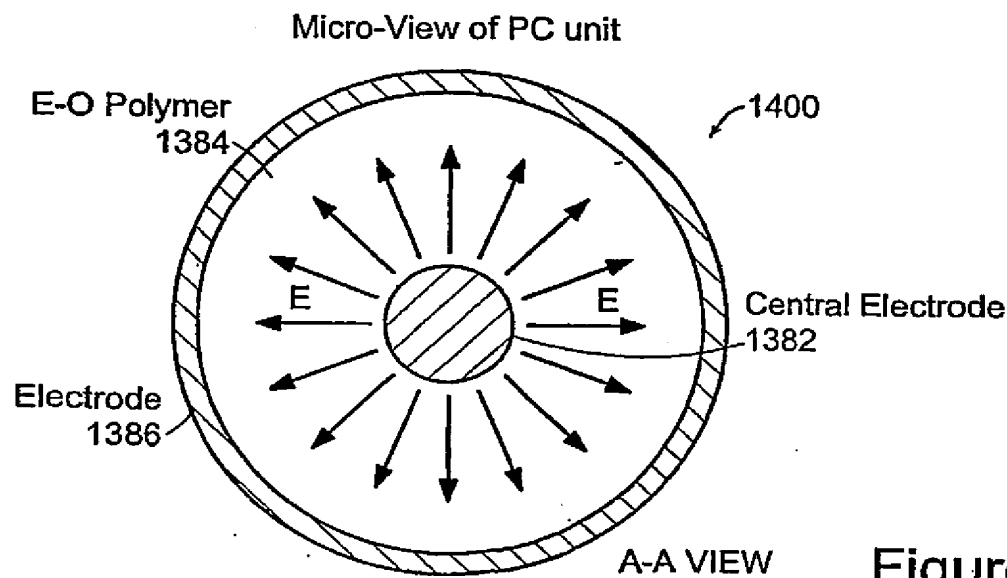
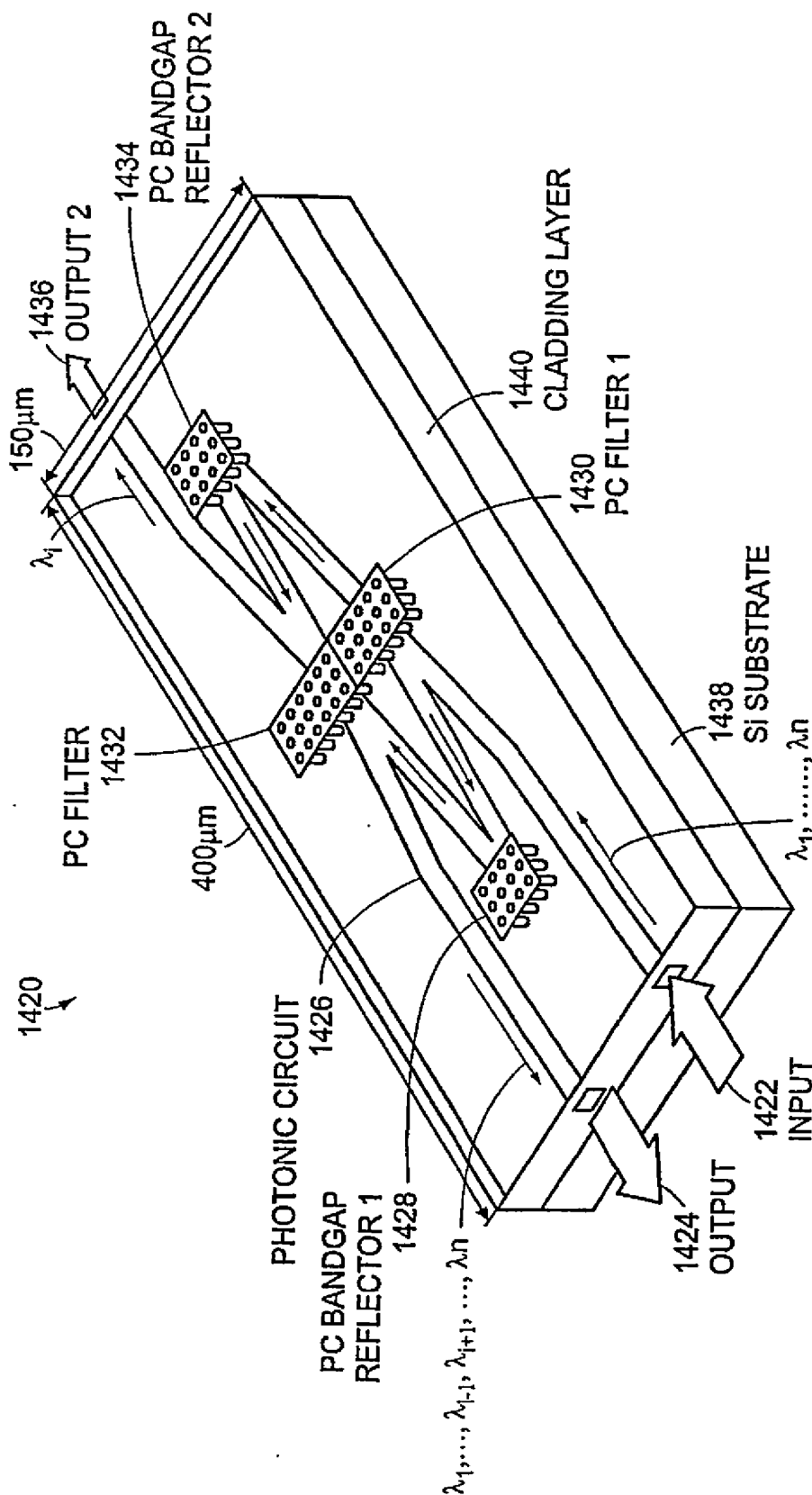


Figure 42D

41/100



TURNTABLE FILTER USING 2D-PC

Figure 43A

42/100

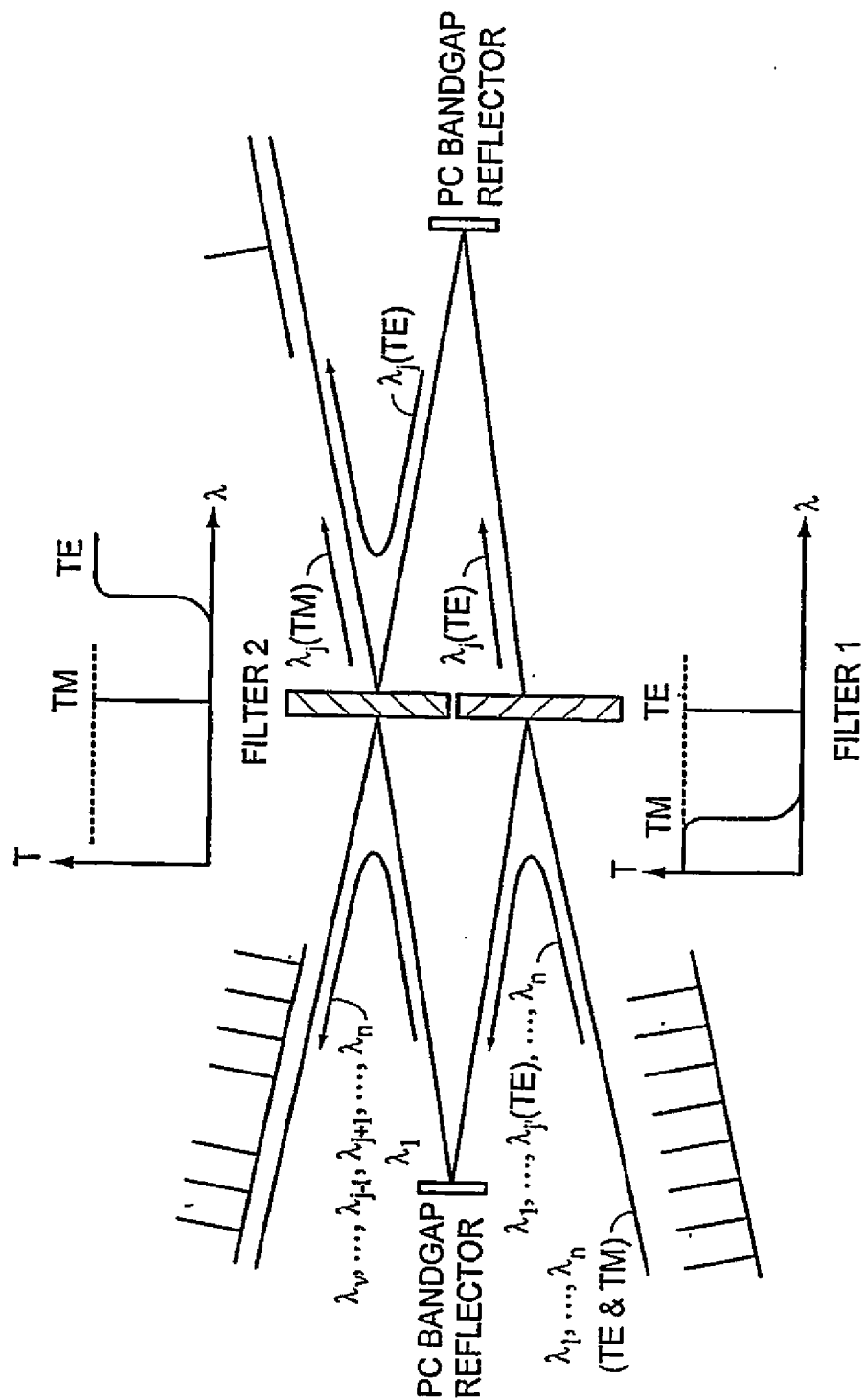


Figure 43B

43/100

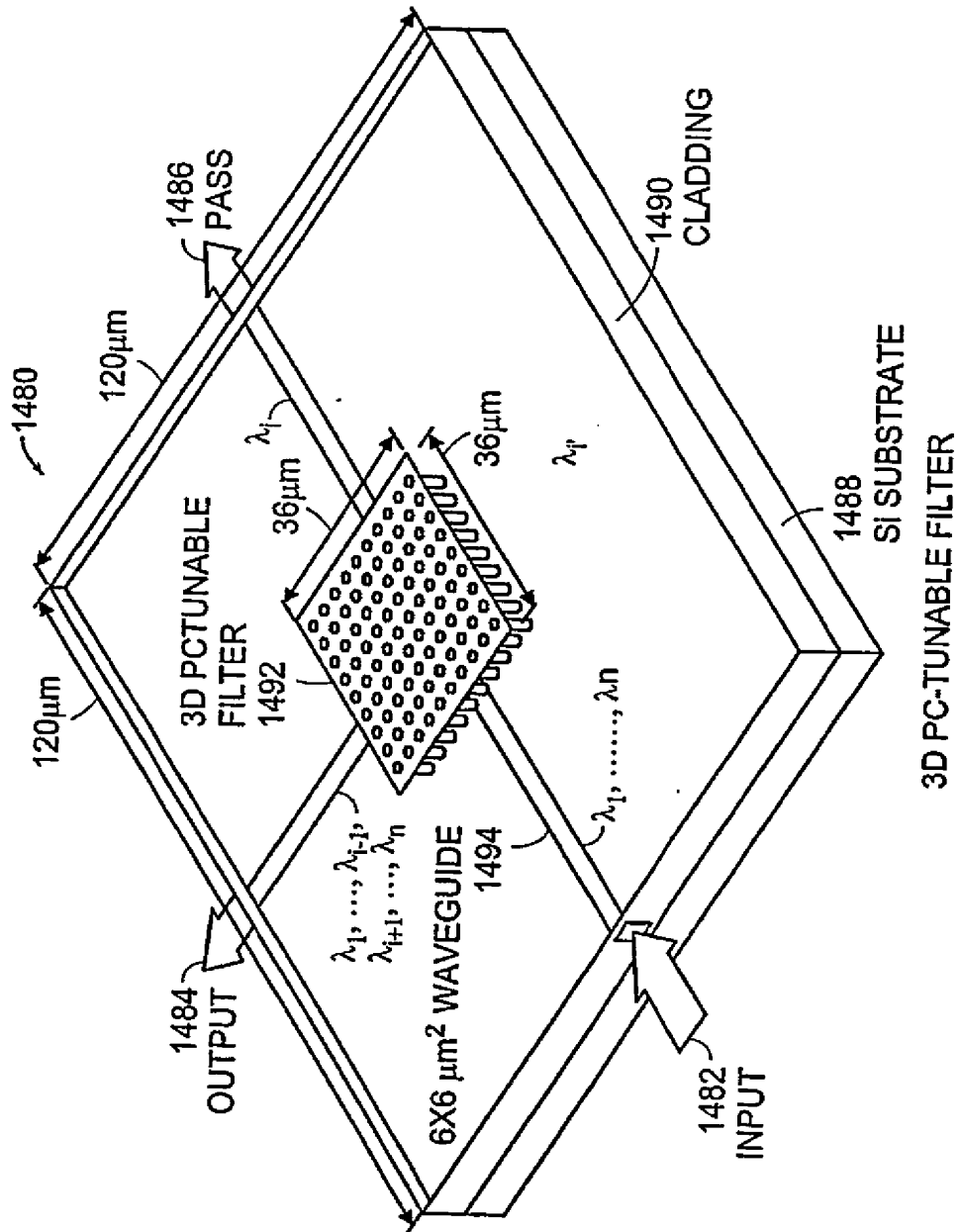


Figure 44A

44/100

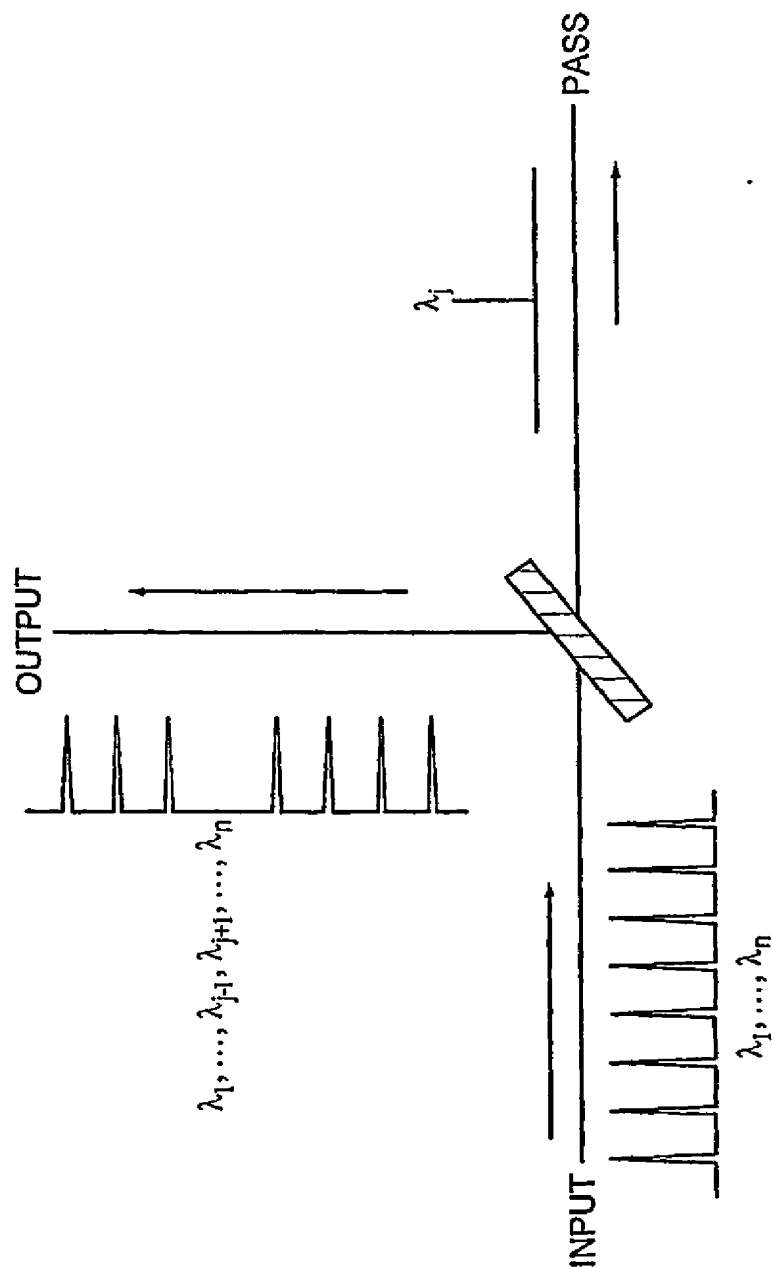


Figure 44B

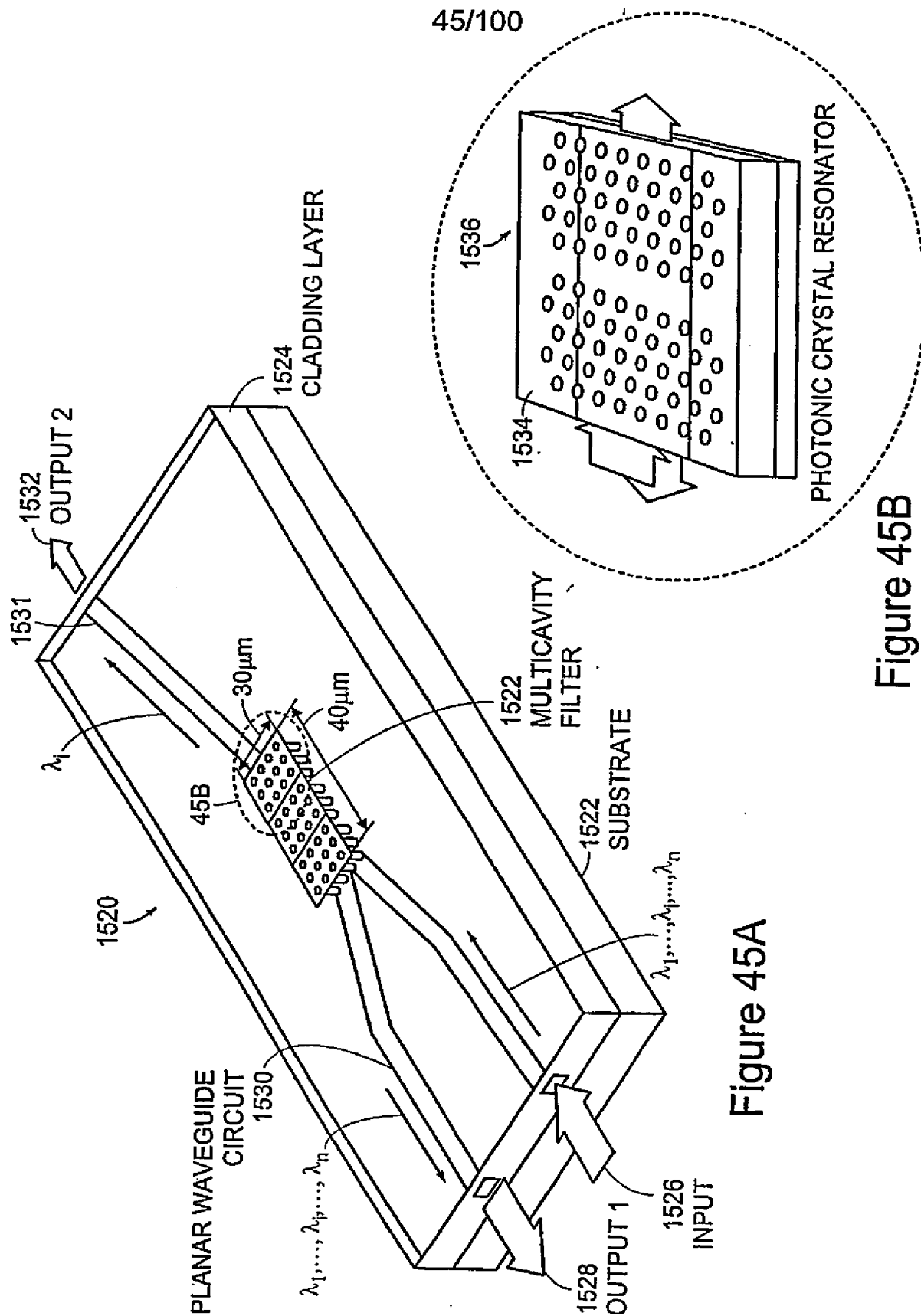


Figure 45B

Figure 45A

46/100

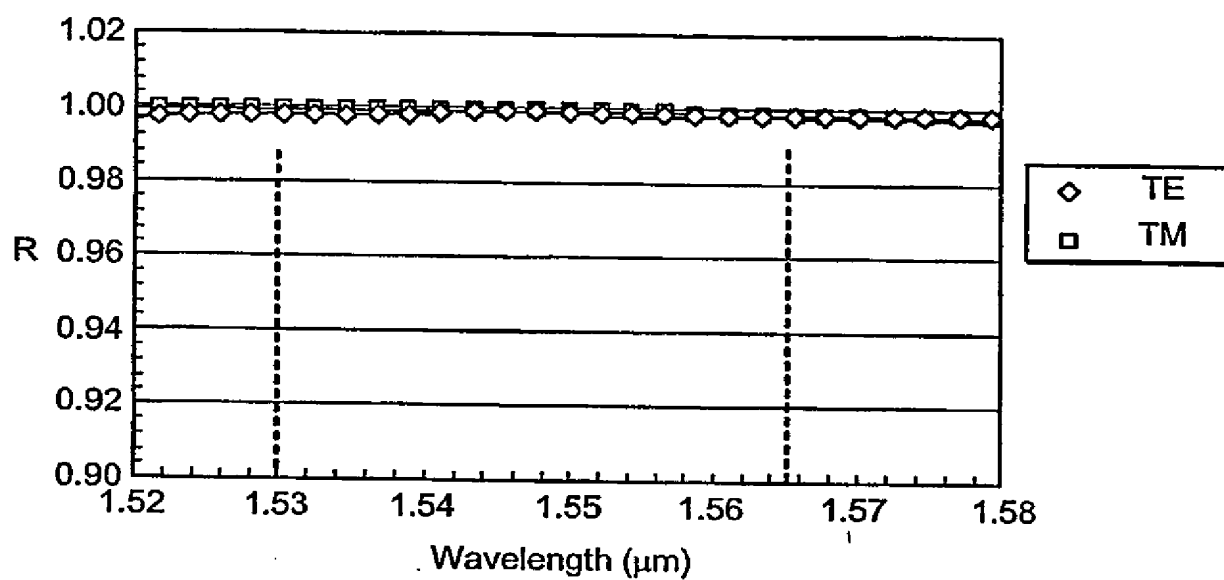


Figure 45C

47/100

1540

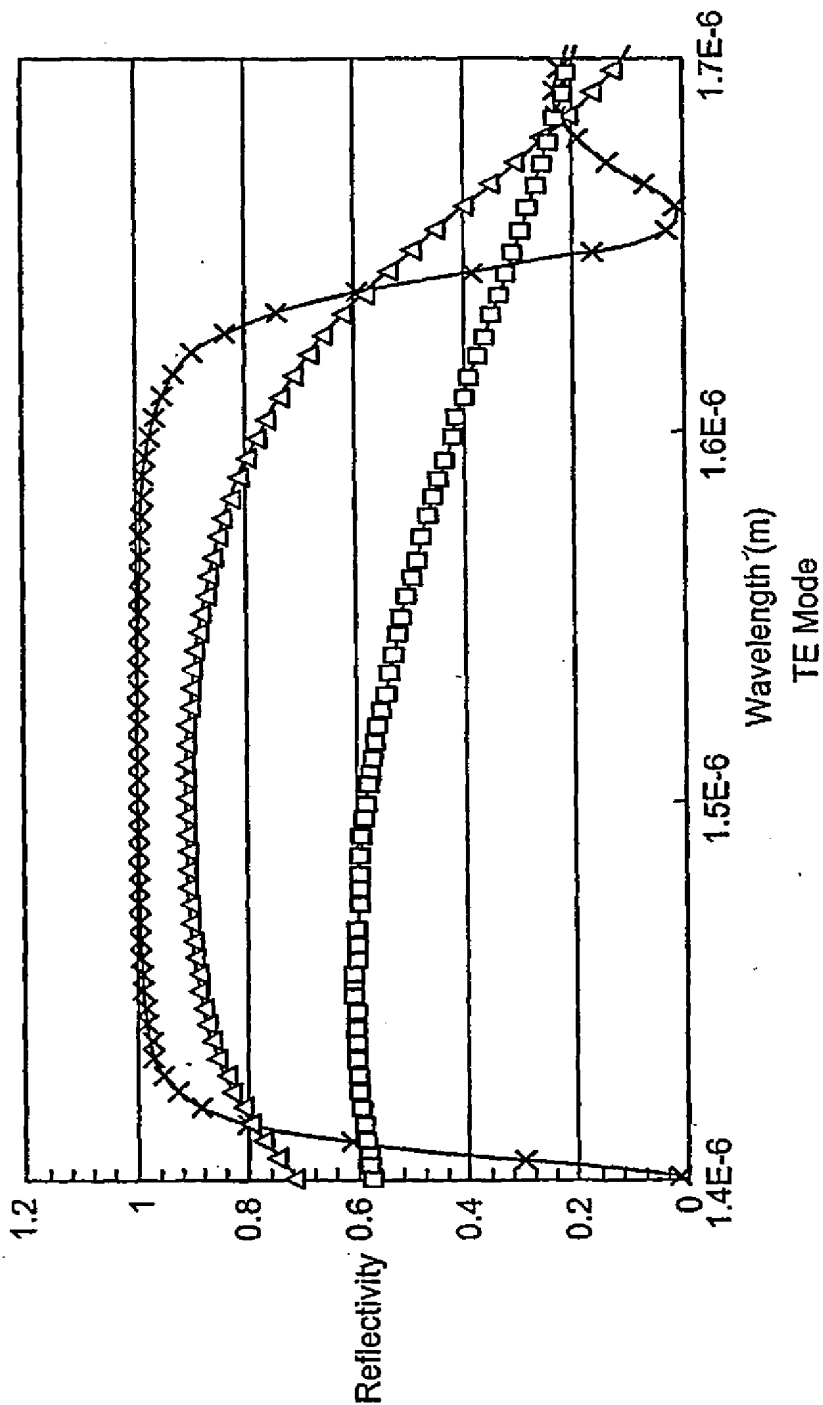


Figure 46A

48/100

1560

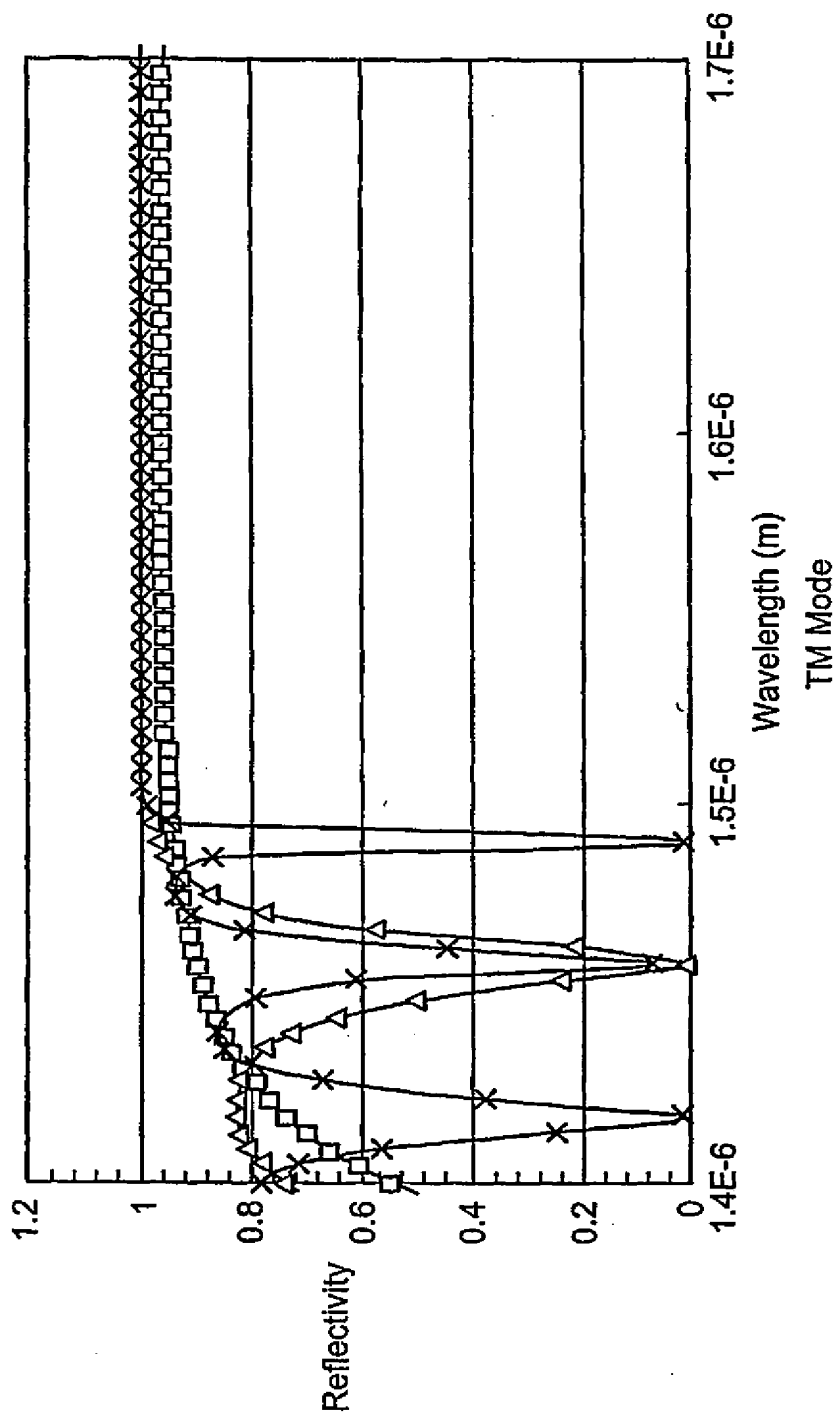


Figure 46B

49/100

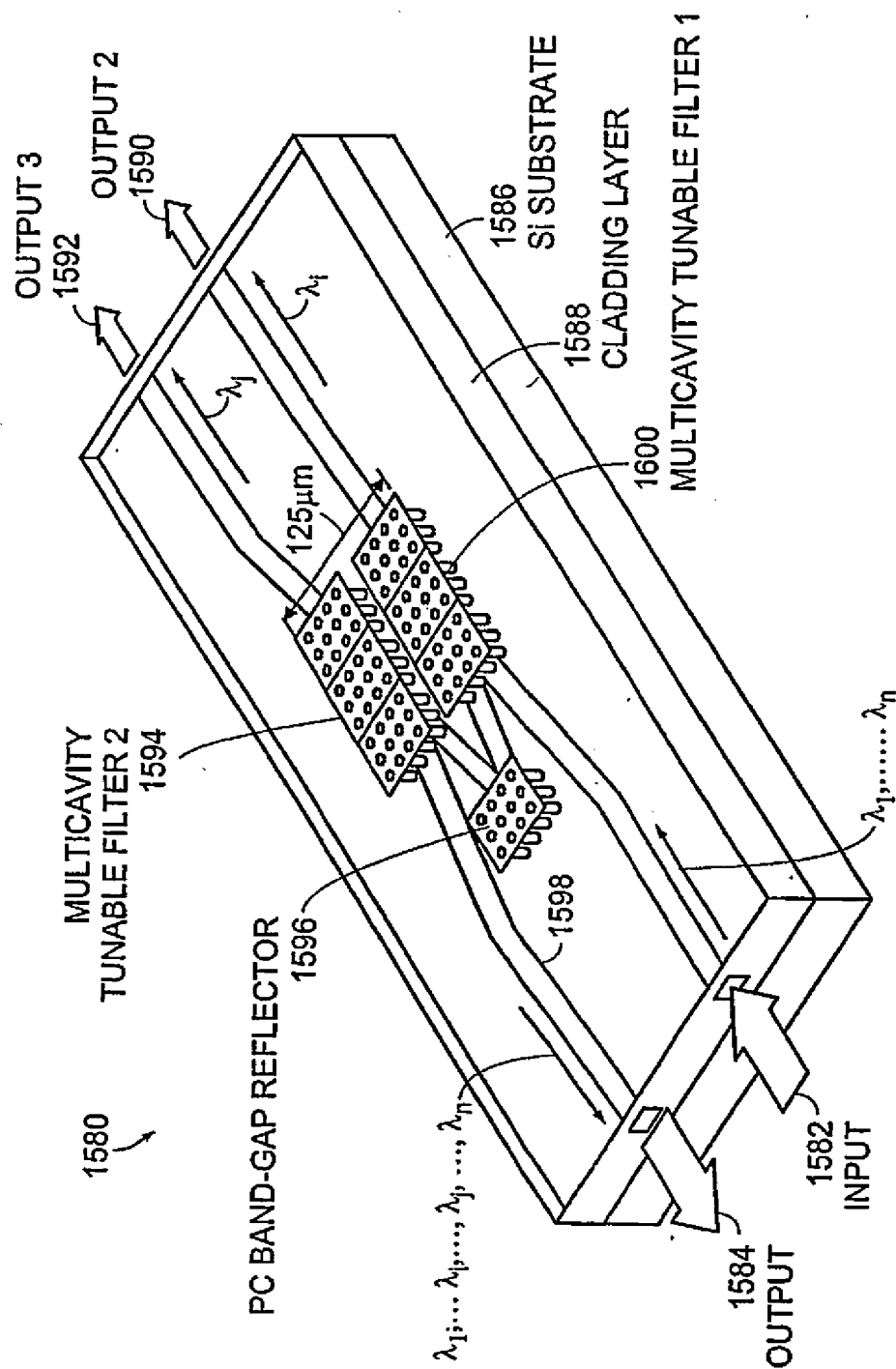


Figure 47

SUBSTITUTE SHEET (RULE 26)

50/100

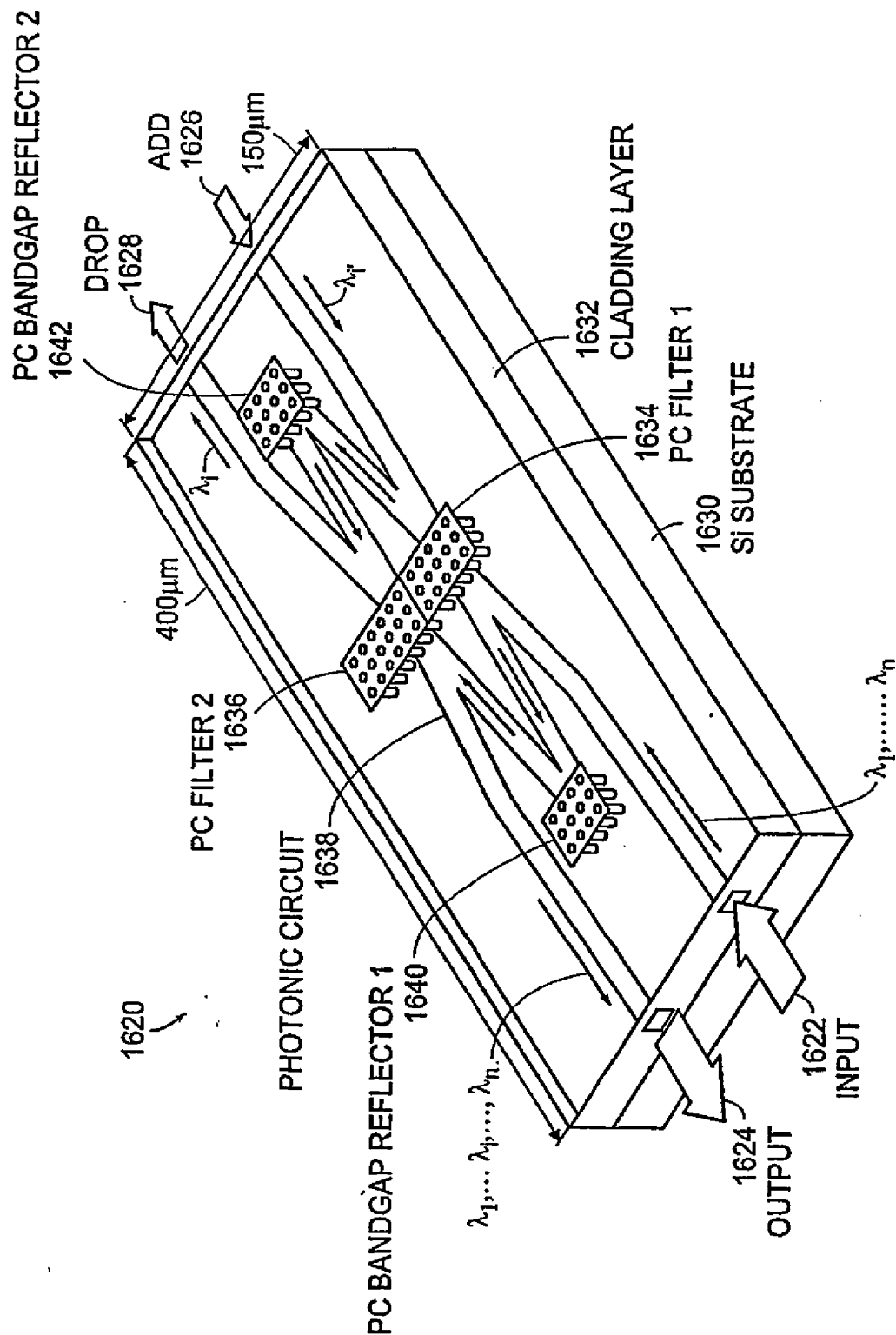


Figure 48A

SUBSTITUTE SHEET (RULE 26)

51/100

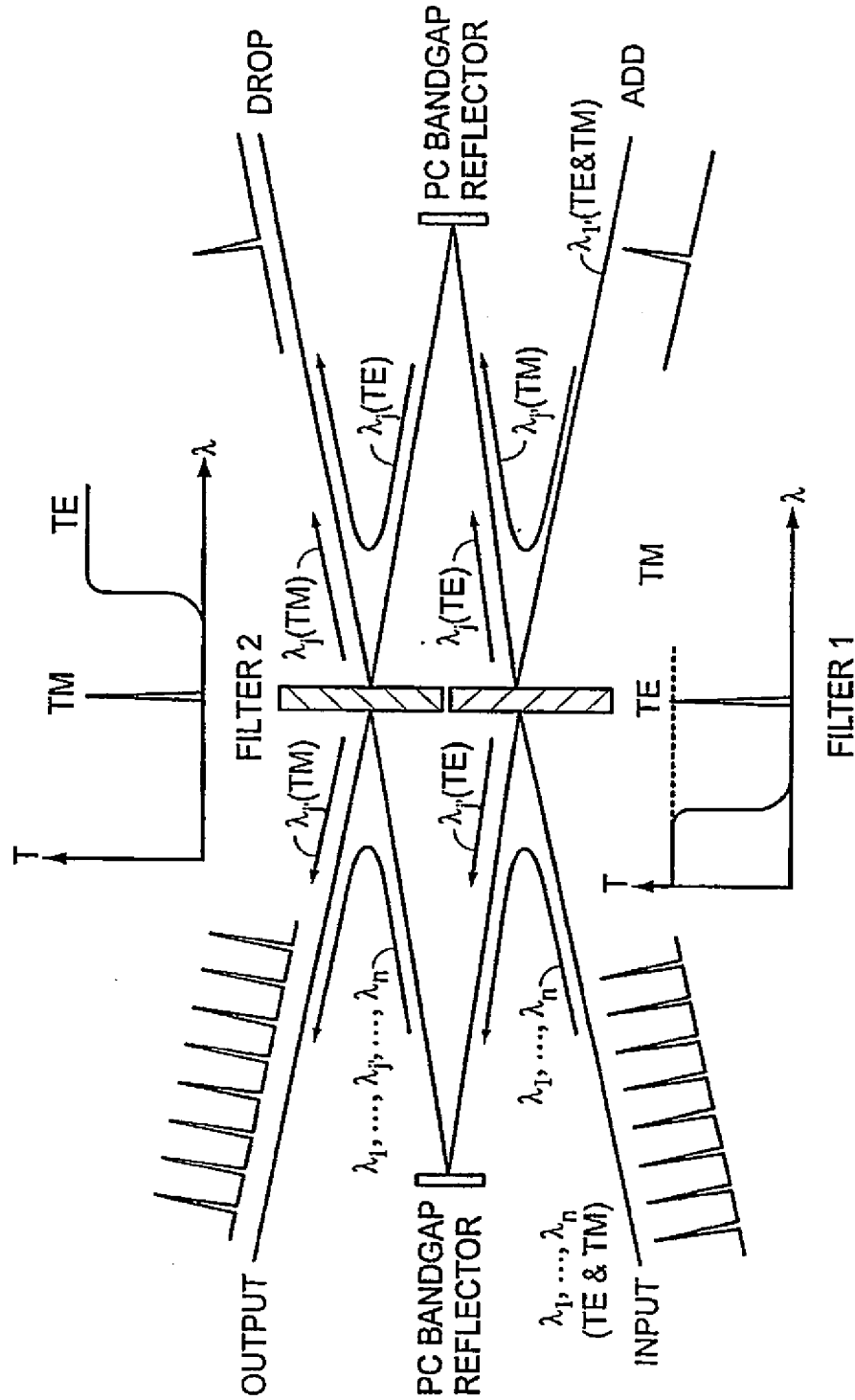


Figure 48B

52/100

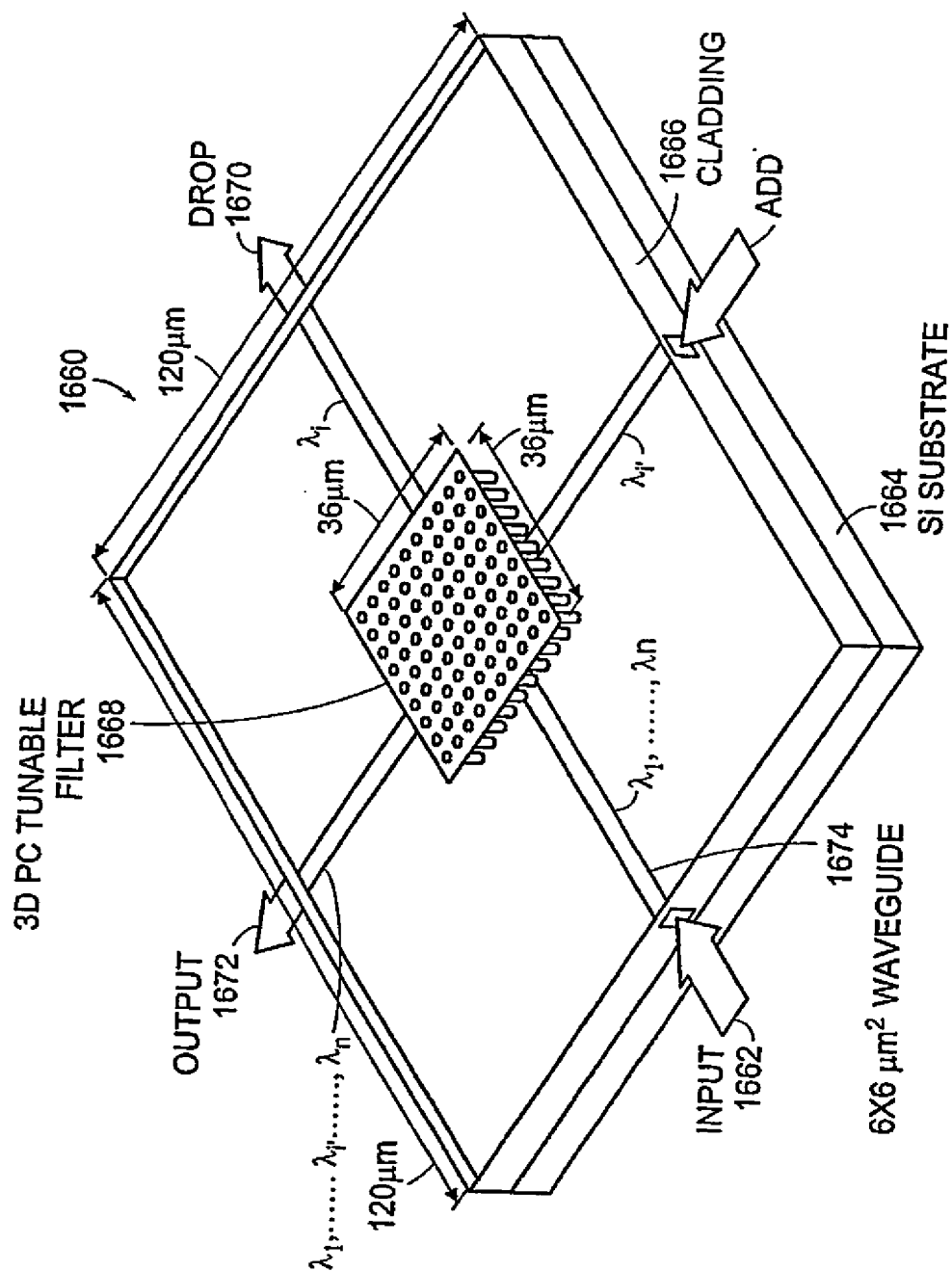


Figure 49A

SUBSTITUTE SHEET (RULE 26)

53/100

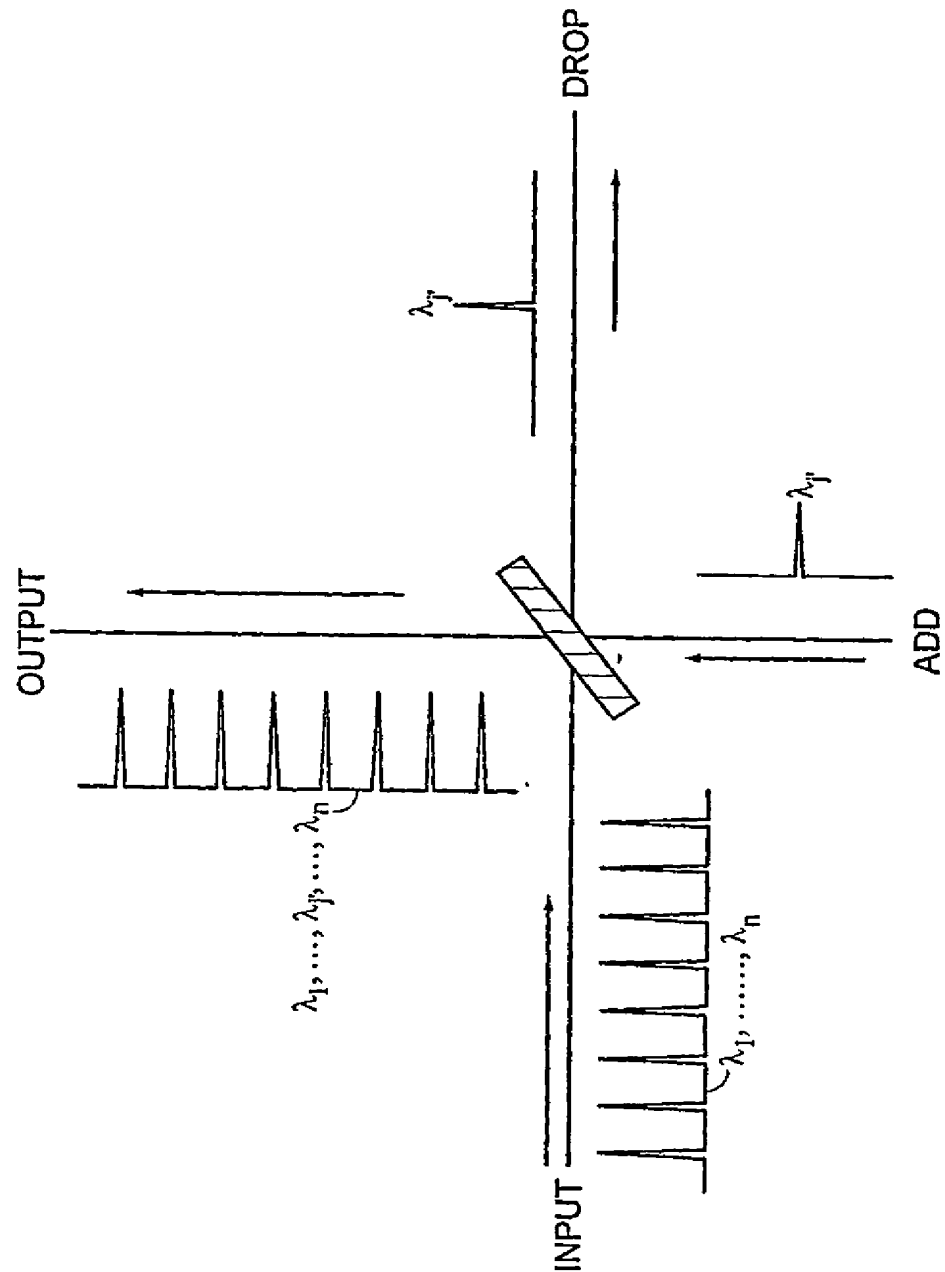


Figure 49B

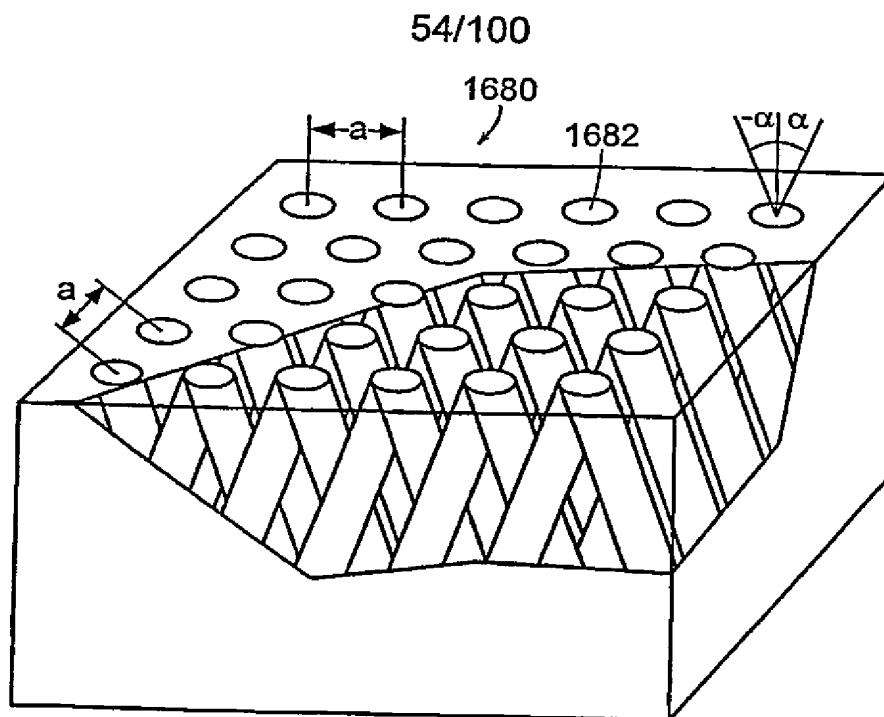


Figure 49C

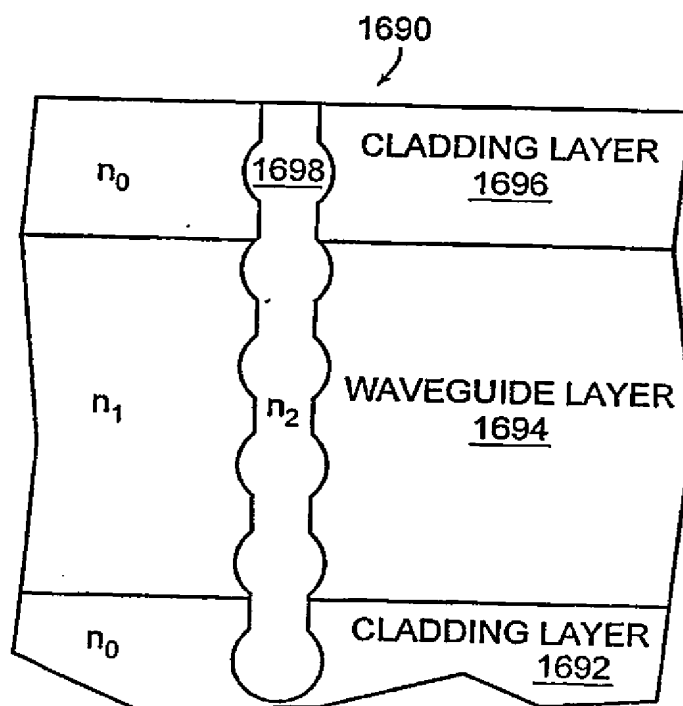


Figure 49D

SUBSTITUTE SHEET (RULE 26)

55/100

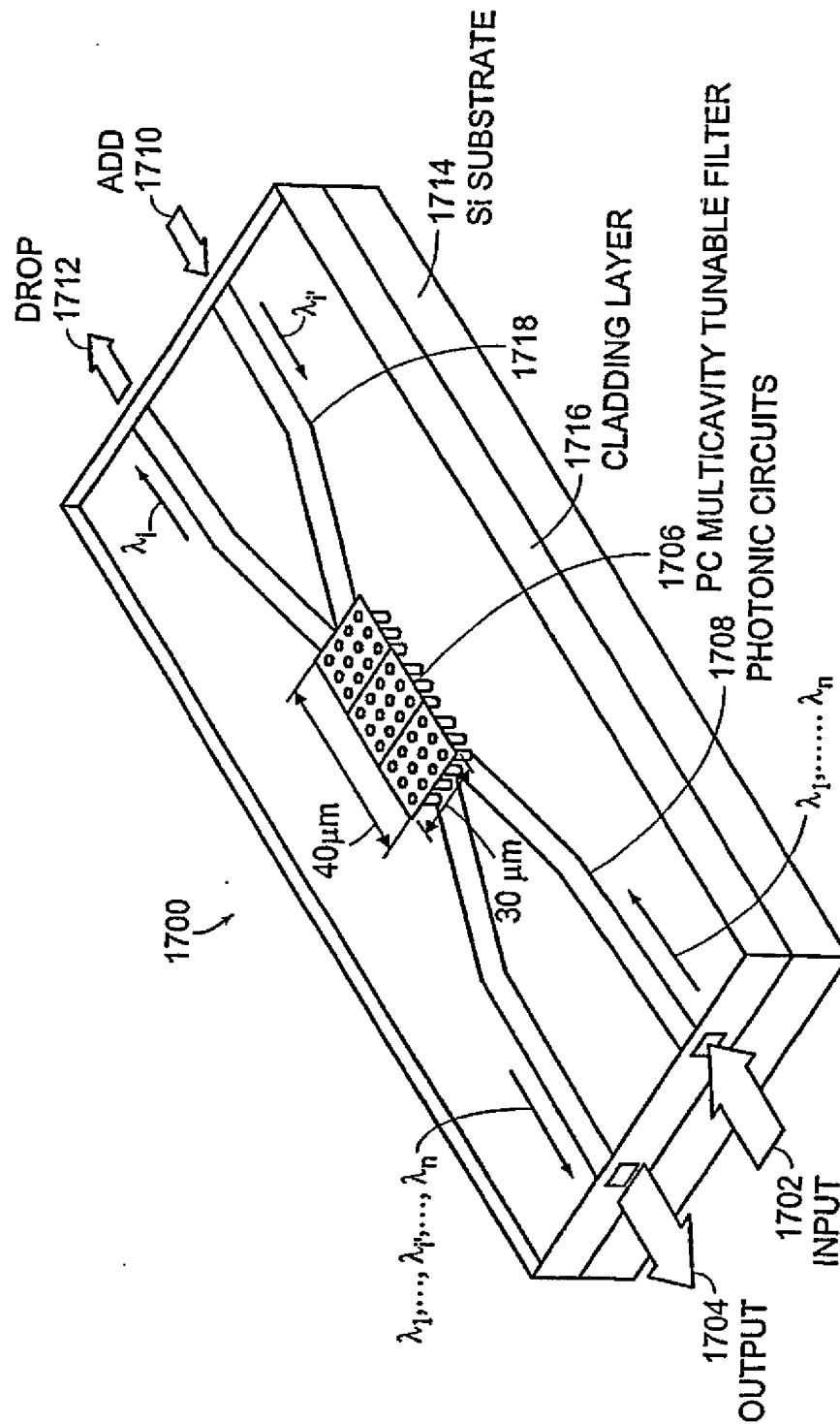
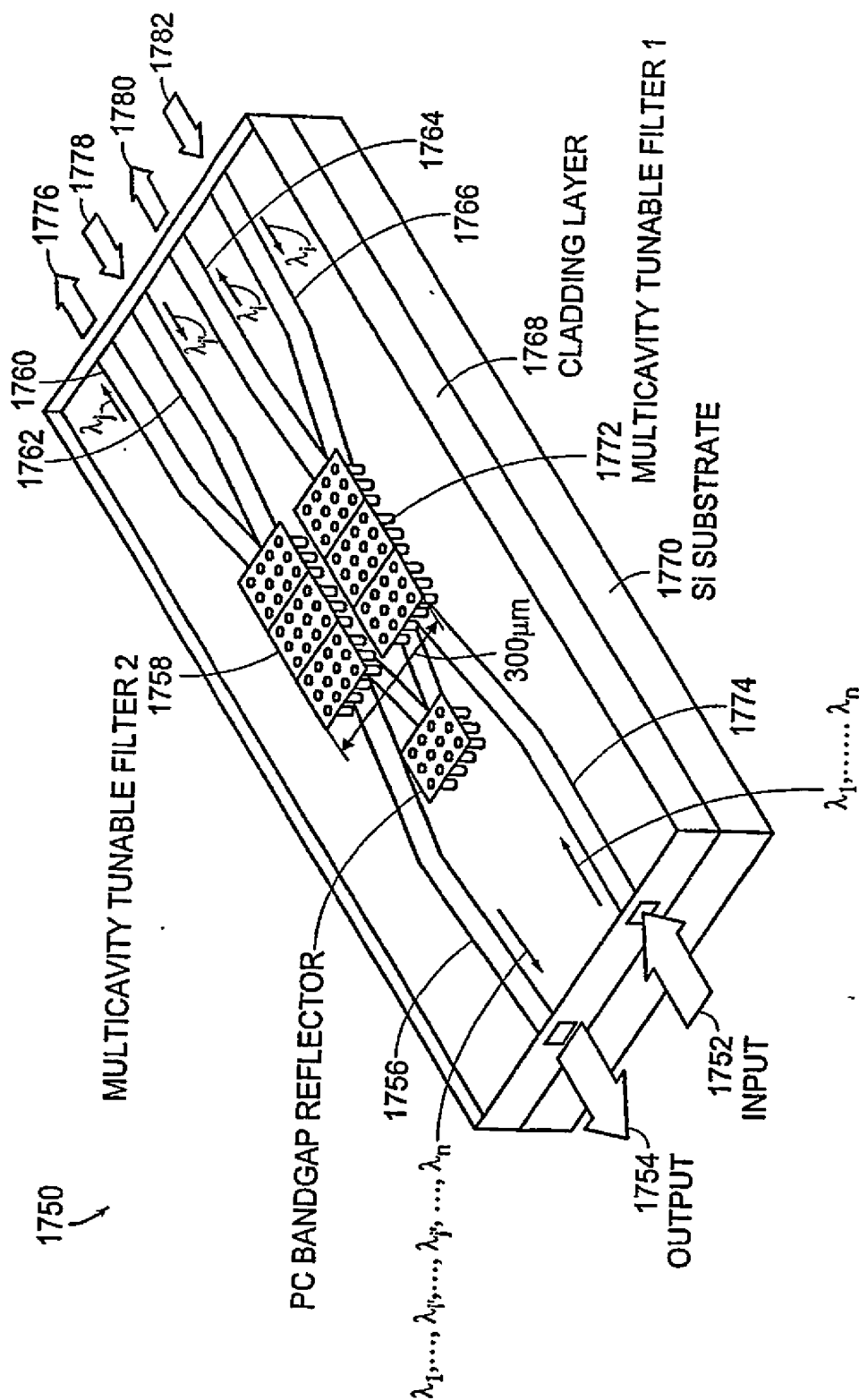


Figure 50

56/100



DUAL-WAVELENGTH DYNAMIC OADM

Figure 51

57/100

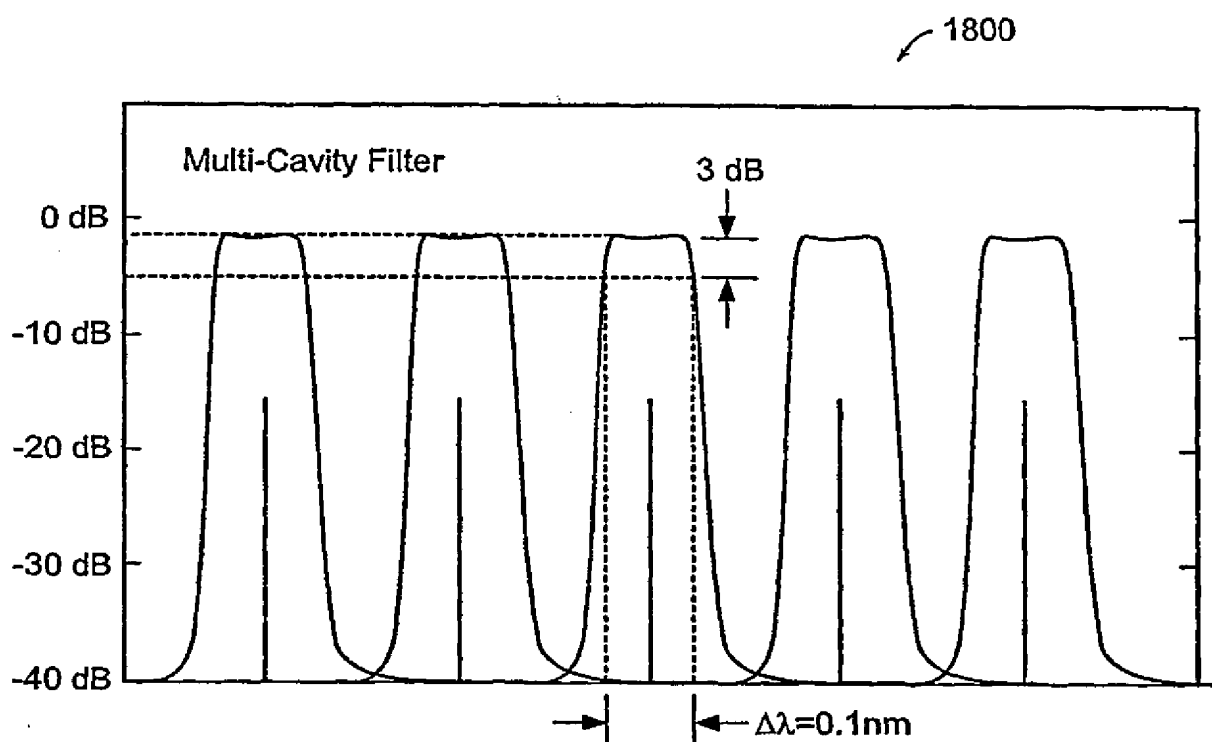


Figure 52A

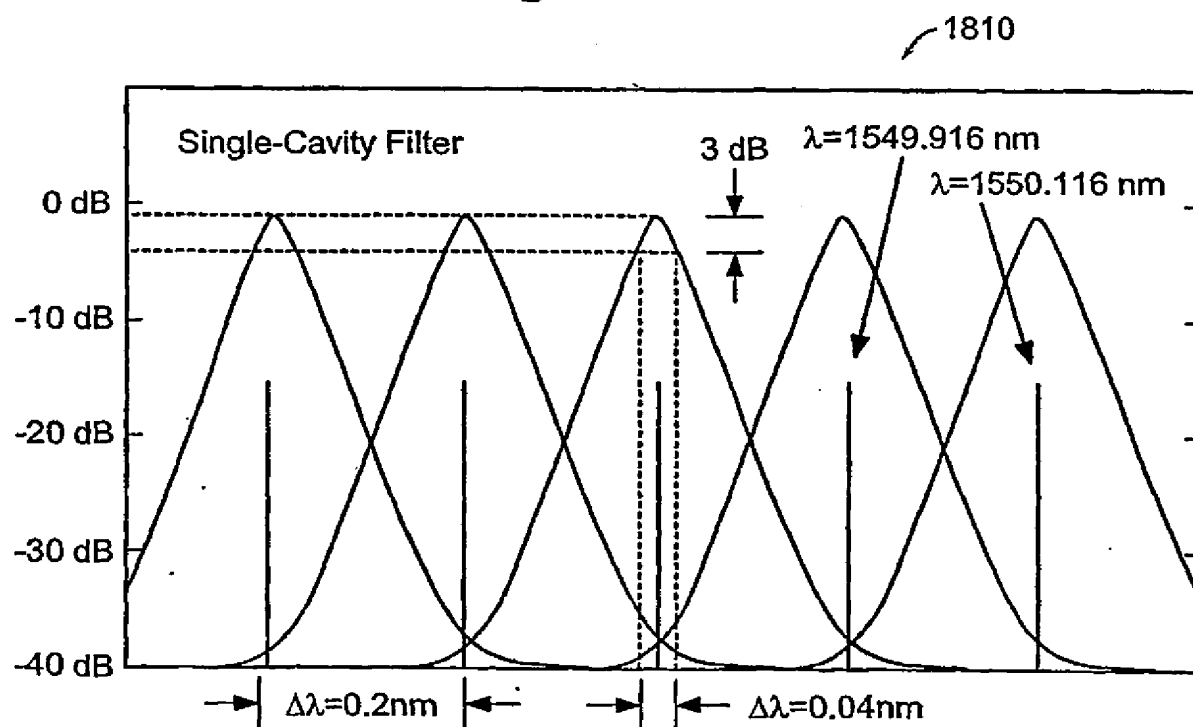


Figure 52B

SUBSTITUTE SHEET (RULE 26)

58/100

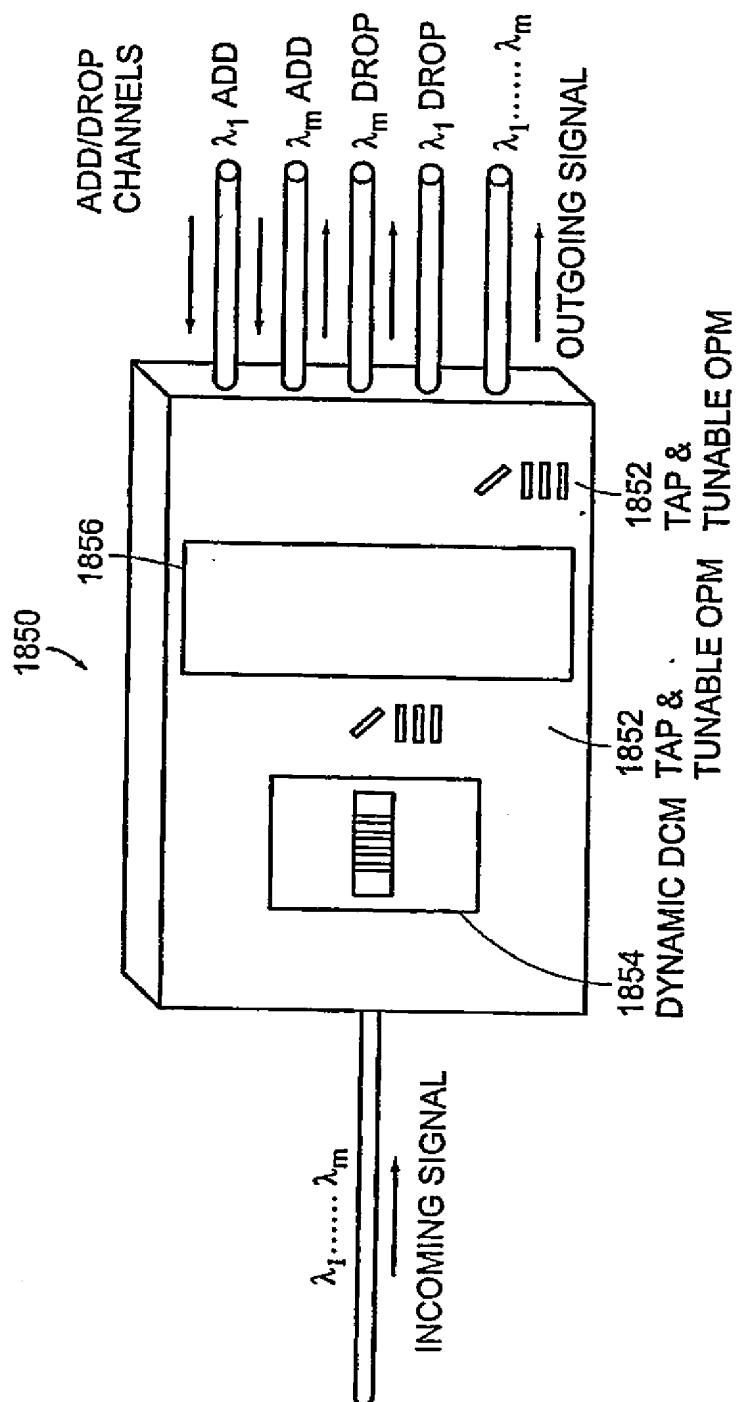


Figure 53A

59/100

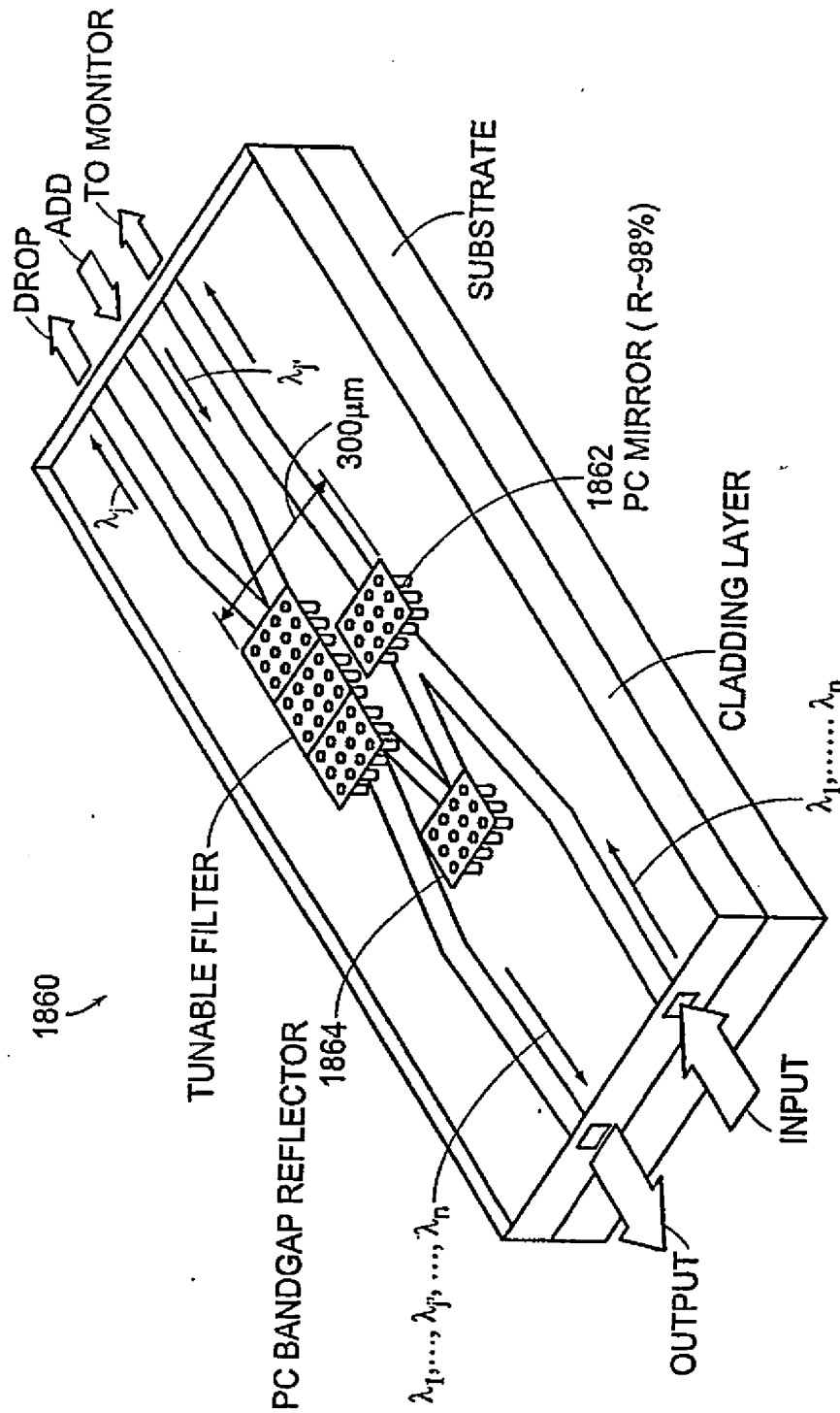


Figure 53B

60/100

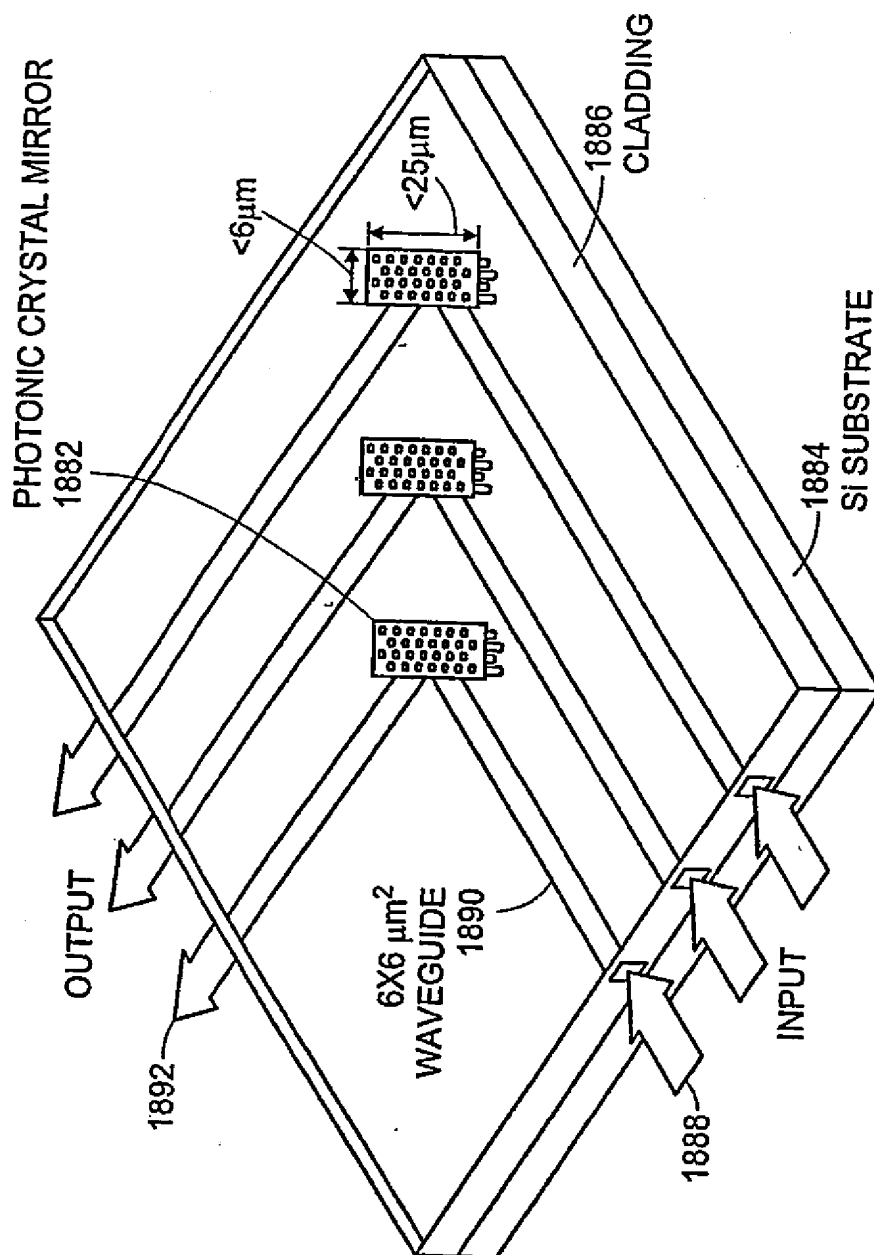


Figure 54A

SUBSTITUTE SHEET (RULE 26)

61/100

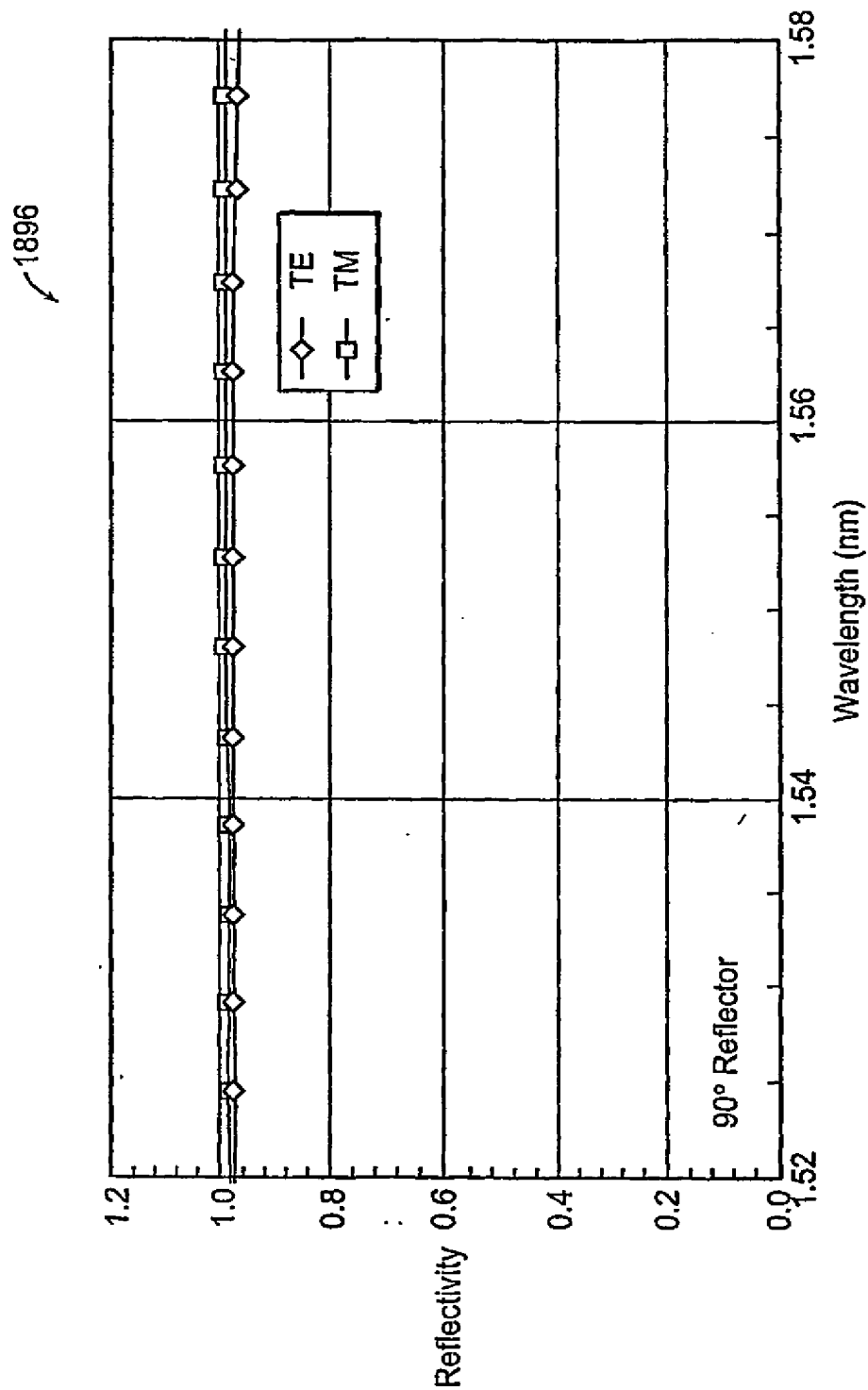
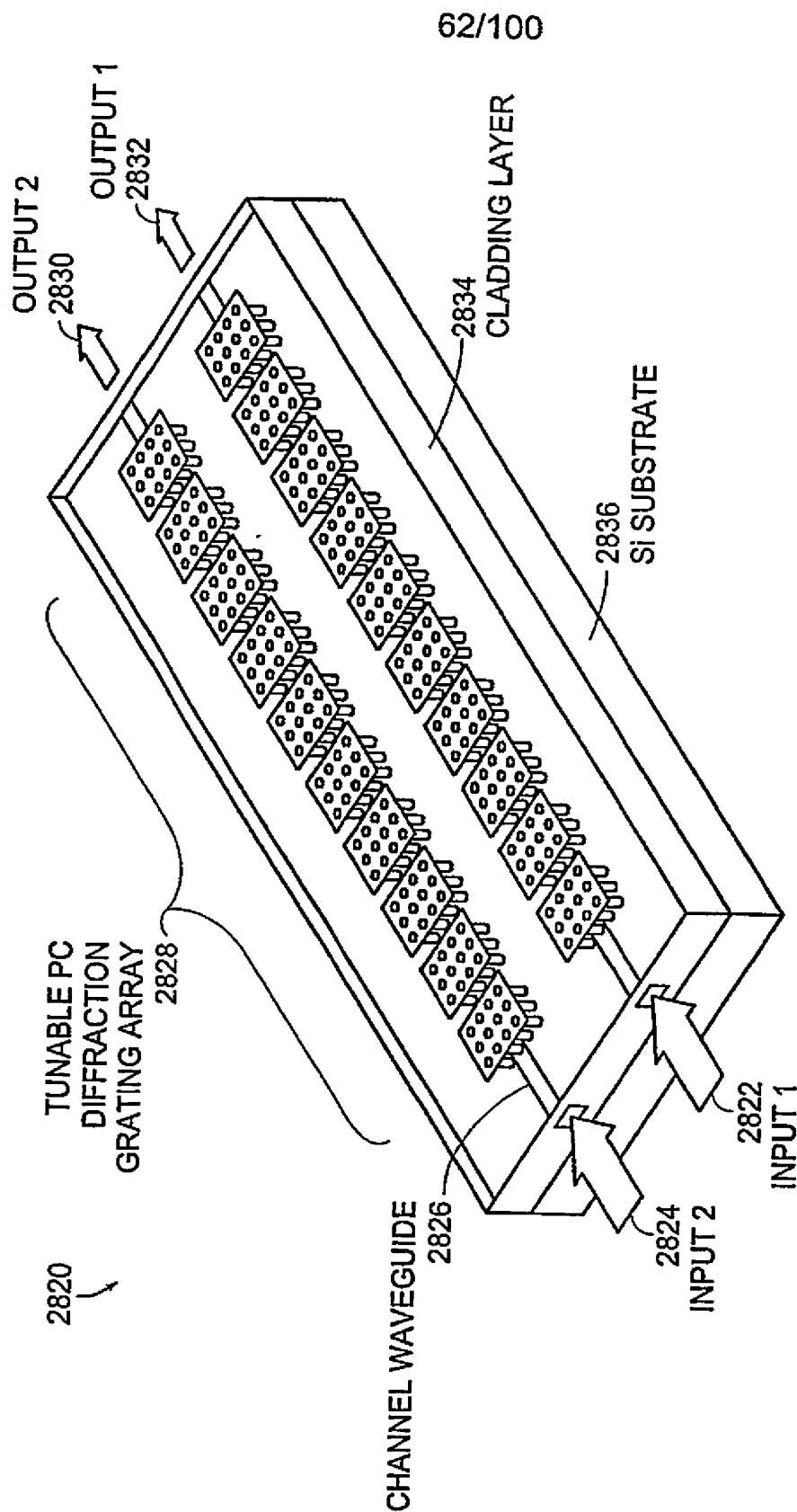


Figure 54B

SUBSTITUTE SHEET (RULE 26)



VARIABLE OPTIC ATTENUATION/SPECTRAL EQUALIZER ARRAY

Figure 55

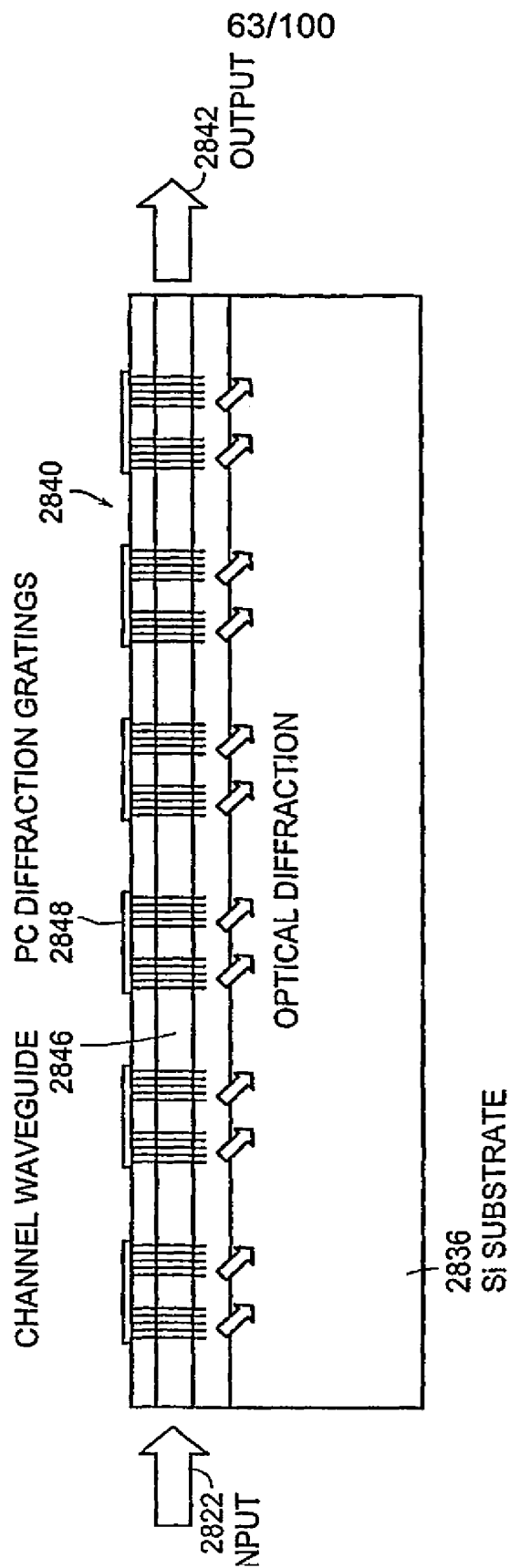


Figure 56

64/100

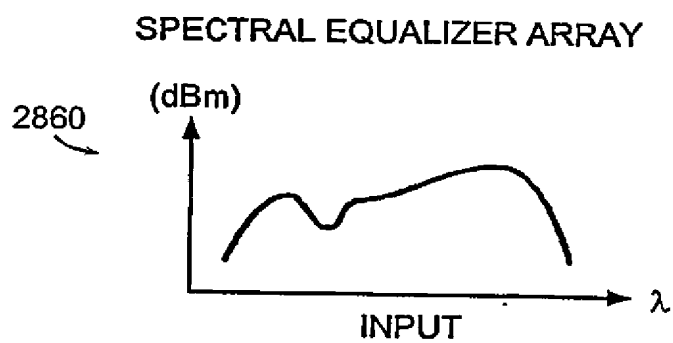


Figure 57A

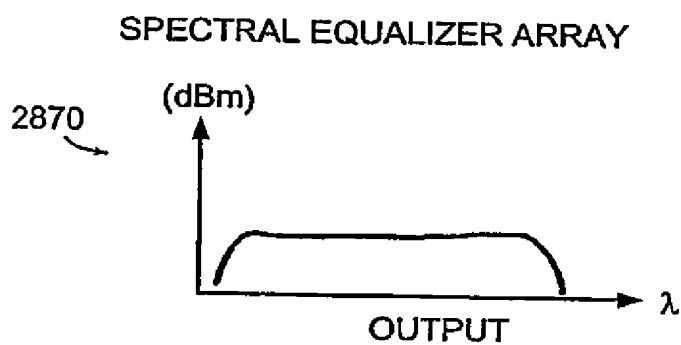


Figure 57B

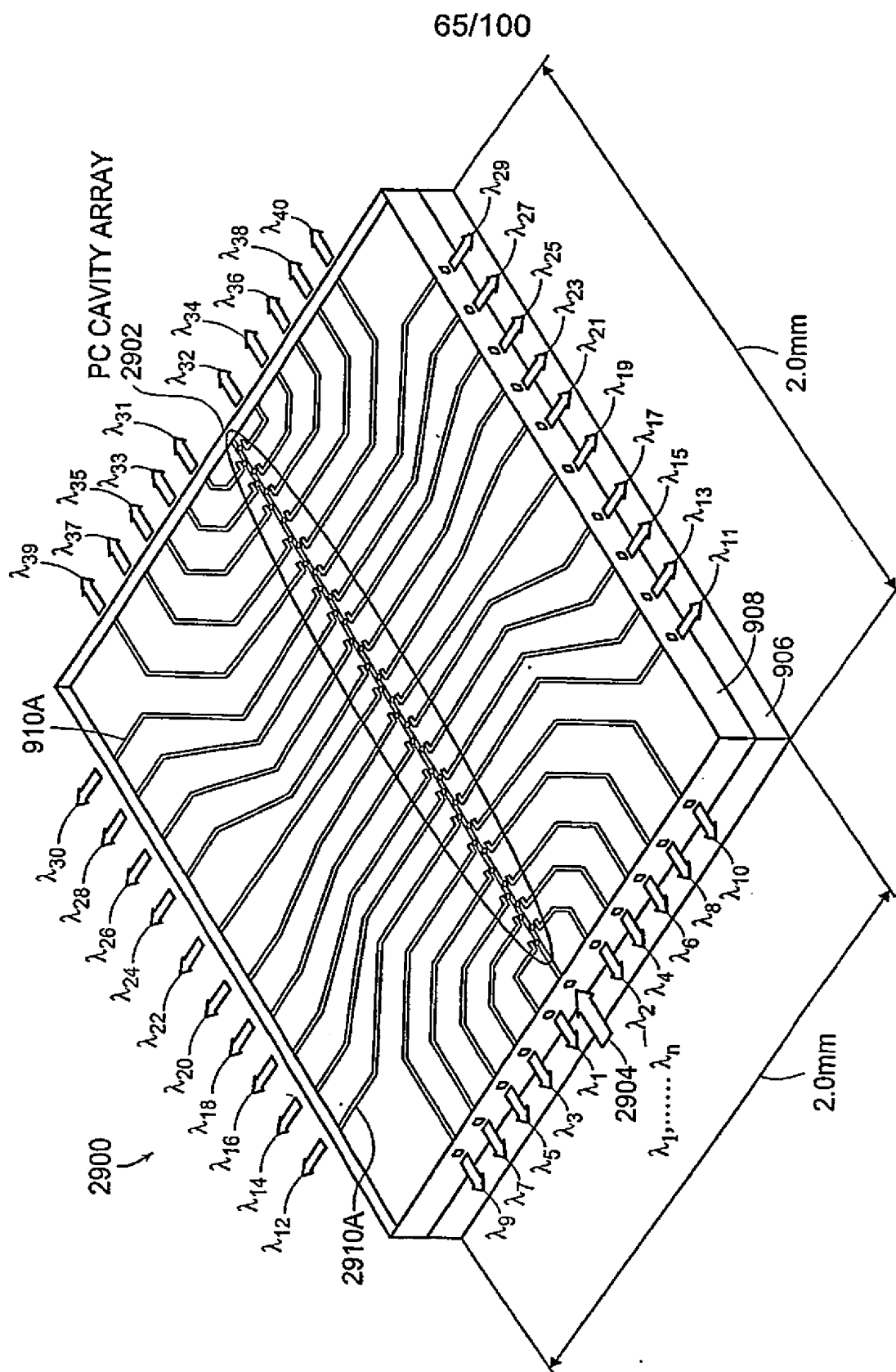


Figure 58

SUBSTITUTE SHEET (RULE 26)

66/100

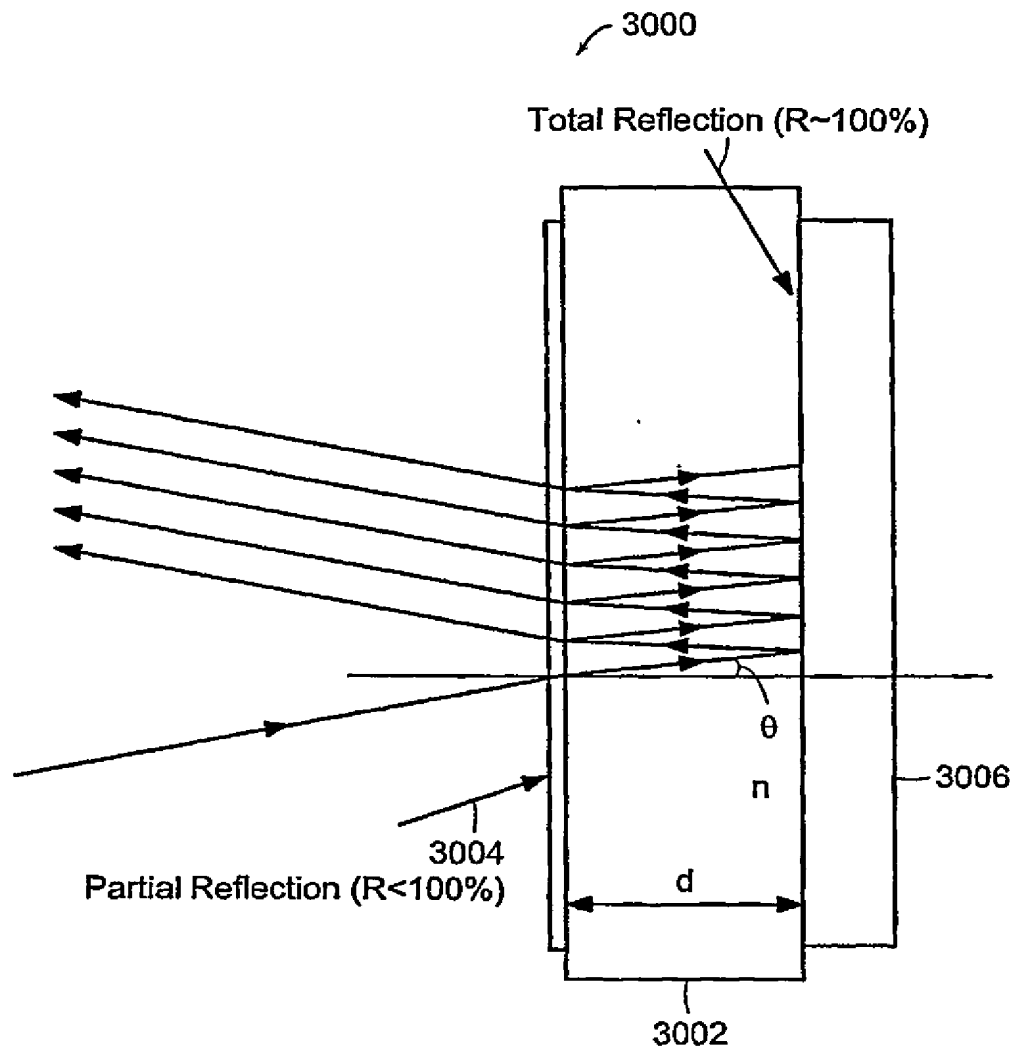


Figure 59

SUBSTITUTE SHEET (RULE 26)

67/100

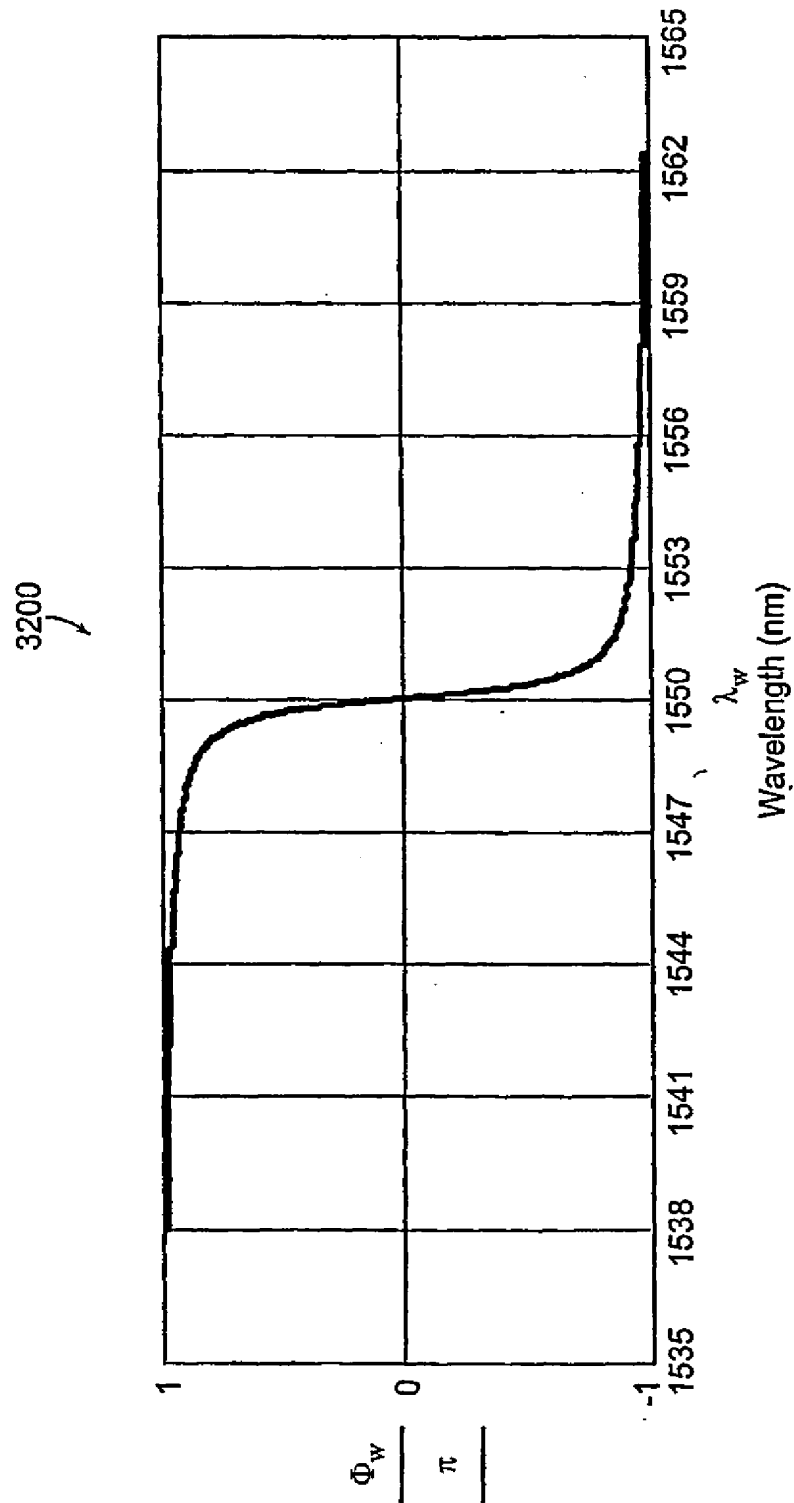


Figure 60

SUBSTITUTE SHEET (RULE 26)

68/100

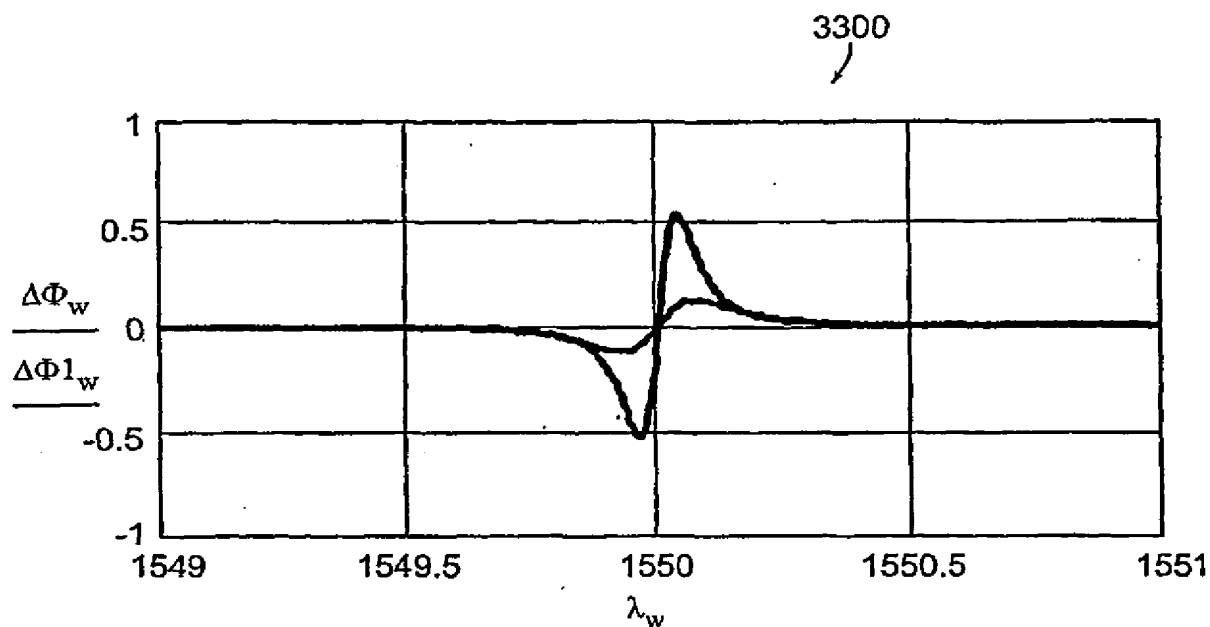


Figure 61

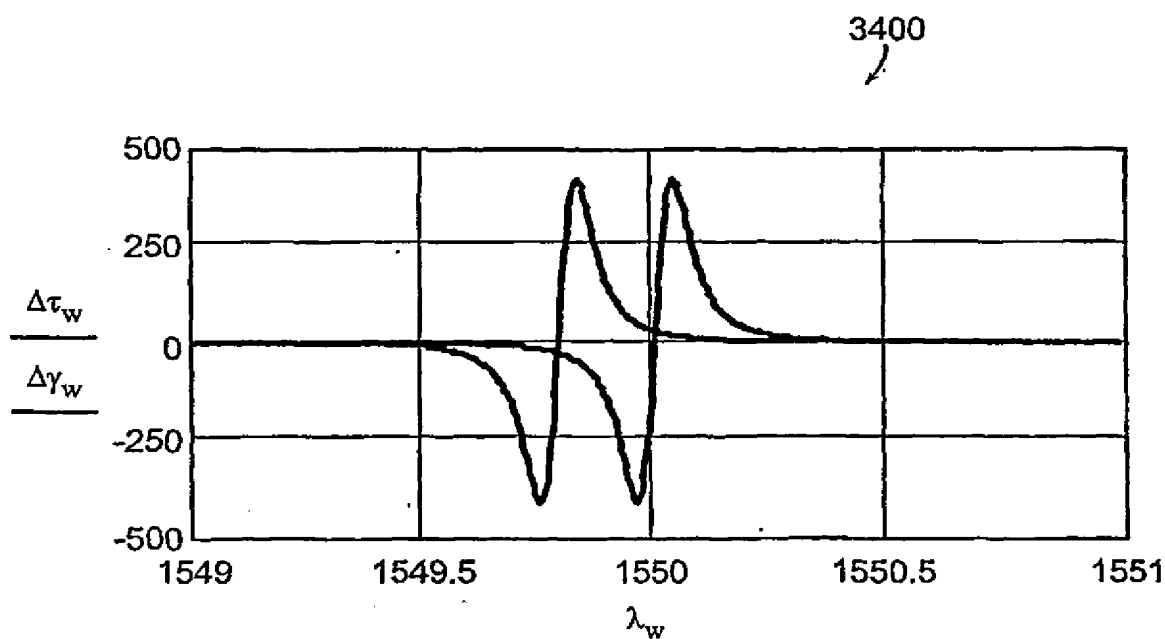


Figure 62

SUBSTITUTE SHEET (RULE 26)

69/100

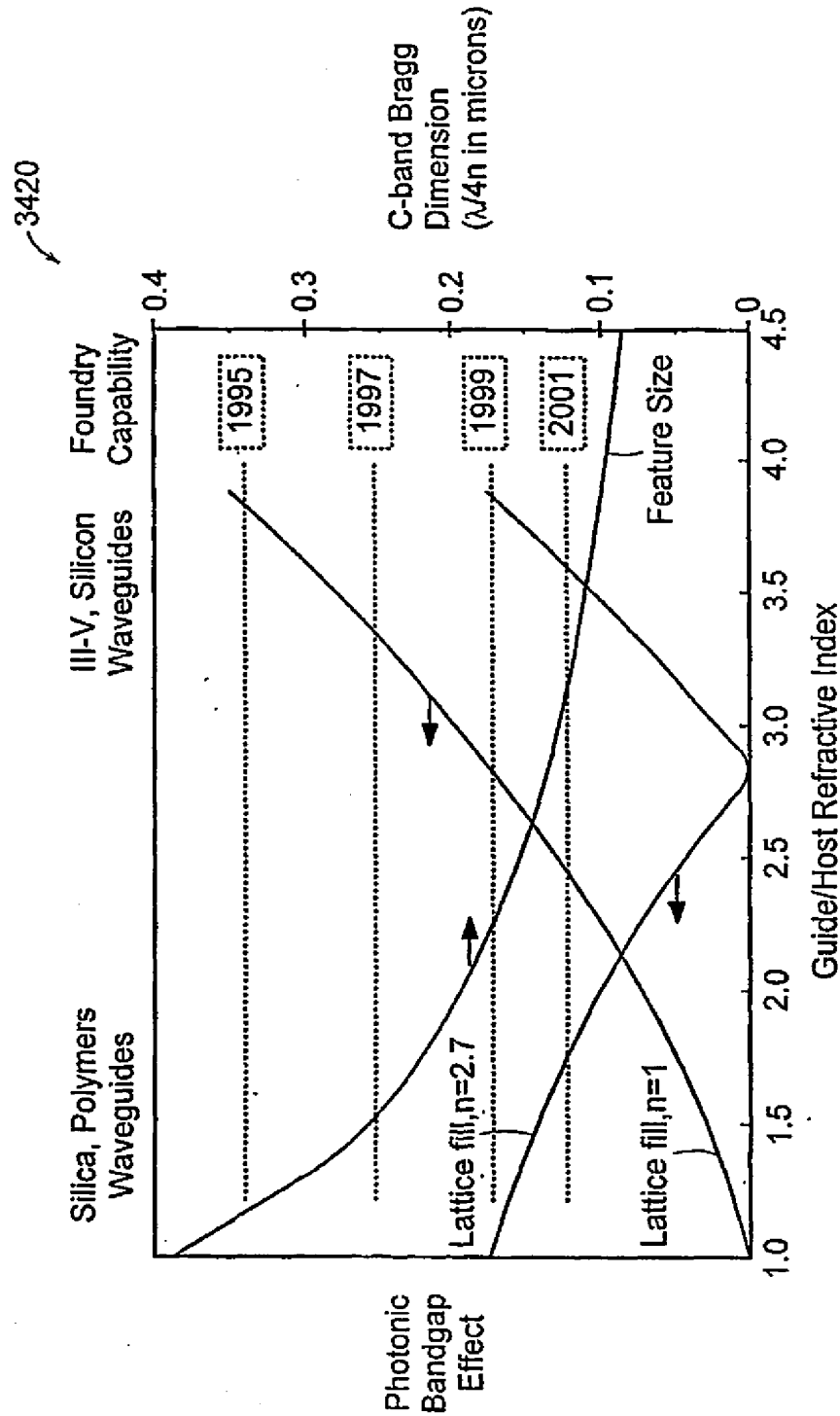


Figure 63

70/100

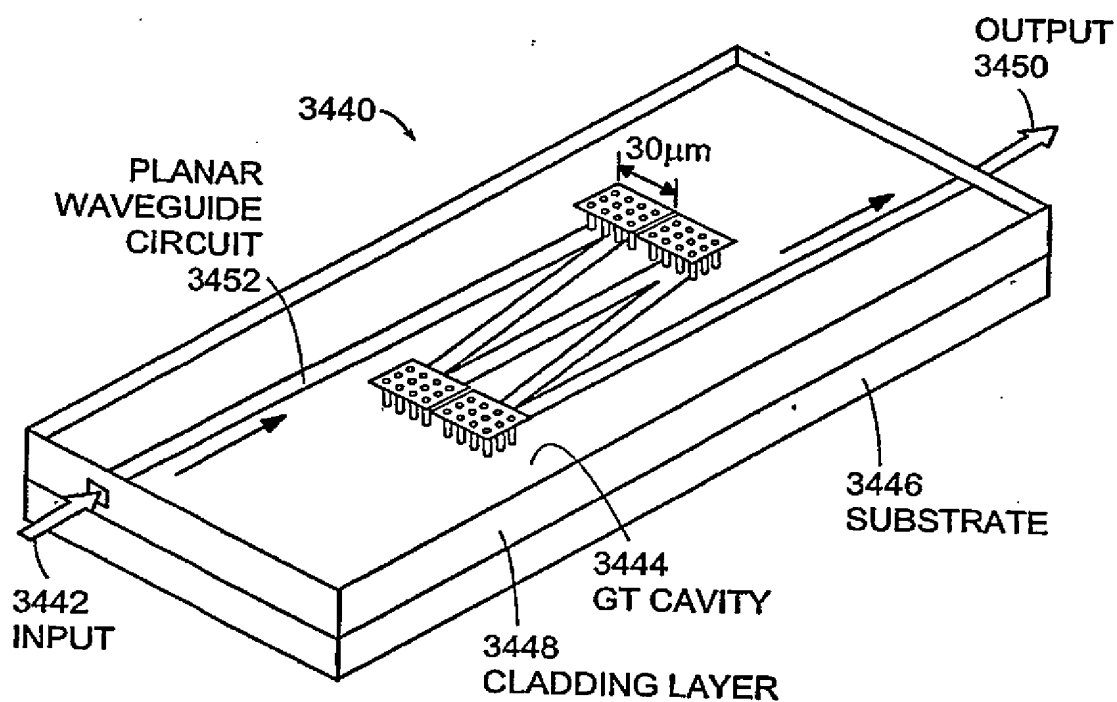


Figure 64A

SUBSTITUTE SHEET (RULE 26)

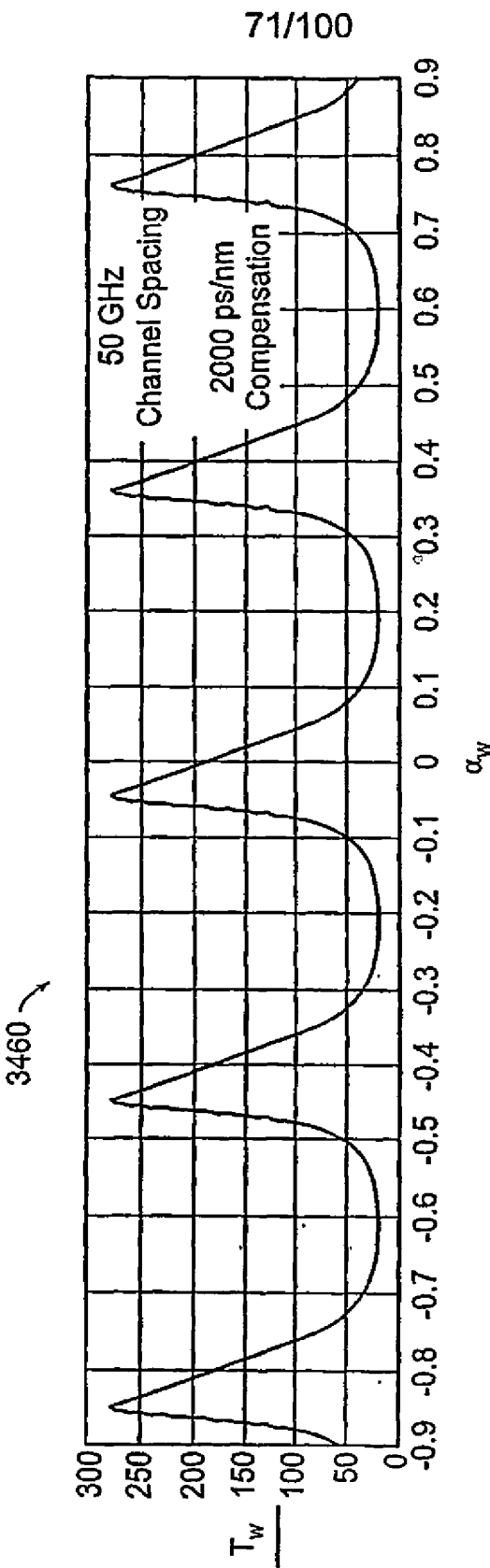


Figure 64B

72/100

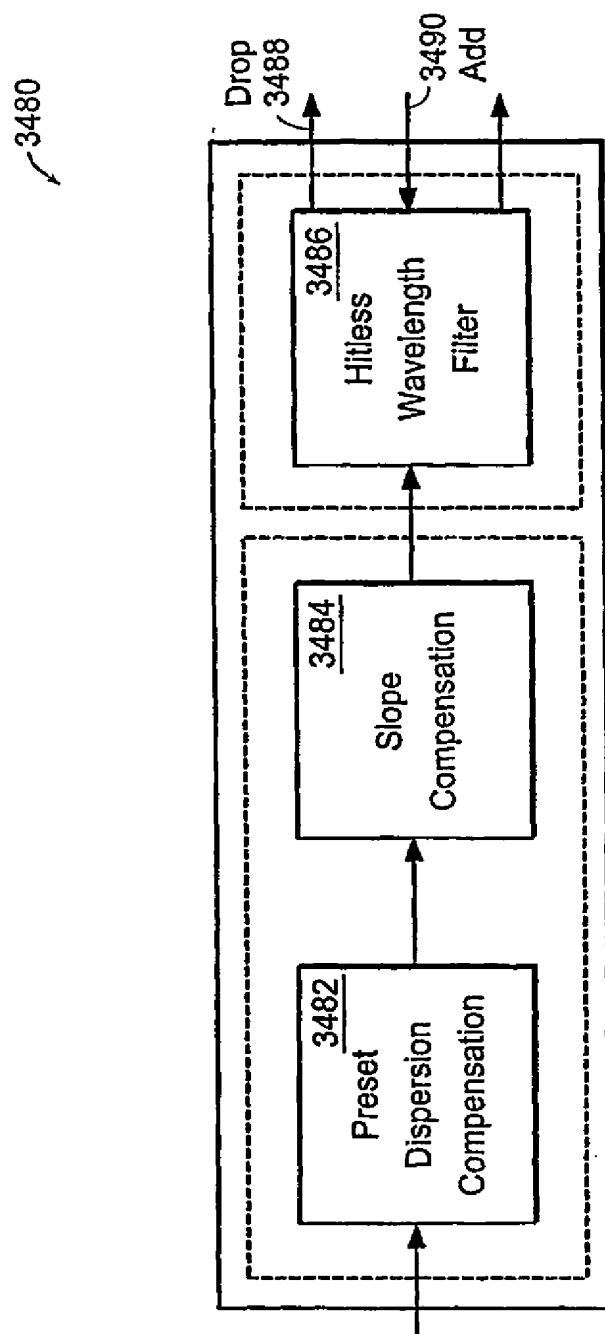


Figure 65A

SUBSTITUTE SHEET (RULE 26)

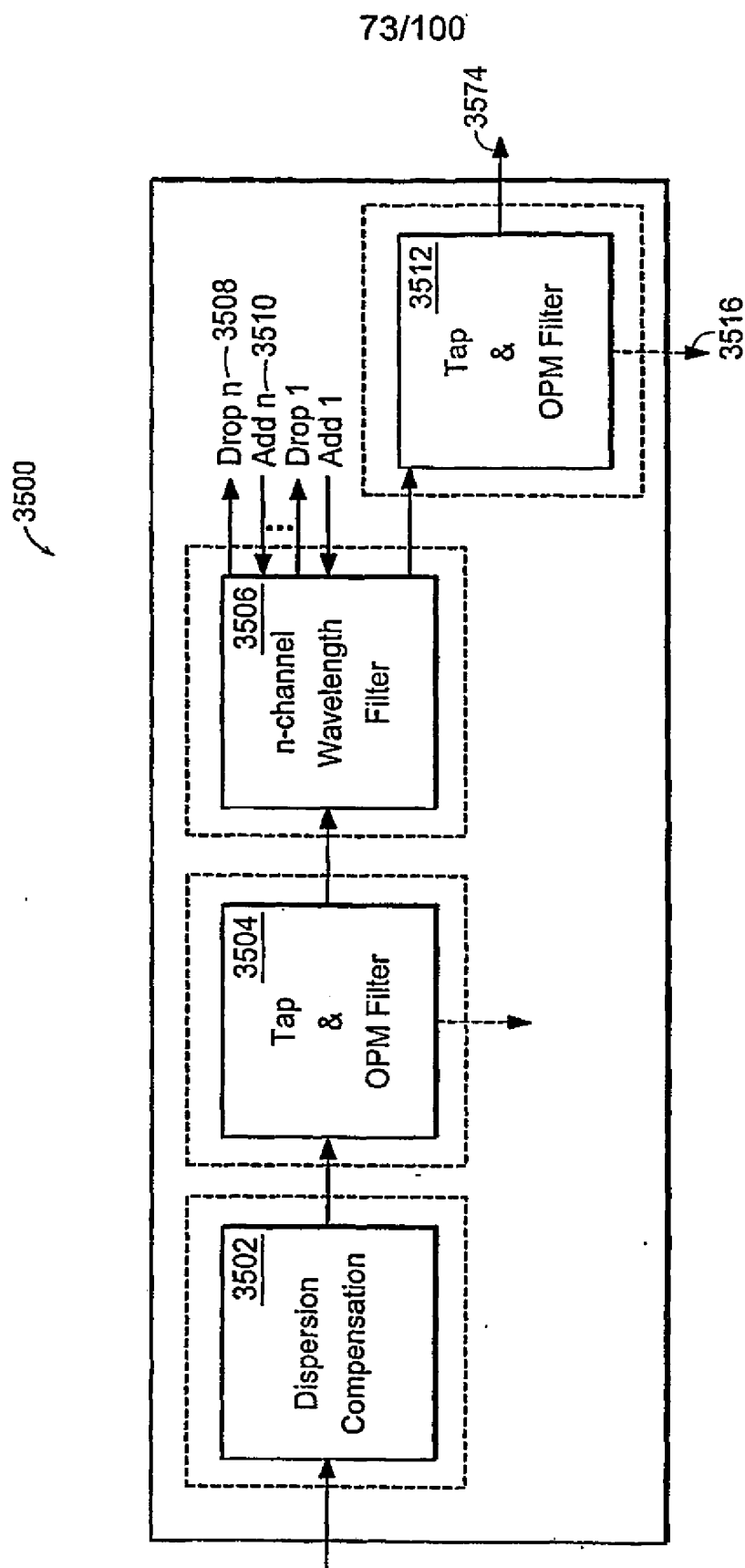


Figure 65B

74/100

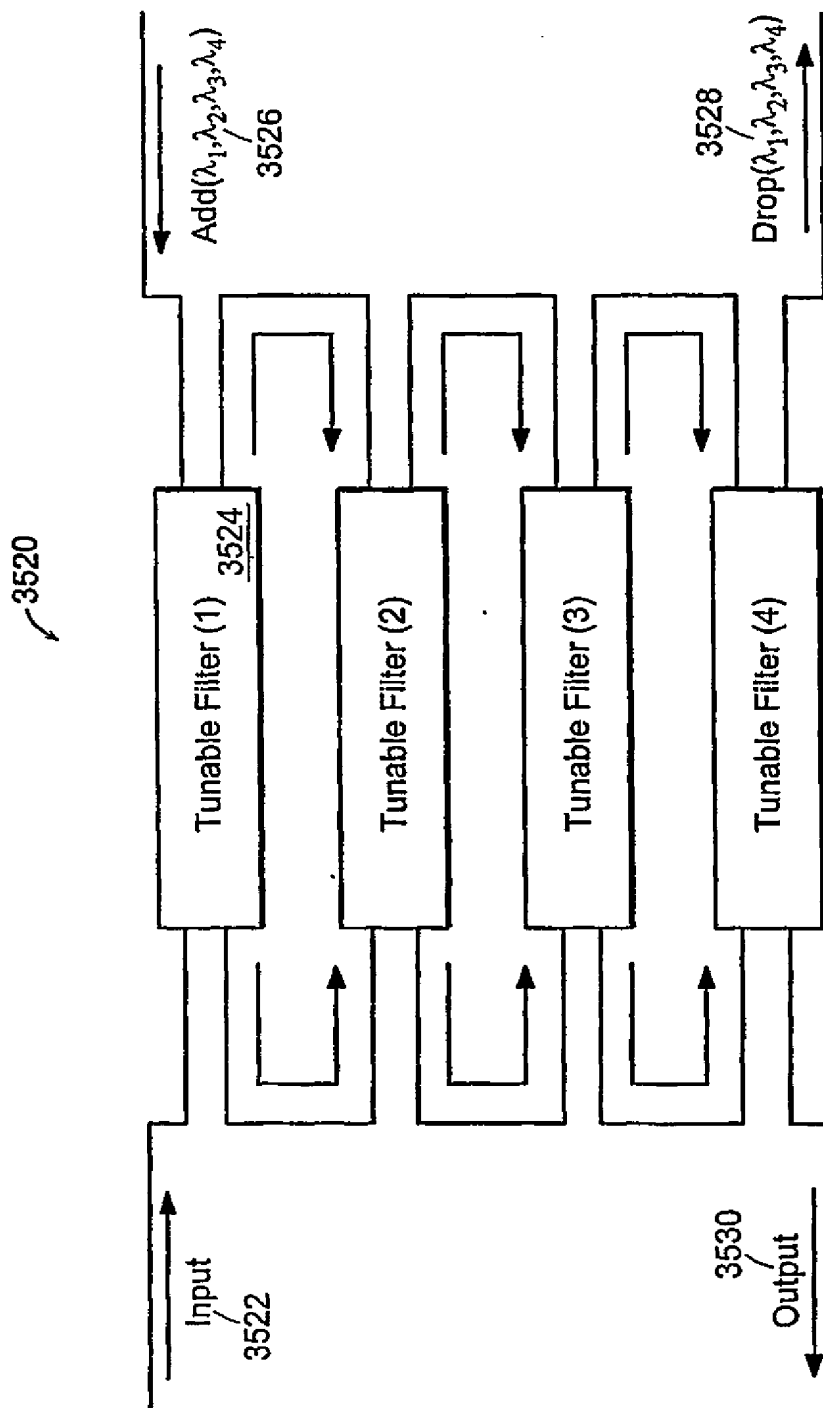


Figure 66A

SUBSTITUTE SHEET (RULE 26)

75/100

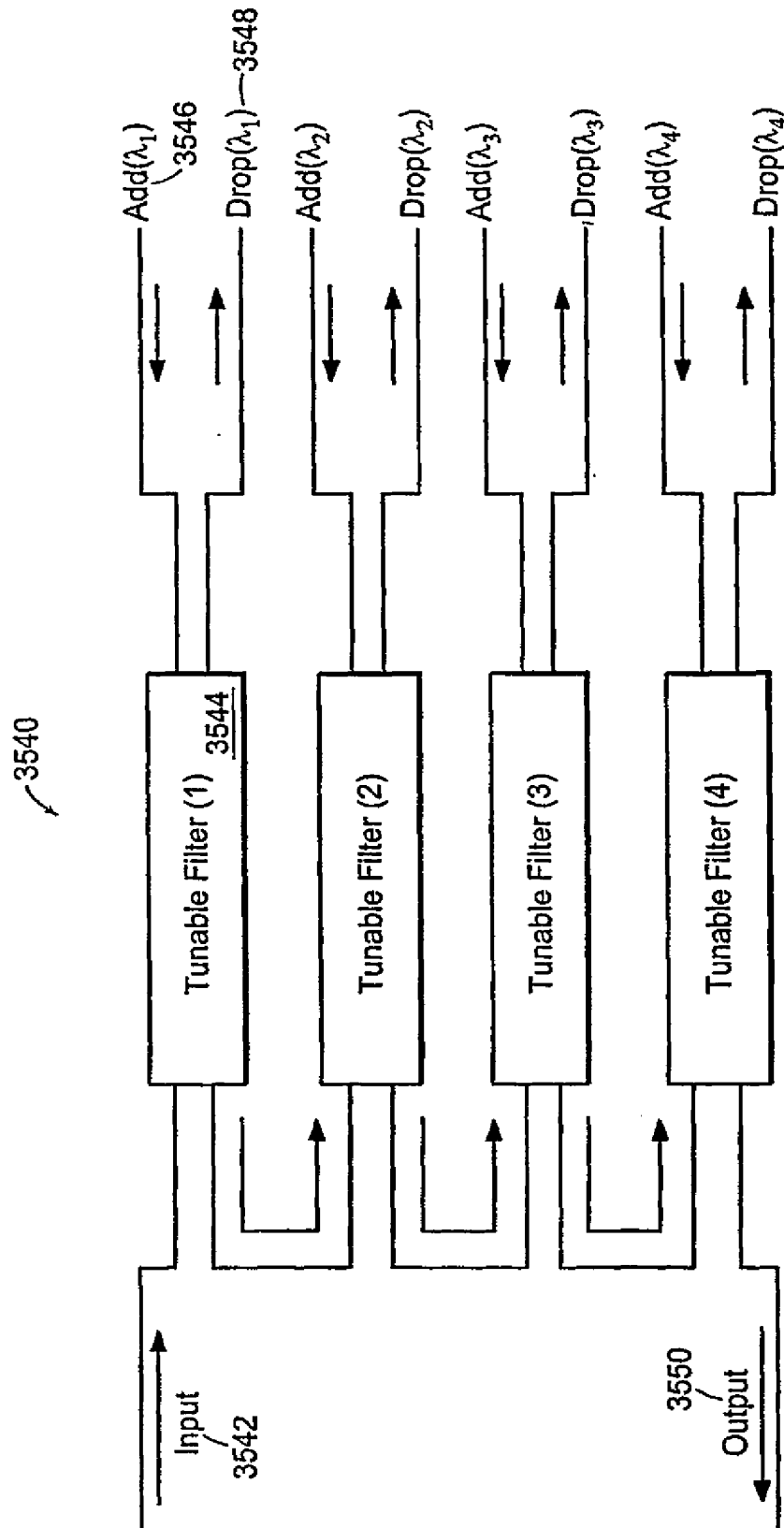


Figure 66B

SUBSTITUTE SHEET (RULE 26)

76/100

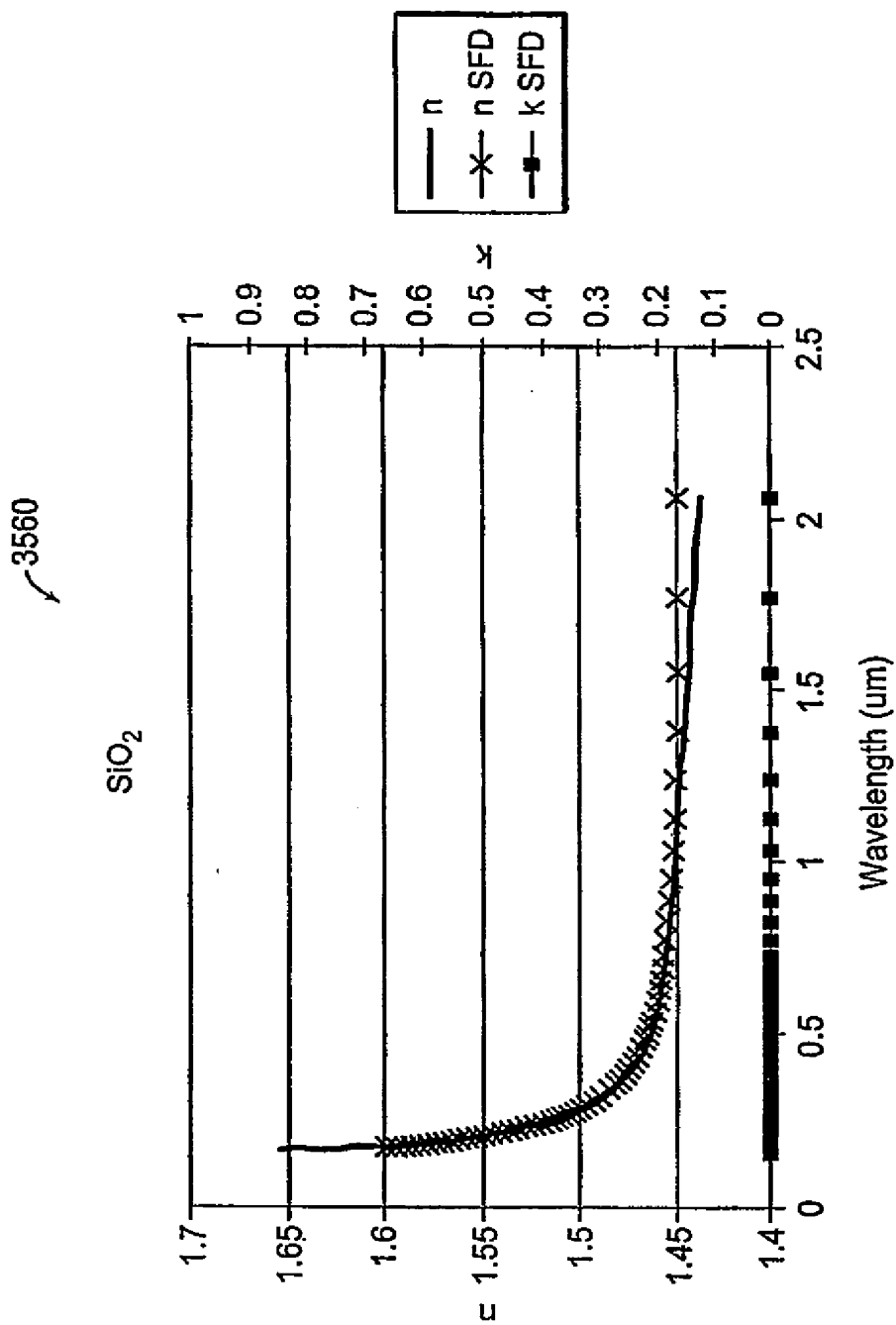


Figure 67

SUBSTITUTE SHEET (RULE 26)

77/100

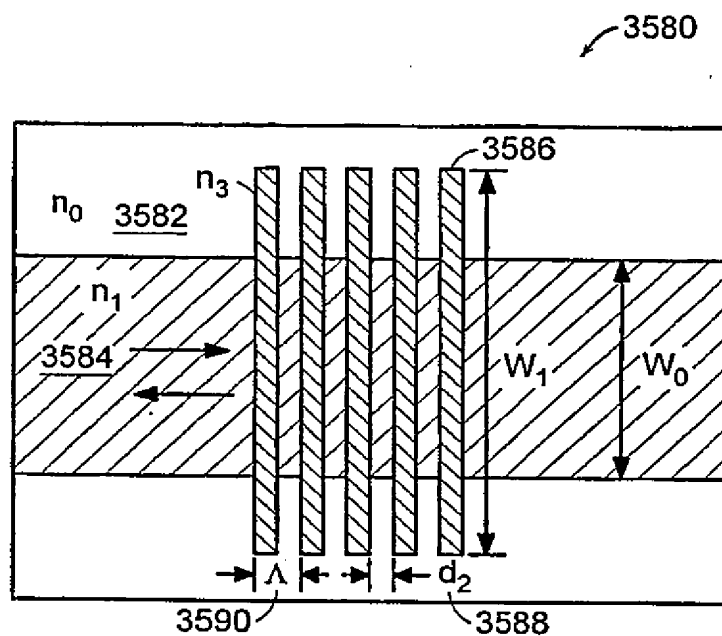


Figure 68A

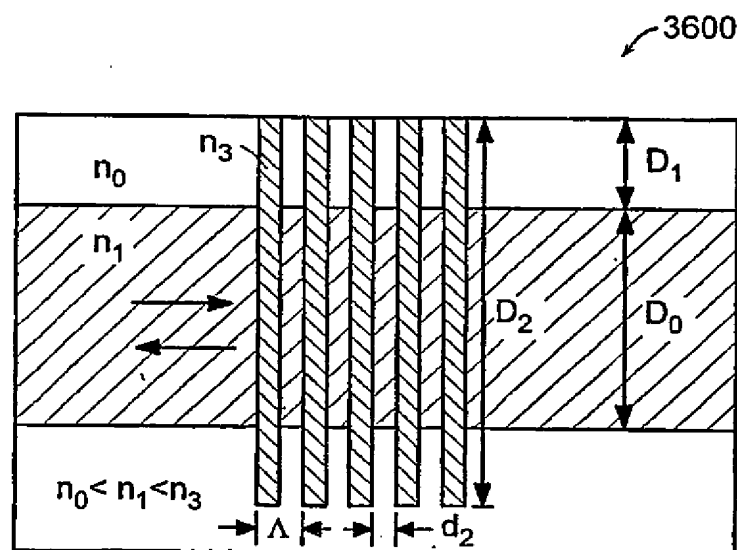


Figure 68B

SUBSTITUTE SHEET (RULE 26)

78/100

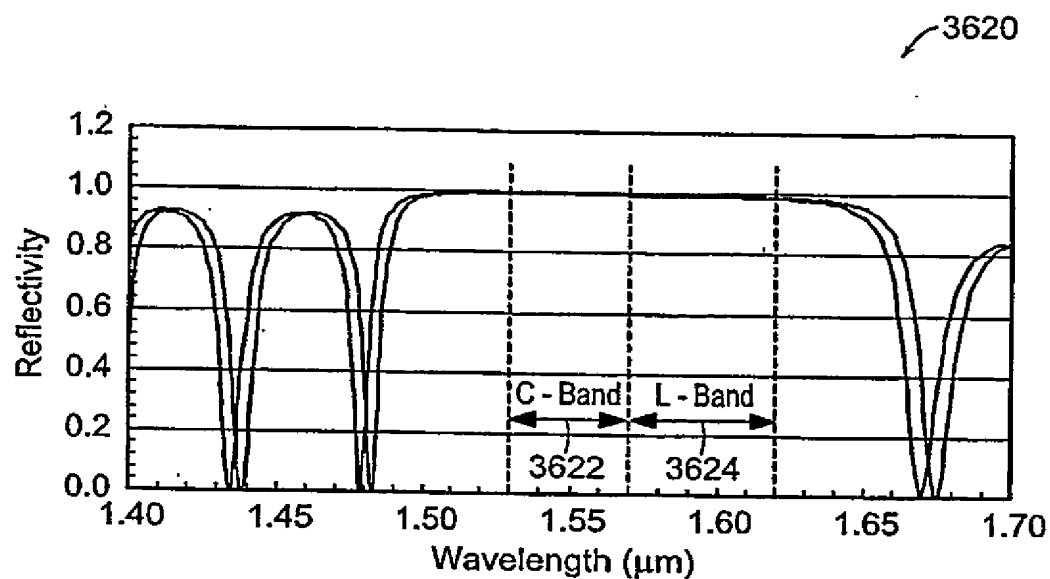


Figure 69

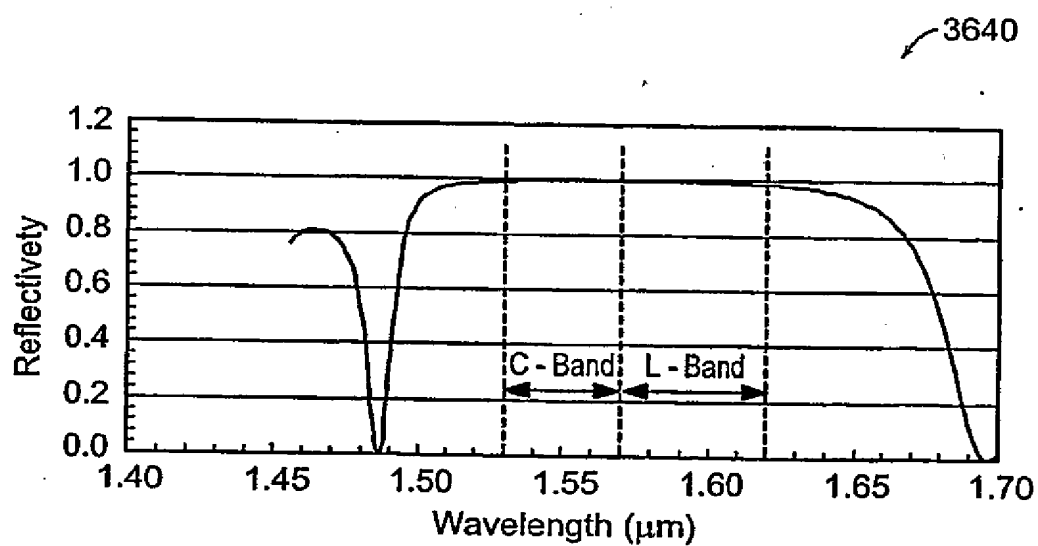


Figure 70

SUBSTITUTE SHEET (RULE 26)

79/100

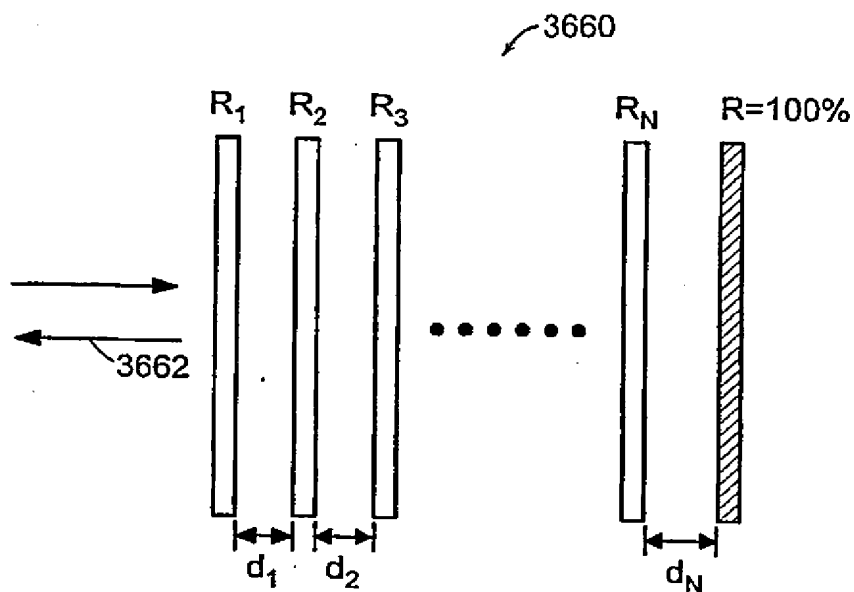


Figure 71

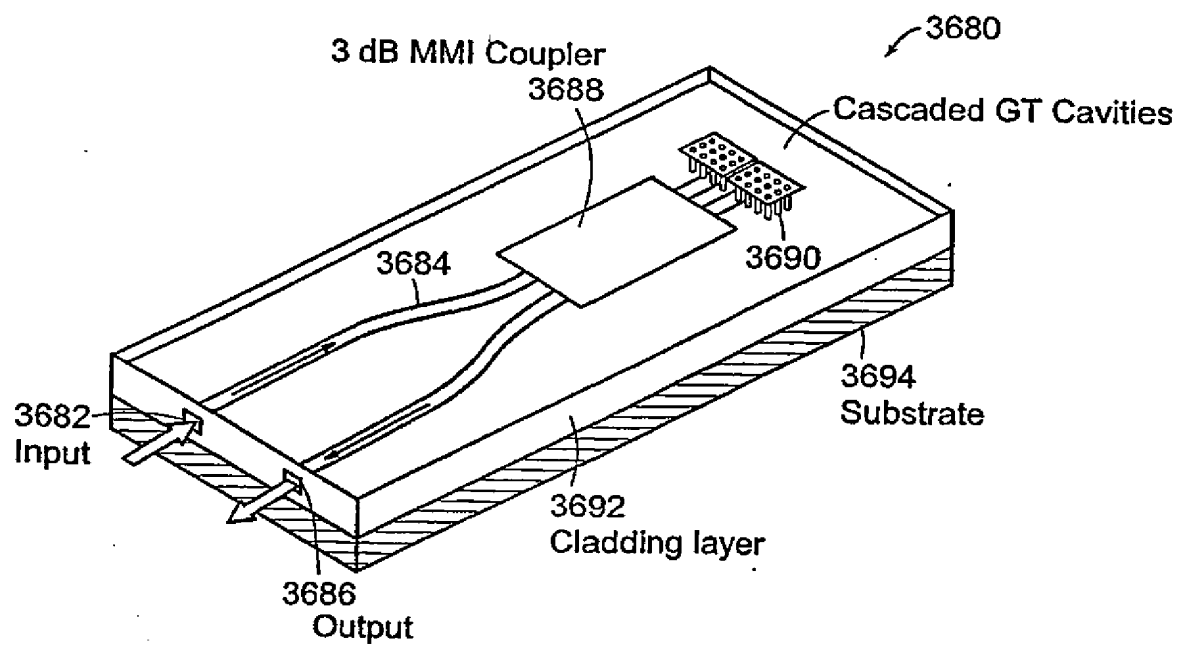


Figure 72

SUBSTITUTE SHEET (RULE 26)

80/100

3695

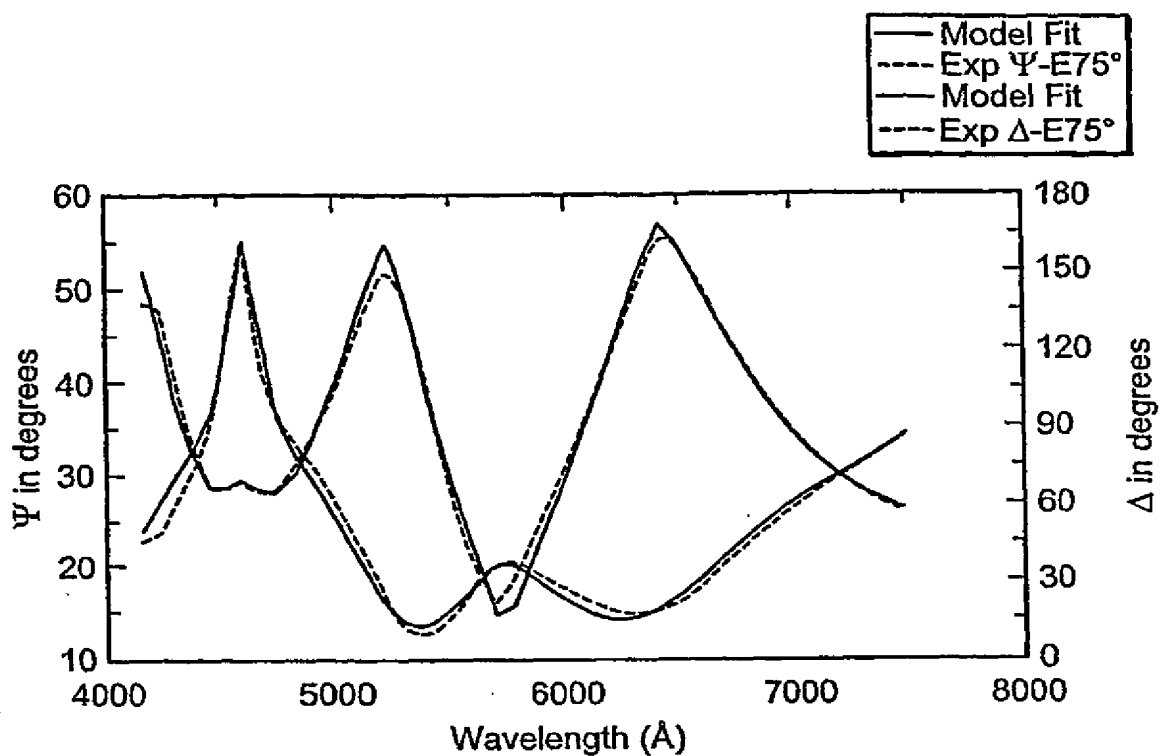


Figure 73A

3696

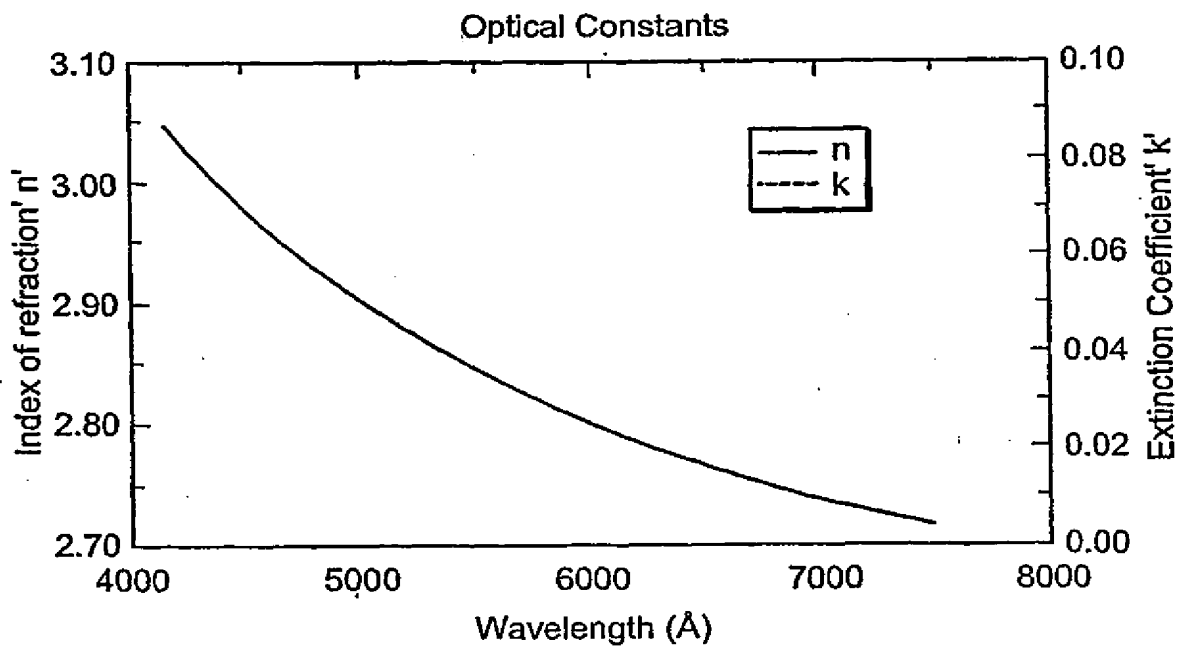


Figure 73B

SUBSTITUTE SHEET (RULE 26)

81/100

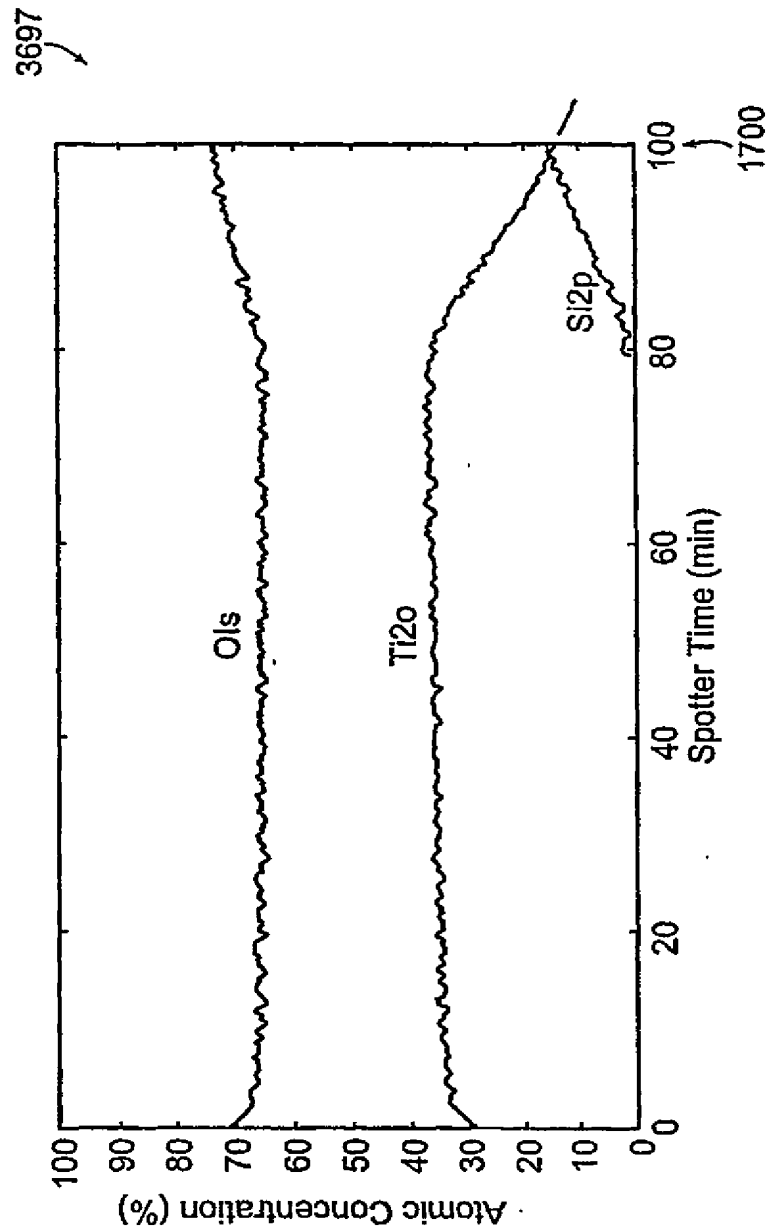


Figure 73C

SUBSTITUTE SHEET (RULE 26)

82/100

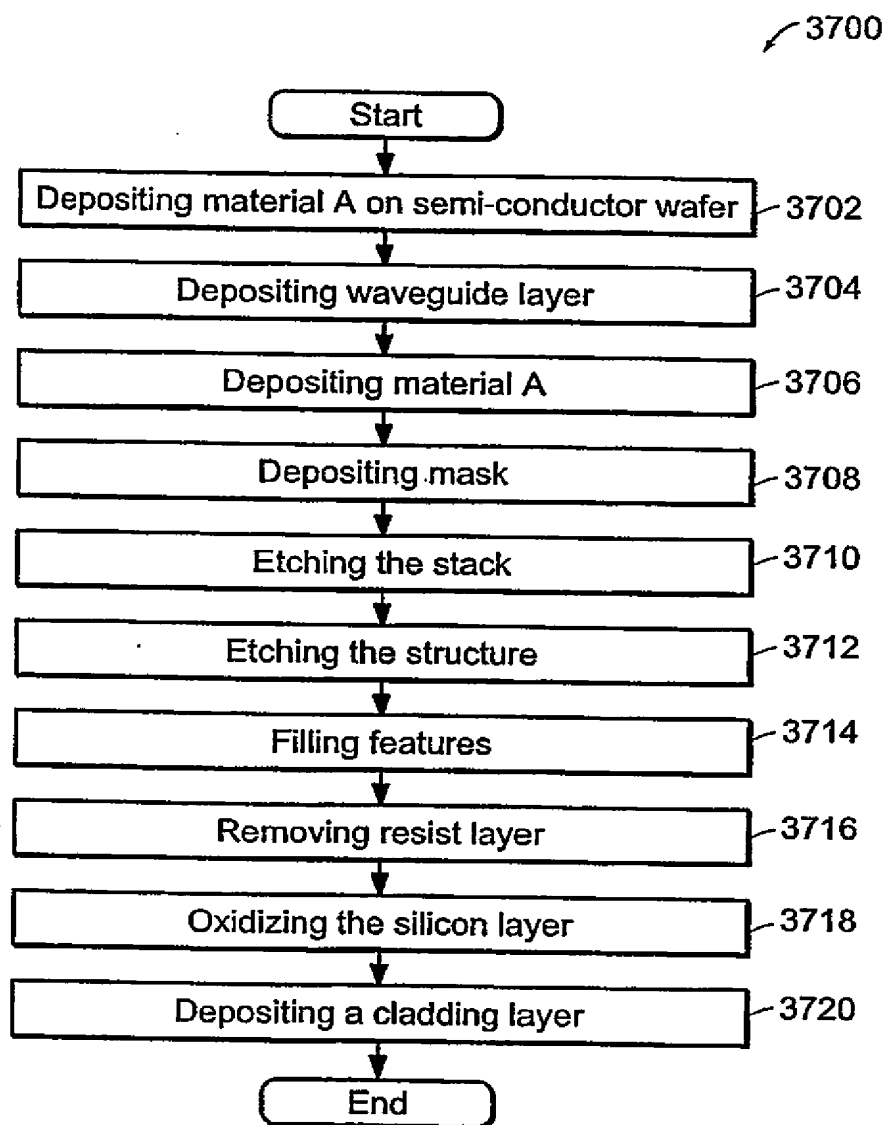


Figure 73D

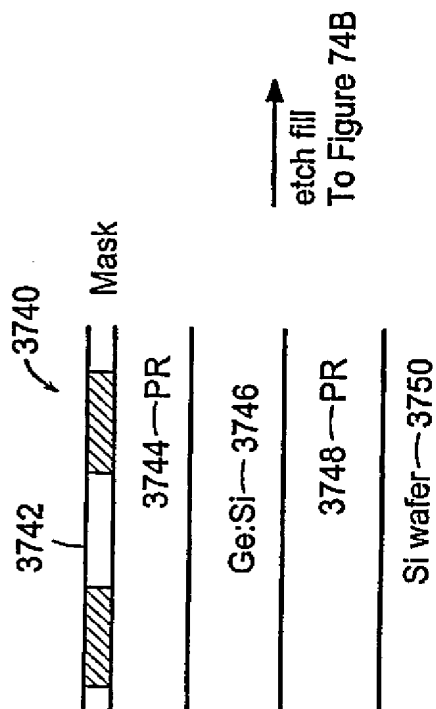


Figure 74A

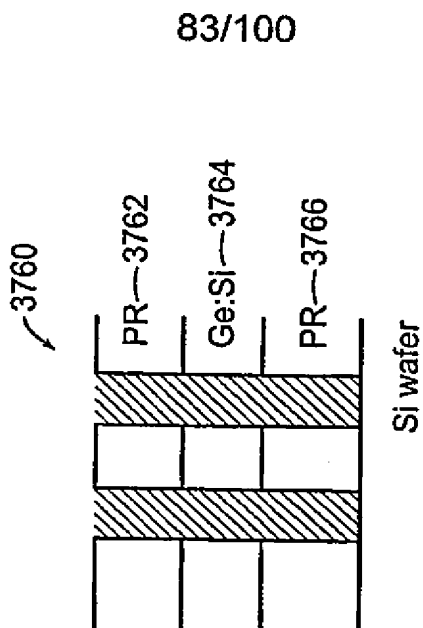
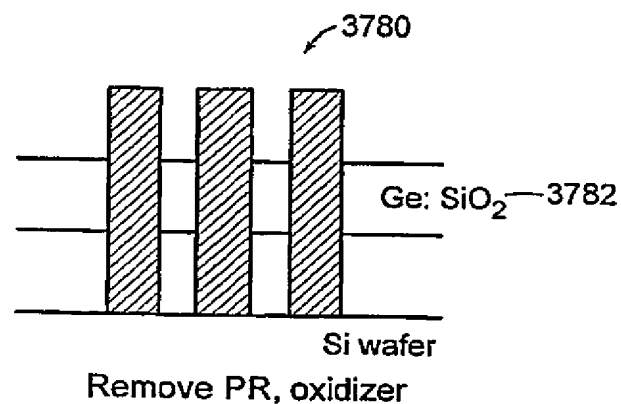


Figure 74B

83/100

84/100



Leave freestanding or encapsulate

Figure 74C

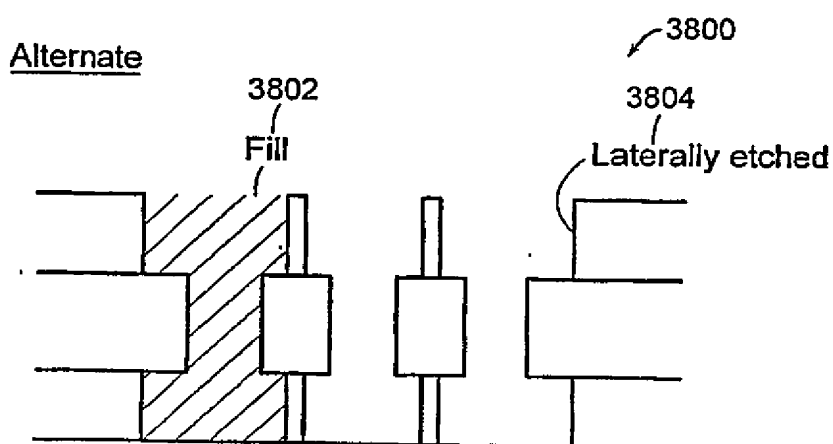


Figure 74D

SUBSTITUTE SHEET (RULE 26)

85/100

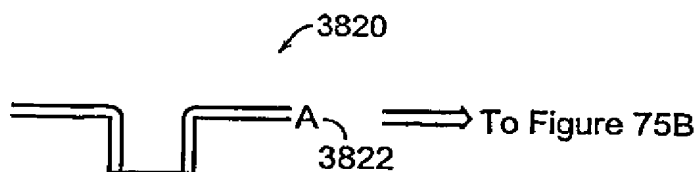


Figure 75A

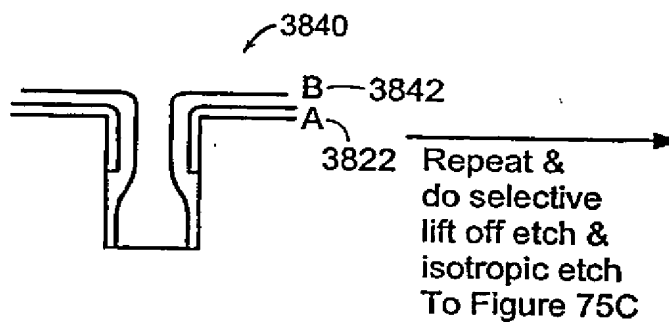


Figure 75B

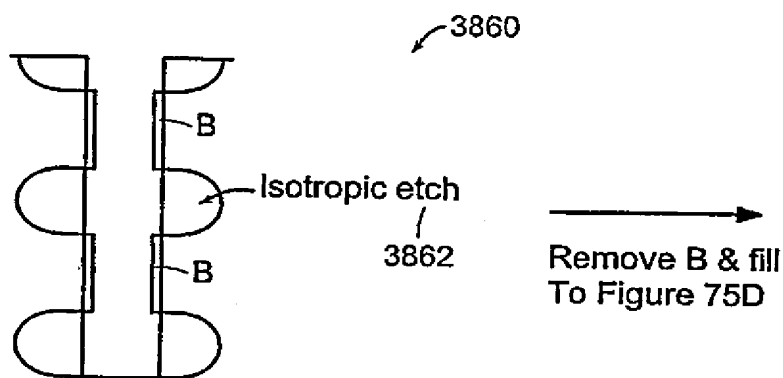


Figure 75C

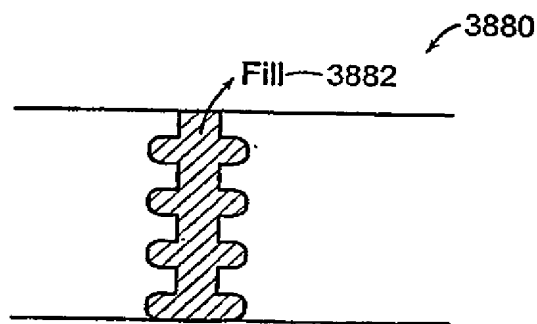


Figure 75D

SUBSTITUTE SHEET (RULE 26)

86/100

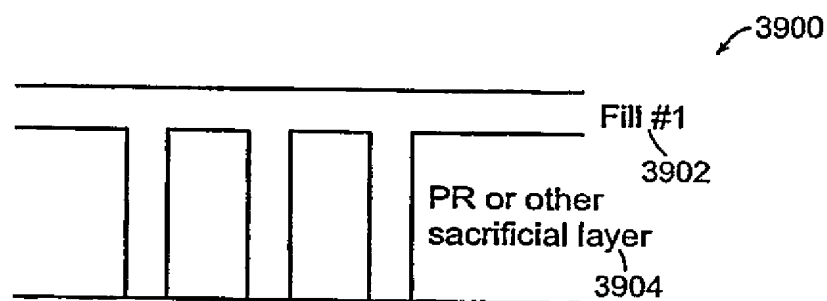


Figure 76A

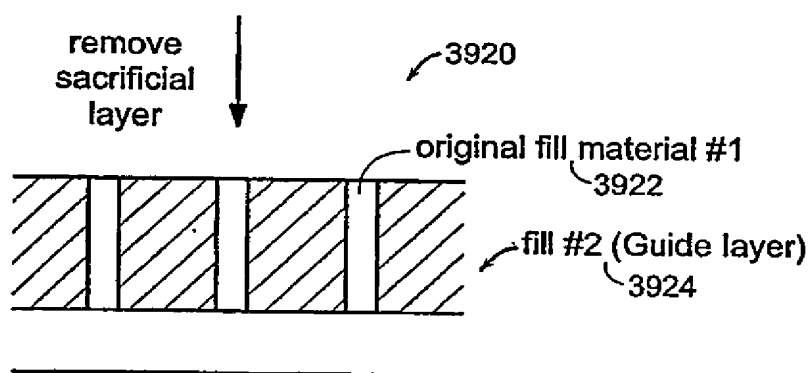


Figure 76B

SUBSTITUTE SHEET (RULE 26)

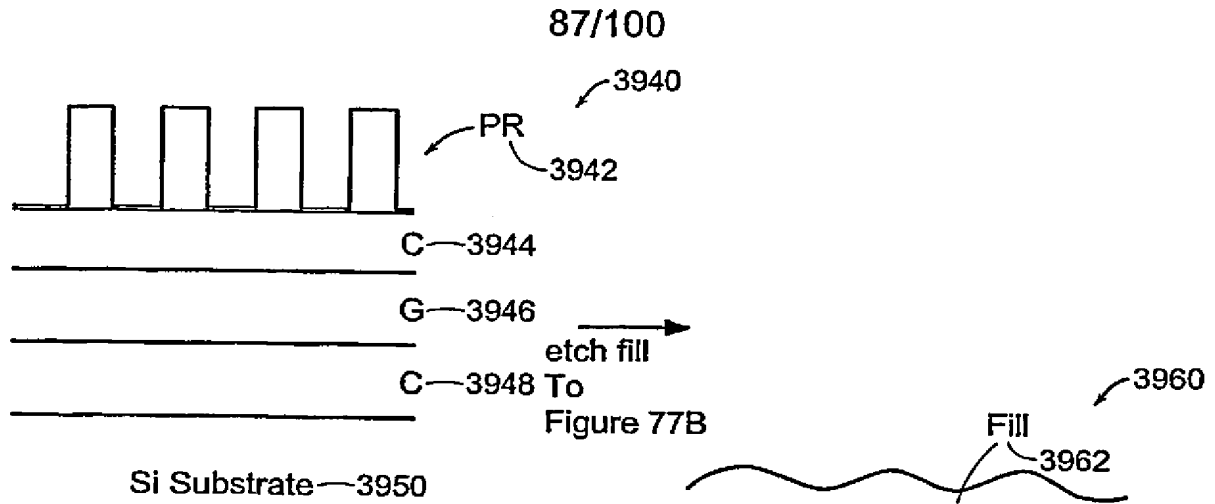


Figure 77A

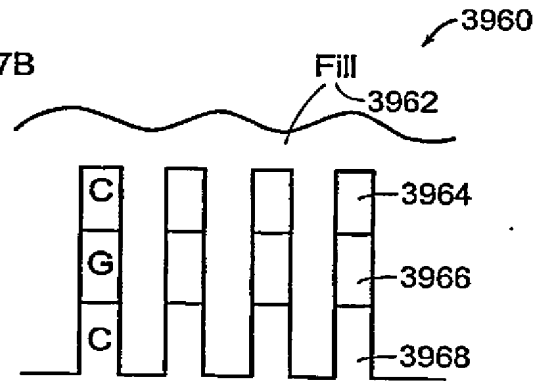


Figure 77B

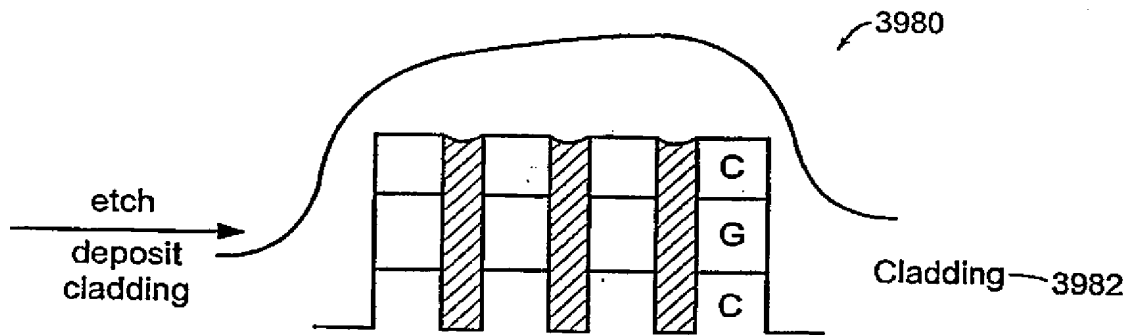


Figure 77C

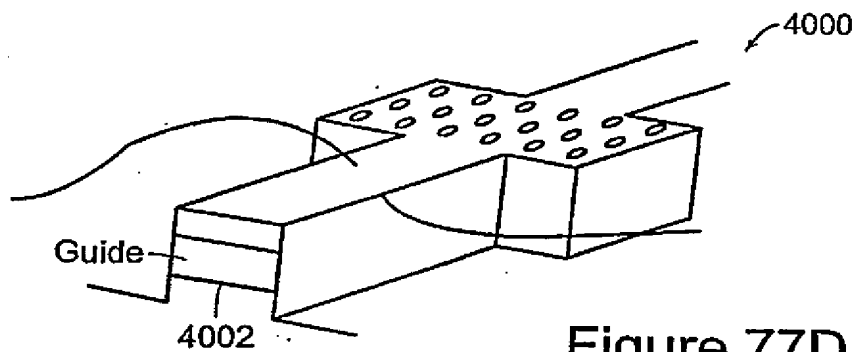


Figure 77D

88/100

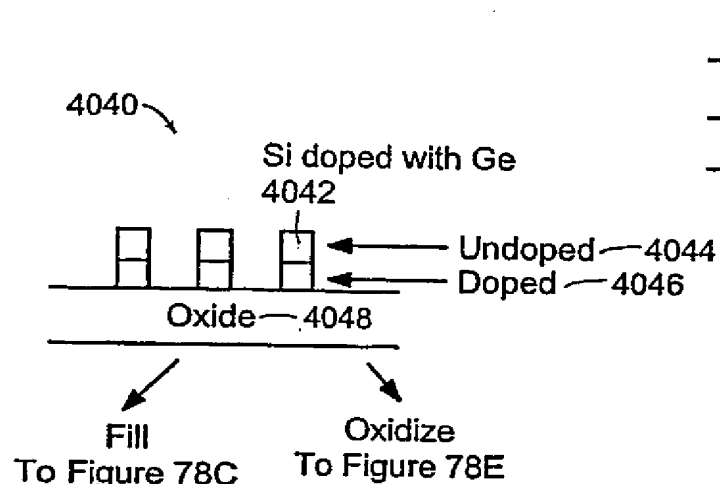


Figure 78B

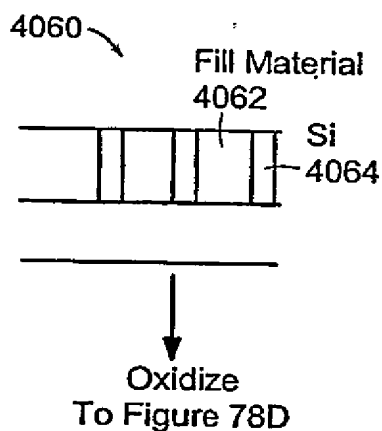


Figure 78C

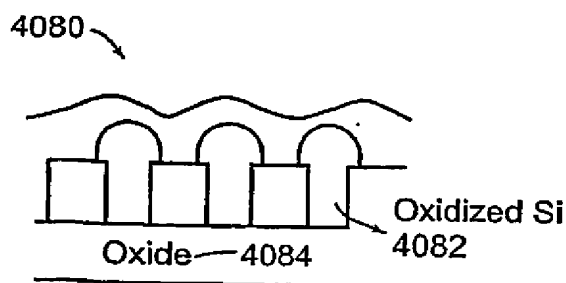


Figure 78D

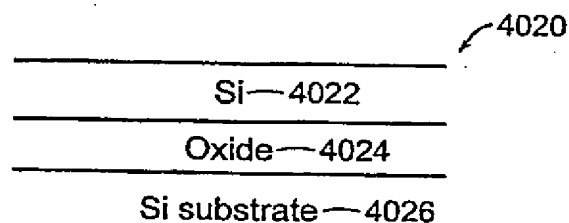


Figure 78A

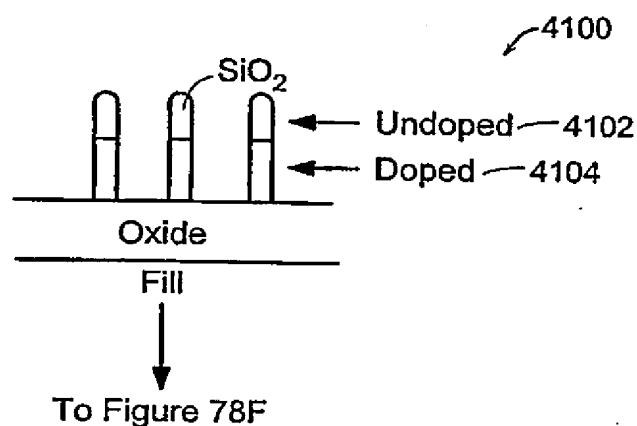


Figure 78E

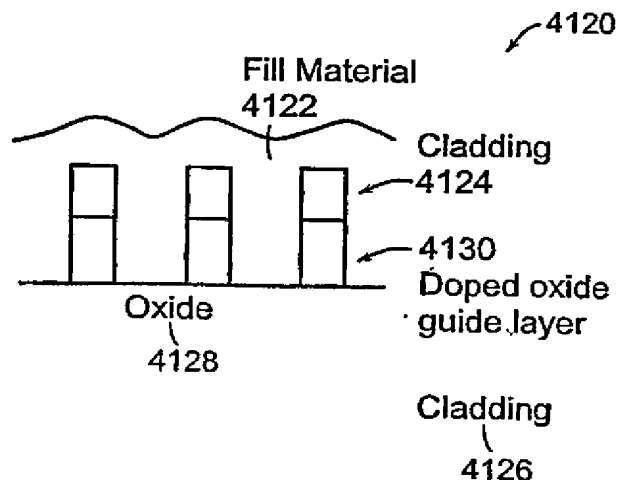


Figure 78F

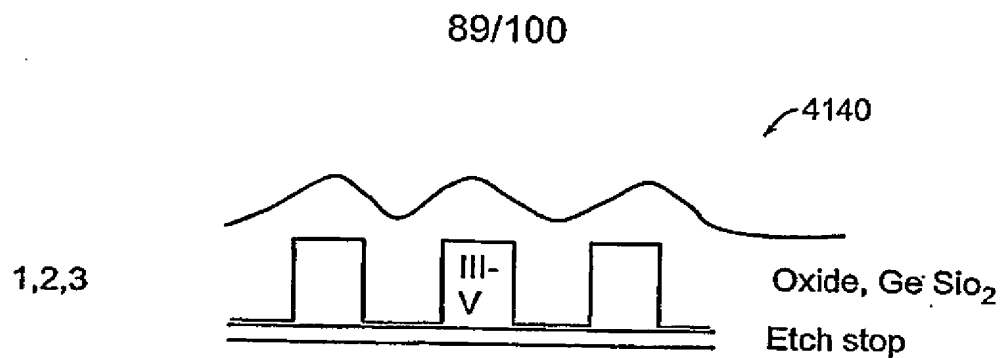


Figure 79A

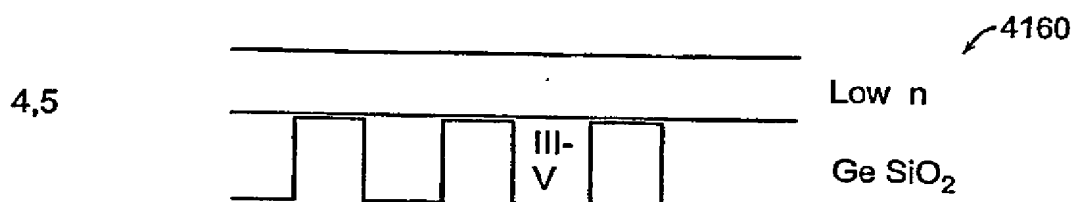


Figure 79B

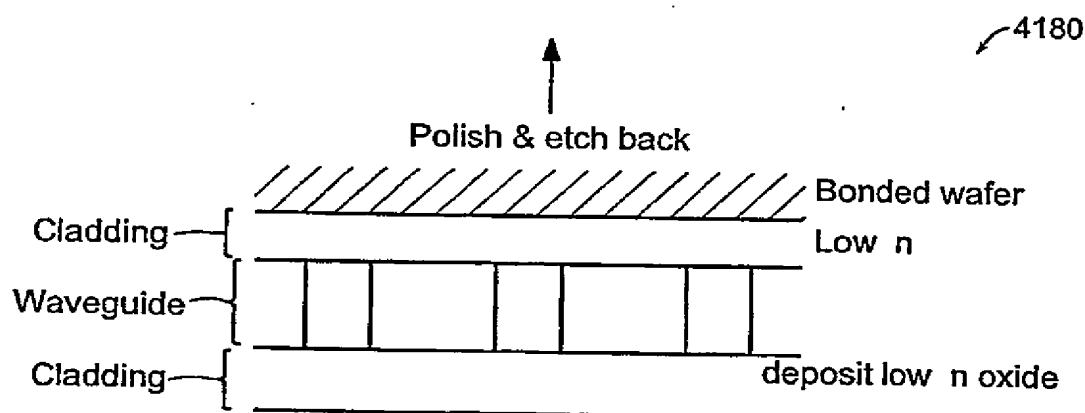


Figure 79C

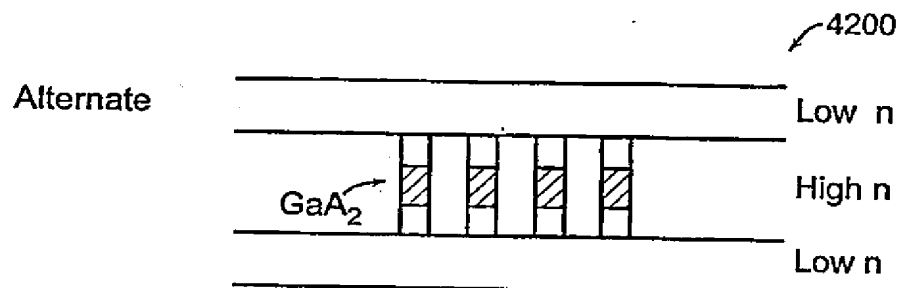


Figure 79D

90/100

4250

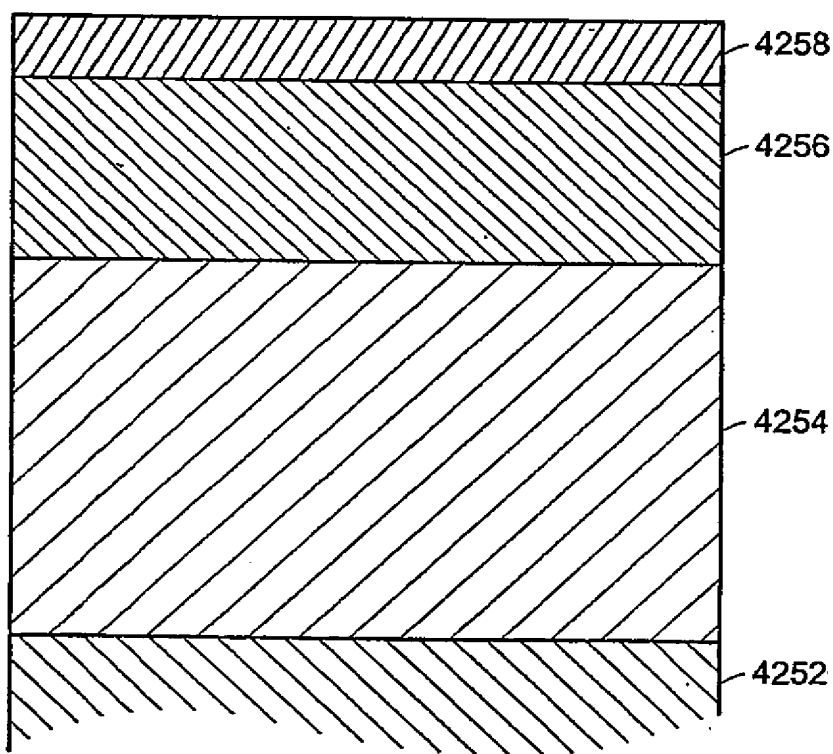


Figure 80A

SUBSTITUTE SHEET (RULE 26)

91/100

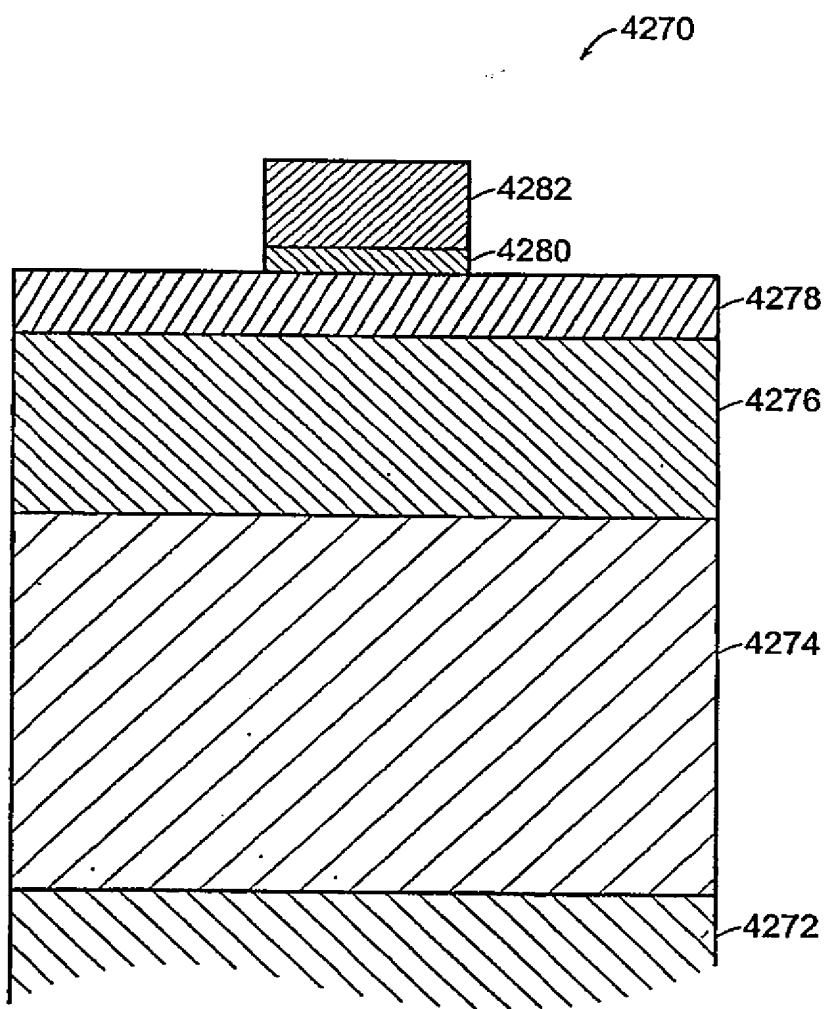


Figure 80B

SUBSTITUTE SHEET (RULE 26)

92/100

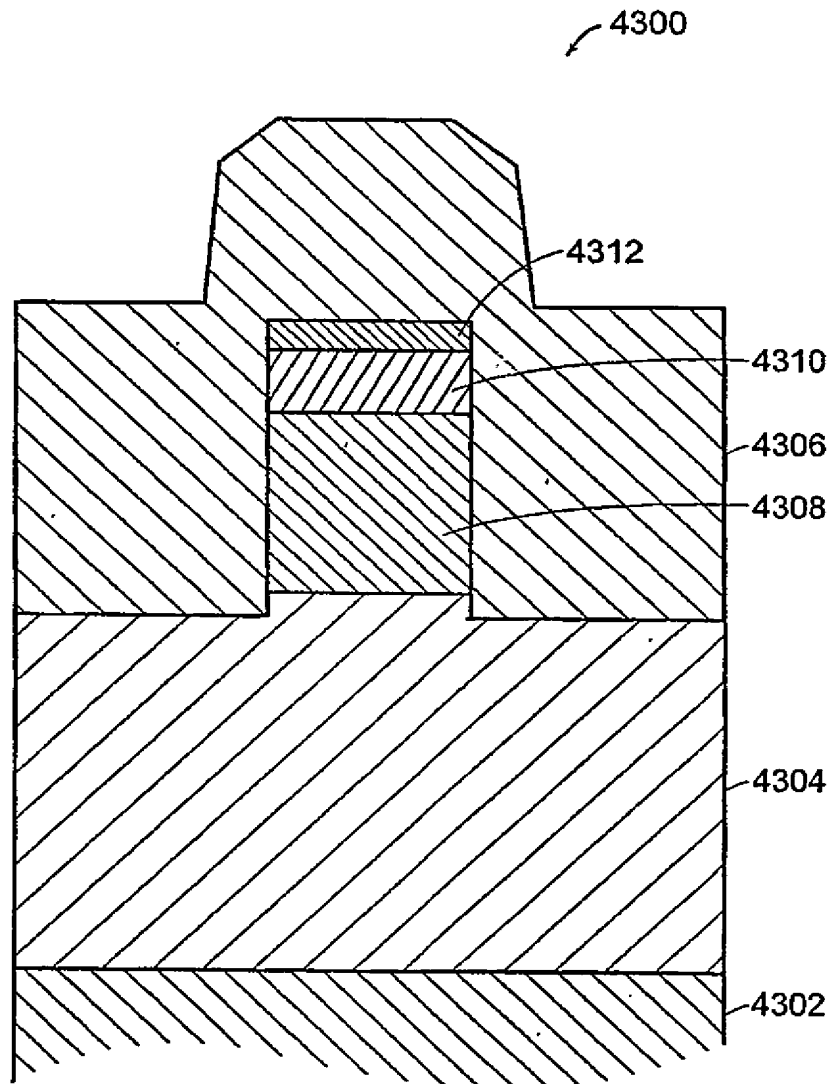


Figure 80C

SUBSTITUTE SHEET (RULE 26)

93/100

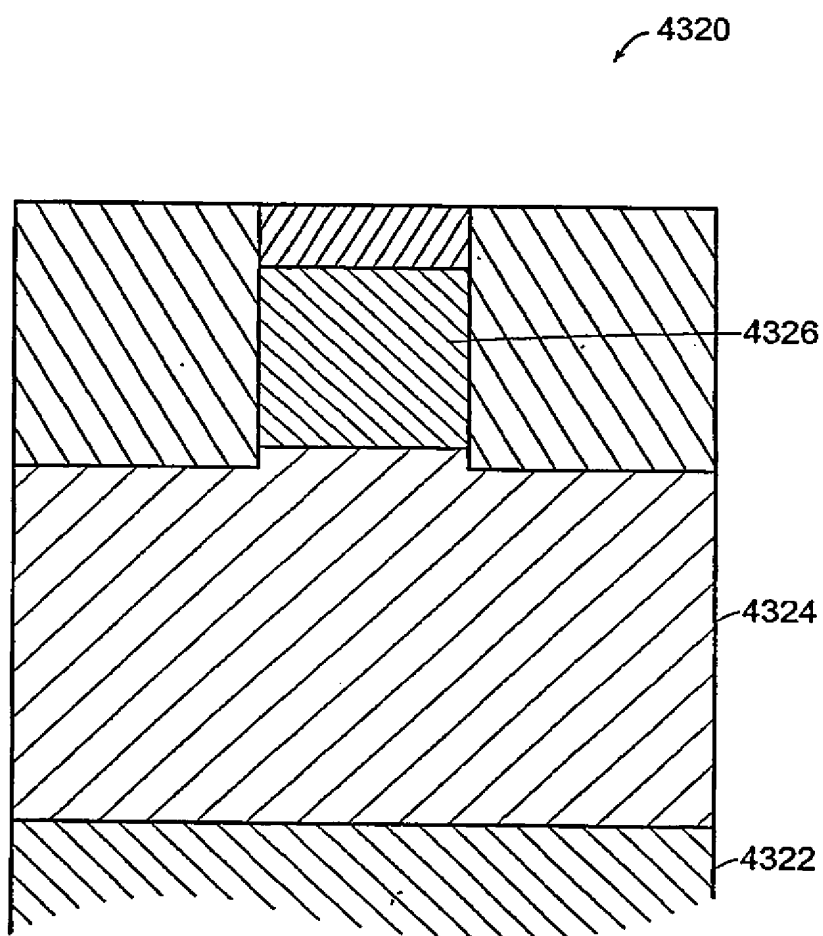


Figure 80D

SUBSTITUTE SHEET (RULE 26)

94/100

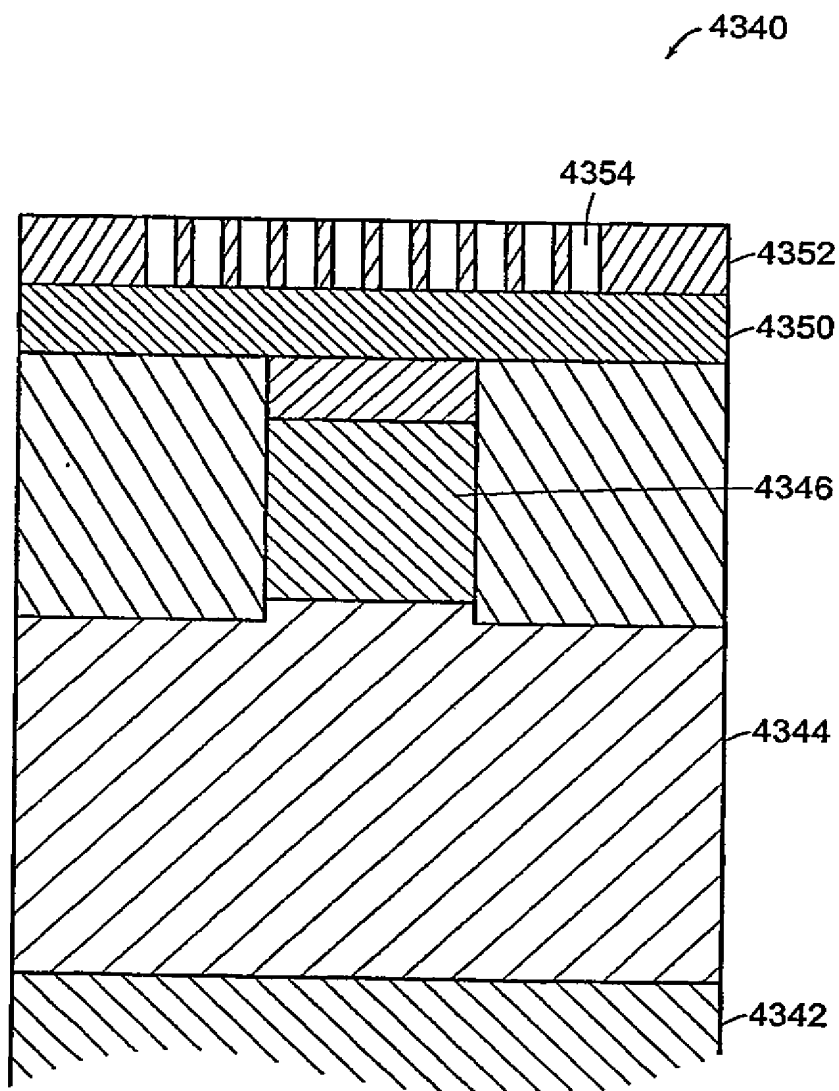


Figure 80E

SUBSTITUTE SHEET (RULE 26)

95/100

4370

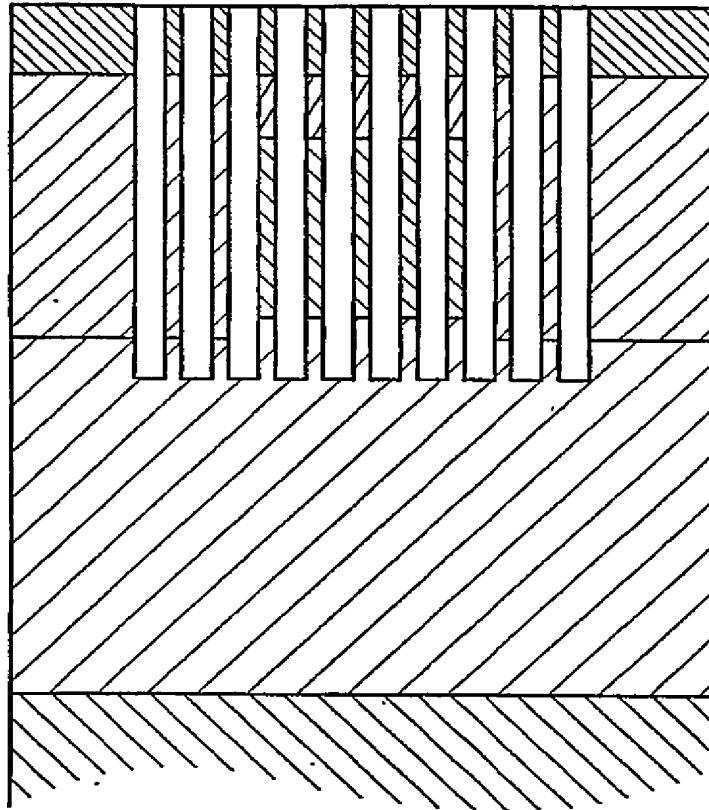


Figure 80F

SUBSTITUTE SHEET (RULE 26)

96/100

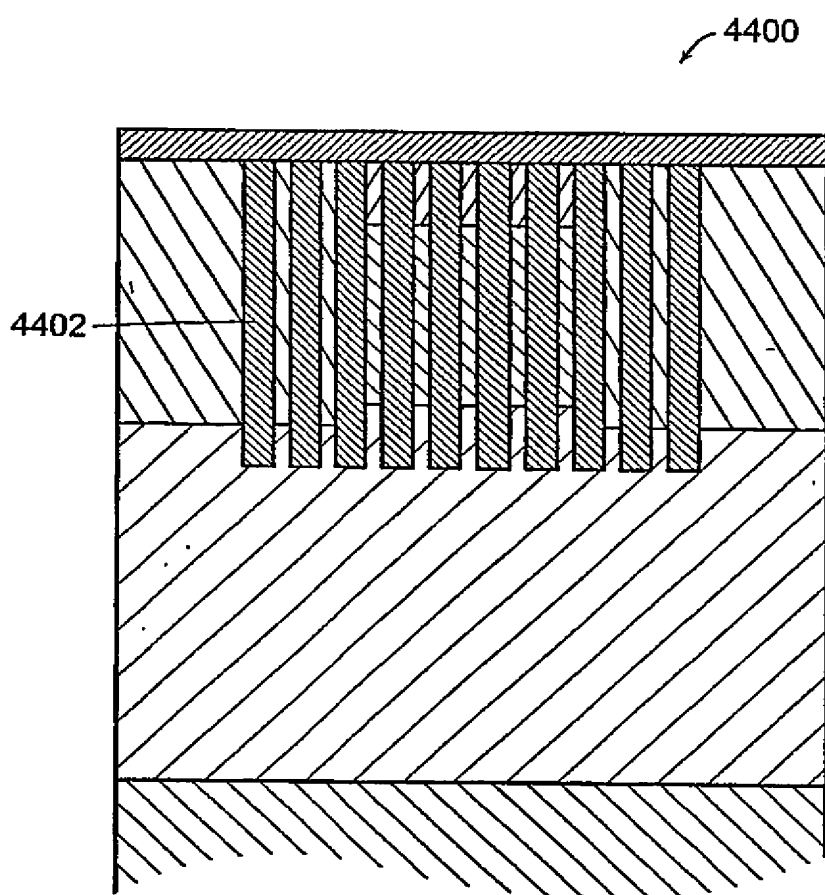


Figure 80G

SUBSTITUTE SHEET (RULE 26)

97/100

4420

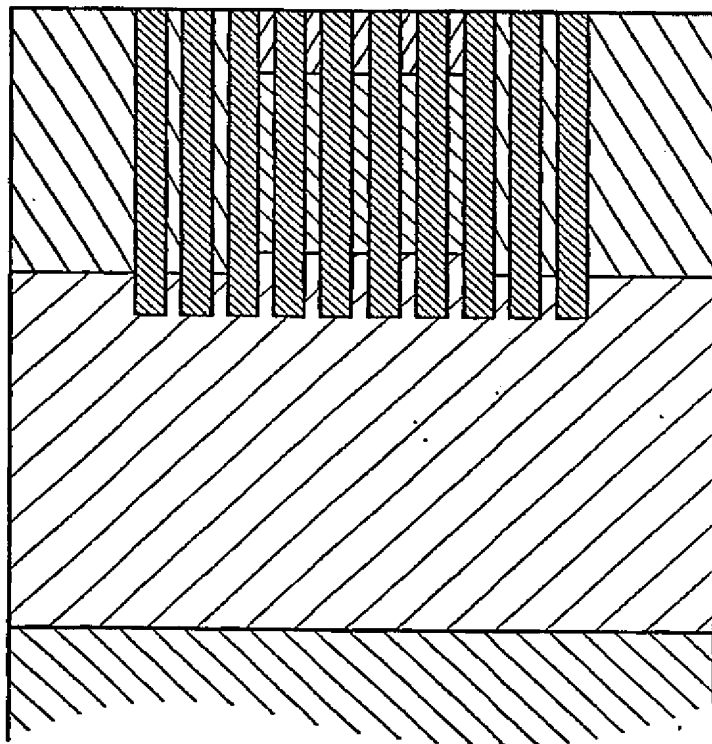


Figure 80H

SUBSTITUTE SHEET (RULE 26)

98/100

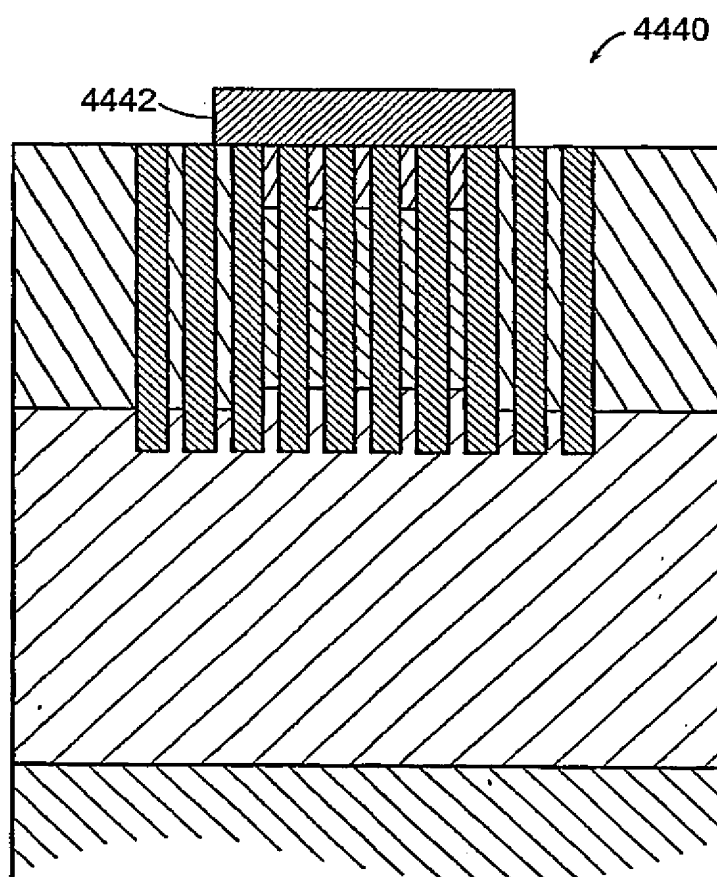


Figure 80I

SUBSTITUTE SHEET (RULE 26)

99/100

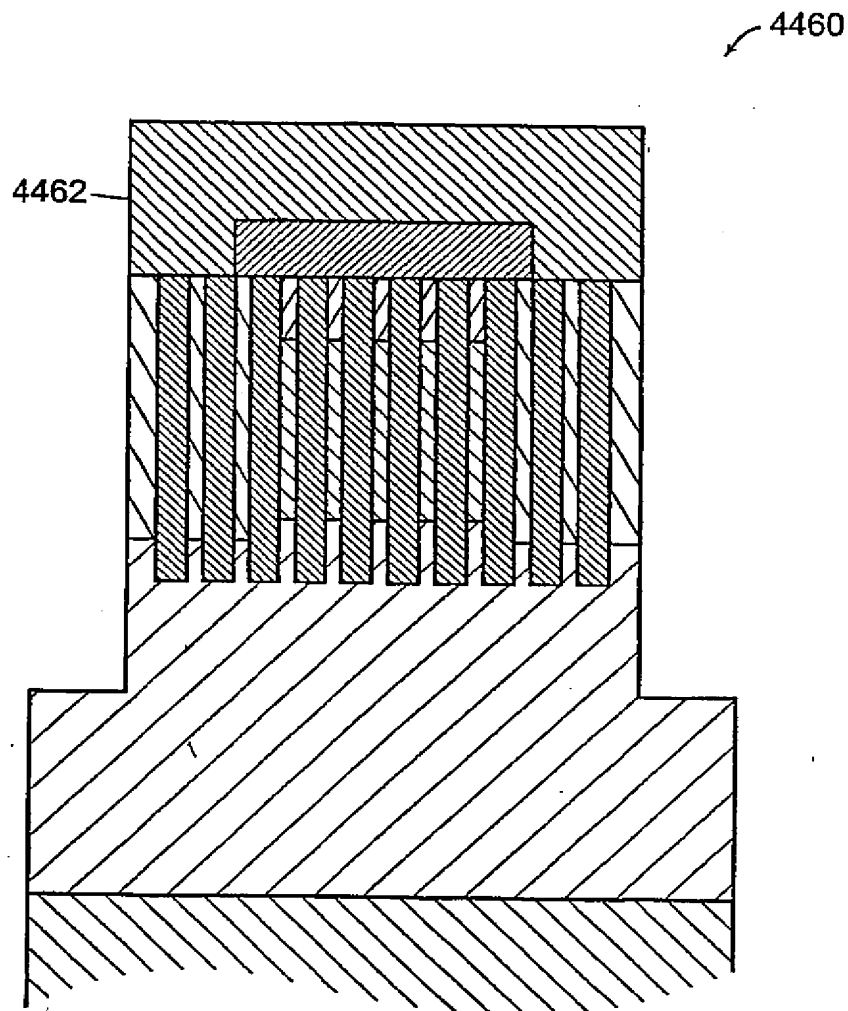


Figure 80J

SUBSTITUTE SHEET (RULE 26)

100/100

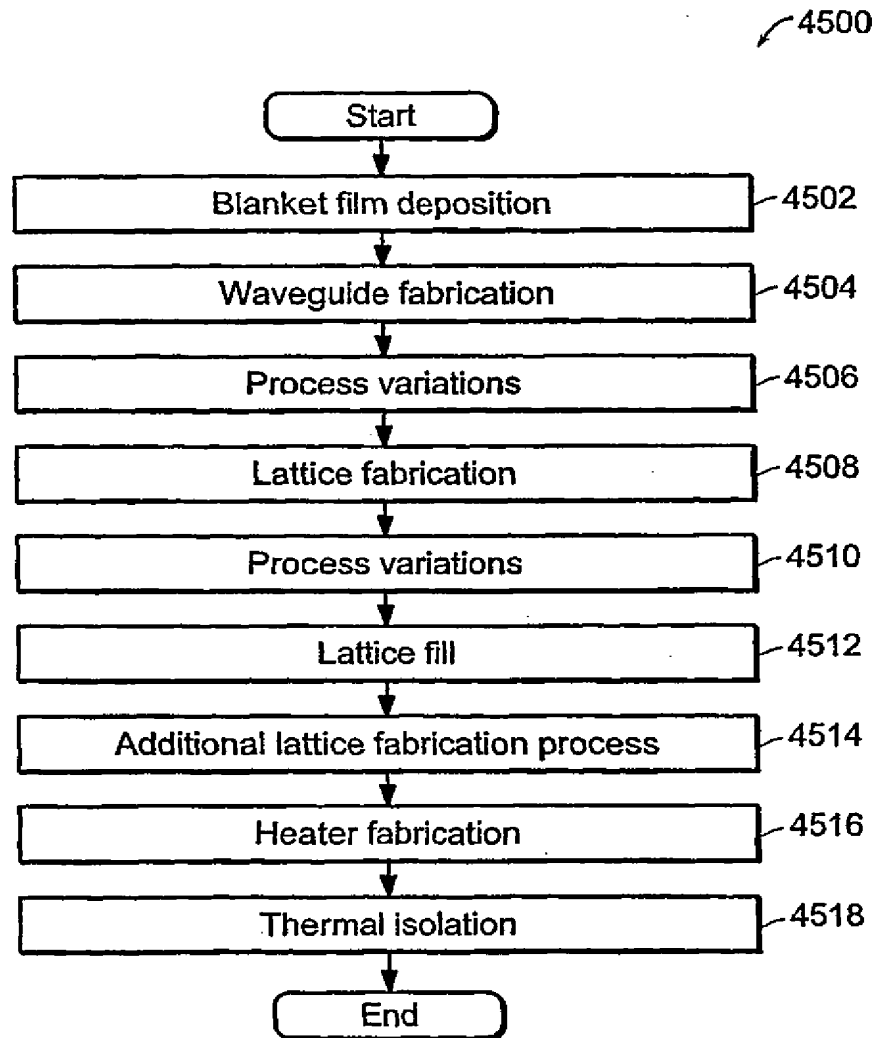


Figure 81

SUBSTITUTE SHEET (RULE 26)

INTERNATIONAL SEARCH REPORT

International Application No

PCT/US 02/41592

A. CLASSIFICATION OF SUBJECT MATTER

IPC 7 G02B6/13

According to International Patent Classification (IPC) or to both national classification and IPC

B. FIELDS SEARCHED

Minimum documentation searched (classification system followed by classification symbols)

IPC 7 G02B

Documentation searched other than minimum documentation to the extent that such documents are included in the fields searched

Electronic data base consulted during the international search (name of data base and, where practical, search terms used)

EPO-Internal, WPI Data, PAJ, INSPEC, COMPENDEX

C. DOCUMENTS CONSIDERED TO BE RELEVANT

Category *	Citation of document, with indication, where appropriate, of the relevant passages	Relevant to claim No.
X	US 6 134 043 A (JOANNOPOULOS JOHN D ET AL) 17 October 2000 (2000-10-17) abstract; figures 1A-1C	1
X	EP 1 039 561 A (SEIKO EPSON CORP) 27 September 2000 (2000-09-27) abstract; figure 1	1
X	US 5 406 573 A (OZBAY EKMEL ET AL) 11 April 1995 (1995-04-11) abstract	1
A	EP 0 453 107 A (UNIV COLORADO FOUNDATION) 23 October 1991 (1991-10-23) abstract page 2, paragraph 1 - paragraph 4 -/--	2

☒ Further documents are listed in the continuation of box C.

☒ Patent family members are listed in annex.

* Special categories of cited documents:

- *A* document defining the general state of the art which is not considered to be of particular relevance
- *E* earlier document but published on or after the international filing date
- *L* document which may throw doubts on priority claim(s) or which is cited to establish the publication date of another citation or other special reason (as specified)
- *O* document referring to an oral disclosure, use, exhibition or other means
- *P* document published prior to the international filing date but later than the priority date claimed

- *T* later document published after the international filing date or priority date and not in conflict with the application but cited to understand the principle or theory underlying the invention
- *X* document of particular relevance; the claimed invention cannot be considered novel or cannot be considered to involve an inventive step when the document is taken alone
- *Y* document of particular relevance; the claimed invention cannot be considered to involve an inventive step when the document is combined with one or more other such documents, such combination being obvious to a person skilled in the art.
- *Z* document member of the same patent family

Date of the actual completion of the international search

28 October 2003

Date of mailing of the international search report

11/11/2003

Name and mailing address of the ISA

European Patent Office, P.B. 5818 Patentlaan 2
NL - 2280 HV Rijswijk
Tel. (+31-70) 340-2040, Tx. 31 651 epo nl,
Fax: (+31-70) 340-3016

Authorized officer

Faderl, I

INTERNATIONAL SEARCH REPORT

International Application No

PCT/US 02/41592

C.(Continuation) DOCUMENTS CONSIDERED TO BE RELEVANT

Category *	Citation of document, with indication, where appropriate, of the relevant passages	Relevant to claim No.
A	EP 1 024 524 A (MATSUSHITA ELECTRIC LTD) 2 August 2000 (2000-08-02) abstract; figure 1 -----	2
A	US 5 997 795 A (BALLATO JOHN ET AL) 7 December 1999 (1999-12-07) column 20, line 29 - line 40 -----	2

FURTHER INFORMATION CONTINUED FROM PCT/ISA/ 210

Continuation of Box I.2

Claims Nos.: 3-80

The initial phase of the search revealed a very large number of documents relevant to the issue of novelty. So many documents were retrieved that it is impossible to determine which parts of the claim(s) may be said to define subject-matter for which protection might legitimately be sought (Article 6 PCT). For these reasons, a meaningful search over the whole breadth of the claim(s) is impossible. Consequently, the search has been restricted to a photonic bandgap device produced by using a supercritical fluid deposition process.

The applicant's attention is drawn to the fact that claims, or parts of claims, relating to inventions in respect of which no international search report has been established need not be the subject of an international preliminary examination (Rule 66.1(e) PCT). The applicant is advised that the EPO policy when acting as an International Preliminary Examining Authority is normally not to carry out a preliminary examination on matter which has not been searched. This is the case irrespective of whether or not the claims are amended following receipt of the search report or during any Chapter II procedure.

INTERNATIONAL SEARCH REPORT

International application No.
PCT/US 02/41592

Box I Observations where certain claims were found unsearchable (Continuation of item 1 of first sheet)

This International Search Report has not been established in respect of certain claims under Article 17(2)(a) for the following reasons:

1. ☐ Claims Nos.:
because they relate to subject matter not required to be searched by this Authority, namely:
2. ☒ Claims Nos.: 3-80
because they relate to parts of the International Application that do not comply with the prescribed requirements to such an extent that no meaningful International Search can be carried out, specifically:
see FURTHER INFORMATION sheet PCT/ISA/210
3. ☐ Claims Nos.:
because they are dependent claims and are not drafted in accordance with the second and third sentences of Rule 6.4(a).

Box II Observations where unity of invention is lacking (Continuation of item 2 of first sheet)

This International Searching Authority found multiple inventions in this international application, as follows:

1. ☐ As all required additional search fees were timely paid by the applicant, this International Search Report covers all searchable claims.
2. ☐ As all searchable claims could be searched without effort justifying an additional fee, this Authority did not invite payment of any additional fee.
3. ☐ As only some of the required additional search fees were timely paid by the applicant, this International Search Report covers only those claims for which fees were paid, specifically claims Nos.:
4. ☐ No required additional search fees were timely paid by the applicant. Consequently, this International Search Report is restricted to the invention first mentioned in the claims; it is covered by claims Nos.:

Remark on Protest

- ☐ The additional search fees were accompanied by the applicant's protest.
- ☐ No protest accompanied the payment of additional search fees.

INTERNATIONAL SEARCH REPORT

Information on patent family members

International Application No

PCT/US 02/41592

Patent document cited in search report		Publication date	Patent family member(s)	Publication date
US 6134043	A	17-10-2000	CA 2340081 A1 EP 1105757 A1 JP 2002522810 T WO 0010040 A1	24-02-2000 13-06-2001 23-07-2002 24-02-2000
EP 1039561	A	27-09-2000	JP 2000277260 A EP 1039561 A2	06-10-2000 27-09-2000
US 5406573	A	11-04-1995	US 5335240 A EP 0676092 A1 WO 9415389 A1	02-08-1994 11-10-1995 07-07-1994
EP 0453107	A	23-10-1991	US 4970093 A AT 119215 T DE 69107656 D1 DE 69107656 T2 EP 0453107 A1 JP 4228574 A	13-11-1990 15-03-1995 06-04-1995 05-10-1995 23-10-1991 18-08-1992
EP 1024524	A	02-08-2000	CN 1264159 A EP 1024524 A2 JP 2000357686 A TW 472295 B US 2003003604 A1 US 2003003770 A1 US 2002083959 A1	23-08-2000 02-08-2000 26-12-2000 11-01-2002 02-01-2003 02-01-2003 04-07-2002
US 5997795	A	07-12-1999	NONE	

(12) INTERNATIONAL APPLICATION PUBLISHED UNDER THE PATENT COOPERATION TREATY (PCT)

(19) World Intellectual Property Organization
International Bureau



(43) International Publication Date
24 July 2003 (24.07.2003)

PCT

(10) International Publication Number
WO 03/060442 A1

(51) International Patent Classification⁷: **G01J 3/28**,
G02B 6/16, G01N 21/25

(21) International Application Number: PCT/EP02/00487

(22) International Filing Date: 19 January 2002 (19.01.2002)

(25) Filing Language: English

(26) Publication Language: English

(71) Applicant (for all designated States except US): **AGILENT TECHNOLOGIES, INC.** [US/US]; 395 Page Mill Road, Palo Alto, CA 94306 (US).

(72) Inventors; and

(75) Inventors/Applicants (for US only): **RUF, Tobias** [DE/DE]; Göttenstrasse 10, 71272 Renningen (DE).
MUELLER, Emmerich [DE/DE]; Finkenweg 7, 71134 Aidlingen (DE).

(74) Agent: **BARTH, Daniel**; Agilent Technologies Deutschland GmbH, Patentabteilung, Herrenbergerstrasse 130, 71034 Boeblingen (DE).

(81) Designated States (national): AE, AG, AL, AM, AT, AU, AZ, BA, BB, BG, BR, BY, BZ, CA, CH, CN, CO, CR, CU, CZ, DE, DK, DM, DZ, EC, EE, ES, FI, GB, GD, GE, GH, GM, HR, HU, ID, IL, IN, IS, JP, KE, KG, KP, KR, KZ, LC, LK, LR, LS, LT, LU, LV, MA, MD, MG, MK, MN, MW, MX, MZ, NO, NZ, OM, PH, PL, PT, RO, RU, SD, SE, SG, SI, SK, SL, TJ, TM, TN, TR, TT, TZ, UA, UG, US, UZ, VN, YU, ZA, ZM, ZW.

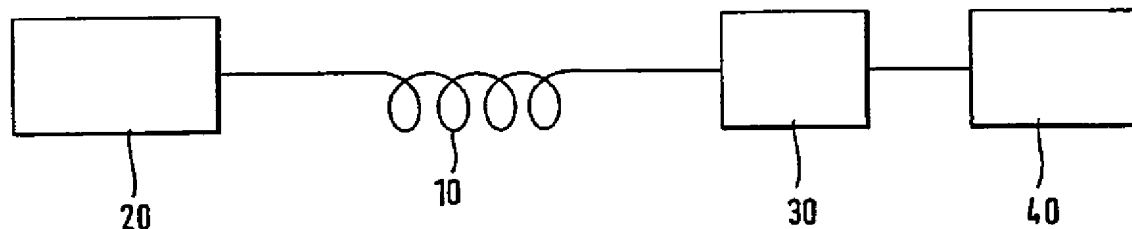
(84) Designated States (regional): ARIPO patent (GH, GM, KE, LS, MW, MZ, SD, SL, SZ, TZ, UG, ZM, ZW), Eurasian patent (AM, AZ, BY, KG, KZ, MD, RU, TJ, TM), European patent (AT, BE, CH, CY, DE, DK, ES, FI, FR, GB, GR, IE, IT, LU, MC, NL, PT, SE, TR), OAPI patent (BF, BJ, CF, CG, CI, CM, GA, GN, GQ, GW, ML, MR, NE, SN, TD, TG).

Published:

— with international search report

For two-letter codes and other abbreviations, refer to the "Guidance Notes on Codes and Abbreviations" appearing at the beginning of each regular issue of the PCT Gazette.

(54) Title: GAS-FILLED OPTICAL FIBER FOR WAVELENGTH CALIBRATION OR MEASUREMENT



(57) Abstract: A gas cell for wavelength calibration or measurement comprises an optical fiber (10) containing a gas having at least one absorption line for providing the wavelength calibration or measurement. The gas is preferably provided in a way that a sufficient part of an optical mode field distribution in the fiber (10) is localized within the gas. The gas may be provided in a hole or an arrangement of holes in or along the fiber (10).

WO 03/060442 A1

GAS-FILLED OPTICAL FIBER FOR WAVELENGTH CALIBRATION OR MEASUREMENT

BACKGROUND OF THE INVENTION

The present invention relates to wavelength calibration.

- 5 Currently, reference signals for wavelength calibration of instruments and systems used, e.g. in telecommunications, are obtained from optical absorption or emission lines of electronic or vibrational states of molecules, such as acetylene, HCN, or CO₂, which are contained in conventional glass cells. Details are disclosed e.g. in US-B-6,249,343, US-A-5,450,193, US-A-
10 5,521,703, or in <http://www.boulder.nist.gov/div815/srms.htm> .

SUMMARY OF THE INVENTION

It is an object of the invention to provide an improved wavelength calibration. The object is solved by the independent claims. Preferred embodiments are shown by the dependent claims.

- 15 According to the present invention, an optical fiber is applied as a gas cell for wavelength calibration purposes. The optical fiber preferably comprises a hole or an arrangement of holes in or along the fiber, in which a sufficient part of the optical mode field distribution is localized. The hole or the arrangement of holes is filled with the gas for providing absorption lines for the wavelength
20 calibration.

Mode-guiding in the fiber can be achieved preferably in two ways:

- An arrangement of holes acts as an effective medium with lower refractive index than other regions of the fiber, e.g., the solid glass core of the fiber. In this case, the mode is usually guided in the glass of the fiber core, and
25 only a small portion of the field distribution is localized in the holes. However, an arrangement of regions (or "shells") with different hole

densities can also be applied which mimics a profile of the effective index of refraction analogous to that in a conventional optical fiber. In this case, the fraction of the mode density localized in the holes will be larger.

- An arrangement of holes acts as a photonic crystal which has very high reflectivity for modes guided in the region surrounded by the photonic crystal region. This region can be a very large diameter "hollow core" which then guides most of the mode intensity.

According to the invention, the holes in such fiber are filled with a defined gas or gas compound used as wavelength reference standard. The use of such fiber gas cells thus allows to enormously increase the interaction length of the light with the gas molecules compared to only a few cm in conventional gas cells. Therefore gases with rather low absorption, such as CO₂, can be used. This is especially useful in the telecommunications L band.

Further, the inventive fiber gas cells can be provided more compact, more flexible and better suited to fiber-optic instruments than the bulky cuvette-type conventional cells used today. Problems of pig-tailing and free-space connections across free path lengths of several cm can be significantly reduced.

Additionally, the volume of toxic gases, e.g. HCN, required for some applications can be significantly smaller. This has benefits for manufacturers, operators, and environment. Finally, fiber gas cells can be provided cheaper than conventional ones. Only a few meters of fiber are needed at most.

In a preferred embodiment for making the inventive fiber gas cells, air-filled hollow cores of "normal" photonic crystal fibers are filled with a desired gas or gas mixture. This can be achieved e.g. by pumping on one side and attaching a gas reservoir on the other side of the fiber. End pieces consisting of flat glass, microlenses as well as other optical, source or detection elements could be attached, for example by gluing or arc welding methods.

Alternatively, small pieces of frozen gas crystals or small amounts of liquid gas can be inserted in the evacuated fiber that is then sealed. The fiber fills with gas as the crystals or the liquid evaporate.

5 Since gas filling of holes with small diameters might suffer from the large resistance of the very narrow channels, the whole fiber growth process is preferably performed in another embodiment in an environment (e.g. under pressure) of the desired gas or gas mixture.

10 In a preferred embodiment, the optical fiber is provided in accordance with a hollow-core fiber as disclosed by J. C. Knight et al., Optics Letters 21, 1547 (1996), a "holey" fiber as disclosed by M. Ibanescu et al., Science 289, 415 (2000), or a photonic crystal fiber as disclosed by J. Broeng et al., Danish Opt. Soc. News, p. 22, June 2000 or J. Broeng et al., J. Opt. A: Pure Appl. Opt. 1, 477 (1999) or J. Broeng et al., Science 285, 1537 (1999).

15 Other applicable fiber structures are disclosed e.g. in WO-A-0022466, WO-A-9964903, WO-A-9964904, US-B-6,301,420, WO-A-0142831, WO-A-0065386, or WO-A-0016141.

20 For providing a wavelength reference measurement, the inventive fiber filled with gas having known absorption wavelengths is preferably coupled to a wavelength source providing the stimulus for the gas-filled fiber. A wavelength response signal of the gas-filled fiber in response to the applied stimulus is detected and analyzed. Comparing the detected wavelength response signal with the known absorption wavelengths then allows calibrating the provided wavelength analysis using the known absorption wavelengths. Calibration schemes and setups as disclosed e.g. in the aforementioned US-B-6,249,343, 25 US-A-5,450,193, US-A-5,521,703, or in <http://www.boulder.nist.gov/div815/srms.htm>, as well as other known wavelength measurement, control and calibration techniques, can be applied accordingly.

Further preferred embodiments are:

- The individual holes of the fiber gas cell are not all uniformly filled with the same gas used for wavelength calibration. Other possibilities include: (1) Some of the holes are filled with the reference gas and some holes are under vacuum ("empty"); (2) some of the holes are filled with the reference gas and others are filled with another gas, e.g. air. The gas cell, however, should be provided in a way that interaction of the light with the reference gas is strong enough to allow for wavelength measurement.
- Different holes of the fiber gas cell are filled with different reference gases, e.g., C_2H_2 and CO_2 in one and the same fiber. This allows the simultaneous measurement of reference wavelengths in different spectral regions, according to the gases used, in a single fiber gas cell.
- At least two fiber gas cells having a certain length and being filled with different reference gases, e.g., C_2H_2 and CO_2 , are spliced together, thereby forming a new fiber gas cell having a greater length. This arrangement allows the simultaneous measurement of reference wavelengths in different spectral regions, according to the gases used, in a single fiber gas cell.
- A fiber gas cell having at least one end piece consisting of a lens or another means to improve the coupling of this fiber gas cell to other fiber-optical components and systems. The at least one end is mechanically coupled or fusion spliced to the fiber gas cell.
- Fiber gas cell in combination with an optical system, such as but not limited to a source or receiver of optical power, to perform wavelength reference measurements.
- An integrated system of fiber gas cell with light source and/or detector mounted directly onto the fiber ends for easy incoupling and/or detection of optical power.

- Fiber gas cell using the broadband light from the spontaneous emission (SSE) of a laser as input illumination. Such a unit may, e.g., replace the combination of light-emitting diode (LED) and conventional gas cell used for wavelength calibration of an optical spectrum analyzer (OSA), since the SSE could be obtained from a tunable laser that is oftentimes used together with an OSA. In an OSA using heterodyne technology, the SSE could also be obtained from a built-in laser source.

BRIEF DESCRIPTION OF THE DRAWINGS

Other objects and many of the attendant advantages of the present invention will be readily appreciated and become better understood by reference to the following detailed description when considering in connection with the accompanied drawings. Features that are substantially or functionally equal or similar will be referred to with the same reference sign(s).

Fig. 1 shows a setup for providing a wavelength reference measurement according to the present invention.

Fig. 2 illustrates, in cross sectional view, in principle an embodiment of the fiber 10 according to the present invention.

DETAILED DESCRIPTION OF THE INVENTION

In Fig. 1, a fiber 10 filled with a gas having known absorption wavelengths is coupled to a wavelength source 20 providing a stimulus signal for the gas-filled fiber 10. A wavelength response signal of the gas-filled fiber 10 in response to the applied stimulus is detected by a detector 30 and analyzed by an analyzing unit 40. The analyzing unit 40 compares the detected wavelength response signal with the expected absorption wavelengths known for the gas in the fiber 10. Differences between actually measured absorption wavelengths and the expected absorption wavelengths then allow calibrating the provided wavelength analysis of the analyzing unit 40.

Fig. 2 illustrates in principle, in cross-sectional view, an applicable embodiment of the fiber 10, as known from: J. Broeng et al., Danish Opt. Soc. News, p. 22, June 22. The regular pattern of circles 100 denotes holes filled with gas. The large cross-sectional area 110 in the center of the figure, having exemplary
5 hexagonal symmetry, represents the hollow core of the fiber 10 and is also filled with gas. The almost circular gray-scale image denotes the field distribution of the fundamental guided mode of the fiber that occurs mainly in the gas-filled region.

CLAIMS:

1. An optical fiber (10) containing a gas providing at least one absorption line for providing a wavelength calibration or measurement.
2. The optical fiber (10) of claim 1, wherein the gas is provided in a way that a sufficient part of an optical mode field distribution in the fiber (10) is localized within the gas.
3. The optical fiber (10) of claim 1 or 2, wherein the gas is provided in a hole or an arrangement of holes in or along the fiber (10), in which a sufficient part of the optical mode field distribution is localized.
4. The optical fiber (10) according to claim 1 or any one of the above claims, wherein an arrangement of holes in the fiber (10) acts as an effective medium with lower refractive index than other regions of the fiber (10).
5. The optical fiber (10) according to claim 1 or any one of the above claims, wherein an arrangement of regions or shells with different hole densities provides a profile of the effective index of refraction analogous to that in a conventional optical fiber.
6. The optical fiber (10) according to claim 1 or any one of the above claims, wherein an arrangement of holes acts as a photonic crystal which has high reflectivity for modes guided in the region surrounded by the photonic crystal region.
7. The optical fiber (10) according to claim 1 or any one of the above claims, wherein some holes in the fiber are filled with the reference gas and some holes are substantially under vacuum or filled with a different gas.
8. The optical fiber (10) according to claim 1 or any one of the above claims, wherein different holes of the fiber are filled with different reference gases.

9. The optical fiber (10) according to claim 1 or any one of the above claims, further comprising at least one end piece, preferably a lens, for better coupling to other fiber-optical components or systems.
- 5 10. A gas cell for wavelength calibration or measurement comprising an optical fiber (10) according to claim 1 or any one of the above claims.
- 10 11. A gas cell for wavelength calibration or measurement comprising a plurality of optical fibers (10) according to claim 1 or any one of the above claims, each having a certain length and being filled with a respective reference gas, wherein the plurality of optical fibers (10) are spliced or otherwise coupled together.
12. An optical system for perform a wavelength reference measurement, comprising:

an optical fiber (10) or a gas cell according to claim 1 or any one of the above claims, adapted for receiving an optical stimulus signal (20),

15 a receiver (30) adapted for receiving a response signal of the optical fiber (10) to an the applied optical stimulus signal (20), and

a processing unit (40) adapted for determining in the response signal one or more wavelengths absorbed by the optical fiber (10) or the gas cell.
- 20 13. The optical system of claim 12, wherein the processing unit (40) is adapted to comparing the one or more determined absorption wavelengths with known one or more absorption wavelengths for providing a wavelength calibration.
14. A method for making an optical fiber (10) or a gas cell according to claim 1 or any one of the above claims, comprising the step of:

25 filling at least one hole or air-filled hollow core of a photonic crystal fiber with a desired gas or gas mixture.

15. The method of claim 14, further comprising the steps of:
- pumping on one side of the fiber, and
- attaching a gas or liquid gas reservoir on the other side of the fiber.
16. The method of claim 14, further comprising the steps of:
- 5 inserting pieces of frozen gas crystals or liquid gas in the evacuated fiber,
- and
- sealing the fiber.
17. The method of claim 14 or any one of the claims 15-16, being performed in an environment of the desired gas or gas mixture.

1 / 1

Fig.1

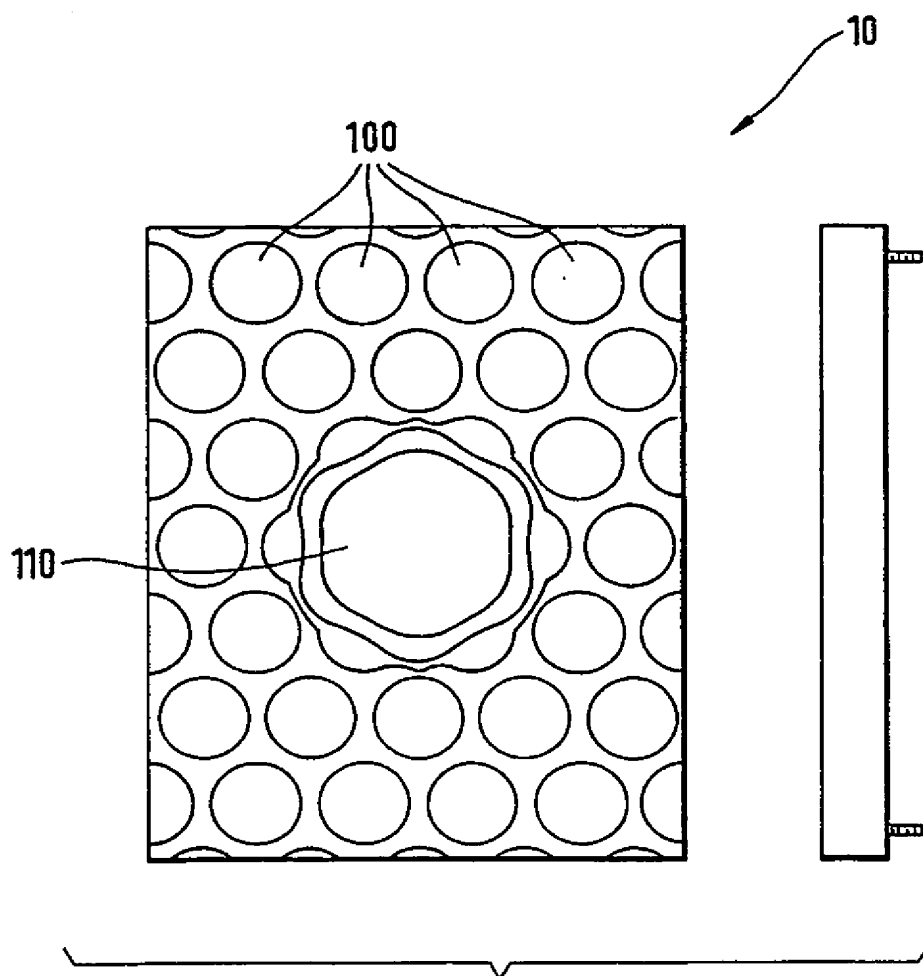
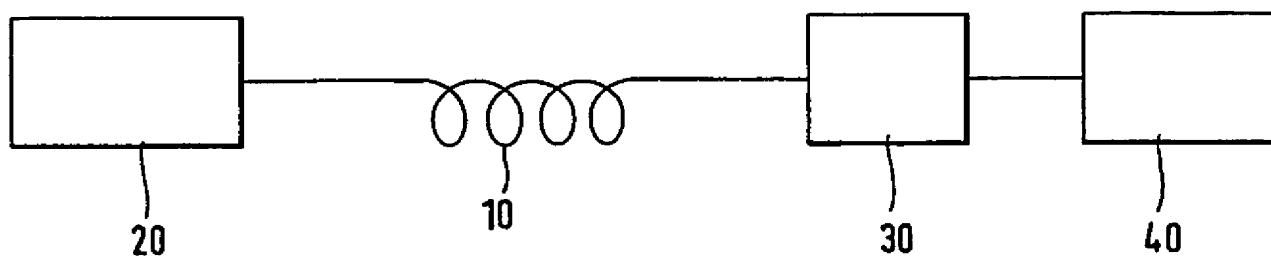


Fig.2

INTERNATIONAL SEARCH REPORT

Int. Application No

PC1/EP 02/00487

A. CLASSIFICATION OF SUBJECT MATTER

IPC 7 G01J3/28 G02B6/16 G01N21/25

According to International Patent Classification (IPC) or to both national classification and IPC

B. FIELDS SEARCHED

Minimum documentation searched (classification system followed by classification symbols)

IPC 7 G01J G02B G01N

Documentation searched other than minimum documentation to the extent that such documents are included in the fields searched

Electronic data base consulted during the International search (name of data base and, where practical, search terms used)

EPO-Internal, INSPEC, PAJ

C. DOCUMENTS CONSIDERED TO BE RELEVANT

Category *	Citation of document, with indication, where appropriate, of the relevant passages	Relevant to claim No.
A	WO 00 60388 A (MANGAN BRIAN JOSEPH ; SECR DEFENCE (GB); BIRKS TIMOTHY ADAM (GB); K) 12 October 2000 (2000-10-12) claims 1,2,13,16 ---	1-6, 10-12
A	US 5 892 861 A (LE FEBRE DAVID A) 6 April 1999 (1999-04-06) abstract ---	1,10-12
A	US 6 249 343 B1 (WILDNAUER KENNETH R ET AL) 19 June 2001 (2001-06-19) abstract ---	1
A	US 2001/029756 A1 (KIM DUK-YOUNG ET AL) 18 October 2001 (2001-10-18) abstract -----	14-17



Further documents are listed in the continuation of box C.



Patent family members are listed in annex.

* Special categories of cited documents:

- *A* document defining the general state of the art which is not considered to be of particular relevance
- *E* earlier document but published on or after the international filing date
- *L* document which may throw doubts on priority claim(s) or which is cited to establish the publication date of another citation or other special reason (as specified)
- *O* document referring to an oral disclosure, use, exhibition or other means
- *P* document published prior to the international filing date but later than the priority date claimed

T later document published after the international filing date or priority date and not in conflict with the application but cited to understand the principle or theory underlying the invention

X document of particular relevance; the claimed invention cannot be considered novel or cannot be considered to involve an inventive step when the document is taken alone

Y document of particular relevance; the claimed invention cannot be considered to involve an inventive step when the document is combined with one or more other such documents, such combination being obvious to a person skilled in the art.

Z document member of the same patent family

Date of the actual completion of the international search

2 December 2002

Date of mailing of the international search report

09/12/2002

Name and mailing address of the ISA

European Patent Office, P.B. 5818 Patentlaan 2
NL - 2280 HV Rijswijk
Tel. (+31-70) 340-2040, Tx. 31 651 epo nl,
Fax: (+31-70) 340-3018

Authorized officer

De Buyzer, H

INTERNATIONAL SEARCH REPORT

Int. Application No

PCT/EP 02/00487

Patent document cited in search report		Publication date	Patent family member(s)	Publication date
WO 0060388	A	12-10-2000	AU 3827400 A	23-10-2000
			CN 1353824 T	12-06-2002
			EP 1166160 A1	02-01-2002
			WO 0060388 A1	12-10-2000
			GB 2350904 A	13-12-2000
			NO 20014740 A	03-12-2001
US 5892861	A	06-04-1999	NONE	
US 6249343	B1	19-06-2001	JP 2001153724 A	08-06-2001
US 2001029756	A1	18-10-2001	JP 2001302268 A	31-10-2001

(19) World Intellectual Property Organization
International Bureau



(43) International Publication Date
2 October 2003 (02.10.2003)

PCT

(10) International Publication Number
WO 03/080524 A1

(51) International Patent Classification⁷: C03B 37/027

(21) International Application Number: PCT/GB03/01298

(22) International Filing Date: 20 March 2003 (20.03.2003)

(25) Filing Language: English

(26) Publication Language: English

(30) Priority Data:
0206573.8 20 March 2002 (20.03.2002) GB
0209001.7 19 April 2002 (19.04.2002) GB

(71) Applicant (for all designated States except US):
BLAZEPHOTONICS LIMITED [GB/GB]; Finance
Office, University of Bath, The Avenue, Claverton Down,
Bath BA2 7AY (GB).

(72) Inventors; and

(75) Inventors/Applicants (for US only): **RUSSELL, Philip**,
St. John [GB/GB]; Shepherds Mead, Southstoke, Bath
BA2 7EB (GB). **MANGAN, Brian, Joseph** [GB/GB]; Flat
5, 41 Grosvenor Place, Bath BA1 6BA (GB). **KNIGHT**,

Jonathan, Cave [GB/GB]; Canteen Cottage, Canteen
Lane, Wellow, Bath BA2 8PY (GB). **KILBRIDE, Ian**,
Patrick [GB/GB]; 45 Eden Vale Road, Westbury, Wiltshire
BA13 3NY (GB). **BIRKS, Timothy, Adam** [GB/GB]; 14
Horsecombe Brow, Combe Down, Bath BA2 5QY (GB).

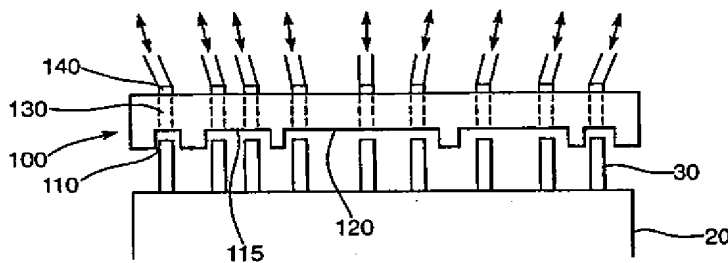
(74) Agents: **CRITTEN, Matthew, Peter** et al.; Abel & Imray,
20 Red Lion Street, London WC1R 4PQ (GB).

(81) Designated States (*national*): AE, AG, AL, AM, AT, AU,
AZ, BA, BB, BG, BR, BY, BZ, CA, CH, CN, CO, CR, CU,
CZ, DE, DK, DM, DZ, EC, EE, ES, FI, GB, GD, GE, GH,
GM, HR, HU, ID, IL, IN, IS, JP, KE, KG, KP, KR, KZ, LC,
LK, LR, LS, LT, LU, LV, MA, MD, MG, MK, MN, MW,
MX, MZ, NI, NO, NZ, OM, PH, PL, PT, RO, RU, SC, SD,
SE, SG, SK, SL, TJ, TM, TN, TR, TT, TZ, UA, UG, US,
UZ, VC, VN, YU, ZA, ZM, ZW.

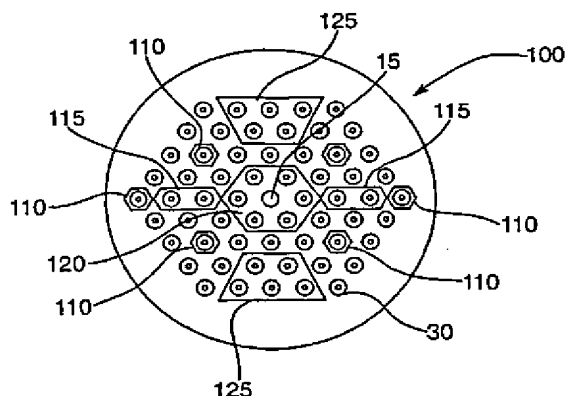
(84) Designated States (*regional*): ARIPO patent (GH, GM,
KE, LS, MW, MZ, SD, SL, SZ, TZ, UG, ZM, ZW),
Eurasian patent (AM, AZ, BY, KG, KZ, MD, RU, TJ, TM),
European patent (AT, BE, BG, CH, CY, CZ, DE, DK, EE,

[Continued on next page]

(54) Title: METHOD OF DRAWING MICROSTRUCTURED GLASS OPTICAL FIBRES FROM A PREFORM



a



b

(57) Abstract: A method of manufacturing a microstructured fibre, comprises: providing a preform comprising a plurality of elongate holes; mating at least one, but not all, of the holes with a connector to connect the hole(s) to an external pressure-controller; drawing the preform into the fibre whilst controlling gas pressure in the hole(s) connected to the pressure-controller. The connector is also claimed.

WO 03/080524 A1



ES, FI, FR, GB, GR, HU, IE, IT, LU, MC, NL, PT, RO,
SE, SI, SK, TR), OAPI patent (BF, BJ, CF, CG, CI, CM,
GA, GN, GQ, GW, ML, MR, NE, SN, TD, TG).

For two-letter codes and other abbreviations, refer to the "Guidance Notes on Codes and Abbreviations" appearing at the beginning of each regular issue of the PCT Gazette.

Published:

— with international search report

METHOD OF DRAWING MICROSTRUCTURED GLASS OPTICAL FIBRES FROM A PREFORM

This invention relates to the field of photonic crystal fibres.

Optical fibres are widely used in applications such as telecommunications. Standard optical fibres are typically made entirely from solid materials such as glass, with each fibre having the same cross-sectional structure along its length. Transparent material in one part (usually the middle) of the cross-section has a higher refractive index than material in the rest of the cross-section and forms an optical core. Light is guided in the optical core by total internal reflection from the material surrounding the core, which forms a cladding region. Most standard fibres are made from fused silica glass, incorporating a controlled concentration of dopant, and have a circular outer boundary typically of diameter 125 microns. Standard fibres can be single-mode or multimode.

Different fibres may provide different functions in a system. For example, a length of fibre designed to provide dispersion compensation may be inserted between lengths of standard fibre. Similarly, a length of fibre may act as an optical amplifier or an optical coupler or a sensor or any of a wide range of other devices.

A perennial problem in fibre optics is achieving smooth transitions from one fibre type to another - the "mode-matching" issue. The requirements of a successful transition are insignificant loss (preferably less than 0.1 dB), no conversion between spatial or polarisation modes (unless required), no back reflections and high tensile strength.

A traditional solution is to heat the fibre to its softening temperature and draw it to a taper. The heat source can be a flame or a carbon dioxide laser beam. Mode field transformations can be achieved in which the mode area is reduced or expanded. A related process involves heating a

fibre without tapering it; that causes the core dopants to spread out into the cladding and thus enlarge the area of the guided mode. Disadvantages of this technique are that the fibre has to be stripped for processing and then recoated; this weakens it and is a lengthy and expensive process.

In the past few years a new type of optical fibre has been demonstrated, called the photonic crystal fibre (PCF), holey fibre or microstructured fibre [J. C. Knight et al., Optics Letters v. 21 p. 203]. Typically, a microstructured fibre is made from a single solid material such as fused silica glass, within which is embedded an array of holes. Those 'holes' are usually air holes but may alternatively be, for example, regions of a solid material (e.g. silica doped with impurities to change its refractive index). The holes run parallel to the fibre axis and extend the full length of the fibre. A region of solid material between holes, larger than neighbouring such regions, can act as a waveguiding fibre core. Light can be guided in this core in a manner analogous to total-internal-reflection guiding in standard optical fibres.

One way to provide such an enlarged solid region in a microstructured fibre with an otherwise periodic array of holes is to omit one or more holes from the structure. However, the array of holes need not be periodic for total-internal-reflection guiding to take place (we may nevertheless refer to such a fibre as a photonic-crystal fibre).

Another mechanism for guiding light in microstructured fibres is based on photonic bandgap effects rather than total internal reflection. For example, light can be confined inside a hollow core (an enlarged air hole) by a suitably-designed array of smaller holes surrounding the core [R. F. Cregan et al., Science v. 285 p. 1537]. True guidance in a hollow core is not possible at all in standard optical fibres.

Microstructured fibres can be fabricated by stacking glass elements (rods and tubes) on a macroscopic scale to form

them in place while fusing them together. This primary preform can then be drawn into a fibre, using the same type of fibre-drawing tower that is used to draw standard fibre from a standard-fibre preform. The primary preform can, for example, be formed from fused silica elements with a diameter of about 0.8 mm.

The microscopic air channels that run along the entire length of a photonic crystal fibre provide the refractive index profile required to guide light at a central defect, either by a modified form of total internal reflection or by photonic band gap effects. It is known in the prior art to alter the properties of those air holes to alter the properties of the fibre.

Conceptually, the simplest method of controlling the size of an air hole in a PCF is, perhaps, to form a preform having a larger-scale approximation to the desired structure, for example by forming the preform from capillaries having different selected hole diameters. However, in practice, it is costly and relatively difficult to manufacture capillaries of different internal diameters and it is difficult to predict the behaviour of such structures during drawing.

International Patent Application No. PCT/GB00/00599 (The University of Bath) teaches that a region of a PCF may be heat-treated after the PCF has been drawn, in order to collapse holes in the heat-treated region.

International Patent Application No. PCT/US99/18089 (Corning Inc.) teaches that the axial properties of a PCF may be varied, for example by varying gas pressure in the preform during the draw. That variation may, in particular, be used to produce a fibre having a dispersion that alternates between positive and negative dispersion in alternate segments of the fibre, producing a net dispersion of zero over the length of the fibre.

International Patent Application No. PCT/GB00/00600 (The University of Bath) teaches a method of making controlled changes in the structure of a photonic crystal fibre whilst it

is being drawn. The Application describes producing the photonic crystal fibre by stacking an array of silica capillaries inside a silica tube, sealing the tube inside an evacuable cylinder, whilst leaving some or all of the capillaries protruding from the cylinder at each end, and then evacuating the inside of the tube whilst leaving the insides of some or all of the capillaries open to the atmosphere, so that they expand during drawing. In a particular example, the Application teaches producing a highly birefringent PCF by having four of the capillaries terminate within the cylinder, so that they do not expand during drawing, so that the drawn fibre has two-fold rotational symmetry.

We have realised that the prior-art manufacturing methods provide only limited control over the structure of the drawn fibre.

An object of the invention is to provide an improved method of manufacturing a PCF and hence to provide PCFs having improved functionality.

According to the invention there is provided a method of manufacturing a microstructured fibre, comprising:

- (i) providing a preform comprising a plurality of elongate holes;
- (ii) mating at least one of the holes with a connector to connect the hole(s) to an external pressure-controller;
- (iii) drawing the preform into the fibre whilst controlling gas pressure in the hole(s) connected to the pressure-controller.

By the term 'external pressure-controller', we mean any suitable means for changing the internal pressure of the holes from atmospheric pressure to another selected value, including, for example, applying a static increased or decreased pressure by means of a piston, but not merely sealing the hole during drawing to create a pressure difference.

Thus, during drawing of the fibre, the size of individual holes can be controlled by individually addressing each hole

in the preform and changing the pressure in that hole. If several holes are addressed simultaneously, then the structure which emerges in the actual fibre can be altered during the drawing process. Radical changes in fibre properties are possible. For example, different devices may be created during the draw along a single length of fibre, with adiabatic transitions provided between each link. Complex arrangements of devices may be produced from a preform comprising a uniform array of holes.

Holes formed in different portions of the cross-section of the drawn fibre may be pressurised by different amounts. For example, the drawn fibre may comprise a cladding region surrounding a core region and holes forming an innermost ring of the cladding region, adjacent to the core region may be pressurised to different pressures from each other.

In general, during drawing of the fibre, larger holes will tend to grow larger and smaller holes will tend to grow smaller. Pressurisation (including depressurisation) may be used to counteract those tendencies, for example in the innermost ring of the cladding region.

Preferably, the preform comprises a plurality of elongate elements, arranged side by side in a bundle, a plurality of the elements being tubes, wherein each tube defines one of the holes in the preform.

Alternatively, the preform comprises a matrix material that defines the holes.

The external pressure-controller may increase the pressure in the hole above atmospheric pressure. Alternatively, the external pressure-controller may decrease the pressure in the hole below atmospheric pressure. The pressure in the hole may be kept constant throughout the drawing of the fibre. Alternatively, the pressure in the hole may be varied during the draw. Thus variations in the cross-sectional area of the hole may be provided along the length of the drawn fibre. The pressure may be pulsed periodically.

As discussed above, the pressure-controller may be any suitable device, which may apply a static or a varying pressure. The pressure-controller may be, for example, a rotary vane pump, a peristaltic pump or a cylinder piston pump.

The hole with which the connector is mated may form a hole in a cladding region of the drawn fibre. The hole with which the connector is mated may form a hole in a core region of the drawn fibre; the core region of the drawn fibre may be a hole. The core region hole may be pressurised to a lower pressure than holes in the cladding region.

Preferably, a plurality of the holes are connected to the external pressure-controller.

The method may include pressurising further groups, each comprising at least one of the holes, to a second pressure or pressures, for example by connecting them to further external pressure-controllers. For example, preferably the method includes connecting at least one (preferably a plurality) of the holes to a second external pressure-controller and the method may include connecting at least one (preferably a plurality) of the holes to a third external pressure-controller.

Preferably, the method includes the step of producing a plurality of devices arranged axially along the PCF by varying over time the pressure applied to the hole or holes. It may be that each of the plurality of devices is the same; the method thus provides a method of mass-producing large numbers of a particular device, spaced at intervals along a single fibre; after production, the devices may then be separated (e.g. by cleaving the fibre). Alternatively, the plurality of devices may comprise a plurality of different devices; thus complex optical effects such as signal processing may be achieved in a single fibre.

The method may include the step of varying over time the rate at which the fibre is drawn from the preform.

The method may include the step of varying over time the preform feed rate. The preform feed rate may even be negative for brief periods of time, such that the preform is being pulled in a direction opposite to the direction in which the fibre is being drawn.

The method may include the step of varying over time the furnace temperature.

Preferably, the pressurisation results in at least one elongate hole formed in the drawn fibre having a different transverse area in one part of the fibre from its transverse area in another part of the fibre. At least one hole may be collapsed completely over a length of the fibre. Such an arrangement may be used for example to create and destroy local cores over particular lengths of the fibre. Similarly, creating and destroying holes adjacent to a core region may be used to create lengths of fibre having an enlarged or reduced core.

Preferably, the pressurisation results in at least one part of the dielectric matrix region having a different transverse area in one part of the fibre from its transverse area in another part of the fibre.

The pressurisation may result, in a transverse cross-section of the drawn fibre, in a plurality of concentric regions, wherein alternate adjacent regions are of a higher and a lower effective refractive index respectively.

The pressurisation may result in the drawn fibre being a W-profile fibre over at least part of its length.

The pressurisation may result in the drawn fibre comprising a long period grating.

The variation in pressurisation may result in a change in the symmetry of the fibre, such that a portion of the fibre is birefringent.

Preferably, two portions of the fibre are birefringent, but their principal polarisation axes are rotated relative to each other by the variation in pressurisation.

Also according to the invention there is provided a photonic crystal fibre comprising a core region and a cladding region comprising a plurality of elongate holes, the fibre comprising a first region of its length in which the holes are arranged in a first pattern having at-most-two-fold rotational symmetry, such that the fibre has in the first region a fast polarisation axis and a slow polarisation axis, and a second region of its length in which the holes are arranged in a second pattern having at-most-two-fold rotational symmetry, such that the fibre in the second region has a fast polarisation axis and a slow polarisation axis, the polarisation axes in the second region being rotated relative to the polarisation axes in the first region, the fibre further comprising a transition region, between the first region and the second region, in which the at least one of the hole changes in cross-sectional area so that the first pattern changes into the second pattern.

Thus, a PCF with low birefringence may be turned adiabatically into a fibre with high birefringence. A twist-compensated PM fibre link (designed to have zero DGD) may be made by simply altering the distribution of pressure in the holes part-way through the draw so as to make the slow axis into a fast axis and vice-versa.

Further portions of the fibre may be birefringent and have rotated polarisations. Any suitable photonic crystal structure may be used to provide birefringence; for example, the structure may be based on a square lattice.

The variation in pressurisation may result in a change in core size in the drawn fibre, such that at least one of the devices comprises a fibre portion having a larger core region and at least one of the devices comprises a fibre portion having a smaller core region; thus, for example, a large core may be turned into a small core by increasing the pressure in surrounding holes and collapsing; a similar effect can be produced by altering the drawing tension.

Also according to the invention there is provided a photonic crystal fibre comprising a core region and a cladding region comprising a plurality of elongate holes, the fibre comprising a region of its length in which the holes adjacent to the core region are of a larger cross-sectional area, and the core region is of a smaller cross-sectional area, than in an adjacent length of the fibre, such that, in use, the fibre has an increased nonlinear response to propagating light in that region of the fibre.

The variation in pressurisation may result in a change in core size, such that at least one of the devices is a nonlinear fibre portion, comprising a core region that is sufficiently small for significant nonlinear optical effects to occur in use. Thus, ultra-small core fibre may be produced in the centre of an otherwise medium-core fibre link - that may allow efficient nonlinear functions to be built seamlessly into a telecommunications system. Because there is no requirement to strip and recoat the fibre, it should have unimpaired tensile strength.

The drawn fibre may comprise a plurality of core regions. Preferably, the variation results in the separation of at least two of the cores being reduced in a region of the fibre, such that at least one of the devices comprises an optical coupler comprising the reduced separation region. Preferably, the devices comprise two optical couplers that form a Mach-Zehnder interferometer. Thus, in-line Mach-Zehnder interferometers may be produced by a simple process of reducing the air hole size between two cores at two points along a dual-core length.

Preferably, the devices comprise a network of switches and/or filters formed from the plurality of couplers.

Also according to the invention there is provided a photonic crystal fibre comprising at least three core regions and a cladding region comprising a plurality of elongate holes, the fibre comprising at least one coupler between a first pair of the core regions and at least one coupler

between a second, different, pair of the core regions, each coupler comprising a region of the fibre in which the cross-sectional area of the holes between the coupled cores is smaller than in adjacent lengths of the fibre, such that the cores are brought closer together.

Such an arrangement would have considerable advantages over taper post-processing, where it is very difficult (if not impossible) to heat-treat selected holes while keeping the rest unaffected. In-line fabrication allows couplers to be created between any group (of two or more) cores while leaving the others unaffected; further down the fibre couplers may be created between different cores.

The fibre may comprise more than two cores. Preferably, the variation results in the separations of the cores being reduced over a plurality of portions of the fibre to form optical couplers between each of the more than two cores. Thus, still more complex networks of devices may be produced.

Preferably, transition regions formed between each of the optical devices are sufficiently gradual to be adiabatic. Alternatively, the transition may be abrupt. Thus, in one draw, a fibre may be produced with many different properties at different positions along its length, all connected by seamless low-loss transitions.

The condition of the draw may be oscillated between two states over time to form a transition region, the first state being matched to the mode of a first of the optical devices and the second state being matched to the mode of a second of the optical devices; for example, one state may be arranged to match a single-mode fibre and the other state may be arranged to match a speciality fibre such as a dispersion compensating fibre (DCF), an amplifier or a highly nonlinear fibre.

Also according to the invention there is provided a photonic crystal fibre comprising a core region and a cladding region comprising a plurality of elongate holes, the fibre comprising a first length in which the holes are arranged in a first transverse pattern providing a first function, a second

length in which the holes are arranged in a second transverse pattern providing a second function, and a transitional length along which at least one of the holes oscillates in cross-sectional area such that the holes oscillate between the first pattern and the second pattern, such that, in use, light is coupled in the transitional length between a mode guided in the first length and a mode guided in the second length.

Similarly, the method may include the step of manufacturing twist-compensated DGD-free fibre by oscillating the structure to and fro periodically (the period being perhaps of a few metres) along the length of the drawn fibre. That would make the exact cutting of length - to achieve DGD-free operation - very easy since an integral number of periods is needed. The accuracy of the actual dispersion would then be within $100 \times dL/L$ percent of the required value.

Similarly, at least one of the holes oscillates between a first value and a second value, such that the holes oscillate between a first pattern and a second pattern and thus substantially avoid an unwanted phase-matching condition.

Also according to the invention there is provided a photonic crystal fibre comprising a core region and a cladding region comprising a plurality of elongate holes, the fibre comprising a length in which the cross-sectional area of at least one of the holes oscillates between a first value and a second value, such that the holes oscillate between a first pattern and a second pattern and thus substantially avoid an unwanted phase-matching condition.

The method may include the step of producing a DCF with graded properties that match the dispersion curve in standard telecomms fibre over the telecommunications bands (dispersion, slope, curvature and slope of curvature etc.). That may be achieved by choosing the functional shape along the length of the fibre appropriately. The dependence of dispersion curve on geometry may be calculated, and used to solve an integral equation for the desired link properties - the required length dependence is given by a function inside the integral.

Parameters of the draw may be controlled during manufacture to produce a desired structure by feedback from direct measurement of the drawn fibre (e.g. the diameter of a hole or a plurality of holes).

Preferably, the method includes the step of calibrating the relationship between parameters of the draw and parameters of the drawn fibre.

Preferably, the method further comprises varying parameters of the draw according to the calibration results to produce a fibre having a selected structure. Thus, the relationship between draw parameters such as pressure, temperature and draw speed and fibre parameters such as hole size and pitch are preferably determined in prior calibration runs. Such calibration may be achieved, for example, by carrying out a large number of sample draws and measuring the results of varying, at any one time, one or more parameters of the draw.

Preferably, the pressure applied to the or each hole is controlled by a digital signal; that is, the pressure may be applied in bursts or pulses of a fixed pressure, with more pulses being applied in a given time interval to apply, effectively, a higher pressure (of course, alternatively an analogue, continuously varying signal may be used).

Elements of the preform may be selected according to the structure desired in the drawn fibre. For example, all of the elements of the preform may be tubes, which may be arranged to provide a triangular lattice of holes in the drawn fibre. At least one of the elements of the preform may be a solid rod; use of such a rod allows for the manufacture of more complex microstructure by providing a larger region of solid dielectric material in the drawn fibre than is provided by a capillary. The preform may further comprise a larger tube that surrounds the bundle of tubes and forms a jacket region in the drawn fibre.

The drawn microstructured fibre may be arranged to guide light in a core by photonic-band-gap guidance. Alternatively,

the drawn microstructured fibre may be arranged to guide light in a core by index-guidance; for example, the core may then be drawn from a solid rod in the preform.

The holes of the preform may be connected to different pressures in any suitable way; examples of possible arrangements are set out below.

A portion of the preform may be retained undrawn during the drawing of the fibre, and individual connections may be made directly, for example via a hose, from one or more external pressure-controllers to each hole or holes to be pressurised by that pressure-controller.

Alternatively, a connector may be provided to connect the holes to the external pressure-controller.

Also according to the invention there is provided a connector for connecting a preform, which is for a microstructured fibre and which comprises a plurality of holes, to a pressure source, the connector comprising a plurality of elements arranged to mate with one or more of the holes, each element being connectable to a pressure source.

Preferably, different ones of the holes are connectable, individually or in groups, to different pressure sources.

Preferably, the preform comprises a plurality of tubes and the elements are chambers in which one or more of the tubes terminate. Preferably, each chamber is in fluid communication with a passage that is connectable to the pressure source. More preferably, the passage terminates in a valve.

The chambers may be distributed in the connector in a plane substantially orthogonal to the direction in which the tubes are intended to pass through the apertures; thus, the chambers may be side-by-side in that plane. The chambers may be adjacent to the apertures. Preferably, the chambers are recesses in a side of the connector. The passages may pass from the chambers to the opposite side of the cap; alternatively, the passages may pass to another side of the

cap. Preferably, the recesses are arranged to be sealed around the ends of the tubes.

The chambers may be distributed in the connector along the direction in which the tubes are intended to pass through the aperture; thus at least one of the tubes may pass through one or more chamber and terminate in a chamber arranged further from the aperture than the chamber(s) through which that tube passes. Such a connector is designed to receive preform tubes of two or more different lengths, such that the tubes of each length, or within different ranges of lengths, terminate in a different chamber.

Also according to the invention there is provided a method of manufacturing a microstructured fibre, comprising:

- (i) providing a preform comprising a plurality of elements arranged side-by-side in a bundle, a plurality of the elements being tubes;
- (ii) connecting at least one of the tubes to an external pressure-controller by attaching a connector to the tube;
- (iii) drawing the preform into the fibre whilst controlling gas pressure in the tube(s) connected to the external pressure controller.

Also according to the invention there is provided a connector for connecting a preform, which is for a microstructured fibre and which comprises a plurality of tubes, to a pressure source, the connector comprising a plurality of apertures arranged to receive the ends of one or more of the tubes and a plurality of chambers in which one or more of the tubes passing through the apertures terminate, each chamber being connectable to a pressure source.

Also according to the invention there is provided a method of manufacturing a microstructured optical waveguide, comprising:

- (i) providing a preform in which there are a plurality of holes running side-by-side through the preform;

(ii) coupling a pressure controller to one or more, but not all, of the holes for controlling the gas pressure in those holes;

(iii) drawing the preform into an optical waveguide while controlling the gas pressure in the holes that are coupled to the pressure controller.

A method, described above as being according to the invention, may thus further comprise the step of mating a connector with an end of the preform such that the elements of the connector mate with at least some of the holes, connecting the elements to one or more external pressure-controllers and pressuring the holes to one or more selected pressure during the draw.

For example, the method may further comprise the step of placing a connector, such as is described above as being according to the invention, over the end of the preform such that the ends of at least some of the tubes pass through the apertures and into the chambers, connecting the chambers to one or more external pressure-controllers and pressuring the tubes to one or more selected pressure during the draw.

Also according to the invention, there is provided a microstructured fibre manufactured according to a method described above as being according to the invention.

Embodiments of the invention will now be described, by way of example only, with reference to the drawings, of which:

Fig. 1 is an example of a preform for use in a method according to the invention;

Fig. 2 is a first arrangement for pressurising the preform of Fig. 1;

Fig. 3 is a second arrangement for pressurising the preform of Fig. 1, shown (a) in vertical cross-section and (b) in plan from underneath;

Fig. 4 is a third arrangement for pressurising the preform of Fig. 1;

Fig. 5 is a fibre according to the invention having polarisation axes that change adiabatically along the length of the fibre;

Fig. 6 is a fibre according to the invention having a small, nonlinear core;

Fig. 7 is a fibre according to the invention that includes a network of Mach-Zehnder interferometers between its cores;

Fig. 8 is a fibre according to the invention in which propagating light is coupled between two states;

Fig. 9 is an arrangement for pressurising a second example of a preform for use in a method according to the invention;

Fig. 10 is a second arrangement for pressurising the preform of Fig. 9.

Fig. 11 is a fibre according to the invention having a core that vanishes and reappears along the fibre's length.

Fig. 12 is a fibre according to the invention having an index-guiding portion and a hollow-core, photonic band-gap guiding portion.

A typical preform 20 (Fig. 1) for a photonic crystal fibre, of a type well known in the prior art, comprises a bundle of thin tubes 30, arranged in a triangular lattice pattern and held together inside a large tube 5. At the centre of the preform 20, a solid cane 15 is provided in place of a tube 30 in the lattice arrangement. A photonic crystal fibre 10 is drawn from the preform in the usual way. In the drawn fibre 10, tubes 30 form a cladding region comprising a plurality of elongate holes embedded in a silica matrix. Cane 15 forms a solid, elongate core region within the fibre. Large tube 5 forms a jacket region that protects the fibre. In this example, light is guided in the core region by total internal reflection from the cladding region, which has a lower effective refractive index than the refractive index of the core region.

In a first method of individually pressurising holes in the preform 20 during drawing into fibre 10 (Fig. 2), tubes 30 are arranged to protrude from jacket tube 5 in preform 20. Hoses 40 are attached to selected ones of the protruding ends of tubes 30; hoses 40 are held in place by O-rings 50. Hoses 40 are connected at their other ends to external pressure-controllers (not shown).

During drawing of fibre 10 from preform 20, the pressures inside tubes 30, and hence the holes into which they are drawn, are varied by varying the pressure produced by the external pressure-controllers in hoses 40. The pressure in hoses 40 is varied in time and also different pressures are applied at any one time to different ones of hoses 40. Thus the holes produced in the cladding region of the drawn fibre 10 vary in their cross-sectional areas both along the fibre and from hole to hole in fibre transverse cross-sections.

In an alternative method (Fig. 3), as an alternative to connecting hoses directly to preform 10, an intermediate connector 100 is used.

Connector 100 is a flat disk into which have been cut a number of chambers in the form of recesses 110, 115, 120, 125. Recesses 110, 115, 120, 125 are arranged to mate with tubes 30 by receiving the ends of tubes 30 where they protrude from the preform 20. Recesses 110 are each arranged to receive the end of one of tubes 30. Recesses 115 are each arranged to receive the end of two of tubes 30. Recess 120 are each arranged to receive the ends of groups of seven of tubes 30 (or six plus cane 15). Recess 125 are each arranged to receive the ends of groups of five of tubes 30. The tubes 30 are sealed in the recesses 110, 115, 120, 125 by means of a gasket.

Passages 130 pass through connector 100 to valves 140. Prior to drawing, hoses 40 are attached to valves 140. The other ends of hoses 40 are attached to external pressure-controllers, as before. In this arrangement, the pressure produced by the controllers affects the pressure in tubes 30 by changing the pressures in recesses 110, 115, 120, 125.

Thus, for example, all seven tubes in each recess 120 are pressurised to the same pressure, whereas the pressures in tubes in recesses 110 may be varied individually.

An alternative form of connector is shown in Fig. 4. In this example, preform 20 is arranged so that different ones of tubes 30 protrude from preform 20 by different lengths. Intermediate connector 200 comprises three chambers 210, 220, 230, arranged in a stack for mating with tubes 30. Each chamber has a valve 240 to which hoses 40 are connected. The other ends of hoses 40 are attached to external pressure-controllers, as before.

Each chamber has a plurality of holes (not shown) in its base; each hole is either sealed or contains an O-ring, through which one of tubes 30 passes. The tubes 30 are divisible into three length ranges. The shortest terminate in the bottom chamber 210 in the stack. The middle-length tubes pass completely through the bottom chamber 210 and terminate in middle chamber 220. The longest tubes pass through chambers 210, 220 and terminate in chamber 230.

During drawing, each of chambers 210, 220, 230 is pressurised (or partially or completely evacuated) to a different pressure. The size of each hole produced in the final fibre depends on the pressure in the particular chamber in which the tube 30 that formed the hole terminates.

The cross-sectional and axial shape and distribution of the holes in fibre 10 will depend on how the pressure in tubes 30 differs from tube to tube and changes over time. In the steady state, the relationship between hole size and hole pressure is given by

$$p = \frac{\sigma}{r},$$

where σ is surface tension of the silica matrix material and r is the radius of the hole.

For any particular device to be provided in fibre 10, the sites of holes that are to be enlarged or reduced are identified and the corresponding pressures required in tubes 30, to produce the required hole diameters, are calculated by computer according to the above relationship. The computer is programmed with the desired transverse hole diameters and their variation with time. The computer is arranged to control the pressures supplied by the external pressure-controllers, according to the relationship given above, to produce the desired hole shapes. A calibration run is carried out to confirm that the fibre material behaves as predicted during the draw and any necessary parametric adjustments made.

Figs. 5 to 8 are examples of devices that can be produced by examples of the method of the invention.

An example of a fibre produced by the method is photonic crystal fibre 300 (Fig. 5), which exhibits substantially no differential group delay (DGD). A fibre having that property is described in British Patent Application No. 0200603.9 (BlazePhotonics Limited), replaced by International Patent Application No. PCT/GB2003/000060, which are hereby incorporated herein by reference. In that patent, DGD is avoided by providing a 90 degree twist, or a series of twists forming a rocking filter, halfway along a photonic crystal fibre, so that the polarisation mode of propagating light and the polarisation axes of the fibre are rotated relative to each other. Thus any DGD experienced by light propagating in the first half of the fibre is cancelled out by propagation through the second half of the fibre.

In the fibre 300 of Fig. 5, the same effect is achieved, during the draw and without the need for twisting the fibre. The polarisation axes of fibre 300 are gradually swapped by changing the size of hole in the cladding region of the fibre 300, by changing the pressurisation of the holes during the draw in accordance with the invention. The fibre 300 comprises a cladding region comprising a square array of holes 330 formed in matrix material 310, and a solid silica core

region 330. In transverse plane A-A' (Fig. 5(ii)), the square lattice pattern of holes 320 results in there being eight holes adjacent to the core 330. Of those eight, four holes 360 at the corners of the square are the same size as holes 320. Holes 340 on opposite sides of the core region 330 are enlarged relative to holes 320. The remaining two holes 350 have a cross-sectional area that is reduced relative to holes 320. The enlarged holes 340 are produced by applying a higher pressure during a first period of drawing to the ones of tubes 30 from which they are formed; the reduced holes 350 are produced by applying a lower pressure to the corresponding ones of tubes 30. The fibre thus has a fast polarisation axis passing through enlarged holes 340 and a slow polarisation axis in a direction orthogonal to the fast axis.

Once a desired length of fibre 300 has been drawn with the hole configuration of Fig. 5(ii), drawing is continued but the pressure in holes 340 is reduced and the pressure in holes 350 is increased. Holes 340, 350 thus gradually change size until at plane B-B' (Fig. 5 (iii)) at what will be the centre of the fibre 300, they are the same size as holes 320, such that the cladding region is a uniform lattice. The change in applied pressure is continued so that at plane C-C', holes 340 are the size at which holes 350 were in plane A-A' and vice versa. The rest of fibre 300 is drawn with fixed pressures, so that from plane C-C' onwards, the fibre has a fast polarisation axis through holes 350 and a slow polarisation axis through holes 340. DGD experienced by light propagating in fibre 300 to plane B-B' is thus cancelled out by propagation onwards from plane B-B' in the half of the fibre in which the polarisation axes have been reversed. The distance from plane A-A' to B-B' and from B-B' to C-C' is approximately 1 m, which is sufficiently long to provide a lossless (adiabatic) transition.

Another example of a fibre produced by the method is photonic crystal fibre 400 (Fig 6.), which includes a small nonlinear core region 450. In transverse planes A-A' and C-C'

(Fig. 6(ii), (iii)) the fibre has a uniform cross-section, comprising a core region 430 surrounded by a cladding region comprising holes 420 arranged on a triangular lattice pattern in matrix material 410. Core region 430 has a diameter of about 5 microns. During drawing of fibre 400, beyond plane A-A', the pressure in the six holes 440, which are adjacent to the core region 430, is increased relative to the pressure in holes 420. Holes 440 expand relative to holes 420 (Fig. 6(iii)) and the expansion forces silica material out of the core region, forming a small core region 450 of diameter about 2 microns. The holes 440 reach a maximum size at plane B-B' and then the pressure is reduced again so that the core region returns at plane C-C' to the size it had in plane A-A'.

Large holes 440 concentrate light in small core region 450 and nonlinear effects, such as self-phase modulation and self-focusing, result for sufficiently high light intensities.

Another example of a fibre produced by the method is photonic crystal fibre 500 (Fig. 7), which comprises a pair of Mach-Zehnder interferometers formed between its cores by the method of the invention. The fibre comprises a cladding region formed from a triangular lattice of holes 502 embedded in a silica matrix 501 and nine core regions (including cores 510, 520 and 530) arranged on a square lattice and formed where holes are missing in the triangular cladding lattice (the triangular lattice is shown only schematically in Fig. 7). One Mach-Zehnder interferometer comprises a pair 540, 542 of couplers formed between cores 520, 530 and the other comprises a pair 550, 552 of couplers formed between cores 510, 520. A long-period grating 545 is formed on fibre 530 between couplers 540, 542 and another long-period grating 555 is formed on fibre 510 between couplers 550, 552.

Each coupler 540, 542 is formed by reducing the pressure in the holes between cores 520 and 530 during the draw so that those holes are reduced in diameter and cores 520, 530 are brought closer together (Fig. 7 (iii)). Similarly, each coupler 550, 552 is formed by reducing the pressure in the

holes between cores 510 and 520 so that those holes are reduced in diameter and cores 510, 520 are brought closer together (Fig. 7 (iv)).

Thus multiple waveguides are provided in fibre 500 in the form of the fibre cores and signals may readily be transferred between cores 510, 520, 530 via the Mach-Zehnder interferometers.

It will readily be appreciated that other, more complex, networks of devices may be formed in fibre 500 by forming couplers between others of the nine core regions at different points along the fibre length.

Another example of a fibre produced by the method is photonic crystal fibre 600 (Fig. 8), which comprises a length of highly birefringent fibre and a length of nonlinear fibre and a region between those lengths in which light is coupled adiabatically between the two fibre types.

Fig. 8 (ii) to (vii) are cross sections through fibre 600 taken at 1 m intervals between transverse plane A-A' and transverse plane B-B'. Fibre 600 comprises a core region 630, surrounded by a cladding region comprising holes 620 embedded in silica matrix 610 (again, the cladding region structure is shown only schematically).

In Fig. 8 (ii) and (iii), fibre 600 has a highly birefringent structure, resulting from two enlarged holes 640, positioned adjacent to and on opposite sides of the core region 630, which are produced by providing increased pressure in the tubes 30 forming those holes during drawing from the preform.

In Fig. 8 (vi) and (vii), fibre 600 has a highly nonlinear structure resulting from a small core region 650 and six adjacent enlarged holes 660 (in a similar arrangement to the embodiment of Fig. 6 (iii)).

In Fig. 8 (iv), (v) and (vi), the structure of fibre 600 oscillates between the highly birefringent structure and the nonlinear structure. That oscillation is achieved by varying during the draw the pressure in the four holes adjacent to the

core region of the fibre that are not holes 640. The changes in hole size and core size along this transitional length of fibre are very gradual and light propagation is essentially loss-less.

Light propagating in the fibre 600 is thus adiabatically coupled between a mode that propagates without loss in the highly birefringent length of the fibre and a (different-shaped) mode that propagates without loss in the highly nonlinear length of the fibre. As light passes along the oscillating structure, more and more light is coupled from the mode of the highly birefringent region to the mode of the highly nonlinear region.

Of course, a photonic crystal fibre according to the invention may be drawn from an alternative form of preform, such as preform 750 shown in Figs. 9 and 10. Holes 760 in preform 750 are not defined by protruding tubes 30 but by a matrix material 770; thus preform 750 is a monolithic one-piece preform. It may be made, for example, by drilling holes 760 into a block of glass. Alternatively, it may be made by using a sol-gel.

Connector 700 (Fig. 9) is an example of a connector for connecting holes 760 to pressure sources. The connector, like connector 100, comprises valves 740, to which are connected hoses 40. The other ends of hoses 40 are attached to external pressure-controllers. However, passages 730 pass through connector 700 from valves 740 to plugs 710. Plugs 710 are arranged to mate with holes 760 by insertion therein.

Connector 800 (Fig. 10) is a second example of a connector for connecting holes 760 to pressure sources. This connector similarly comprises valves 840 and passages 830, corresponding to valves 740 and passages 730 in connector 700. However, this connector does not have plugs 710 or recesses 110, 115, 120; rather, passages 830 are mated to holes 760 by direct abutment, the join being sealed with an appropriate sealant (e.g. a sealant gel) and connector 800 and preform 750 being held in place by any appropriate means (e.g. a clamp).

As will be understood, the invention is particularly advantageous for providing transitions between lengths of fibre having different properties. For example, an embodiment of the invention is a mode filter; that is, a fibre comprising
5 a first section that supports a smaller number of modes and a second section that supports a larger number of modes. A transition between the first and second sections (and back again, if desired) is readily provided by gradually changing the size of holes in the fibre cross-section. A relatively
10 short section supporting a smaller number of modes in a fibre otherwise supporting a larger number of modes is sufficient to eliminate the extra, unwanted modes downstream of that section. A particularly important case is when the first section is a section supporting only a single mode.

15 Another example of a transition provided according to the invention is a transition between core shapes. Thus, an embodiment of the invention is a fibre comprising a core having a first shape in a first section and a second shape in a second section. Again, a transition between the first and
20 second sections (and back again, if desired) is readily provided by gradually changing the size of holes in the fibre cross-section. The gradual change in hole size results in an equal number of modes being guided in the first and second sections. An application of such a arrangement would be to
25 provide a double-clad fibre in which light is coupled from diode bars into a pump waveguide.

Another embodiment of the invention is in a fibre comprising a core region that vanishes or appears at a point along the fibre's length. Fibre 900 (Fig. 11) is such a
30 fibre. In transverse cross-section, it comprises a cladding region comprising a plurality of holes 910 (only four are shown, for ease of illustration) arranged to provide a photonic band-gap at a desired propagation wavelength. Fibre 900 is divided into five regions A, B, C, B' and A'. Regions
35 A and A' are lengths of photonic-band-gap guiding microstructured fibres in which light of wavelength within the

band-gap is guided in a large air hole forming core 920. Region B includes a long-period grating, which couples desired components of light guided in core 920 in region A into a cladding mode of fibre 900. Undesired components of the propagating light remain in core 920. However, in region C fibre 900 does not include core 920, and so the undesired light is eliminated. The desired light is coupled from the cladding mode back into core 920 by a second long-period grating, in region B'. The desired components of the light then continue their propagation in core 920 in region A'. Region C does not include core 920 because the hole forming 920 has been collapsed during drawing of the fibre. Abrupt transition regions 930 remain, in which core 920 decreases in cross-sectional area to zero.

In another embodiment (not shown), core 920 is a core of a multicore fibre.

Another embodiment of the invention is a fibre having a first region arranged to guide light in a solid core by total internal reflection and a second region arranged to guide light in an elongate hole by photonic band-gap guidance, the two regions being connected by a transition region in which the elongate hole collapses.

An example of such a fibre is fibre 1000 (Fig. 12). Fibre 1000 comprises a first region A comprising a plurality of holes 1010 (only four are shown, for ease of illustration) embedded in a silica matrix material. The holes 1010 are arranged to provide a band-gap for light of a selected wavelength propagating in air. However, in region A, light is guided in solid silica core region 1005; guidance occurs because holes 1010 lower the effective refractive index of the cladding region of fibre 1000, resulting in total internal reflection between core region 1005 and the cladding region containing holes 1010.

In region B, on the other hand, fibre 1000 includes a low-index core in the form of an elongate air hole 1020, and the band-gap provided by holes 1010 causes light of the

selected wavelength to be confined to that hole 1020. Region A does not include air-core 1020 because hole 1020 has been collapsed during drawing of fibre 1000. An abrupt transition region 1030 exists where hole 1020 decreases in cross-sectional area to zero.

Thus the invention provides an arrangement for readily transferring light between regions of fibre that guide by the two different guidance mechanisms known for microstructured fibres. The fibre may thus benefit from advantages of each mechanism; for example, devices only possible in index-guiding fibre may be incorporated in-line in an otherwise photonic band-gap guiding fibre. In the example of Fig. 12, holes 1010 retain the periodicity for photonic band-gap guiding, even in region A. Of course, in other embodiments, the holes in index-guiding regions such as region A may be transferred by selective pressurisation into any configuration that retains an effective refractive index step with the core region.

Set out above are some examples of devices that may be produced in a method according to the invention. It is envisaged that a great many other devices may also be produced according to the method, due to the great range of possible fibre structures that may result from controlling pressure in selected holes of a preform for a microstructured fibre. Also, it may be that the devices described above may be made by methods not according to the invention, for example by post-processing a microstructured fibre (for example, by heat treatment).

Claims

1. A method of manufacturing a microstructured fibre, comprising:
 - (i) providing a preform comprising a plurality of elongate holes;
 - (ii) mating at least one of the holes with a connector to connect the hole(s) to an external pressure-controller;
 - (iii) drawing the preform into the fibre whilst controlling gas pressure in the hole(s) connected to the pressure-controller.
2. A method as claimed in claim 1, in which the preform comprises a plurality of elongate elements, arranged side by side in a bundle, a plurality of the elements being tubes, wherein each tube defines one of the holes in the preform.
3. A method as claimed in claim 1, in which the preform comprises a matrix material that defines the holes.
4. A method as claimed in any preceding claim, in which the external pressure-controller increases the pressure in the hole above atmospheric pressure.
5. A method as claimed in any of claims 1 to 3, in which the external pressure-controller decreases the pressure in the hole below atmospheric pressure.
6. A method as claimed in any preceding claim, in which the pressure in the hole is kept constant throughout the drawing of the fibre.
7. A method as claimed in any of claims 1 to 5, in which the pressure in the hole is varied during the draw.
8. A method as claimed in claim 6, in which the pressure is pulsed periodically.
9. A method as claimed in any preceding claim, in which a plurality of the holes are connected to the external pressure-controller.
10. A method as claimed in any preceding claim, the method including the step of pressurising further groups, each

comprising at least one of the holes, to a second pressure or pressures.

11. A method as claimed in any preceding claim, the method including the step of varying over time the rate at which the fibre is drawn from the preform.

12. A method as claimed in any preceding claim, the method including the step of varying over time the preform feed rate.

13. A method as claimed in any preceding claim, the method including the step of varying over time the furnace temperature.

14. A method as claimed in any preceding claim, in which the pressurisation results in at least one elongate hole formed in the drawn fibre having a different transverse area in one part of the fibre from its transverse area in another part of the fibre.

15. A method as claimed in any preceding claim, in which the pressurisation results in at least one part of the dielectric matrix region having a different transverse area in one part of the fibre from its transverse area in another part of the fibre.

16. A method as claimed in claim 15, in which at least one hole is completely collapsed over a length of the fibre.

17. A method as claimed in any preceding claim, in which the pressurisation results, in a transverse cross-section of the drawn fibre, in a plurality of concentric regions, wherein alternate adjacent regions are of a higher and a lower effective refractive index respectively.

18. A method as claimed in any preceding claim, in which the pressurisation results in the drawn fibre being a W-profile fibre over at least part of its length.

19. A method as claimed in any preceding claim, the method including the step of producing a plurality of devices arranged axially along the PCF by varying over time the pressure applied to the hole or holes.

20. A method as claimed in any preceding claim, in which the pressurisation results in the drawn fibre comprising a long period grating.
21. A method as claimed in any preceding claim, in which the variation in pressurisation results in a change in the symmetry of the fibre, such that a portion of the fibre is birefringent.
22. A method as claimed in claim 21, in which two portions of the fibre are birefringent and their principal polarisation axes are rotated relative to each other by the variation in pressurisation.
23. A method as claimed in claim 22, in which the distribution of pressure in the holes is altered part-way through the draw so as to make the slow axis into a fast axis and vice-versa.
24. A method as claimed in any of claims 21 to 23, in which further portions of the fibre may be birefringent and have rotated polarisations.
25. A method as claimed in any preceding claim, in which the variation in pressurisation results in a change in core size in the drawn fibre, such that the fibre comprises a fibre portion having a larger core region and a fibre portion having a smaller core region.
26. A method as claimed in any preceding claim, in which the variation in pressurisation results in a change in core size, such that the fibre comprises a nonlinear fibre portion, comprising a core region that is sufficiently small for significant nonlinear optical effects to occur in use.
27. A method as claimed in any preceding claim, in which the drawn fibre comprises a plurality of core regions.
28. A method as claimed in claim 27, in which the variation results in the separation of at least two of the cores being reduced in a region of the fibre, such that the fibre comprises an optical coupler comprising the reduced separation region.

29. A method as claimed in claim 28, in which the fibre comprises two such optical couplers that form a Mach-Zehnder interferometer.

30. A method as claimed in claim 28 or claim 29, in which the
5 fibre comprises a network of switches and/or filters formed from a plurality of such couplers.

31. A method as claimed in claim 27, in which the fibre comprises more than two cores.

32. A method as claimed in claim 31, in which the variation
10 results in the separations of the cores being reduced over a plurality of portions of the fibre to form optical couplers between each of the more than two cores.

33. A method as claimed in any preceding claim, in which a
15 transition region formed between each of a plurality of optical devices formed in the fibre is sufficiently gradual to be adiabatic.

34. A method as claimed in any preceding claim, in which the
condition of the draw is oscillated between two states over
time to form a transition region, the first state being
20 matched to the mode of a first optical device comprised within the fibre and the second state being matched to the mode of a second of optical device comprised within the fibre.

35. A method as claimed in any preceding claim, the method
includes the step of manufacturing twist-compensated DGD-free
25 fibre by oscillating the structure to and fro periodically along the length of the drawn fibre.

36. A method as claimed in any preceding claim, in which the
pressure is oscillated during the draw to avoid unwanted
nonlinear effects by oscillating the fibre structure around a
30 desired structure that satisfies an unwanted phase-matching condition.

37. A method as claimed in any preceding claim, in which the
method includes the step of producing a DCF with graded
properties that match the dispersion curve in standard
35 telecomms fibre over the telecommunications bands.

38. A method as claimed in any preceding claim, in which the method includes the step of calibrating the relationship between parameters of the draw and parameters of the drawn fibre.

5 39. A method as claimed in claim 38, in which the method further comprises varying parameters of the draw according to the calibration results to produce a fibre having a selected structure.

10 40. A method as claimed in any preceding claim, in which the pressure applied to the or each hole is controlled by a digital signal.

15 41. A method as claimed in any preceding claim, in which a portion of the preform is retained undrawn during the drawing of the fibre, and individual connections are made directly, for example via a hose, from one or more external pressure-controllers to each hole or holes to be pressurised by that pressure-controller.

20 42. A method as claimed in any of claims 1 to 40, in which a connector is provided to connect the holes to the external pressure-controller.

25 43. A connector for connecting a preform, which is for a microstructured fibre and which comprises a plurality of holes, to a pressure source, the connector comprising a plurality of elements arranged to mate with one or more of the holes, each element being connectable to a pressure source.

44. A connector as claimed in claim 43, in which different ones of the elements are connectable, individually or in groups, to different pressure sources.

30 45. A connector as claimed in claim 43 or claim 44, in which the preform comprises a plurality of tubes and the elements are chambers in which one or more of the tubes terminate.

46. A connector as claimed in claim 45, in which each chamber is in fluid communication with a passage that is connectable to the pressure source.

35 47. A connector as claimed in claim 45 or claim 46, in which the chambers are distributed in the connector in a plane

substantially orthogonal to the direction in which the tubes are intended to pass through the apertures.

48. A connector as claimed in claim 47, in which the chambers are adjacent to the apertures.

5 49. A connector as claimed in claim 48, in which the chambers are recesses in a side of the connector.

10 50. A connector as claimed in any of claims 43 to 48, in which the chambers are distributed in the connector along the direction in which the tubes are intended to pass through the aperture.

15 51. A method as claimed in any of claims 1 to 42, further comprising the step of mating a connector as claimed in any of claims 41 to 50 with an end of the preform such that the elements of the connector mate with at least some of the holes, connecting the elements to one or more external pressure-controllers and pressuring the holes to one or more selected pressure during the draw.

52. A method of manufacturing a microstructured optical waveguide, comprising:

20 (i) providing a preform in which there are a plurality of holes running side-by-side through the preform;

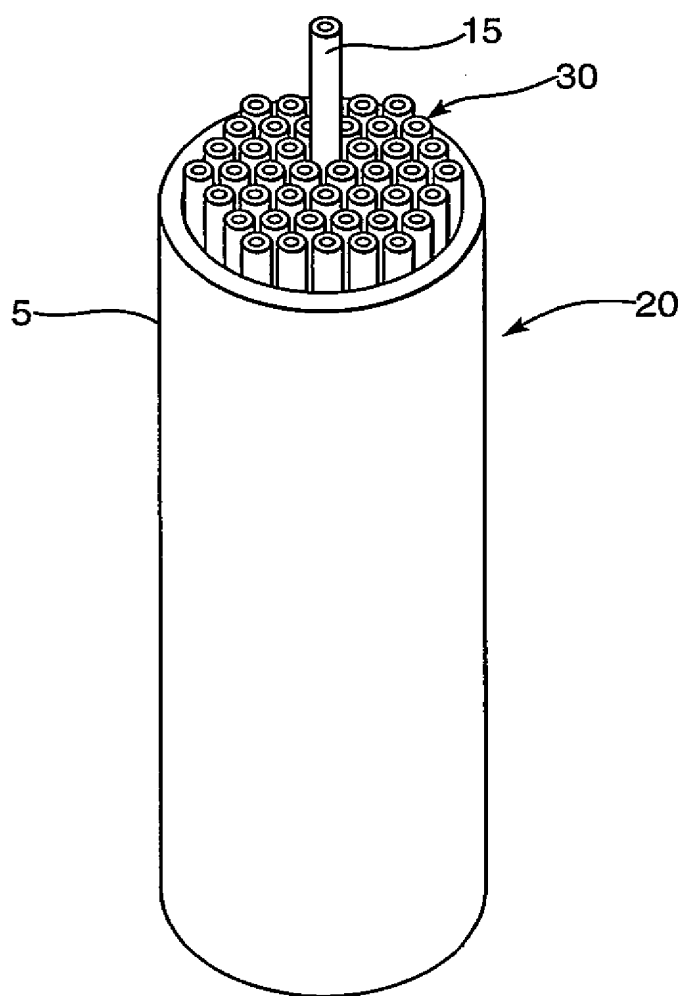
(ii) coupling a pressure-controller to one or more, but not all, of the holes for controlling the gas pressure in those holes;

25 (iii) drawing the preform into an optical waveguide while controlling the gas pressure in the holes that are coupled to the pressure-controller.

53. A fibre made by a method according to any of claims 1 to 43, 51 or 52.

1/8

Fig.1.



2/8

Fig.2.

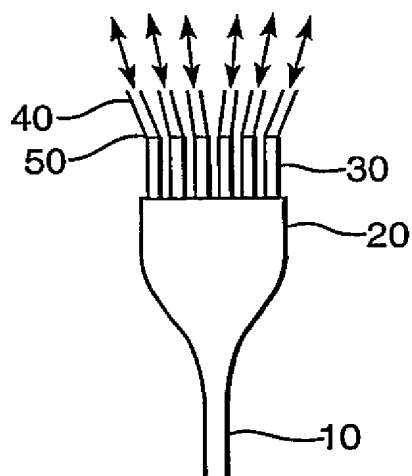


Fig.3(a).

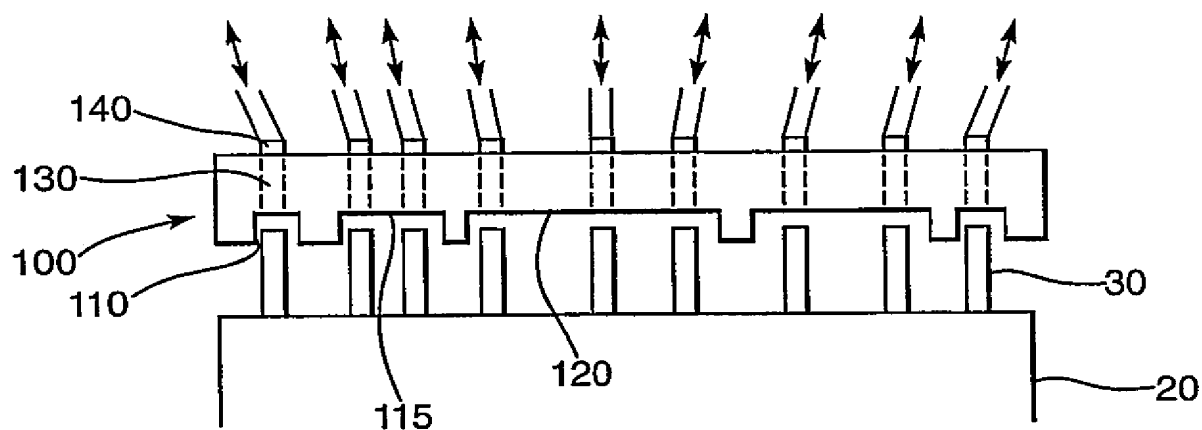


Fig.3(b).

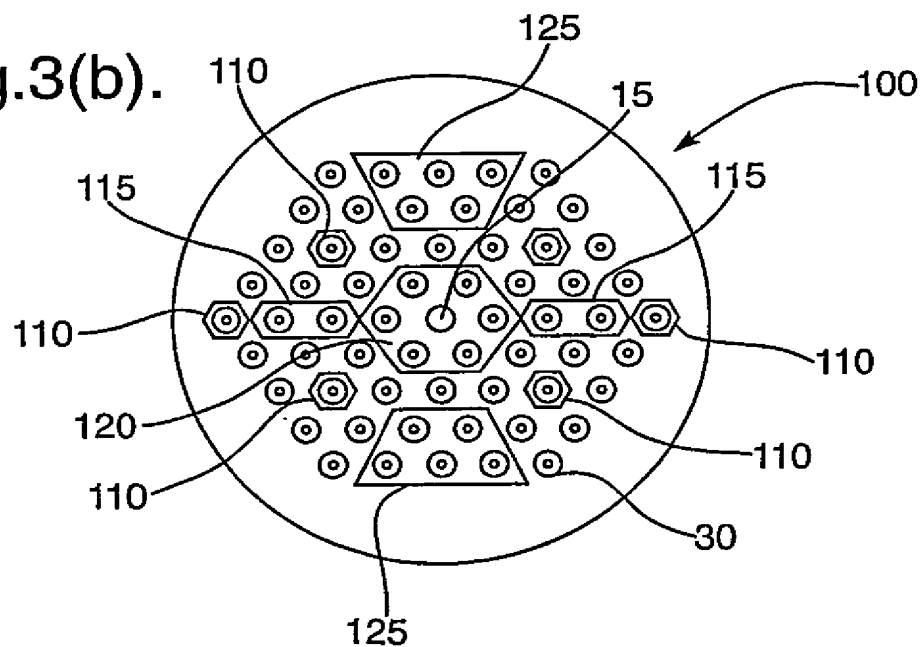
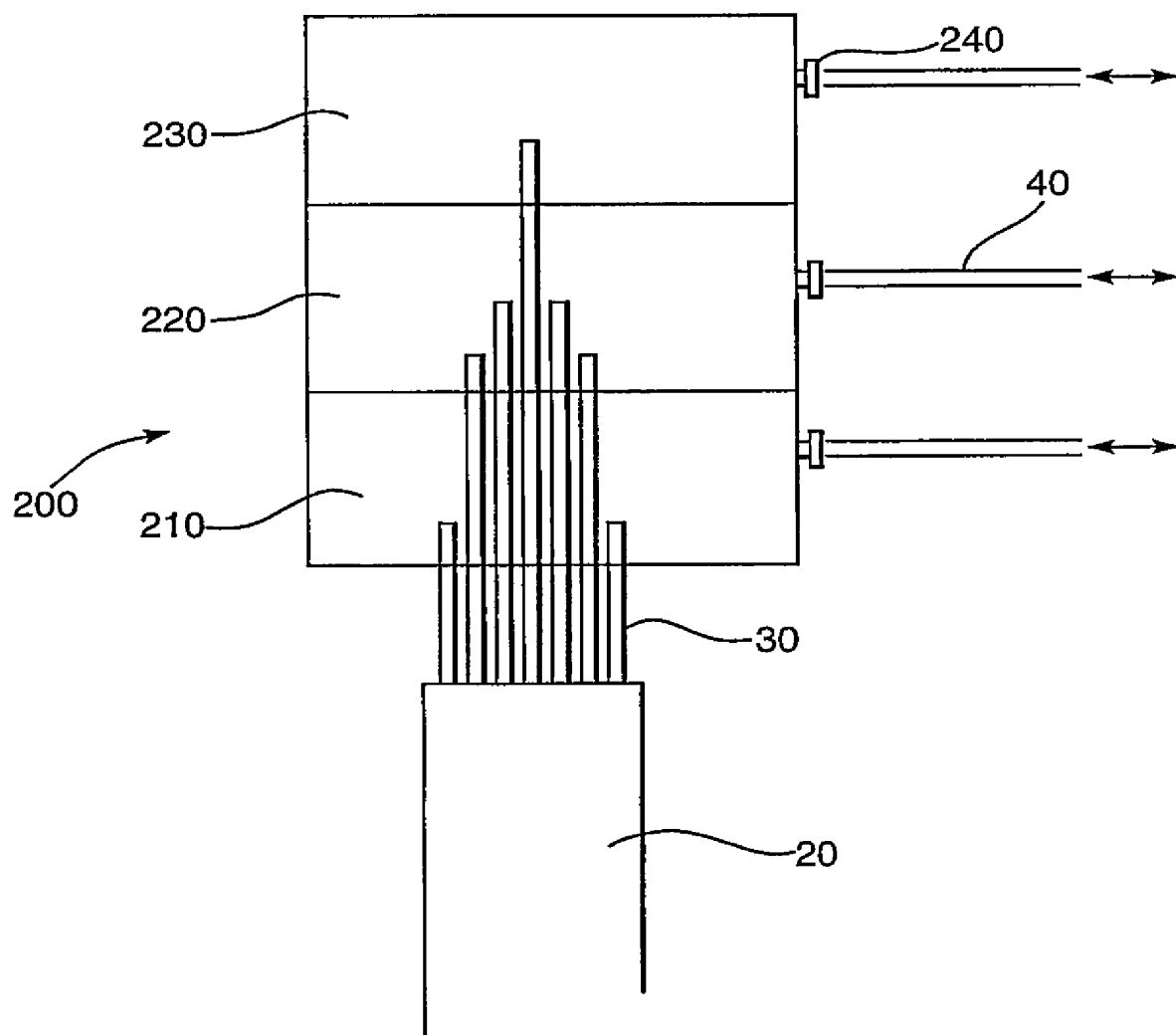


Fig.4.



4/8

Fig.5.

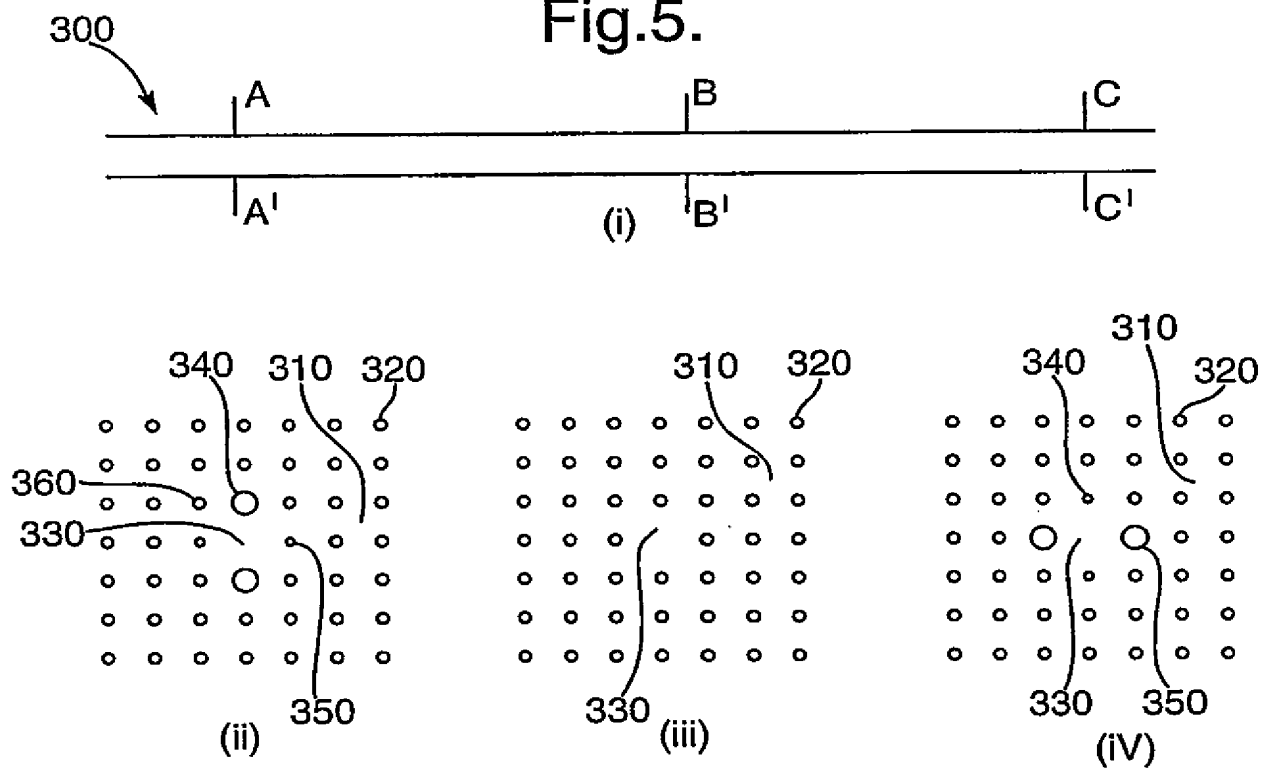


Fig.6.

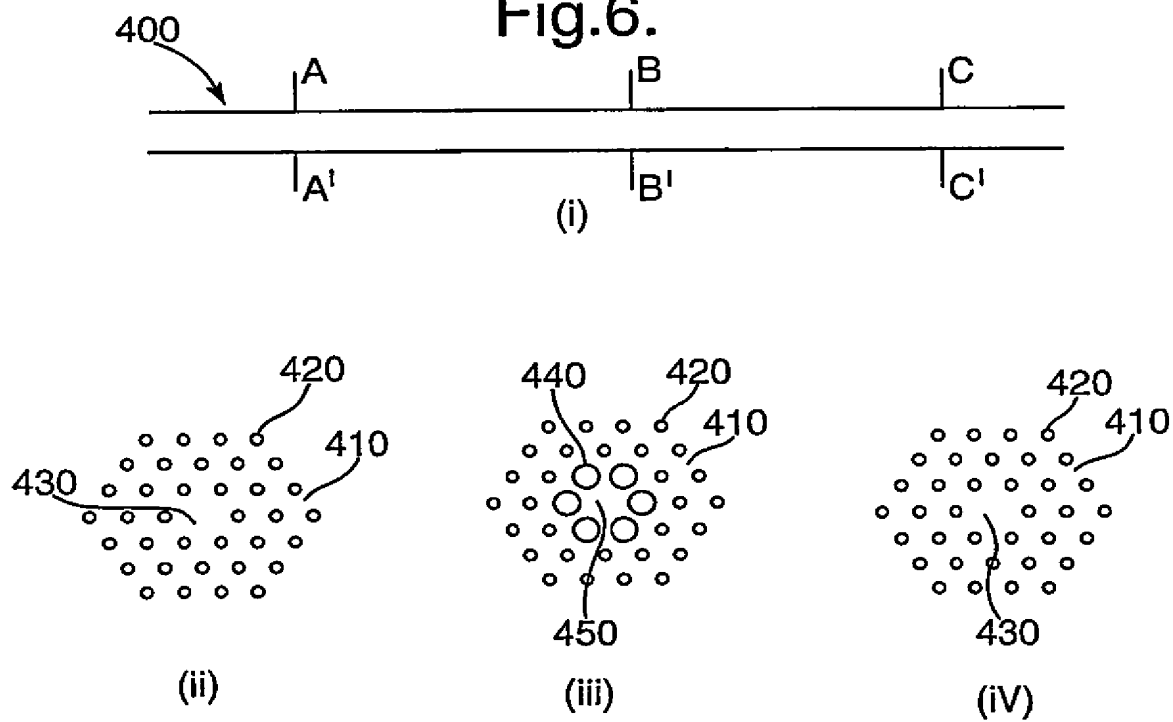
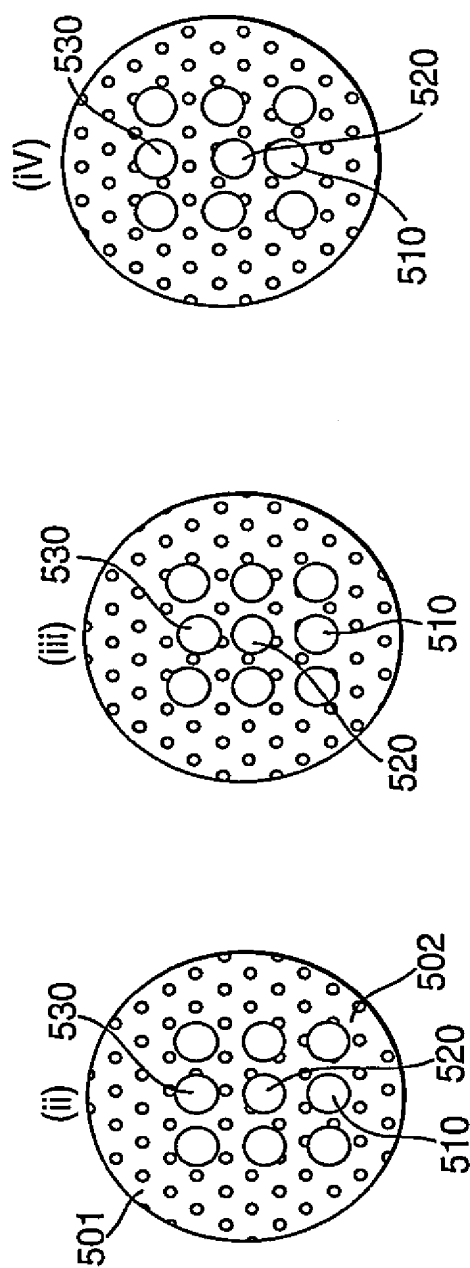
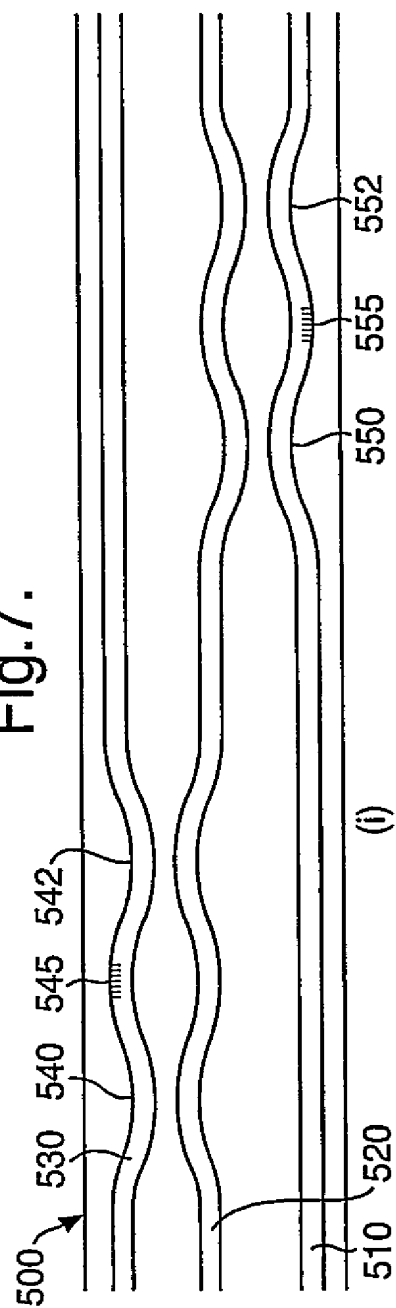
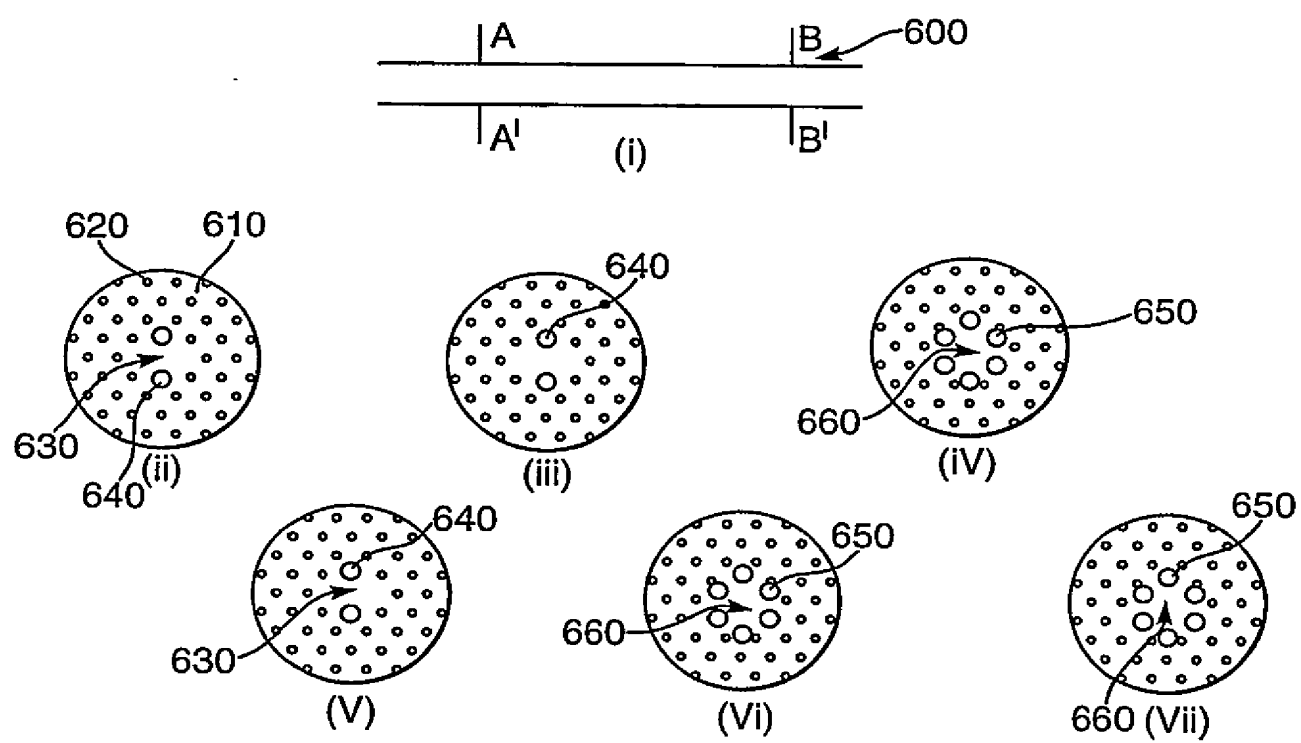


Fig.7.



6/8

Fig.8.



7/8

Fig.9.

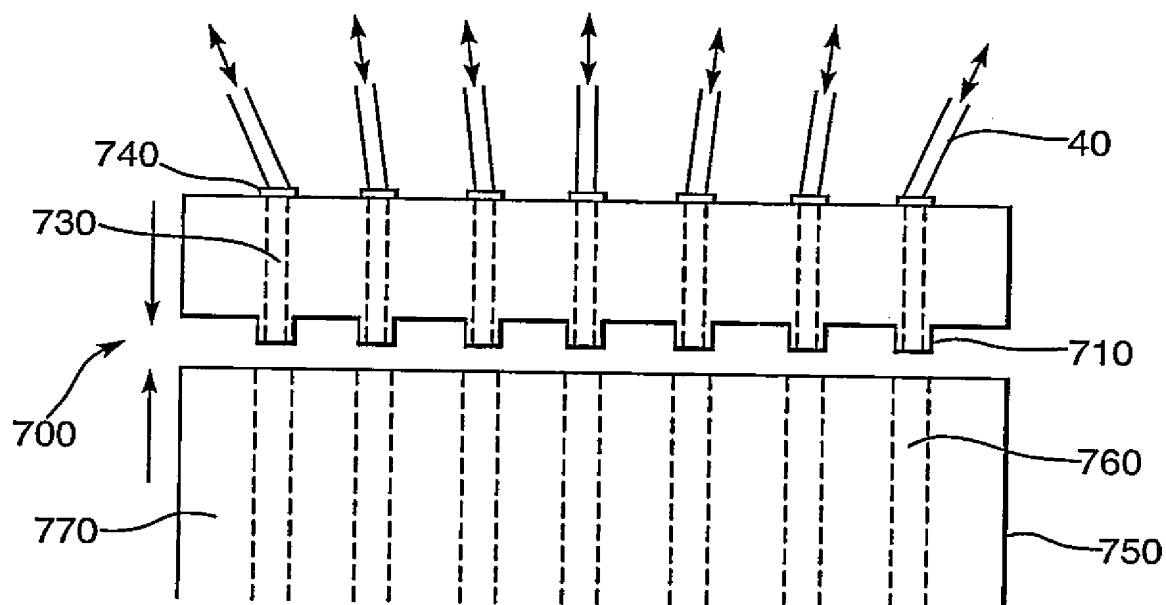


Fig.10.

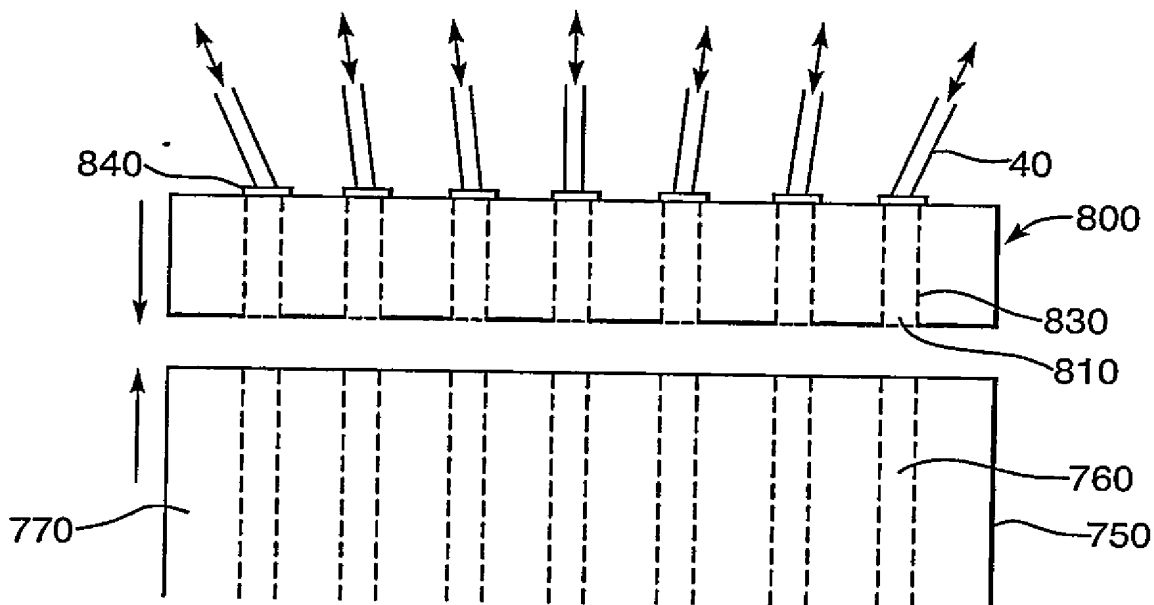


Fig.11.

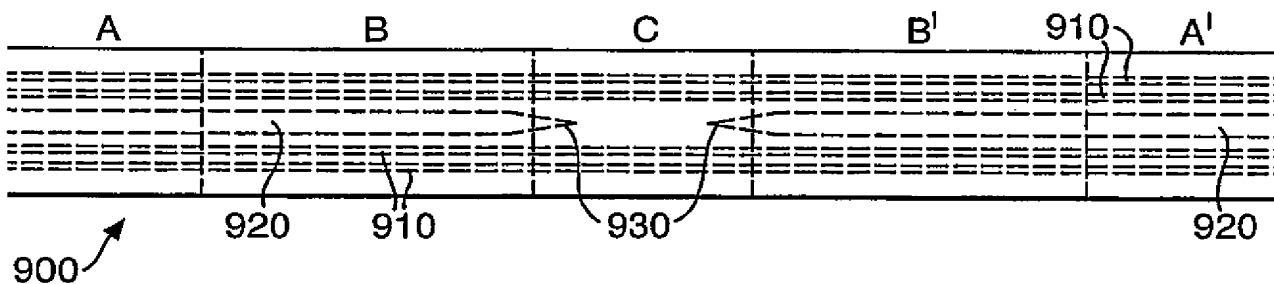
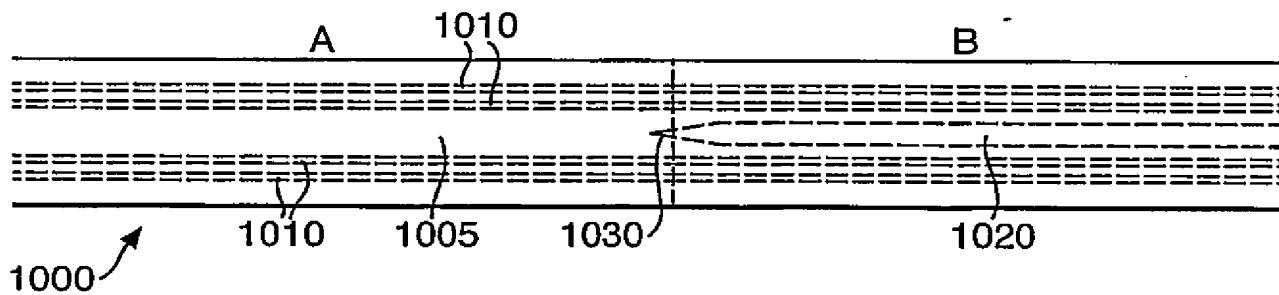


Fig.12.



INTERNATIONAL SEARCH REPORT

PCT/GB 03/01298

A. CLASSIFICATION OF SUBJECT MATTER
IPC 7 C03B37/027

According to International Patent Classification (IPC) or to both national classification and IPC

B. FIELDS SEARCHED

Minimum documentation searched (classification system followed by classification symbols)

IPC 7 C03B

Documentation searched other than minimum documentation to the extent that such documents are included in the fields searched

Electronic data base consulted during the international search (name of data base and, where practical, search terms used)

C. DOCUMENTS CONSIDERED TO BE RELEVANT

Category *	Citation of document, with indication, where appropriate, of the relevant passages	Relevant to claim No.
X A	WO 00 49436 A (UNIVERSITY OF BATH, GB) 24 August 2000 (2000-08-24) cited in the application claims 37-43	1-15, 20-22, 52,53 43
X A	WO 00 16141 A (CORNING INC) 23 March 2000 (2000-03-23) cited in the application claims 35-39	1,53 43,52
X A	US 2001/029756 A1 (PAEK U-C ET AL) 18 October 2001 (2001-10-18) claims 1,5,8; figure 3	1,53 43,52
A	WO 00 49435 A (UNIVERSITY OF BATH) 24 August 2000 (2000-08-24) page 4	1,52,53

☐ Further documents are listed in the continuation of box C.☒ Patent family members are listed in annex.

* Special categories of cited documents:

A document defining the general state of the art which is not considered to be of particular relevance

E earlier document but published on or after the international filing date

L document which may throw doubts on priority claim(s) or which is cited to establish the publication date of another citation or other special reason (as specified)

O document referring to an oral disclosure, use, exhibition or other means

P document published prior to the international filing date but later than the priority date claimed

T later document published after the international filing date or priority date and not in conflict with the application but cited to understand the principle or theory underlying the invention

X document of particular relevance; the claimed invention cannot be considered novel or cannot be considered to involve an inventive step when the document is taken alone

Y document of particular relevance; the claimed invention cannot be considered to involve an inventive step when the document is combined with one or more other such documents, such combination being obvious to a person skilled in the art

Z document member of the same patent family

Date of the actual completion of the international search

12 June 2003

Date of mailing of the international search report

20/06/2003

Name and mailing address of the ISA

European Patent Office, P.B. 5818 Patentlaan 2
NL - 2280 HV Rijswijk
Tel. (+31-70) 340-2040, Tx. 31 651 epo nl,
Fax (+31-70) 340-3016

Authorized officer

Stroud, J

INTERNATIONAL SEARCH REPORT

PCT/GB 03/01298

Patent document cited in search report		Publication date	Patent family member(s)	Publication date
WO 0049436	A	24-08-2000	AU 2564900 A	04-09-2000
			AU 2565000 A	04-09-2000
			CA 2362992 A1	24-08-2000
			CA 2362997 A1	24-08-2000
			CN 1341219 T	20-03-2002
			CN 1341221 T	20-03-2002
			EP 1153324 A1	14-11-2001
			EP 1153325 A1	14-11-2001
			WO 0049435 A1	24-08-2000
			WO 0049436 A1	24-08-2000
			JP 2002537574 A	05-11-2002
			JP 2002537575 A	05-11-2002
WO 0016141	A	23-03-2000	AU 5772699 A	03-04-2000
			BR 9913724 A	29-05-2001
			CA 2341727 A1	23-03-2000
			CN 1317099 T	10-10-2001
			EP 1121615 A1	08-08-2001
			JP 2002525256 T	13-08-2002
			TW 455709 B	21-09-2001
			WO 0016141 A1	23-03-2000
			ZA 9905897 A	04-04-2000
US 2001029756	A1	18-10-2001	KR 2001096260 A	07-11-2001
			JP 2001302268 A	31-10-2001
WO 0049435	A	24-08-2000	AU 2564900 A	04-09-2000
			AU 2565000 A	04-09-2000
			CA 2362992 A1	24-08-2000
			CA 2362997 A1	24-08-2000
			CN 1341219 T	20-03-2002
			CN 1341221 T	20-03-2002
			EP 1153324 A1	14-11-2001
			EP 1153325 A1	14-11-2001
			WO 0049435 A1	24-08-2000
			WO 0049436 A1	24-08-2000
			JP 2002537574 A	05-11-2002
			JP 2002537575 A	05-11-2002

Optical devices based on liquid crystal photonic bandgap fibres

Thomas Tanggaard Larsen and Anders Bjarklev

COM Center, Technical University of Denmark, DK-2800 Lyngby, Denmark.
tl@com.dtu.dk, ab@com.dtu.dk

David Sparre Hermann

Photonics Laboratory, Department of Microtechnology and Nanoscience MC2, Chalmers University of Technology,
 412 96 Gothenburg, Sweden.
David.Hermann@fy.chalmers.se

Jes Broeng

Crystal Fibre A/S, Blokken 84, DK-3460 Birkerød, Denmark
jh@crystal-fibre.com

Abstract: Photonic Crystal Fibers (PCFs) have appeared as a new class of optical waveguides, which have attracted large scientific and commercial interest during the last years. PCFs are microstructured waveguides, usually in silica, with a large number of air holes located in the cladding region of the fiber. The size and location of these air holes opens up for a large degree of design freedom within optical waveguide design. Further, the existence of air holes in the PCF gives access close to the fiber core and by introducing new materials into the air holes, a high interaction between light and hole material can be obtained, while maintaining the microstructure of the waveguide. In this paper, we describe what we call Liquid Crystal Photonic Bandgap Fibers, which are PCFs infiltrated with Liquid Crystals (LCs) in order to obtain increased fiber functionality. We describe a thermo-optic fiber switch with an extinction ratio of 60dB and tunable PBGs using thermo-optic tuning of the LC. These devices operate by the PBG effect and are therefore highly sensitive to the refractive index distributions in the holes.

©2003 Optical Society of America

OCIS codes: (060.2310) Fiber optics, (230.3990) Microstructure devices

References and Links

1. D. B. Keck, R. D. Maurer, and P. C. Schultz, "On the ultimate lower limit of attenuation in glass optical waveguides," *Appl. Phys. Lett.* **22**, 307-309 (1973).
2. R. Symms and J. Cozens, *Optical Guided Waves and Devices*, (McGraw-Hill Book Company England, 1992).
3. J. C. Knight, J. Broeng, T. A. Birks, and P. St. J. Russell, "Photonic bandgap guidance in optical fibers," *Science* **283**, 1476-1478 (1998).
4. E. Yablonovitch, "Inhibited spontaneous emission in solid-state physics and electronics," *Phys. Rev. Lett.* **58**, 2059-2062 (1987).
5. J. D. Joannopoulos, R. D. Meade, and J. N. Winn, *Photonic Crystals: Molding the Flow of Light*, (Princeton Univ. Press, 1995).
6. P. Russell, "Photonic crystal fibers," *Science* **299**, 358-362 (2003).
7. K. P. Hansen, *et al.*, "Highly nonlinear photonic crystal fiber with zero-dispersion at 1.55 μ m," Optical Fiber Communication Conference (Optical Society of America, Washington, D.C., 2002) PDF A9.
8. R.F. Cregan *et al.*, "Single-mode photonic band gap guidance of light in air," *Science* **285**, 1537-1539 (1999).
9. B. Temelkuran, S. D. Hart, G. Benoit, J. D. Joannopoulos, and Y. Fink, "Wavelength-scalable hollow optical fibres with large photonic bandgaps for CO₂ laser transmission," *Nature* **420**, 650-653 (2002).

#2871 - \$15.00 US
 (C) 2003 OSA

Received August 07, 2003; Revised September 29, 2003
 6 October 2003 / Vol. 11, No. 20 / OPTICS EXPRESS 2589

10. J. Limpert, *et al.*, "High-power air-clad large-mode-area photonic crystal fiber laser," *Opt. Express* 11, 818 (2003), <http://www.opticsexpress.org/abstract.cfm?URI=OPEX-11-7-818>
11. J. Jasapara, R. Bise, T. Her, and J. Nicholson, "Effect of Mode Cut-Off on Dispersion in Photonic Bandgap Fibers," *Optical Fiber Communication Conference Th13* (2003).
12. P. S. Westbrook, *et al.*, "Cladding-mode resonances in hybrid polymer-silica microstructured optical fiber gratings," *IEEE Photonics Technol. Lett.* 12, (2000).
13. B. J. Eggleton, C. Kerbage, P. S. Westbrook, R. S. Windeler, and A. Hale, "Microstructured optical fiber devices," *Optics Express* 9, 698-713 (2001).
14. E. Yablonovitch, "Liquid versus photonics crystals," *Nature* 401, 539-541 (1999).
15. K. Busch and S. John, "Liquid-Crystal Photonic-Band-Gap Materials: The Tuneable Electromagnetic Vacuum," *Phys. Rev. Lett.* 83, 967-970 (1999).
16. C. Wenyi, A. Munoz, P. Palffy-Muhoray, and B. Taheri, "Lasing in a three-dimensional photonics crystal of the liquid crystal blue phase II," *Nature Materials* 1, 111-113 (2002).
17. P. G. de Gennes and J. Prost, J. *The Physics of liquid crystals*, 2nd edition, (Clarendon Press, Oxford, 1993).
18. S. Chandrasekhar, *Liquid crystals*, (Cambridge University Press, 1977).
19. P. Rudquist, M. Buivydas, L. Komitov, and S. T. Lagerwall, "Linear electro-optic effect based on flexoelectricity in a cholesteric with sign change of dielectric anisotropy," *J. Appl. Phys.* 76, (1994).
20. H. -S. Kitzerow, B. Liu, F. Xu, and P. P. Crooker, "Effect on chirality on liquid crystals in capillary tubes with parallel and perpendicular anchoring," *Phys. Rev. E* 54, 568-575, (1996).
21. S. K. Lo, L. M. Galarneau, D. J. Rogers, and S. R. Flom, "Smectic Liquid Crystal Waveguides with cylindrical Geometry," *Mol. Cryst. Liq. Cryst.* 201, 137-145 (1991).
22. J. T. Mang, K. Sakamoto, and S. Kumar, "Smectic Layer Orientation in Confined Geometries," *Mol. Cryst. Liq. Cryst.* 223, 133-142 (1992).
23. S. Kralj and S. Zumer, "Smectic-A structures in submicrometer cylindrical cavities," *Phys. Rev. E*, 54(2), 1610-1617 (1996).
24. K. Abeeluck, N. M. Litchinitser, C. Headley, and B. J. Eggleton, "Analysis of spectral characteristics of photonic bandgap waveguides," *Opt. Express* 10, 1320-1333 (2002), <http://www.opticsexpress.org/abstract.cfm?URI=OPEX-10-23-1320>
25. J. B. Jensen, *et al.*, "Photonic Crystal Fibre based evanescent-wave sensor for detection of aqueous solutions," *Conference on Lasers and Electro-Optics* (Optical Society of America, Washington, D.C., 2003).
26. V. K. Gupta, J. J. Skaife, T. B. Dubrowsky, and N. L. Abbott, "Optical Amplification of Ligand-Receptor Binding Using Liquid Crystals," *Science* 278, 2077-2080 (1998)

Introduction

Standard optical waveguides guide light by total internal reflection, which requires that the refractive index of the waveguide core is larger than that of the surrounding (often homogeneous) cladding. Such waveguides have been extremely successful as transmission fibres [1] in world-spanning telecommunication systems or in the emerging field of integrated optics [2]. With the appearance of photonic crystal fibres [3] (PCFs) and, more generally, three-dimensional periodic structures for control of electromagnetic waves [4], a more diverse field of optical waveguides has appeared, relying on the properties of structural repeatable index contrasts often in air-solid combinations [5]. The waveguiding properties of photonic crystal structures may (depending on structure) either be explained as modified total internal reflection [6], or as Photonic BandGap (PBG) guiding, in which a periodic cladding structure exhibit strong reflection through a two-dimensional destructive interference process. PCFs have shown numerous unique properties, e.g., as non-linear fibres with highly extended dispersion control [7], as air-guiding fibres [8] or Bragg fibres [9] allowing for transmission of light at new wavelengths, or as fibres with very high numerical apertures, which are specifically attractive in very-high-power cladding-pumped fibre lasers [10].

Photonic crystal structures have also opened for a highly extended access to the guided light through the hollow voids in or around the core region of the waveguide.

Important examples include the demonstration of large waveguide dispersion in a PCF with high-index liquid [11] filled holes, or as devices combining Bragg grating technology and Microstructured Optical Fibres (MOFs) with polymer-filled air holes [12]. The work by Kerbage and Eggleton [13] is particularly interesting, because it shows the possibility of realising active waveguide control, by dynamic positioning of a microfluid inside a MOF. Further, Yablonovitch [14] states that a combination of liquid and photonic crystals may hold new potential also for 3-dimensional waveguide structures.

The perspectives of design and active control of optical waveguides are further widened, if we bring the idea of self-organised material components into action. A very interesting candidate is the use of Liquid Crystals (LCs), which according to theoretical work by Busch and John [15] may be used in three-dimensional photonic crystals to obtain tuneable light localization, or to allow mirrorless lasing through the formation of a self-assembled PBG material [16]. It is, therefore, fundamentally interesting to study the potential application of LCs as means of introducing enhanced periodicity and controllability, and in a further sense make the two-dimensional PCF a three-dimensional structure. Even more, it is relevant to consider the fundamental differences between optical waveguiding resulting from total internal reflection in contrast to the PBG effect, because enhanced active waveguide control must be expected, if e.g., switching between these two waveguiding principles is brought in action.

Here we report the first liquid-crystal-filled photonic crystal fibres, which guide light by the photonic bandgap effect as shown on Fig. 1. We demonstrate the first use of an actively controlled photonic bandgap fibre device, and describe how liquid-crystal-filled PCFs can serve as a highly sensitive, tuneable signal-processing element operating by the photonic bandgap effect. We demonstrate a tuneable filter function and low-voltage controlled broadband optical switching with an extinction ratio of as much as 60 dB, and an insertion loss of only 1dB.

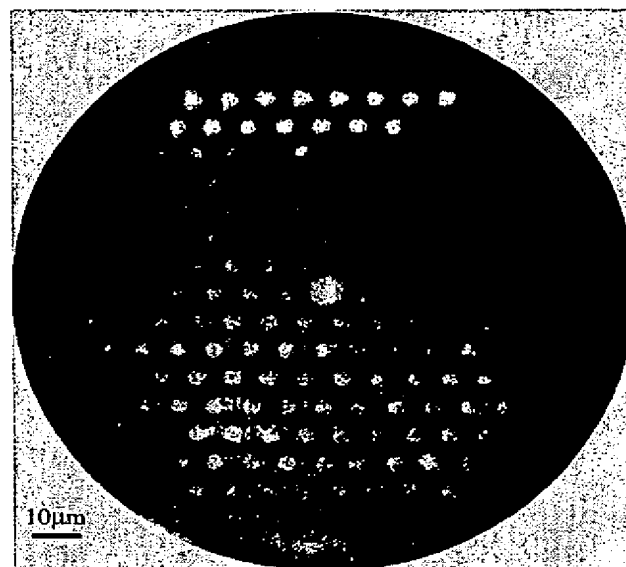


Fig. 1. Micrograph of the end facet of a liquid-crystal-filled photonic crystal fibre. The periodic structure, consisting of silica and liquid crystal, gives rise to a cladding with photonic bandgaps, and the fibre supports only guided modes at certain wavelength bands. In this case, a blue mode is supported in the visible region of the spectrum.

Mesophases of liquid crystals

Liquid crystals are organic materials consisting of geometrically anisotropic molecules, leading to long-range orientational [17], [18] order and a number of *mesophases*, which are thermodynamic phases with physical properties intermediate between those of pure liquids and pure solids. Phase transitions occur either when temperature is varied (thermotropics) or when the concentration of solute molecules is varied (lyotropics). Thermotropics are mainly used for electro-optic applications, such as flat-panel laptop displays. Lyotropics occur abundantly in nature, such as in DNA and cell membranes. We are presently concerned with

thermotropic, rodlike (calamitic) LCs and examples of mesophases within this class are shown in Fig. 2. *Nematics* have only long-range orientational order, while *smectics A and C* in addition have long-range positional order in one dimension, resulting in a structure of thin (2-5 nm) layers; several hundred smectic layers thus average up to determine the local optical properties. In case of *chiral* molecules, all phases become noncentrosymmetric, leading to a helical superstructure in chiral nematic (N^* =cholesteric) and chiral smectic C (SmC^*), but not in chiral smectic A (SmA^*). The *helical structures* are self-organized PBG materials, provided the helical pitch p is on the same order of magnitude as the wavelength of the light.

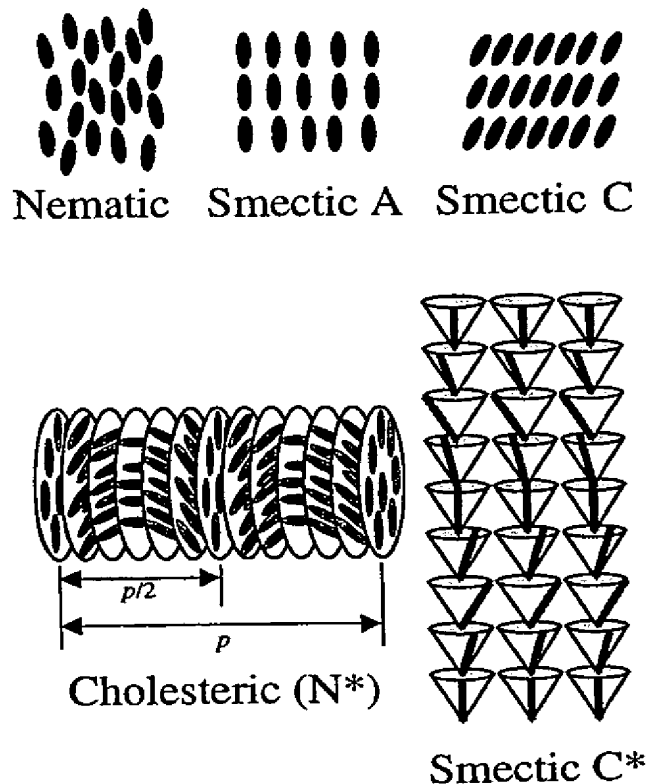


Fig. 2. Examples of phases of thermotropic liquid crystals: Nematic, Smectic A and Smectic C phases (non-chiral molecules), appearing in that order upon cooling, if the same material possesses all of these phases. If the molecules are chiral, we instead have N^* (=cholesteric), SmA^* and SmC^* . These phases all lack mirror planes. A helical superstructure due to the molecular chirality appears in the N^* and SmC^* phases (shown), but not in the SmA^* phase (not shown).

Liquid crystal photonic bandgap fibres

In this work, we have filled LCs into the circular voids of a triangular structured PCF, with inter-hole distance of $7\mu\text{m}$ and hole size of $3.5\mu\text{m}$. We examined the alignment of the LC by polarizing microscopy observations of a single hole. We have used two different types of LCs:

#2871 - \$15.00 US
(C) 2003 OSA

Received August 07, 2003; Revised September 29, 2003
6 October 2003 / Vol. 11, No. 20 / OPTICS EXPRESS 2592

MDA-00-1445 from Merck and TM216 from BDH. The first is a short-pitch cholesteric having a N* to isotropic phase transition at 94°C, a reflection wavelength of 470nm and extraordinary and ordinary refractive indices of $n_{e,589nm}=1.6844$ and $n_{o,589nm}=1.5070$, respectively. The latter has both a chiral Smectic A and a cholesteric phase, with the phase transition temperatures SmA* 26.2°C N* 42.3°C Isotropic. TM216 is a short-pitch LC with a highly temperature sensitive pitch around the SmA* to N* phase transition [19].

Alignment study

Polarized microscopy observations of MDA-00-1445 in its cholesteric phase indicated that the helix axis of the cholesteric was aligned in a radial symmetry and perpendicular to the fibre axis. These observations are consistent with the ones found by Kitzrow *et al.* [20]. Similar observations of TM216 in the SmA* phase indicated a homeotropic alignment of the director in a region extending from the inner walls of the holes and in towards the central region of the holes. This central region had no or little transmission dependence in the polarized microscope. These observations suggest that the LC is aligned radially within the PCF holes - equivalent to a smectic layer structure forming concentric cylinders along the axis of the PCF holes, and wrapped around an optically isotropic core region. This alignment is consistent with observations by Lo *et al.* [21] and by Mang *et al.* [22] and is further substantiated by a theoretical study by Kralj and Zumer [23].

Device description

After the alignment study, all voids of a PCF were filled with LCs, where the relatively high and controllable refractive index of the LC, together with the periodic arrangement of holes in the PCF, gives rise to a fibre cladding with photonic bandgaps [24]. The spectral characteristics of the filled fibre, thereby, depend on the original PCF structure and on the alignment and optical properties of the LC.

To access the potential of controllability, we coated the filled section of the fibre with a thin conducting layer - forming a resistive microheater. By applying a small current through the microheater, the temperature of the LC and, thereby, the photonic bandgaps of the cladding structure could be controlled. The device-principle is illustrated in Fig. 3(a). The inset in Fig. 3(a) shows a polarized micrograph of the SmA* phase of TM216 inside a PCF hole.

Waveguiding principle

While accurate simulation of fibre operation is difficult for the exact LC composition in the holes, Fig. 3(b) qualitatively illustrates the bandgap effects that are in play. The figure illustrates mode indices of allowed states of the fibre as function of wavelength. We have made the approximation of a uniform refractive index material filling the holes. The rods were simulated for a refractive index of 1.59(chosen to be approximately equal to the average value of the ordinary and extra-ordinary refractive indices). Although this is an approximation it serve to explain the basic waveguiding mechanism, but cannot be used for accurate simulation of cladding modes and bandgap edges, since it is expected that the actual alignment of the LC will have a significant influence on these solutions. The fibre has LC-filled holes of diameter, d , equal to 3.5 μ m, and pitch, Λ , of 7.0 μ m. Intuitively, the operation of the LC-filled fibre may be explained as individual rods (the LC-filled holes) forming isolated waveguides at short wavelengths, whereas, for increasing wavelength, the rods become resonant and finally strongly coupled waveguides. Most importantly, forbidden regions with mode index below the low-index background material ($n = 1.45$) appear for narrow spectral ranges. Within these spectral ranges, the fibre is capable of confining and guiding light in the core, despite its lower refractive index compared to the surrounding rods. The spectral position and extend of these 'light-guide' ranges are highly dependent on the exact composition of the rod material. Hence, the strong sensitivity of LCs makes them ideal candidates for control of light guidance by very small external influences.

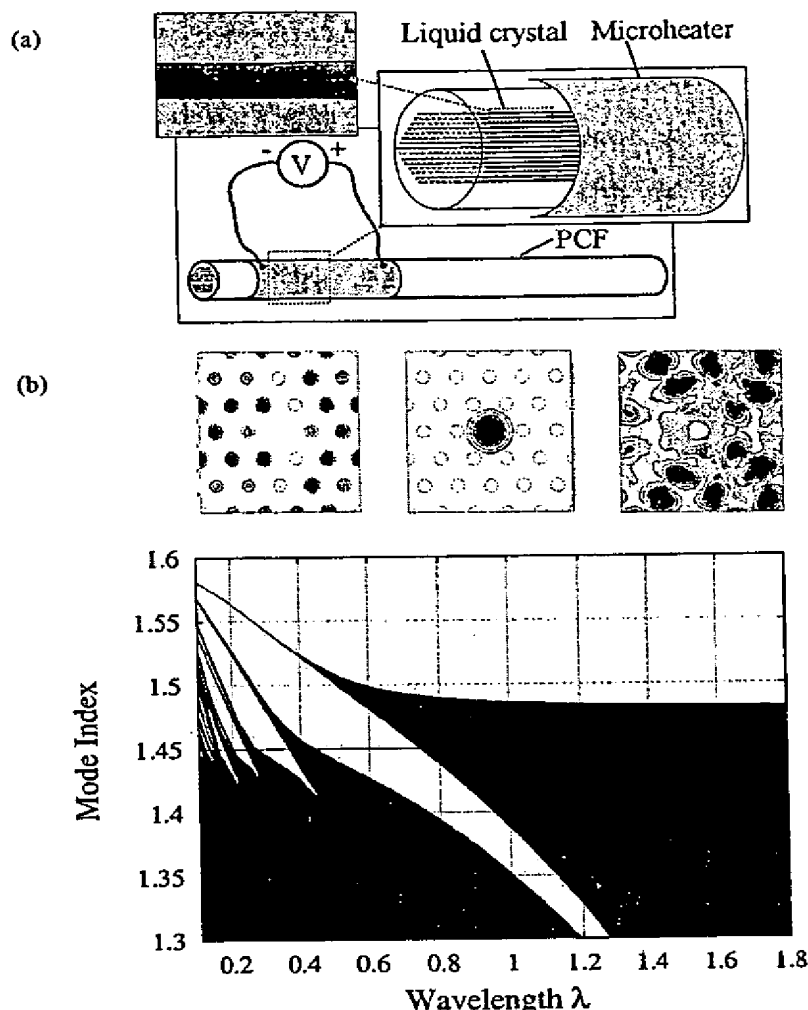


Fig. 3. (a) Device principle. The voids of a triangular structured PCF is filled with a liquid crystal and coated with a thin conducting layer, which forms a resistive microheater. Upper left inset shows a polarized micrograph of a liquid crystal inside a PCF void. (b) Mode index simulation of rod-type photonic crystal. At short wavelengths, the individual rods form isolated waveguides, for increasing wavelength the rods become resonant and finally strongly coupled waveguides. A forbidden region with mode index below the low-index background material (blue line) appears for narrow spectral ranges. These spectral ranges are utilized to guide light in the core and they are highly dependent on the exact composition of the rod material. Liquid crystals provide a very high sensitivity to the spectral location of these 'light-guide' ranges, thereby opening up the possibilities of low-voltage driven all-optical functional devices. Field distributions of a high-index cladding mode (left), a defect mode guided by the core (middle), and a low-index cladding mode (right) are shown in the top panel.

Device Characterization

Due to phase transitions, the LC shows large thermo-optical effects, whereby the photonic bandgaps of the cladding may be shifted spectrally. We found bandgap location sensitivities of 3nm/°C and 1nm/°C at infrared and visible wavelengths, respectively. However, when operating the LC around the phase transition temperatures, significantly stronger effects were observed - thereby causing large modifications of the refractive index distribution. This is demonstrated in Fig. 4, where a 20mm length of PCF is filled with a cholesteric LC (MDA-00-1445) and heated from 77°C to 94°C. The dominant bandgap changes from green to yellow, into an off state, and then to blue. The off-state is attributed to a highly scattering behavior of the LC at the phase transition, where the molecules tend to dis-align from their cholesteric phase.

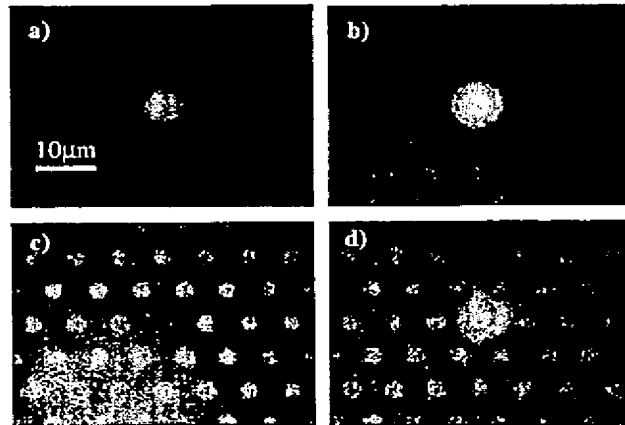


Fig. 4. Micrographs of the guided modes in a PCF filled with a short-pitch cholesteric LC.(MDA-00-1445). Well below the N^* to Isotropic phase transition temperature ($T_c=94^\circ\text{C}$), the bandgap location sensitivity is approximately 1nm/°C and 3 nm/°C in the visible and infrared region, respectively. Closer to T_c , the transmission characteristics changes more rapidly, and the color of the guided modes changes from a) green@ $T=77^\circ\text{C}$ to b) yellow@ $T=89^\circ\text{C}$ and then into an c) off state@ $T=91^\circ\text{C}$ for thereafter to change to d) blue@ $T=94^\circ\text{C}$

The experimental observation of this effect encouraged us to investigate other LC phase transitions at lower temperatures to explore the potential of low-voltage controlled fibre functionalities. For this purpose, we filled 10mm of the PCF voids with TM216 and examined the characteristics of the photonic bandgaps at the SmA^* to N^* phase transition. Figure 5(a) shows the transmission spectrum of the filled fibre, when the LC is in its SmA^* and N^* phase. In the SmA^* case there are 3 bandgaps around 670nm, 1000nm and 1600nm, with the 670nm and 1000nm bandgap having insertion loss as low as 1dB. When slightly heated to above the SmA^* phase, which only required a voltage of 5mV, all the transmission bands disappear due to a highly scattering dis-alignment of the LC in the N^* phase. Figure 5(b) shows the spectrum of a 974nm pump laser coupled to the fibre, where a 60dB extinction ratio occurs for a temperature interval of only 0.4°C. Further experiments have shown a 60dB extinction ratio, where the required temperature interval only was 0.1°C, but this was difficult to maintain due to thermal fluctuation in the laboratory.

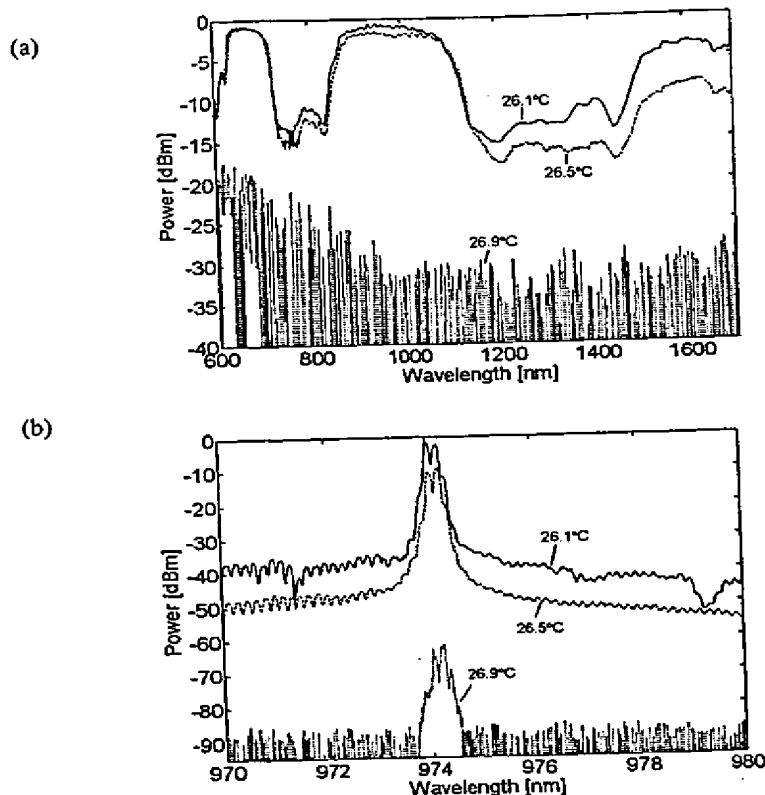


Fig. 5. (a) Transmission spectrum for a triangular structured PCF filled with a liquid crystal (TM216). Spectrum is shown for 3 temperatures around the SmA* to N* phase transition temperature: 26.1°C, 26.5°C and 26.9°C. (b) Spectrum of a 974nm pump laser beam coupled into the fiber and shows an extinction ratio of 60dB with a switching temperature difference of 0.4°C.

Conclusion

These results indicate that small, high-performance optical devices may be designed that requires a minimum of external influence to obtain tuneability, and allow for in-fibre functionalities with a minimum of insertion loss. Further, the high optical nonlinearity of LCs makes them an ideal candidate for all-optical signal processing devices and by using the self-organizing PBG effect of the LC, the possibility of designing more advanced signal processing devices may open up. Combining this with the knowledge of LCs in biological system, such as DNA and cell membranes, could open up for a new class of PBG fibre based biosensors with sub-microliter sample volume [25]. Further, it has been shown that LCs could act as an optical amplifier of protein-ligand bindings [26], which further strengthens the possibility of using liquid crystal PBG fibres as biosensors for detection of receptor binding of certain molecules, e.g., proteins.

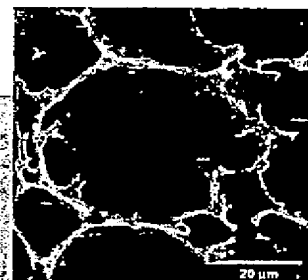
Acknowledgment

This work was supported by the NKT Academy in Denmark.

Porous Materials and Supercritical Fluids**

By Andrew I. Cooper*

Porous materials are used in a wide variety of applications, including catalysis, chemical separation, and tissue engineering. The synthesis and processing of these materials is frequently solvent intensive. In addition to reducing organic solvent emissions, supercritical fluids offer a number of specific physical, chemical, and toxicological advantages as alternative solvents for the production of functional porous materials. The figure shows an electron image of a porous polyacrylate produced by the templating of a concentrated CO₂-in-water emulsion—a process that would otherwise be highly solvent intensive.



1. Introduction

1.1. Alternative Solvents

Almost 15 billion kilograms of organic and halogenated solvents are produced worldwide each year. The use of organic solvents in manufacturing and processing on this scale represents a major ecological problem. Similarly, both the generation of polluted aqueous waste streams and the energy used to remove water from products (i.e., drying steps) make significant contributions to global environmental pollution. As such, there is a real need to consider either solvent-free processes or alternative solvents.^[1-3] In recent years, a number of research groups have proposed alternatives to conventional organic solvents or water. These include supercritical fluids (SCFs),^[4,5] ionic liquids,^[6] and fluorinated solvents.^[7,8]

This review focuses specifically on the use of SCFs for the synthesis and processing of porous materials. In particular, the aim is to highlight areas where the unique properties of SCF solvents can be exploited to generate materials that would be difficult or inconvenient to obtain by other routes. The general properties of SCFs in relation to chemical synthesis^[4] and extraction^[5] have been reviewed previously and will not be reiterated here. The specific benefits associated with SCFs in connection with porous materials will be discussed throughout.

1.2. Supercritical Fluids in Materials Chemistry

SCF solvents are being evaluated in a diverse range of materials applications,^[9,10] such as polymer synthesis,^[11-13] particle formation,^[14-16] coatings, lithography,^[1,17] dyeing,^[18] and waste management.^[19,20] All of these applications exploit at least one of the unique properties associated with SCFs. There are several specific reasons to consider SCFs as alternative solvents for the synthesis and processing of porous materials:

i) The production of porous materials is often solvent intensive—more sustainable alternatives could offer significant environmental benefits.

ii) Drying steps can be energy intensive—with the exception of water, most of the SCF solvents studied so far are gases under ambient conditions.

iii) Pore collapse can occur in certain materials (e.g., aerogels) when removing conventional liquid solvents—this can be avoided by the use of SCF solvents, which do not give rise to a liquid–vapor interface.

iv) Porous structures are important in biomedical applications (e.g., tissue engineering) where there are strict limits on the amounts of residual organic solvent that may remain in the materials—this provides a strong driving force to seek non-toxic solvent alternatives.

v) Surface modification of porous materials frequently requires the use of solvents that will wet the pore structure efficiently—SCFs (and certain liquefied gases, such as CO₂) are extremely versatile wetting agents due to their low surface tensions (e.g., liquid CO₂ will wet Teflon).

vi) Surface modification or templating of nanoporous materials presents special problems because organic solvents are often too viscous to fill such small pores. Even gaseous species (when below the critical temperature) can condense within small pores, thus forming a relatively viscous liquid “plug” that blocks the pore to further penetration. SCF solvents have much lower viscosities than organic liquids and cannot condense into the liquid state. Moreover, mass-trans-

[*] Dr. Andrew I. Cooper
Donnan and Robert Robinson Laboratories
Department of Chemistry, University of Liverpool
Crown Street, Liverpool, L69 3BX (UK)
E-mail: aicooper@liv.ac.uk

[**] The author thanks the Royal Society for provision of a Royal Society University Research Fellowship and acknowledges EPSRC for funding (GR/R15597, GR/N39999 and GR/23653). Mr. I. Hussain, Dr. K. Senoo, Dr. B. Tan, and Dr. H. Zhang are acknowledged for their help in preparing this review.

fer rates in SCF solvents tend to be high owing to low solvent viscosity.

vii) As a result of their compressed state, SCF solvents are highly suited to the generation of polymer foams. Moreover, polymer foaming requires that the material is either melted or highly plasticized—many SCF solvents are excellent plasticizing agents (while being non-solvents) for a wide range of polymers.

In many applications, more than one these considerations is important. As such, the synthesis and processing of porous materials is a particularly fertile area for SCF research. This review will summarize recent advances in the use of SCF solvents for the generation or modification of porous structures, with special attention to the points listed above.

To avoid confusion, we have restricted our use of the terms micropore, mesopore, and macropore to the definitions recommended by IUPAC,^[21] i.e., micropores < 2 nm, mesopores 2–50 nm, and macropores > 50 nm.

2. Generation of Porous Materials by Supercritical Fluid Processing

2.1. Foaming

2.1.1. Microcellular Polymer Foams

SCFs are useful for the production of expanded microcellular polymer foams, as reviewed previously.^[13] For example, "solvent-free"^[22–29] approaches have been developed whereby a polymer is saturated with supercritical carbon dioxide (scCO₂) (usually at moderately elevated temperatures), followed by rapid depressurization at constant temperature (i.e., a pressure quench as opposed to a temperature quench). This method takes advantage of the large depression in the glass-transition temperature (T_g) found for many polymers in the presence of CO₂, which means that the polymer may be kept in the liquid state at relatively low temperatures. By lowering the pressure at a fixed temperature, the amount of diluent absorbed by the polymer is decreased. Thus, T_g begins to rise, eventually to the point where the T_g for the polymer is higher

than the foaming temperature: at this point the cellular structure can grow no further and is locked in. The sudden reduction in pressure leads to the generation of nuclei due to supersaturation, and these nuclei grow to form the cellular structure until vitrification occurs.

Ultralow- k dielectric materials have been produced by foaming polyimides (e.g., Matrimid) using scCO₂.^[30] This approach allows the formation of both microcellular and bicontinuous, nanoporous structures, with dielectric constants as low as $k = 1.77$. A process was also developed for the production of porous polyetherimide monofilaments by semicontinuous solid-state foaming using a modified "pressure-cell" technique.^[31] Dense, CO₂-saturated fibers were spun at rates up to 1 ms⁻¹ with porosity being introduced at the spinning head (Fig. 1). The process was designed to allow the production of closed microcellular as well as open nanoporous filaments.

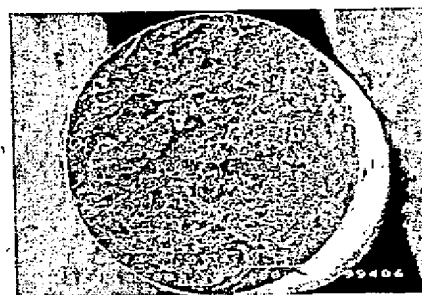


Fig. 1. Electron image of the cross-section of a foamed polyetherimide fiber, saturated for 8 h at 10 bar CO₂ saturation pressure and foamed at 180 °C for 30 s. Scale bar = 100 μ m. Reproduced with permission; copyright 2002, American Chemical Society [31].

The generation of microcellular poly(vinylidene fluoride) (PVDF) foams using scCO₂ by continuous extrusion has also been described.^[32] Both semicrystalline PVDF and blends of PVDF with polystyrene (PS) and poly(methyl methacrylate) (PMMA) were foamed using a single-screw extruder. For PVDF/PMMA blends, it was found that the cell density decreased (from 10⁸ to 10¹⁰ cell cm⁻³) and the bulk density increased (from 0.85 to 1.25 g cm⁻³) as the foaming temperature was raised from 140 to 200 °C.^[32]



Andrew Cooper obtained both B.Sc. (1991) and Ph.D. (1994) degrees in Chemistry at the University of Nottingham (UK). Upon completing his Ph.D., he was awarded an 1851 Research Fellowship which he held in the Chemistry Department at the University of North Carolina, Chapel Hill (USA) (1995–1996). He then held a Ramsay Memorial Research Fellowship in the Melville Laboratory for Polymer Synthesis, University of Cambridge (UK) (1997–1998). In 1999, he moved to the Chemistry Department at the University of Liverpool (UK) where he holds a Royal Society University Research Fellowship. He was recently awarded the Royal Society of Chemistry MacroGroup UK Young Researchers' Award (2002). His research interests include organometallic reaction mechanisms, dendrimers, supercritical fluids, polymer synthesis, porous polymers, emulsion-templated materials, and high-throughput approaches for accelerated materials discovery.

2.1.2. Biocomposite Foams

It is clearly desirable to use non-toxic solvents for the synthesis or processing of biocomposite materials (e.g., for tissue engineering).^[33,34] Carbon dioxide is an obvious choice for such applications, although SCF alkanes (e.g., ethane, propane) and certain hydrofluorocarbons (e.g., R134a)^[35] could, in principle, fulfil similar requirements from a toxicological perspective. A major challenge in this area is to incorporate biologically active guest species into polymer hosts without loss of activity. For example, there are well-documented problems in maintaining protein activity under conventional processing methods due to either the presence of an organic-aqueous interface (e.g., double-emulsion techniques), elevated temperatures (e.g., polymer melt processing), or vigorous mechanical agitation. A further challenge is to control the morphology of the composites (e.g., to generate porosity that optimizes release characteristics or allows cell infiltration into a scaffold).

SCF mixing can be used to overcome many of these limitations in a single processing step. For example, CO₂-induced plasticization has been exploited to lower the viscosity of biodegradable polymers, such as poly(D,L-lactide) (PLA), polylactide-co-polyglycolide (PLGA), and polycaprolactone, to such an extent that bioactive guests could be mixed into the polymer at temperatures close to ambient (e.g., 35 °C, 200 bar).^[36] Foaming occurred upon venting the CO₂, which introduced a high degree of porosity into the composite materials. Biocomposites were formed encapsulating enzymes (e.g., ribonuclease A, catalase, β -D-galactosidase) and it was found that the enzyme activity was retained. Adenoviral osteoprogenitor constructs were also produced by scCO₂ foaming of PLA (Fig. 2).^[37,38] The replacement of bone tissue is a major clinical and socioeconomic need, and again the avoidance of organic solvent residues is appealing.

Microporous PLGA foams containing encapsulated proteins (e.g., basic fibroblast growth factor) have also been prepared by SCF processing of water-in-oil (W/O) emulsions.^[39]



Fig. 2. Demonstration of sub-cutaneous new bone formation using human osteoprogenitor cells seeded onto a porous SCF-processed poly(lactic acid) scaffold, adsorbed with a bone growth factor (osteoblast stimulating factor-1) in MF1 nude mice. Note the extensive new woven bone formation (dark areas in image) as confirmed using birefringence microscopy demonstrating organized collagen and matrix formation. Scale bar = 1 μ m. Reproduced with permission; copyright 2003; American Society for Bone and Mineral Research [38].

In this process, an aqueous protein phase was emulsified in a concentrated solution of PLGA in methylene chloride followed by SCF extraction of the organic solvent and subsequent SCF foaming. Residual methylene chloride levels in the foams were found to be higher than the 600 μ g g⁻¹ limit established by the US Pharmacopoeia, although it was suggested that these levels could be reduced by longer periods of SCF extraction,^[39,40] or by prolonged vacuum drying.^[39] The synthesis of PLGA by ring-opening precipitation copolymerization of lactide and glycolide monomers in scCO₂ using stannous octoate as the initiator was also reported.^[41] Relatively low molecular weight PLGA (M_w ~3500 g mol⁻¹) was produced and the material could be recovered as an expanded porous foam after depressurization.

2.2. Crystallization of SCF-Swollen Crosslinked Polymers (CSX)

An alternative process for the generation of porous polymer structures is crystallization of swollen, crosslinked polymers, or "CSX".^[42] Candidate materials for this process require i) a crystallizable block in the polymer; ii) chemical crosslinking between the polymer chains; and (iii) the possibility of swelling by an appropriate fluid. In the CSX process (Fig. 3), a preshaped, crosslinked polymer is heated above the crystal melting temperature (point 2) before a SCF solvent is added in order to transform the polymer into the swollen gel

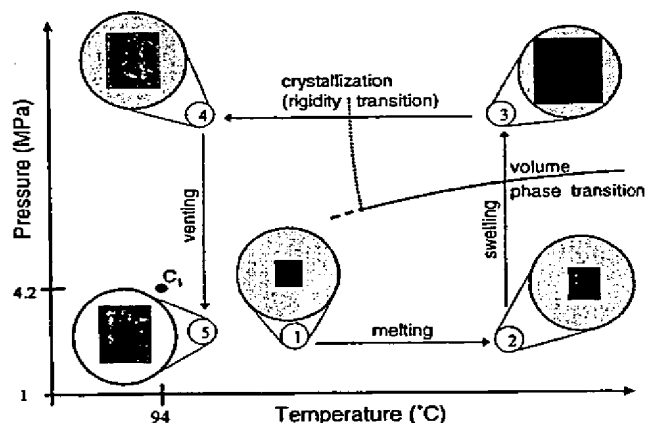


Fig. 3. Schematic pressure-temperature (P - T) diagram of the CSX process for generating porous structures through an intermediate gel state. The critical point (T_c , P_c) is denoted by " C_1 ". The various states are as follows: 1) initial polymer specimen; 2) amorphous network; 3) swollen gel; 4) bicontinuous structure of polymer and SCF; 5) porous polymer structure after venting of SCF. Reproduced with permission; copyright 2002, American Chemical Society [42].

state (point 3). Subsequent crystallization leads to the development of two continuous phases: a solid polymer-rich phase intertwined with a fluid phase (point 4). After removal of the fluid, a bicontinuous pore structure remains (point 5). It should be noted that this process is *not* a foaming process since the swollen CSX gel consists mostly of swelling fluid,

which does not expand or contract significantly during pore formation. This technique has been used to process linear low-density polyethylene (LLDPE) with a gel content of 15.9% using supercritical propane to give materials with pore diameters in the range 10 nm–10 μm and void volumes of more than 80% (Fig. 4).^[42] The resulting pore structure was ultraclean, and preliminary results suggested that the materials were ready for biomedical applications (e.g., the culture of HEPG2 liver cells) without any further purification.

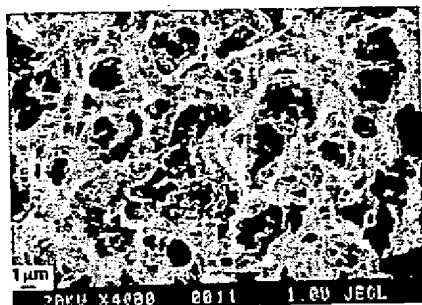


Fig. 4. Electron image of porous radiation crosslinked LLDPE (15.9% gel content), produce by the CSX process outlined in Figure 3. Void volume = 83%. Scale bar = 100 μm . Reproduced with permission; copyright 2002, American Chemical Society [42].

A different strategy is to crystallize polymer materials from *homogeneous* SCF solutions, although this may be somewhat limited in scope by solubility considerations.^[43,44] An example of this approach is the production of mesoporous open-cell foams (surface area = 120–150 $\text{m}^2 \text{g}^{-1}$) by crystallization of isotactic polypropylene from homogeneous solution in supercritical propane.^[45]

2.3. SCF Antisolvent-Induced Phase Separation

Since scCO_2 is such a poor solvent for common, organic hydrocarbon polymers,^[44] it has broad potential as an antisolvent for the preparation of porous polymeric materials. Porous PS^[46] (Fig. 5) and cellulose acetate^[47] membranes were formed by precipitation from a suitable organic solvent.

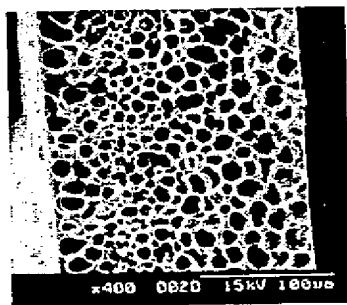


Fig. 5. Porous PS membrane produced by wet phase inversion from toluene using scCO_2 as the antisolvent (25 $^\circ\text{C}$, 20 wt.-% polymer solution in toluene, $M_w = 280\,000 \text{ g mol}^{-1}$). Reproduced with permission; copyright 2001, Elsevier Science [46].

The membranes were prepared by a wet phase-inversion method, in which a homogeneous polymer solution is immersed in a non-solvent bath (in this case containing scCO_2). The approach is analogous to methods used to produce polymer particles (e.g., precipitation with a compressed fluid antisolvent or “PCA”) except that the two solvents are mixed much more slowly. (In PCA, the organic polymer solution is typically sprayed rapidly into the antisolvent in order to produce particles, see Sec. 2.5 below.) As in the case of the CSX process,^[42] the porosity in the membranes was not generated by foaming; turbidity was observed in the solutions after addition the scCO_2 and little change was observed during depressurization, suggesting that the porous structures were formed by antisolvent-induced phase separation rather than by physical expansion.^[46]

2.4. Non-Reactive Gelation of SCF Solutions Using Organogelators

The formation of low-density porous materials with nanoscopic features by using low molecular mass organic gelators (LMOGs) is currently a subject of considerable interest.^[48] Materials produced by this route are often highly fragile and subject to structural collapse during drying because of capillary forces. As such, SCF solvents offer a distinct advantage for the synthesis and processing of these materials, for the same reasons that SCFs are used to dry silica aerogels.^[49,50] Low-density microcellular fluorinated materials were generated by a one-step process which uses scCO_2 and requires no organic solvents.^[51,52] Highly fluorinated, low molar mass compounds^[51,52] and polymers^[52] were synthesized which dissolve in scCO_2 and then associate to form gels. Upon removal of the CO_2 phase, the gels produced free-standing foams with average cell diameters smaller than 1 μm and density reductions of 97% relative to the parent compound (Fig. 6). This technique combines gelation and foaming in one process. It is likely that less expensive, non-fluorinated gelators (e.g., based on peracetylated sugar derivatives^[53]) could be developed in the future for similar applications.

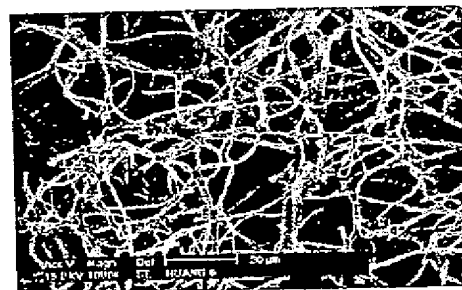


Fig. 6. SEM image of a free-standing foam produced from a CO_2 -soluble tri-functional urea by gelation of a 5 wt.-% solution in scCO_2 (scale bar = 20 μm). Bulk density of the foam is approximately 0.09 g cm^{-3} . Reproduced with permission; copyright 1999, the American Association for the Advancement of Science [51].

Similarly, LMOG aerogels have been produced from 2,3-dicyloxyanthracene, both by SCF drying of gels formed in ethanol, and by direct gelation of scCO_2 without the use of any organic solvents.^[54]

2.5. Porous Particle Formation

The preparation of micrometer-sized particles using SCFs is particularly useful for the processing of pharmaceutical formulations.^[55] Broadly speaking, there are two main strategies to achieve this; rapid expansion of supercritical solutions^[14,56,57] (where the material must be soluble in the fluid) and antisolvent precipitation^[15,58,59] (where the material should be insoluble). Antisolvent precipitation has potential for generating porous microparticles from a wide variety of substrates, particularly since it does not require that the starting material is soluble in the SCF solvent (see also discussion on membranes,^[46,47] Sec. 2.3).

Porous PS microspheres and microballoons (hollow microspheres) were produced by spraying a toluene solution of PS through a capillary into CO_2 vapor to form droplets, which then fell into liquid CO_2 where they were rapidly dried and vitrified.^[60] Both the thickness and porosity of the microcellular shells could be controlled by changing the initial solution composition. The cell sizes and surface areas of the microspheres were approximately 1–20 μm and 3–40 $\text{m}^2 \text{g}^{-1}$, respectively.

A non-steroidal drug, $\text{Cu}_2(\text{indomethacin})_4\text{L}_2$ [L = dimethylformamide (DMF)] was formulated into micrometer-sized particles using both gas antisolvent (GAS) techniques and aerosol extraction systems (ASES).^[61] In both cases, DMF was used as the solvent and CO_2 as the antisolvent. Under certain conditions, the material processed by ASES could be isolated as large (> 50 μm), porous spheres.

The main requirement for these processes is that the solvent and the SCF antisolvent are miscible. While the approach is therefore quite general, a disadvantage is that the use of organic solvents is not avoided.

3. Chemical Synthesis of Porous Materials Using Supercritical Fluids

3.1. Chemical Gelation of SCF Solutions

The use of SCF solvents to avoid pore collapse during drying of inorganic, organic, and organic-inorganic hybrid aerogels,^[51] and other nanoscale porous materials such as semiconductors,^[62] has been reviewed by others and will not be discussed in detail here. In the supercritical state there is no liquid-vapor interface so capillary stresses are suppressed, although other stresses can occur because of differential strain between the SCF in the pores and the porous matrix.^[62] More recently, the same advantages have been exploited to allow the preservation of high-aspect-ratio, nanometer-sized fea-

tures in microlithography using scCO_2 as the developing solvent (Fig. 7).^[1]

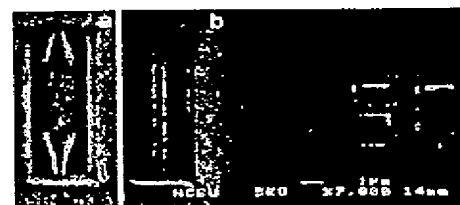


Fig. 7. Electron images of 150 nm microlithographic features (6:1 aspect ratio) developed by a) aqueous-based development and b) scCO_2 -based development using appropriate adjuncts. The use of a SCF solvent for pattern development avoids feature collapse, in a similar way that pore collapse is avoided in the SCF drying of aerogels. Scale bar = 1 μm . Provided by Micell Technologies and reproduced with permission [1].

In addition to the use of SCF solvents for the controlled drying of preformed porous materials, researchers have exploited SCF solvents as media for the in-situ preparation of porous materials by chemical reaction (i.e., direct chemical gelation of SCF solutions). The primary advantages of this approach are that separation is simple and that it is possible to avoid the use of large volumes of organic solvents, both in the synthesis step itself and by eliminating further solvent usage during sample purification.

3.1.1. Sol-Gel Polymerization of Alkoxysilanes in SCFs

Aerogels have been synthesized by sol-gel polymerization of alkoxysilanes in scCO_2 .^[50] Instead of forming gels in alcohol solvents before exchanging the alcohol for CO_2 , scCO_2 was used directly as the sol-gel polymerization solvent. Standard sol-gel formulations require large quantities of water (typically 2–3 equivalents) for the hydrolysis and condensation of the alkoxysilane monomers.^[51] Alcohols are good solvents for these processes because they are capable of dissolving both water and non-polar alkoxysilane monomers. Since the solubility of water in CO_2 is very low, an alternative water-free method was used.^[50] Alkoxysilanes such as tetramethoxysilane or 1,4-bis(triethoxysilyl) benzene were polymerized at 35–45 $^{\circ}\text{C}$ in scCO_2 (410 bar) in the presence of 13–36 wt.-% formic acid. Gelation occurred within 12 h and the gel was aged for a further 12–18 h. At the end of the reaction, the CO_2 pressure was released to yield silica aerogels in almost 100 % yield to give materials with surface areas in the range 250–600 $\text{m}^2 \text{g}^{-1}$.

3.1.2. Free-Radical Polymerization using scCO_2 as a "Pressure-Adjustable" Porogen

We have investigated the formation of permanently porous crosslinked poly(acrylate) and poly(methacrylate) monoliths using scCO_2 as the porogenic solvent.^[63,64] Materials of this type^[65,66] are useful in applications such as high-performance liquid chromatography, high-performance membrane chroma-

tography, capillary electrochromatography, microfluidics,^[67] molecular imprinting,^[68] and high-throughput bioreactors.^[69] In our process, no organic solvents are used, either in synthesis or in purification. It is possible to synthesize the monoliths in a variety of containment vessels, including chromatography columns and narrow-bore capillary tubing. Moreover, we have exploited the variable density associated with SCF solvents in order to "fine-tune" the polymer morphology. Figure 8 shows the variation in the Brunauer-Emmett-Teller (BET) surface area for a series of crosslinked poly(trimethyl-

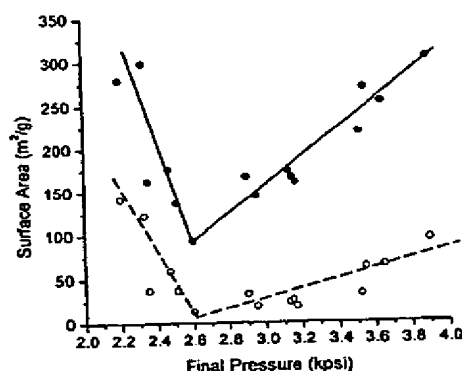


Fig. 8. Variation in BET surface area (●) and micropore surface area (○) as a function of reaction pressure for a series of porous poly(trimethylolpropane trimethacrylate) monoliths synthesized using scCO_2 as the porogen. The variable density associated with SCF solvents can be used to "fine-tune" porous structures. Reproduced with permission; copyright 2002, American Chemical Society [70a].

olpropane trimethacrylate) monoliths synthesized using scCO_2 as the porogen over a range of reaction pressures.^[70] The average pore size and surface area in these materials could be tuned continuously over a considerable range (BET surface area = 90–320 $\text{m}^2 \text{g}^{-1}$) just by varying the SCF solvent density. It is interesting to note that a minimum in surface area (and a maximum in the average pore diameter, not shown) was observed at a reaction pressure of around 2600 psi (–18 MPa). This can be rationalized by considering the variation in solvent quality as a function of CO_2 density and the resulting influence on the mechanism of nucleation, phase separation, aggregation, monomer partitioning, and pore formation.^[71] We have also applied the same concept to the synthesis of well-defined porous, crosslinked poly(methacrylate) beads (diameters = 100–200 μm) by suspension polymerization, again without the use of any organic solvents (Fig. 9).^[72] The surface area of the beads could be tuned over a wide range (5–500 $\text{m}^2 \text{g}^{-1}$) by varying the CO_2 density. Both of these techniques demonstrate how the variable density associated with SCF solvents can be exploited to precisely control the structure of porous materials produced by reaction-induced phase separation.

3.2. Templating of Supercritical Fluid Emulsions

Emulsion templating is useful for the synthesis of highly porous inorganic^[73–76] and organic materials.^[77–79] In principle, it

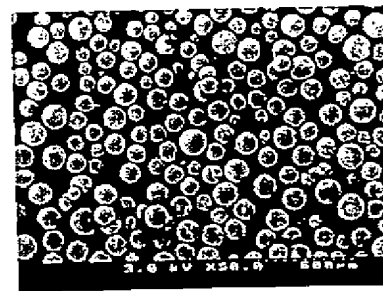


Fig. 9. Macroporous polymer beads synthesized by suspension polymerization using scCO_2 as the porogen (scale bar = 600 μm). Reaction pressure = 300 bar. Average pore size = 100 nm. BET surface area = 253 $\text{m}^2 \text{g}^{-1}$. Average bead diameter = 130 μm . Reproduced with permission; copyright 2001, American Chemical Society [72].

is possible to access a wide range of porous hydrophilic materials by reaction-induced phase separation (i.e., chemical "locking") of concentrated oil-in-water (O/W) emulsions. In practice, a significant drawback to this approach is that large quantities of a water-immiscible oil or organic solvent are required as the internal phase (typically > 80 vol.-%). Moreover, it may be difficult to remove this oil phase from the templated material after the reaction. Inspired by studies on SCF emulsion formation and stability,^[80] we have developed methods for templating high internal phase CO_2 -in-water (C/W) emulsions to generate highly porous materials in the absence of any organic solvents—only water and CO_2 are used.^[81] Providing that the emulsions are sufficiently stable (which depends strongly on the surfactant system), it is possible to generate low-density materials (–0.1 g cm^{-3}) with relatively large pore volumes (up to 6 $\text{cm}^3 \text{g}^{-1}$) from water-soluble vinyl monomers such as acrylamide and hydroxyethyl acrylate. Figure 10 shows a crosslinked polyacrylamide material synthesized from a high internal phase C/W emulsion, as characterized by scanning electron microscopy (SEM) and confocal microscopy (scale = 230 × 230 μm). Comparison of the two images illustrates quite clearly how the porous structure shown in the SEM image is templated from the C/W emulsion (as represented by the confocal microscopy image of the pores). In general, the confocal image gives a better measure of the CO_2 emulsion droplet size and size distribution immediately before gelation of the aqueous phase. From analysis of the confocal images, cell densities in the materials were found to be in the range 0.5×10^8 – $5 \times 10^8 \text{ cells cm}^{-3}$. Initially, we used low molecular weight (M_w = 550 g mol^{-1}) perfluoropolyether ammonium carboxylate surfactants to stabilize the C/W emulsions,^[81] but a significant practical disadvantage is that this surfactant is expensive and non-degradable. We have subsequently shown that it is possible to use inexpensive hydrocarbon surfactants to stabilize the C/W emulsions and that these emulsions can also be templated to yield low-density porous materials.

3.3. Nanoscale Casting

A wide variety of nanoporous structures can be formed by templating both natural and synthetic materials.^[82–86] The

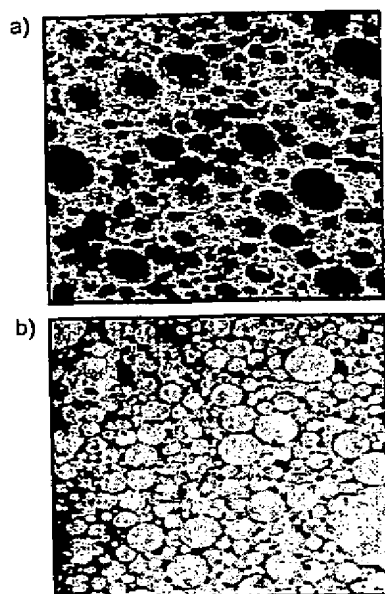


Fig. 10. Emulsion-templated crosslinked polyacrylamide materials synthesized by polymerization of a high internal phase CO_2 -in-water emulsion (C/W HIPE). a) SEM image of sectioned material. b) Confocal image of same material, obtained by filling the pore structure with a solution of a fluorescent dye. As such, (a) shows the "walls" of the material while (b) shows the "holes" formed by templating the scCO_2 emulsion droplets. Both images = $230 \times 230 \mu\text{m}$. Ratio of CO_2 /aqueous phase = 80/20 v/v. Pore volume = $3.9 \text{ cm}^3 \text{ g}^{-1}$. Average pore diameter = $3.9 \mu\text{m}$. Adapted from Butler et al. [81].

viscosities and surface tensions associated with conventional liquid solvents and reagents may prohibit the replication of very small features. Even gaseous reagents, when used below the critical temperature, may capillary condense into the liquid phase within nanometer and sub-nanometer-sized pores. As such, SCF solvents possess specific advantages for templating structures on the nanometer scale since they have low viscosity, high diffusivities, and never condense into the liquid phase. A number of porous inorganic materials have been prepared by the process of "nanoscale casting using SCFs" (Fig. 11).^[87–92] In this technique, low molecular weight precursors such as tetraethyl orthosilicate (TEOS),^[87,90] platinum



Fig. 11. Electron image of porous titania sample produced by nanoscale casting using supercritical fluids. An activated carbon cloth was treated with a solution of titanium isopropoxide in CO_2 and the carbon template was then removed by calcining in air at 873 K (scale bar = $100 \mu\text{m}$). This method can be used to replicate features on the macro-, meso-, and microscopic length scales. Reproduced with permission; copyright 2001, Elsevier Science [91].

acetylacetonate $[\text{Pt}(\text{acac})_2]$,^[88] titanium isopropoxide $[\text{Ti}(\text{O}i\text{-Pr})_4]$,^[91,92] and aluminium acetylacetonate $[\text{Al}(\text{acac})_3]$ ^[91] were dissolved in scCO_2 and contacted with porous template materials such as activated carbon^[87–92] and palm nutshell.^[89] After treatment in the SCF, the samples were recovered and the template material was removed by calcination or oxygen plasma treatment. Using this method, it was possible to produce templated nanoporous platinum,^[88,89] silica,^[87,89,90] titania,^[89,91,92] and alumina materials.^[91] In the case of silica, it was shown that the samples prepared using solutions of TEOS in scCO_2 had much higher surface areas ($900\text{--}1400 \text{ m}^2 \text{ g}^{-1}$) than samples which were produced by immersion in neat liquid TEOS ($440\text{--}540 \text{ m}^2 \text{ g}^{-1}$).^[87,89,90] Nitrogen adsorption-desorption isotherms for the materials formed by immersion in neat TEOS did not exhibit a manifested step corresponding to the existence of micropores or mesopores.^[89] It was assumed that silica only covered the entrances of the mesopores and micropores in the activated carbon template because of the high viscosity of the neat precursor medium. By contrast, the SCF-assisted approach led to silica penetration of the smallest pores in the activated carbon template.

4. Modification of Porous Materials Using Supercritical Fluids

In addition to generating porous structures by processing and chemical synthesis (Sects. 2,3), it is also possible to modify preformed porous materials using SCFs.

4.1. Chemical Deposition within Porous Substrates

Several groups have investigated the reactive deposition of metals, polymers, and other materials in order to modify the properties of porous substrates by using SCFs. Potential advantages include rapid mass transfer, easy separations, and the ability to fill even small mesopores and micropores.

4.1.1. Deposition of Metal Nanoparticles in Porous Materials

There are a number of reports of the synthesis^[93–95] or purification^[96,97] of metal nanoparticles using SCF solvents. Recent results suggest that this is an area where fine control over solvent properties (e.g., by varying solvent density) may offer distinct advantages. For example, silver and gold nanocrystals, sterically stabilized with dodecanethiol ligands, were dispersed in supercritical ethane.^[96] Since the van der Waals attraction between the nanocrystal cores increases significantly with size, an increase in ethane density and thus solvent strength was found to disperse larger nanocrystals with size selectivity. A reduction in ethane density precipitated the nanocrystals, again with size selectivity. This suggests that SCF solvents may be useful for size separation of metal nanoparticles, which is important in a number of emerging technologies.^[96,97]

Metal nanoparticles have been synthesized *in situ* within non-porous, SCF-swollen polymer substrates (e.g., poly(4-methyl-1-pentene), polytetrafluoroethylene, polyethylene).^[98,99] This approach takes advantage of plasticization and swelling effects associated with SCF solvents. It is also possible to synthesize metal nanoparticles within permanently porous structures,^[100,101] thereby exploiting wetting behavior, pore filling, and low viscosity. For example, silver nanoparticles have been introduced into the pore structure of porous crosslinked PS beads and silica aerogels by *scCO*₂-assisted impregnation of silver coordination complexes followed by depressurization and subsequent addition of H₂ (1000 psi (~6.9 MPa), 60 °C, 24 h) in order to reduce the complexes to metallic silver.^[100] Mass increases of 2–10 % were observed, and mean particle diameters were found to be in the range 20–40 nm.

4.1.2. Chemical Fluid Deposition of Thin Metal Films in Porous Supports

Thin metal films are important for a wide variety of applications involving optics, microelectronics, sensors, membranes, and catalysis. Micrometer-thick metal films do not have the mechanical integrity to be freestanding and must be supported in some manner. In an extension of studies involving the chemical fluid deposition (CFD) of thin metal films on surfaces,^[102–104] thin palladium films have been formed within porous alumina disks by *in-situ* H₂ reduction of CO₂-soluble organopalladium compounds.^[105] The film position in the disks was controlled by adjusting the relative concentrations of H₂ and the palladium precursor (π -2-methylallyl(cyclopentadienyl)palladium or palladium hexafluoroacetylacetonate) on opposite sides of the alumina substrate (see Fig. 12). Palladium films between 2 and 80 μ m thick were deposited at prescribed depths between 80 and 600 μ m, as measured from the metal precursor side. The deposition of supported thin metal films *within* the bulk of a porous substrate (rather than on the surface) has certain advantages (e.g., the film is protected from abrasion and is less likely to suffer from adhesion problems). Hydrogen has low solubility in most organic solvents but is highly soluble in *scCO*₂,^[106,107] thus facilitating the reduction step. This process genuinely exploits the gas-liquid “hybrid” properties of *scCO*₂: it is solution-based (therefore, eliminating precursor volatility constraints) while retaining most of the rapid transport properties and conformal coverages associated with chemical vapour deposition. A potential restriction for CFD is that the reduction chemistry must proceed readily at low temperatures.^[102–104]

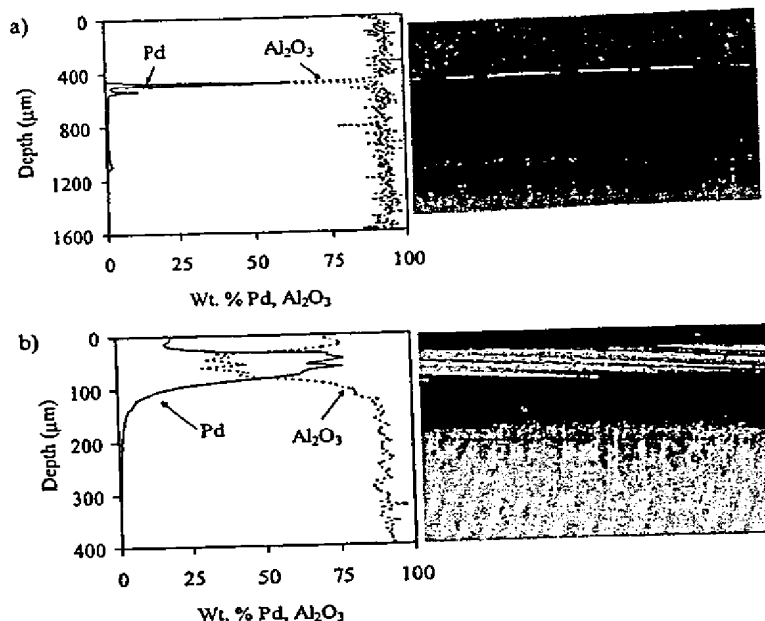


Fig. 12. Electron probe microanalysis (EPMA, left) and optical microscopy cross-section analysis (right) of palladium films deposited within porous α -alumina disks by reduction of a CO₂-soluble precursors in *scCO*₂ solution. a) Precursor = CpPd(π -C₄H₇), 0.53 wt.-% in CO₂, 0.47 wt.-% H₂ in CO₂. b) Precursor = CpPd(hfac) (hfac = hexafluoro acetylacetonate), 0.76 wt.-% in CO₂, 0.61 wt.-% H₂ in CO₂. Note that the more concentrated precursor solution gives rise to a thicker Pd film. The position of the film can be controlled by varying the relative concentrations of precursor and H₂. Reproduced with permission; copyright 2001, American Chemical Society [105].

4.1.3. Supercritical Fluid-Mediated Metallization of Mesoporous Silica

Mesoporous aluminosilicates are important as solid acids and ion exchangers.^[108] A key requirement in these applications is hydrothermal stability. Postsynthesis aluminization offers potential advantages over directly synthesized materials with respect to accessibility of active Al sites and structural ordering, but there are difficulties to be overcome in obtaining a uniform distribution of Al throughout the host silica. This arises from the fact that the Al is first contacted with the outer surface of the host silica during grafting before being transported into the internal pore structure, or bulk. The low viscosity and high diffusivity inherent to SCFs are ideally suited to rapid transport of reagent species into mesoporous substrates. For example, MCM-41 silica materials have been aluminized by reaction with aluminium isopropoxide using either *scCO*₂ or supercritical propane as the solvent (reaction temperature = 40 °C for CO₂, 110 °C for propane).^[109] The samples were then calcined at 600 °C for 4 h to obtain the Al-grafted materials.^[27] Al magic-angle spinning (MAS) NMR spectroscopy indicated that ca. 40 % of the Al in the dry samples was tetrahedrally coordinated, increasing to at least 60 %

after calcination. The samples showed very high stability after steaming at 900 °C for 4 h, with both samples retaining 80–85 % of their surface area and pore volume, and 80 % of their acid content. To investigate whether or not there was any specific advantage of using the solvents in the supercritical state, an Al-grafted material was synthesized under the equivalent conditions but using liquefied propane instead of SCF propane.^[109] This material was found to have lower hydrothermal stability, suggesting that the SCF route led to better dispersion of the Al, a change in the way that the Al interacts with the host silica surface, or a combination of both.

4.1.4. Growth of Dimensionally Ordered Nanowires within Mesoporous Silica

Nanoscale structures of semiconductor wires are expected to play a role as materials in emerging technologies because of their unique optical, electrical, and mechanical properties.^[110,111] Alkanethiol-coated gold nanocrystals (2.5 nm diameter) have been used as uniform seeds for the growth of defect-free silicon nanowires from SCF solution.^[112] It was found that the orientation of the nanowires could be controlled by varying the reaction pressure, once again taking advantage of the variable density associated with SCFs. More recently, semiconductor silicon nanowires have been synthesized within the pores of surfactant-templated mesoporous silica using scCO_2 as the solvent.^[113,114] Diphenyl silane was degraded within the pore structure at 500 °C to create silicon nanowires. The low viscosity of the SCF phase enabled rapid diffusion of the reactant precursor into the mesoporous structure. Discrete transitions in the UV-vis absorption spectrum suggested quantum confinement effects.^[114]

4.1.5. Synthesis of Conducting Polymer Foams

The polymerization of monomers within non-porous SCF-swollen polymer hosts to form polymer blends has been described for a number of monomer-polymer combinations.^[115–119] Related techniques have been applied to the formation of porous composite materials such as foams. For example, conducting polypyrrole-polyurethane composite foams have been formed by SCF impregnation of polyurethane substrates with an oxidant, $\text{Fe}(\text{CF}_3\text{SO}_3)_3$, followed by exposure to pyrrole vapor.^[120–122] The in-situ precipitation polymerization of pyrrole in scCO_2 and in supercritical fluoroform has also been reported.^[123]

4.1.6. Porous Coordination-Polymer Crystals

Very recently, Kitaura et al. reported the synthesis of copper-based coordination polymers that show fascinating adsorption behavior for “supercritical gases” such as CO_2 , CH_4 , O_2 , and N_2 .^[124] In particular, these materials exhibit “gate-opening” and “gate-closing” pressures (i.e., the micro-

porous structure is pressure-responsive). Because of the relatively flexible nature of these materials, the channels can open and close reversibly with pressure. Hysteretic adsorption is observed because the gas molecules stabilize the porous phase. In principle, SCF solvents such as scCO_2 could be versatile media for the structural modification of microporous coordination polymers, although solubility considerations (e.g., the relative insolubility of most metal salts and complexes) may restrict the types of reactions that are readily achieved.

4.2. Surface Treatment Porous Materials with Low Surface Energy Coatings

The protection of historical buildings and other structures made of stone can be achieved by coating with perfluoropolyethers. These polymers are water repellent and stable to corrosive acids, high temperatures, UV radiation, and oxidizing agents. The materials are also transparent and colorless, thus maintaining the appearance of natural stone. A practical drawback is that these materials are not soluble in common organic solvents. By contrast, perfluoropolyethers are readily soluble in chlorinated fluorocarbons (CFCs) and in CO_2 .^[125] Perfluorinated polyether coatings have been applied onto surfaces of marble, sandstone, and limestone by spraying from solutions in scCO_2 .^[126] The penetration depth of the fluorinated coating was found to strongly depend on the mean size and porosity of the stones. These results suggest that CO_2 could be used for the application of weather-proof fluorinated coatings for which there are no other viable, environmentally acceptable alternatives.

5. Conclusions

This review has shown that there are a number of specific benefits that can be derived from the use of SCFs for the synthesis and modification of porous materials. SCFs are useful for the production of microcellular foams, both by expansion and by using crystallization or antisolvent phase-separation routes. In the case of biocomposite foams, the introduction of toxic solvent residues into the final product can be avoided. For materials that possess nanoscale pores or features (e.g., aerogels, LMOG foams, nanolithographic images), supercritical drying can avoid feature collapse due to the lack of capillary forces. Likewise, templating of nanoscale features and surface modification of nanoscale porous structures using SCFs holds promise because these solvents penetrate small pores more effectively than liquid solvents. Direct gelation of SCFs and templating of SCF emulsions are two new routes to produce low density porous materials. In the case of chemical gelation of SCF solutions, the variable density associated with SCFs can be used to fine-tune the resultant pore structure. Lastly, all of these processes offer the potential of reducing organic solvent usage in the production of porous materials and

composites. This is particularly important for processes that currently use large volumes of organic solvents (e.g., O/W emulsions, organic sol-gel routes, suspension polymerization, etc.). SCF routes to porous materials that exploit more than one of these specific advantages are likely to be profitable subjects for future research.

Received: January 8, 2003
Final version: April 16, 2003

- [1] J. M. Desimone, *Science* 2002, 297, 799.
- [2] M. Poliakoff, J. M. Fitzpatrick, T. R. Farren, P. T. Anastas, *Science* 2002, 297, 807.
- [3] E. J. Beckman, *Environ. Sci. Tech.* 2002, 36, 347A.
- [4] P. G. Jessop, W. Leitner, *Chemical Synthesis Using Supercritical Fluids*, Wiley-VCH, Weinheim, Germany 1999.
- [5] M. A. McHugh, V. J. Krukons, *Supercritical Fluid Extraction*, 2nd ed., Butterworth-Heinemann, Stoneham, MA 1994.
- [6] M. J. Earle, K. R. Seddon, *ACS Symp. Ser.* 2002, 819, 10.
- [7] L. P. Barthel-Rosa, J. A. Gladysz, *Coord. Chem. Rev.* 1999, 192, 587.
- [8] E. de Wolf, G. van Koten, B. J. Deelman, *Chem. Soc. Rev.* 1999, 28, 37.
- [9] A. I. Cooper, *Adv. Mater.* 2001, 13, 1111.
- [10] C. A. Eckert, B. L. Knutson, P. G. Debenedetti, *Nature* 1996, 383, 313.
- [11] J. M. DeSimone, Z. Guan, C. S. Elsbernd, *Science* 1992, 257, 945.
- [12] J. L. Kendall, D. A. Canelas, J. L. Young, J. M. DeSimone, *Chem. Rev.* 1999, 99, 543.
- [13] A. I. Cooper, *J. Mater. Chem.* 2000, 10, 207.
- [14] P. G. Debenedetti, J. W. Tom, X. Kwauk, S.-D. Yeo, *Fluid Phase Equilib.* 1993, 82, 311.
- [15] E. Reverchon, *J. Supercrit. Fluids* 1999, 15, 1.
- [16] P. G. Shah, J. D. Holmes, R. C. Doty, K. P. Johnston, B. A. Korgel, *J. Am. Chem. Soc.* 2000, 122, 4245.
- [17] C. K. Ober, A. H. Gabor, P. Gallagher-Wetmore, R. D. Allen, *Adv. Mater.* 1997, 9, 1039.
- [18] S. G. Kazarian, *Macromol. Symp.* 2002, 184, 215.
- [19] S. Yesodharan, *Curr. Sci.* 2002, 82, 1112.
- [20] J. Abeln, M. Kluth, G. Petrich, H. Schmieder, *High Press. Res.* 2001, 20, 537.
- [21] K. S. W. Sing, D. H. Everett, R. A. W. Haul, L. Moscou, R. A. Pierotti, J. Rouquerol, T. Siemieniowska, *Pure Appl. Chem.* 1985, 57, 603.
- [22] S. K. Goel, E. J. Beckman, *Polymer* 1993, 34, 1410.
- [23] S. K. Goel, E. J. Beckman, *Polym. Eng. Sci.* 1994, 34, 1137.
- [24] K. L. Parks, E. J. Beckman, *Polym. Eng. Sci.* 1996, 36, 2404.
- [25] K. L. Parks, E. J. Beckman, *Polym. Eng. Sci.* 1996, 36, 2417.
- [26] K. A. Arora, A. J. Lesser, T. J. McCarthy, *Macromolecules* 1998, 31, 4614.
- [27] K. A. Arora, A. J. Lesser, T. J. McCarthy, *Polym. Eng. Sci.* 1998, 38, 2055.
- [28] K. N. Lee, Y. J. Suh, H. J. Lee, J. H. Kim, *Polymer (Korea)* 1999, 23, 181.
- [29] P. H. Nam, P. Maiu, M. Okamoto, T. Kotaka, T. Nakayama, M. Takada, M. Ohshima, A. Usuki, N. Hasegawa, H. Okamoto, *Polym. Eng. Sci.* 2002, 42, 1907.
- [30] B. Krause, G. H. Koops, N. F. A. van der Vegt, M. Wessling, M. Wubbenhorst, J. van Turnhout, *Adv. Mater.* 2002, 14, 1041.
- [31] B. Krause, M. Kloth, N. F. A. van der Vegt, M. Wessling, *Ind. Eng. Chem. Res.* 2002, 41, 1195.
- [32] S. Siripurapu, Y. J. Gay, J. R. Royer, J. M. DeSimone, R. J. Spontak, S. A. Khan, *Polymer* 2002, 43, 5511.
- [33] R. Langer, J. P. Vacanti, *Science* 1993, 260, 920.
- [34] M. J. Whitaker, R. A. Quirk, S. M. Howdle, K. M. Shakesheff, *J. Pharm. Pharmacol.* 2001, 53, 1427.
- [35] C. D. Wood, K. Senoo, C. Martin, J. Cuellar, A. I. Cooper, *Macromolecules* 2002, 35, 6743.
- [36] S. M. Howdle, M. S. Watson, M. J. Whitaker, V. K. Popov, M. C. Davies, F. S. Mandel, J. D. Wang, K. M. Shakesheff, *Chem. Commun.* 2001, 109.
- [37] X. B. Yang, H. I. Roach, N. M. P. Clarke, S. M. Howdle, R. A. Quirk, K. M. Shakesheff, R. O. C. Oreffo, *Bone* 2001, 29, 523.
- [38] X. Yang, R. S. Tare, K. A. Partridge, H. I. Roach, N. M. P. Clarke, S. M. Howdle, K. M. Shakesheff, R. O. C. Oreffo, *J. Bone Miner. Res.* 2003, 18, 47.
- [39] D. D. Hile, M. L. Amirpour, A. Akgerman, M. V. Pishko, *J. Controlled Release* 2000, 66, 177.
- [40] W. S. Koegler, C. Patrick, M. J. Cima, L. G. Griffith, *J. Biomed. Mater. Res.* 2002, 63, 567.
- [41] D. D. Hile, M. V. Pishko, *Macromol. Rapid Commun.* 1999, 20, 511.
- [42] H. H. Winter, G. Gappert, H. Ito, *Macromolecules* 2002, 35, 3325.
- [43] F. Rindfleisch, T. P. DiNoia, M. A. McHugh, *J. Phys. Chem.* 1996, 100, 15581.
- [44] C. F. Kirby, M. A. McHugh, *Chem. Rev.* 1999, 99, 565.
- [45] P. D. Whaley, S. Kulkarni, P. Ehrlich, R. S. Stein, H. H. Winter, W. C. Conner, G. Beauchage, *J. Polym. Sci. B, Polym. Phys.* 1998, 36, 617.
- [46] H. Matsuyama, H. Yano, T. Maki, M. Teramoto, K. Mishima, K. Matsuyama, *J. Membrane Sci.* 2001, 194, 157.
- [47] H. Matsuyama, A. Yamamoto, H. Yano, T. Maki, M. Teramoto, K. Mishima, K. Matsuyama, *J. Membrane Sci.* 2002, 204, 81.
- [48] D. J. Abdallah, R. G. Weiss, *Adv. Mater.* 2000, 12, 1237.
- [49] N. Husing, U. Schubert, *Angew. Chem. Int. Ed.* 1998, 37, 23.
- [50] D. A. Loy, E. M. Russick, S. A. Yamanaka, B. M. Baugher, K. J. Shea, *Chem. Mater.* 1997, 9, 2264.
- [51] C. Shi, Z. Huang, S. Kilic, J. Xu, R. M. Enick, E. J. Beckman, A. J. Carr, R. E. Melendez, A. D. Hamilton, *Science* 1999, 286, 1540.
- [52] Z. H. Huang, C. M. Shi, R. Enick, E. Beckman, *Chem. Mater.* 2002, 14, 4273.
- [53] V. K. Potluri, J. H. Xu, R. Enick, E. Beckman, A. D. Hamilton, *Org. Lett.* 2002, 4, 2333.
- [54] F. Placin, J. P. Desvergne, F. Cansell, *J. Mater. Chem.* 2000, 10, 2147.
- [55] J. W. Tom, P. G. Debenedetti, *J. Aerosol Sci.* 1991, 22, 555.
- [56] Y. Chernyak, F. Henon, R. B. Harris, R. D. Gould, R. K. Franklin, J. R. Edwards, J. M. DeSimone, R. G. Carbonell, *Ind. Eng. Chem. Res.* 2001, 40, 6118.
- [57] A. Blasig, C. M. Shi, R. M. Enick, M. C. Thies, *Ind. Eng. Chem. Res.* 2002, 41, 4976.
- [58] J. L. Owens, K. S. Anseth, T. W. Randolph, *Macromolecules* 2002, 35, 4289.
- [59] R. Y. Hsu, C. S. Tan, J. M. Chen, *J. Appl. Polym. Sci.* 2002, 84, 1657.
- [60] D. J. Dixon, G. Luna-Bárcenas, K. P. Johnston, *Polymer* 1994, 35, 3998.
- [61] B. Warwick, F. Dehghani, N. R. Foster, I. R. Biffin, H. L. Regtop, *Ind. Eng. Chem. Res.* 2002, 41, 1993.
- [62] J. vonBehren, E. H. Chimowitz, P. M. Fauchet, *Adv. Mater.* 1997, 9, 921.
- [63] A. I. Cooper, A. B. Holmes, *Adv. Mater.* 1999, 11, 1270.
- [64] A. I. Cooper, C. D. Wood, A. B. Holmes, *Ind. Eng. Chem. Res.* 2000, 39, 4741.
- [65] F. Svec, J. M. J. Fréchet, *Science* 1996, 273, 205.
- [66] F. Svec, J. M. J. Fréchet, *Ind. Eng. Chem. Res.* 1998, 38, 34.
- [67] C. Yu, M. C. Xu, F. Svec, J. M. J. Fréchet, *J. Polym. Sci. A, Polym. Chem.* 2002, 40, 755.
- [68] M. J. Whitcombe, E. N. Vulfson, *Adv. Mater.* 2001, 13, 467.
- [69] M. Petro, F. Svec, J. M. J. Fréchet, *Biotechnol. Bioeng.* 1996, 49, 355.
- [70] a) A. K. Hebb, K. Senoo, R. Bhat, A. I. Cooper, *Chem. Mater.* 2003, 15, in press; b) A. K. Hebb, A. I. Cooper, *Comp. Sci. Technol.* 2003, 63, 2061.
- [71] D. C. Sherrington, *Chem. Commun.* 1998, 2275.
- [72] C. D. Wood, A. I. Cooper, *Macromolecules* 2001, 34, 5.
- [73] A. Imhof, D. J. Pine, *Adv. Mater.* 1998, 10, 697.
- [74] P. Schmidt-Winkel, W. W. Lukens, P. D. Yang, D. I. Margolese, J. S. Lettow, J. Y. Ying, G. D. Stucky, *Chem. Mater.* 2000, 12, 686.
- [75] V. N. Manoharan, A. Imhof, J. D. Thorne, D. J. Pine, *Adv. Mater.* 2001, 13, 447.
- [76] H. Zhang, G. C. Hardy, M. J. Rosseinsky, A. I. Cooper, *Adv. Mater.* 2003, 15, 78.
- [77] N. R. Cameron, D. C. Sherrington, *Adv. Polym. Sci.* 1996, 126, 163.
- [78] W. Busby, N. R. Cameron, C. A. B. Jahoda, *Biomacromolecules* 2001, 2, 154.
- [79] H. Zhang, A. I. Cooper, *Chem. Mater.* 2002, 14, 4017.
- [80] C. T. Lee, P. A. Psathas, K. P. Johnston, J. deGrazia, T. W. Randolph, *Langmuir* 1999, 15, 6781.
- [81] R. Butler, C. M. Davies, A. I. Cooper, *Adv. Mater.* 2001, 13, 1459.
- [82] R. A. Caruso, M. Giersig, F. Willig, M. Antonietti, *Langmuir* 1998, 14, 6333.
- [83] B. J. Zhang, S. A. Davis, S. Mann, *Chem. Mater.* 2002, 14, 1369.
- [84] E. Dujardin, S. Mann, *Adv. Mater.* 2002, 14, 775.
- [85] Y. N. Xia, B. Gates, Z. Y. Li, *Adv. Mater.* 2001, 13, 409.
- [86] O. D. Velev, E. W. Kaler, *Adv. Mater.* 2000, 12, 531.
- [87] Y. Fukushima, H. Wakayama, *J. Phys. Chem. B* 1999, 103, 3062.
- [88] H. Wakayama, Y. Fukushima, *Chem. Commun.* 1999, 391.
- [89] H. Wakayama, Y. Fukushima, *Ind. Eng. Chem. Res.* 2000, 39, 4641.
- [90] H. Wakayama, Y. Fukushima, *Chem. Mater.* 2000, 12, 756.
- [91] H. Wakayama, H. Itahara, N. Tetsuda, S. Inagaki, Y. Fukushima, *Chem. Mater.* 2001, 13, 2392.
- [92] H. Wakayama, S. Inagaki, Y. Fukushima, *J. Am. Ceram. Soc.* 2002, 85, 161.
- [93] H. Ohde, M. Ohde, F. Bailey, H. Kim, C. M. Wai, *Nano Lett.* 2002, 2, 721.
- [94] H. Ohde, J. M. Rodriguez, Y. Xiang-Rong, C. M. Wai, *Chem. Commun.* 2000, 2353.
- [95] M. Ji, X. Y. Chen, C. M. Wai, J. L. Fulton, *J. Am. Chem. Soc.* 1999, 121, 2631.

- [96] P. S. Shah, J. D. Holmes, K. P. Johnston, B. A. Korgel, *J. Phys. Chem. B* 2002, 106, 2545.
- [97] N. Z. Clarke, C. Waters, K. A. Johnson, J. Satherley, D. J. Schiffrin, *Langmuir* 2001, 17, 6048.
- [98] J. J. Watkins, T. J. McCarthy, *Chem. Mater.* 1995, 7, 1991.
- [99] a) P. B. Webb, P. C. Marr, A. J. Parsons, H. S. Gidda, S. M. Howdle, *Pure Appl. Chem.* 2000, 72, 1347. b) J. Zhang, A. J. Busby, C. J. Roberts, X. Chen, M. C. Davies, S. J. B. Tendler, S. M. Howdle, *Macromolecules*, 2002, 35, 8869.
- [100] K. S. Morley, P. C. Marr, P. B. Webb, A. R. Berry, F. J. Allison, G. Moldovan, P. D. Brown, S. M. Howdle, *J. Mater. Chem.* 2002, 12, 1898.
- [101] K. M. K. Yu, A. M. Steele, J. Zhu, Q. J. Fu, S. C. Tsang, *J. Mater. Chem.* 2003, 13, 130.
- [102] J. J. Watkins, J. M. Blackburn, T. M. McCarthy, *Chem. Mater.* 1999, 11, 213.
- [103] J. M. Blackburn, D. P. Long, J. J. Watkins, *Chem. Mater.* 2000, 12, 2625.
- [104] D. P. Long, J. M. Blackburn, J. J. Watkins, *Adv. Mater.* 2000, 12, 913.
- [105] N. E. Fernandes, S. M. Fisher, J. C. Poshusta, D. G. Vlachos, M. Tsapatsis, J. J. Watkins, *Chem. Mater.* 2001, 13, 2023.
- [106] B. Subramaniam, *Appl. Catal. A* 2001, 212, 199.
- [107] P. G. Jessop, T. Ikariya, R. Noyori, *Chem. Rev.* 1999, 99, 475.
- [108] J. Y. Ying, C. P. Mehnert, M. S. Wong, *Angew. Chem. Int. Ed.* 1999, 38, 56.
- [109] A. S. O'Neil, R. Mokaya, M. Poliakoff, *J. Am. Chem. Soc.* 2002, 124, 10636.
- [110] C. Y. Yeh, S. B. Zhang, A. Zunger, *Phys. Rev. B* 1994, 50, 14405.
- [111] L. Brus, *J. Phys. Chem.* 1994, 98, 3575.
- [112] J. D. Holmes, K. P. Johnston, R. C. Doty, B. A. Korgel, *Science* 2000, 287, 1471.
- [113] N. R. B. Coleman, M. A. Morris, T. R. Spalding, J. D. Holmes, *J. Am. Chem. Soc.* 2001, 123, 187.
- [114] N. R. B. Coleman, N. O'Sullivan, K. M. Ryan, T. A. Crowley, M. A. Morris, T. R. Spalding, D. C. Steytler, J. D. Holmes, *J. Am. Chem. Soc.* 2001, 123, 7010.
- [115] J. J. Watkins, T. J. McCarthy, *Macromolecules* 1994, 27, 4845.
- [116] J. J. Watkins, T. J. McCarthy, *Macromolecules* 1995, 28, 4067.
- [117] E. Kung, A. J. Lesser, T. J. McCarthy, *Macromolecules* 1997, 31, 4160.
- [118] P. Rajagopalan, T. J. McCarthy, *Macromolecules* 1998, 31, 4791.
- [119] K. A. Arora, A. J. Lesser, T. J. McCarthy, *Macromolecules* 1999, 32, 2562.
- [120] Y. Fu, D. R. Palo, C. Erkey, R. A. Weiss, *Macromolecules* 1997, 30, 7611.
- [121] S. L. Shenoy, D. Cohen, C. Erkey, R. A. Weiss, *Ind. Eng. Chem. Res.* 2002, 41, 1484.
- [122] S. L. Shenoy, P. Kaya, C. Erkey, R. A. Weiss, *Synth. Met.* 2001, 123, 509.
- [123] F. M. Kerton, G. A. Lawless, S. P. Armes, *J. Mater. Chem.* 1997, 7, 1965.
- [124] R. Kitaura, K. Seki, G. Akiyama, S. Kitagawa, *Angew. Chem. Int. Ed.* 2003, 42, 428.
- [125] F. E. Henon, M. Camaiti, A. L. C. Burke, R. G. Carbonell, J. M. DeSimone, F. Piacenti, *J. Supercrit. Fluids* 1999, 15, 173.
- [126] F. E. Henon, R. G. Carbonell, J. M. DeSimone, *AIChE J.* 2002, 48, 941.

Microstructured optical fiber devices

B. J. Eggleton*, C. Kerbage, P. S. Westbrook, R. S. Windeler, and A. Hale
Optical Fiber Solutions, Lucent Technologies, Murray Hill, NJ 07974

*Also with *Specialty Fiber Devices, Optical Fiber Solutions, Lucent Technologies, Somerset, NJ 08873*

*Phone: 908 582 3087, Fax: 908 582 6055, Email: egg@lucent.com

Abstract: We present several applications of microstructured optical fibers and study their modal characteristics by using Bragg gratings inscribed into photosensitive core regions designed into the air-silica microstructure. The unique characteristics revealed in these studies enable a number of functionalities including tunability and enhanced nonlinearity that provide a platform for fiber device applications. We discuss experimental and numerical tools that allow characterization of the modes of the fibers.

©2001 Optical Society of America

OCIS code: (060.0060) Fiber optics and optical communications; (060.2270) Fiber characterization; (230.3990) Microstructure devices; (160.5470) Polymers.

References and Links

1. P.V. Kaiser and H.W. Astle, "Low-loss single-material fibers made from pure fused silica," *The Bell System Technical Journal*, **53**, 1021-1039 (1974).
2. J. Broeng, D. Mogilevstev, S.E. Barkou, and A. Bjarklev, "Photonic crystal fibers: A new class of optical waveguides," *Optical Fiber Technology*, **5**, 305-330, (1999).
3. J.C. Knight, T.A. Birks, P.S.J. Russell, and D.M. Atkin, "All-silica single mode optical fiber with photonic crystal cladding," *Opt. Lett.* **21**, 1547-1549, (1996).
4. J.C. Knight, T.A. Birks, R.F. Cregan, P.S.J. Russell, and J.P. Sandro, "Photonic crystals as optical fibers: physics and applications," *Optical Materials*, **11**, 143-151, (1999).
5. R.S. Windeler, J.L. Wagener, and D.J. DiGiovanni, "Silica-air microstructured fibers: Properties and applications," *Optical Fiber Communications conference*, San Diego (1999).
6. T.A. Birks, J.C. Knight, and P.S.J. Russell, "Endlessly single-mode photonic crystal fiber," *Opt. Lett.* **22**, 961-963, (1997).
7. R.F. Cregan, B.J. Mangan, J.C. Knight, T.A. Birks, P. S. J. Russell, P.J. Roberts, and D.C. Allan, "Single-mode photonic bandgap guidance of light in air," *Science*, **285**, 1537-1539, (1999).
8. T.M. Monro, W. Belardi, K. Furusawa, J.C. Baggett, N.G.R. Broderick, and D.J. Richardson, "Sensing with microstructured optical fibres," *Meas. Sci. and Tech.* **12**, 854-858, (2001).
9. R. Holzwarth, M. Zimmermann, Th. Udem, T.W. Hansch, P. Russbuldt, K. Gabel, R. Poprawe, J.C. Knight, W.J. Wadsworth, and P.S.J. Russell, "White-light frequency comb generation with a diode-pumped Cr:LiSAF laser," *Opt. Lett.* **17**, 1376-1378, (2001).
10. T.A. Birks, D. Mogilevstev, J.C. Knight, and P.S.J. Russell, "Dispersion Compensation Using Single-Material Fibers," *IEEE Phot. Tech. Lett.* **11**, 674-676, (1999).
11. J.K. Ranka, R.S. Windeler, and A.J. Stentz, "Optical properties of high-delta air-silica microstructure optical fibers," *Opt. Lett.* **25**, 796-798, (2000).
12. T.M. Monro, D.J. Richardson, N.G.R. Broderick, and P.J. Bennet, "Holey optical fibers: An efficient modal model," *J. Lightwave Tech.* **17**, 1093-1102, (1999).
13. J.C. Knight, T.A. Birks, R.F. Cregan, P.S.J. Russell, and J.P. Sandro, "Large mode area photonic crystals," *Opt. Lett.* **25**, 25-27, (1998).
14. T. Erdogan, "Fiber Grating Spectra," *J. Lightwave Tech.* **155**, 1277-1294, (1997).
15. R. Kashyap, *Fiber Bragg gratings*, 1st ed. ed. 1999: Academic Press.
16. B.J. Eggleton, P.S. Westbrook, C.A. White, C. Kerbage, R.S. Windeler, and G.L. Burdge, "Cladding mode resonances in air-silica microstructure fiber," *J. Lightwave Tech.*, **18**, 1084-1100, (2000).
17. B. J. Eggleton, P. S. Westbrook, R. S. Windeler, S. Spalter, and T.A. Strasser, "Grating resonances in air-silica microstructured optical fibers," *Opt. Lett.* **24**, 1460-1462, (1999).
18. C. Kerbage, B.J. Eggleton, P.S. Westbrook, and R.S. Windeler, "Experimental and scalar beam propagation analysis of an air-silica microstructure fiber," *Opt. Express*, **7**, 113-123, (2000), <http://www.opticsexpress.org/oearchive/source/22997.htm>
19. P.S. Westbrook, B.J. Eggleton, R.S. Windeler, A. Hale, T.A. Strasser, and G.L. Burdge, "Cladding-Mode Resonances in Hybrid Polymer-Silica Microstructured Optical Fiber Gratings," *IEEE Phot. Tech. Lett.* **12**, 495-497, (2000).

#37441 - \$15.00 US

(C) 2001 OSA

Received October 31, 2001; Revised December 05, 2001

17 December 2001 / Vol. 9, No. 13 / OPTICS EXPRESS 698

20. J. K. Chandalia, B. J. Eggleton, R. S. Windeler, S. G. Kosinski, X. Liu, and C. Xu, "Adiabatic Coupling in Tapered Air-Silica Microstructured Optical Fiber," *IEEE Phot. Tech. Lett.* **13**, 52-54, (2001).
21. X. Liu, C. Xu, W.H. Knox, J.K. Chandalia, B.J. Eggleton, S.G. Kosinski, and R.S. Windeler, "Soliton self-frequency shift in a tapered air-silica microstructured fiber," *Opt. Lett.* **26**, 358-360, (2000).
22. C. Kerbage, A. Hale, A. Yablon, R.S. Windeler, and B.J. Eggleton, "Integrated all-fiber variable attenuator based on hybrid microstructure fiber," *App. Phys. Lett.* **79**, 3191-3193, (2001).
23. M.J. Steel, T.P. White, C. Martijn de Sterke, R.C. McPhedran, L.C. Botten, "Symmetry an degeneracy in microstructured optical fibers," *Opt. Lett.* **26**, 488-490, (2001).

1. Introduction

Microstructured optical fibers (MOFs) [1] are typically all silica optical fibers in which air-holes are introduced in the cladding region and extend in the axial direction of the fiber [1-6]. These fibers, which have been known since the earliest days of silica light guide research [1], come in a variety of different shapes, sizes, and distributions of air-holes. Recent interest in such fibers has been generated through potential applications in optical communications [1-8], optical fiber based sensing [8], frequency metrology and optical coherence tomography [9]. The earliest work reported by Kaiser *et al.* and shown in Figure 1(a), demonstrated low loss single material fibers made entirely from silica. A number of years later Russell and coworkers demonstrated the so-called *photonic crystal* MOF, shown in Fig. 1(b) [6]. These fibers incorporate a periodic array of air-holes in the cladding region and guide light through modified total internal reflection [4,8]. This advance generated enormous interest in this new class of MOFs leading to the first demonstration of a true *photonic bandgap* MOF by Cregan *et al.* in 1999 [7]. These fibers, shown in Fig. 1 (c), can guide light in a central air-core region through coherent Bragg scattering off the periodic array of air-holes [2]. MOFs that incorporate an array of air-holes surrounding a very small silica core, as shown in Fig. 1 (d), can provide unique dispersion [10] and nonlinear characteristics that have been used to demonstrate a number of novel effects, including the generation of a broadband supercontinuum and a zero GVD as low as 765 nm[11].

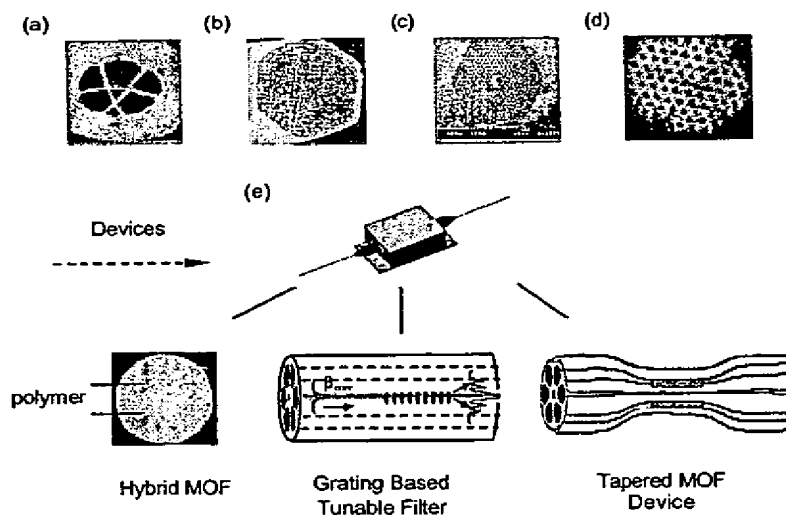


Fig. 1. Historical outline of different MOFs (a) Air-silica MOF, Kaiser *et al.* (1974) (b) Photonic crystal MOF, Russell *et al.* (1996), (c) Photonic bandgap MOF, Cregan *et al.* (1999),

and (d) Dispersion control MOF, Ranka *et al.* (1999). (e) Possible device applications based on MOFs.

Most research activities in this field have been concerned with the guidance properties of the fundamental mode localized in the core region of these fibers, for example, bend loss, cutoff wavelength [6], mode field diameter [12], and dispersion [10,12] and have focused on potential applications requiring long lengths of fiber where, for example, the fiber provides unique dispersion characteristics [11], reduced nonlinearity [13], or broad single-mode spectral ranges [6].

Another important application that we explore in this paper is the use of MOFs for optical fiber devices. In these applications the microstructured cladding region is designed to manipulate the propagation of core and leaky cladding modes. The core region can incorporate a doped region allowing for the inscription of grating structures and the air-holes can allow for the infusion of active materials yielding novel tunable hybrid waveguide devices. The resulting hybrid waveguide can be exploited in the design of optical devices, such as grating-based filters, tunable optical filters, tapered fiber devices and variable optical attenuators. We present a detailed modal characterization of different MOFs with limiting characteristics (e.g., air-fill fraction, ratio of propagation wavelength to air-hole diameter and air-hole distribution). By inspection of the transmission spectrum of the fiber Bragg grating written into the core of these fibers, we obtain a "mapping" of the different modes of the fiber. The spectra of these gratings are analyzed and explained qualitatively and compared to simulations using beam-propagation method (BPM). We discuss the implications of these results in more detail for the design of grating based devices and describe a range of applications of MOFs.

The paper is structured as follows: In Section 2, we present a brief background on the propagation of core and cladding modes in optical fibers and how they manifest in optical fiber grating devices. We then briefly describe the BPM for computation of waveguide properties. In section 3, we present characterization of grating spectra and near-field mode distributions for different MOFs. The transmission spectra are analyzed and compared to numerical simulations using BPM. In section 4, we demonstrate a number of device applications of MOFs including applications to fiber Bragg gratings with reduced cladding mode loss, tunable resonant filters, variable optical attenuators and nonlinear devices.

2. Background

Fig. 2 shows several MOFs with different geometries of the air-holes. Each fiber incorporates a germanium-doped core to allow for the inscription of periodic waveguide gratings. In order to fully characterize both core and higher order modes, we can examine the transmission spectra of gratings written in the core of the MOFs. Fiber Bragg gratings (FBG) and long period gratings (LPG) written into the core of such fibers facilitate phase matching to counter and co-propagating modes, respectively [14]. When excited, these modes manifest themselves as resonant loss in the corresponding transmission spectrum thus providing a modal spectrum of the waveguide, revealing effective indices (propagation constants) and mode profiles. As we show below these characteristics can be compared to simulations using BPM.

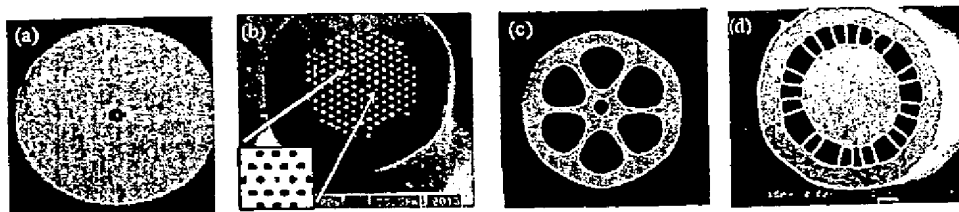


Fig. 2. SEMs and photographs of respective MOF (a) high delta MOF (b) photonic crystal MOF; (c) grapefruit MOF; (d) air-clad MOF.

2.1 Fiber gratings and cladding mode resonances

The transmission spectra of a FBG and LPG written in the core of a conventional fiber are shown in Fig. 3(a)-(b). Also shown in Fig. 3, is a schematic illustrating grating induced coupling from a guided core mode to higher order modes, which are confined by the glass air interface; these are referred to as *cladding modes*. The sharp resonant loss on the short wavelength side of the Bragg resonance in Fig. 3(a) is due to coupling to the counter-propagating cladding modes. Similarly, the coupling to the co-propagating cladding modes by the LPG manifests as peak loss at a certain wavelength in the transmission of the fiber.

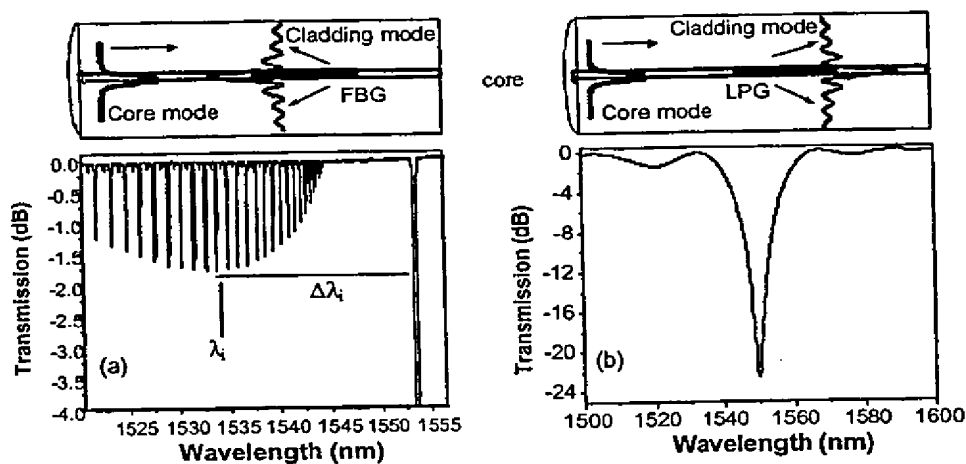


Fig.3. (a) Typical transmission spectrum of FBG in standard fibers exhibiting short wavelength loss. Each dip in the transmission spectrum is associated with grating facilitated phase matching to a counter-propagating cladding mode. The inset shows a schematic of Bragg grating in the core of a conventional optical fiber. Fig. 3. (b) The corresponding transmission spectrum of LPG.

A simple description of the core and cladding modes can be obtained through inspection of the transmission spectrum of a FBG written into a photosensitive core of a MOF. The effective index of the fundamental mode localized in the core region (n_{co}) can be determined using the Bragg condition $\lambda_B = 2n_{co}\Lambda_{FBG}$ [15], where Λ_{FBG} is the period of the FBG. The effective indices of the cladding modes ($n_{clad,i}$) can then be determined using the phase matching condition for a cladding resonance: $\beta_{clad,i} + \beta_{01} = 2\pi/\Lambda_{FBG}$, where $\beta_{clad,i}$ is the propagation constant of the i th cladding mode propagating in the opposite direction to the

fundamental LP_{01} with propagation constant β_{01} . The phase matching condition is then given by:

$$\lambda_{FBG,i} = (n_{co} + n_{clad,i})\Lambda_{FBG} \quad (1)$$

The effective indices obtained from inspection of the FBG spectrum can be used in the design of LPGs, which couple the fundamental core mode to co-propagating cladding modes. For the co-propagating grating couplers the phase matching condition can be written as,

$$\lambda_{LPG,i} = (n_{co} - n_{clad,i})\Lambda_{LPG} \quad (2)$$

where $\lambda_{LPG,i}$ is the resonant coupling wavelength and Λ_{LPG} is the period of the LPG. Neglecting chromatic dispersion of the core and cladding modes, the LPG resonance wavelength is then proportional to the wavelength interval between the Bragg resonance and the i^{th} cladding resonance in the FBG [16]:

$$\frac{\lambda_{LPG,i}}{\Lambda_{LPG}} = \frac{\Delta\lambda_i}{\Lambda_{FBG}} \quad (3)$$

where $\Delta\lambda_i = \lambda_B - \lambda_{clad,i}$ is the difference between the fundamental Bragg resonance (given by the Bragg condition) and the wavelength of the i^{th} cladding mode resonance. Predicting the peak intensities of the experimental grating spectra, however requires detailed knowledge of the modal distributions and use of coupled mode theory.

For uniform gratings (constant index modulation and grating period), which we consider in this paper, the transmission coefficient at the peak of the n th resonance is given by:

$$T_i = 1 - \tanh^2(\kappa_i L) \quad (4)$$

where L is the length of the grating [15] and κ_i is the coupling coefficient between the core and cladding mode i [15]. The spectra consist of the contribution of each mode at wavelengths determined by the modal composition, multiplied by a grating dependent shape factor.

2.2 Beam propagation method applied to MOF

The BPM provides a simple intuitive method of determining the modal spectrum and modal profiles for complex waveguides. The beam-propagation correlation method has been used extensively in the study of complex waveguides and is particularly well suited to computing mode evolution in waveguides that vary in the longitudinal direction and in geometries where leaky modes are important [16]. This latter point is of particular interest in this work where we consider the propagation of leaky modes in the claddings of different MOFs. Briefly, the BPM correlation method, summarized schematically in Fig. 4, propagates a launched field profile within a waveguide. The propagation of the field along the z direction through a transverse guide can be written as:

$$E(x, y, z) = \sum_i \alpha_i E_i(x, y) e^{-i\beta_i z} \quad (5)$$

where for each mode i , $E_i(x, y)$ is the transverse modal profile, α_i is the amplitude strength of each mode, and $\beta_i = 2\pi n_i/\lambda$ is the wave vector in the propagation direction z .

The correlation function computes the initial launched profile and the profile at each z value given by:

$$P(z) = \int E(x, y, 0) E^*(x, y, z) dx dy \quad (6)$$

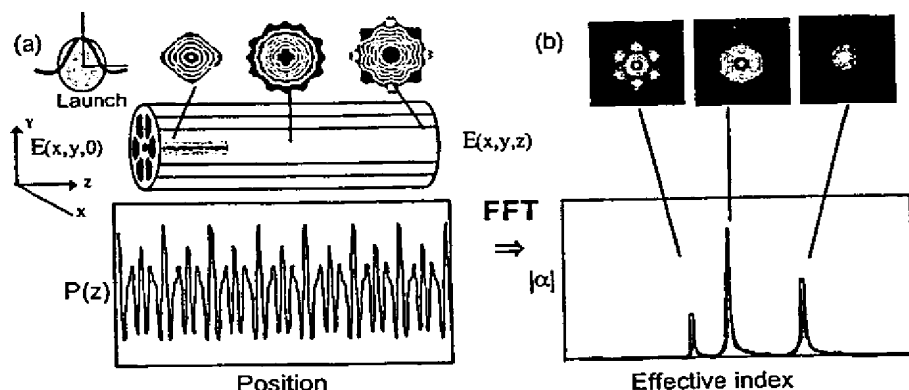


Fig. 4. Launch mode field along MOF structure (a) the correlation function and (b) its Fourier transform revealing the effective indices of the modes.

The BPM computes this function, $E(x,y,z)$, for all z given only the initial starting field $E(x,y,0)$ and the refractive index profile of the waveguide

$$E(x,y,0) = \Delta n(x,y) E_{core}(x,y) \quad (7)$$

where $\Delta n(x,y)$ is the grating index profile [16].

This propagation is accomplished without a priori knowledge of the modal decomposition, however; the propagation contains all the information about the modes. Here the strengths α_i within the launched profile are identical to the coupling constants (κ_i) necessary for a coupled mode analysis.

$$\alpha_i = \int E_i(x,y) \Delta n(x,y) E_{core}(x,y) dx dy = \left(\frac{\lambda}{\pi} \right) \kappa_i \quad (8)$$

where the relative intensities of the Fourier transformed peaks determine the squares of the coupling coefficients.

3. Modal characterization

By examining the transmission spectrum of a FBG written into an MOF, we expect to gain insight into the guidance properties of the core and cladding modes and to correlate these properties with calculations of the cladding mode fields using BPM. The experimental setup is shown in Fig. 5. A 1550 nm tunable source is launched into the fiber with a FBG written in the core, using a 10× microscope objective and a beam-splitter. When the wavelength of the incident light satisfies the Bragg conditions, different counter-propagating cladding modes, are excited; facilitated by phase matching provided by the FBGs. Light reflected off the FBG is imaged in the near field on an IR camera using a 40× microscope objective. When capturing images of the reflected mode-field the far end of the fiber is placed in index-matching gel so as to minimize back reflections.

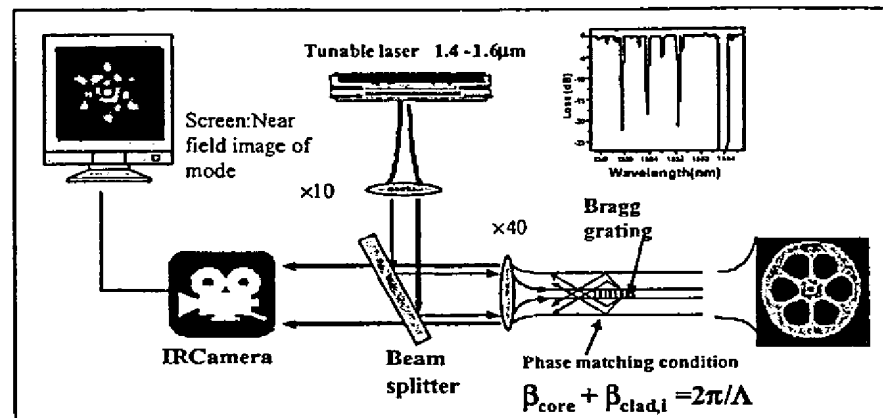


Fig. 5. Experimental setup used to characterize near field images for respective air-silica MOFs. Bragg grating selectively excited counter-propagating “cladding modes” which are imaged in the near field on the VIDECON camera.

3.1 Photonic crystal fiber

Fig. 6 shows a cross section of the “photonic crystal MOF” and the transmission spectrum of a FBG written in its core. The fiber was designed with a sufficiently small photosensitive germanium-doped core such that it would appear as a small perturbation on the guided modes of the fiber but contain sufficient germanium to write a grating. The core radius is $\sim 1\mu\text{m}$ and $\Delta = (n_{\text{core}} - n_{\text{clad}})/n_{\text{core}} \sim 0.5\%$, where n_{core} and n_{clad} are the refractive indices of the germanium-doped core and silica cladding, respectively. The core is surrounded by a hexagonal array of holes in a silica matrix with an air-hole diameter $d \sim 2\mu\text{m}$ and spacing $\Lambda \sim 10\mu\text{m}$ extending to a radius $\sim 60\mu\text{m}$, corresponding to 7 layers. This MOF guides by total internal reflection and satisfies the criterion provide in Ref. [6] for being endlessly single mode. In particular the fiber should support only one single bound mode in the $1.5\mu\text{m}$ wavelength regime.

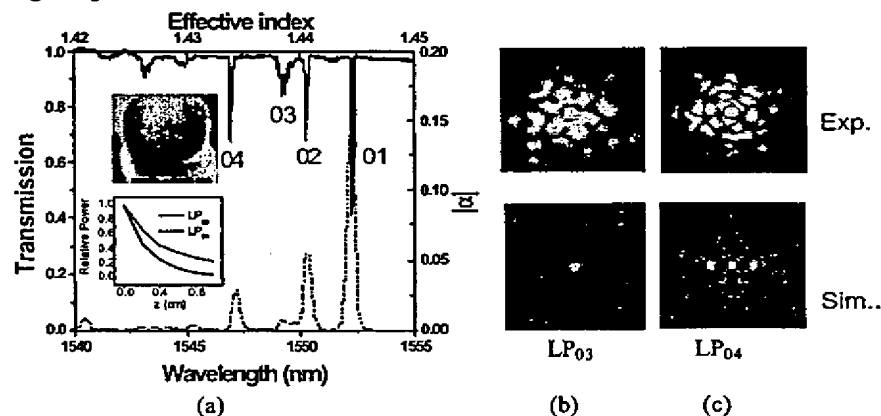


Fig. 6. (a) Measured transmission spectrum of FBG written in photonic crystal MOF (solid line), calculated modal spectrum (dashed line). Light from the near field images reflected off FBG when the tunable laser wavelength is tuned to: (a) 1549.196nm, corresponding to the resonance labeled “LP₀₃”; and (c) 1546.990nm corresponding to the resonance labeled “LP₀₄”.

The solid line in Fig. 6 (a) is the measured transmission spectrum of the FBG. The dashed line is the computed modal spectrum. The right vertical axis is the mode overlap, defined in Eq.8, and calculated using BPM assuming symmetric launch conditions. Note that a number of discrete resonances appear in the transmission spectrum of the FBG indicating excitation of higher order modes propagating in the PCF, apparently contradicting the single-modedness of the PCF. In fact, these higher order modes correspond to leaky cladding modes that are quickly dissipated upon propagation. The cladding modes of this PCF, have effective indices below that of silica, and are stripped off by the high index outer silica region and that there is negligible coherent feedback from the outer silica air interface [16,17]. The measured and calculated mode profiles for the lower order cladding modes LP_{03} and LP_{04} are shown in Fig. 6(b) and (c) respectively. The shape of these modes reveals the hexagonal symmetry of the lattice and that most of the energy is confined in the inner few rings or holes. Simulations confirm that these modes have a relatively high propagation loss and complex propagation constants [17]. The energy of the modes tunnels between the air-holes into the cladding and is revealed as loss (~ 2 dB/cm) as depicted in the simulations (see inset in Fig. 6), these are thus leaky modes.

3.2 "Grapefruit" MOF

Fig. 7(a) shows the experimental transmission spectrum and the corresponding mode images (bottom) of a MOF ("grapefruit" MOF) with six large air-holes surrounding an inner cladding region of ~ 30 μm in diameter. A Bragg grating with a period of 0.5 μm was written in the germanium core of diameter 8 μm and $\Delta = ((n_1 - n_2)/n_1) \sim 0.35\%$, where n_1 and n_2 are the refractive indices of the germanium core and silica cladding, respectively. The first peak on the right side of the transmission spectrum, labeled A in Fig. 7, corresponds to excitation of the backward propagating core mode. The other resonances on the shorter wavelength side of the main peak correspond to coupling to higher order cladding modes. Only the four lowest order-cladding modes (labeled B, C, D and E) in the transmission spectrum of the MOF are surrounded by the holes and their propagation is governed by the total internal reflection at the interface of the cladding-holes. Higher order mode (F) spreads throughout the fiber through the interstitial region in the cladding between the holes [18]. Also note that the cladding mode resonances are spaced farther apart in wavelength due to the reduced inner effective cladding of the MOF. As the inner cladding diameter decreases the cladding mode spacing increases. We return to this point further below.

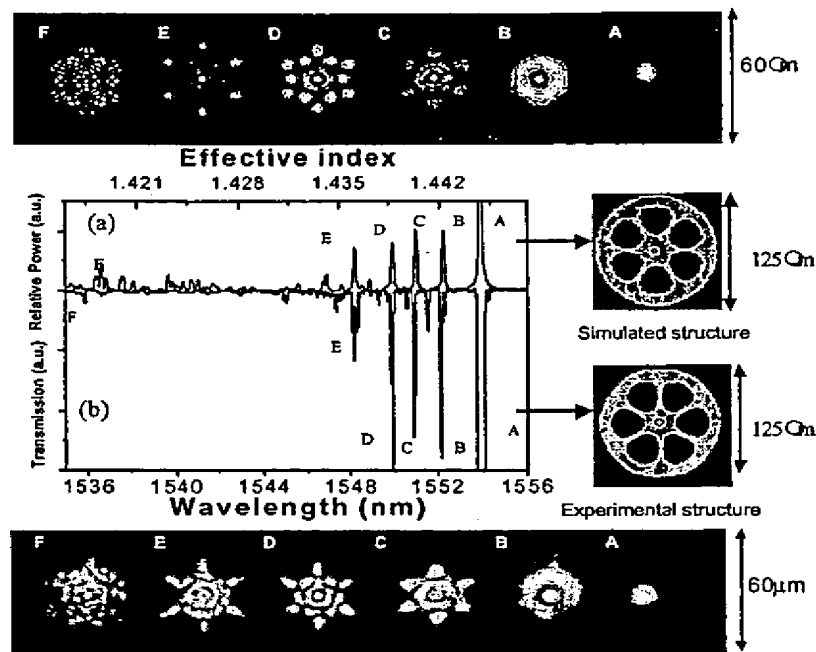


Fig. 7. (a) Part of transmission spectrum of FBG written into the core of the grapefruit MOF (solid line) with the corresponding observed near field images of light reflected off FBG when the laser was tuned to (A) 1553.96nm (the LP_{01} mode); (B) 1552.39nm (LP_{02}); (C) 1550.84nm (LP_{03}) mode; (D) 1547.82nm (LP_{04} mode); (E) 1547.36nm (LP_{05} mode); (F) 1535.82nm, and (b) calculated modal spectrum of the grapefruit MOF (dashed line) and its corresponding simulated modes.

Fig. 7 (b) shows the simulated mode spectrum and the simulated mode profiles using BPM (top). The simulated plot reveals the values of the relative power, which is related to the overlap ratio between the core and each of the excited modes, versus wavelength. The profile and the distribution of the energy of the modes are in good agreement with experiments and are clearly affected by the presence of the holes. The circular shapes of the modes of a conventional fiber are lost in this MOF. Instead the images exhibit symmetry of the air-hole geometry. The optical devices described further in this paper exploit lower order cladding modes that are predominantly confined to the inner cladding region.

4. Applications

The unique characteristics revealed in the above mentioned studies enable a number of functionalities including tunability and enhanced nonlinearity that provide a platform for fiber device applications.

4.1 Reduction of cladding mode loss in optical fiber Bragg gratings.

Cladding mode resonances are exploited in the design of FBG [16] and LPG [17] devices. In the case of LPGs these cladding modes are exploited in the design of band-rejection filters for flattening of optical amplifiers. In the case of a FBG the cladding mode loss is often regarded as a nuisance where the short wavelength loss reduces the usable bandwidth. As described above the microstructured cladding region manipulates cladding mode propagation. This

manifests in the spectral characteristics of optical fiber gratings, as is evident in Fig. 7. When the microstructured cladding region creates an inner effective cladding the fiber resembles a fiber with a reduced cladding diameter. We show that in such fiber the cladding mode loss can be reduced significantly.

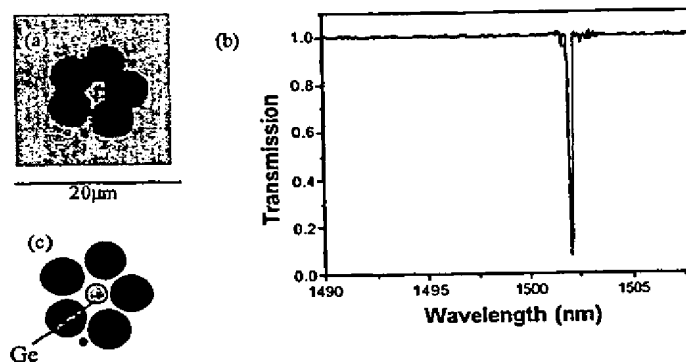


Fig. 8. (a) Transmission spectrum of FBG written into the core of the MOF (b) photo of the inner region and (c) schematic diagram

Fig. 8(a) shows a photo and schematic of a high-delta microstructured optical fiber that was designed to suppress cladding mode loss in a FBG MOF. This fiber incorporates five air-holes that are placed very close to a Germanium doped core. A length of the fiber was first loaded with deuterium to enhance the photosensitivity of the germanium region that and then was exposed using 242nm through a conventional phase mask with a period of $\Lambda_{mask}=1.075\mu\text{m}$ where $\Lambda_{FBG}=\Lambda_{mask}/2$. This produced a peak index modulation of $\Delta n\sim 10^{-5}$. The transmission spectrum of the FBG is shown in Fig. 8(b) where the Bragg resonance is at $\lambda_B=1504\text{ nm}$. The effective index of the core mode is then determined to be $n_{eff}\sim 1.405$. Note the absence of any significant cladding mode loss for wavelengths shorter than the Bragg resonance. Because of the small effective inner cladding diameter of this fiber, the cladding modes are offset significantly from the Bragg resonance.

The computed modal spectrum using BPM, shows a core mode with an effective index of $n_{eff}\sim 1.405$, in good agreement with the experimental measurements described above, and indicates a second mode of the inner cladding region with an effective index of $n_{eff}\sim 1.25$. Indeed the difference between the lowest modes of the inner cladding region is $\Delta\sim 10\%$, and is much larger than the core-cladding index step in standard fiber; it exhibits similar modal properties to a step-index fiber with $\Delta\sim 30\%$. The corresponding cladding mode spectrum in this fiber is thus offset from the Bragg resonance by as much as 80nm, consistent with the measured grating spectra shown above. These cladding modes (with $n_{eff}>n_{core}$) have negligible spatial overlap with the grating in the central core region and thus are not excited by interaction of core guided light with the grating.

4.2 Hybrid tunable optical fiber waveguides

Active materials, such as polymers, can be infused into the relatively large air-holes of the grapefruit MOF. Fig. 9(a) shows one end of the fiber immersed in a reservoir of material and sealed on the other end where vacuum is applied. The material then can be introduced into the air-holes of the fiber as shown in Fig. 9(b). In our case, the material is an acrylate monomer mixture (viscosity ~ 30 centipoise), which was infused into the air-holes at a rate of 0.03 cm/sec and was UV-cured for about 15 minutes to form a polymer with a desired

refractive index The refractive index of the polymer (n_p) has higher temperature dependence than that of glass (n_{silica}) sketched in Fig. 9(c). Since the fundamental mode is not affected by the presence of the air-holes, mode guidance in the cladding can be strongly affected simply by changing the hybrid waveguide temperature by 10-50°C [19].

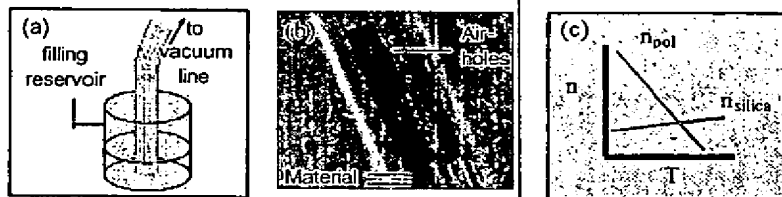


Fig. 9. (a) Schematic drawing of material (polymer) infused in the air-holes of the MOF. (b) Picture showing material in the air-holes of the fiber. (c) Refractive indices of the polymer and silica dependence on temperature.

4.3 Tunable grating filters

When polymer is infused into an MOF with a LPG written in the core the cladding resonances may be wavelength shifted and also suppressed entirely through temperature tuning. Fig. 9(a) shows a cross section of such a fiber with the infused polymer and silica regions as well as a conventional Ge-doped core.

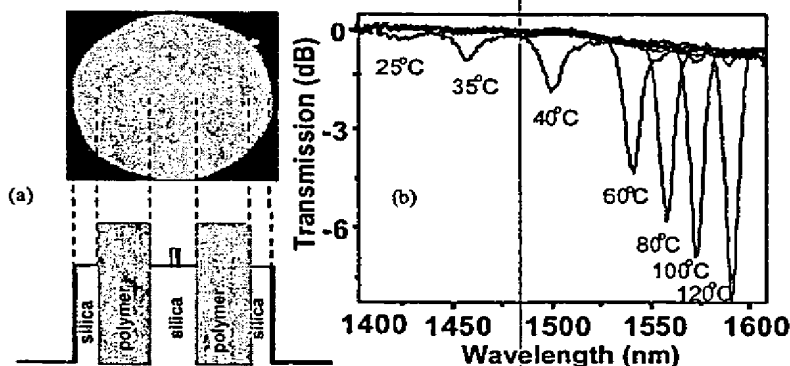


Fig. 10. (a) Photo of hybrid polymer air-silica microstructured optical fiber and a schematic diagram (b) Spectrum of LPG in hybrid polymer-silica fiber at different temperatures

Fig. 10(b) shows the transmission spectrum of an LPG written into the hybrid MOF. The LPG is first UV written in the waveguide, then the polymer is infused into the air regions and UV cured to form the hybrid waveguide at the grating. The LPG resonance shows over 100nm of tunability, 10 times more than in a standard LPG. The tunability results from both the high temperature dependence of the polymer refractive index and the geometry of the microstructure.

After polymer infusion into a LPG at room temperature, the cladding resonances have been completely suppressed, indicating that the waveguide defined by the polymer cladding interface has become very lossy. The polymer refractive index decreases with increased temperature, while that of silica increases. Moreover, the polymer refractive index varies about 10 times as fast as that of silica. Therefore, as the temperature increases, and the

polymer index drops below that of silica, the waveguide defined by the inner polymer-silica interface becomes guiding. The large tuning range is due to the geometry of the microstructure because it creates a small inner cladding whose cladding modes have relatively large wavelength spacing. Because the phase shift upon total internal reflection is proportional to the spacing, the tuning range is enhanced.

4.4 Tapered MOF

Another interesting characteristic of MOFs is that they allow for both the group velocity dispersion and the mode field diameter to be controlled. This can be exploited in a range of different applications, including compensating chromatic dispersion [11] and allows for fiber designs with very small effective area for enhanced nonlinear interactions [12]. Although these fibers exhibit interesting and attractive properties, they have several practical difficulties, such as coupling light into the small core. Here, we demonstrate efficient coupling into an MOF, which has been tapered to very small diameter sizes and exhibits similar dispersion characteristics to previous work [20]. Furthermore, because of the supporting cladding region, the tapered MOF is mechanically stronger, and more robust than tapered conventional fibers that have demonstrated similar nonlinear effects [11], and also exhibit negligible sensitivity to external index, potentially allowing for packaging.

Fig. 11 shows a schematic of the tapered MOF device and the evolution of the computed and observed fundamental intensity mode profile of the MOF. The un-tapered grapefruit fiber is well matched to standard single-mode fiber, ensuring low loss due to splicing (< 0.1 dB) [20,21].

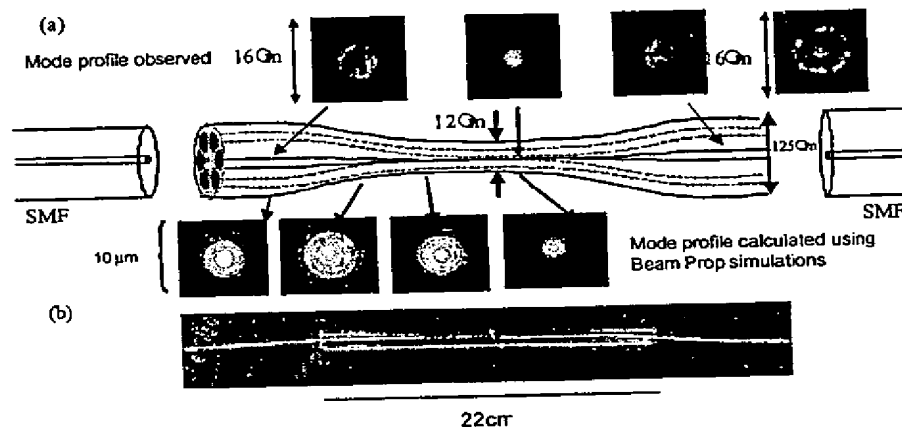


Fig. 11. (a) Schematic of the tapered MOF to 10 μm with calculated and observed cross-sectional intensity plots of the mode field at different points along the taper. (b) Packaged tapered MOF device.

The fiber is tapered by heating and stretching in a flame to reduce the outer diameter while maintaining the same cross-sectional profile. The flame temperature is chosen such that the air holes do not collapse, ensuring that the fiber cross section does not change throughout the taper. The MOF can be tapered down to less than 10 μm in outer-diameter with a waist length of 20 cm. Tapering of the MOF is adiabatic so that the fundamental mode evolves into the fundamental mode of the central silica region with low loss (< 0.1 dB), where it is confined by the ring of air-holes. Because the mode is confined within the air-ring, the total fiber diameter can be maintained at an acceptable level, which increases robustness and allows for

packaging as shown in Fig. 11(b). In addition, the fundamental mode is guided in the germanium-doped core after adiabatic expansion, allowing for splicing to standard fibers.

4.5 Enhanced nonlinear interactions

Tapered MOF provide an ideal structure for demonstrations of dramatic nonlinear effects. Laser pulses at $1.3 \mu\text{m}$ generated by a femtosecond Ti-sapphire pumped optical parametric oscillator were free-space coupled into the un-tapered portion of the MOF and then propagated through the taper. Tunable self-frequency shifting solitons were generated over the important communications windows from $1.3 \mu\text{m}$ to $1.65 \mu\text{m}$ with input pulse at $1.3 \mu\text{m}$ [21]. As the light propagates through the MOF the light is continually shifted towards the red due to intrapulse Raman scattering, which transfers the energy of the high frequency part of the pulse spectrum to the low frequency part, we observe 60% of the input photons being self-frequency shifted. The soliton wavelength can be tuned from 1.2 to $1.8 \mu\text{m}$ by adjusting the input power. These dramatic results are possible because the fiber exhibits a large anomalous dispersion over a wide wavelength range as shown in Fig. 12, which ensure that the pulse is stable against modulational instability at high peak intensities. These dramatic nonlinear effects confirm the adiabaticity and low loss of the taper.

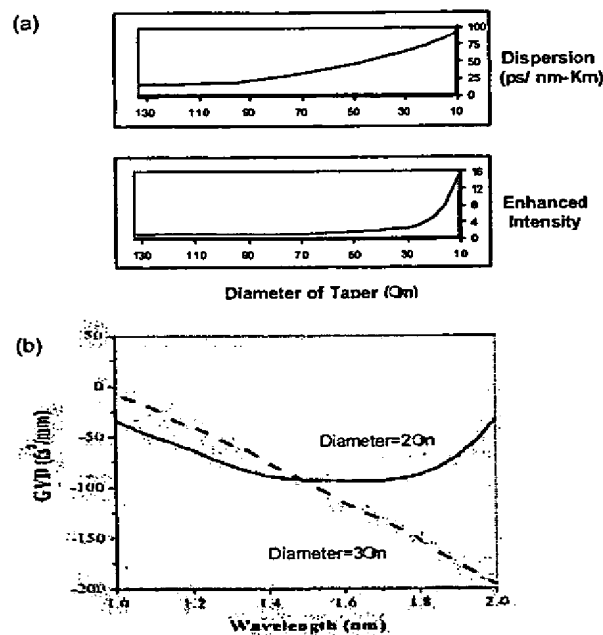


Fig. 12 (a) Dispersion and intensity plots along the taper calculated at wavelength $1.5 \mu\text{m}$.
(b) Group velocity dispersion as a function of wavelength for different diameters in the waist.

4.6 Variable optical attenuator microstructure fiber device

In this section we present a tunable all-fiber optical device based on an MOF that exploits the temperature dependence of the refractive index of a polymer incorporated into the air-holes of the MOF, which has been tapered. The fiber design enables efficient interaction between

tunable materials with the propagating mode field thus permitting a range of different functionalities [22]. Here we demonstrate an electrically tunable attenuator device (loss-filter), which is fully integrated, packaged and spliced with about 30 dB dynamic range, insertion loss of less than 0.8 dB, and minimal polarization dependence.

Fig. 13 shows the schematic of the MOF fiber used in the modulation device. As mentioned before, the lowest order mode of the fiber is guided in the germanium doped core of the fiber by total internal reflection at the core-cladding interface and is unaffected by the presence of the air voids in the cladding.

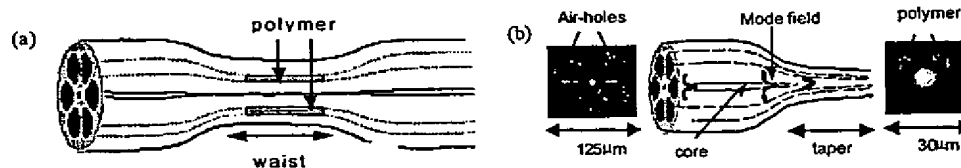


Fig. 13 (a) Schematic diagram of the all-fiber variable attenuator device based on tapered MOF and (b) mode profile evolution along the fiber.

In order to achieve an efficient field interaction between the core mode and the air voids, the fiber needs to be adiabatically tapered. Again, the fiber is heated and stretched such that the fiber diameter is decreased while the cross-sectional profile remains approximately the same. As shown in Fig. 13, by tapering the fiber down to small diameter sizes, the core diameter decreases and becomes extremely small. The core mode spreads into the cladding region where it is confined by the air-hole interface. In the waist of the tapered fiber, the waveguide resembles a very high-delta fiber ($\Delta \sim 35\%$) similar to a glass rod surrounded by air. The large modal field interaction with the surrounding air voids in the waist of the fiber makes the core mode very sensitive to any index change at the air-holes-cladding interface. Tunable refractive index materials, such as polymers, with a thermal coefficient that is an order of magnitude larger than that of silica may be introduced into the holes and will affect the guiding mechanisms of light in the optical fiber.

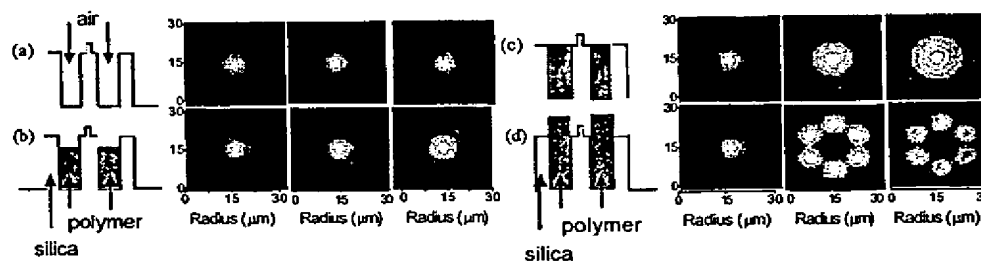


Fig. 14 Index cross-sectional profile in the waist of the fiber (a) with no polymer and with polymer of index (b) lower ($n_p=1.42$), (c) same as ($n_p=1.44$) and (d) higher ($n_p=1.5$) than that of silica. The corresponding calculated intensity cross sectional mode profile are shown at (1) $z=0$ cm, (2) $z=1$ cm and (3) $z=2$ cm along the length of the waist.

Fig. 14 shows the cross sectional index profile for different values of polymer refractive index, and the corresponding calculated mode field cross-sectional intensities,

calculated using BPM. The outer diameter of the waist of the taper is 30 μm with corresponding inner diameter of $\sim 8 \mu\text{m}$. The simulation includes absorption losses in the polymer of 0.2 dB/mm [19]. Fig. 14(a) shows the device when no polymer is infused in the air-holes and the mode field propagates in the fiber without any change. Fig. 14(b)-(d) show the corresponding waveguide index profiles and the associated intensity mode profiles for the case when the air-holes are infused with polymer of varying refractive index. If the index of the infused polymer is lower than that of silica ($n_p=1.42$) as shown in Fig. 14(b), the mode is confined in the cladding by total internal reflection, and only a small percentage of the optical field will be in the material. In this case the mode propagates through the taper with minimal loss. On the other hand, if the index of the material is close to that of silica, as shown in Fig. 14(c) ($n_p=1.44$) or higher than that of silica ($n_p=1.5$), as in Fig. 14(d), the mode field will refract into the high index medium, resulting in dramatic loss and attenuation for the propagating mode, exacerbated by material losses of the polymer and interstitial region between air-holes, which results in leakage of modes.

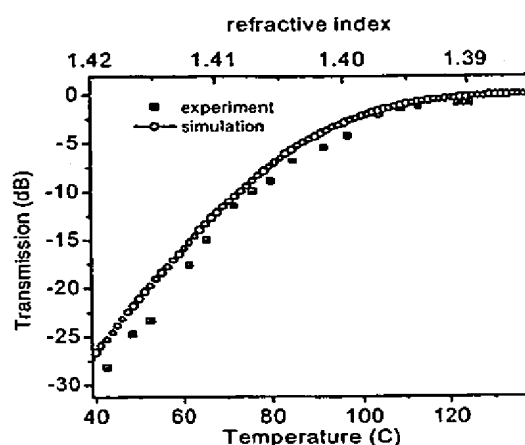


Fig. 15 Transmission (output) of the tapered microstructure fiber plotted in dB scale as a function of temperature and refractive index at 1550 nm.

Fig. 15 shows both the experimental (dots) and simulated (circular) plot of the transmission through the fiber as a function of temperature (bottom axis) and corresponding polymer refractive index (top axis) at 1550 nm. The attenuation of the device varies from -30dB to -0.8dB with the highest insertion loss occurring at the lowest temperature. The circular dots in Fig. 14 represent the results of numerical simulations using BPM. The simulated waveguide, defined by the geometry and the index profile, closely matches the real cross section and dimensions of the tapered fiber. A Gaussian beam profile centered on the core axis was launched into the structure. The simulated results are in very good agreement with the experimental measurements. The measured PDL was less than 0.5 dB, which may be attributed to the material absorption and irregular boundaries that vary along the tapered fiber, between the cladding and air-holes. We note that microstructured fiber exhibits 6fold rotational symmetry and is expected to exhibit very low birefringence and thus minimal PDL [23]. The wavelength dependence of the device is about 0.3 dB over a range of 30 nm (1530-1560 nm). The maximum power consumption is 375mW, corresponding to about 2V of applied voltage. Even though the fiber is tapered to a small diameter size, the device is robust and easily packaged with very low loss.

5. Conclusion

In summary, we have presented different device applications of MOFs and we have reviewed mode propagation in these MOFs. By inspection of the transmission spectra of FBG and LPG written in the core of the MOFs, we obtain knowledge of the optical properties of higher order modes that are unique to the geometry of the microstructure fiber. The mode profiles and guidance properties of these modes are measured experimentally and calculated using BPM. By gaining insight into the properties of these modes, we demonstrate fiber designs whose characteristics are unique providing a platform for future photonic devices.

#37441 - \$15.00 US
(C) 2001 OSA

Received October 31, 2001; Revised December 05, 2001
17 December 2001 / Vol. 9, No. 13 / OPTICS EXPRESS 713

the voids in the colloidal crystal film–substrate system, we carefully peeled the crystal films off the gold substrates with adhesive tape, and subsequently imaged the peeled lower surfaces of the crystal films using SEM and AFM.

Received: July 25, 2002
Final version: October 4, 2002

Incorporation of Proteins into Polymer Materials by a Novel Supercritical Fluid Processing Method**

By Michael S. Watson, Martin J. Whitaker,
Steven M. Howdle,* and Kevin M. Shakesheff

- [1] a) O. D. Velev, T. A. Jede, R. F. Lobo, A. M. Lenhoff, *Nature* 1997, 389, 447. b) B. T. Holland, C. F. Blanford, A. Stein, *Science* 1998, 281, 538. c) J. E. G. J. Wijnhoven, W. L. Vos, *Science* 1998, 281, 802. d) A. A. Zakhidov, R. H. Baughman, Z. Iqbal, C. Cui, I. Khayrullin, S. O. Dantas, J. Marti, V. G. Ralchenko, *Science* 1998, 282, 897. e) S. H. Park, Y. Xia, *Adv. Mater.* 1998, 10, 1045. f) Q. Luo, Z. Liu, L. Li, S. Xie, J. Kong, D. Zhao, *Adv. Mater.* 2001, 13, 286.
- [2] a) M. D. Sacks, T.-Y. Tseng, *J. Am. Ceram. Soc.* 1984, 67, 526. b) P. Calvert, *Nature* 1985, 317, 201.
- [3] a) S. H. Park, Y. Xia, *Langmuir* 1999, 15, 266. b) S.-Y. Chang, L. Liu, S. A. Asher, *J. Am. Chem. Soc.* 1994, 116, 6739.
- [4] a) J. H. Holtz, S. A. Asher, *Nature* 1997, 389, 829. b) J. H. Holtz, J. S. W. Holtz, C. H. Munro, S. A. Asher, *Anal. Chem.* 1998, 70, 780. c) O. D. Velev, E. W. Kaler, *Langmuir* 1999, 15, 3693.
- [5] a) G. A. Ozin, S.-M. Yang, *Adv. Funct. Mater.* 2001, 11, 95. b) S.-M. Yang, H. Miguez, G. A. Ozin, *Adv. Funct. Mater.* 2002, 12, 425.
- [6] a) R. Mayoral, J. Requena, J. S. Moya, C. López, A. Cintas, H. Miguez, F. Meseguer, L. Vázquez, M. Holgado, A. Blanco, *Adv. Mater.* 1997, 9, 257. b) L. N. Donselaar, A. P. Philipse, J. Suurmond, *Langmuir* 1997, 13, 6018. c) H. Miguez, F. Meseguer, C. López, A. Milsud, J. S. Moya, L. Vázquez, *Langmuir* 1997, 13, 6009.
- [7] a) N. Ise, *Angew. Chem. Int. Ed. Engl.* 1986, 25, 323. b) H. B. Sunkara, J. M. Jethmalani, W. T. Ford, *Chem. Mater.* 1994, 6, 362. c) A. E. Larsen, D. G. Grier, *Nature* 1997, 385, 230.
- [8] a) N. D. Denkov, O. D. Velev, P. A. Kralchevsky, I. B. Ivanov, H. Yoshimura, K. Nagayama, *Langmuir* 1992, 8, 3183. b) C. D. Dushkin, K. Nagayama, T. Miwa, P. A. Kralchevsky, *Langmuir* 1993, 9, 3695. c) A. S. Dimitrov, K. Nagayama, *Langmuir* 1996, 12, 1303. d) S. Rakers, L. F. Chi, H. Fuchs, *Langmuir* 1997, 13, 7121.
- [9] S. H. Park, D. Qin, Y. Xia, *Adv. Mater.* 1998, 10, 1028.
- [10] a) P. Jiang, J. F. Bertone, K. S. Hwang, V. L. Colvin, *Chem. Mater.* 1999, 11, 2132. b) Y. A. Vlasov, X.-Z. Bo, J. C. Sturm, D. J. Norris, *Nature* 2001, 414, 289. c) Z.-Z. Gu, A. Fujishima, O. Sato, *Chem. Mater.* 2002, 14, 760.
- [11] a) O. D. Velev, K. Furusawa, K. Nagayama, *Langmuir* 1996, 12, 2374. b) O. D. Velev, A. M. Lenhoff, E. W. Kaler, *Science* 2000, 287, 2240. c) G.-R. Yi, J. H. Moon, S.-M. Yang, *Adv. Mater.* 2001, 13, 1185.
- [12] a) A. van Blaaderen, R. Ruel, P. Wiltzius, *Nature* 1997, 385, 321. b) K.-H. Lih, J. C. Crocker, V. Prasad, A. Schofield, D. A. Weitz, T. C. Lubensky, A. G. Yodh, *Phys. Rev. Lett.* 2000, 85, 1770. c) E. Kim, Y. Xia, G. M. Whitesides, *Adv. Mater.* 1996, 8, 245. d) S. M. Yang, G. A. Ozin, *Chem. Commun.* 2000, 2507. e) Y. Yin, Y. Lu, B. Gates, Y. Xia, *J. Am. Chem. Soc.* 2001, 123, 8718.
- [13] a) K. M. Chen, X. Jiang, L. C. Kimerling, P. T. Hammond, *Langmuir* 2000, 16, 7825. b) J. Aizenberg, P. V. Braun, P. Wiltzius, *Phys. Rev. Lett.* 2000, 84, 2997.
- [14] a) R. C. Hayward, D. A. Saville, I. A. Aksay, *Nature* 2000, 404, 56. b) S.-R. Yeh, M. Seul, B. I. Shraiman, *Nature* 1997, 386, 57.
- [15] Z.-Z. Gu, A. Fujishima, O. Sato, *Angew. Chem. Int. Ed.* 2002, 41, 2067.
- [16] a) H. A. Biebuyck, G. M. Whitesides, *Langmuir* 1994, 10, 2790. b) C. B. Gorman, H. A. Biebuyck, G. M. Whitesides, *Chem. Mater.* 1995, 7, 252.
- [17] A. Kumar, H. A. Biebuyck, G. M. Whitesides, *Langmuir* 1994, 10, 1498.
- [18] N. L. Abbott, G. M. Whitesides, L. M. Racz, J. Szekeley, *J. Am. Chem. Soc.* 1994, 116, 290.
- [19] A. T. Skjeltorp, P. Meakin, *Nature* 1988, 335, 424.
- [20] a) G. Subramanian, K. Constant, R. Biswas, M. M. Sigalas, K.-M. Ho, *Appl. Phys. Lett.* 1999, 74, 3933. b) G. Subramanian, V. N. Manoharan, J. D. Thorne, D. J. Pine, *Adv. Mater.* 1999, 11, 1261. c) Q.-B. Meng, Z.-Z. Gu, O. Sato, *Appl. Phys. Lett.* 2000, 77, 4313.
- [21] X. Chen, Z. Cui, Z. Chen, K. Zhang, G. Lu, G. Zhang, B. Yang, *Polymer* 2002, 43, 4147.

Considerable advances have been made in tissue engineering since the advent of the field in the early 1990s.^[1,2] One of the challenges faced by researchers in this field, and in pharmaceutical science in general, is that of supplying drugs, nutrients, hormones, growth factors etc. to well-targeted locations in the body,^[3–8] and specifically to cells growing in the interiors of tissue engineering scaffolds.^[9–13] Recently, the use of supercritical carbon dioxide (scCO₂) to enable the mixing of dry powders of thermally and/or solvent-sensitive biological factors into biodegradable polymers has been described.^[14–16] These techniques yield porous or particulate devices capable of the sustained, controlled release of the factor. However, these methods are not appropriate when very low loadings of the biological factor are required, because the dry powder cannot be handled and mixed on the nanogram scale. This is a major limitation for growth factors and other biotechnology drugs where therapeutic concentrations are often of the order of parts per billion.^[17,18] Therefore, we have developed a new solution-based process to enable accurate and efficient handling of therapeutic quantities of proteins while retaining the manifold advantages of supercritical fluid processing.^[19,20]

Avidin tagged with rhodamine was used as a model protein for confocal microscopy studies of protein distribution. Avidin–rhodamine solutions of 10 and 1 µg mL^{−1} were prepared using distilled water, and 0.5 mL aliquots were pipetted onto the poly(D,L-lactide) (PLA) scaffolds. Control scaffolds without any protein addition were also prepared. All the samples were freeze-dried for 48 h, leaving the avidin–rhodamine on the surface.

From these dried samples, one scaffold from each of the protein concentrations was removed to act as a single positive control. The remaining samples were then reprocessed in scCO₂ using the same procedure as described in the experimental section. At each stage of the procedure, representative samples were sectioned, gold coated, and their pore structure examined by scanning electron microscopy (SEM). The pores are interconnected and a bimodal distribution was observed,

* Prof. S. M. Howdle, Dr M. S. Watson
School of Chemistry, University of Nottingham
Nottingham, NG7 2RD (UK)
E-mail: steve.howdle@nottingham.ac.uk
M. J. Whitaker, Prof. K. M. Shakesheff
School of Pharmaceutical Sciences, University of Nottingham
Nottingham, NG7 2RD (UK)

** The authors gratefully acknowledge Dr. Susan Anderson for her assistance with the confocal microscopy. A studentship (MJW), postdoctoral fellowship (MSW) and Advanced Fellowship (KMS) were funded by the EPSRC. We acknowledge also the University of Nottingham Institute of Materials Technology (UNIMAT).

with larger ($\sim 300\text{--}600\text{ }\mu\text{m}$) and smaller ($\sim 10\text{--}20\text{ }\mu\text{m}$) diameter pores. Mercury intrusion porosimetry confirms the presence of the smaller pores. The larger pores are not detected, but are clearly visible by SEM. These findings are very similar to those reported previously in PLA- CO_2 systems.^[14,15] Porosimetry data also confirmed that the total pore volume for these samples lies reproducibly in the range of 60–70 %. The larger pores were not observed in other foamed polymer systems.^[21,22]

Sectioned specimens were studied by confocal microscopy using a Leica TCS4D system with a Leica DMRBE upright fluorescence microscope and an argon-krypton laser. The red fluorescence of tetramethylrhodamine isothiocyanate (TRITC) avidin-rhodamine was excited with the 568 nm laser line.

For the activity studies, samples were prepared by adsorbing $100\text{ }\mu\text{L}$ of 250 mg cm^{-3} aqueous solution of ribonuclease A onto PLA powder, and freeze-drying for a period of 48 h before processing as above. The enzyme was released from the scaffolds into a tris(hydroxymethyl)aminomethane (Tris) buffer solution (pH 7.13) at $37\text{ }^\circ\text{C}$ for 15 min. The activity of the enzyme after processing and release from the scaffold was monitored by measuring the rate of conversion of a ribonuclease-specific substrate, cytidine-2',3'-monophosphate, to a form that could be detected spectrophotometrically. The activity was normalized to the total amount of protein present, determined by Coomassie protein assay.

Figure 1 (upper) shows a schematic of the supercritical fluid process. Concentration profiles of the fluorescent avidin-rhodamine complex are shown after the freeze-drying step and after supercritical CO_2 reprocessing. Following the initial freeze-drying, fluorescence is localized at the exposed surfaces of the scaffold, i.e., the top surface and the walls of pores. After supercritical CO_2 reprocessing, the complex is

now uniformly distributed, and the resulting fluorescence is homogeneous throughout the sample.

The schematic is supported by data from confocal microscopy. On the left are eight images from the sample immediately after freeze-drying. These follow the edge of a pore from the top surface to a depth of $77.4\text{ }\mu\text{m}$. The images show that fluorescence intensity decreases with depth from the top surface except for a narrow region at the edge of the pore, indicating that the complex is localized on the surfaces. The series on the right depicts a sample that was reprocessed in supercritical CO_2 . The series follows the edge of a pore to a depth of $82.5\text{ }\mu\text{m}$. In contrast to the unprocessed scaffold, fluorescence is clearly observed throughout the scaffold with appreciable intensity detected in both the bulk of the polymer and at the pore surfaces. The porosities obtained for the control and re-processed scaffolds were found to be comparable.

Ribonuclease activity was measured after release into Tris buffer solution from scaffolds, after processing in scCO_2 (Fig. 2). The rate of conversion of cytidine-2',3'-monophosphate to cytidine-3'-phosphate was measured by the change in absorbance at 284 nm . The black circles (samples) represent the activity of the enzyme compared to the standards (open circles). The mean recovery of activity was $100.8 \pm 9.8\%$, indicating that enzyme activity is retained throughout the process. The correlation between sample and standard activity is high ($R^2 = 0.9959$).

Figure 3 displays the protein release behavior as a function of time. Where the protein has been dried, i.e., adsorbed onto the polymer scaffold without a second supercritical fluid (SCF) processing step, the protein is released very quickly, with nothing remaining after two days (black triangles). In samples that have been subjected to the SCF reprocessing step, the release is far more protracted. After an initial "burst" phase (0–1 days), the rate of release stabilizes for

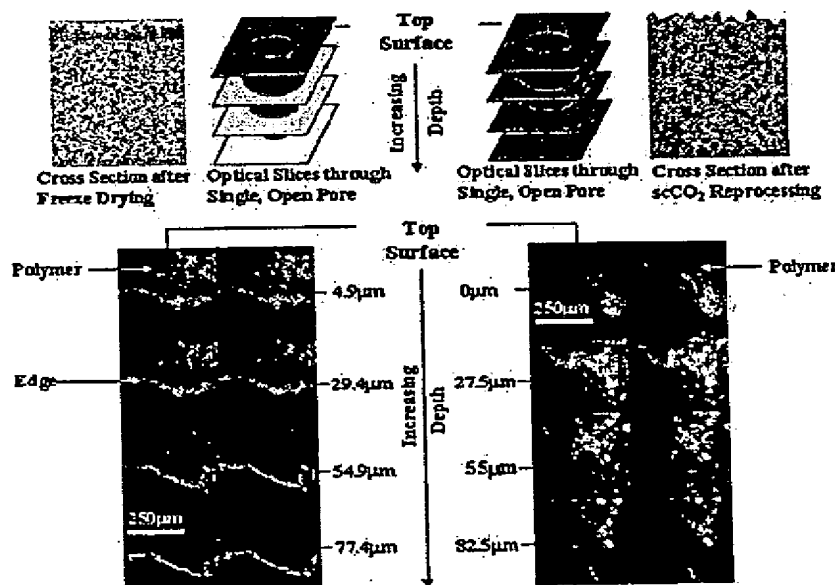


Fig. 1. Schematic cross-section and confocal micrographs of polymer samples during processing. Note the uniform distribution of fluorescent material throughout the scaffold after scCO_2 processing.

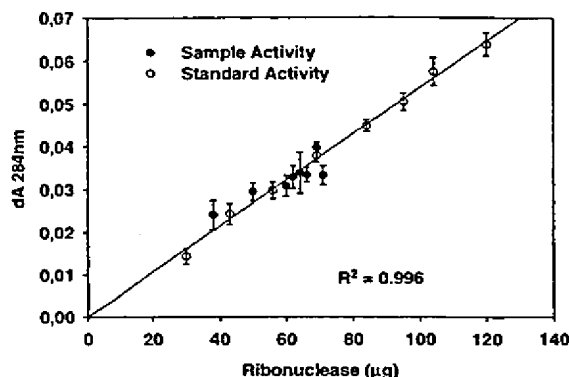


Fig. 2. Recovery of ribonuclease A activity after double processing in scCO_2 . Samples: black circles, standards: open circles. Error bars ± 1 standard deviation. The scCO_2 does not denature the enzyme.

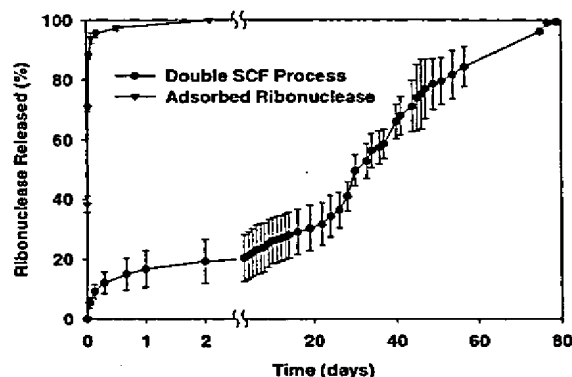


Fig. 3. Ribonuclease A release in Tris buffer (pH 7.13) 37°C from PLA scaffolds after double processing. $N = 3$. Error bars ± 1 SD (black circles). Percentage release of ribonuclease compared to the total dose adsorbed onto PLA powder. $N = 4$. Error bars ± 1 SD (black triangles). Note that after scCO_2 processing the release profile is significantly improved.

approximately three weeks, before degradation of the polymer matrix allows the protein to escape. The profile then follows a rectilinear relationship until the exhaustion of the protein after approximately 80 days.

We have combined conventional solution and supercritical fluid processing to prepare porous tissue engineering scaffolds that contain biologically active material for controlled release. This combination allows the accurate dosing of the biological agent whilst retaining the advantages of supercritical fluid technology i.e., a very clean route to porous materials. We have also demonstrated the retention of biological activity throughout the scCO_2 processing using the enzyme ribonuclease A, with $100 \pm 9.8\%$ activity after processing. The scaffolds control the rate of protein release with kinetics typical of other PLA systems. The significant attraction of this new technique is that there is no exposure at any stage of manufacture to either raised temperatures or organic solvent. Additionally, a wide range of alternative morphologies including microparticles may be accessed simply by controlling the method of depressurization.

Experimental

Materials: The first step in our novel processing was to prepare a high surface area polymer substrate by grinding the polymer into a fine powder. Subsequent processing used supercritical CO_2 to prepare porous scaffolds. Scaffolds and powders were prepared from a commercially sourced poly(D,L-lactide) (PLA) (Alkermes Medisorb, low inherent viscosity (I.V.) $M_w = 85$ kD, polydispersity = 1.4) used without further purification. Food grade carbon dioxide (BOC) was supplied to a stainless steel autoclave through stainless steel piping using a PM101 pump from NWA, Germany. Sigma UK supplied avidin-rhodamine protein conjugate and ribonuclease A. Tris buffer (pH 7.13) comprised 25 mM tris(hydroxymethyl)aminomethane, 25 mM sodium chloride, and 25 mM hydrochloric acid.

Scaffold preparation: Porous scaffolds were prepared in moulds prepared from 48-well tissue culture plates (Costar, USA). $12 \times 100 \pm 1$ mg PLA were weighed out into the mould, which was then sealed inside the autoclave. The autoclave was heated to 35°C before filling with CO_2 over 30 min to a pressure of 207 ± 2 bar. This filling time minimizes the potentially detrimental effects of excessive Joule-Thompson heating on the biologically active substrate as the system is pressurized, while the high pressure minimizes the formation of a non-porous "skin" on the outside of the scaffold [23]. The polymer- CO_2 mixture was allowed to equilibrate for 20 min before venting to atmospheric pressure over 8 min. The pressure was controlled throughout the preparation using a JASCO BP-1580-81 programmable backpressure regulator. The autoclave temperature remained below 38°C throughout the filling step, and the flow rate of CO_2 during the equilibration step was $12 \text{ cm}^3 \text{ min}^{-1}$. After the initial scCO_2 processing, the mould containing the foamed polymer scaffolds was removed from the autoclave and the residual gas allowed to escape for 2 h. Studies in our laboratories have shown this to be sufficient time for the complete release of dissolved CO_2 .

Received: March 30, 2002
Final version: October 9, 2002

- [1] U. A. Stock, J. P. Vacanti, *Annu. Rev. Med.* 2001, 52, 443.
- [2] Y. Tabata, *Drug Discovery Today* 2001, 6, 483.
- [3] B. Gander, L. Meinel, E. Walter, H. P. Merkle, *Chimia* 2001, 55, 212.
- [4] M. Nof, L. D. Shea, *J. Biomed. Mater. Res.* 2002, 59, 349.
- [5] W. L. Murphy, M. C. Peters, D. H. Kohn, D. J. Mooney, *Biomaterials* 2000, 21, 2521.
- [6] S. Stolnik, C. R. Heald, J. Neal, M. C. Garnett, S. S. Davis, L. Illum, S. C. Purkis, R. J. Barlow, P. R. Gellert, *J. Drug Targeting* 2001, 9, 361.
- [7] J. J. Kim, K. Park, *J. Controlled Release* 2001, 77, 39.
- [8] F. Li, W. G. Liu, K. De Yao, *Biomaterials* 2002, 23, 343.
- [9] C. M. Agrawal, R. B. Ray, *J. Biomed. Mater. Res.* 2001, 55, 141.
- [10] R. N. B. Bhandari, L. A. Riccalton, A. L. Lewis, J. R. Fry, A. H. Hammond, S. J. B. Tendler, K. M. Shakesheff, *Tissue Eng.* 2001, 7, 345.
- [11] E. J. Caterson, L. J. Nesti, W. J. Li, K. G. Danielson, T. J. Albert, A. R. Vaccaro, R. S. Tuan, *J. Biomed. Mater. Res.* 2001, 57, 394.
- [12] Y. M. Elcin, V. Dixit, T. Gitnick, *Artif. Organs* 2001, 25, 558.
- [13] M. J. Whitaker, R. A. Quirk, S. M. Howdle, K. M. Shakesheff, *J. Pharm. Pharmacol.* 2001, 53, 1427.
- [14] S. M. Howdle, M. S. Watson, M. J. Whitaker, V. K. Popov, M. C. Davies, F. S. Mandel, J. D. Wang, K. M. Shakesheff, *Chem. Commun.* 2001, 109.
- [15] M. H. Sheridan, L. D. Shea, M. C. Peters, D. J. Mooney, *J. Controlled Release* 2000, 64, 91.
- [16] T. P. Richardson, M. C. Peters, A. B. Ennett, D. J. Mooney, *Nat. Biotechnol.* 2001, 19, 1029.
- [17] J. J. Vallbacka, J. N. Nobrega, M. V. Sefton, *J. Controlled Release* 2001, 72, 93.
- [18] K. Y. Lee, M. C. Peters, K. W. Anderson, D. J. Mooney, *Nature* 2000, 408, 998.
- [19] A. I. Cooper, *Adv. Mater.* 2001, 13, 1111.
- [20] S. Alsou, J. L. Duda, *Chem. Eng. Technol.* 1999, 22, 971.
- [21] K. A. Arora, A. J. Lesser, T. J. McCarthy, *Macromolecules* 1998, 31, 4614.
- [22] S. K. Goel, E. J. Beckman, *Polym. Eng. Sci.* 1994, 34, 1137.
- [23] S. K. Goel, E. J. Beckman, *Polym. Eng. Sci.* 1994, 34, 1148.

Propagation of Cold Atoms along a Miniature Magnetic Guide

M. Key, I. G. Hughes,* W. Rooijakkers, B. E. Sauer, and E. A. Hinds†

Sussex Centre for Optical and Atomic Physics, University of Sussex, Brighton, BN1 9QH, United Kingdom

D. J. Richardson and P. G. Kazansky

Optoelectronics Research Centre, Southampton University, SO17 1BJ, United Kingdom

(Received 4 October 1999)

A cloud of laser-cooled ^{85}Rb atoms is coupled through a magnetic funnel into a miniature waveguide formed by four current-carrying wires embedded in a silica fiber. The atom cloud has a $\sim 100\text{ }\mu\text{m}$ radius within the fiber and propagates over cm distances. We study the coupling, propagation, and transverse distribution of atoms in the fiber, and find good agreement with theory. This prototype demonstrates the feasibility of miniature guides as a tool in the new field of integrated atom optics, leading to single-mode propagation of de Broglie waves and the possible preparation of 1D atom clouds.

PACS numbers: 03.75.Be, 32.80.Pj, 39.10.+j

There is widespread interest in guiding cold atoms [1,2]. For atom lithography, the goal is to dispense precise quantities of atoms onto specific regions of a surface [3]. In atom optics, the guide can be a "hosepipe," delivering large quantities of atoms to an inaccessible region, or it can be a "single-mode fiber" permitting coherent propagation of de Broglie waves for applications such as interferometry [4] or integrated atom optics [5–7]. In statistical physics, a quantum guide for atoms permits the study of degenerate quantum gases in 1D. Here one might realize a Tonks gas of bosons whose elementary excitations obey Fermi statistics or observe Luttinger liquid behavior with correlation functions that decay algebraically [8].

In several previous experiments [9], cold atoms have been guided inside hollow optical fibers where optical dipole forces confined them on axis. With this approach it is a challenging problem to avoid heating the atoms through intensity fluctuations and spontaneous emission. Confinement by static magnetic fields provides an alternative. On the macroscopic scale, magnetic guiding has been demonstrated using arrangements of permanent magnets [10] and along the side of a current-carrying wire [11]. Here we report on a miniature magnetic quadrupole guide in which we observe an atom cloud of $100\text{ }\mu\text{m}$ radius propagating for several centimeters [12]. We study the motion of atoms in this guide and we discuss the prospects for achieving single-mode de Broglie wave propagation.

Our guide is illustrated in Fig. 1. The supporting structure is a 25 mm-long silica tube fabricated by the Optoelectronics Research Centre at Southampton. Five parallel holes, each of radius $R = 261(5)\text{ }\mu\text{m}$, run through the length of the tube parallel to the vertical z axis. Four of them intersect the (x, y) plane on the corners of a square at $(\pm a, \pm a)$, with $a = 522(10)\text{ }\mu\text{m}$. These contain copper wires which carry a current I to produce the guiding magnetic field. The fifth hole is on the tube axis where the atoms are guided. To a good approximation the magnetic field vector is a purely quadrupole one: $\mathbf{B} = (B'x, -B'y)$ with $B' = \mu_0 I / \pi a^2 = 1.46(6)I\text{ T/m}$. An atom at radius

ρ interacting with this field has Zeeman energy $-B'\mu_z\rho$, where μ_z is the projection of its magnetic moment onto the local magnetic field direction. For the modest field strengths of interest here, the gyromagnetic ratio is independent of field strength, so, provided the spin does not flip, μ_z is a constant of the motion and the potential is linear in ρ . For $\mu_z < 0$ the atom then experiences a constant force directed toward the axis. Nonadiabatic behavior is suppressed at the center by adding a $\sim 300\text{ mG}$ magnetic field along the z direction to maintain an adequate splitting of the magnetic sublevels [13]. This causes the potential to become harmonic at distances less than a few μm from the axis. At the top of the guide the wires spread out (Fig. 1) to form a magnetic funnel of apex angle $\sim 90^\circ$, centered on the axis. A "pinch coil" wound

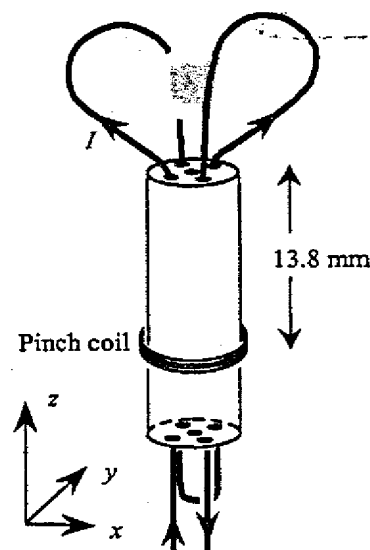


FIG. 1. Schematic view of the quadrupole guide. A cloud of cold atoms falls into the central hole where it is guided down to the pinch coil, reflected, and guided back up to the top. The diameter of the guide is greatly exaggerated.

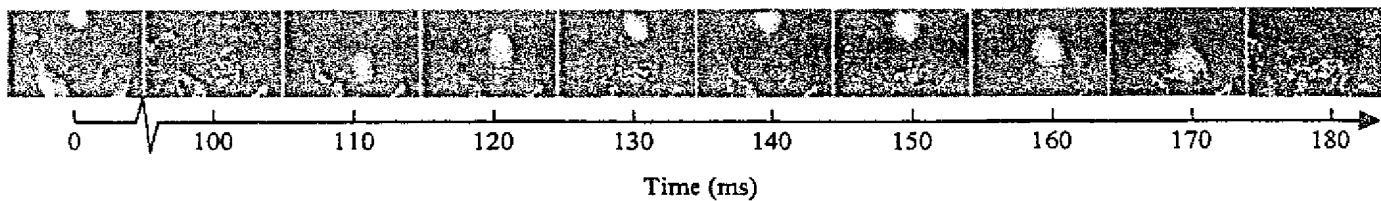


FIG. 2. Atoms released from the MOT at $t = 0$ propagate down the guide and back up again, rising to their original height after 139 ms. Some of the laser light scattered from the input funnel is visible in the background.

on the outside of the guide, 13.8 mm below the top, allows us to add a field in the z direction to close off the guide.

The guide is mounted in a vacuum chamber (10^{-9} Torr) with its entrance 10 mm below a magneto-optical trap (MOT) of standard design [2]. The MOT collects $\sim 5 \times 10^6$ ^{85}Rb atoms from the background vapor (filling lifetime ~ 5 s). These are then cooled in optical molasses to form a $T = 25$ μK cloud with rms radius $\sigma = 0.72$ mm, which we optically pump into the ($F = 3, m_F = 3$) ground-state sublevel relative to a uniform magnetic field $B_x \hat{x}$. As the atoms fall in the dark, B_x is reduced to zero and the guide current is adiabatically turned on. With a field of 40 G at the center of the pinch coil, atoms traveling down the guide should be reflected to reemerge from the entrance aperture. These are detected by a 2 ms pulse of laser light (10 mW/cm², -10 MHz molasses), which produces enough fluorescence for a CCD camera to record the distribution of the atoms without appreciably moving them under radiation pressure. We made CCD pictures with the pinch coil on and off. Figure 2 shows the cloud at the moment of release and the subsequent on-off differences as a function of the propagation time. The cloud clearly reemerges from the fiber and rises to its original height, 139 ms after being released, demonstrating that the atoms are indeed being guided in the fiber. Since the total drop height is $h = 2.38$ cm, this round-trip time indicates that the vertical component of the motion is close to free fall. The velocity of atoms along the guide is therefore approximately 45 cm/s near the top and 65 cm/s near the bottom.

When the cloud released from the MOT expands freely, only 0.7% of the atoms enter the guide aperture. By contrast, we find that the funnel gives an optimum efficiency for coupling atoms into the guide of 11% when the guide current I is set at 4.68 A, the value used in all the experiments reported here. The existence of an optimum can be understood as follows. The gravitational energy released by a ^{85}Rb atom falling 10 mm from the MOT to the guide entrance is equal to the magnetic interaction with a field of 15 G. If the field at the edge of the guide exceeds this, the magnetic aperture of the funnel becomes narrower than the physical diameter of the guide, making a constriction which reduces the coupling efficiency. At the same time, the field cannot be much smaller if the atoms are to be confined within the guide because an appreciable fraction of this energy goes into the transverse motion through deflections in the magnetic funnel. The angular momentum of the atoms around the guide axis $L \approx \sqrt{2mkT} \sigma$

imposes the additional constraint that the guiding force must be large enough to overcome the centrifugal force $L^2/(m\rho^3)$. Our optimum current makes a field of 17.9 G at the wall of the guide and exerts a force of $B'\mu_z \approx 6 \times 10^{-23}$ N on the atoms, compared with a typical centrifugal force at the wall of $\approx 2 \times 10^{-23}$ N. The coupling is thus a compromise between constriction of the entrance aperture to the guide and rejection of higher angular momenta. A Monte Carlo simulation of the experiment gives 21% coupling efficiency when the MOT is perfectly placed on the symmetry axis, dropping to 10% for an offset of 1 mm between the center of the MOT and the axis of the guide. Such a misalignment is possible in our apparatus.

In Fig. 3 we plot the number of atoms returning from the guide versus the field in the pinch coil. The vertical line marks the field $mgh/\mu_B = 35.8$ G at which the magnetic interaction energy is equal to the entire gravitational energy released by falling. Most of the atoms are reflected at lower fields than this because some of their energy is in transverse motion. Empirically we find that the measured step fits well to the integral of a Gaussian distribution, shown in Fig. 3 by the solid curve. Our Monte Carlo simulation gives the very similar step shown by the dashed line. The slight discrepancy in the absolute position of the step is due to our systematic uncertainty in the conversion from current in the pinch coil to field. The same theoretical model gives a mean energy in the transverse motion

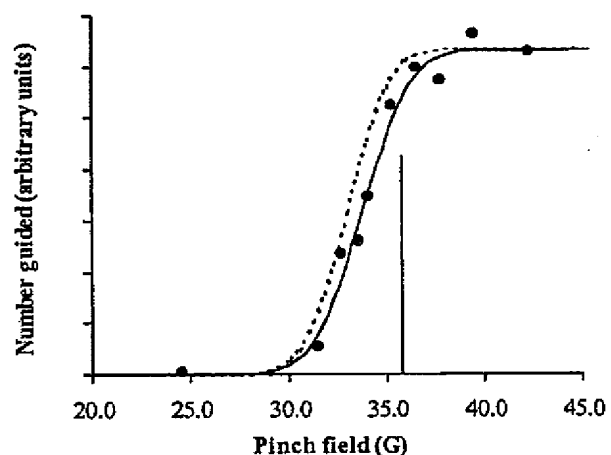


FIG. 3. Reflected atom signal versus magnetic field in the pinch coil. Points: experimental data. Solid line: simple empirical fit described in text. Dashed line: numerical model. Vertical line: mgh/μ_B .

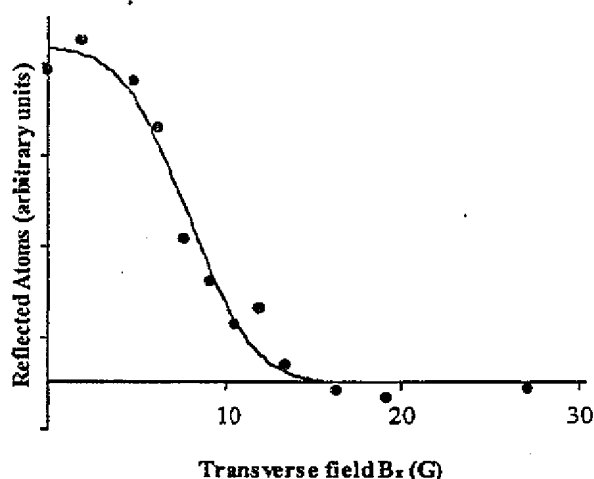


FIG. 4. When a transverse magnetic field is applied, the number of guided atoms decreases because of loss to the wall. Dots: experiment. Line: simple theory described in text.

(divided by μ_B) of 9.6 G, with a standard deviation over the ensemble of 3.3 G. In order to make a direct measurement of this, we adiabatically add a transverse magnetic field B_x to the guide while the atoms are propagating in it. This translates the magnetic potential to the side, lowering the energy required for atoms to escape onto the wall by $\mu_B B_x$. Figure 4 shows how the number of atoms returning from the guide decreases. Fitting these points to the integral of a Gaussian distribution, shown by the solid line, we find a mean transverse energy of 9.9 G with a standard deviation of 3.0 G, in excellent agreement with the numerical model. Expressed as a temperature, this is 670 μ K, which is much larger than the initial 25 μ K temperature of the atom cloud because the atoms are adiabatically compressed by gravity in the funnel. Noting that the mean potential energy is 2/3 of this total (virial theorem for a linear potential) we deduce from the known field gradient that the radius of the atom cloud in the guide is 98 μ m.

In order to increase the distance over which the atoms propagate in the guide, we added a second pinch coil at the top, which is switched on once the atoms have entered to form a very long Ioffe trap. After holding them for any desired length of time, the upper coil is turned off and the atoms emerge to be recaptured in the MOT. The decay time determined in this way is typically 300 ms, depending on the state of the vacuum, and does not appear to be any shorter than the collisional loss lifetime measured for atoms in free flight in the chamber. This shows as predicted [14] that there is no appreciable thermal coupling to the room-temperature glass wall, even at distances of order 100 μ m. For a storage time of 300 ms the atoms propagate a distance of ~ 10 cm along the guide.

The quantum mechanical eigenmodes of this guide [13] are characterized by an energy $(\hbar \mu_B B' / \sqrt{m})^{2/3}$, which scales with current and wire spacing as $I^{2/3} / a^{4/3}$. For our experimental parameters, this energy divided by Boltzmann's constant is ~ 1 μ K, indicating that many trans-

verse modes of the de Broglie waves are occupied in our present experiment. However, we have already demonstrated that similar currents can be passed through structures that are 20 times smaller, in which the mode spacings are ~ 50 μ K. In order to achieve good coupling to such a waveguide, it will be important to introduce some dissipation into the funnel or, alternatively, to use an atom source of smaller phase-space volume, such as a Bose-Einstein condensate.

In conclusion, we have demonstrated that cold atoms can be efficiently coupled into a miniature magnetic quadrupole waveguide where they propagate within a 100 μ m radius over tens of cm without appreciable loss other than background gas collisions. This is a prototype which shows the feasibility of miniature guides as a tool in the new field of integrated atom optics, leading to single-mode propagation of de Broglie waves and the possible preparation of 1D atom clouds.

We thank Malcom Boshier for many valuable discussions, and Per Seltborg and Sotiria Arabatzoglou for technical contributions. This work was supported by grants from EPSRC (U.K.), the British Council, the Royal Society, and the European Union.

*Present address: Department of Physics, Durham University, South Road, Durham DH1 3LE, United Kingdom.

†Email address: e.a.hinds@sussex.ac.uk

- [1] J.P. Dowling and J. Gea-Banacloche, *Adv. At. Mol. Opt. Phys.* **37**, 1 (1996); V. Balykin, *Adv. At. Mol. Opt. Phys.* **41**, 181 (1999).
- [2] E.A. Hinds and I.G. Hughes, *J. Phys. D* **32**, R119 (1999).
- [3] Jabez J. McClelland, in *Handbook of Nanostructured Materials and Nanotechnology*, edited by H.S. Nalwa (Academic Press, San Diego, 1999).
- [4] *Atom Interferometry*, edited by P.R. Berman (Academic Press, Boston, 1997).
- [5] E.A. Hinds, M.G. Boshier, and I.G. Hughes, *Phys. Rev. Lett.* **80**, 645 (1998).
- [6] J. Schmiedmayer, *Eur. Phys. J. D* **4**, 57 (1998).
- [7] J.H. Thywissen, R.M. Westervelt, and M. Prentiss, *Phys. Rev. Lett.* **83**, 3762 (1999).
- [8] M. Olshanii, *Phys. Rev. Lett.* **81**, 938 (1998); H. Monien, M. Linn, and N. Elstner, *Phys. Rev. A* **58**, R3395 (1998).
- [9] M.J. Renn *et al.*, *Phys. Rev. Lett.* **75**, 3253 (1995); *Phys. Rev. A* **53**, R648 (1996); **55**, 3684 (1997); H. Ito *et al.*, *Appl. Phys. Lett.* **70**, 2496 (1997).
- [10] C.J. Myatt *et al.*, *Opt. Lett.* **21**, 290 (1996); A. Goepfert *et al.*, *Appl. Phys. B* **69**, 217 (1999).
- [11] J. Schmiedmayer, *Phys. Rev. A* **52**, R13 (1995); J. Denschlag, D. Cassettari, and J. Schmiedmayer, *Phys. Rev. Lett.* **82**, 2014 (1999).
- [12] While this manuscript was in preparation, we learned that atoms have also been guided in miniature magnetic guides constructed on a surface by lithography. Müller *et al.*, physics/9908031; Dekker *et al.*, physics/9908929.
- [13] E.A. Hinds and C.C. Eberlein, *Phys. Rev. A* (to be published).
- [14] C. Henkel and M. Wilkens, *Europhys. Lett.* **47**, 414 (1999).

Electrically Stimulated Light-Induced Second-Harmonic Generation in Glass: Evidence of Coherent Photoconductivity

P. G. Kazansky and V. Pruneri

Optoelectronics Research Centre, University of Southampton, Southampton SO17 1BJ, United Kingdom
(Received 1 November 1996)

A strong electrostatic field applied to glass is spatially modulated by intense light at frequencies ω and 2ω . The phenomenon is explained in terms of photoconductivity being dependent on the relative phase of the light fields at different frequencies. [S0031-9007(97)02913-X]

PACS numbers: 42.70.Cc, 42.50.Hz, 42.65.Ky, 42.81.Dp

Recently, the interference between different quantum processes has been the subject of considerable attention in many areas of physics. One of the reasons for this growing interest is that such kinds of interference open a prospect of a new degree of freedom in the control of physical processes—not only by the intensity or the polarization of light, but also by the phase of light. It was observed in the experiments on rubidium atoms [1] and photoemission from Sb-Cs photocathodes [2] that the interference between the one- and two-photon transition moments changes the angular distribution of the photoelectrons and excites a phase dependent current (coherent photocurrent). Recently, coherent photocurrent via quantum interference of electrons produced by one- and two-photon bound-to-free intersubband transitions was observed in AlGaAs/GaAs quantum well superlattices [3]. However, second-harmonic generation (SHG) via photo-induced spatially oscillating electrostatic fields in glass was probably the first observed phenomenon where coherent photocurrent was involved [4–6]. Indeed, SHG is forbidden in glass due to the inversion symmetry of the glass matrix. However, when a sample of glass or glass fiber (e.g., Ge-doped silica glass) is illuminated for some time (preparation time) with intense light containing frequencies at ω (pump) and 2ω (second-harmonic seeding) and afterwards the seeding is removed, it is still possible to observe light at frequency 2ω (second harmonic) generated in the glass [7]. In experiments on optical glass fibers strong amplification of a weak seeding radiation at frequency 2ω , generated inside a fiber as a result of magnetic dipole or quadrupole effects, is observed after launching only intense light at frequency ω [8]. In this phenomenon the coherent photocurrent, excited in glass as a result of interference between one-photon ionization by light at frequency 2ω and two-photon ionization by light at frequency ω , gives rise to a spatially oscillating electrostatic field E_g (photogalvanic field): $E_g = j_{\text{coh}}/\sigma$, where j_{coh} is the coherent photocurrent and σ is the photoconductivity. The amplitude of the photogalvanic field E_g in glass is typically $\sim 10^4$ – 10^5 V/cm and this field can induce the second-order nonlinear susceptibility ($\chi^{(2)}$), responsible for SHG, via the third-order susceptibility: $\chi^{(2)} = 3\chi^{(3)}E_g$. Assuming $\chi^{(3)} = 10^{-22}$ (m/V)² for silica glass, the magnitude of

$\chi^{(2)}$ is $\sim 10^{16}$ – 10^{15} m/V. It turns out that the $\chi^{(2)}$ periodicity can compensate for the phase velocity mismatch, thus making the SHG process efficient. In nonlinear optics the process that allows such compensation is known as quasi-phase-matching.

Unlike mixing between one- and two-photon processes, which leads to a modulation in the angular distribution of photoelectrons, it was shown in experiments on mixing between one- and three-photon processes in xenon gas [9], HCl molecular beam [10], and between five- and three-photon process in mercury vapor [11] that the total cross section of the ionization transition can be directly modulated by changing the relative phase between two light fields oscillating at different frequencies. However, to our knowledge, two interesting aspects of the phenomenon have not been yet investigated. First, experiments on quantum interference have been carried out only in centrosymmetric media although it was already widely discussed that in media without inversion symmetry the interference between one- and two-photon transitions induced by light at frequencies 2ω and ω can lead to a modulation of the total cross section for the overall transition [12]. Second, the modulation of the total cross section of ionizing transitions due to quantum interference (coherent photoconductivity) has been observed only in atomic systems. In this Letter we report the observation of *efficient* second-harmonic generation in glass subjected to a strong external electrostatic field. The spatial periodic modulation of the applied electric field, responsible for the second-harmonic signal, arises from the interaction of the intense light at frequencies ω and 2ω with glass, which has its inversion symmetry broken by the applied field. The process could represent the first evidence of coherent photoconductivity in glass.

Let us consider the interaction of light beams of frequencies ω and 2ω in glass when a strong dc electric field ($E_0 \gg E_g$) is applied. The probability of simultaneous ionization of the defect site by two photons at frequency ω and one photon at frequency 2ω in the presence of E_0 is given by

$$\begin{aligned}
 P &\sim |a_2 E_\omega E_\omega + b_2 E_0 E_{2\omega}|^2 \\
 &= |a_2|^2 I_\omega^2 + |b_2|^2 I_{2\omega}^2 E_0^2 \\
 &\quad + 2 \operatorname{Re}(a_2 b_2^* E_0 E_\omega E_\omega E_{2\omega}^*), \quad (1)
 \end{aligned}$$

where E_ω and $E_{2\omega}$ are the field amplitudes at frequency ω and 2ω , respectively, I_ω and $I_{2\omega}$ are the corresponding intensities, and a_2 and b_2 are two complex coefficients which determine the weight of the different processes in the probability P . All terms in this expression are even powers of the electric field regardless of the fact that they are uniform (first two terms) or modulated [being dependent on the relative phase of the fields at frequencies ω and 2ω (the last term)]. The modulated part of the probability leads to modulation of the total ionization cross section and hence to a corresponding modulation of the photoconductivity:

$$\sigma = \sigma_0 + \sigma_{\text{coh}}, \quad (2)$$

where

$$\sigma_0 \sim |a_2|^2 I_\omega^2 + |b_2|^2 I_{2\omega} E_0^2$$

is the uniform part of the photoconductivity and $\sigma_{\text{coh}} \sim 2 \text{Re}(a_2 b_2^* E_0 E_\omega E_{2\omega})$ is the part of the photoconductivity being dependent on the relative phase between E_ω and $E_{2\omega}$ (coherent photoconductivity). Therefore the coherent photoconductivity spatially oscillates with a period Λ determined by the refractive index mismatch between light waves at frequencies ω and 2ω :

$$\sigma_{\text{coh}} \sim \cos 2\pi z / \Lambda, \quad \Lambda = \lambda / 2(n_{2\omega} - n_\omega),$$

where λ is the wavelength in vacuum of the light at frequency ω and $n_{2\omega}$, and n_ω are the refractive indices at frequencies 2ω and ω , respectively. It should be pointed out that the process of quantum interference considered above is qualitatively different from the already observed process of quantum interference in glass without strong ($E_0 \gg E_g$) dc electric field applied [4–8]. In the latter case a modulation of the angular distribution of photoelectrons (*coherent photocurrent*) rather than a modulation of the total cross section of ionization (*coherent photoconductivity*) takes place.

In fact the coefficients a_2 and b_2 in the expression of the probability P can depend on the intensities of light at frequencies 2ω and ω : $a_2 = a_2(I_\omega^2, I_\omega^3, I_{2\omega})$, $b_2 = a_2(I_\omega^2, I_\omega^3, I_{2\omega})$ and this can result in even higher order nonlinear processes [5].

The Ohmic current ($j = \sigma E_0$) induced by the applied electric field separates photocarriers which accumulate at the boundaries of the illuminated region and screen the applied electric field E_0 . The resulting internal electric field inside the glass E_c , assuming intensities of light waves at frequencies 2ω and ω to be constant, evolves accordingly to

$$dE_c/dt = -E_c/\tau, \quad \tau = \epsilon/\sigma,$$

where τ is the dielectric relaxation time and ϵ is the dielectric constant of glass. An approximate solution for E_c in the limit $\sigma_{\text{coh}} \ll \sigma_0$, $\tau = \tau_0 = \epsilon/\sigma_0$ is

$$\begin{aligned} E_c &= \sigma_{\text{coh}}/\sigma_0 E_0 [1 - \exp(-t/\tau_0)] \\ &\quad \times \exp(-t/\tau_0) + E_0 \exp(-t/\tau_0) \\ &= E_c^{\text{coh}} + E_c^0, \end{aligned} \quad (3)$$

where E_c^{coh} and E_c^0 are the modulated and uniform parts of the internal dc electric field. The modulated part of the electric field, proportional to σ_{coh} , and the corresponding $\chi^{(2)}$ grating ($\chi^{(2)} = 3\chi^{(3)}E_c^{\text{coh}}$) are zero at the beginning ($t = 0$), reach maximum values at $t = \tau_0 \ln 2$, and finally decrease to zero in the steady state condition ($t = \infty$). The $\chi^{(2)}$ periodicity compensates exactly for the phase velocity mismatch (refractive index mismatch), thus making the second-harmonic generation process efficient [$I_{2\omega} \propto (\chi^{(2)})^2 I^2(I_\omega)^2$, where l is the interaction length]. In fact, the evolution of the dc electric field can be more complicated since the second-harmonic electromagnetic field and the $\chi^{(2)}$ grating, i.e., modulated dc electric field itself, can vary in time and along the sample. However, even in a more general case, Eq. (3) still provides a qualitative physical description (in particular at the beginning of the process and in the steady state condition). A more detailed mathematical analysis for the general case will be presented elsewhere.

In our experiments we used Ge-doped silica fibers with built-in capillaries on both sides of the core, suitable for introducing wire electrodes (Fig. 1). A typical fiber used in our experiments had a 0.32 numerical aperture, 3 μm core diameter, 165 μm outer diameter, 50 μm hole diameter, and 9 μm interhole spacing. Metal wires of 25 μm diameter were inserted into the fiber over length varying from 5 to 500 mm. A mode-locked (76 MHz repetition rate, 300 ps pulse duration) and Q -switched (1 kHz repetition rate, 300 ns envelope duration) Nd-YAG laser operating at 1064 nm was used as the pump source.

First, we launched only infrared light (pump) of ~ 12 mW average power (1 kW peak power) for ~ 1 h into the fiber, ~ 25 cm long. No SHG was observed in the fiber. Then we launched simultaneously the pump of ~ 12 mW average power and the SH seeding of ~ 40 μW average power, generated in a (KTiOPO₄) crystal. The SH seeding was removed after preparation of ~ 10 min and a SH signal (being generated in the fundamental LP₀₁ fiber mode) of ~ 20 μW average power was observed, corresponding to a conversion efficiency of $\sim 0.16\%$. This was confirmed by monitoring the growth of the SH signal in the fiber when the SH seeding was blocked for a short time during the preparation (Fig. 2). Our result is in good agreement with previous observations on photoinduced SHG in Ge-doped

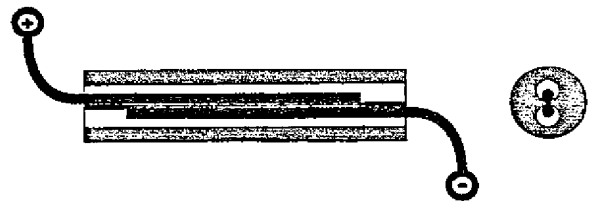


FIG. 1. Cross section of a Ge-doped silica fiber with internal electrodes. The fiber had a 0.32 numerical aperture, 3 μm core diameter, 165 μm outer diameter, 50 μm hole diameter, and 9 μm interhole spacing. Metal wires of 25 μm diameter were inserted into the fiber over length varying from 5 to 500 mm.

fibers [7] and may be explained by the appearance of a modulated second-order nonlinearity ($\chi^{(2)}$ grating) in the fiber as a result of the charge separation due to coherent photocurrent.

We then applied voltages up to 10 kV (corresponding to electrical fields $\sim 10^7$ V/cm, which are probably among the highest values ever applied to glass materials) across the electrodes inside the fiber and launched into the fiber (25 cm long) IR pump light of ~ 1 kW peak power. The length of the region over which the electric field had been applied (electrode superposition) was ~ 20 cm long. For applied voltages greater than ~ 2 kV a strong increase of weak electric-field-induced second-harmonic (EFISH) signal of ~ 10 nW (i.e., generated immediately after the electric field was applied) was observed (Fig. 2). In fact the SH signal (being generated in the fundamental LP_{01} mode) grows rapidly, within a 1 min time scale, reaching the maximum value of ~ 250 μ W average power and then slowly decreases (Fig. 2). After this first growth and decrease an interesting "echo" behavior was observed when the voltage was repeatedly switched off and on (Fig. 3). After disconnecting the voltage, the SH signal rapidly drops, remaining zero for a short time period, then increases, reaching almost 60% of the maximum value when the voltage was applied and finally slowly decreases again (Fig. 3). During these experiments we achieved conversion efficiencies as high as $\sim 2\%$ for a peak pump power of ~ 1 kW, which is ~ 10 times higher than in our experiments carried out without applying an external electric field. We detected a ~ 4 times smaller SH signal and ~ 2

times smaller growth rate in a fiber with electrode superposition ~ 10 cm long, thus two times shorter than in the previous fiber used.

We excluded a simple explanation of this phenomenon by the EFISH seeding of the $\chi^{(2)}$ grating in a fiber on the basis of two experimental observations. First, we observed that the second-harmonic growth took place only in the region where the electric field was applied (where the electrodes superposed) and the SH output was quadratic dependent on the length of this region. Second, no SHG signal was observed in any of the used fibers after preparation for more than 1 h with a weak external SH seeding of the same and even an order of magnitude higher level of power compared to the EFISH maximum signal. The maximum SH signal and the time, necessary to reach half of the maximum, when the voltage is switched on and switched off (Fig. 4), clearly depend on the applied voltage: The maximum SH signal increases with the applied voltage whereas the half-growth time decreases with the applied voltage.

The high conversion efficiency measured in our experiments and the observed quadratic dependence of the SHG efficiency on the fiber length represent clear evidences of quasi-phase-matched SHG due to the presence of a $\chi^{(2)}$ grating in the fiber. Moreover, the enhancement of SHG in glass due to a strong applied electric field ($\sim 5.5 \times 10^6$ V/cm) was confirmed by experimental observation that the amplitude of the $\chi^{(2)}$ grating increases at least ~ 3 times (corresponding to an increase of conversion efficiency ~ 10 times) compared to the experimental situation where no electric field is applied to the fiber. From our measurements we can also estimate the amplitude of the second-order susceptibility $\chi^{(2)} \approx 10^{-14}$ m/V, which corresponds to a modulation of $\sim 8\%$ of the applied electric

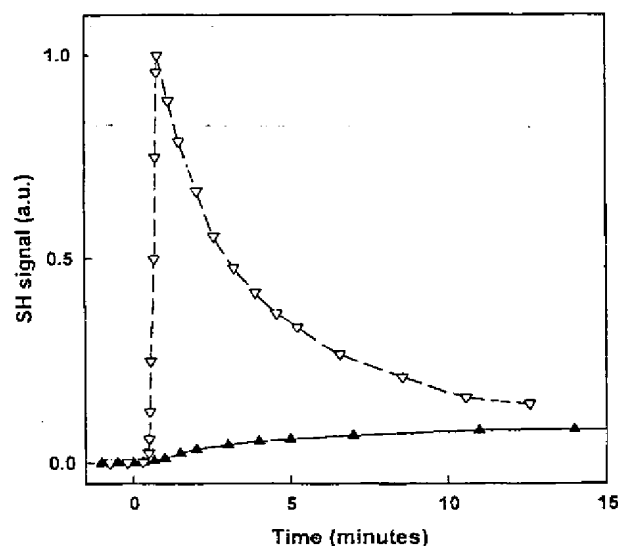


FIG. 2. Time dependence of a SH signal in a fiber with external SH seeding of ~ 40 μ W average power (opened triangles). The seeding was launched at $t = 0$. The SH growth was monitored by blocking the SH seeding. Time dependence of a SH signal in a fiber with applied voltage of 5 kV (filled triangles). The voltage was switched on at $t = 0$. The length of the fiber is ~ 25 cm and the superposition of the electrodes is ~ 20 cm. Average pump power is ~ 12 mW.

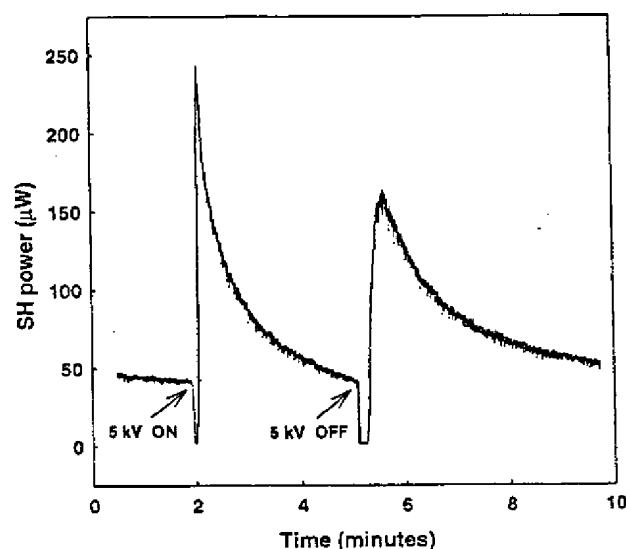


FIG. 3. Time dependence of a SH signal in a fiber when an applied voltage of 5 kV was repeatedly switched on and off. The instants when the voltage is on and off are shown by arrows.

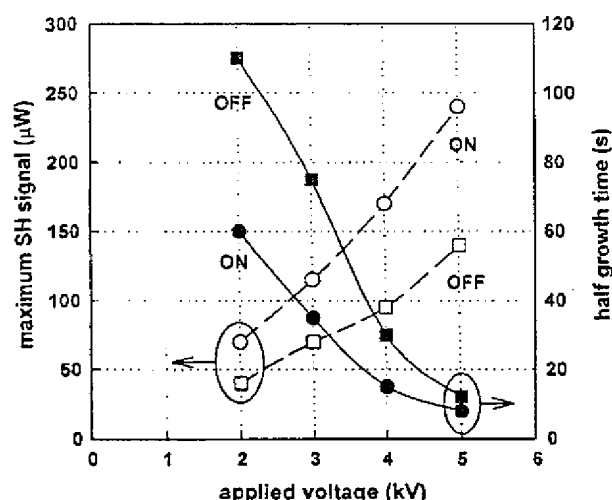


FIG. 4. Dependencies of the maximum SH signal and the time necessary to reach half of this signal on applied voltage when the voltage is switched on and off, respectively.

field. The possibility of a $\chi^{(2)}$ grating due to the interference between different fiber modes at the same frequency of light [13] was excluded since both the SH and the pump signals propagated in the fundamental LP_{01} mode.

Our experimental results can be qualitatively interpreted in light of the mechanism presented above, i.e., on the basis of photoconductivity being dependent on the relative phase between interacting waves at frequencies ω and 2ω , which provides quasi-phase-matching for the SHG. More important this model is consistent with the increase in conversion efficiency with the applied voltage and is also in good agreement with the experimental time dependence of the SH signal growth to a maximum value followed by a gradual decay. It is possible to estimate from (2), assuming $a_2 = b_2$, and using the experimental values for the electric fields ($E_0 = 5.5 \times 10^6$ V/cm, $|E_\omega| = 3.2 \times 10^6$ V/cm, $|E_{2\omega}| = 4.5 \times 10^5$ V/cm), the theoretical ratio $\sigma_{coh}/\sigma_0 \approx 2E_0|E_\omega|^2|E_{2\omega}|/(|E_\omega|^4 + |E_{2\omega}|^2E_0^2) \approx 0.4$. Experimental estimation of the ratio σ_{coh}/σ_0 can be obtained from (3): $\sigma_{coh}/\sigma_0 \approx 4E_m^{coh}/E_0$, where E_m^{coh} is the maximum amplitude of the modulated dc electric field. Using experimentally obtained $E_m^{coh}/E_0 \approx 0.08$, the experimental ratio $(\sigma_{coh}/\sigma_0)_{exp} \approx 0.3$ is in good agreement with the theoretical prediction. Moreover, an interesting feature in the time dependence of the SH signal—the origin of an unexpected growth (echo) of the SH signal after switching off the voltage (Fig. 3)—can be explained. Indeed, as follows from Eq. (3) in steady state conditions the internal electric field E_c is zero, which means that the applied dc electric field E_0 is locally compensated by the electric field E_s due to the screening charges,

accumulated at the boundaries of the illuminated region: $E_c = E_0 + E_s = 0$, $E_0 = -E_s$. After switching off the voltage ($E_0 = 0$) the internal electric field rapidly increases almost to its initial value $E_c = E_s = -E_0$. This rapid increase induces in the glass, due to the dc Kerr effect, a change in the phase mismatch between pump and SH waves which cannot be compensated any longer by the remaining weak $\chi^{(2)}$ grating of a period given by the previous phase mismatch (before switching off the voltage). The lack of quasi-phase-matching makes the SH signal drop quickly to zero. However, due to the fact that the internal electric field increases almost to its initial value (with opposite polarity) a new quasi-phase-matching grating (with a new period given by the new phase mismatch) will start growing and the process of electrically stimulated growth of $\chi^{(2)}$ grating via coherent photoconductivity repeats itself for a second time.

In conclusion we observed electrically stimulated light-induced second-harmonic generation in glass due to the modulation of a strong applied electrostatic field induced by light at frequencies ω and 2ω . This phenomenon in glass is interpreted as the first evidence of photoconductivity being dependent on the relative phase between light waves of different frequencies.

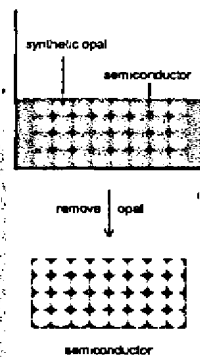
We thank L. Dong for fabricating the fibers used in the experiments.

- [1] Y. Y. Yin, C. Chen, D. S. Elliot, and A. V. Smith, *Phys. Rev. Lett.* **69**, 2353 (1992).
- [2] N. B. Baranova, A. N. Chudinov, A. A. Shulginov, and B. Ya. Zel'dovich, *Opt. Lett.* **16**, 1346 (1991).
- [3] E. Dupont, P. B. Corkum, H. C. Liu, M. Buchanan, and Z. R. Wasilevski, *Phys. Rev. Lett.* **74**, 3596 (1995).
- [4] E. M. Dianov, P. G. Kazansky, and D. Yu. Stepanov, *Sov. J. Quantum Electron.* **19**, 575 (1989).
- [5] D. Z. Anderson, V. Mizrahi, and J. E. Sipe, *Opt. Lett.* **16**, 796 (1991).
- [6] V. Dominic and J. Feinberg, *Phys. Rev. Lett.* **71**, 3446 (1993).
- [7] R. H. Stolen and H. W. K. Tom, *Opt. Lett.* **12**, 585 (1987).
- [8] U. Osterberg and W. Margulis, *Opt. Lett.* **11**, 516 (1986).
- [9] J. C. Miller, R. N. Compton, M. G. Payne, and W. R. Garrett, *Phys. Rev. Lett.* **45**, 114 (1980).
- [10] S. M. Park, S. P. Lu, and R. J. Gordon, *J. Chem. Phys.* **94**, 8622 (1991).
- [11] C. Chen, Y. Y. Yin, and D. S. Elliot, *Phys. Rev. Lett.* **64**, 507 (1990).
- [12] R. J. Glauber, in *Quantum Optics*, edited by R. J. Glauber, Proceedings of the E. Fermi International School in Physics Vol. 62 (Academic Press, New York, London, 1969).
- [13] M. E. Fermann, L. Li, M. C. Farries, L. J. Poyntz-Wright, and L. Dong, *Opt. Lett.* **14**, 748 (1989).

Chemical Approaches to Three-Dimensional Semiconductor Photonic Crystals

By David J. Norris* and Yurii A. Vlasov

We review recent efforts to make three-dimensional semiconductor photonic crystals using self-assembly techniques. These approaches, which utilize a synthetic opal as a template to shape the semiconductor material (see Figure), provide a simple and inexpensive alternative to lithographic methods. Since the resulting structures can, in principle, have a complete photonic bandgap – a property that would allow ultimate control over the flow of light – these materials may have serious implications for modern photonics.



1. Introduction

As exemplified by this special issue, many materials that are periodically structured on a micrometer length scale can now be fabricated with chemical assembly. While many forces are driving research in this area, one important motivation is to obtain optical photonic crystals, materials that are periodic on an optical length scale.^[1] When this periodicity is three-dimensional (3D), these structures have potential for novel optical properties. The most striking is the possibility of obtaining a complete photonic bandgap, a range of energy for which the photon cannot propagate in any direction inside the structure.^[2,3] With this property, 3D photonic crystals would allow us to inhibit unwanted spontaneous emission and manipulate the flow of light. Thus, these materials could have serious implications for modern photonics.^[4]

Unfortunately, a thorough experimental investigation of these implications has been hindered by the difficulty in making 3D photonic crystals that exhibit a complete photonic bandgap at optical wavelengths. The structure must be extremely porous (~80 % air), with a very specific sub-micrometer 3D periodicity (i.e., a specific lattice symmetry). Recently, state-of-the-art nanofabrication has succeeded in making the appropriate structures with a bandgap at 1.5 μm .^[5,6] However, in parallel to these efforts, chemical assembly has also been studied as an alternate route to photonic crystals. This has been stimulated by its simplicity, its ability to yield structures that are three-dimensionally periodic over

macroscopic length scales, and its potential to be much less expensive than traditional nanofabrication.

One approach has been to use sub-micrometer colloidal spheres (silica or polymer), which can be induced to spontaneously organize on a crystalline lattice. In nature, this process leads to gemstone opals.^[7,8] In analogy, sub-micrometer spheres assembled in the laboratory are sometimes referred to as synthetic opals.^[9] Although these structures are (by definition) photonic crystals, they do not have a complete photonic bandgap (since, e.g., the final porosity is too small). However, by using the opal as a template a much more interesting photonic crystal can be made—the so-called inverted opal. This is achieved by filling the interstitial spaces between the spheres with another material and then selectively removing the spheres by chemical etching or calcination. The final structure, which is a replica of the original opal, consists of air spheres arranged on a face-centered cubic (fcc) lattice. Using this simple approach, inverted opals from a variety of materials have been made, as shown by many recent reports^[10–27] and reviews.^[28–31] These results are important since theory predicts that inverted opals can have a complete photonic bandgap at optical wavelengths.^[32,33] The bandgap arises since this structure automatically has the appropriate porosity, lattice spacing, and lattice symmetry. On the other hand, the bandgap will occur only if we can utilize a material with a refractive index >2.8 .

Unfortunately, this last requirement has proven extremely challenging to satisfy, since few materials simultaneously have a high refractive index and negligible absorption at optical wavelengths. However, as shown in Table 1, one suitable class of materials is conventional semiconductors. At wavelengths longer than the absorption edge (or electronic bandgap), a semiconductor has both a high refractive index and low absorption. In addition, these materials can have other very useful electrical

[*] Dr. D. J. Norris, Dr. Yu. A. Vlasov
NEC Research Institute
4 Independence Way
Princeton, NJ 08540 (USA)
E-mail: dnorris@research.nj.nec.com

Table 1. Key parameters for several semiconductors that can be used to make photonic crystals. To obtain a complete photonic bandgap, the semiconductor must not only have a high refractive index, but also be transparent. Thus, each material is limited to wavelengths longer than its absorption edge. The refractive index is quoted at the onset of the transparency region, where the absorption coefficient becomes $<1 \text{ cm}^{-1}$. Both the ordinary and extraordinary indices are listed for uniaxial semiconductors. Data are compiled from the *Handbook of Optical Constants of Solids* [56] and *Properties of Optical and Laser Related Materials* [57].

Semiconductor	Index of refraction (at specified wavelength)	Absorption edge (at 300 K)
CdS	2.46/2.45 (0.65 μm)	0.50 μm
GaP	3.42 (0.56 μm)	0.55 μm
Se	2.82/3.64 (1.0 μm)	0.67 μm
CdSe	2.75/2.77 (0.75 μm)	0.71 μm
GaAs	3.54 (0.95 μm)	0.87 μm
InP	3.33 (1.0 μm)	0.97 μm
Si	3.53 (1.1 μm)	1.10 μm
Ge	4.12 (2.0 μm)	1.87 μm
Te	4.93/6.37 (4.0 μm)	3.49 μm

and optical properties. For example, modern integrated electronics is driven by manipulating the electrical conductivity of silicon. Similarly, optical telecommunications is based upon solid-state lasers made from direct bandgap semiconductors, such as GaAs, which can efficiently convert electrons to photons. Thus, not only can semiconductor photonic crystals exhibit a complete photonic bandgap, but they also have potential to be integrated into current optoelectronic technology.

Here, we review recent efforts to use chemical approaches to move toward this goal.^[34] Using a variety of infiltration methods, several groups have succeeded in making inverted opals from high-refractive-index semiconductors.^[24–27] Since these structures can, in principle, satisfy all the requirements

necessary to obtain a complete photonic bandgap at optical wavelengths, they provide the first opportunity to explore the existence of the bandgap in chemically assembled photonic crystals. Thus, they represent an important milestone in photonic crystal research.

2. Early Work

Almost immediately after the realization that synthetic opals could act as interesting photonic crystals,^[35] researchers began attempts to fill their pores with semiconductors. While the earliest efforts used vapor phase syntheses to grow semiconductor particles inside the opal, e.g., CdS^[35,36] or InP,^[37,38] liquid phase syntheses have also been used.^[39–41] These efforts were motivated by a need not only to increase the refractive index of the photonic crystal, but also to obtain a luminescent material with which phenomena, such as the modification of spontaneous emission^[39–41] or optical gain enhancement,^[42] could be studied. In parallel to these optical studies, opals were also filled with semiconductors, such as GaAs and Te, to probe the influence of periodic structure on thermal and electrical conductivity.^[43,44]

However, in most of these early attempts, the pores of the opal were only partially filled. Furthermore, since small clusters of nanoparticles often grew inside the opal, the filling was inhomogeneous. While such nanoparticles can be advantageous for utilizing quantum confinement effects in luminescence,^[35,36,40,42] it does not allow inverted opals to be formed.



David Norris received his B.S. in chemistry from the University of Chicago in 1990. He then pursued his doctorate in physical chemistry at the Massachusetts Institute of Technology, where he investigated the optical properties of nanometer-scale semiconductor particles with Prof. Mouni Bawendi. After receiving his Ph.D. in 1995, he then studied single-molecule spectroscopy with Prof. W. E. Moerner as a postdoctoral fellow at the University of California, San Diego. In 1997, David joined the NEC Research Institute in Princeton, New Jersey, where he currently heads a research group. His research focuses on developing and investigating novel materials, including photonic crystals and other nano-structured materials.



Yurii Vlasov graduated from the University of St. Petersburg, Russia in 1988 with a B.S. in physics. Since then, he has been working as a research scientist at the Ioffe Institute of Physics and Technology, St. Petersburg, where he obtained his Ph.D. in 1994 on optical properties of semiconductor heterostructures under the supervision of Prof. Alexander Kaplyanskii. He then began a project to study the optics of self-organized photonic crystals, which was continued during his postdoctoral fellowship at the Strasbourg Institute of Physics and Chemistry of Materials (IPCMS) with Prof. Bernd Honerlage. Since 1998 Yuri has been working at the NEC Research Institute in Princeton, NJ, first as a postdoctoral scientist and later as a staff scientist with Dr. David Norris on semiconductor photonic crystals. He also continues to hold a research scientist position at the Ioffe Institute in Russia. His research interests span from fabrication of novel nanophotonic materials to optics of strong light localization and quantum optical phenomena in resonant media.

As soon as the template is removed, the inhomogeneous semiconductor structure collapses.

In general, these difficulties with filling arise since the interstitial voids of the opal are connected by small channels. Thus, the challenge is to transport and deposit material into the voids without obstructing these channels. This must be achieved while satisfying two requirements. First, to obtain an inverted opal, the voids must be homogeneously filled, i.e., the infill material must be contiguous. Second, to obtain a complete photonic bandgap, the voids must be sufficiently filled with high refractive index material. The optimal bandgap has been predicted to occur when the filling is ~80%.^[33]

In one of the early attempts, complete filling was obtained by using Te, a narrow-gap semiconductor.^[44] Due to its low melting temperature, the semiconductor could be melted and forced under high pressure into the voids of the opal. Although these structures were made for conductivity measurements, Te inverted opals could also have a complete photonic bandgap at infrared wavelengths $>4\ \mu\text{m}$ (see Table 1). Unfortunately, this simple approach does not work for wider-gap semiconductors, which all have melting temperatures that are too high for an opal to survive.

3. Recent Advances

To overcome these difficulties, four new approaches have recently been reported.^[24–27] Below we briefly outline and discuss these methods. Since each approach begins with a synthetic opal as a template and then ends by selectively removing it, we concentrate on the intermediate steps required for filling with semiconductor material.

3.1. Nanocrystal Sintering

Due to well-developed chemical syntheses for semiconductor nanocrystals,^[45] nanometer-scale colloidal particles provide a convenient method of transporting semiconductor material into the template. Nanocrystals, which are typically $\sim 10\times$ smaller than the smallest channel of the opal, can be synthesized before filling, dissolved in a solvent, and then deposited in the voids. In fact, such particles were used to dope synthetic opals in early luminescence studies.^[40] However, it has also been demonstrated, as in Figure 1, how they can be used to obtain inverted opals.^[24] Since nanocrystals that are nearly monodisperse can be assembled into densely packed solids by slowly evaporating away the solvent,^[46] this process was used in the presence of a synthetic opal to completely fill its pores with semiconductor nanoparticles. Once the template was filled, the nanocrystals were then sintered inside the opal at moderate temperatures (750°C) due to the reduction of the melting temperature in nanometer-scale particles.^[47] The result, demonstrated for CdSe,^[24] is an inverted opal made from a bulk semiconductor.

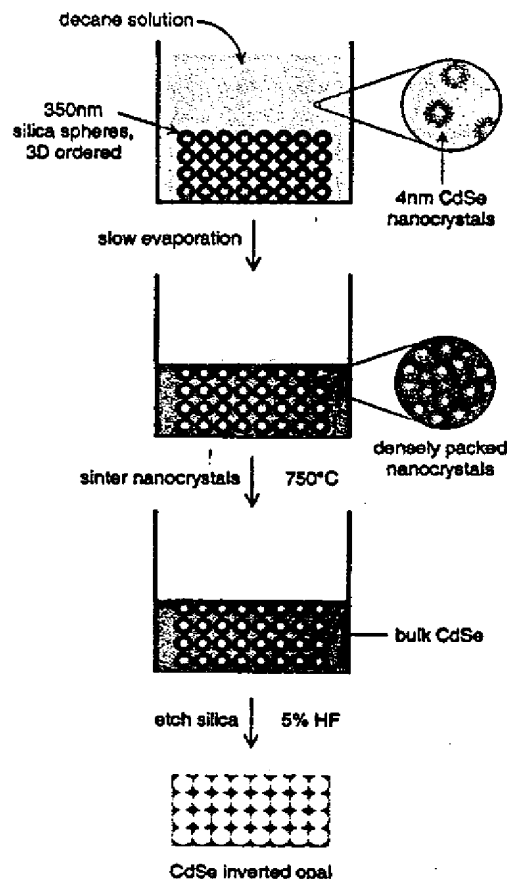


Fig. 1. Procedure for obtaining CdSe inverted opals by nanocrystal sintering, as discussed in [24].

One of the advantages of the nanocrystal-sintering approach is that it is completely general to any of the materials that can be synthesized as colloidal nanoparticles. For example, Ag and Au inverted opals have already been made with this approach.^[20,28,48] In the future, it should also be possible to adapt this method to Si^[49] or GaP^[50] nanocrystals. Thus, many high-refractive-index inverted opals should be obtainable. However, a potential problem is that, although the template is initially completely filled with nanocrystals, they are condensed during sintering. Thus, similar to the sol-gel methods that produce metal-oxide inverted opals, this approach can have difficulties in obtaining infiltration of the high refractive index material greater than 50%. Although methods exist which may solve this problem, they have yet to be demonstrated.

3.2. Electrodeposition

As shown in Figure 2, a second approach is to utilize chemical electrodeposition. By placing the template directly on the cathode of an electrochemical cell, II–VI semiconductors such as CdSe have been deposited in the interstitial voids of an opal.^[25] An exciting feature of the deposition is

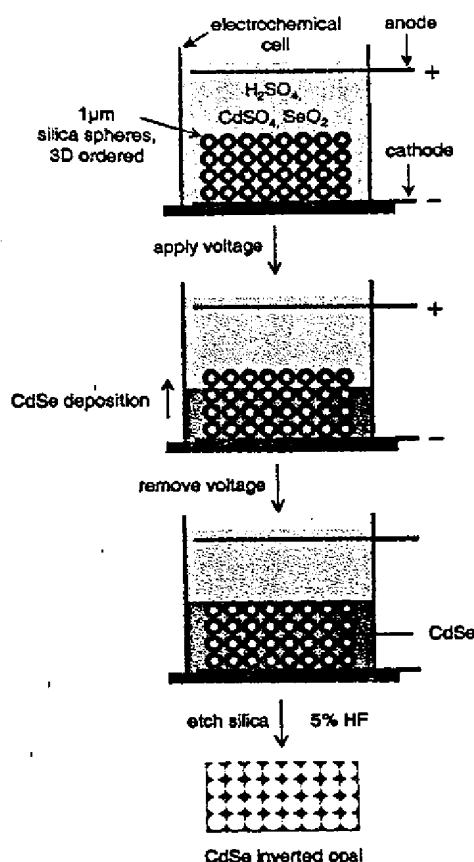


Fig. 2. Procedure for obtaining CdSe inverted opals using electrodeposition, as discussed in [25].

that it proceeds sequentially from the bottom to the top of the template. Thus, an important advantage of this approach is that the voids can be completely filled. Consequently, an exact replica of the initial opal template can be obtained. However, a potential difficulty is that, while many materials can be electrodeposited, it is not yet clear whether the bottom-to-top growth, crucial to the success of this method, is possible in other high-refractive-index semiconductors, besides CdS and CdSe. This problem, which requires further study, must be overcome in order to obtain a complete photonic bandgap at visible or near visible wavelengths with this approach.

Currently, both the nanocrystal-sintering and electrodeposition methods have succeeded in making inverted opals from II-VI semiconductors that, according to Table 1, have refractive indexes that can be very close to, but below, the threshold for a photonic bandgap. While II-VI compounds are direct-gap semiconductors, which may be useful for studying the strong modification of luminescence, gain, and optical nonlinearities by the photonic crystal, it is necessary to further increase the refractive index to achieve a complete photonic bandgap. Efforts to extend these methods to higher refractive index semiconductors, such as GaP, are in progress.

3.3. Chemical Vapor Deposition

A third approach, which has already succeeded in going beyond II-VI semiconductors, is chemical vapor deposition (CVD). While it had been commonly assumed, after early attempts failed to achieve homogeneous filling, that CVD was inappropriate for obtaining inverted opals, a recent success with silicon has shown this to be incorrect.^[26,31] Following the scheme in Figure 3, disilane gas has been used as a precursor to uniformly deposit silicon nanoclusters throughout the interior surfaces of an opal. Subsequently, these nanoclusters were annealed at moderate temperatures (600 °C) to obtain polycrystalline Si. A remarkable feature of this method is that, unlike previous attempts to use CVD, the resulting infill is extremely homogeneous. Furthermore, in the initial report,^[26,31] it was claimed that the amount of filling was not only controllable but could be as high as 100 %. Although these findings need to be further quantified, the implications of this approach are clear. As shown in Table 1, the resulting inverted opals can have an extremely high refractive index, which may allow a complete photonic bandgap to be obtained (see Sec. 4). Thus, these materials have great potential for applications in telecommunications at near infrared wavelengths.

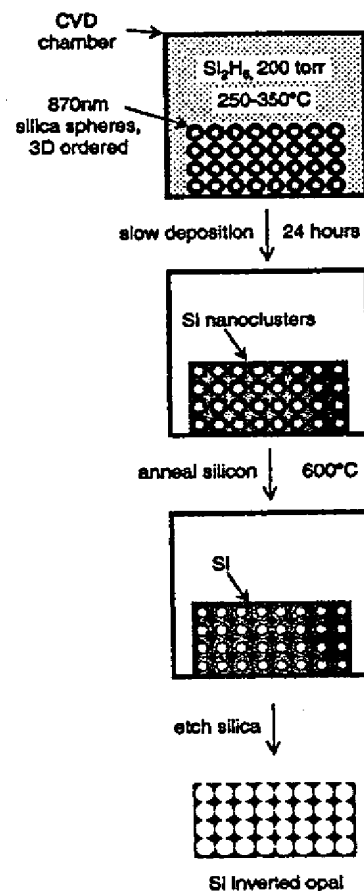


Fig. 3. Procedure for obtaining Si inverted opals using CVD, as discussed in [26].

However, due to the absorption of silicon, these structures are inappropriate for wavelengths shorter than 1.1 μm . Whether this technique can be extended to wider bandgap semiconductors, which would enable complete bandgaps at visible wavelengths, remains an open question. Certainly, the success of the CVD approach with Si suggests that it should be reconsidered as a general method for infiltration.

3.4. Oxide Reduction

For inverted opals with a refractive index even higher than silicon, the fourth approach^[27] has been used to yield germanium structures. As outlined in Figure 4, this method begins by forming germanium oxide inside the template by hydrolyzing tetramethoxygermane in situ. Ge^0 is subsequently obtained by reducing the oxide with H_2 at 550 °C. Significant infiltration follows if these steps are repeated several times. Similar to the silicon approach, the success of this method is significant since germanium has a refractive index that is well above the theoretical threshold for formation of a complete photonic bandgap. Thus, it may provide a material where the existence of the bandgap in self-assembled photonic crystals

can be probed for the first time (see Sec. 4). However, due to the absorption edge of Ge, these structures can only achieve a photonic bandgap above 2 μm . Nonetheless, they might have many important applications.

While the CVD and oxide reduction methods have successfully produced high-refractive-index inverted opals, the photonic bandgap is limited to infrared wavelengths. This follows as a general consequence of Moss' rule for semiconductors, which states that the wavelength of the absorption edge is proportional to the fourth power of the refractive index.^[51] As shown in Table 1, this tendency makes it difficult to satisfy the index requirement for a complete photonic bandgap at visible wavelengths. However, it would be very desirable to extend the above methods to GaP, which is an obvious candidate for this goal.

4. Future Directions

In the quest to obtain a complete photonic bandgap, most of the work to date has focused on fabricating three-dimensionally periodic semiconductor structures that have the necessary symmetry, porosity, lattice spacing, and refractive index. While, of course, further work on these issues needs to be done, this focus has clearly led to significant progress, as demonstrated by the materials outlined above. Indeed, several of these structures may satisfy all the requirements necessary to exhibit a complete bandgap. Thus, with these materials now in hand, one might imagine that the existence of the bandgap will be simple to verify. Unfortunately, this is not the case. While several factors complicate the analysis of the bandgap,^[52] the most significant is the role of disorder in these materials. For example, it is not known whether the imperfections present in current inverted opals are small enough to observe the complete photonic bandgap. In chemical assembly, such "residual" disorder can arise from several different sources. First, defects in the initial opal template, such as stacking faults^[53] or small deviations in sphere size, are directly imprinted in the final inverted structure. While great strides have been made in reducing these defects, it has been predicted that even a 2 % deviation in sphere size can destroy the complete bandgap in inverted opals.^[54] Second, significant disorder can be caused by the infiltration process itself. Even the best samples to date have variations in the amount of filling from point to point in the lattice. Since these inhomogeneities must be much smaller than the optical wavelength, the elimination of residual disorder remains a challenge, even with the above methods.

Thus, now that high-refractive-index, self-assembled photonic crystals have been made, only half the problem has been solved. It is necessary to experimentally explore the photonic bandgap properties of these new structures and obtain a better understanding of the underlying physics. We have recently argued^[52] that this can be achieved by combining recently developed optical techniques^[55] with further refinements in the materials. With this approach, it should be possible to address questions such as the influence of disorder on photon-

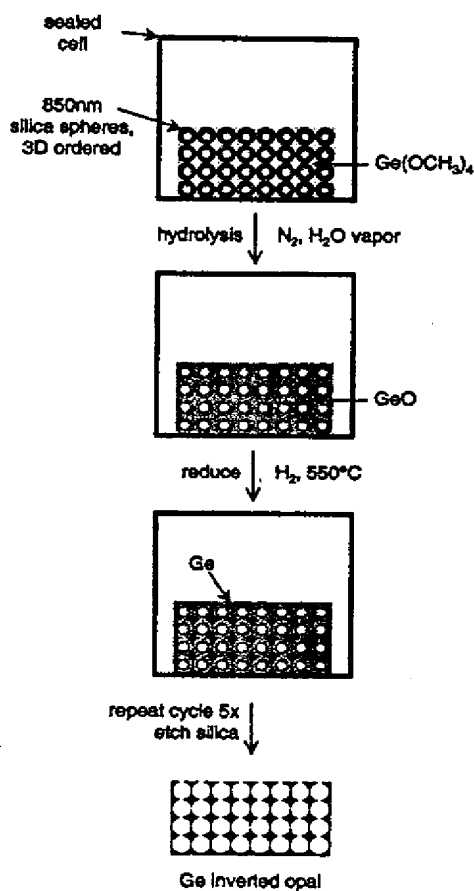


Fig. 4. Procedure for obtaining Ge inverted opals using oxide reduction, as discussed in [27].

ic properties. More importantly, we should finally be able to answer the crucial question of whether a complete photonic bandgap can exist in self-assembled photonic crystals.

Received: October 5, 2000

- [1] a) J. D. Joannopoulos, P. R. Villeneuve, S. Fan, *Nature* 1997, 386, 143.
b) J. D. Joannopoulos, R. D. Meade, J. N. Winn, *Photonic Crystals*, Princeton Press, Princeton, NJ 1995.
- [2] E. Yablonovitch, *Phys. Rev. Lett.* 1987, 58, 2059.
- [3] S. John, *Phys. Rev. Lett.* 1987, 58, 2486.
- [4] For recent reviews, see articles in *Photonic Bandgap Materials* (Ed: C. M. Soukoulis), Kluwer, Dordrecht, The Netherlands 1996 and *Photonic Crystals and Light Localization* (Ed: C. M. Soukoulis), Kluwer, Dordrecht, The Netherlands 2001, in press.
- [5] S. Y. Lin, J. G. Fleming, D. L. Hetherington, B. K. Smith, R. Biswas, K. M. Ho, M. M. Sigalas, W. Zubrzycki, S. R. Kurtz, J. But, *Nature* 1998, 394, 251.
- [6] S. Noda, K. Tomoda, N. Yamamoto, A. Chutinan, *Science* 2000, 289, 604.
- [7] J. V. Sanders, *Nature* 1964, 204, 1151.
- [8] J. V. Sanders, *Acta Cryst. A* 1968, 24, 427.
- [9] Here, we focus on synthetic opals, where it is assumed that the colloidal spheres are close-packed. Charged colloids can also be crystallized in certain liquids to yield photonic crystals where the spheres are spaced by distances much larger than their diameter. For example, see the work of S. A. Asher et al. in this issue and elsewhere.
- [10] O. D. Velev, T. A. Jede, R. F. Lobo, A. M. Lenhoff, *Nature* 1997, 389, 447.
- [11] B. T. Holland, C. F. Blanford, A. Stein, *Science* 1998, 281, 538.
- [12] J. E. G. J. Wijnhoven, W. L. Vos, *Science* 1998, 281, 802.
- [13] G. Subramanian, K. Constant, R. Biswas, M. M. Sigalas, K.-M. Ho, *Appl. Phys. Lett.* 1999, 74, 3933.
- [14] G. Subramania, V. N. Manoharan, J. D. Thorne, D. J. Pine, *Adv. Mater.* 1999, 11, 1261.
- [15] A. A. Zakhidov, R. H. Baughman, Z. Iqbal, C. Cui, I. Khayrullin, S. O. Dantas, J. Marti, V. G. Ralchenko, *Science* 1998, 282, 897.
- [16] H. Kajii, Y. Kawagishi, H. Take, K. Yoshino, A. A. Zakhidov, R. H. Baughman, *J. Appl. Phys.* 2000, 88, 758.
- [17] S. H. Park, Y. Xia, *Adv. Mater.* 1998, 10, 1045.
- [18] P. Jiang, K. S. Hwang, D. M. Mittleman, J. F. Bertone, V. L. Colvin, *J. Am. Chem. Soc.* 1999, 121, 11630.
- [19] M. Deutsch, Yu. A. Vlasov, D. J. Norris, *Adv. Mater.* 2000, 12, 1176.
- [20] O. D. Velev, P. M. Tessier, A. M. Lenhoff, E. W. Kaler, *Nature* 1999, 401, 548.
- [21] P. Jiang, J. Cizeron, J. F. Bertone, V. L. Colvin, *J. Am. Chem. Soc.* 1999, 121, 7957.
- [22] J. E. G. J. Wijnhoven, S. J. M. Zevenhuizen, M. A. Hendriks, D. Vanmaekelbergh, J. J. Kelly, W. L. Vos, *Adv. Mater.* 2000, 12, 885.
- [23] N. Eradat, J. D. Huang, Z. V. Vardeny, A. A. Zakhidov, R. H. Baughman, in *Photonic Crystals and Light Localization* (Ed: C. M. Soukoulis), Kluwer, Dordrecht, The Netherlands 2001, in press.
- [24] Yu. A. Vlasov, N. Yao, D. J. Norris, *Adv. Mater.* 1999, 11, 165.
- [25] P. V. Braun, P. Wiltzius, *Nature* 1999, 402, 603.
- [26] A. Blanco, F. Chomski, S. Gratchak, M. Ibsate, S. John, S. W. Leonard, C. López, F. Meseguer, H. Míguez, J. P. Mondia, G. A. Ozin, O. Toader, H. M. v. Driel, *Nature* 2000, 405, 437.
- [27] H. Míguez, F. Meseguer, C. López, M. Holgado, G. Andreasen, A. Mifsud, V. Fornés, *Langmuir* 2000, 16, 4405.
- [28] O. D. Velev, E. W. Kaler, *Adv. Mater.* 2000, 12, 531.
- [29] Y. Xia, B. Gates, Y. Yin, Y. Lu, *Adv. Mater.* 2000, 12, 693.
- [30] K. M. Kułowski, P. Jiang, H. Vaswani, V. L. Colvin, *Adv. Mater.* 2000, 12, 833.
- [31] E. Chornski, G. A. Ozin, *Adv. Mater.* 2000, 12, 1071.
- [32] H. S. Sözüer, J. W. Haus, R. Inguva, *Phys. Rev. B* 1992, 45, 13962.
- [33] K. Busch, S. John, *Phys. Rev. E* 1998, 58, 3896.
- [34] Although titania (TiO₂) is a semiconductor for which interesting inverted opals have been made and studied (e.g., see [12–14]), these structures are not considered here, as they are treated elsewhere in this issue.
- [35] V. N. Astratov, V. N. Bogomolov, A. A. Kaplyanskii, A. V. Prokofiev, L. A. Samoilovich, S. M. Samoilovich, Yu. A. Vlasov, *Nuova Cimento D* 1995, 17, 1349.
- [36] Yu. A. Vlasov, V. N. Astratov, O. Z. Kurimov, A. A. Kaplyanskii, V. N. Bogomolov, A. V. Prokofiev, *Phys. Rev. B* 1997, 55, 13357.
- [37] S. G. Romanov, N. P. Johnson, A. V. Fokin, V. Y. Butko, H. M. Yates, M. E. Pemble, C. M. Sotomayor Torres, *Appl. Phys. Lett.* 1997, 70, 2091.
- [38] H. M. Yates, M. E. Pemble, H. Míguez, A. Blanco, C. López, F. Meseguer, L. Vázquez, *J. Cryst. Growth* 1998, 193, 9.
- [39] A. Blanco, C. López, R. Mayoral, H. Míguez, F. Meseguer, A. Mifsud, J. Herrero, *Appl. Phys. Lett.* 1998, 73, 1781.
- [40] S. V. Gaponenko, A. M. Kapitonov, V. N. Bogomolov, A. V. Prokofiev, A. Fychmüller, A. L. Roguch, *JETP Lett.* 1998, 68, 142.
- [41] S. G. Romanov, A. V. Fokin, R. M. D. L. Rue, *Appl. Phys. Lett.* 1999, 74, 1821.
- [42] Yu. A. Vlasov, K. Luterova, I. Pelant, B. Hönerlage, V. N. Astratov, *Appl. Phys. Lett.* 1997, 71, 1616.
- [43] V. N. Bogomolov, S. A. Kitorov, D. A. Kurdyukov, A. V. Prokofiev, S. M. Samoilovich, D. V. Smirnov, *JETP Lett.* 1995, 61, 753.
- [44] V. N. Bogomolov, L. M. Sorokin, D. A. Kurdyukov, T. M. Pavlova, J. L. Hutchison, *Phys. Solid State* 1997, 39, 1869.
- [45] C. B. Murray, D. J. Norris, M. G. Bawendi, *J. Am. Chem. Soc.* 1993, 115, 8706.
- [46] C. B. Murray, C. R. Kagan, M. G. Bawendi, *Science* 1995, 270, 1335.
- [47] A. N. Goldstein, C. M. Echer, A. P. Alivisatos, *Science* 1992, 256, 1425.
- [48] Yu. A. Vlasov, M. Deutsch, T. Thio, E. Dujardin, N. Yao, A. A. Sirenko, I. A. Akimov, D. J. Norris, *Abstracts of the Fall Meeting of the Materials Research Society* 1999, p. 134.
- [49] L. Brus, *J. Phys. Chem.* 1994, 98, 3575.
- [50] A. J. Nozik, O. I. Micic, *MRS Bull.* 1998, February, 24.
- [51] T. S. Moss, *Optical Properties of Semiconductors*, Butterworths, London 1959, p. 48.
- [52] D. J. Norris, Yu. A. Vlasov, in *Photonic Crystals and Light Localization* (Ed: C. M. Soukoulis), Kluwer, Dordrecht, The Netherlands 2001, in press.
- [53] Yu. A. Vlasov, V. N. Astratov, A. V. Baryshev, A. A. Kaplyanskii, O. Z. Kurimov, M. F. Limonov, *Phys. Rev. E* 2000, 61, 5784.
- [54] Z.-Y. Li, Z.-O. Zhang, *Phys. Rev. B* 2000, 62, 1516.
- [55] Yu. A. Vlasov, M. Deutsch, D. J. Norris, *Appl. Phys. Lett.* 2000, 76, 1627.
- [56] *Handbook of Optical Constants of Solids*, Vols. I and II (Ed: F. D. Palik), Academic, Boston, MA 1991.
- [57] *Properties of Optical and Laser Related Materials* (Ed: D. N. Nikogosyan), Wiley, New York 1997.

Enhancement of optical gain of semiconductors embedded in three-dimensional photonic crystals

Yu. A. Vlasov,^{a)} K. Luterova,^{b)} I. Pelant,^{b)} and B. Hönerlage

Institut de Physique et Chimie des Matériaux de Strasbourg, Groupe d'Optique Non Linéaire et d'Optoelectronique, UMR 46 CNRS-ULP-ECMP, 23 rue du Loess, 67037 Strasbourg Cedex, France

V. N. Astratov

A. F. Ioffe Physical Technical Institute, 26 Polytechnicheskaya, 194021 St. Petersburg, Russia

(Received 14 May 1997; accepted for publication 23 July 1997)

The three-dimensional photonic crystals used in this study were synthetic opals, composed of submicron silica spheres, close-packed in a face-centered cubic structure with a period of 200 nm, that exhibit photonic stopbands around 600 nm. We present measurements of the optical gain of CdS quantum dots (QDs) embedded inside the interstitials between the silica spheres. Unlike the usual gain spectra of CdS QDs in glass matrices, which display maximum gain at energies of the first quantum-confined transitions, for QDs embedded in photonic crystals the gain maximum is shifted toward the high-frequency edge of the photonic stopband (2.2 eV) far below the absorption edge of the semiconductor (2.5 eV). Studies of temperature, intensity, and orientation dependencies of the gain spectra allow one to ascribe the observed effect to gain enhancement caused by multiple coherent Bragg scattering of light in the periodic photonic crystal. © 1997 American Institute of Physics. [S0003-6951(97)04538-5]

In recent years a great attention has been paid to the fabrication and studies of artificial three-dimensional (3D) periodic dielectric structures whose periodicity matches the wavelength of electromagnetic waves.¹ Owing to this periodicity, the frequency-momentum dispersion relationship for photons is strongly modified in such *photonic crystals* and a photonic band gap (PBG) can develop in which the density of photonic states (DOS) is zero.² The emission spectra of an active medium placed within a photonic crystal should, therefore, be drastically altered.²⁻⁶ This may play an important role in low threshold microlasers based on photonic band gap engineering.

The fabrication of a 3D photonic crystal with a submicron lattice constant for operating in the visible spectral region, however, still remains a challenge. It was recently found that synthetic opals, composed of α -SiO₂ spheres, closely packed in a 3D face-centered-cubic (FCC) structure with a period of about 200 nm, possess photonic stopbands throughout the visible spectrum (400–600 nm).⁷⁻⁹ According to numerous theoretical calculations of the photonic band structure of opal-like FCC photonic lattices composed of spherical “atoms,”^{10,11} an absolute PBG with zero DOS between the lowest photonic zones is prohibited by symmetry. It is possible, however, to expel the propagating photonic modes along all but a few directions, thus creating a very large depletion of the photonic DOS—a “pseudogap.”^{13,10,11} It was shown recently that the pseudogap criterion could be met in opals by impregnating the interstitials between the silica spheres with a high refractive index semiconductor.⁹

Our synthetic opal samples were fabricated by three subsequent technological procedures: sol-gel synthesis of monodisperse (standard deviation less than 3%) suspension of silica spheres, sedimentation of the suspension into a solid

state ordered array, followed by thermal annealing. The exposure of the porous opal matrices to a vapor flow of Cd and S results in the formation of wurtzite CdS nanocrystals of about 6 nm mean diameter,^{7,9} that homogeneously fill all the empty voids between the spheres. Atomic force microscopy (AFM) reveals the hexagonal-type close packing of the silica spheres on the base surface of the platelet sample, characteristic of the (111) plane of a FCC lattice with a lattice constant of $a=260$ nm and volume fraction of the spheres $\beta=0.96$. This is consistent with previously obtained transmission electron microscopy (TEM) data.^{7,9}

A transmission spectrum of an opal/CdS sample, measured at normal incidence to the (111) face, is presented in Fig. 1A in a semilogarithmic scale. Besides the drastic decrease of transmission at short wavelengths above 480 nm, due to the absorption of light in the semiconductor nanocrystals, a large drop centered at 600 nm can also clearly be seen. It is ascribed to a photonic stopband at the L point on the photonic Brillouin zone (BZ).⁷⁻⁹

For high intensity excitation in our optical gain measurements, a XeCl excimer laser emitting ultraviolet light pulses (308.5 nm) of 20 ns duration at 5 Hz repetition rate is used. The optical gain is measured using the variable-stripe-length (VSL) method.¹² The laser beam is focused onto the (111) face of the sample in the form of a narrow rectangular stripe of about 20 μ m in width and a variable length D . The emitted light [i.e., amplified spontaneous emission (ASE)] is collected from the cleaved edge of the sample in the direction of the stripe, as shown in the inset of Fig. 2A.

Figure 1B shows a set of ASE spectra measured at 10 K in the stripe direction for a fixed stripe length of $D=150$ μ m for various excitation intensities. At low pumping rates the spectrum consists of a single broad band (band A) with its maximum at 500 nm and a very wide tail extending to longer wavelengths (see spectrum 1 in Fig. 1B). It can be seen (spectra 2–4) that an increase of the pumping intensity results in the appearance of a well-defined long-wavelength band centered at 570 nm (band B). This band exhibits rapid

^{a)}On leave from A. F. Ioffe Physical Technical Institute, 26 Polytechnicheskaya, 194021 St. Petersburg, Russia; electronic mail: vlasov@valholl.u-strasbg.fr

^{b)}Permanent address: Institute of Physics, Czech Academy of Sciences, 10 Cukrovnicka, 162 00 Prague, Czech Republic.

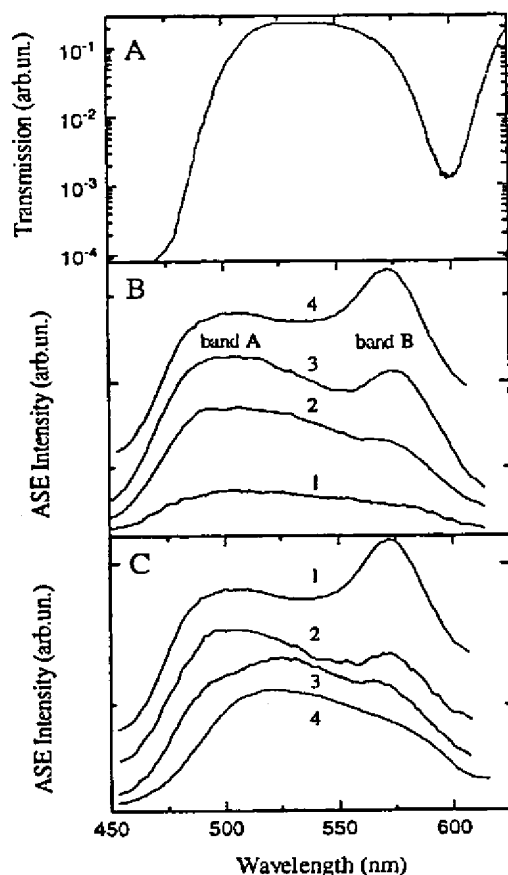


FIG. 1. (A) Transmission spectrum of an opal/CdS sample having the thickness of 100 μm taken at 10 K at a normal incidence to a (111) face. (B) Set of ASE spectra measured at 10 K with 150 μm stripe length oriented along the (211) direction as a function of excitation intensity: 1–0.25, 2–0.55, 3–0.77, and 4–1 MW/cm^2 . (C) Set of ASE spectra measured at 1 MW/cm^2 excitation intensity with 150 μm length stripe oriented along the (211) direction as a function of temperature: 1–10, 2–40, 3–80, and 4–300 K.

temperature quenching illustrated in Fig. 1C. These observations strongly contradict an assignment of the B band to a defect-related emission band usually observed in luminescence spectra of QD in glass.^{13–15} The latter is typically very broad (200 nm FWHM^{13–15}), and exhibits slower temperature quenching¹⁵ and slower growth with increasing pumping¹³ than the intrinsic near-band-edge luminescence band A. The band B cannot be assigned to the emission from the silica host itself, because luminescence spectra taken from the region of the sample, which was not exposed to the vapor flow during the semiconductor synthesis, are very weak and do not exhibit such structured luminescence bands. It can be supposed, therefore, that the B band originates from the same intrinsic states as band A, but the long-wavelength portion of their spontaneous emission is greatly amplified due to increased gain at these wavelengths.

In order to verify this hypothesis, the optical gain measurements were performed at various excitation intensities and for different temperatures. The ASE intensity I_{ASE} measured at 10 K as a function of the stripe length D for various excitation intensities is presented in Fig. 2. The $I_{\text{ASE}}(D)$ dependencies shown in Fig. 2A correspond to the light detection at the wavelength of 500 nm, i.e., at the maximum of

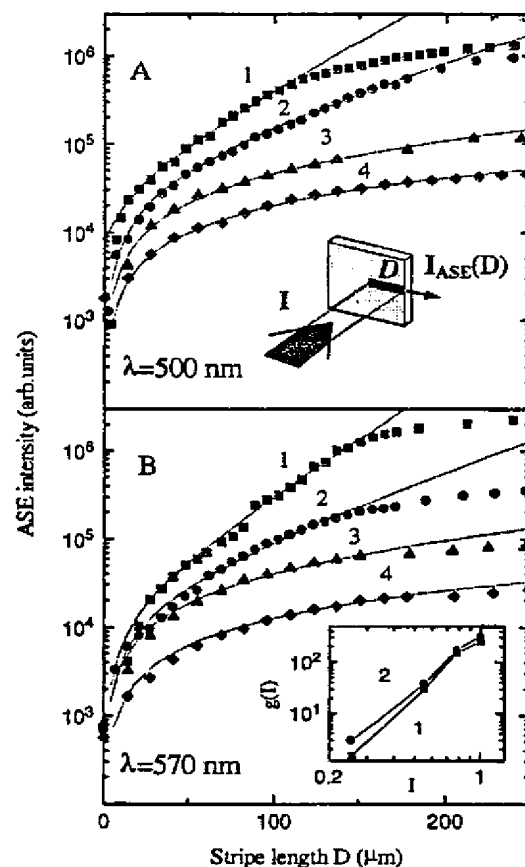


FIG. 2. ASE intensity at 10 K as a function of the stripe length measured for (211) oriented stripes for different intensities of excitation: 1–1, 2–0.77, 3–0.55, and 4–0.25 MW/cm^2 . (A) ASE is detected at the maximum of band A (500 nm); (B) at the maximum of band B (570 nm). Inset (A) Geometry of gain measurements using the VSL method. Inset (B) Log-log plot of the gain g as a function of the excitation intensity I for band A (1) and band B (2).

band A. It can be seen that at our highest excitation intensity of 1 MW/cm^2 the I_{ASE} increases exponentially over at least two orders of magnitude (see line 1 in Fig. 2A) and exhibits saturation for D larger than 120 μm . The effective gain coefficient g (total gain minus loss) can be obtained by fitting the $I_{\text{ASE}}(D)$ dependence using the expression¹² $I_{\text{ASE}}(D) = S/g \cdot [\exp(g \cdot D) - 1]$, where S is a spontaneous emission intensity constant. The result of this procedure yields a value of $g = 220 \text{ cm}^{-1}$ for an excitation intensity of 1 MW/cm^2 . This value is comparable to that usually observed in CdS QDs in glass matrices for a similar temperature and excitation intensity.^{13,14} The gain diminishes as the intensity of excitation I is reduced and it practically disappears when $I = 0.2 \text{ MW}/\text{cm}^2$. The $g(I)$ dependence reveals a quadratic increase of the gain with increasing excitation intensity. This is shown in a log-log plot in the inset of Fig. 2B (see curve 1). This behavior is expected for gain processes involving two electron-hole pairs (biexciton) recombination. It has been shown^{13,14} that biexcitonic gain, originating from biexciton to exciton recombination, is favored in QD embedded in glass matrices. It results in a broad gain spectrum with a maximum near the absorption band edge and a long tail extending to lower energies.^{13,14}

Parallel with gain measurements taken at a wavelength

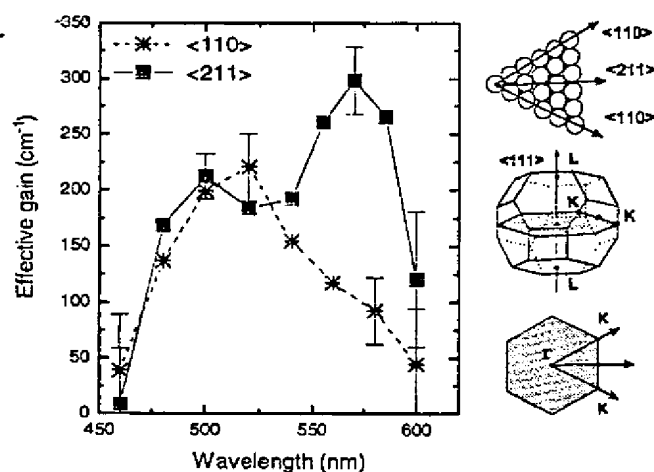


FIG. 3. Gain spectra measured at 10 K for 1 MW/cm² excitation intensity for a stripe oriented along the (211) direction (squares) and along the (110) direction (stars). Inset: Sketch of sphere packaging on the (111) face of the sample, corresponding photonic BZ, and its projection on the (111) plane.

of 500 nm (Fig. 2A) the gain is also measured at longer wavelengths. Figure 2B represents a set of $I_{\text{ASE}}(D)$ dependencies taken at the spectral position of 570 nm, i.e., at the maximum of band B. The gain in this spectral region far from the absorption edge is surprisingly large. Moreover, for our maximum excitation intensity of 1 MW/cm², it reaches a value of $g=300 \text{ cm}^{-1}$, which is nearly 1.5 times larger than the value $g=220 \text{ cm}^{-1}$ measured for band A. The intensity dependence of the gain at band B repeats the quadratic $g(P)$ trend characteristic of the gain for band A, which indicates that it is also due to biexcitonic recombination. See curve 2 in the inset of Fig. 2B.

We would like to emphasize at this point that these observations clearly demonstrate that the B band is mainly composed of amplified spontaneous emission originating from the same transitions as band A. It can be supposed that the enhancement of the gain at these wavelengths which is quite unusual for QDs in glass, is due to distributed Bragg reflections, provided by the periodic photonic lattice of the dielectric opal matrix. If this is the case, then the B band gain should possess well-defined directional properties according to the symmetry of the opal photonic lattice. Indeed, the (111) face of the opal photonic lattice, onto which the stripe is focused in the VSL gain experiments, possesses two inequivalent directions (<110> and <211>, see inset in Fig. 3), which can be clearly identified by the analysis of AFM images. For the <110> oriented stripe the wavevector k of photons, which are collected in the VSL method in the stripe direction, increases in the $\Gamma-K$ direction of the photonic BZ. When k approaches the boundary of the first BZ at point K with coordinates $2\pi/a^*(3/4, 3/4, 0)$ (see inset in Fig. 3), the photonic stopband develops. The photonic stopband for the <211> direction should occur at longer wavelengths, since the absolute value of the wavevector $|k|$, which corresponds to the boundary of BZ in the <211> direction, is about 10% smaller than that at the point K (see inset in Fig. 3).

In all the gain measurements described above, the excitation stripe was oriented along one and the same <211> direction. Measurements of the orientation dependence of the

gain were performed by rotating the sample around the [111] axis. Figure 3 depicts the gain spectra measured for <211> and <110> oriented stripes for one and the same excitation intensity of 1 MW/cm² at 10 K. It can be clearly seen that band B dominates in the gain spectra only for stripes oriented along the <211> direction. Rotation of the sample around the [111] axis by only 30° (the stripe is then oriented along the <110> direction) results in a blueshift and disappearance of the band B, as expected. Comparison of the gain spectra shows that the gain value is enhanced at 570 nm by at least a factor of 3. Several mechanisms predicted to occur in 3D photonic crystals can be responsible for the observed effect.³⁻⁶ We would like to note at this stage that, accounting for even one of the proposed mechanisms caused by slowing down of the photon group velocity at the photonic band edge, which implies an exceedingly long optical path length in the structure,⁵ may explain the observed magnitude of gain enhancement.

In conclusion, optical gain was observed for the first time with semiconductor nanocrystals embedded in a 3D photonic crystal. We found that light interference on a photonic lattice of opal results in an enhancement of the long-wavelength portion of the gain at the high-frequency edge of the photonic stopband far below the absorption edge of the semiconductor. Well-defined spatial directionality of ASE at these wavelengths, exponential increase of its intensity with a threshold pumping value and a relatively small spectral width enabled us to describe the observed effect as a lasing action, which occurs without any external mirrors or cavities.

The authors are indebted to Dr. V. N. Bogomolov and Dr. A. V. Prokofiev for furnishing the samples of synthetic opals. They would like to thank M. Robino for providing AFM measurements and Dr. P. Gilliot, Dr. Ch. Hirleimann, and Dr. R. Levy for many helpful discussions. Three of the authors (Yu.V., K.L. and I.P.) gratefully acknowledge financial support from the French government, MENESR (C.I.E.S.). One author (V.A.) acknowledges partial support from the RFBR (Grant No. 960217928).

¹For a recent review, see, for example, articles in *Photonic Band Gap Materials*, edited by C. M. Soukoulis, NATO ASI Ser. E Vol. 315 (Kluwer, Dordrecht, 1996).

²E. Yablonovitch, *Phys. Rev. Lett.* **58**, 2059 (1987).

³T. Suzuki and P. K. L. Yu, *J. Opt. Soc. Am. B* **12**, 570 (1995).

⁴S. John and T. Quang, *Phys. Rev. Lett.* **74**, 3419 (1995).

⁵J. P. Dowling, M. Scalora, M. J. Bloemer, and C. M. Bowden, *J. Appl. Phys.* **75**, 1896 (1994).

⁶S. John and J. Wang, *Phys. Rev. B* **43**, 12772 (1991).

⁷V. N. Astratov, V. N. Bogomolov, A. A. Kaplyanskii, A. V. Prokofiev, L. A. Samoilovich, S. M. Samoilovich, and Yu. A. Vlasov, *Nuovo Cimento D* **17**, 1349 (1995).

⁸V. N. Astratov, Yu. A. Vlasov, O. Z. Karimov, A. A. Kaplyanskii, Yu. G. Musikhin, N. A. Bert, V. N. Bogomolov, and A. V. Prokofiev, *Phys. Lett. A* **222**, 349 (1996).

⁹Yu. A. Vlasov, V. N. Astratov, O. Z. Karimov, A. A. Kaplyanskii, V. N. Bogomolov, and A. V. Prokofiev, *Phys. Rev. B* **55**, 13 357 (1997).

¹⁰H. S. Sözüer, J. W. Haus, and R. Inguva, *Phys. Rev. B* **45**, 13962 (1992).

¹¹Z. Zhang and S. Satpathy, *Phys. Rev. Lett.* **65**, 2650 (1990).

¹²K. L. Shaklee, R. E. Nahory, and R. F. Leheny, *J. Lumin.* **7**, 284 (1973).

¹³J. Butty, N. Peyghambarian, Y. H. Kuo, and J. D. Mackenzie, *Appl. Phys. Lett.* **69**, 3224 (1996).

¹⁴J. Butty, Y. Z. Hu, N. Peyghambarian, Y. H. Kuo, and J. D. Mackenzie, *Appl. Phys. Lett.* **67**, 2672 (1995).

¹⁵M. G. Bawendi, P. J. Carroll, W. L. Wilson, and L. E. Brus, *J. Chem. Phys.* **96**, 946 (1992).

this mixture was kept standing in a refrigerator overnight. The red solid that precipitated was collected by vacuum filtration and recrystallized from $\text{CH}_2\text{Cl}_2/\text{MeOH}$ to give 1.1 g (68% yield) of red crystals: m.p. 129 °C (127 °C from second heating in DSC); ^1H NMR (300 MHz, CDCl_3): δ 0.90 (t, J = 6.6 Hz, 6H), 1.34 (m, 12H), 1.63 (m, 4H), 1.82 (s, 6H), 3.40 (t, J = 7.8 Hz, 4H), 6.70 (d, J = 9.6 Hz, 2H), 7.99 (d, J = 9.6 Hz, 2H); ^{13}C NMR (75 MHz, CDCl_3): δ 13.97, 22.60, 26.66, 27.37, 27.69, 31.57, 51.43, 53.74, 90.43, 97.23, 112.06 (two carbons), 113.08, 113.13, 113.32, 132.57, 152.98, 173.66, 177.15; infrared (IR) (neat, cm^{-1}) 2950, 2928, 2856, 2223, 1607, 1564, 1538, 1491, 1472, 1422, 1355, 1333, 1220, 1187, 1119, 1002, 981, 920, 826; ultraviolet-visible (UV-vis) (THF) λ_{max} nm (ϵ) 491 (72 455).

NMR-spectra were measured with a Bruker AMX 300, UV-vis spectra with a HP 8453 spectrophotometer, Fourier transform IR (FTIR) spectra with a Bruker Vector 33, melting points with TA Instruments DSC 2920 and Olympus BH-2 polarized light microscopy equipped with a Mettler FP5 temperature controller and FP52 hot stage. MDSC was also performed on the TA Instruments DSC 2920 and the temperature is raised by 5 °C min^{-1} and modulated every 60 s by ± 0.8 °C.

For sample preparation, the components are either dissolved in chlorobenzene and cast on the substrate or dissolved in benzene and freeze-dried. The resulting composites are melted at 140–150 °C, sandwiched between two indium tin oxide (ITO) coated glass slides and cooled by placement on a cold (room temperature) metal plate.

The DC photoconductivity is measured at a wavelength λ = 647 nm (Kr ion laser) by applying a high voltage on one electrode and monitoring the current from the other electrode to the ground by a sensitive current amplifier (Keithley 428). All measurements are taken in steady state after opening the laser shutter.

For transient ellipsometry, the sample is placed between crossed polarizers at an angle of 54° between the sample normal and the laser beam. A laser diode at a wavelength λ = 905 nm is employed and the residual birefringence of the sample is compensated by a crystal compensator. The transmission through the ellipsometry setup is measured in response to a step function of the electric field applied to the sample with a rise time of ~ 100 μs .

The two-wave mixing is measured in a standard geometry [29] with the two beams having external angles of 30° and 60° to the sample normal and beam ratio 1:1. The laser source is a Kr ion laser at a wavelength of 647 nm. The time transients are measured by opening a shutter for both beams with a switching time of about 150 μs . After the measurements, the gratings are erased by a larger, non-Bragg matched erasing beam.

In the beam fanning experiments, the same setup as in the two-wave mixing is used except only one beam is present. The angle of the beam to the sample normal is 60° and the applied electric field is inverted compared to two-wave mixing to enhance the fanning. Additionally, an aperture is placed in the beam path 50 cm behind the sample, which clips only 5% of the unperturbed beam.

Received: September 17, 2001
Final version: November 22, 2001

- [1] P. Guenter, J. P. Huignard, *Photorefractive Materials and Their Applications*, Vols. 1–2, Springer, Berlin 1988–1989.
- [2] P. Yeh, *Introduction to Photorefractive Nonlinear Optics*, Wiley, New York 1993.
- [3] L. Solymar, D. J. Webb, A. Grunnet-Jepsen, *The Physics and Applications of Photorefractive Materials*, Clarendon, Oxford 1996.
- [4] M. B. Klein, *Opt. Lett.* 1984, 9, 350.
- [5] K. Sutter, J. Hüller, P. Günter, *Solid State Commun.* 1990, 74, 867.
- [6] S. Ducharme, J. C. Scott, R. J. Twieg, W. E. Moerner, *Phys. Rev. Lett.* 1991, 66, 1846.
- [7] E. V. Rudenko, A. V. Sukhov, *JETP Lett.* 1994, 59, 142.
- [8] W. E. Moerner, A. Grunnet-Jepsen, C. L. Thompson, *Annu. Rev. Mater. Sci.* 1997, 27, 585.
- [9] B. Kippelen, K. Meerholz, N. Peyghambarian, in *Nonlinear Optics of Organic Molecules and Polymers* (Eds: H. S. Nalwa, S. Miyata), CRC Press, Boca Raton, FL 1997, p. 465.
- [10] S. J. Zilker, *ChemPhysChem* 2000, 1, 72.
- [11] P. M. Lundquist, R. Wortmann, C. Geletnicky, R. J. Twieg, M. Jurich, V. Y. Lee, C. R. Moylan, D. M. Burland, *Science* 1996, 274, 1182.
- [12] Y. D. Zhang, T. Wada, H. Sasabe, *J. Mater. Chem.* 1998, 8, 809.
- [13] A. Grunnet-Jepsen, D. Wright, B. Smith, M. S. Bratcher, M. S. DeClue, J. S. Siegel, W. E. Moerner, *Chem. Phys. Lett.* 1998, 291, 553.
- [14] T. K. Daubler, R. Bittner, K. Meerholz, V. Cimrova, D. Neher, *Phys. Rev. B* 2000, 61, 13515.
- [15] W. E. Moerner, S. M. Silence, F. Hache, G. C. Bjorklund, *J. Opt. Soc. Am. B—Opt. Phys.* 1994, 11, 320.
- [16] M. A. Diaz-Garcia, D. Wright, J. D. Casperson, B. Smith, E. Glazer, W. E. Moerner, L. I. Sukhomlinova, R. J. Twieg, *Chem. Mater.* 1999, 11, 1784.

- [17] E. Hendrickx, B. Kippelen, S. Thayumanavan, S. R. Marder, A. Persoons, N. Peyghambarian, *J. Chem. Phys.* 2000, 112, 9557.
- [18] K. Meerholz, R. Bittner, Y. DeNardin, C. Bräuchle, E. Hendrickx, B. L. Volodin, B. Kippelen, N. Peyghambarian, *Adv. Mater.* 1997, 9, 1043.
- [19] D. Wright, U. Gubler, Y. Roh, W. E. Moerner, M. He, R. J. Twieg, *Appl. Phys. Lett.* 2001, 79, 4274.
- [20] R. Bittner, C. Bräuchle, K. Meerholz, *Appl. Opt.* 1998, 37, 2843.
- [21] A. Grunnet-Jepsen, C. L. Thompson, W. E. Moerner, *Mater. Res. Soc. Symp. Proc.* 1997, 479, 199.
- [22] A. Grunnet-Jepsen, C. L. Thompson, R. J. Twieg, W. E. Moerner, *J. Opt. Soc. Am. B—Opt. Phys.* 1998, 15, 901.
- [23] K. Meerholz, R. Bittner, Y. DeNardin, *Opt. Commun.* 1998, 150, 205.
- [24] F. Wurthner, S. Yao, J. Schilling, R. Wortmann, M. Redi-Abshiro, E. Mecher, F. Gallego-Gomez, K. Meerholz, *J. Am. Chem. Soc.* 2001, 123, 2810.
- [25] L. M. Wang, M. K. Ng, L. P. Yu, *Appl. Phys. Lett.* 2001, 78, 700.
- [26] A. Grunnet-Jepsen, C. L. Thompson, W. E. Moerner, *Science* 1997, 277, 549.
- [27] M. R. Leahy, D. J. McGee, *Opt. Commun.* 2001, 187, 277.
- [28] G. Melikian, F. Rouessac, C. Alexandre, *Synth. Commun.* 1995, 25, 3045.
- [29] A. Grunnet-Jepsen, C. L. Thompson, W. E. Moerner, *J. Opt. Soc. Am. B* 1998, 15, 905.

Lasing from Semiconductor Quantum Rods in a Cylindrical Microcavity**

By Miri Kazes, David Y. Lewis, Yuval Ebenstein, Taleb Mokari, and Uri Banin*

Colloidal semiconductor nanocrystals are a class of nanomaterials with significant potential for serving as luminescent chromophores in applications ranging from lasers^[1] and optoelectronic devices,^[2] to biological fluorescence tagging.^[3,4] An obvious advantage of such nanostructures over conventional chromophores is the remarkable spectral coverage for luminescence from the ultraviolet to the near infrared. Such coverage is afforded through size control of a variety of available high-quality nanocrystals of II–VI and III–V semiconductors, a direct manifestation of the well-known quantum confinement effect.^[5–8]

Shape control of such colloiddally prepared nanostructures has been recently achieved by modifying the colloidal synthesis to obtain rod-shaped particles—quantum rods,^[9] which display the transition from zero-dimensional quantum dots (QDs) to one-dimensional quantum wires. Unlike the spherical dots, quantum rods have linearly polarized emission as demonstrated recently by fluorescence measurements on single quantum rods and by theoretical calculations.^[10] This property of linearly polarized emission, along with the prospect of broad spectral coverage and the chemical accessibility to quantum rods, renders them highly attractive as potential laser materials. Furthermore, low lasing thresholds are predicted for quantum dots and quantum wires compared with

* Prof. U. Banin, M. Kazes, D. Y. Lewis, Y. Ebenstein, T. Mokari
Institute of Chemistry and the Center for Nanoscience and Nanotechnology, The Hebrew University of Jerusalem
Jerusalem 91904 (Israel)
E-mail: banin@chem.huji.ac.il

** We thank Dr. Nir Tessler for helpful discussions and Dr. Oded Millo for comments on the manuscript. This research was funded in part by a grant from the Israel Science Foundation (grant #99/00-12.5) and by a grant from the James-Frank program.

two-dimensionally confined quantum wells, the basis of present semiconductor diode laser devices ubiquitous in information and telecommunication technologies.^[11,12] However, in spite of intense research, amplified spontaneous emission was only recently observed for spherical colloidal CdSe QDs in close-packed films where pumping with an amplified femtosecond laser source was used to compete with fast non-radiative Auger decay processes.^[1] The observation of an induced absorption feature at the region of potential optical gain for the same nanocrystals in solution was thought to be a limiting factor for lasing in this natural solution environment of colloidal particles.^[13] In this paper, we report the first observation of lasing for CdSe/ZnS quantum rods in solution using a cylindrical microcavity, with nanosecond (ns) excitation from a commonly available pump source. The simple microcavity setup used here provides much needed uncomplicated means for screening colloidal nanocrystals as potential laser chromophores directly in solution, avoiding further sample processing required for film preparation. Lasing in a similar configuration at room temperature was also observed for the spherical QDs while previously detection of lasing in solution was unsuccessful. While for QDs the lasing is not polarized, for quantum rods we detected a linearly polarized laser signal directly related to their symmetry.

The cylindrical microcavity, comprising an optical fiber (radius $r = 62.5 \mu\text{m}$) within a glass capillary tube (inner radius $100 \mu\text{m}$), is shown schematically in Figure 1c, left inset. Cylindrical or spherical microcavities have extremely low loss whispering gallery modes (WGMs) due to light trapping by total internal reflection at the cavity boundaries.^[15] This, accompanied by the fast cavity round trip times, makes them suitable laser cavities for semiconductor quantum rods and nanocrystals. The cylindrical microcavity configuration we implemented was recently used with a Rhodamine 6G dye solution as the laser active medium, occupying the space between the fiber and enclosing capillary tube.^[14] Evanescent wave coupling and optical mode confinement were achieved for the fiber with a refractive index higher than that of the surrounding dye solution. Low threshold pump levels for the dye were observed, due to the ultrahigh microcavity quality factors (Q). The lasing in this microcavity is based on the gain in the evanescent field region of WGMs near the fiber surface. Each WGM is characterized by the azimuthal mode number n , and the radial mode order l . In our experiments the microcavity was pumped from the side using the second harmonic of a Nd-YAG laser at 532 nm (beam radius $w \sim 0.3 \text{ mm}$), with the emission collected at 90° and detected using a spectrograph/charge coupled device (CCD) setup. All experiments were carried out in ambient conditions.

Figure 1 presents results of lasing for CdSe/ZnS quantum rods, along with their structural and optical characteristics. The quantum rods were grown using the well-developed methods of colloidal nanocrystal synthesis utilizing high-temperature pyrolysis of organometallic precursors in coordinating solvents,^[16,17] and are overcoated by hexadecylamine (HDA) and trioctylphosphine oxide (TOPO). The rod-shell

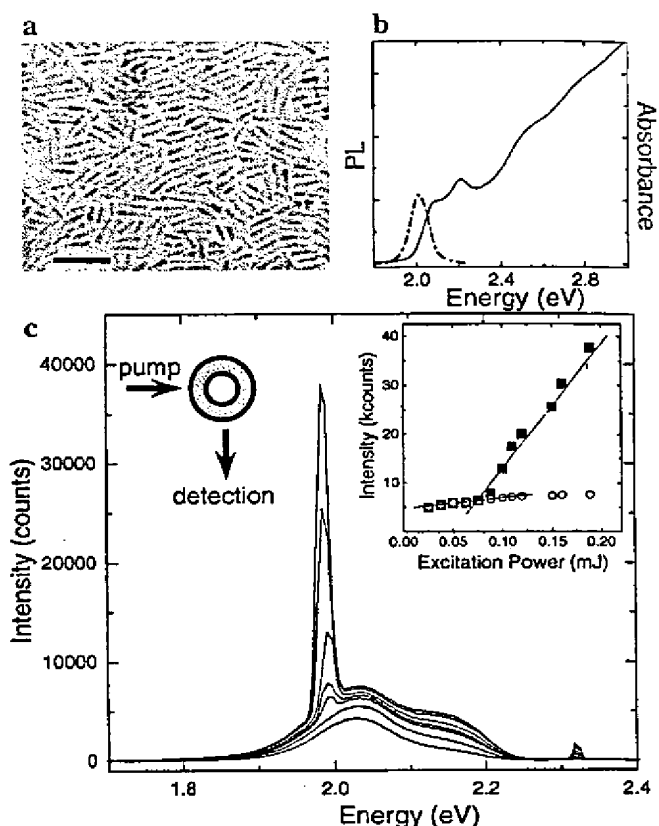


Fig. 1. a) TEM image of the quantum rod sample (scale bar 50 nm). b) The absorption (solid line) and emission (dot-dashed line) for the quantum rods in solution. c) Emission spectra for the quantum rods loaded in the microcavity at different pump powers. The peak at 2.33 eV is the residual scattering of the pump laser. The pump intensities from low to high are: 0.016 mJ, 0.038 mJ, 0.075 mJ, 0.088 mJ, 0.10 mJ, 0.15 mJ, 0.19 mJ. The narrow peak at 1.98 eV emerging above the fluorescence is the laser signal that appears at a threshold pump level of $\sim 0.08 \text{ mJ}$. The right inset of (c) displays the intensity of the laser peak (filled squares) and the fluorescence peak (empty circles) versus the pump power. Lasing shows a clear threshold behavior as accentuated by the solid lines. The left inset in (c) is a schematic top view of the cylindrical microcavity experimental setup as described in the text, with the gray shaded area representing the quantum rod solution occupying the volume between the fiber and inner capillary walls.

configuration was chosen since the growth of ZnS on the organically coated CdSe quantum rods enhances the fluorescence quantum yield from $\sim 2\%$ to 14% . The shell, composed of ZnS that has a bandgap enclosing that of CdSe, passivates potential surface traps that in the organically coated CdSe rods provide efficient non-radiative decay routes for the excited charge carriers, and therefore enables more easily the achievement of population inversion required for lasing.

A transmission electron microscopy (TEM) image of the quantum rods deposited on a grid from a solution of hexanes is presented in Figure 1a. Good size and shape monodispersity is observed, demonstrating the extent of control over the sample preparation. The average nanorod length is 25 nm, with an average diameter of 4 nm. The monodispersity assists the achievement of lasing by reducing the inhomogeneous spectral broadening of the gain profile. The optical

characteristics of the nanorod sample are summarized in Figure 1b. The absorption spectrum of the quantum rods in solution (solid line) has an onset at ~ 2.1 eV, considerably blue shifted compared with the bulk CdSe gap (at 1.7 eV). The bandgap in quantum rods is strongly dependent on the smallest dimension—the diameter at which quantum confinement is most significant, with a weak dependence on length.^[18] Upon excitation at 532 nm, a well-defined photoluminescence (PL) peak of bandgap emission centered at 2.0 eV is observed (dot-dashed line, Fig. 1b).

In Figure 1c, emission spectra collected from the cylindrical microcavity, loaded with a quantum rod sample in hexanes, are shown for several laser excitation intensities where each spectrum corresponds to a single laser shot. The peak at 2.33 eV is due to scattering of the pump laser. At low excitation intensities (e.g., 0.016 mJ), the spectrum resembles that measured for the quantum rods in solution (Fig. 1b). At higher intensities, changes in the spectral shape are observed. Most significantly, above ~ 0.08 mJ a narrow peak clearly emerges at 1.98 eV, to the red of the fluorescence peak. This narrow peak signifies lasing from the quantum rods in the cylindrical microcavity. The dependence of the intensity of the lasing peak on pump power is shown in the right inset of Figure 1c (filled squares), along with the dependence of the fluorescence peak intensity (empty circles). The lasing peak intensity exhibits an abrupt change of slope at the onset of laser action, while at the same time the peak fluorescence intensity is in effect saturated. This threshold behavior of the laser peak intensity provides an additional important signature of lasing.^[19]

Figure 2 shows a sequence of high-resolution single-shot emission spectra measured at an excitation level well above threshold. Each spectrum exhibits a detailed peak structure of discrete lasing modes in a similar spectral range, with intensities much higher than that of the background fluorescence. Each peak corresponds to lasing in a WGM of the microcavity, with different azimuthal mode number n . The average peak spacing is 0.65 nm. This value is in good agreement with the theoretical separation between WGMs with consecutive n values corresponding to $-\lambda_n^2/(m_2^2 2\pi r)$, with $m_2 = 1.455$ the refractive index of the fiber and λ_n the detected mode wavelength. These results, along with the data discussed in the previous paragraph, provide unambiguous confirmation for lasing from the quantum rods in the microcavity. The choice of hexanes as solvent with index of refraction $m_1 = 1.375$ affords the proper conditions for optical confinement of the WGMs near the fiber surface, and the high Q of the cavity provides the necessary conditions to achieve lasing, overcoming the competing non-radiative loss mechanisms. Among the loss mechanisms, Auger quenching has been reported to be ~ 300 ps for CdSe nanocrystals with a diameter similar to that of the quantum rods,^[20] and may also be a significant loss mechanism in this case.

Consecutive spectra exhibit intensity variations between the different lasing modes that may be due to the high sensitivity of the WGMs to the local surface quality of the fiber.

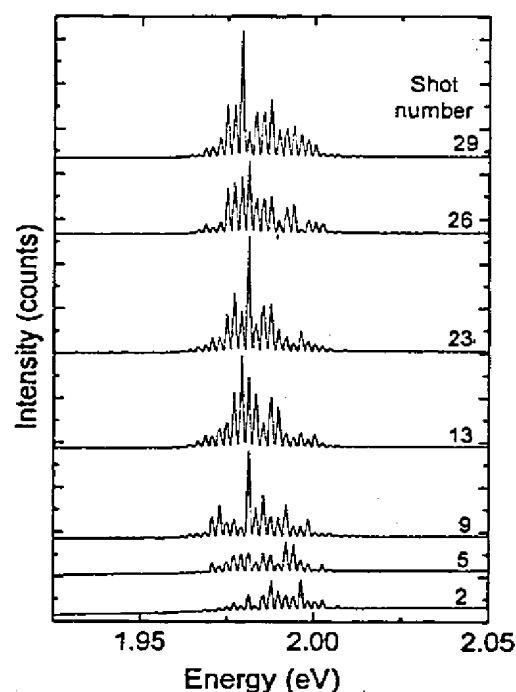


Fig. 2. Representative single-shot high-resolution emission-lasing spectra of the quantum rods in the cylindrical microcavity pumped well above threshold. Shot number is indicated. Each spectrum shows clearly discrete peaks corresponding to lasing in WGMs of the microcavity.

Eventually, after tens of shots and at higher pump levels, the modes decrease in intensity until finally they are quenched due to burning of the illuminated spot. It is then possible to move to a different position on the long axis of the microcavity and observe lasing again. However, lasing could not be observed in every spot and threshold levels varied by a factor of up to 5. Furthermore, the spectra, all showing discrete WGMs with similar spacings, differed slightly in the central wavelength position and relative intensities of the different modes. These changes are attributed to the local quality of the fiber surface or cleanliness of the microcavity.

As an interesting point of comparison, we also examined lasing in the cylindrical microcavity configuration from a solution of spherical CdSe/ZnS core-shell nanocrystals prepared as published previously.^[21–23] The left inset of Figure 3 depicts the core-shell absorption spectra (solid line), portraying several discrete transitions typical of the atomic-like highly monodisperse QDs. Compared with quantum rods (Fig. 1b), the absorption spectrum for the dots is more structured due to the more discrete nature of their density of states above the bandgap. The left inset also shows the PL spectra (dot-dashed line), exhibiting a peak of bandgap emission centered at 2.2 eV with a high quantum yield (60%). The gap is shifted further to the blue compared with the quantum rods, due to the smaller diameter of the core in these nanocrystals serving as a demonstration of the microcavity laser color tunability afforded through control of the nanostructure size and shape.

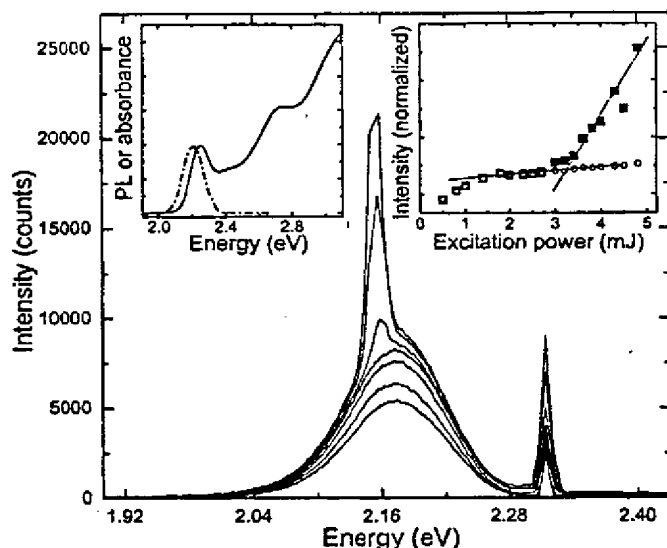


Fig. 3. Lasing in CdSe/ZnS core-shell nanocrystals. Above ~ 3 mJ, a narrow lasing peak appears at 2.16 eV (the peak at 2.33 eV is the scatter from the pump laser). The pump levels from low to high are: 0.5 mJ, 0.8 mJ, 1.4 mJ, 2.5 mJ, 3.4 mJ, 4.3 mJ, 4.8 mJ. The right inset shows the intensity of the lasing peak (filled squares) and the normalized intensity of the fluorescence at 2.21 eV (empty circles) versus the pump power. Lasing shows a clear threshold behavior as accentuated by the solid lines. The left inset shows the absorption (solid line) and emission (dash-dotted line) spectra for the nanocrystals in solution.

For the hexanes solution of nanocrystals in the microcavity at low pump powers, we observed the typical emission spectrum as can be seen in Figure 3. At higher excitation powers, as for the quantum rods, a narrow lasing peak is clearly observed emerging on top of the envelope of the fluorescence spectrum. A distinct threshold behavior is exhibited, as shown in the right inset of Figure 3. At higher resolution we could clearly resolve the lasing in discrete WGMs as in the quantum rods (Fig. 4a). Pump-probe experiments revealed induced absorption features in the region of potential gain for the QDs in solution and were thought to limit the possibility of achieving lasing in this medium.^[13] However, in these experiments the nanocrystals were excited far to the blue of the bandgap while here the pump is closer to the bandgap. Lasing was achieved here by pumping the nanocrystal solution with a nanosecond laser source, due to the favorable conditions afforded by the cylindrical microcavity. This clearly demonstrates an important aspect of the cylindrical microcavity configuration used here. The relative simplicity of the setup utilizing a commonly available nanosecond pump laser source with the sample directly in solution provides straightforward means for screening colloidal nanostructured materials as potential laser chromophores.

The remarkable control over the particle shape allowing the preparation of quantum rods directly impacts their optical and electronic properties.^[10] Figure 4 shows the results of polarized emission measurements from the cylindrical microcavity loaded with nanocrystals (Fig. 4a), versus quantum rods (Fig. 4b). The pump laser was polarized parallel to the microcavity axis, and we measured the emission polarized either

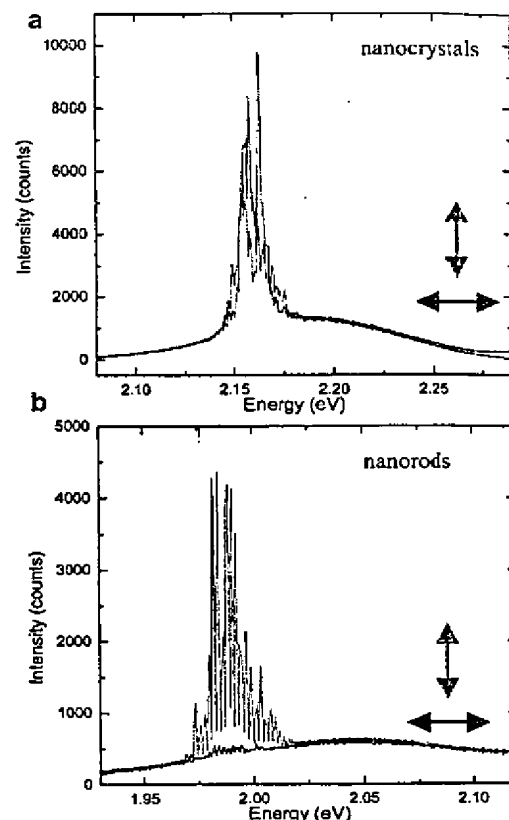


Fig. 4. Polarized emission measurements for lasing in nanocrystals (a) and quantum rods (b). The pump laser is polarized parallel to the cylindrical microcavity axis. Spectra for the VV configuration (detection polarization parallel to the pump polarization) are in magenta, while spectra for the VH configuration (detection polarization perpendicular to the pump polarization) are in blue. Lasing in nanocrystals shows no polarization dependence, while in quantum rods the lasing is clearly linearly polarized.

parallel (VV, denoted by vertical arrow, magenta color) or perpendicular (VH, horizontal arrow, blue color) to this axis. Spectra for VV or VH configurations were measured in consecutive shots. For QDs, the VH and VV spectra presented in Figure 4a show lasing in similar WGMs but with varying intensities. These kinds of fluctuations were observed also for consecutive shots measured at the same polarization. Taking into account the tens of shots measured either in VV or VH, we could not detect essential intensity differences between lasing in the different polarizations for the QDs. In contrast, the lasing from quantum rods is highly linearly polarized as can be seen clearly in Figure 4b. While for the VH case only residual WGMs were resolved, in VV we detected strong distinct modes showing that the lasing in quantum rods is linearly polarized parallel to the cavity and the pump laser axis. This difference between quantum rods and dots is directly related to the nanostructure shape, representing a fundamental distinction between the quasi-one-dimensional rods versus the zero-dimensional QDs. The linearly polarized lasing appears even though the quantum rods are randomly oriented in the solution. The lasing for Rhodamine dye in the cylindrical mi-

croavity is also polarized^[14] and, in dye lasers in general, the lasing polarization is known to be parallel to the polarization of the pumping beam. The polarized lasing arises because of photoselection by the linearly polarized pumping process, which in effect induces sufficient partial orientation for the emitting dipoles. Alignment of quantum rods by electric fields, for example, may further improve the optical gain characteristics.

Lasing was detected for colloidal CdSe quantum rods and nanocrystals in solution. The straightforward cylindrical microcavity setup used can facilitate rapid and efficient screening to identify the major determining factors for the function of colloidal nanostructures in laser applications. This information can be implemented in future formulations of improved samples with tailored properties for laser action. There are differences between quantum rods and QDs that may prove advantageous for the utility of the rods as laser chromophores. The non-resonant Stokes shift between absorption and emission is larger in rods compared with dots, leading to decreased reabsorption losses. Further, the Auger rates in rods may be smaller because of their larger size while still allowing color tunability through control of the rod diameter. Finally, quantum rods show linearly polarized lasing, a significant difference compared with QDs for which lasing is not polarized.

Experimental

Materials Used for Quantum Rod Synthesis: Anhydrous hexanes, toluene, methanol, Se powder (99.999 %), trioctylphosphine oxide (TOPO, 90 %), trioctylphosphine (TOP, 95 %), tributylphosphine (TBP, 99 %), hexadecylamine (HDA, 98 %), and diethylzinc (ZnEt_2 , 1 M in hexane) were purchased from Aldrich and used as received aside from TOP, which was distilled under vacuum. Dimethylcadmium (CdMe_2) was purchased from Strem and purified by vacuum transfer. Bis(trimethylsilyl) sulfide ($(\text{TMS})_2\text{S}$) was purchased from Fluka. Tetradecylphosphonic acid (TDPA) was purchased from Alfa.

Typical Quantum Rod Preparation: 4 g of TOPO and 0.4 g of TDPA were heated to 360 °C and vigorously stirred. The Cd stock solution (0.16 g CdMe_2 + 0.34 g TBP) was added to the flask over about 10 s. After 60 s, 1.5 g of Se stock (0.15 g Se + 1.35 g TBP) was injected rapidly, resulting in the immediate nucleation of quantum rods. The temperature was decreased to 250 °C for rod growth. After 20 min, new Cd stock (0.0303 g Cd + 0.12 g TBP) was added to the reaction and 2 min later Se stock solution (0.017 g of Se + 0.13 g of TBP) was added dropwise. Such sequences of secondary injections were repeated three times and the reaction was stopped by cooling the flask. After cooling,

the ZnS shell was grown in the same flask: 2 g of HDA was added and the flask was heated to 170 °C. A significant increase in PL quantum yield was observed. The ZnS stock solution was prepared by dissolving 100 μL of bis(trimethylsilyl) sulfide and 230 μL of diethylzinc (1 M in hexane) in 2 mL TOP. 1 mL of the solution was added dropwise (0.2 mL doses at 10 min intervals) to the vigorously stirred solution of CdSe quantum rods and the solution was cooled and maintained for 1 h at 90 °C. The CdSe/ZnS quantum rods were precipitated with methanol, separated by centrifugation, and dispersed in hexanes for optical measurements.

Preparation of Capillaries: Typically ~3 mg of quantum rods or nanocrystals were dissolved in 100 μL of anhydrous hexanes forming a highly concentrated solution. The solution was sonicated briefly to better dissolve the particles. A fiber segment was inserted into the capillary tube and the solution was loaded by capillary action.

Received: October 29, 2001

- [1] V. I. Klimov, A. A. Mikhailovsky, S. Xu, J. A. Hollingsworth, C. A. Leatherdale, H. J. Eisler, M. G. Bawendi, *Science* 2000, 290, 314.
- [2] V. L. Colvin, M. C. Schlamp, A. P. Alivisatos, *Nature* 1994, 370, 354.
- [3] M. P. Bruchez, M. Moronne, P. Gin, S. Weiss, A. P. Alivisatos, *Science* 1998, 281, 2013.
- [4] W. C. W. Chan, S. Nie, *Science* 1998, 281, 2016.
- [5] A. P. Alivisatos, *Science* 1996, 271, 933.
- [6] L. E. Brus, *J. Chem. Phys.* 1984, 80, 4403.
- [7] C. B. Murray, D. J. Norris, M. G. Bawendi, *J. Am. Chem. Soc.* 1993, 115, 8706.
- [8] Y. W. Cao, U. Banin, *J. Am. Chem. Soc.* 2000, 122, 9692.
- [9] X. G. Peng, L. Manna, W. D. Yang, J. Wickham, E. Scher, A. Kadavanich, A. P. Alivisatos, *Nature* 2000, 404, 59.
- [10] J. Hu, L. S. Li, W. Yang, L. Manna, L. W. Wang, A. P. Alivisatos, *Science* 2001, 292, 2060.
- [11] M. Asada, M. Y. Miyamoto, Y. Suematsu, *IEEE J. Quantum Electron.* 1986, QE-22, 1915.
- [12] E. Grundmann, *Physica E* 2000, 5, 167.
- [13] V. I. Klimov, C. J. Schwarz, D. W. McBranch, C. A. Leatherdale, M. G. Bawendi, *Phys. Rev. B* 1999, 60, R2177.
- [14] H. J. Moon, Y. T. Chough, K. An, *Phys. Rev. Lett.* 2000, 85, 3161.
- [15] *Optical Processes in Microcavities* (Eds: R. K. Chang, A. J. Campillo), Advanced Series in Applied Physics, Vol. 3, World Scientific, Singapore 1996.
- [16] L. Manna, E. C. Scher, A. P. Alivisatos, *J. Am. Chem. Soc.* 2000, 122, 12700.
- [17] Z. A. Peng, X. Peng, *J. Am. Chem. Soc.* 2001, 123, 1389.
- [18] L. S. Li, H. Jiangtao, W. Yang, A. P. Alivisatos, *Nano Lett.* 2001, 1, 349.
- [19] A. Yariv, *Quantum Electronics*, 3rd ed., Wiley, New York 1986.
- [20] V. I. Klimov, A. A. Mikhailovsky, D. W. McBranch, C. A. Leatherdale, M. G. Bawendi, *Science* 2000, 287, 1011.
- [21] M. A. Hines, P. J. Guyot-Sionnest, *J. Phys. Chem.* 1996, 100, 468.
- [22] B. O. Dabbousi, J. Rodriguez-Vicjo, F. V. Mikulec, J. R. Heine, H. Mattoussi, R. Ober, K. F. Jensen, M. G. Bawendi, *J. Phys. Chem. B* 1997, 101, 9463.
- [23] D. V. Talapin, A. L. Rogach, A. Kornowski, M. Haase, H. Weller, *Nano Lett.* 2001, 1, 207.

Integrated fiber Mach-Zehnder interferometer for electro-optic switching

VN: 2412 P: 15-09-2002

P: 1643-1645

M. Fokine, L. E. Nilsson, Å. Claesson, D. Berlemont, L. Kjellberg, L. Krummenacher, and W. Margulis

Acero, Electrum 236, SE-164 40 Kista, Sweden

XP-001161779

P: 1643-1645 = (3)

Received February 19, 2002

Molten alloys under high pressure were used to obtain fibers with long internal electrodes that are solid at room temperature. An integrated Mach-Zehnder interferometer was constructed from a twin-core twin-hole fiber that permitted application of an electric field preferentially to one of the cores. Good stability and a switching voltage of 1.4 kV were measured with a 1-m-long fiber device with a quadratic voltage dependence. © 2002 Optical Society of America

OCIS codes: 060.4370, 190.4360.

With the growing importance of optics in access and metro networks, the need for inexpensive high-performance optical components becomes more acute. With fiber-based devices, one can exploit the qualities associated with the fibers developed for transport applications, such as low cost per meter, excellent transparency, reproducibility, and stability. This capacity adds to the obvious compatibility of such devices with the fiber network in splicing and mode matching. Fiber modulators and switches would therefore be an attractive alternative to their semiconductor and ferroelectric-crystal-based counterparts. The low intrinsic (third-order) nonlinearity of fibers has been exploited in a number of instances in Kerr-effect fiber modulators.^{1,2} Poled fiber devices with a thermally induced effective second-order nonlinearity have also been demonstrated.³⁻⁶ Although progress has been made, even after poling the typical voltages required for switching in glass-based devices are still too high for commercial exploitation. Ways to improve the efficiency of electro-optic fibers are to record very large electric fields by poling (5×10^8 V/m) and to increase the nonlinearity of the material by special doping. A complementary approach is to make longer devices. This approach raises the problem of how to obtain fibers with long internal electrodes. The already-developed technique of side polishing fibers with holes and inserting thin wires⁷ brings the important benefit of not hindering splicing. However, this wire-insertion technique requires skill and is time consuming (i.e., costly). Further, the position of the wire in the holes varies along the fiber and from device to device, leading to uncertainty in the performance before and after poling (varying electric field and impedance along the fiber). The use of long-fiber devices also increases the problems of thermal and mechanical stability. To transform phase modulation into amplitude modulation, it is usual to use Mach-Zehnder fiber interferometers comprising two fiber couplers and two independent arms, one of which contains the electro-optic device. Environmental, thermal, mechanical, and acoustic fluctuations lead to time variations in the interferometer, even for zero driving signal. Further, the cost of the fiber device increases with the number of required components and with the degree of difficulty in packaging for noise compensation.

In this Letter, details are given of a simple technique that permits fabrication of long-fiber devices with internal electrodes that are solid at room temperature. An integrated Mach-Zehnder interferometer that consisted of a single twin-core fiber with two internal electrodes was designed. Preliminary experiments with such an arrangement are also presented.

The electrode fabrication technique consists of heating an alloy with a relatively low melting point in an oven so that a liquid is available. One end of the fiber with holes is inserted into the molten metal, and the other end is kept free in the atmosphere, as shown schematically in Fig. 1. The liquid metal is contained in a small crucible in a sealed cell that is pressurized. In this way the liquid metal is forced up into the fiber. The difference in pressure can greatly exceed the 1 atm of pressure that is obtained with vacuum. The technique of pressurizing or sucking liquids into silica fibers and capillaries was previously used in various fields and to make fiber components (see, for example, Ref. 8). For the experiments reported here, two different cylindrical pressure cells were constructed, with a typical length of ~10 cm and an internal diameter of ~2.5 cm. A lid with a small hole (~1-mm diameter) through which the fiber passed was provided. The lid sealed the cell hermetically, and a conical Teflon piece was squeezed around the fiber and against the lid, preventing

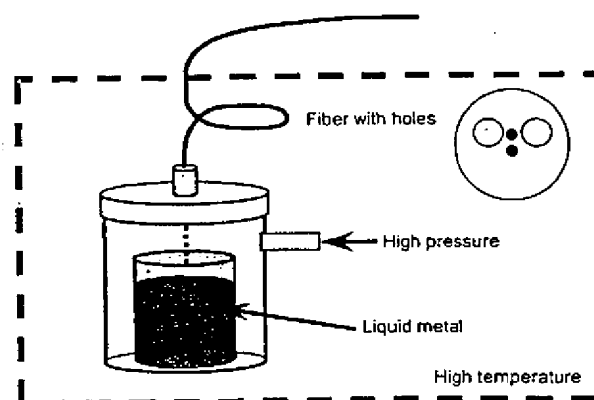


Fig. 1. Schematic diagram of the metal-insertion technique. The fiber cross section is also shown.

0146-9592/02/181643-03\$15.00/0

© 2002 Optical Society of America

leakage. It was found that the compressed air available in the laboratory at 8 atm was sufficient to push at least 22 m of metal into the fibers (the longest device that was made). Therefore, no attempts were made to use higher pressure or to use purer or less-reactive gasses, such as Ar.

Various types of alloy were inserted into fibers. For most experiments, an eutectic alloy of Bi (43%) and Sn (57%) was used. The melting temperature of this alloy was 137°C, which allowed us to keep the acrylate primary coating intact while filling the holes with the molten metal. The oven was normally heated to 170°C. Figure 2 shows the protruding electrodes after the fiber was stretched and cleaved. It is clear that the metal electrode is smooth and continuous. If the fiber was reheated, the volume change of the alloy on melting was sufficiently small for the contact not to be broken when the alloy underwent a phase transition.

The time taken to fill the fiber with the molten alloy depends on the hole size, type of alloy, temperature, and pressure. Typically, a 1-m-long fiber device was filled in less than 1 min. Fibers with outer diameters of 125 and 150 μm were filled with the setup, and the hole size ranged from 20 to 40 μm . We obtained access to the internal electrodes by side polishing the fiber with a 2.8-cm-diameter brass cylinder covered and 2400-mesh sandpaper. The cylinder automatically revolved backward and forward by almost a turn. To avoid fiber breakage, we prevented the sandpaper joint from contacting the fiber by use of two position sensors. The cylinder was also automatically translated so that abrasion would take place uniformly along the polishing surface. Typically, the electrodes were exposed after 2 min, and the fibers were polished with the primary coating still on. Electrical contact was made with a thin wire or with conductive epoxy.

Splicing the fibers with holes to standard telecommunications fibers gave nonoptimized losses of ~ 1 dB. It was found necessary to avoid having metal alloy near the fiber surface that was to be spliced. The usual technique used to prevent the metal from extending to the fiber end was to have a length of the fiber outside the oven, as shown schematically in Fig. 1. The other side (initially filled) could be conveniently emptied by means of pressing the molten metal further into the fiber without supplying new metal (e.g., by removal of the crucible from the pressure chamber).

As mentioned above, phase modulation is usually transformed into amplitude modulation with a fiber Mach-Zehnder interferometer (MZI) that comprises two couplers and two independent optical paths. The twin-core fiber design shown in Fig. 1 allows coupling of light between cores through the evanescent wave. Since any electric field established between the electrodes is preferentially applied to one of the cores, the entire interferometer is embodied by a single piece of fiber. Therefore, in principle it should be possible to perform amplitude modulation with a fiber MZI spliced between two pieces of standard telecommunications fiber. The main disadvantage of integrating the MZI is that the twin-core fiber is generally a single output port device, because it is difficult to obtain access to both cores with spliced

fibers. On the other hand, the proximity of the cores also makes the interferometer insensitive to thermal, acoustic, and mechanical noise. The main advantages of integrating the MZI, however, are its potential simplicity and low price.

A preliminary fiber was drawn, and tests were carried out. The schematic setup is illustrated in Fig. 3. The two cores had a center-to-center separation of ~ 21 μm . The two holes had a diameter of ~ 24 μm and center-to-center separation of 62 μm . The separation between the electrodes surrounding the core that was subjected to the electric field was approximately 46 μm . The cores were designed to have an ~ 8 - μm diameter, but during fiber fabrication one of the cores lost its original round shape. The outer diameter of this fiber was 150 μm . Numerical simulations showed that the beat length at 1.55 μm increased from 10 cm for 20- μm center-to-center core separation to 1 m for 26- μm separation. Increasing the distance between the cores makes it easier to subject the electric field preferentially to one core only. However, it becomes difficult to guarantee efficient coupling of light between cores, because the geometrical dimensions and refractive indices of the cores must match to an accuracy of within 0.1%.

An ~ 1.5 -m-long fiber piece was filled along 1 m with molten metal that was allowed to solidify at room temperature. Contacts were established by side polishing of the fiber, as described above. The electrodes did not extend to the end of the fiber, preventing electrical breakdown. In the tests, light was not intended to couple between cores, so the stringent fabrication requirements mentioned above were bypassed. Rather, an unfocused 633-nm-wavelength He-Ne laser beam illuminated one fiber end so that both cores were excited. Light propagated as two independent beams guided by the twin cores to the output side and exited the fiber, diffracting. After weak collimation, the



Fig. 2. Fiber with holes showing protruding electrodes inserted in molten form at high pressure.

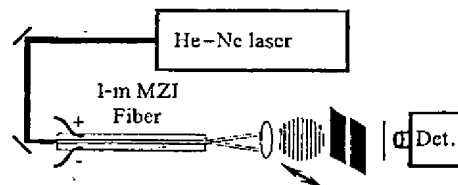


Fig. 3. Experimental setup. A single fringe is detected after the slit. Det., detector.

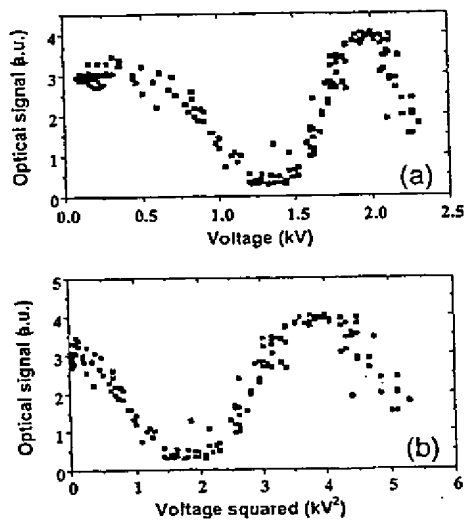


Fig. 4. Intensity of the optical signal detected after the slit as a function of (a) applied voltage to the MZI fiber and (b) applied voltage squared.

far-field pattern consisted of interference vertical lines if at the fiber output the two cores were disposed along a horizontal plane. Provided that the fiber was cleaved and aligned properly, the pattern observed was sufficiently clean, in spite of the fact that the fiber was multimode at this wavelength and that one of the cores was not round. A single fringe was detected with a photomultiplier through a 0.5-mm-wide slit.

The fiber was not poled. Rather, the weak intrinsic Kerr nonlinearity was exploited. The optical signal measured without the application of voltage was quite stable in time (2.7% standard deviation in power level without further packaging). The voltage was increased and reduced manually a number of times, and all the data were recorded. Figure 4(a) shows a plot of the optical signal measured as a function of voltage, and Fig. 4(b) illustrates the signal detected as a function of the square of the applied voltage. The periodicity seen in Fig. 4(b) confirms the expected quadratic dependence, and the required voltage for a π shift is measured to be 2 kV^2 , which implies that $V_\pi \sim 1.4 \text{ kV}$. Assuming for simplicity that the electric field created by an applied DC voltage is uniform between the electrodes, the voltage required for the optical paths of the two arms to become different by $\lambda_{He-Ne}/2$ is given by⁷

$$V_\pi = [n\lambda d^2/6L\chi^{(3)}]^{1/2}, \quad (1)$$

where d is the electrode separation and L is the device length. Assuming that in the unpoled fiber $\chi^{(3)} \sim 1.9 \times 10^{-22} \text{ m}^2/\text{V}^2$, we estimate that $V_\pi \sim 1.3 \text{ kV}$. The good agreement with the measured value is somewhat coincidental, since there is a large uncertainty caused by the noncircular core shape and the nonuniform electric field distribution and possible contributions caused by electrostrictive effects.⁹

A short-wavelength laser was used in the test described above. For the large core spacing of the fiber, no light coupling was expected between the cores at this wavelength, even if their shapes were round and identical. More-comprehensive testing will require a fiber fabricated with a cross section closer to that illustrated in Fig. 1. Poling studies are also under way to reduce the voltage required for switching.

In conclusion, the technique presented for obtaining fibers with solid internal electrodes helps in fabricating long devices with a scalable procedure for cheap manufacture. The twin-core twin-hole fiber design that was presented should also contribute to the effort to make stable low-cost electro-optic fiber devices.

Partial funding from the European IST Project GLAMOROUS is gratefully acknowledged. The authors thank R. Kashyap and J. L. Archimbault for useful critical comments. M. Fokine's e-mail address is michael.fokine@acreo.se.

References

1. L. Li, R. D. Birch, and D. N. Payne, in *Digest of IEE Colloquium on Advanced Fibre Waveguide Devices* (Institution of Electrical and Engineers, London, 1986), p. 10.
2. M. V. Bergot, M. C. Farries, M. E. Fermann, L. Li, L. J. Poyntz-Wright, P. St. J. Russell, and A. Smithson, *Opt. Lett.* **13**, 592 (1988).
3. X. C. Long, R. A. Myers, and S. R. J. Brueck, *Electron. Lett.* **30**, 2162 (1994).
4. P. G. Kazansky, L. Dong, and P. St. J. Russell, *Opt. Lett.* **19**, 701 (1994).
5. P. G. Kazansky, P. St. J. Russell, L. Dong, and C. N. Pannell, *Electron. Lett.* **31**, 62 (1995).
6. T. Fujiwara, D. Wong, and S. Fleming, *IEEE Photon. Technol. Lett.* **7**, 1177 (1995).
7. D. Wong, W. Xu, S. Fleming, M. Janos, and K.-M. Lo, *Opt. Fiber Technol.* **5**, 235 (1999).
8. B. J. Eggleston, C. Kerbage, P. Westbrook, R. S. Windeler, and A. Hale, *Opt. Express* **9**, 698 (2001), <http://www.optics.express.org>.
9. A. C. Liu, J. F. Digonnet, and G. S. Kino, *J. Opt. Soc. Am. B* **18**, 187 (2001).

Fabrication inside Microchannels Using Fluid Flow

PAUL J. A. KENIS, RUSTEM F. ISMAGILOV,
SHUICHI TAKAYAMA, AND
GEORGE M. WHITESIDES*

*Department of Chemistry and Chemical Biology,
Harvard University, Cambridge, Massachusetts 02138*

SHULONG LI† AND HENRY S. WHITE*

*Department of Chemistry, University of Utah,
Salt Lake City, Utah 84112*

Received April 18, 2000

ABSTRACT

This Account summarizes techniques for carrying out microfabrication of structures with dimensions down to 10 μm in microchannels that are 0.02–2 mm wide. These methods are largely based on the exploitation of laminar flow at low Reynolds number (Re) to control the spatial delivery of reagents. These methods are illustrated by fabrication of fibers, microelectrode arrays, arrays of crystals, and patterns of proteins and cells.

Introduction

Channels that are 0.02–2 mm wide—channels which, in this Account, we call almost interchangeably “microchan-

Paul J. A. Kenis was born in 1970 in Arcen, The Netherlands. He received his masters degree from Nijmegen University (NL) with R. J. M. Nolte in 1993 and his Ph.D. degree in supramolecular chemistry from the University of Twente (NL) with D. N. Reinhoudt in 1997, after which he joined the group of G. M. Whitesides at Harvard University as a postdoctoral fellow. He joined the faculty of the department of Chemical Engineering at the University of Illinois at Urbana—Champaign in the fall of 2000. His research interests include (organic) materials science, surface chemistry, microfluidics, and microfabrication.

Rustem F. Ismagilov was born in 1973 in Ufa, Russia. He received his undergraduate degree from the Higher Chemical College of the Russian Academy of Sciences in 1994 and his Ph.D. degree in chemistry from the University of Wisconsin, Madison, with S. F. Nelsen in 1998. Currently he is a postdoctoral fellow in the group of Professor G. M. Whitesides at Harvard University. His research interests include physical organic chemistry, microfluidics, and nonlinear dynamics.

Shuichi Takayama was born in 1968 in Tokyo, Japan. He received his masters degree from the University of Tokyo with K. Mori in 1994 and his Ph.D. degree in chemistry from the Scripps Research Institute with C.-H. Wong in 1998, after which he joined the Whitesides group as a Leukemia and Lymphoma Society postdoctoral fellow. He joined the faculty of the department of Biomedical Engineering at the University of Michigan, Ann Arbor, in the fall of 2000. His major research interests are in the areas of bioorganic chemistry, biomaterials, bioengineering, and microfluidics.

George M. Whitesides received his A.B. degree from Harvard College in 1960, and his Ph.D. from the California Institute of Technology with J. D. Roberts in 1964. He was a member of the faculty of the Massachusetts Institute of Technology from 1963 to 1982, at which time he joined the Department of Chemistry at Harvard University. His present research interests include micro- and nanofabrication, microfluidics, self-assembly, rational drug design, and cell biology.

Shulong Li was born in 1964 in Sichuan, China. He received his B.S. degree in chemistry and M.S. degree in polymer science from the University of Science and Technology of China, and his Ph.D. in materials science from the University of Minnesota in 1993, working with Professor H. S. White. He spent one year as a postdoctoral research associate at the National Renewable Energy Laboratory in Golden, CO, before joining the Milliken Research Corp. in 1994. He is currently conducting industrial research in the area of textiles and fibers.

Henry S. White is a Professor of Chemistry at the University of Utah. He received his B.S. degree from the University of North Carolina in 1978, and his Ph.D. from the University of Texas at Austin with A. J. Bard in 1983. He held a postdoctoral research appointment at the Massachusetts Institute of Technology from 1983 to 1984, and was on the faculty of the Department of Chemical Engineering and Materials Science at the University of Minnesota between 1984 and 1993. His present research interests include electroanalytical chemistry, molecular transport at nanostructured electrodes, iontophoretic transport in biological membranes, and magnetic field effects in electrochemistry.

nels” or “capillaries”—can be considered as reaction vessels with two unusual characteristics. First, their interior volumes are small, but readily and rapidly accessible from the outside by pumping fluids or gases into them. Second, fluids moving in them at low to moderate velocities flow laminarily, that is, without turbulence. This laminar flow can be used to deliver reagents spatially inside capillaries with remarkable precision. These characteristics, combined with the ease with which microchannels can be assembled and disassembled using soft lithography and other techniques, suggest them as a new system of reactors with which to carry out microfabrication.¹

This Account summarizes projects in our two laboratories that are aimed at developing techniques for microfabrication that use microchannels as reactors. We had two objectives. First, we wished to use the small volume of the microchannel to generate microstructures that would be removed once formed and used independently of the channel in which they were formed; that is, the microchannel would serve as a reactor for the fabrication of a structure to be used elsewhere. Second, we wished to fabricate small, functional structures inside capillaries, with the intention of leaving the structures in place once fabricated. These structures would be integrated with other uses of the channel (for example, as microelectrodes in a microanalytical system in which separations are carried out in the capillary). The techniques that are reviewed in this Account provide routes to structures that are difficult to fabricate by other techniques. These methods are especially useful in handling proteins, cells, and other delicate biological structures.

To accomplish either task, it is necessary to perform a set of elementary operations: (i) transfer reagents from reservoirs outside the channel to the inside; (ii) deliver these reagents to locations where reactions are to occur; (iii) allow or cause the desired reactions; and (iv) remove waste products from the regions where reaction takes place. We have used fluids to accomplish these operations. In principle, one could also work with gases, although their distinct physical properties—for example, high diffusion constants—make their application in fabrication inside microchannels more challenging than that of liquids.

We organize this Account into four sections. In the first, we give a brief overview of the technologies that have been used to carry out microfabrication in microchannels. In the second, we review the characteristics of liquid flow in capillaries at low and high values of the Reynolds number, Re . The emphasis in this section is on the potential of laminar or near-laminar flow as a strategy to control the spatial delivery of reagents inside small channels. This strategy can be adapted either to a single liquid stream, or to two or more different streams of liquid in laminar flow. In the third, we describe examples of microfabrica-

* To whom correspondence should be addressed.

† Current address: Milliken Research Corp., Spartanburg, SC 29304.

Table 1. Techniques Used for Microfabrication inside Microchannels

Strategy for Microfabrication Process or Technology	Reference
Multilayer Photolithography	2
Single-Stream Liquid Flow	
Chemical Vapor Deposition	3
Light Tweezers assisted Deposition	4
Polymer Deposition	8
Electroless Deposition	9
Electrochemical Fiber Growth	10
Etching of Optical Fibers	11,12
Micromolding in capillaries (MIMIC)	13-17
Deposition of Proteins	18
Multiple-Stream Liquid Flow	
Electroless Deposition	20
Etching	20
Nucleation and Crystallization (CaCO_3)	20
Deposition of Proteins	24
Deposition of Cells	24

tion that use a single stream of liquid. In the fourth, we sketch applications of microfabrication (and closely related methods used for micropatterning of bacterial and mammalian cells) based on multiple streams of liquid in laminar flow.

I. Overview of Microfabrication in Microchannels

Table 1 lists technologies (including our own) that have been used to carry out microfabrication in capillaries. Conventional photolithography is the basis of the methods most commonly used to fabricate microchannels containing functional microstructures.² In this type of fabrication, the capillary and its internal features are generated by a series of planar pattern-transfer steps. Until recently, there were few alternatives to photolithography (and the processes intimately associated with it: evaporation, CVD, RIE, lift-off, and others). Miyagi et al. have, for example, patterned the inner walls of hollow waveguides by chemical vapor deposition of dielectric films consisting of Cu_2O .³ Renn and Pastel have shown that laser-induced forces (light tweezers) can be used to manipulate and position atoms, clusters, and micrometer-sized particles (e.g., NaCl and KI crystals) inside hollow optical fibers.⁴

II. Laminar and Turbulent Flow of Liquids: The Reynolds Number

The Reynolds number, $Re = \nu\rho/\mu$, characterizes the tendency of a fluid to develop turbulence, or to flow without turbulence (that is, laminarly).⁵ Here, ρ is the density in kilograms per cubic meter, μ is the viscosity in kilograms per meter per second, l is the diameter of the capillary in meters, and ν is the flow rate in meters per second. The value of Re at which flow changes from turbulent to laminar depends on the geometry of the channel. For a straight pipe, this transition occurs at $Re \approx 2100$. Flow past an object or flow in a channel in which



FIGURE 1. Optical micrograph of two-phase laminar flow: two aqueous phases, each colored with a different dye (black ink and Congo red), brought together with a "Y" junction in an elastomeric microfluidic system.

the geometry changes, however, develops eddies at lower Reynolds numbers ($Re \approx 40-300$). Liquid flows in capillaries (that is, tubes having small values of l ; $l \approx 50-100 \mu\text{m}$) often have low values of Re and are therefore laminar, even for liquid flow velocities as high as 0.5 m s^{-1} . Most usefully, two or more streams that are brought together in a narrow channel flow laminarly, in parallel, without turbulent mixing (Figure 1). The only mechanism of mixing of their components is diffusion across the interface between the streams.

Laminar flow permits control of the spatial delivery of reagents within a capillary. The application of different chemistries from different streams of a multiphase, laminar flow system allows reactions to take place exclusively at certain regions of the capillary: either between a stream and the interior surface of the capillary, or at the interface between adjacent streams. Levin et al. pioneered the use of laminar flow in microfluidic devices to fractionate samples by taking advantage of the fast diffusion of small molecules or ions from one stream into an adjacent stream, relative to the slow diffusion of proteins, colloids, etc.⁶ Weigl and Yager implemented these principles elegantly in a micromachined device for the analysis of heterogeneous biological samples such as blood by taking advantage of the fast diffusion of analyte molecules from the sample stream into an adjacent stream that contained, for example, a fluorescent indicator.⁷

In small capillaries, turbulent flow of aqueous solutions (or eddy-like flow in the region of transition from laminar to turbulent) occurs only at high velocities of flow. Turbulence facilitates mass transport. In laminar flow, the only mechanism for mixing is diffusion. This difference in mechanisms and rates of mass transport can be used to increase the rate of delivery of reagents to specific regions inside a capillary where flow is turbulent, and thus to increase the rate of chemical reaction in the turbulent regions, relative to regions where flow is laminar.

III. Microfabrication Using Single Streams of Liquid in Microchannels

We distinguish different methods of fabrication inside microchannels using a single stream of liquid: one that results in a uniform modification of the inner surface of the capillary, and several others that allow for fabrication with spatial resolution.

Uniform In-Channel Coatings. A uniform coating—either covalently attached or physically adsorbed—on the inner surface of capillaries can easily be achieved from a single liquid stream—laminar or turbulent—that contains

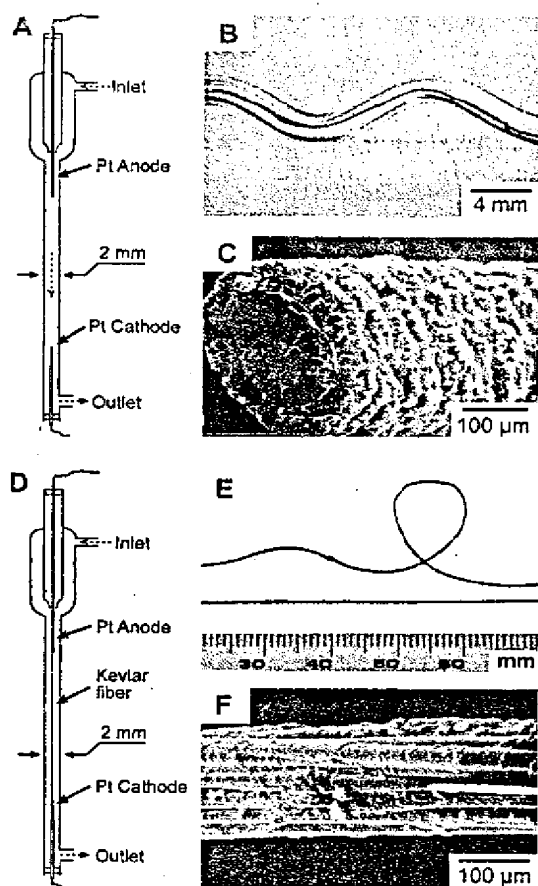


FIGURE 2. (A) Schematic diagram of the electrochemical flow cell used to grow single-phase conducting polymer fibers. (B) Optical micrograph of a zigzag poly(3-methylthiophene) fiber grown in a zigzag glass capillary. (C) SEM image of a fracture cross section of a poly(3-methylthiophene) fiber. (D) Schematic diagram of the electrochemical flow cell used to grow composite Kevlar/conducting polymer fibers. (E) Optical micrograph and (F) SEM image of Kevlar/polypyrrole composite fibers.

the necessary chemicals. This strategy is frequently used to produce coatings: examples include organic films that reduce sticking of proteins in capillary electrophoresis capillaries⁸ and metal films (by electroless deposition of silver) with polymer coatings inside hollow waveguides to reduce optical losses.⁹

Conducting Polymer Fibers. An example of fabrication from a single homogeneous stream that creates a free-standing microstructure is the electrochemical processing of conducting polymer fibers.¹⁰ Figure 2A shows an electrochemical cell used to synthesize macroscopically long fibers of polypyrrole and poly(3-methylthiophene). Hydrodynamic flow patterns inside a 2-mm-diameter glass tube (separating the anode and cathode) are employed to control both the spatial direction and the rate of polymerization. A solution containing the monomer flows through the cell at an average velocity between 10 and 60 cm s^{-1} (corresponding to $700 < Re < 4200$). Nucleation and growth of a single conductive fiber from the anode in the direction of flow occur when an electrical current ($\sim 1 \text{ mA}$) is passed between the electrodes. Controlling the

applied current or the flow velocity in the glass tube controls the rate of polymer growth as well as the shape of the resulting fiber: The application of larger currents typically resulted in faster growth of uniform fibers with larger diameters, whereas high flow rates ($\sim 50 \text{ cm s}^{-1}$) resulted in nonuniform, cone-shaped fibers. Polypyrrole and poly(3-methylthiophene) fibers of 10 cm length and between 0.01 and 0.1 cm diameter have been grown using this one-step process (Figure 2B,C) with a wide variety of shapes (e.g., tapered fibers, zigzag-shaped fibers) by changing the shape of the glass tubing.

The key element of this procedure that gives directional polymer growth is the coupling of the flow patterns with mass transport of the monomer to the surface. Hydrodynamic flow past the tip of the growing fiber produces a relatively stagnant boundary layer or a recirculating flow in which intermediates produced by chemical reaction can be trapped. The result is an increased rate of deposition of polymerization intermediates (oligomers) at surfaces adjacent to the boundary layer or the fluid eddy, here the tip of the fiber. Consequently, the polymer fiber grows only along the direction of the flow within the glass tube, never touching the sides of the tube.

Kevlar/Polypyrrole Composite Fibers. Kevlar/polypyrrole composite fibers that exhibit excellent electrical conductivity and that are flexible and strong—in contrast with the brittle polypyrrole and poly(3-methylthiophene) fibers (see above) that break when flexed—have been synthesized in electrochemical flow cells using a different approach (Figure 2D).¹⁰ A woven Kevlar thread, containing 70 filaments each of $17 \mu\text{m}$ diameter, was suspended between the anode and cathode of the cell. When pyrrole was oxidized at the anode in the presence of flow (20 cm s^{-1}), the resulting polymer grew onto the Kevlar thread and coated the entire 10-cm length in $\sim 20 \text{ min}$. The conductive polymer phase deposits uniformly between the filaments of the Kevlar thread and produces an electrically conductive and flexible composite fiber (Figure 2E,F) that may be of interest for antistatic weaves and as flexible electrodes for in vivo measurements.

Near-Field Optical Probes. In a different strategy, Lambelet et al. and Stöckle et al. have used the film of polymer (the cladding layer) on the outside of optical fibers as capillaries with 3–200- μm inside diameters, and then used convectively driven laminar flows inside these capillaries to fabricate high-quality, near-field optical probes with regular conical tips.^{11,12} Hanging the ends of optical fibers with polymer cladding attached in an aqueous phase containing HF resulted in anisotropic etching of the glass cores, even without the application of bulk flow. The authors explain the formation of conical tips inside the cladding capillary by the combination of local flows induced by chemically driven convection and increases in the density of the solution on dissolution of the glass (Figure 3).

Selective Patterning on Substrates. We have demonstrated selective electroless deposition of metallic copper on one wall of a rectangular microchannel using a variation of the MIMIC ("micromolding in capillaries")

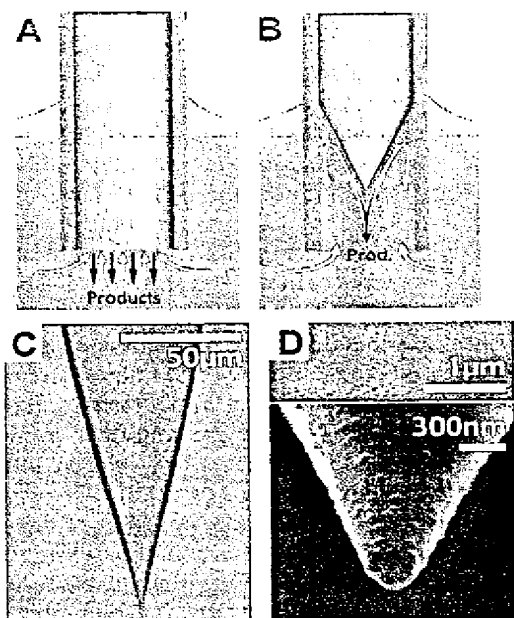


FIGURE 3. Fabrication of near-field optical probes by tube etching as proposed by Stöckle et al. Schematic of the convection mechanism: (A) initial diffusion-controlled etching—more etchant available to the outer regions of the fiber—and (B) convection-controlled tip formation inside the tube driven by concentration gradients and the gravitational removal of reaction products. (C) Optical micrograph of an uncoated tip. (D) Scanning electron micrographs of an Al-coated tube-etched fiber tip. Top: the glass surface close to the tip apex. Bottom: the tip apex. Reproduced with permission from ref 12.

technique.¹³ The channel consisted of a poly(dimethylsiloxane) (PDMS) membrane with a channel structure embossed in its surface placed on a gold-covered substrate. The channel was filled with an electroless deposition solution containing copper ions and formaldehyde as the reducing agent. The activity of the gold surface in catalyzing the electroless deposition process resulted in selective deposition of copper on the wall of the channel formed by the gold surface and not on the walls of the channel formed by the PDMS mold.

Similarly, Biebuyck et al. patterned regions of a substrate with immunoglobulins from a single liquid flow in a microfluidic network embossed in PDMS that was placed on the substrate.¹⁴ This PDMS mold was passivated with poly(ethylene glycol) or bovine serum albumin prior to placement on the substrate to avoid deposition of immunoglobulins on its surface.

Arrays of Beads. A related technique also gives access to crystalline arrays of 0.1–3- μm beads inside 10–100- μm channels. The liquid flow (driven by evaporation from one end of the capillary, or by capillary filling of the tube) delivered the beads from suspension to a region in which they are, in essence, filtered from the flowing stream; this flow led to crystalline arrays. Harrison et al. and Manz et al. have used such arrays as packed reactor beds in microanalytical devices.¹⁵ Xia et al. have exploited related flow behavior between narrowly spaced plates to fabricate crystalline arrays of beads; these crystals may be useful

as macroporous membranes,¹⁶ tunable optical filters,¹⁷ and 3D photonic band gap materials.¹⁸

These studies established the concept of using the capillary as a small reactor, and identified some of the types of chemistry that can be carried out using this type of reactor. The range of structures that one can fabricate inside microchannels using only a single stream of liquid is, however, limited.

IV. Microfabrication Using Multiple Streams of Liquid in Laminar Flow

Soft lithography allows the fabrication of branching capillary networks rapidly, so long as the capillaries are $>20\ \mu\text{m}$ in lateral dimension.¹⁹ The procedure we use—which we call “rapid prototyping”—consists of four steps: (i) high-resolution printing of a mask with $>20\text{-}\mu\text{m}$ features; (ii) photolithography with this mask to fabricate a bas-relief master; (iii) micromolding against this master to form three sides of the channel system; and (iv) sealing to form the complete microchannel. It is straightforward to create multiple streams of fluids flowing laminarly in parallel inside these channels²⁰ and to use these streams for microfabrication and micropatterning by localized delivery of reagents from the laminar flows. This method—sometimes in combination with the use of prepatterned channels—allows fabrication of complex functional structures inside preformed capillaries without the registration steps required by planar photolithography.

Microfabrication by delivery of reactants from parallel laminar flows generates structures (etched or deposited) having edges tapered along their longitudinal direction as a result of diffusion transverse to the direction of flow.^{20,26} This diffusional broadening can be minimized by using high flow rates ($v \approx 0.50\ \text{m s}^{-1}$); high rates of flow result in short residence times in the region being patterned. The resolution one can achieve depends on the details of the process being used for patterning.

Area-Selective Crystal Growth. A two-stream laminar flow can be used for the localized nucleation and growth of crystals inside a microchannel.²⁰ The capillary is fabricated by placing a patterned PDMS membrane on a gold-coated wafer covered with a self-assembled monolayer (SAM) of $\text{HS}(\text{CH}_2)_{15}\text{COOH}$; this SAM nucleates formation of calcite crystals.²¹ Figure 4A shows a line of calcite crystals—with diameters of 2–5 μm —that have nucleated and grown at the interface between two parallel streams, one containing calcium ions (as CaCl_2) and the other containing carbonate ions (as NaHCO_3).

Patterned Etching of Silver and PDMS. Figure 4B shows the result of patterning the inside of a glass capillary by electroless deposition of silver from one stream of a two-stream fluid flow system. The glass capillary is connected to a Y-shaped channel in PDMS in order to create the two-stream flow system; the method can be extended to four or more streams.²² Figure 4C shows the creation of topographical features inside of a PDMS capillary using patterned flow of etchant and inert solvent.²³ In general, the position (or edges) of the etched or deposited micro-

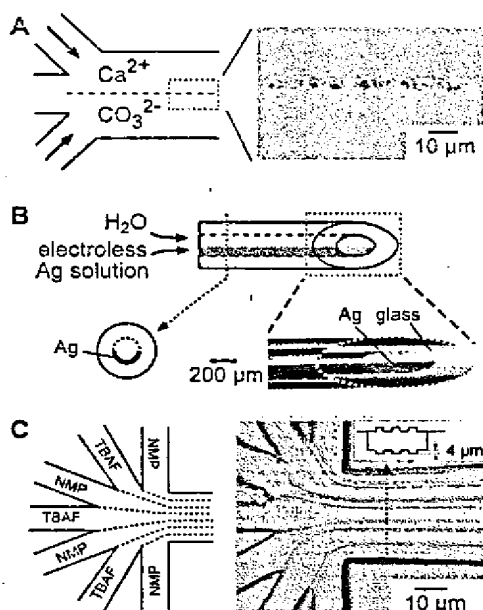


FIGURE 4. (A) Scanning electron microscopy images of calcite deposited on a self-assembled monolayer at the interface of aqueous laminar flows of NaHCO_3 (100 mM, buffered to pH 7.4) and CaCl_2 (25 mM). (B) Optical micrograph of a glass capillary that has half of the inner surface plated with silver. (C) Optical micrograph of topographical features created inside of a PDMS capillary using patterned flow of NMP (*N*-methylpyrrolidinone, an inert liquid) and TBAF (tetrabutylammonium fluoride in NMP; an etchant). Inset: Schematic cross section of the topographically patterned channel. structure can be controlled with a precision down to $\sim 5 \mu\text{m}$ by adjustment of the relative volumes of the streams being injected.

Three-Electrode System. Figure 5 outlines a two-step fabrication of a three-electrode array inside a preformed channel. This procedure starts by placing a PDMS membrane with the "crow's foot" channel system embossed in its surface on a glass slide having a 200- μm -wide evaporated gold stripe.²⁰ A three-phase laminar flow through the channel—a central gold-etchant solution, and adjacent water streams—selectively removes the gold in a strip in the middle of the channel. This etching creates two isolated Au electrodes that serve as working and counter electrodes. In a subsequent step, flowing the two components of a commercial electroless silver plating solution laminarly in parallel through the channel results in the deposition of a metallic silver wire on the glass at the interface between the two phases. Figure 5 also shows a typical example of tapering or broadening of a microstructure—here the silver wire—along the longitudinal direction of the channel as a result of diffusion transverse to the direction of flow. After treatment with 1% HCl to form AgCl on the surface, the silver wire serves as the reference electrode. We have shown that continuous, conductive silver wires as thin as 10 μm can be fabricated by using high flow rates (up to 1 m s^{-1}). For the fabrication of the silver wire in the three-electrode system, we typically used lower flow rates. The lower rates gave wider and less uniform wires, but these wires were also desirable (in this instance) for durability in use. We successfully recorded

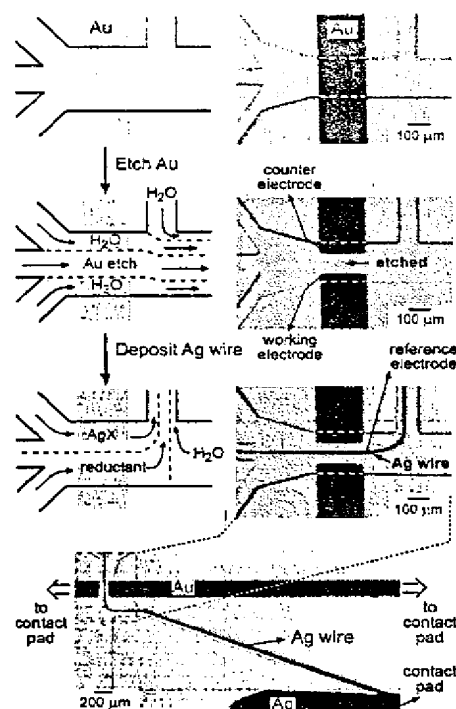


FIGURE 5. Optical micrographs of the stepwise fabrication of a three-electrode system using multiphase laminar flow. A PDMS mold with a channel system embossed in its surface is placed on a glass slide covered with an evaporated gold stripe. Two electrodes (counter and working) are formed by selectively etching the gold stripe in the middle of the channel with a three-phase laminar flow system. The gold stripe widens beyond the outer edge of the PDMS membrane into contact pads. A silver (reference) electrode is fabricated at the interface of a two-phase laminar flow and is directed into a side channel toward a contact pad.

cyclic voltammograms of, for example, a 5-nL volume of 2 mM $\text{Ru}(\text{NH}_3)_6\text{Cl}_3$ in water.²⁰

Patterning Proteins and Cells on Capillary Surfaces. Multistream laminar flow systems are useful in fabricating biologically relevant structures and patterns in sizes similar to those of cells (typically 5–100 μm). Figure 6 shows three examples of patterning within a capillary: (A) proteins adsorbed on the substrate; (B) the location of cells; and (C) the delivery of biochemicals to cells.²⁴ These methods will be useful in fabricating microfluidic systems for cell-based sensors and screening systems based on cells and for studying chemotaxis, cell–cell communication, and cellular ecology.

Conclusions

Microfabrication with liquids flowing in capillaries has characteristics that are fundamentally different from those of microfabrication with photolithography. The former relies on microfluidic channels to deliver reagents in patterns of flowing liquids to specific regions of a surface; the latter relies on masks to pattern light. Fabrication of the microchannels is a relatively straightforward task, using a rapid prototyping strategy based on soft lithography;¹⁹ photolithography usually requires more specialized tools. Microfluidic systems are limited in the patterns

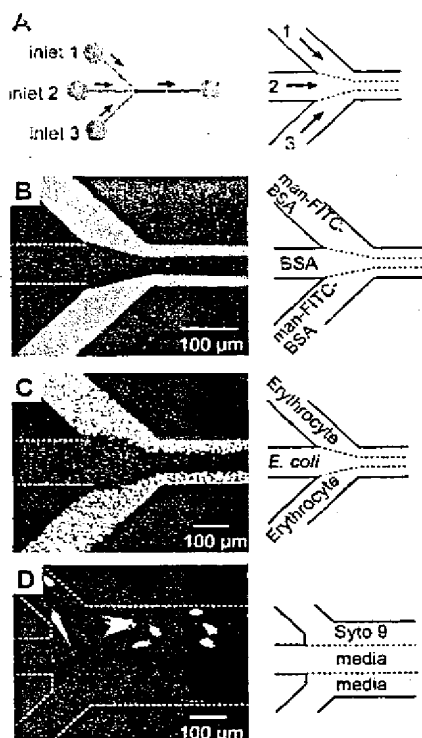


FIGURE 6. Examples of biologically relevant patterns generated using multiphase laminar flow. (A) Top view of a capillary network used for biological patterning. Optical micrographs B–D (fluorescence) represent close-up views of the junctions where the inlets converge into a single main channel. (B) Creating patterns of proteins inside a capillary. Solutions of bovine serum albumin (BSA) and BSA colabeled with mannose and fluorescein (man-FITC-BSA) were allowed to flow through the designated channels. (C) Patterned deposition of cells inside a capillary. Chick erythrocytes and *Escherichia coli* were deposited selectively in their designated lanes by patterned flow of cell suspensions. Adherent cells were visualized with a fluorescent nucleic acid stain (Syto 9). (D) Using patterned flow of media to stain part of the bovine capillary endothelial cells that were attached to the entire bottom face of a capillary. Only those cells over which a solution of dye (Syto 9) was allowed to flow were labeled. Syto 9 and media were allowed to flow from the designated inlets.

they can form; photolithography is a very general method of forming patterns.

The occurrence of laminar flow on the microscopic scale allows liquid streams to be maintained as entities that are separate and capable of delivering different reagents. The width of the separate streams (or the interfacial width as governed by the rates of diffusion) internal to the channel determines the feature sizes, and the relative volumes of the streams control the position of the liquid–liquid interfaces. External positioning tools or masks determine feature sizes and positions in photolithography. The usual problem in microfabrication based on photolithography of determining position in superimposing patterns in multilayer fabrication (registration) translates into a problem of controlling relative rates of flow in microfluidic fabrication.

Microfluidic and photolithographic patterning are sufficiently different in the physical principles on which they

rest that they are complementary in their applications. Fluidic microfabrication inside capillaries is presently best suited for one-at-a-time, research, or prototyping demonstrations. Its strengths are convergence, specific applicability to problems involving channels (e.g., microanalytical devices), and compatibility with biological reagents and systems. Photolithography is highly developed for in-plane microfabrication and can be used to make many devices in parallel. Its strengths are generality in patterning, the ability to make small features, the ability to manufacture small systems in large numbers, and performance highly optimized for use with semiconductors and ceramics.

Fluid flow in microchannels allows the fabrication of a variety of useful structures ranging from conducting organic fibers to electrode systems integrated into microanalytical devices. Fluid flow also has the ability to deposit or carve away material on the interior surface of the capillary, and thus to change the surface properties or topography of a channel. Such patterns can have a profound effect on the flow profiles. For example, electroosmotic flow in capillaries that are patterned with regions of opposite surface charge leads to unusual low-*Re* flows.²⁵ Studies of the details of the fluid flow in microfluidic systems—by visualization or modeling—should make it possible to fabricate a broader range of structures using fluid flow.²⁶

Fluid flows have clear potential to pattern delicate biological structures. They are also applicable to patterning the topography of the surfaces, the proteins absorbed on these surfaces, cells attached to those surfaces, and the medium to which the cells are exposed. We expect these methods to facilitate the study of, for example, cell–surface adhesion, chemotaxis, and cell–cell communication, and to contribute to cell-based microfluidic sensors.

The work at Harvard was supported financially by DARPA through NSF Grant ECS-97294505, and MRSEC-shared facilities supported by the NSF under Grant NSF DMR-9809363 were used. Work at the University of Utah was supported by the Office of Naval Research. P.J.A.K. acknowledges the Netherlands Organization for Scientific Research (NWO) for a postdoctoral fellowship. S.T. thanks the Leukemia and Lymphoma Society for a postdoctoral fellowship.

References

- (1) Duffy, D. C.; McDonald, J. C.; Schueller, O. J. A.; Whitesides, G. M. Rapid Prototyping of Microfluidic Systems in Poly(dimethylsiloxane). *Anal. Chem.* 1998, 70, 4974–4984.
- (2) Madou, M. *Fundamentals of Microfabrication*; CRC Press: New York, 1997.
- (3) Matsuura, Y.; Miura, D.; Miyagi, M. Fabrication of Copper Oxide-Coated Hollow Waveguides for CO₂ Laser Radiation. *Appl. Opt.* 1999, 38, 1700–1703.
- (4) Renn, M. J.; Pastel, R. Particle Manipulation and Surface Patterning by Laser Guidance. *J. Vac. Sci. Technol. B.* 1998, 16, 3859–3863.
- (5) The characteristics of fluid flow in capillaries have been studied extensively in the past. See, for example: Rosenhead, L. *Laminar Boundary Layers*; Dover Publications: New York, 1988. Tritton, D. J. *Physical Fluid Dynamics*, 2nd ed.; Oxford University Press: New York, 1988.

- (6) Fuh, C. B.; Levin, S.; Giddings, J. C. Rapid Diffusion Coefficient Measurements Using Analytical SPLITT Fractionation: Application to Proteins. *Anal. Biochem.* 1993, 208, 80–87. Levin, S.; Tawil, G. Analytical SPLITT Fractionation in the Diffusion Mode Operating as a Dialysis-like System Devoid of Membrane. Application to Drug-Carrying Liposomes. *Anal. Chem.* 1993, 65, 2254–2261.
- (7) Weigl, B. H.; Yager, P. Silicon Microfabricated Diffusion-Based Optical Chemical Sensor. *Sens. Actuators B* 1997, 38–39, 452–457. Weigl, B. H.; Yager, P. Microfluidic Diffusion based Separation and Detection. *Science* 1990, 283, 346–347.
- (8) Rodriguez, I.; Li, S. F. Y. Surface Deactivation in Protein and Peptide Analysis by Capillary Electrophoresis. *Anal. Chim. Acta* 1999, 383, 1–26. Altria, K. D. Overview of Capillary Electrophoresis and Capillary Electrochromatography. *J. Chromatogr. A* 1999, 856, 443–463.
- (9) Abe, Y.; Matsuura, Y.; Shi, Y.-W.; Wang, Y.; Uyama, H.; Miyagi, M. Polymer-Coated Hollow Fiber for CO₂ Laser Delivery. *Opt. Lett.* 1998, 23, 89–90.
- (10) Li, S.; Macosko, C. W.; White, H. S. Electrochemical Processing of Conducting Polymer Fibers. *Science* 1993, 259, 957–960. Li, S.; Macosko, C. W.; White, H. S. Electrochemical Processing of Electrically Conductive Polymer Fibers. *Adv. Mater.* 1993, 5, 575–576. Li, S.; White, H. S. Synthesis of Conducting Polymer Composite Fibers in Electrochemical Flow Cells. *J. Electrochem. Soc.* 1993, 140, 2473–2476.
- (11) Lambelet, P.; Sayah, A.; Pfeffer, M.; Philippon, C.; Marquis-Weible, F. Chemically Etched Fiber Tips for Near-Field Optical Microscopy: A Process for Smoother Tips. *Appl. Opt.* 1998, 37, 7289–7292.
- (12) Stöckle, R.; Fokas, C.; Deckert, V.; Zenobi, R.; Sick, B.; Hecht, B.; Wild, U. P. High-Quality Near-Field Optical Probes by Tube Etching. *Appl. Phys. Lett.* 1999, 75, 160–162.
- (13) Xia, Y.; Kim, E.; Whitesides, G. M. Micromolding in Capillaries: Applications in Materials Science. *J. Am. Chem. Soc.* 1996, 118, 5722–5731.
- (14) Delamarche, E.; Bernard, A.; Schmid, H.; Michel, B.; Biebuyck, H. Patterned Delivery of Immunoglobulins to Surfaces Using Microfluidic Networks. *Science* 1997, 276, 779–781. Delamarche, E.; Bernard, A.; Schmid, H.; Bietsch, A.; Michel, B.; Biebuyck, H. Microfluidic Networks for Chemical Patterning of Substrates: Design and Application to Bioassays. *J. Am. Chem. Soc.* 1998, 120, 500–508.
- (15) Ocivirk, G.; Verpoorte, E.; Manz, A.; Grasserbauer, M.; Widmer, H. M. High-Performance Liquid-Chromatography Partially Integrated onto a Silicon Chip. *Anal. Methods Instrum.* 1995, 2, 74–82. Oleschuk, R. D.; Schultz-Lockyear, L. L.; Ning, Y.; Harrison, D. J. Trapping of Bead-Based Reagents within Microfluidic Systems: On-Chip Solid-Phase Extraction and Electrochromatography. *Anal. Chem.* 2000, 72, 585–590.
- (16) Park, S. H.; Xia, Y. Macroporous Membranes with Highly Ordered and Three-Dimensionally Interconnected Spherical Pores. *Adv. Mater.* 1998, 10, 1045–1048. Park, S. H.; Xia, Y. Fabrication of Three-Dimensional, Macroporous Membranes with Assemblies of Microspheres as Templates. *Chem. Mater.* 1998, 10, 1745–1747.
- (17) Park, S. H.; Xia, Y. Assembly of Mesoscale Particles over Large Areas and Its Application in Fabricating Tunable Optical Filters. *Langmuir* 1999, 15, 266–273.
- (18) Park, S. H.; Gates, B.; Xia, Y. A Three-Dimensional Photonic Crystal Operating in the Visible Region. *Adv. Mater.* 1999, 11, 462–466.
- (19) Xia, Y.; Whitesides, G. M. Soft Lithography. *Angew. Chem., Int. Ed.* 1998, 37, 550–575.
- (20) Kenis, P. J. A.; Ismagilov, R. F.; Whitesides, G. M. Microfabrication Inside Capillaries Using Multiphase Laminar Flow Patterning. *Science* 1999, 285, 83–85.
- (21) Aizenberg, J.; Black, A. J.; Whitesides, G. M. Controlling Local Disorder in Self-Assembled Monolayers by Patterning the Topography of their Metallic Supports. *Nature* 1998, 394, 868–871. Aizenberg, J.; Black, A. J.; Whitesides, G. M. Control of Crystal Nucleation by Patterned Self-Assembled Monolayers. *Nature* 1999, 398, 495–498.
- (22) Ismagilov, R. F.; Kenis, P. J. A.; Stroock, A. D.; Rosmarin, D.; Whitesides, G. M., unpublished results.
- (23) Takayama, S.; Ostuni, E.; McDonald, J. C.; Bowden, N.; Wu, M.-H.; Whitesides, G. M., unpublished results.
- (24) Takayama, S.; McDonald, J. C.; Ostuni, E.; Liang, M.; Kenis, P. J. A.; Ismagilov, R. F.; Whitesides, G. M. Patterning Cells and their Environments Using Multiple Laminar Fluid Flows in Capillary Networks. *Proc. Natl. Acad. Sci. U.S.A.* 1999, 96, 5545–5548.
- (25) Stroock, A. D.; Chiu, D. T.; Huck, W. T. S.; Ismagilov, R. F.; Kenis, P. J. A.; Weck, M.; Stone, H. A.; Whitesides, G. M. Patterning of Electro Osmotic Flow with Patterned Surface Charges. *Phys. Rev. Lett.* 2000, 84, 3314–3317.
- (26) Ismagilov, R. F.; Stroock, A. D.; Kenis, P. J. A.; Stone, H. A.; Whitesides, G. M. Experimental and Theoretical Scaling Laws for Transverse Diffusive Broadening in Two-Phase Laminar Flows in Microchannels. *Appl. Phys. Lett.* 2000, 76, 2376–2378. General reference: Merzkirch, W. *Flow Visualization*, 2nd ed.; Academic Press: Orlando, FL, 1987.

AR000062U